How farm dust prevents asthma *pp. 1034 & 1106*

Engineering yeast factories *pp. 1050 & 1095*

Shaking down tall structures in Nepal's earthquake *p. 1091*

Science

$10
4 SEPTEMBER 2015
sciencemag.org

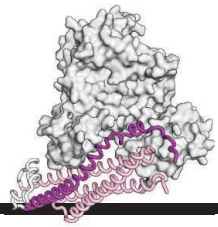
AAAS



Science in Iran

Nuclear pact brightens prospects for science *pp. 1029 & 1038*

CONTENTS



1111
A key mechanism in membrane fusion

4 SEPTEMBER 2015 • VOLUME 349 • ISSUE 6252

1063 **BIO ART**
By W. Myers

LETTERS

1064 **HOT GENOME LEAVES NATURAL HISTORIES COLD**
By X. Lu

1064 **DOCUMENTING RARE DISEASE DATA IN CHINA**
By H. Lin et al.

1064 **ACKNOWLEDGING AI'S DARK SIDE**
By C. Didier et al.

1065 **TECHNICAL COMMENT ABSTRACTS**

RESEARCH

IN BRIEF

1066 From *Science* and other journals

REVIEW

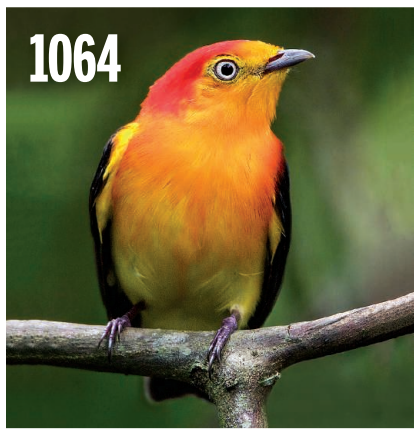
1069 **EPIDEMIOLOGY**
Why infectious disease research needs community ecology *P. T. J. Johnson* et al.
REVIEW SUMMARY; FOR FULL TEXT: dx.doi.org/10.1126/science.1259504

RESEARCH ARTICLES

1070 **MACROECOLOGY**
The predator-prey power law: Biomass scaling across terrestrial and aquatic biomes *I. A. Hatton* et al.
RESEARCH ARTICLE SUMMARY; FOR FULL TEXT: dx.doi.org/10.1126/science.aac6284
▸ PERSPECTIVE P. 1053



PHOTO (BOTTOM): JOHN GALETZKA, TECTONICS OBSERVATORY, CALIFORNIA INSTITUTE OF TECHNOLOGY



1071 **T CELL CHEMOTAXIS**
Neutrophil trails guide influenza-specific $CD8^+$ T cells in the airways *K. Lim* et al.
RESEARCH ARTICLE SUMMARY; FOR FULL TEXT: dx.doi.org/10.1126/science.aaa4352
▸ PERSPECTIVE P. 1055

1072 **PLANT SCIENCE**
Monodehydroascorbate reductase mediates TNT toxicity in plants *E. J. Johnston* et al.
▸ PERSPECTIVE P. 1052

REPORTS

1075 **CHEMISTRY**
Transient assembly of active materials fueled by a chemical reaction *J. Boekhoven* et al.
▸ PERSPECTIVE P. 1056

1080 **METALLURGY**
Linear complexions: Confined chemical and structural states at dislocations *M. Kuzmina* et al.
▸ PERSPECTIVE P. 1059

1083 **MATERIALS SCIENCE**
Highly thermally conductive and mechanically strong graphene fibers *G. Xin* et al.

1087 **CATALYSIS**
Sustainable Fe–ppm Pd nanoparticle catalysis of Suzuki-Miyaura cross-couplings in water *S. Handa* et al.

1091 **NATURAL HAZARDS**
Slip pulse and resonance of the Kathmandu basin during the 2015 Gorkha earthquake, Nepal *J. Galetzka* et al.

1095 **SYNTHETIC BIOLOGY**
Complete biosynthesis of opioids in yeast *S. Galanie* et al.
▸ PERSPECTIVE P. 1050

1101 **MICROBIOME**
Growth dynamics of gut microbiota in health and disease inferred from single metagenomic samples *T. Korem* et al.
▸ PERSPECTIVE P. 1058

1106 **ALLERGY**
Farm dust and endotoxin protect against allergy through A20 induction in lung epithelial cells *M. J. Schuijs* et al.
▸ NEWS STORY P. 1034

1111 **MEMBRANE FUSION**
A direct role for the Sec1/Munc18-family protein Vps33 as a template for SNARE assembly *R. W. Baker* et al.

1115 **RNA EDITING**
RNA editing by ADAR1 prevents MDA5 sensing of endogenous dsRNA as nonself *B. J. Liddicoat* et al.

1120 **DNA SEGREGATION**
Structures of archaeal DNA segregation machinery reveal bacterial and eukaryotic linkages *M. A. Schumacher* et al.

DEPARTMENTS

1029 **EDITORIAL**
Iran, science, and collaboration
By Mohammad Farhadi
▸ SCIENCE IN IRAN SECTION P. 1038

1134 **WORKING LIFE**
When science fails a scientist
By Kim Hunter-Schaedle

Science Staff 1028
New Products 1125
Science Careers 1126

SCIENCE (ISSN 0036-8075) is published weekly on Friday, except the last week in December, by the American Association for the Advancement of Science, 1200 New York Avenue, NW, Washington, DC 20005. Periodicals mail postage (publication No. 484460) paid at Washington, DC, and additional mailing offices. Copyright © 2015 by the American Association for the Advancement of Science. The title SCIENCE is a registered trademark of the AAAS. Domestic individual membership and subscription (51 issues): $153 ($74 allocated to subscription). Domestic institutional subscription (51 issues): $1282; Foreign postage extra: Mexico, Caribbean (surface mail) $55; other countries (air assist delivery) $85. First class, airmail, student, and emeritus rates on request. Canadian rates with GST available upon request, GST #1254 88122. Publications Mail Agreement Number 1069624. **Printed in the U.S.A.**
Change of address: Allow 4 weeks, giving old and new addresses and 8-digit account number. **Postmaster:** Send change of address to AAAS, P.O. Box 96178, Washington, DC 20090–6178. **Single-copy sales:** $10.00 current issue, $15.00 back issue prepaid includes surface postage; bulk rates on request. **Authorization to photocopy** material for internal or personal use under circumstances not falling within the fair use provisions of the Copyright Act is granted by AAAS to libraries and other users registered with the Copyright Clearance Center (CCC) Transactional Reporting Service, provided that $30.00 per article is paid directly to CCC, 222 Rosewood Drive, Danvers, MA 01923. The identification code for *Science* is 0036-8075. *Science* is indexed in the *Reader's Guide to Periodical Literature* and in several specialized indexes.

Published by AAAS

Science
AAAS
1200 New York Avenue, NW, Washington, DC 20005
Bateman House, 82-88 Hills Road, Cambridge, UK CB2 1LQ

Editor-in-Chief Marcia McNutt
Executive Editor Monica M. Bradford **News Editor** Tim Appenzeller
Managing Editor, Research Journals Katrina L. Kelner
Deputy Editors Barbara R. Jasny, Andrew M. Sugden(UK), Valda J. Vinson, Jake S. Yeston

Research and Insights

SR. EDITORS Caroline Ash(UK), Gilbert J. Chin, Lisa D. Chong, Julia Fahrenkamp-Uppenbrink(UK), Pamela J. Hines, Stella M. Hurtley(UK), Paula A. Kiberstis, Marc S. Lavine(Canada), Kristen L. Mueller, Ian S. Osborne(UK), Beverly A. Purnell, L. Bryan Ray, Guy Riddihough, H. Jesse Smith, Jelena Stajic, Peter Stern(UK), Phillip D. Szuromi, Brad Wible, Nicholas S. Wigginton, Laura M. Zahn **ASSOCIATE EDITORS** Brent Grocholski, Keith T. Smith, Sacha Vignieri **ASSOCIATE BOOK REVIEW EDITOR** Valerie B. Thompson **ASSOCIATE LETTERS EDITOR** Jennifer Sills **CHIEF CONTENT PRODUCTION EDITOR** Cara Tate **SR. CONTENT PRODUCTION EDITOR** Harry Jach **CONTENT PRODUCTION EDITORS** Jeffrey E. Cook, Chris Filiatreau, Cynthia Howe, Lauren Kmec, Barbara P. Ordway, Catherine Wolner **SR. EDITORIAL COORDINATORS** Carolyn Kyle, Beverly Shields **EDITORIAL COORDINATORS** Ramatoulaye Diop, Joi S. Granger, Lisa Johnson, Anita Wynn **PUBLICATIONS ASSISTANTS** Aneera Dobbins, Jeffrey Hearn, Dona Mathieu, Le-Toya Mayne Flood, Shannon McMahon, Scott Miller, Jerry Richardson, Rachel Roberts(UK), Alice Whaley(UK), Brian White **EXECUTIVE ASSISTANT** Anna Bashkirova **ADMINISTRATIVE SUPPORT** Janet Clements(UK), Lizanne Newton(UK), Maryrose Madrid, Laura-Nadine Schuhmacher (UK, Intern), Alix Welch (Intern), John Wood(UK)

News

NEWS MANAGING EDITOR John Travis **INTERNATIONAL EDITOR** Richard Stone **DEPUTY NEWS EDITORS** Daniel Clery(UK), Robert Coontz, Elizabeth Culotta, David Grimm, David Malakoff, Leslie Roberts **CONTRIBUING EDITOR** Martin Enserink(Europe) **SR. CORRESPONDENTS** Jeffrey Mervis, Elizabeth Pennisi **NEWS WRITERS** Adrian Cho, Jon Cohen, Jennifer Couzin-Frankel, Carolyn Gramling, Eric Hand, Jocelyn Kaiser, Catherine Matacic, Kelly Servick, Robert F. Service, Erik Stokstad(Cambridge, UK), Emily Underwood **INTERNS** Hanae Armitage, Emily DeMarco, Annick Laurent, Laura Olivieri, Juan David Romero **CONTRIBUTING CORRESPONDENTS** Michael Balter(Paris), John Bohannon, Ann Gibbons, Mara Hvistendahl, Sam Kean, Eli Kintisch, Kai Kupferschmidt(Berlin), Andrew Lawler, Christina Larson(Beijing), Mitch Leslie, Charles C. Mann, Eliot Marshall, Virginia Morell, Dennis Normile(Tokyo), Heather Pringle, Tania Rabesandratana(London), Gretchen Vogel(Berlin), Lizzie Wade(Mexico City) **CAREERS** Donisha Adams, Rachel Bernstein **COPY EDITORS** Julia Cole, Jennifer Levin (Chief) **ADMINISTRATIVE SUPPORT** Jessica Williams

Executive Publisher Rush D. Holt
Publisher Kent R. Anderson **Chief Digital Media Officer** Rob Covey

BUSINESS OPERATIONS AND PORTFOLIO MANAGEMENT DIRECTOR Sarah Whalen **BUSINESS SYSTEMS AND FINANCIAL ANALYSIS DIRECTOR** Randy Yi **MANAGER OF FULFILLMENT SYSTEMS** Neal Hawkins **SYSTEMS ANALYST** Nicole Mehmedovich **ASSISTANT DIRECTOR, BUSINESS OPERATIONS** Eric Knott **MANAGER, BUSINESS OPERATIONS** Jessica Tierney **BUSINESS ANALYSTS** Cory Lipman, Cooper Tilton, Celeste Troxler **FINANCIAL ANALYST** Robert Clark **RIGHTS AND PERMISSIONS ASSISTANT DIRECTOR** Emilie David **PERMISSIONS ASSOCIATE** Elizabeth Sandler **RIGHTS, CONTRACTS, AND LICENSING ASSOCIATE** Lili Kiser

MARKETING DIRECTOR Ian King **MARKETING MANAGER** Julianne Wielga **MARKETING ASSOCIATE** Elizabeth Sattler **SR. MARKETING EXECUTIVE** Jennifer Reeves **SR. ART ASSOCIATE, PROJECT MANAGER** Tzeitel Sorrosa **ART ASSOCIATE** Seil Lee **JR. ART ASSOCIATE** Kim Huynh **ASSISTANT COMMERCIAL EDITOR** Selby Frame **MARKETING PROJECT MANAGER** Angelissa McArthur **PROGRAM DIRECTOR, AAAS MEMBER CENTRAL** Peggy Mihelich **FULFILLMENT SYSTEMS AND OPERATIONS** membership@aaas.org **MANAGER, MEMBER SERVICES** Pat Butler **SPECIALISTS** LaToya Casteel, Terrance Morrison, Latasha Russell **MANAGER, DATA ENTRY** Mickie Napoleoni **DATA ENTRY SPECIALISTS** JJ Regan, Brenden Aquilino, Fiona Giblin

DIRECTOR, SITE LICENSING Tom Ryan **DIRECTOR, CORPORATE RELATIONS** Eileen Bernadette Moran **SR. PUBLISHER RELATIONS SPECIALIST** Kiki Forsythe **PUBLISHER RELATIONS MANAGER** Catherine Holland **PUBLISHER RELATIONS, EASTERN REGION** Keith Layson **PUBLISHER RELATIONS, WESTERN REGION** Ryan Rexroth **SALES RESEARCH COORDINATOR** Aiesha Marshall **MANAGER, SITE LICENSE OPERATIONS** Iquo Edim **SENIOR PRODUCTION SPECIALIST** Robert Koepke **SENIOR OPERATIONS ANALYST** Lana Guz **FULFILLMENT ANALYST** Judy Lillibridge **ASSOCIATE DIRECTOR, MARKETING** Christina Schlecht **MARKETING ASSOCIATES** Thomas Landreth, Isa Sesay-Bah

DIRECTOR OF WEB TECHNOLOGIES Ahmed Khadr **SR. DEVELOPER** Chris Coleman **DEVELOPERS** Dan Berger, Jimmy Marks **SR. PROJECT MANAGER** Trista Smith **SYSTEMS ENGINEER** Luke Johnson

CREATIVE DIRECTOR, MULTIMEDIA Martyn Green **DIRECTOR OF ANALYTICS** Enrique Gonzales **SR. WEB PRODUCER** Sarah Crespi **WEB PRODUCER** Alison Crawford **VIDEO PRODUCER** Nguyen Nguyen **SOCIAL MEDIA PRODUCER** Meghna Sachdev

DIRECTOR OF OPERATIONS PRINT AND ONLINE Lizabeth Harman **DIGITAL/PRINT STRATEGY MANAGER** Jason Hillman **QUALITY TECHNICAL MANAGER** Marcus Spiegler **PROJECT ACCOUNT MANAGER** Tara Kelly **DIGITAL PRODUCTION MANAGER** Lisa Stanford **ASSISTANT MANAGER DIGITAL/PRINT** Rebecca Doshi **SENIOR CONTENT SPECIALISTS** Steve Forrester, Antoinette Hodal, Lori Murphy, Anthony Rosen **CONTENT SPECIALISTS** Jacob Hedrick, Kimberley Oster

DESIGN DIRECTOR Beth Rakouskas **DESIGN EDITOR** Marcy Atarod **SENIOR DESIGNER** Garvin Grullón **DESIGNER** Chrystal Smith **GRAPHICS MANAGING EDITOR** Alberto Cuadra **SENIOR SCIENTIFIC ILLUSTRATORS** Chris Bickel, Katharine Sutliff **SCIENTIFIC ILLUSTRATOR** Valerie Altounian **SENIOR ART ASSOCIATES** Holly Bishop, Preston Huey **SENIOR PHOTO EDITOR** William Douthitt **PHOTO EDITORS** Leslie Blizard, Christy Steele

DIRECTOR, GLOBAL COLLABORATION, CUSTOM PUBLICATIONS, ADVERTISING Bill Moran **EDITOR, CUSTOM PUBLISHING** Sean Sanders: 202-326-6430 **ASSISTANT EDITOR, CUSTOM PUBLISHING** Tianna Hicklin: 202-326-6463 **ADVERTISING MARKETING MANAGER** Justin Sawyers: 202-326-7061 science_advertising@aaas.org **ADVERTISING MARKETING ASSOCIATE** Javia Flemmings **ADVERTISING SUPPORT MANAGER** Karen Foote: 202-326-6740 **ADVERTISING PRODUCTION OPERATIONS MANAGER** Deborah Tompkins **SR. PRODUCTION SPECIALIST/GRAPHIC DESIGNER** Amy Hardcastle **PRODUCTION SPECIALIST** Yuse Lajiminmuhip **SR. TRAFFIC ASSOCIATE** Christine Hall **SALES COORDINATOR** Shirley Young **ASSOCIATE DIRECTOR, COLLABORATION, CUSTOM PUBLICATIONS/CHINA/TAIWAN/KOREA/SINGAPORE** Ruolei Wu: +86-186 0082 9345, rwu@aaas.org **COLLABORATION/ CUSTOM PUBLICATIONS/JAPAN** Adarsh Sandhu + 81532-81-5142 asandhu@aaas.org **EAST COAST/E. CANADA** Laurie Faraday: 508-747-9395, FAX 617-507-8189 **WEST COAST/W. CANADA** Lynne Stickrod: 415-931-9782, FAX 415-520-6940 **MIDWEST** Jeffrey Dembski: 847-498-4520 x3005, Steven Loerch: 847-498-4520 x3006 **UK EUROPE/ASIA** Roger Goncalves: TEL/FAX +41 43 243 1358 **JAPAN** Katsuyoshi Fukamizu(Tokyo): +81-3-3219-5777 kfukamizu@aaas.org **CHINA/TAIWAN** Ruolei Wu: +86-186 0082 9345, rwu@aaas.org

WORLDWIDE ASSOCIATE DIRECTOR OF SCIENCE CAREERS Tracy Holmes: +44 (0) 1223 326525, FAX +44 (0) 1223 326532 tholmes@science-int.co.uk **CLASSIFIED** advertise@sciencecareers.org **U.S. SALES** Tina Burks: 202-326-6577, Nancy Toema: 202-326-6578 **SALES ADMINISTRATOR** Marci Gallun **EUROPE/ROW SALES** Axel Gesatzki, Sarah Lelarge **SALES ASSISTANT** Kelly Grace **JAPAN** Hiroyuki Mashiki(Kyoto): +81-75-823-1109 hmashiki@aaas.org **CHINA/TAIWAN** Ruolei Wu: +86-186 0082 9345 rwu@aaas.org **MARKETING MANAGER** Allison Pritchard **MARKETING ASSOCIATE** Aimee Aponte

AAAS BOARD OF DIRECTORS RETIRING PRESIDENT, CHAIR Gerald R. Fink **PRESIDENT** Geraldine (Geri) Richmond **PRESIDENT-ELECT** Barbara A. Schaal **TREASURER** David Evans Shaw **CHIEF EXECUTIVE OFFICER** Rush D. Holt **BOARD** Bonnie L. Bassler, May R. Berenbaum, Carlos J. Bustamante, Stephen P.A. Fodor, Claire M. Fraser, Michael S. Gazzaniga, Laura H. Greene, Elizabeth Loftus, Mercedes Pascual

SUBSCRIPTION SERVICES For change of address, missing issues, new orders and renewals, and payment questions: 866-434-AAAS (2227) or 202-326-6417, FAX 202-842-1065. Mailing addresses: AAAS, P.O. Box 96178, Washington, DC 20090-6178 or AAAS Member Services, 1200 New York Avenue, NW, Washington, DC 20005

INSTITUTIONAL SITE LICENSES 202-326-6755 **REPRINTS:** Author Inquiries 800-635-7181 **COMMERCIAL INQUIRIES** 803-359-4578 **PERMISSIONS** 202-326-6765, permissions@aaas.org **AAAS Member Services** 202-326-6417 or http://membercentral.aaas.org/discounts

Science serves as a forum for discussion of important issues related to the advancement of science by publishing material on which a consensus has been reached as well as including the presentation of minority of conflicting points of view. Accordingly, all articles published in *Science*—including editorials, news and comment, and books reviews—are signed and reflect the individual views of the authors and not official points of view adopted by AAAS or the institutions with which the authors are affiliated.

INFORMATION FOR AUTHORS See pages 678 and 679 of the 6 February 2015 issue or access www.sciencemag.org/about/authors

SENIOR EDITORIAL BOARD
Robert H. Grubbs, *California Institute of Technology,* **Gary King,** *Harvard University*
Susan M. Rosenberg, *Baylor College of Medicine,* **Ali Shilatifard,** *Northwestern University*
Feinberg School of Medicine, **Michael S. Turner**, *U. of Chicago*

BOARD OF REVIEWING EDITORS (Statistics board members indicated with **(S)**)

Adriano Aguzzi, *U. Hospital Zürich*
Takuzo Aida, *U. of Tokyo*
Leslie Aiello, *Wenner-Gren Foundation*
Judith Allen, *U. of Edinburgh*
Sonia Altizer, *U. of Georgia*
Sebastian Amigorena, *Institut Curie*
Kathryn Anderson, *Memorial Sloan-Kettering Cancer Center*
Meinrat O. Andreae, *Max-Planck Inst. Mainz*
Paola Arlotta, *Harvard U.*
Johan Auwerx, *EPFL*
David Awschalom, *U. of Chicago*
Jordi Bascompte, *Estación Biológica de Doñana CSIC*
Facundo Batista, *London Research Inst.*
Ray H. Baughman, *U. of Texas, Dallas*
David Baum, *U. of Wisconsin*
Carlo Beenakker, *Leiden U.*
Kamran Behnia, *ESPCI-ParisTech*
Yasmine Belkaid, *NIAID, NIH*
Philip Benfey, *Duke U.*
Stephen J. Benkovic, *Penn State U.*
May Berenbaum, *U. of Illinois*
Gabriele Bergers, *U. of California, San Francisco*
Bradley Bernstein, *Massachusettes General Hospital*
Peer Bork, *EMBL*
Bernard Bourdon, *Ecole Normale Supérieure de Lyon*
Chris Bowler, *École Normale Supérieure*
Ian Boyd, *U. of St. Andrews*
Emily Brodsky, *U. of California, Santa Cruz*
Ron Brookmeyer, *U. of California Los Angeles* **(S)**
Christian Büchel, *U. Hamburg-Eppendorf*
Joseph A. Burns, *Cornell U.*
Gyorgy Buzsaki, *New York U. School of Medicine*
Blanche Capel, *Duke U.*
Mats Carlsson, *U. of Oslo*
David Clapham, *Children's Hospital Boston*
David Clary, *U. of Oxford*
Joel Cohen, *Rockefeller U., Columbia U.*
James Collins, *Boston U.*
Robert Cook-Deegan, *Duke U.*
Alan Cowman, *Walter & Eliza Hall Inst.*
Robert H. Crabtree, *Yale U.*
Roberta Croce, *Vrije Universiteit*
Janet Currie, *Princeton U.*
Jeff L. Dangl, *U. of North Carolina*
Tom Daniel, *U. of Washington*
Frans de Waal, *Emory U.*
Stanislas Dehaene, *Collège de France*
Robert Desimone, *MIT*
Claude Desplan, *New York U.*
Ap Dijksterhuis, *Radboud U. of Nijmegen*
Dennis Discher, *U. of Pennsylvania*
Gerald W. Dorn II, *Washington U. School of Medicine*
Jennifer A. Doudna, *U. of California, Berkeley*
Bruce Dunn, *U. of California, Los Angeles*
Christopher Dye, *WHO*
Todd Ehlers, *U. of Tuebingen*
David Ehrhardt, *Carnegie Inst. of Washington*
Tim Elston, *U. of North Carolina at Chapel Hill*
Gerhard Ertl, *Fritz-Haber-Institut, Berlin*
Barry Everitt, *U. of Cambridge*
Ernst Fehr, *U. of Zurich*
Anne C. Ferguson-Smith, *U. of Cambridge*
Michael Feuer, *The George Washington U.*
Toren Finkel, *NHLBI, NIH*
Kate Fitzgerald, *U. of Massachusetts*
Peter Fratzl, *Max-Planck Inst.*
Elaine Fuchs, *Rockefeller U.*
Daniel Geschwind, *UCLA*
Andrew Gewirth, *U. of Illinois*
Karl-Heinz Glassmeier, *TU Braunschweig*
Ramon Gonzalez, *Rice U.*
Julia R. Greer, *Caltech*
Elizabeth Grove, *U. of Chicago*
Nicolas Gruber, *ETH Zurich*
Kip Guy, *St. Jude's Children's Research Hospital*
Taekjip Ha, *U. of Illinois at Urbana-Champaign*
Christian Haass, *Ludwig Maximilians U.*
Steven Hahn, *Fred Hutchinson Cancer Research Center*
Michael Hasselmo, *Boston U.*
Martin Heimann, *Max-Planck Inst. Jena*
Yka Helariutta, *U. of Cambridge*
James A. Hendler, *Rensselaer Polytechnic Inst.*
Janet G. Hering, *Swiss Fed. Inst. of Aquatic Science & Technology*
Kai-Uwe Hinrichs, *U. of Bremen*
Kei Hirose, *Tokyo Inst. of Technology*
David Hodell, *U. of Cambridge*
David Holden, *Imperial College*
Lora Hooper, *UT Southwestern Medical Ctr. at Dallas*
Raymond Huey, *U. of Washington*
Steven Jacobsen, *U. of California, Los Angeles*
Kai Johnsson, *EPFL Lausanne*
Peter Jonas, *Inst. of Science & Technology (IST) Austria*
Matt Kaeberlein, *U. of Washington*
William Kaelin Jr., *Dana-Farber Cancer Inst.*
Daniel Kahne, *Harvard U.*
Daniel Kammen, *U. of California, Berkeley*
Masashi Kawasaki, *U. of Tokyo*
V. Narry Kim, *Seoul National U.*
Joel Kingsolver, *U. of North Carolina at Chapel Hill*
Robert Kingston, *Harvard Medical School*
Etienne Koechlin, *Ecole Normale Supérieure*
Alexander Kolodkin, *Johns Hopkins U.*
Alberto R. Kornblihtt, *U. of Buenos Aires*
Leonid Kruglyak, *UCLA*
Thomas Langer, *U. of Cologne*
Mitchell A. Lazar, *U. of Pennsylvania*
David Lazer, *Harvard U.*
Thomas Lecuit, *IBDM*
Virginia Lee, *U. of Pennsylvania*
Stanley Lemon, *U. of North Carolina at Chapel Hill*
Ottoline Leyser, *Cambridge U.*
Marcia C. Linn, *U. of California, Berkeley*
Jianguo Liu, *Michigan State U.*
Luis Liz-Marzan, *CIC biomaGUNE*
Jonathan Losos, *Harvard U.*
Ke Lu, *Chinese Acad. of Sciences*
Christian Lüscher, *U. of Geneva*
Laura Machesky, *CRUK Beatson Inst. for Cancer Research*
Anne Magurran, *U. of St. Andrews*
Oscar Marin, *CSIC & U. Miguel Hernández*
Charles Marshall, *U. of California, Berkeley*
C. Robertson McClung, *Dartmouth College*
Graham Medley, *U. of Warwick*
Tom Misteli, *NCI*
Yasushi Miyashita, *U. of Tokyo*
Mary Ann Moran, *U. of Georgia*
Richard Morris, *U. of Edinburgh*
Alison Motsinger-Reif, *NC State U.* **(S)**
Sean Munro, *MRC Lab. of Molecular Biology*
Thomas Murray, *The Hastings Center*
James Nelson, *Stanford U. School of Med.*
Daniel Neumark, *U. of California, Berkeley*
Kitty Nijmeijer, *U. of Twente*
Pär Nordlund, *Karolinska Inst.*
Helga Nowotny, *European Research Advisory Board*
Ben Olken, *MIT*
Joe Orenstein, *U. of California Berkeley & Lawrence Berkeley National Lab*
Harry Orr, *U. of Minnesota*
Andrew Oswald, *U. of Warwick*
Steve Palumbi, *Stanford U.*
Jane Parker, *Max-Planck Inst. of Plant Breeding Research*
Giovanni Parmigiani, *Dana-Farber Cancer Inst.* **(S)**
Donald R. Paul, *U. of Texas, Austin*
John H. J. Petrini, *Memorial Sloan-Kettering Cancer Center*
Joshua Plotkin, *U. of Pennsylvania*
Albert Polman, *FOM Institute AMOLF*
Philippe Poulin, *CNRS*
Jonathan Pritchard, *Stanford U.*
David Randall, *Colorado State U.*
Colin Renfrew, *U. of Cambridge*
Felix Rey, *Institut Pasteur*
Trevor Robbins, *U. of Cambridge*
Jim Roberts, *Fred Hutchinson Cancer Research Ctr.*
Barbara A. Romanowicz, *U. of California,Berkeley*
Jens Rostrup-Nielsen, *Haldor Topsoe*
Mike Ryan, *U. of Texas, Austin*
Mitinori Saitou, *Kyoto U.*
Shimon Sakaguchi, *Kyoto U.*
Miquel Salmeron, *Lawrence Berkeley National Lab*
Jürgen Sandkühler, *Medical U. of Vienna*
Alexander Schier, *Harvard U.*
Randy Seeley, *U. of Cincinnati*
Vladimir Shalaev, *Purdue U.*
Robert Siliciano, *Johns Hopkins School of Medicine*
Denis Simon, *Arizona State U.*
Alison Smith, *John Innes Centre*
Richard Smith, *U. of North Carolina* **(S)**
John Speakman, *U. of Aberdeen*
Allan C. Spradling, *Carnegie Institution of Washington*
Jonathan Sprent, *Garvan Inst. of Medical Research*
Eric Steig, *U. of Washington*
Paula Stephan, *Georgia State U. and National Bureau of Economic Research*
Molly Stevens, *Imperial College London*
V. S. Subrahmanian, *U. of Maryland*
Ira Tabas, *Columbia U.*
Sarah Teichmann, *Cambridge U.*
John Thomas, *North Carolina State U.*
Shubha Tole, *Tata Institute of Fundamental Research*
Christopher Tyler-Smith, *The Wellcome Trust Sanger Inst.*
Herbert Virgin, *Washington U.*
Bert Vogelstein, *Johns Hopkins U.*
Cynthia Volkert, *U. of Göttingen*
Douglas Wallace, *Dalhousie U.*
David Wallach, *Weizmann Inst. of Science*
Ian Walmsley, *U. of Oxford*
Jane-Ling Wang, *U. of California, Davis*
David A. Wardle, *Swedish U. of Agric. Sciences*
David Waxman, *Fudan U.*
Jonathan Weissman, *U. of California, San Francisco*
Chris Wikle, *U. of Missouri* **(S)**
Ian A. Wilson, *The Scripps Res. Inst.* **(S)**
Timothy D. Wilson, *U. of Virginia*
Rosemary Wyse, *Johns Hopkins U.*
Jan Zaanen, *Leiden U.*
Kenneth Zaret, *U. of Pennsylvania School of Medicine*
Jonathan Zehr, *U. of California, Santa Cruz*
Len Zon, *Children's Hospital Boston*
Maria Zuber, *MIT*

BOOK REVIEW BOARD
David Bloom, *Harvard U.,* **Samuel Bowring,** *MIT,* **Angela Creager,** *Princeton U.,*
Richard Shweder, *U. of Chicago,* **Ed Wasserman,** *DuPont*

Published by AAAS

EDITORIAL

Iran, science, and collaboration



Mohammad Farhadi is Iran's Minister of Science, Research and Technology in Tehran, Iran.

More than 35 years since its revolution, Iran is embarking on a new era of international interaction and cooperation. On the road to becoming a nation with scientific clout, Iran takes the role of science for peace, progress, and dialogue very seriously.

Iran is now a nation of 78 million people, with about 4.5 million university students, 2500 higher education institutions, 36 science and technology parks, 400 nongovernmental scientific associations, more than 800 research centers, and 1000 scientific journals. Our scientists publish about 30,000 international scientific papers annually, a growth of at least 20-fold since 1979. These achievements could not have been reached without the intensive participation of individual scientists and scientific societies and government support. This participation sprang from a model of development for postrevolutionary Iran that respects the rights of all Iranians to have access to higher education. It is this philosophy that has helped the country weather internal and external disturbances. Sanctions on Iran, for example, pushed its science, industry, and service sectors to cooperate in new and fruitful ways and also forced scientists to work more creatively and promote a knowledge-based economy for the first time in Iran's history. This environment further spurred science-driven political discourse in the country. A prominent example is the role of the scientific community in the recent negotiations on Iran's nuclear program. This could not have materialized without the participation of scientists to provide technical expertise and to clarify scientific language.



"...Iran is embarking on a new era of international interaction and cooperation."

Today, Iran is in a position to fine-tune its development model and move toward qualitative improvement of its science and technology. This includes growing its international scientific collaborations. Given that cooperation is most effective through direct contacts between scientists rather than through government-driven agreements, the Iranian government will encourage and support collaborations initiated by individual scientists from within the country or in any part of the world. There are already such efforts in place, such as the Gondishapour program, in which Iran has partnered with France to support the travel of scientists to and from Iran once a mutual project between the scientists of the countries has begun. A similar program has been negotiated between Iran and some other European countries. Iran will continue to encourage its universities to be international in all aspects of science and education.

In looking at Iran's history, it is clear that international scientific institutions such as the Maragheh observatory, which was established in the 13th century by a couple of hundred scientists from all over the world, can be vivid guides for science diplomacy in all areas of science, research, and technology. Iran plans to have big science projects, such as the Iranian National Observatory, which will bridge Iranian scientists with the international science community.

In addition to the increasing number of scientific personnel and growing the scientific infrastructure, Iran offers a unique environment for certain research areas such as archaeology, desert studies, ecological studies, and study of the fauna and flora of the Irano-Turanian region. Thus, prospects for collaboration in the natural sciences, humanities, engineering, and medical and biosciences are all on the horizon. We invite scientists from all over the world to initiate a collaborative program with our scientists. Iran is ready.

– Mohammad Farhadi

10.1126/science.aad3016

PHOTOS: (TOP RIGHT) IRAN MINISTRY OF SCIENCE, RESEARCH AND TECHNOLOGY; (INSET) © GEORGE STEINMETZ/CORBIS

Downloaded from www.sciencemag.org on September 5, 2015

Published by AAAS

NEWS

3,000,000,000,000

Number of trees on Earth—eight times as many as previous estimates—according to a study that models tree density at the scale of a square kilometer based on a combination of satellite imagery and forest inventory data (*Nature*).

IN BRIEF



U.S. President Barack Obama at the Conference on Global Leadership in the Arctic: Cooperation, Innovation, Engagement and Resilience, or GLACIER.

Obama calls for more icebreakers

The Obama administration wants to build a new heavy-duty icebreaker 2 years faster than planned. But even completing it in 2020 will still leave the United States four icebreakers short of what experts say is needed to cover the nation's anticipated needs in the Arctic and Antarctic. On Tuesday, President Barack Obama announced the accelerated schedule in opening remarks to a Department of State–hosted climate change conference, calling on the world's nations to take urgent action on climate change. The U.S. Coast Guard currently has only two active icebreakers—the 40-year-old heavy icebreaker *Polar Star* and the medium research icebreaker *Healy*—and a report earlier this year to the Coast Guard cited the need for three heavy-duty and three medium-duty ships; funding for the construction of new icebreakers has been stalled for years in Congress. The conference amplified U.S. priorities for the Arctic Council, an intergovernmental forum that it is chairing from 2015 to 2017, including climate change, stewardship of the Arctic Ocean, and the economic plight of native communities.

AROUND THE WORLD

China adopts new stem cell rules

BEIJING | Chinese stem cell scientists may now have a legal way to move forward with new clinical trials, on hold in the country since January 2012. That was when China's Ministry of Health imposed a temporary moratorium in an effort to clamp down on unproven therapies. The new rules, announced last month, require informed consent from patients, "sufficient" animal testing, and the use of stem cell lines approved by the newly named National Health and Family Planning Commission. The regulations also require that all clinical studies take place at authorized hospitals, which aren't allowed to advertise their services or charge patients. This last requirement could introduce some restraint into China's flourishing "grey market" in stem cell therapy, but critics worry that the rules—which don't lay out any punishment for violators—don't go far enough.

India eliminates neonatal tetanus

NEW DELHI | The World Health Organization officially confirmed last week that India has eliminated maternal and neonatal tetanus (MNT). Elimination means reducing the incidence of the disease to less than one case per 1000 live births in every district in the country; just a few decades ago, India was reporting 150,000 to 200,000 neonatal tetanus cases each year, and tetanus was responsible for 15% of the neonatal deaths in the country. India's health officials credit the elimination to a countrywide immunization push and an increase in the numbers of children born in the hospital. There are 22 countries remaining that have yet to eliminate MNT.

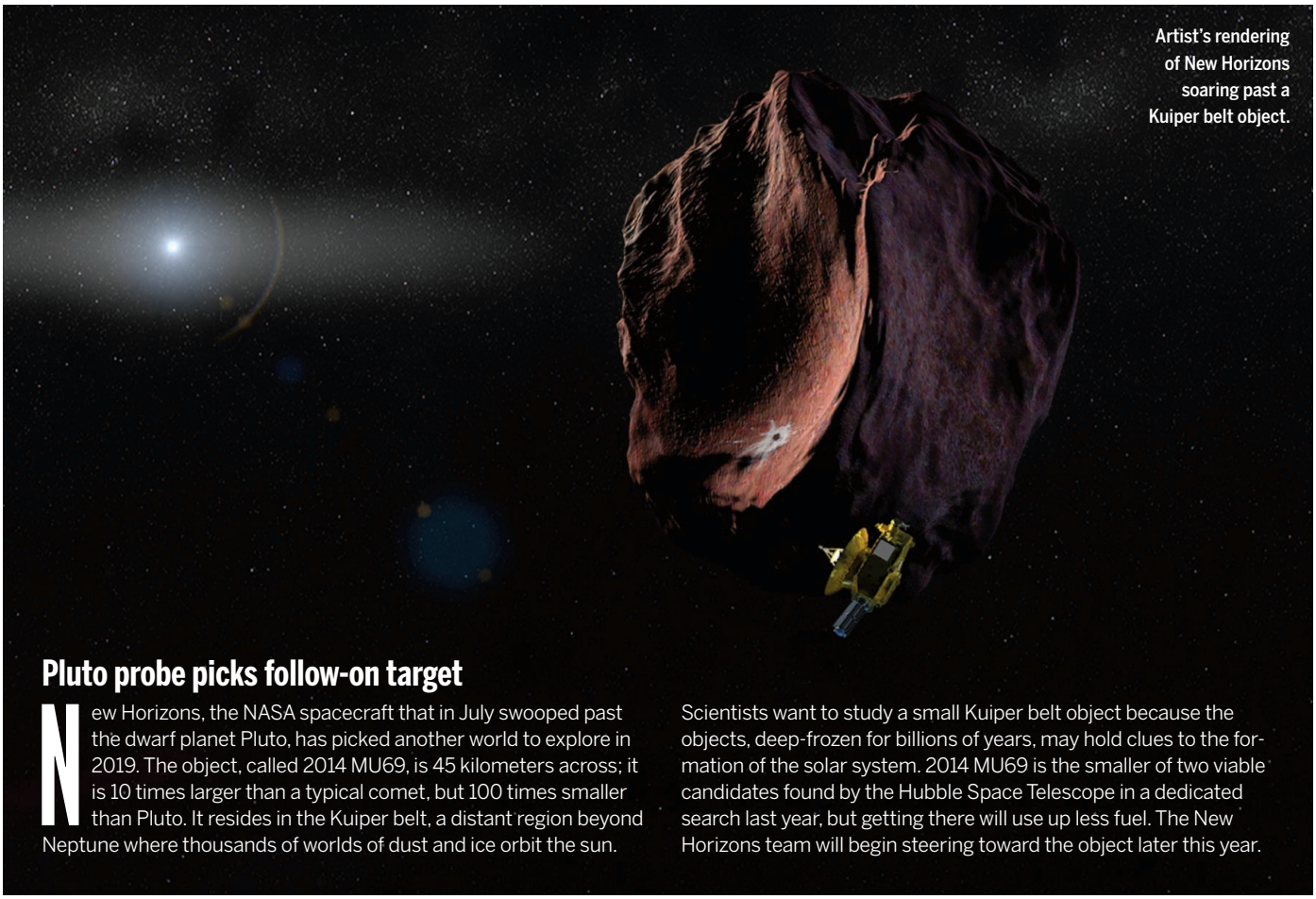
Fuzzy nautilus spotted

NDROVA ISLAND, PAPUA NEW GUINEA | For the first time in nearly 30 years, scientists have observed the "crusty nautilus," also known as *Allonautilus scrobiculatus*. *A. scrobiculatus* is a cousin of the famous chambered nautilus, but instead of being smooth, its shell is covered with tiny hairs.

PHOTO: REUTERS/JONATHAN ERNST

Downloaded from www.sciencemag.org on September 5, 2015

Published by AAAS



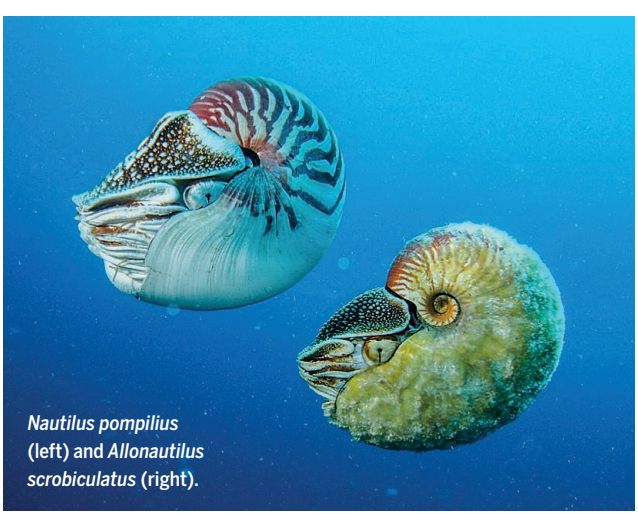
Artist's rendering of New Horizons soaring past a Kuiper belt object.

Pluto probe picks follow-on target

New Horizons, the NASA spacecraft that in July swooped past the dwarf planet Pluto, has picked another world to explore in 2019. The object, called 2014 MU69, is 45 kilometers across; it is 10 times larger than a typical comet, but 100 times smaller than Pluto. It resides in the Kuiper belt, a distant region beyond Neptune where thousands of worlds of dust and ice orbit the sun.

Scientists want to study a small Kuiper belt object because the objects, deep-frozen for billions of years, may hold clues to the formation of the solar system. 2014 MU69 is the smaller of two viable candidates found by the Hubble Space Telescope in a dedicated search last year, but getting there will use up less fuel. The New Horizons team will begin steering toward the object later this year.

The creature was discovered in 1984 but has rarely been seen since. Researchers rediscovered it this summer as they studied nautiluses—relatives of octopuses and squid—in waters 150 to 400 meters deep. Hoping to determine whether *A. scrobiculatus* still existed—and, if so, to collect the first videos and DNA samples of them—the team lured nautiluses to a cage filled with fish and chicken bait and filmed them with a deep-water camera. They also tracked the movements of four *A. scrobiculatus* by attaching small acoustic transmitters to their shells.



Nautilus pompilius (left) and *Allonautilus scrobiculatus* (right).

Climate pledges fall short

BONN, GERMANY | With fewer than 100 days remaining before 195 nations are scheduled to gather in Paris to finalize a new global deal to curb climate change, just 56 countries have submitted their pledges to reduce greenhouse gas emissions to the United Nations. That tally came as diplomats gathered in Bonn this week for a penultimate negotiating session before the Paris meeting. Although the pledges come from countries responsible for some 60% of current emissions, U.N. chief Ban Ki-moon on 26 August expressed frustration with the pace of the talks at a meeting in France. "We don't have time to waste," he said. In a bid to speed things up, he has reportedly invited world leaders to discuss the climate pact at a 27 September meeting in New York City.

Hubris and Fukushima

VIENNA | The widespread assumption that a major accident "was simply unthinkable" led to the multiple meltdowns at Japan's Fukushima nuclear power plant after the earthquake and tsunami that struck northeastern Japan on 11 March 2011, according to the International Atomic Energy Agency's final report on the incident. The report, released this week, says that although there are still uncertainties about the health effects of radioactive contamination from the stricken reactors, a rise in childhood thyroid cancer cases is unlikely. The 200-page report and five accompanying technical volumes are intended to provide lessons for nuclear plant operators, regulators, and governments worldwide. "There can be no grounds for complacency," the report warns, because many of the safety shortcomings "were not unique to Japan."

CREDITS: (TOP TO BOTTOM) NASA/JOHNS HOPKINS UNIVERSITY APPLIED PHYSICS LABORATORY/SOUTHWEST RESEARCH INSTITUTE/STEVE GRIBBEN; PETER WARD

Published by AAAS

IN DEPTH

GEOPHYSICS

Mantle plumes seen rising from Earth's core

Fat tubes of hot rock could alter views of how the planet cools

By **Eric Hand**

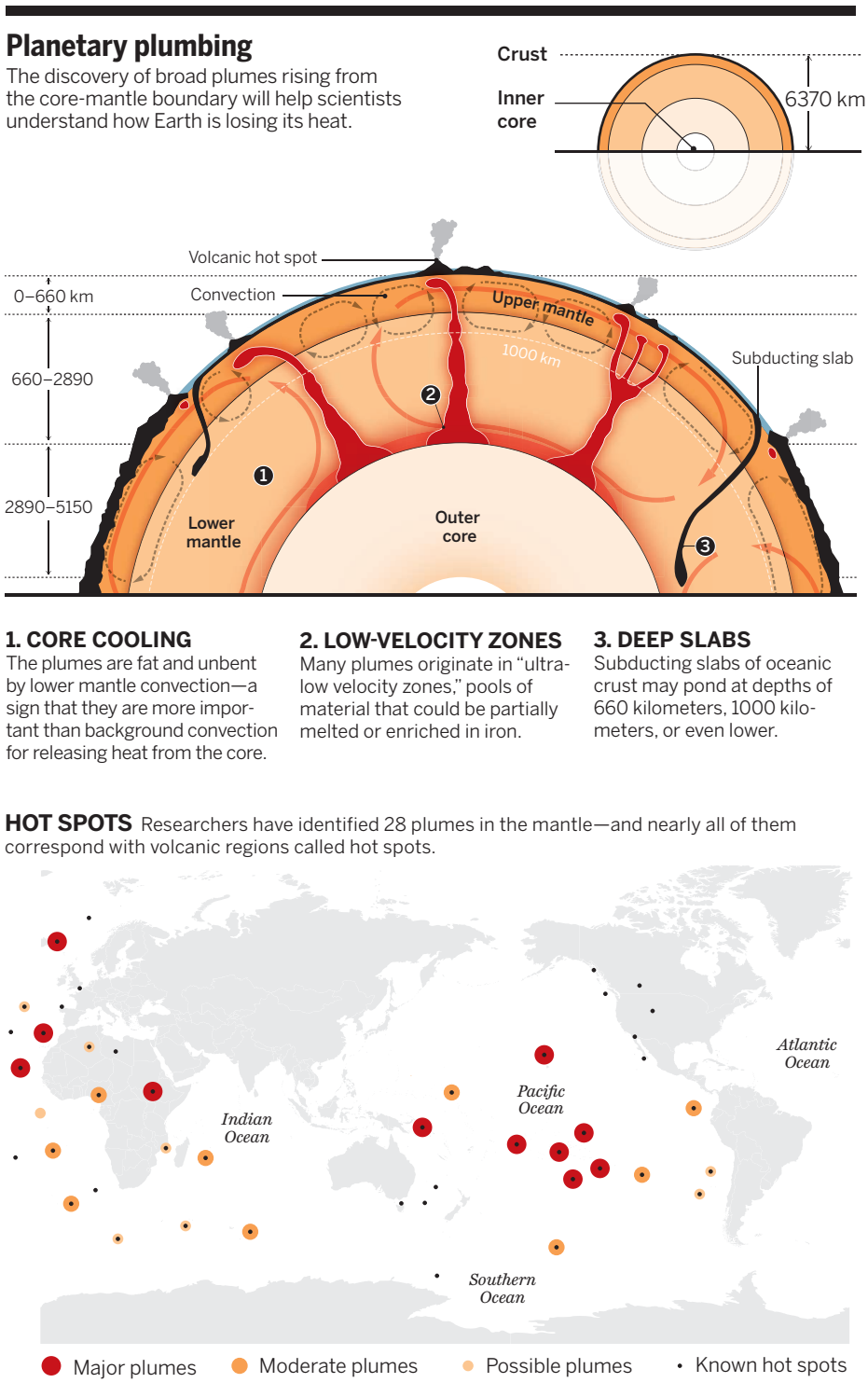
A key internal feature of Earth has come into focus. For more than 40 years, geoscientists have debated whether Earth's hot spots—several dozen volcanic regions that bulge upward as if something hot and insistent were pushing up from below—are fed by mantle plumes, columns of hot rock thought to rise from the core nearly 3000 kilometers below the surface. Proponents cited physical models that suggest that plumes form naturally, like bubbles in a boiling pot, as the mantle is heated from below. And seismologists, using earthquake waves to perform MRI-like tomographies on the planet, have seen signs of plumes in the upper parts of the mantle. But absent evidence of mantle plumes stretching continuously up from the core, a small minority of scientists has argued that hot spots could be fed by shallower reservoirs.

Now, a new study finds that it's plumes all the way down. Using a sophisticated technique to wring unprecedented detail from earthquake records, researchers have found evidence for 28 mantle plumes, most of them beneath volcanic hot spots, rising continuously, and vertically, from the core. "If our picture makes sense, then we've settled the debate. Plumes exist," says Barbara Romanowicz, a geophysicist at the University of California, Berkeley, who published the study on 2 September in *Nature* along with her colleague, Scott French.

The confirmation comes with surprises. The plumes are 600 to 800 kilometers wide, more than three times as big as simple models have predicted, Romanowicz says. As a result, plumes can carry more heat away from the core than was thought. Moreover, their deepest reaches are ramrod straight and do not appear to sway in the currents of rock believed to circulate in the lower mantle. "It's quite likely that people will need to rethink how the lower mantle is working," she says.

Other researchers have hailed the study. "The tomography work they did is a great tour de force," says Peter van Keken, a geodynamicist at the University of Michigan, Ann Arbor. "What was really fuzzy in previous models has become sharper." Van Keken is intrigued by the shearing and bending of the plumes seen at depths shallower than 1000 kilometers. He thinks the change in plume behavior at 1000 kilometers could represent an unknown phase change in the rising rock, which makes it a little less stiff.

As for the surprising size of the plumes, van Keken says it jibes with an emerging notion that the hot plumes may be made of different stuff from the surrounding mantle. If a



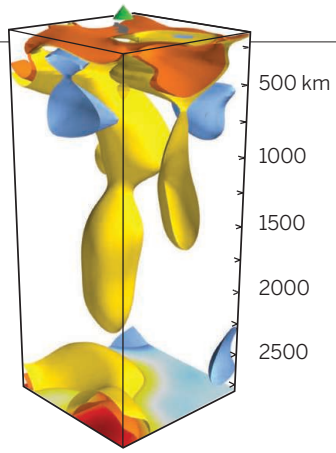
CREDITS: (ILLUSTRATION) A. CUADRA/*SCIENCE*; (DATA) ADAPTED FROM S. FRENCH *ET AL.*, *NATURE* **525**, 95 (3 SEPTEMBER)

Downloaded from www.sciencemag.org on September 5, 2015

Published by AAAS

plume gathers dense basaltic material near the core-mantle boundary, says van Keken, "it helps the plume to slow down, it helps the plume to be broader."

Guust Nolet, an emeritus geophysicist at the University of Nice Sophia Antipolis in France, says previous studies have indicated the existence of deep mantle plumes (see *Science*, 16 January 2004, p. 338), but this one sharpens the view at the top and bottom of the mantle. He says the surprising size of the plumes will change the accounting of how Earth sheds internal heat—a flux estimated at 44 terawatts. Perhaps half of that heat flux is thought to come from radioactive elements within Earth, and the other half from residual heat in the core. Geophysicists have assumed that mantle convection, a broad cellular pattern of circulating rock, carried most of the heat away from the core. "We need to review that view and give the plumes a much larger role," Nolet says. "It might be that the lower mantle isn't convecting at all."



FROM THE DEEP
This rendering of the plume beneath Hawaii shows a lateral bending above a depth of 1000 kilometers. The level could mark an undiscovered mineral phase transition in lower mantle rock.

The new result takes advantage of a technique called seismic tomography. Large earthquakes that shake Earth's surface send waves that travel all the way through the planet, bouncing off internal boundaries and slowing down when they encounter anomalously hot, less dense structures, such as plumes. From measurements of many earthquakes, a picture of Earth's interior can be derived.

Many tomographic studies rely on just the arrival times, or initial pulses, of different earthquake waves. A relatively new modeling technique called whole waveform tomography uses the full rupture duration of each earthquake—in effect, most of the squiggles in a seismogram. The process is computationally intensive: Romanowicz and French's analysis using records of 273 large earthquakes required the equivalent of 3 million computer hours on a Department of Energy supercomputer called Hopper.

That result is not enough to persuade Gillian Foulger, a geophysicist at Durham University in the United Kingdom, and a longtime skeptic of deep mantle plumes. Although she applauds the computational effort, she says that the whole waveform technique is still in its embryonic stages. She also notes that most of the plumes found by Romanowicz and French sit under hotspots in the ocean, where seismic data is extremely limited. "If your data is poor, you see a lot of noise," she says. Some researchers are pushing for programs to help fill that information gap (see sidebar, below).

But van Keken says the evidence for deep mantle plumes is strong. "The naysayers are few and far between," he says. Not that he wouldn't also like to improve the resolution of the models. If they could see features as small as 100 kilometers across, they could reveal the fate of slabs of ocean crust plummeting into Earth's interior from subduction zones, he says. Some slabs may pool at intermediate depths, whereas others may fall all the way to the core. But to achieve that sort of view, models will need to tap into the higher frequency content embedded in seismograms—and that will require much more computing power. "You'll need a really big computer if you don't want your grad student to wait forever for their Ph.D.," van Keken says. ■

Ocean robots listen for earthquake echoes

By **Eric Hand**

The discovery of large mantle plumes rising from the core-mantle boundary (see main story, p. 1032) underscores how far seismologists have come in using earthquake waves to probe Earth's interior. Unfortunately, two-thirds of the planet—the part covered by oceans—is a virtual blank spot for seismology. Ocean islands with stations gathering continuous seismic data are scarce, and deploying ocean-bottom sensors from ships is time-consuming and expensive.

Now, researchers are talking about a way to fill the data gap: autonomous submersibles that listen for large earthquakes. Their measurements would not match those of land-based instruments, but "I think the way to go forward is to sacrifice quality for quantity," says Guust Nolet, an emeritus geophysicist at the University of Nice Sophia Antipolis in France, who described the approach in a paper he and colleagues published last month in *Nature Communications*.

Nolet calls his instruments Mobile Earthquake Recording in Marine Areas by Independent Divers (MERMAIDs). They are 30-kilogram floats just over a meter tall, equipped with a hydrophone, which can drift at a depth of 1.5 kilometers and listen for as long as 2 years. When strong earthquake waves course through Earth's interior and reach the ocean floor, they turn into acoustic waves that a MERMAID can hear. The device then rises to the surface and transmits its data via a satellite link. Nolet says MERMAIDs cost $30,000 apiece—about as much as one day of ship time.

In tests in the Mediterranean Sea, the Indian Ocean, and the Pacific Ocean, the robots captured between one-third and two-thirds of earthquakes of magnitude 6.5 and larger. In the Indian Ocean, they even recorded a small swarm of earthquakes that were never detected on land. MERMAIDS have drawbacks: Because their locations can be determined only when they surface and transmit data, they cannot locate earthquakes in real time. Moreover, the instruments can only record compressional earthquake waves, or P waves. Other waves useful for tomography don't turn into sound at the sea floor.

Jonathan Berger, a geophysicist at the Scripps Institution of Oceanography in San Diego, California, says Nolet's study is a good proof of principle. "His paper demonstrates quite well that they can do what they said they'd do," he says. Berger is testing wave gliders, surfboardlike devices that harness the power of ocean waves to saunter along the surface at speeds of 1 knot and could also capture earthquake noise. The gliders, which cost about $200,000 apiece, can be navigated away from shore—and back to shore for maintenance—without the need for expensive ship time. ■

ILLUSTRATION: ADAPTED FROM S. FRENCH *ET AL*., *NATURE* **525**, 95 (3 SEPTEMBER)

Published by AAAS



Farm chores may provide an unexpected benefit: asthma prevention.

IMMUNOLOGY

How farm life prevents asthma

Lung reaction to bacteria may explain protection for farm children, bolstering hygiene hypothesis

By **Jocelyn Kaiser**

For researchers trying to untangle the roots of the current epidemic of asthma, one observation is especially intriguing: Children who grow up on dairy farms are much less likely than the average child to develop the respiratory disease. Now, a European team studying mice has homed in on a possible explanation: Bits of bacteria found in farm dust trigger an inflammatory response in the animals' lungs that later protects them from asthma. An enzyme involved in this defense is sometimes disabled in people with asthma, suggesting that treatments inspired by this molecule could ward off the condition in people.

The study, published on page 1106, offers new support for the so-called hygiene hypothesis, a 26-year-old idea that posits that our modern zeal for cleanliness and widespread use of antibiotics have purged the environment of microorganisms that once taught a child's developing immune system not to overreact to foreign substances. "This gives us a tantalizing molecular mechanism for understanding the epidemiological evidence," says pediatric immunologist Stuart Turvey of the University of British Columbia in Vancouver, Canada, who was not involved with the new work. But others caution that the finding is probably far from the only explanation for why early exposure to microbes can make kids less allergy-prone.

About 20 studies in Europe and elsewhere have found that children raised on farms have relatively low rates of allergies and asthma. Some researchers suspect a key reason is that the kids breathe in air full of molecules from the cell wall of certain bacteria, called lipopolysaccharides for their fat-sugar structure. Also known as endotoxins, these fragments—from dying bacteria in cow manure and fodder—cause a temporary low state of inflammation in the lungs that somehow dampens the immune system's response to allergens, the thinking goes.

Pulmonologist Bart Lambrecht and immunologist Hamida Hammad of Ghent University and Flanders Institute for Biotechnology in Belgium and their collaborators wanted to probe the mechanism for endotoxins' protective effect. They first showed that injecting the molecules into the noses of 6- to 12-week-old mice every other day for 2 weeks protects the rodents from developing asthma later, in response to dust mites. In the endotoxin-exposed mice, the epithelial cells lining the lungs made lower levels of proinflammatory molecules called cytokines when they encountered the dust mites; the mice also had fewer dendritic cells, the immune sentinels activated by cytokines.

An enzyme made by the epithelial cells, called A20, seemed to play a role in reducing these inflammatory responses. In mice engineered to lack the gene for A20 in their lung epithelial cells, endotoxins did not protect the animals from asthma. The team got similar results when they repeated the mouse experiments with farm dust, which includes not just endotoxins but other potentially inflammatory fragments from bacteria, fungi, and plants as well.

The Ghent team then tested bronchial cells from healthy people and found that exposure to endotoxins lowers the levels of the same inflammatory molecules studied in the mice. The levels didn't drop as much in cells from people with asthma, and their cells also made less A20 protein. Finally, the researchers found that among nearly 500 farm children, those carrying a mutation that lowers A20 activity were five times more likely to develop asthma.

Until now, Lambrecht says, most explanations for the hygiene hypothesis assumed it acts directly on the immune system's T cells. The new finding shows that with endotoxins, "it's not happening in the immune system. It's in the structural cells of the airway," Lambrecht says. "We need this environmental exposure to cool down the epithelium so it knows what's dangerous and not dangerous." He points out that A20 plays a similar restraining role in the gut of a newborn, helping it tolerate the beneficial microbes that contribute to digesting food. The new study suggests that a drug that boosts A20's activity could help protect children with a family history of asthma from developing the disease, Lambrecht says. (Dosing children with endotoxins is risky because the mechanism is apparently finely tuned; large exposures promote asthma.)

Others who study the hygiene hypothesis caution that the newly uncovered mechanism does not entirely explain the protective effect of dairy farm life. Drinking unprocessed milk also seems to ward off asthma in kids, points out Gary Huffnagle of the University of Michigan, Ann Arbor—and that effect is unlikely to involve the lung epithelium. What's more, endotoxin levels are not that much higher on farms than in cities, suggesting "it's too simple an answer," says asthma genetics researcher William Cookson of Imperial College London, who thinks changes in living microbial communities in the lungs and gut may be just as important.

Harvard University immunologist Richard Blumberg would also like to see the Ghent team show that the protective response lasts from birth into adulthood—experiments that Lambrecht's group is now planning. For now, says Blumberg, the new study is "another important layer of our community's search to understand the biology behind the hygiene hypothesis." ■

PHOTO: © IMAGE SOURCE/CORBIS

Downloaded from www.sciencemag.org on September 5, 2015

Published by AAAS

REGENERATIVE MEDICINE

Trachea surgeon cleared of misconduct

Independent investigator had incomplete information, Karolinksa Institute says

By **Gretchen Vogel**

Some of the work of pioneering trachea surgeon Paolo Macchiarini may be flawed, but it doesn't constitute scientific misconduct. That is the conclusion of the Karolinska Institute in Stockholm, where Macchiarini is a visiting professor, after completing a second investigation of his studies.

Although Karolinska did say he acted "without due care" in some instances, Macchiarini says he feels vindicated by the decision, announced on 28 August by Karolinska Vice-Chancellor Anders Hamsten. "I and my team are not guilty of anything," he says. "The sense of innocence is prevailing." In May, an independent investigator had reported evidence of misconduct in seven papers, but Hamsten rejected that conclusion after Macchiarini and others submitted more than a thousand pages of additional documentation.

Karolinska hired Macchiarini in 2010 after he captured the media spotlight with a revolutionary solution for people with trachea damage due to cancer, injury, or birth defects. Macchiarini removed living cells from an organ-donor trachea and seeded it with a patient's own stem cells, which were supposed to grow into and over the scaffold to create a functional trachea. At Karolinska, he took the technique a step further: Three patients there received a fully artificial trachea consisting of a polymer scaffold seeded with stem cells.

Some scientists questioned whether the cells had grown as Macchiarini had hoped, however, and charged that his papers didn't fully describe the patients' fate (*Science*, 19 April 2013, p. 266). The first Karolinska patient survived for 2.5 years after the operation; the second died a few months after receiving his transplant, and the third has been in intensive care since receiving her transplant in August 2012.

In June 2014, trachea surgeon Pierre Delaere at UZ Leuven in Belgium filed a complaint with Karolinska, charging that Macchiarini's claim of regenerating tracheae was not possible. In June and August 2014, four physicians at Karolinska lodged complaints as well, documented with patient and lab records. Three were co-authors on Macchiarini's papers who felt he deceived them; they alleged that the papers failed to mention complications from the transplants, that medical records didn't support the positive descriptions of the grafts' development, and that Macchiarini didn't obtain proper ethical approval for the surgeries.



Critics say Paolo Macchiarini failed to mention complications from his artificial trachea transplant in scientific papers.

Delaere's complaint was handled by Karolinska's ethics council, which concluded in April that his issues were of a "philosophy-of-science kind rather than of a research-ethical kind," and found no evidence of misconduct. In response to the other complaints, the institute commissioned an inquiry by Bengt Gerdin, a professor emeritus of surgery at Uppsala University in Sweden.

In May, Gerdin concluded that there were significant discrepancies between available medical records and the published results, and that these constituted misconduct. He also said there were serious questions about the ethical permission for the surgeries. Swedish prosecutors are still investigating those charges.

But Hamsten says Macchiarini's rebuttal, as well as additional testimony by doctors outside Sweden who had treated some of the patients, have convinced him that Gerdin's conclusion was wrong. "From the university side, we are very impressed with the meticulousness and structure of Gerdin's report," Hamsten says. "But he did not at that point in time have all the relevant information." Much of the additional information is not public because of patient confidentiality rules.

Gerdin says that he hasn't yet read the new documents, but that Macchiarini and Karolinska should have made them available during his investigation, not afterward. "It's a meaningless process" to commission an independent review if the final decision is based on documents available only to Karolinska officials, Gerdin says. Macchiarini says he didn't have access to all of the material at the time and assumed that Gerdin would track it down himself.

Hamsten acknowledges that Macchiarini should have had all of the data available at Karolinska. "Good research practice requires that all the documentation should be assembled in one place," he says. That is one reason that Macchiarini's work "does not meet the university's high quality standards in every respect," Hamsten says. Karolinska will ask Macchiarini to submit errata on several of the papers in question; Macchiarini says he doesn't think errata are necessary, but that the final decision is up to the journals involved.

Macchiarini still hopes to develop his technique further, but a trial at the University Hospital of Krasnodar in Russia is on hold after nine patients received a transplant. "We are trying to improve the technology," he says. Harvard Apparatus Regenerative Technology, the Massachusetts company that helped develop the scaffolds used in the Karolinska transplants, says it stopped working with Macchiarini in 2014. It plans to launch a clinical trial of a second-generation scaffold with U.S.-based collaborators in 2016. ■

PHOTO: © ITAR-TASS PHOTO AGENCY/ALAMY

Downloaded from www.sciencemag.org on September 5, 2015

Published by AAAS

SCIENTIFIC PUBLISHING

PubPeer co-founder reveals identity—and new plans

Neuroscientist Brandon Stell wants to raise funds to expand postpublication critiques

By **Jennifer Couzin-Frankel**

After 3 years in the shadows, the anonymous founder of a popular and controversial website that allows users to critique published research revealed himself this week. "I'm a bit nervous … I wouldn't call myself a risk-taker," admits Brandon Stell, a 41-year-old neuroscientist and the main force behind PubPeer. The site has become an influential outlet for identifying flawed, and sometimes fraudulent, studies, but it has also drawn criticism—and a lawsuit—from researchers who say they've been maligned by anonymous comments posted there.

Stell, an American who co-leads a brain physiology team at Paris Descartes University (PDU), went public with a 31 August announcement on PubPeer. Joining him in the limelight are two friends who have acted as counselors: Boris Barbour, a neuroscientist in Paris and a running buddy of Stell's who contributes regularly to PubPeer, and Gabor Brasnjo, who was in graduate school with Stell and is now a patent attorney in San Francisco, California (but will be involved in PubPeer in a nonlegal capacity).

Two other PubPeer founders are brothers Richard and George Smith. Stell says Richard Smith worked with him in Paris for several months as a graduate student. George Smith is a web developer who built the site and handles its technical elements. The Smith brothers shared no other identifying information, and in a conversation and email exchange with *Science*, Richard Smith explained that he believes PubPeer "shouldn't be about any one scientist," but that he's excited about PubPeer's next chapter.

The founders, Barbour, and Brasnjo are publicly joining forces because they want to raise money for The PubPeer Foundation, which was quietly registered in California this past December. They couldn't register a nonprofit with no names attached, Stell says, so had to make a choice. He says the foundation will aim to encourage postpublication peer review, improve PubPeer's transparency, and enhance the site.

Stell says PubPeer was inspired by the freewheeling paper critique groups he attended as an undergraduate. Brasnjo, who was a year ahead of Stell in graduate school, says the two often discussed the idea that a paper's publication was just the beginning of its scholarly life. "The real significance of it takes shape over time," Brasnjo says, "as people have lab meetings, discuss the paper, consider the findings … [do] follow-on experiments."

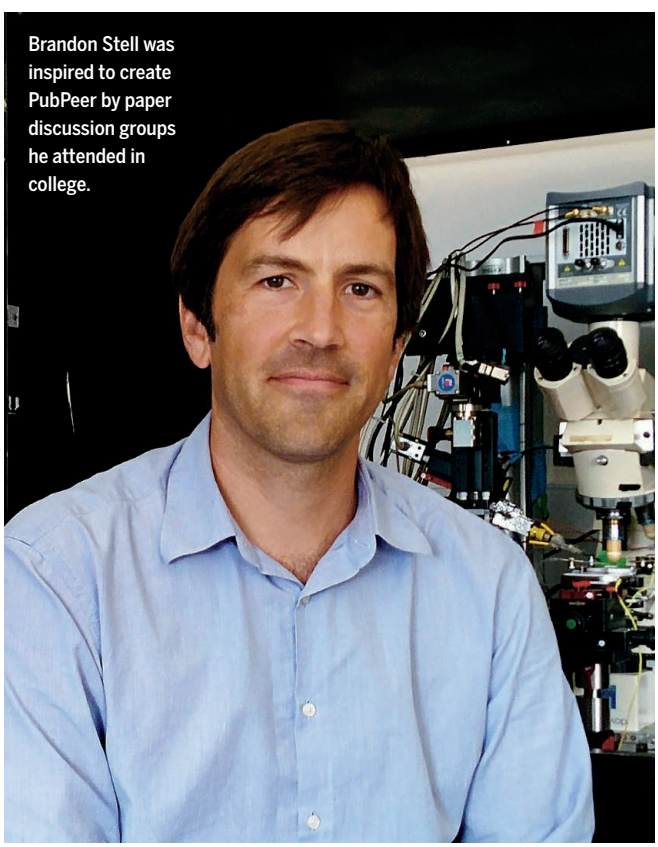
PubPeer is designed to facilitate that discussion. It allows users to post under their names or anonymously; it currently holds some 35,000 comments. The site's popularity—it gets more than 300,000 page views a month—suggests that PubPeer has tapped into a hunger for candid conversation about published research.

The site has also become known as a place to flag problems. By identifying anomalies, commenters have prompted numerous paper corrections and retractions. But they've also attracted the ire of scientists who say they've been unfairly smeared by anonymous postings. Last year, a cancer researcher at Wayne State University in Detroit, Michigan, filed suit against some anonymous users, alleging that their negative comments cost him a job offer. PubPeer's lawyers are currently appealing a judge's order to hand over information on one anonymous commenter.

Researchers who know Stell say they're not startled to learn that PubPeer, which launched in late 2012, is his baby. "He's a surprising character all around," says fisheries biologist Chris Jordan, who taught Stell in the mid-1990s, when the neuroscientist was an undergraduate at the University of Colorado, Boulder. Even then, Stell nurtured "a pretty deeply held belief about scientific integrity … about wanting to either hold everybody accountable, or have the community hold [itself] accountable," says Jordan, who now works for the National Oceanic and Atmospheric Administration in Corvallis, Oregon.

"I think ethics may be a part of" Stell's motivation for creating PubPeer, agrees Isabel Llano, who, like Stell, is a researcher with France's National Center for Scientific Research, and heads the PDU research unit that includes Stell's team. "If knowledge is not transmitted directly and with real honesty, then there is not a basis for science. … This is his way of reacting, of saying: 'OK, I will do something about this.'"

Stell, who says he has not posted comments on PubPeer and won't do so in the future, believes he'll now be freer to engage in public debates about scientific integrity and postpublication review. That's a far cry from 2 years ago, when he declined to identify himself when being interviewed for a *Science* story about PubPeer (*Science*, 9 August 2013, p. 606). He used a temporary phone number and an anonymous email. He didn't want PubPeer "to impact my scientific life or my personal life," he said at the time. But he also conceded that it was "going to be very hard to stay anonymous forever." ■



Brandon Stell was inspired to create PubPeer by paper discussion groups he attended in college.

PHOTO: FEDERICO TRIGO

Downloaded from www.sciencemag.org on September 5, 2015

Published by AAAS



PHOTO: NEIL PALMER/CIAT/FLICKR

As part of its Two Degrees Up project, CGIAR's International Center for Tropical Agriculture examined the impact of climate change on agriculture in the Mount Kenya region.

FOOD SECURITY

Global agricultural research network is overhauled again

CGIAR looks for antidote to tapering funds, internal woes

By **Dennis Normile**

A key guardian of global food security is looking shaky. Funding for the Consultative Group on International Agricultural Research (CGIAR), the world's premier group of agricultural research centers, is sagging in the global economic downturn. Its flagship backer—the World Bank—threatened to pull the plug on its contributions. And now CGIAR is about to undergo internal convulsions: It's reorganizing for the second time in just 5 years.

Backers say the move will give CGIAR a more coherent strategy and make the most of available funding. Critics are dubious. Such "endless reorganization" suggests "you are not identifying the main problems," says Robert Zeigler, director-general of the International Rice Research Institute (IRRI) in Los Baños, the Philippines, a CGIAR center. He thinks greater effort should go into securing stable funding and prioritizing research.

CGIAR traces its origins to two institutes founded in the 1960s: the International Maize and Wheat Improvement Center in El Batán, Mexico, and IRRI. Both were major players in developing the crop varieties key to the Green Revolution, which enabled developing countries to feed their burgeoning populations. CGIAR centers proliferated, and by the early 2000s there were 15 of them working in areas as varied as livestock, marine resources, and arid land crops. But efforts overlapped and there was little coordination. And money grew scarcer, as donors—primarily aid agencies in developed countries—emphasized other concerns such as the environment and gender issues.

In 2010, CGIAR embarked on a reboot. While maintaining their independence, the institutes formed a consortium to foster collaboration, set priorities, and evaluate results. One objective "was to get the centers to work more effectively together, and that has worked well," says Jimmy Smith, director-general of the International Livestock Research Institute in Nairobi. He and others point to the consortium's collaborative projects, such as the Global Rice Science Partnership, in which three CGIAR centers and three national labs study rice genes that affect yield and tolerance of adverse conditions. Donors responded favorably: CGIAR's funding shot up from $531 million in 2008 to $1.057 billion in 2014.

Under the realignment, donor countries and foundations formed a seperate group, the CGIAR Fund, to develop long-term funding. The separation was intended to allow researchers and funders to concentrate on what each does best (*Science*, 4 February 2011, p. 522). But the split made it harder for center managers to keep in touch with donors, leading to funding uncertainties that complicate planning, Smith says. Evaluating the reform last year, a panel chaired by John Beddington, former chief science adviser to the U.K. government, concluded that ambiguities in roles and responsibilities have hindered setting consistent strategies, planning, and decision-making. The panel strongly recommended merging the constituents back into a single CGIAR system.

In April, the CGIAR Fund Council agreed and ordered up a transition plan, which it is slated to approve this month. "There is a huge amount of evidence" supporting the move to a single organization, says Jonathan Wadsworth, executive secretary of the CGIAR Fund. By the end of 2016, a new board will set a research strategy and approve the next round of collaborative research projects.

The board must confront a gloomy financial picture. Contributions are slipping this year to between $975 million and $990 million, Wadsworth says. CGIAR narrowly escaped a bigger hit. The World Bank quietly told officials early this year that it intended to phase out the $50 million in annual support it had provided for years. The bank never publicized its decision or the reasons behind it, "but everybody in the community knew about it," says Peter McPherson, president of the Association of Public and Land-grant Universities in Washington, D.C., and a long-time CGIAR supporter. He and others drafted a letter signed by 46 organizations to World Bank President Jim Yong Kim and U.S. Treasury Secretary Jacob Lew urging the bank to continue its support. "The role played by CGIAR is too critical to the future of the world's food supply to ignore," they wrote. Two members of the U.S. Senate's agricultural committee, Pat Roberts (R–KS) and Debbie Stabenow (D–MI), sent their own letter to Lew expressing concern about the cuts.

That support apparently rescued CGIAR's World Bank lifeline. A spokesperson confirmed in an email to *Science* that the bank will provide $30 million to CGIAR in 2016 and that it "is pursuing additional funding options." Wadsworth is grateful, but he notes that global agricultural research "is still tremendously underfunded."

Zeigler, for one, worries that CGIAR's latest overhaul will be an unwelcome distraction as it grapples with a harsh fundraising environment. "We're burning up another year to 2 years in a reorganization," he says, when the time and effort would be better spent shoring up CGIAR's finances and making tough decisions about which programs deserve the precious support. ■

Downloaded from www.sciencemag.org on September 5, 2015

Published by AAAS



UNSANCTIONED SCIENCE

Despite penury and isolation, Iran's scientists have pursued an ambitious agenda. If sanctions end, research will blossom

By **Richard Stone**, *in Tehran*

Not far from Qazvin, an ancient Persian capital known for fine calligraphy, a new monument to learning will soon be built. If all goes well, construction of Iran's first synchrotron, a source of brilliant x-ray light for studies of everything from biological molecules to advanced materials, will begin in 2018. The $300 million Iranian Light Source Facility (ILSF) is the country's biggest basic science project ever—and expectations are high inside and outside the Islamic republic. The synchrotron "will offer Iran the potential to do world-class science," says David Attwood, an applied physicist at the University of California, Berkeley, who visited the ILSF's office in Tehran last year.

The project is a testament to the country's determination to do science in spite of turmoil, political interference, and the viselike grip of economic sanctions imposed by the United States and its allies to block Iran's suspected effort to develop nuclear weapons. The sanctions largely prohibit high-tech exports to Iran and bar U.S. scientists from conducting research in Iran—or even providing advice—without a license from the U.S. Department of the Treasury. They prevent computers in Iran from downloading most scientific software, and the nation's disconnection from the international banking system makes it virtually impossible for Iranians to subscribe to overseas journals.

ONLINE

For more on Iran, see http://scim.ag/sciiran

Yet Iran's synchrotron builders have pushed ahead. They have smuggled essential parts, built what they could not buy, and done without whenever possible. "Failure is not an option," says Javad Rahighi, a nuclear physicist and the ILSF's director. Animated by the same spirit, an array of other homegrown initiatives has flourished, despite the sanctions, in areas ranging from seismology to stem cell research. The result is a surprisingly robust scientific enterprise, as was evident when the Iranian government recently granted *Science* rare access to select facilities and researchers.

Iran's pariah status may soon be ending. In July, Iran and world powers signed a deal that should limit Iran's nuclear program and block its pathways toward a nuclear weapon in exchange for relief from economic sanctions. So long as U.S. and Iranian domestic politics don't interfere, implementation will begin by year's end.

Until sanctions are lifted, Western science engagement with Iran will proceed haltingly. But the pas de deux with the West is already underway. An Iranian delegation was in Vienna in July, striking agreements for joint research with the U.N. Industrial Development Organization and

PHOTO: BABAK TAFRESHI/THE WORLD AT NIGHT

Downloaded from www.sciencemag.org on September 5, 2015

Published by AAAS



Iran is gearing up to build a national astronomy observatory with a 3.4-meter telescope here on the summit of Mount Gargash in central Iran.

other international partners. And earlier this summer, a group of U.S. university officials led by Allan Goodman, president of the Institute of International Education in New York City, traveled to Iran to assess where the United States and Iran might forge scientific ties. "We got a pretty consistent message that their science is alive and well," Goodman says.

THAT IS A TRIUMPH over the country's recent history, which is still on vivid display. At Behesht-e Zahra cemetery on the southern outskirts of Tehran, row upon row of graves, many marked by simple concrete slabs, stretch to the horizon. A vast section of the cemetery, one of the world's largest, is set aside for the troops—many of them teenage boys—who died during the Iran-Iraq War, a World War I–style conflict featuring trench warfare and poison gas attacks that lasted from 1980 to 1988. Images of the martyrs, as they are called, adorn bridges, billboards, and facades—a constant reminder of the hard years in the wake of the 1979 revolution that toppled the shah. The iconography "was an eye-opener for us," Goodman says. "We completely underestimated the profound effect that it's still having on Iranians."

For 3 years in the early 1980s, all Iranian universities were shuttered. Most able-bodied men were mobilized for the war—spurring a catastrophic brain drain. After the war was over, academia slowly clawed its way out of the abyss. Iran moved aggressively to bolster its higher education system, opening scores of new universities; student enrollment skyrocketed. As part of that revival, Sharif University of Technology (SUT) in Tehran launched the nation's first Ph.D. program, in physics. The government, meanwhile, started rolling out mission-oriented research centers, including one in Tehran for seismic risk now called the International Institute of Earthquake Engineering and Seismology (IIEES).



"We're entering the post-sanctions era," says Iran's deputy science minister Vahid Ahmadi. He's counting on Iran's diaspora to help his country's scientific community connect with the rest of the world.

Seeking its own brand of postrevolution science, Iran's Supreme Council of the Cultural Revolution, established in the early 1980s to ensure that universities adhered to Islamic thought, launched Jihad-e Daneshgahi. Known in English as the Academic Center for Education, Culture and Research (ACECR), it aims to yoke science to societal needs. The center has funded practical efforts such as building high-voltage transmission lines and securing oil drilling equipment, and it teamed up with engineers in the city of Isfahan to make drones for Iran's military.

PHOTO: EBRAHIM MIRMALEK

Published by AAAS



More improbably, ACECR has notched up an achievement in basic research. In 1991, it founded the Royan Institute in Tehran to help infertile Iranians, who until then had to travel abroad for treatment. (Royan is Farsi for "embryo" and "ever-growing.") The institute has since become a heavyweight in stem cell research, publishing hundreds of papers and scoring successes in animal cloning despite Iran's isolation.

On a grander scale, The Supreme Council aspired to set the pace for science in the Middle East. Its National Master Plan for Science and Education, released in 2011, lists as one objective "bolstering the promotion of science and technology in the Islamic world." According to the plan, the "revival of the great Islamic civilization" is "contingent upon all-out progress in science." The council set up an Islamic World Science Citation Center in Tehran in 2004, and it promoted Persian as an international scientific language. It even attempted to create an Islamic Internet.

By the early 2000s, Iran was thinking big in basic science, with planning underway for the ILSF and a world-class astronomical observatory (see sidebar, p. 1042). But the science push faced long odds. Iran was hemorrhaging talent, with many top students and scholars going abroad—and staying abroad. And science spending couldn't keep pace with the lofty ambitions. Although the official government target for science spending is 3% of gross domestic product, the reality is closer to 0.5%, which in 2014 amounted to $1.75 billion, says Vahid Ahmadi, Iran's deputy science minister and a specialist in optoelectronics. The science ministry, he says, controls only about 27% of that budget, he says. And that small pie is sliced thinly: Last year, SUT's research budget was only a few hundred thousand dollars, says Jawad Salehi, a professor of electrical engineering there. "90% of our papers are intellectual ideas. We don't have the budget to make prototypes," says Salehi, who worked for 10 years at Bellcore in Morristown, New Jersey. Compounding woes, take-home pay for scientists has withered because of the country's dire economic straits.

Faced with such penury, the scientific community was aghast in 2012 when the government of Mahmoud Ahmadinejad, a religious hardliner who served as Iran's president from 2005 to 2013, picked 40 projects for lavish support that over several years would amount to the science ministry's entire annual budget. "Most of those projects are suspect and would never pass real review," says a senior scientist in Tehran. Many awards went to political cronies of Ahmadinejad, critics contend.



But the biggest blow was the one Iran's government provoked from the world community. In 2002, Iranian dissidents revealed the existence of a secret uranium enrichment facility in Natanz. More revelations followed, prompting the United States and the United Nations to ratchet up sanctions. Stoking tensions, former U.S. President George W. Bush anointed Iran a member of his "axis of evil," whereas Ahmadinejad labeled the Holocaust a "myth" and Israel a cancer cell "that must be removed from the body."

AS THE PROHIBITIONS ON IRAN multiplied, they snared scientists along with the broader economy. For example, no stone can be imported from or exported to Iran—a ban meant to crimp the construction industry. "No stone means no fossils," says Erfan Khosravi, a paleontologist at the University of Tehran. "We can't borrow fossils to compare specimens or send fossils abroad for analysis," he says. And because radionuclide exports to Iran are barred, he says, "we can't date specimens."

Nor can Iranian scientists readily publish in international journals. Some editors reject Iranian submissions outright, claiming, wrongly, that reviewing a manuscript with any Iranian author would contravene sanctions. (Sanctions do bar U.S. citizens from reviewing work by an author from an Iranian government entity, such as its nuclear organization.) A few

CREDITS: (MAP) C. SMITH/*SCIENCE*; (PHOTO) EBRAHIM MIRMALEK

Published by AAAS



A female scientist in the Royan Institute's andrology lab. Women comprise more than half of Iran's workforce in the biological sciences.

years ago, after SUT was singled out for sanctions, Elsevier severed its agreement to publish the university's top journal, *Scientia Iranica*.

"The sanctions became so brutal," says IIEES President Mohammad Kazem Jafari. For years, the seismologist notes, his institute imported seismic sensors from Canada, the United Kingdom, and the United States; the accelerometers are deployed at faults to warn of nascent earthquakes and to monitor shaking and structural integrity at bridges, dams, and other vital infrastructure. Earthquake-wracked Iran needs such data, but such devices can also be used to monitor nuclear tests. Around 2010, Iran could no longer import seismic sensors, "even for humanitarian purposes," Jafari says.

His solution? Institute engineers designed their own sensor. In his office at IIEES, below a hazard map of Iran in which the entire country is crisscrossed with thick red lines depicting high seismic risk, Jafari cradles his institute's HAT accelerometer, a heavy black device resembling a child-size bowler hat. HAT sensors have been deployed, for instance, at Bushehr Nuclear Power Plant and the Hirvy dam in Kermanshah province, and in systems that would shut off Tehran's natural gas lines after a major earthquake.

"If something stops us, we find our way around it," geneticist Massoud Houshmand says. "We are like a river finding a new way." At the sprawling campus of the National Institute for Genetic Engineering and Biotechnology, Houshmand leads a team that can now diagnose more than 300 rare mitochondrial diseases, including some unique to Iran. He chalks up his success to his 50 current and former students now overseas who help his Tehran team carry out experiments.

Similar ingenuity is keeping Iran's synchrotron project on track. When preparatory work for the ILSF began at the Institute for Research in Fundamental Sciences (IPM) in 2010, the ILSF group knew they would not be able to import a key component, an ultrastable power supply for the machine's electromagnets. So they set out to make their own. "People laughed at us," Rahighi says. Five years later, the homegrown device works better than comparable equipment at some operating synchrotrons, he says. "People aren't laughing anymore."

When homespun resourcefulness fails, however, Iranian scientists have been forced to pay jacked-up prices on the black market, where smuggled instrumentation usually comes without service agreements. After the Iran Polymer and Petrochemical Institute here managed to lay hands on a first-rate nuclear magnetic resonance machine, the German manufacturer had a stark warning. "They said, 'You can send your parts for repair, but we cannot guarantee that we can send them back,'" says Director Mehdi Nekoomanesh.

And needed materials are often slow to arrive. That's especially aggravating when scientists are racing peers in a fast-moving field such as stem cell research. "Many times we've been scooped" because of sanction-related delays in tying up experimental loose ends, says Royan Institute President Hamid Gourabi.

NOW, IRANIAN SCIENTISTS ARE HOPING that the nuclear pact will bring changes: an opening to the West, a more benign political environment, and an improving economy that will allow more generous science funding. "It's a new era for science in Iran," Ahmadi says hopefully. "We're entering the postsanctions era."

The nuclear agreement calls for converting the Fordow uranium enrichment facility into an international research center, and designates cooperation in areas as diverse as fusion, astrophysics, and radiomedicine. IPM particle physicist Shahin Rouhani, president of the Physics Society of Iran, says Fordow's underground lab could host detectors for cosmic dark matter particles, and for neutrinos beamed through Earth from CERN, the European organization for nuclear research near Geneva.

Iran's entire scientific enterprise should benefit from the thaw. "By reintroducing the Iranian community as intellectual equals in the international scientific community, cultural understanding develops and bridges are built," says Gerry Gilmore, an

Published by AAAS

An eye on the sky

By **Richard Stone**, *on Mount Gargash, Iran*

As the sun sets on an early August evening at this 3600-meter peak in central Iran, village lights shimmer in the distance and the temperature plummets. Alireza Behnam, a physicist, ducks into a cozy trailer parked at the site and heats water for tea. His immediate task on the mountain is to study the weather. His larger goal: help his country recapture some of its past astronomical glory.

A millennium ago, when Europe was in its Dark Ages, Persia and the rest of the Muslim world were dotted with observatories. Copernicus even drew on the meticulous records of planetary motion from the observatory at Maragheh in northwestern Iran for his proposal that Earth revolves around the sun. That astronomical tradition is due to resume next spring, not far from Behnam's trailer, as construction begins on the $30 million Iranian National Observatory (INO), a 3.4-meter optical telescope.

When completed in 4 or 5 years, it could be the best general-purpose telescope for thousands of kilometers, says Piero Salinari of the Arcetri Astrophysical Observatory in Florence, Italy. "INO has very good potential for becoming an important facility for astronomy in the world, not only in Iran," he adds. The telescope will study exoplanets and gamma ray bursts, hunt for dark matter, and probe galaxy formation. Although it is dwarfed by the largest instruments elsewhere, "an awful lot of state-of-the-art science is still being carried out with 2- to 4-meter telescopes," says Hendrik Hildebrandt, an astronomer at the Argelander Institute for Astronomy in Bonn, Germany.

The INO testifies to the persistence of Iran's tiny astronomy community in the face of shifting political winds. The push for an observatory began in the 1980s, when an Iranian-born philanthropist in Spain, inspired by the Isaac Newton Telescope at La Palma in the Canary Islands, offered to bankroll a similar facility in his homeland. The philanthropist "offered to bequeath his entire fortune to the University of Kerman, so long as it built an observatory," says INO Director Reza Mansouri, an astrophysicist at the Institute for Research in Fundamental Sciences (IPM) in Tehran. But Iran was at the tail end of a long, draining war with Iraq and did not grasp the opportunity.

A decade later, the National Research Council of Iran endorsed two big science projects: the observatory and a high-energy particle accelerator. But the INO soon went off the rails. Mahmoud Ahmadinejad, a religious hard-liner, was elected president in 2005, and his science minister took a dim view of the telescope project, Mansouri says.

Counting on a change of heart—or a change of minister—astronomers continued to lay the groundwork. Mountaintop instruments showed that the steadiness of the air above Mount Gargash—its "seeing"—is outstanding. According to the percentage of "super-seeing nights," says Arne Ardeberg, an astronomer at Lund University in Sweden, "it beats Mauna Kea," the peak in Hawaii that's home to some of the world's largest and best optical telescopes. In 2009, IPM Director Mohammad-Javad Larijani, whose family wields tremendous clout in Iran, wrote to the supreme leader, Seyyed Ali Khamenei, about the observatory's plight.



Two big assists this year may help Reza Mansouri complete his long quest for a world-class telescope in Iran.

Ten days later, the government authorized 70 billion rials (about $4 million at the time) for the INO—enough to order a primary mirror from Germany and have it polished in Finland. Engineers quickly began devising solutions to the challenges of the site: large temperature swings in the dry desert air, brutal winter conditions, and earthquakes. Because Iran is one big seismic zone, the INO's design team came up with platform supports that will be decoupled from the rock to minimize vibrations, Mansouri says. "That part of the construction is very delicate," he says.

When reformist President Hassan Rouhani took power in August 2013, the stars at last seemed to be aligned for the INO. But last summer, as design work was wrapping up and the primary mirror was being readied for its long journey by ship and truck to Iran, the INO got some dispiriting news. Even though Iran's parliament had approved another $1 million for the project, sanctions over Iran's nuclear program were biting, and the government's planning department refused to allocate the money. "It was such a discouraging moment. Our lowest point," Mansouri says.

This year saw two "absolutely critical" developments, he says. The first was a visit to Gargash by Iran's vice president for science and technology, Sorena Sattari. After returning to Tehran, Mansouri says, the vice president, a mechanical engineer by training, wrote an enthusiastic note to Rouhani, who then instructed the planning department to help the INO.

The second boost is from an improbable source: the United States. Last September, Alireza Shabani, an Iranian-American who is helping build a quantum computer at Google's Quantum Artificial Intelligence Lab in Mountain View, California, read a news report about the INO's dire straits. "I was very sad. I really wanted to find a way to make this project survive," Shabani says. After contacting Mansouri, he pledged to enlist the Iranian-American diaspora to the cause. In July, Shabani and two colleagues launched Biruni Inc., a foundation named after an ancient Persian scholar, to raise money for the observatory.

Transferring the money won't be easy, given U.S. sanctions. This month, Shabani says, he and a lawyer will make their case for an exemption to the Treasury Department rules. The nuclear detente with Iran should strengthen their case.

Mansouri hopes the INO will lead to other new relationships. Iran has perhaps 10 observational astronomers, he says; another 100 of Iranian origin work in the United States, and 50 or so in Europe. "If even 10% of them come back to work in Iran," Mansouri says, "it would make a big difference." But the view from Gargash won't be limited to Iranians. "This is a project that all astronomers can use." ■

PHOTO: © EBRAHIM MIRMALEK

Downloaded from www.sciencemag.org on September 5, 2015

Published by AAAS

astronomer at the University of Cambridge in the United Kingdom, who serves on the international oversight committee for Iran's national observatory.

In what many take as a promising omen, Ali Brivanlou, the Iranian-born head of the laboratory of molecular embryology at The Rockefeller University in New York City, is due to arrive in Tehran this week for a lecture tour hosted by the Royan Institute. He expects an "extremely emotional" homecoming. Brivanlou was among the first wave of researchers to derive human embryonic stem cells (hESCs), and he made the seminal discovery that all embryonic cells will develop into nerve cells unless they receive signals directing them otherwise. Brivanlou had declined previous invitations because of the tensions over Iran's nuclear program. But the agreement changed his mind—as did his respect for the science at Royan.

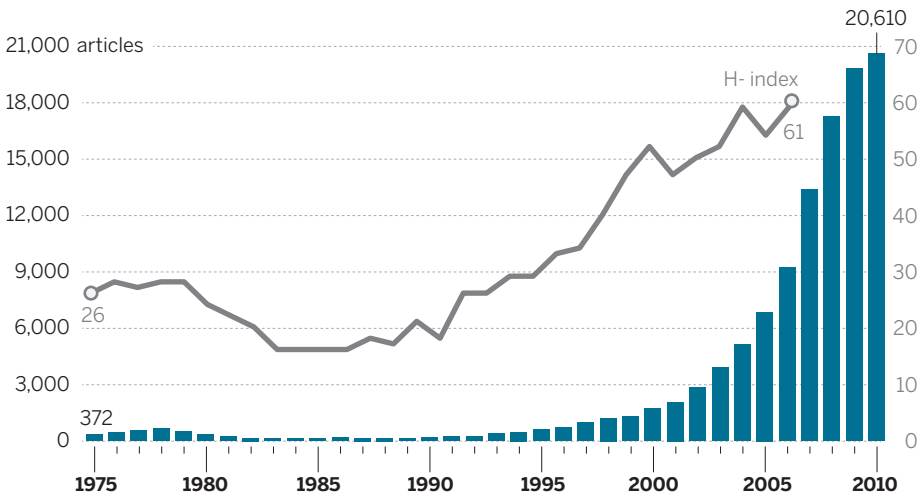
"Surprisingly, Iran has some of the most liberal laws on stem cell research in the world," Brivanlou says, thanks to a 2002 fatwa from Iran's Supreme Leader Seyyed Ali Khamenei declaring such research permissible under Islamic law. (Reproductive cloning in humans is out of bounds.) Royan established its first hESC line, Royan H1, in 2003 and has performed more than 40 clinical trials with stem cell transplantation.

Royan researchers were the first in the Middle East to succeed in somatic cell cloning—a lamb in 2006—and last month they scored another first when they cloned a mouflon, an endangered species of wild sheep. Royan is also a participant in the international Human Proteome Project: It is responsible for characterizing all of the proteins coded by the Y chromosome.

"We are a small flower," Royan Director Hossein Baharvand says of his institute, which is filled with female researchers. (Nationwide, about half of the scientific workforce is women.) Yet Brivanlou is impressed with what they have accomplished. "They're on par with Western European and U.S. labs," he says. "The papers they produce are extremely high quality." Still, Royan scientists are unable to perform many experiments that are routine in the West, says Rudolf Jaenisch, a stem cell researcher at the Whitehead Institute for Biomedical Research in Cambridge, Massachusetts, who visited Royan in 2007 and 2010. "It was sad to see the consequences of the embargo on their work."

A rising science power

Even while laboring under sanctions, Iran has aspired to set the pace for science in the Middle East. In journals indexed by the Web of Science, the articles from Iran are skyrocketing, as is its H-index, a metric for productivity and citation impact.



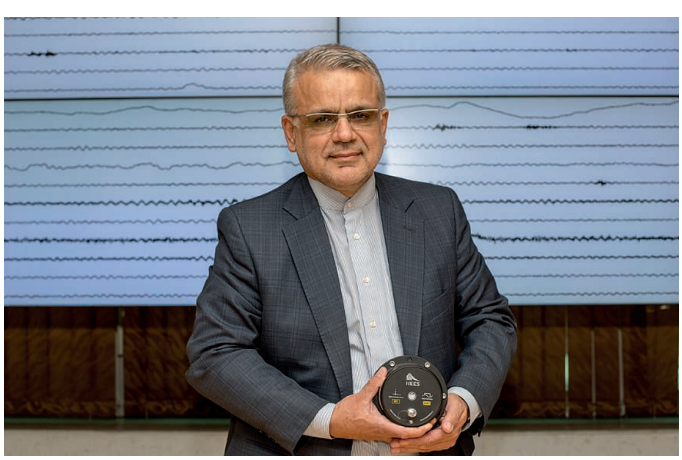
IRAN'S SCIENCE ESTABLISHMENT hopes that ties with Brivanlou and other Iranians who have made their mark abroad will help elevate research at home. "Policymakers are very keen to collaborate with overseas Iranian scientists and engineers," says Mohammad Abooyee, director of the National Research Institute for Science Policy in Tehran. The science ministry is stepping up efforts to sponsor overseas Iranians on short-term visits to Iran. And the government is drawing up plans for a more ambitious program to entice expats to accept permanent positions, Abooyee says. "It is time for them to come home."

To attract Iranians now working in the West, Iran will have to bolster both funding and academic freedom. Optimists see glimmers of progress on both fronts. This summer the government upped the budget of the National Elites Foundation, which hands out research grants to top scientists and enables elite science postgrads to spend 2 years on a research project in lieu of mandatory military service. And in October 2013, 3 months after being sworn in as Iran's president, Hassan Rouhani called on his nation's intelligence ministry to relax its scrutiny of academia "so all faculty members would feel safe to express themselves and participate in debates on campus."

"Resistance to change is deep rooted in our culture," says a senior science policy analyst in Iran. But "little by little," he says, "hardliners are being pushed to the side."

Rahighi returned to Iran in 1986—long before it was fashionable for expats to come home—after a stint in Europe using radioactive ion beams to study the nuclear reactions inside stars. He joined the Atomic Energy Organization of Iran, but says he bailed out of the nuclear program to head up the ILSF. "I've kept this project very transparent from the beginning," he says. That's good, says Attwood, who emphasizes that Iran "will need help to build this thing."

Rahighi is counting on it. The ISLF "will be a place where we can meet with the West," he says. He pictures his machine not just as an x-ray source—but also as a citadel of basic research in a transformed scientific landscape. ■



As sanctions tightened, Iran's seismology institute could no longer import seismic sensors. Director Mohammad Kazem Jafari cradles a homemade version.

CREDITS: (GRAPH) A. CUADRA/*SCIENCE*; (DATA SOURCE) S. KHARABAF *ET AL.*, *JOURNAL OF RESEARCH IN MEDICAL SCIENCES* **17**, 3 (MARCH 2012); (PHOTO) EBRAHIM MIRMALEK

Published by AAAS

SAVING IRAN'S GREAT SALT LAKE

Stopping Lake Urmia from turning into salt desert is the country's top environmental priority

By **Richard Stone**, *at Lake Urmia, Iran*



Lake Urmia's retreat has imperiled ecosystems and agriculture, and dislocated whole communities, in northwestern Iran.



PHOTOS: (LEFT TO RIGHT) ALESSANDRO MARONGIU/DEMOTIX; US DEPARTMENT OF THE INTERIOR/USGS (2)

In a wetland dying of thirst, Hossein Akhani, a botanist at the University of Tehran, mourns a verdant past. "Fifteen years ago, the lake was here," he says. "Every time I come back, the water is farther away."

Lake Urmia, in Iran's northwestern corner, was once the planet's sixth largest salt lake, covering about 5200 square kilometers—a bit larger than the Great Salt Lake in Utah. Flamingos, egrets, and other waterfowl feasted on brine shrimp, and resorts catered to tourists who believed that bathing in the saline waters improves health. But after gradually receding for years, the water body that the local Azeri people once revered as their "turquoise solitaire" shriveled last year to a mere 10% of its maximum. Salt lakes pulse like lungs, swelling during wet periods and contracting during the dry season. But Urmia's contraction at the end of 2014 was more like a death rattle.

"The crisis in Lake Urmia is clearly a disaster of hemispheric proportions," says Brad Marden, an ecologist at Great Salt Lake Artemia in Ogden, Utah. He is one of several U.S. experts who traveled to Tehran in March 2014 for a brainstorming session, sponsored by Iran's Environment Department and the United Nations Development Programme (UNDP), on how to rescue the lake. Like the Aral Sea, a better known vanishing salt lake in Central Asia, Lake Urmia is exposing a salt desert that generates noxious dust, threatening crops and people. Wildlife is vanishing, all the way down to its endemic brine shrimp, and recreation is also on the extinction list.

Some Iranian officials have tended to blame the weather—droughts and rising temperatures. But others concede that policy has had a major impact. Water management in the basin "has played the central role in the lake's demise," says Soroosh Sorooshian, director of the Center for Hydrometeorology and Remote Sensing at the University of California, Irvine. The three rivers that supply nearly 90% of the water flowing into Urmia have all been dammed for irrigation and hydropower. And groundwater recharge to those rivers has tapered thanks to an estimated 40,000 illegal wells that have lowered the water table, Iranian experts say.

A cure will be neither cheap nor easy. President Hassan Rouhani's government plans to spend about $6 billion over the next decade on Urmia's revival—the largest environmental project in the country. In 2015, his cabinet approved $660 million for 88 projects, most targeting better irrigation systems and other infrastructure. Other measures will follow, including water conservation, walling off and protecting arms of the lake to provide havens for wildlife, and steps to combat desertification. Still, more needs to be done, Akhani says. "Almost nothing is being spent on research and ecological restoration," he says, or on paying villagers to quit destructive practices like grazing and mining near the lake. And whether Urmia can still be saved remains "the million-dollar question," Sorooshian says.





By 2014, Urmia had shriveled to a mere 10% of its maximum.

NEAR THE LAKE'S eastern edge, birds steer clear of a former wetland, now a blinding expanse of salt. Crunching across salt-crusted soil, Akhani heads to a still-moist area where clumps of sedges are making their last stand. He crouches and points out a few kinds of halophytes, or salt-loving plants. Then his eyes light up. "There it is!" he exclaims. "This plant changed my life." As a student in 1986, he found this rare halophyte, *Microcnemum coralloides*, in a salt marsh near his hometown of Arak—a discovery that set him on a lifelong pursuit of halophytes. The marsh in Arak dried up, taking *M. coralloides* with it, but 8 years ago, Akhani happened on this population. Now, he says, "this plant has no future here." He presses a sprig between sheets of paper, preserving it for study in Tehran.

Just to the west of Rahmanlu, a former port and resort on the former eastern shore, is one culprit in the lake's decline: breathtaking fields of sunflowers. Before the 1979 revolution, the region grew grapes and made wine. After Iran became an Islamic republic, wine was forbidden. Farmers turned to thirstier crops, including sunflowers, wheat, apples, and sugar beets; to slake that thirst, authorities dammed local rivers for irrigation. Water-intensive crops

Published by AAAS

just 6% of the country. Chief culprits are forest conversion to cropland, logging, urbanization, and holiday villas. Wildfires have taken a heavy toll in recent years, especially in the Zagros Mountains and in Golestan National Park, Iran's first biosphere reserve and home to almost 20% of Iran's plant species. And a few years ago, Zagros oaks—which account for almost half of Iran's remaining forest cover—began succumbing to a fatal fungal pathogen, *Biscogniauxia mediterranea*, which causes a malady called charcoal disease. Meanwhile, Iran's Environment Department is attempting to block construction of two dams: Shafarud Dam in Gilan province, which would flood vast swathes of Hyrcanian relict forest, assemblages of tree species such as the Persian ironwood near the Caspian Sea; and Khersan-3 Dam in Chaharmahal and Bakhtiari province, which would submerge 2400 hectares of Zagros oaks.

A CHEETAH RACES EXTINCTION

Asiatic cheetahs once ranged from the Arabian Peninsula to India. Today, the critically endangered subspecies is making its last stand on the arid plains of central Iran. Fewer than 100 are left, Lewis says. Over the past decade, Iran's Environment Department, UNDP, and others have been working together to try to save the predator through the Conservation of Asiatic Cheetah Project. The project aims to crack down on poaching while curbing livestock grazing to restore cheetah habitat and boost the numbers of its prey, including the Jebeer gazelle and wild sheep. Project leaders say they want to balance habitat preservation with the needs of local villagers.

The hope is that the cheetah won't go the way of another big cat, the Persian tiger. This close cousin of the Siberian tiger went extinct in Iran 40 years ago. "The decline in the number of these beautiful animals may have stopped," Lewis says. Camera traps show an increase of cubs, and a survey is underway to get a better handle on numbers. Although the animal's fate still hangs in the balance, Lewis says, "I strongly believe that it is not too late to save the Asiatic cheetah." ■

PHOTO: R. STONE/*SCIENCE*



At the northern end of Lake Urmia, Sirous Ebrahimi and his team are watering sand dunes with a bacterial medium that is meant to both stimulate plant growth and form a crust that stabilizes the dunes.

"quadrupled, if not more, water consumption in the region," Sorooshian says.

As the lake receded, winds blew salt onto the surrounding agricultural lands, poisoning the soil. "With agriculture under threat, livelihoods come under threat," says Gary Lewis, who represents UNDP in Iran and is the top U.N. official in the country. "As the sea has dried out, people moved away in the hundreds of thousands." (The same scenario played out at the dying Aral Sea in nearby Central Asia.)

To avoid a human and ecological crisis, Iranians "have to go after low-hanging fruits," such as stemming the diversion of water flowing naturally to the lake, Sorooshian says. Improved irrigation practices could reduce water use by 45% nationwide, easing demands on the lake's tributaries, says Masoud Tajrishy, vice president of research at the Sharif University of Technology in Tehran, which is implementing some of the restoration effort. A tougher task, he says, will be weaning farmers off water-intensive crops.

Equally tough will be deciding what to do about a 15-kilometer-long causeway built 20 years ago across a narrowing in the middle of Lake Urmia. Today, the causeway separates mostly dry lakebed to the south from a relict lake that resembles the Arctic Ocean—cerulean water dotted with what look like ice floes but are in fact islands of salt. "Interrupting the natural circulation had to have an impact" on the lake's resilience, Sorooshian says.

Yet to prevent desertification from taking over the entire lake, engineers are contemplating further barriers to seal off its salvageable arms. Brine shrimp could be revived inside the embayments, possibly attracting back waterfowl. The strategy has been in use for a century at the Great Salt Lake in Utah. Akhani and other ecologists vehemently oppose partitioning, however. "We have experienced the impact of the causeway," he says. "We have a saying in Farsi: 'A wise man does not fall in a well twice.'"

At the northern end of Lake Urmia, a man in a straw hat is trying a smaller scale remedy. He is watering a sand dune with a garden hose. Sirous Ebrahimi, an environmental biotechnologist at the Sahand University of Technology in Tabriz, takes a break from this seemingly Sisyphean task to explain. He's spraying a bacterial medium that is meant to stimulate plant growth; it also forms a crust that stabilizes the dune.

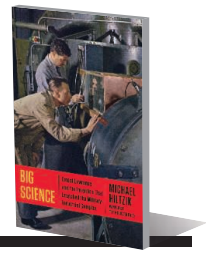
Ebrahimi's effort is one of five pilot projects on dune stabilization that are vying for a sizable share of the Urmia restoration funds. Kiumars Pourjebeli, a horticulturist in Jebel village, plucks small purple berries from a bushy plant, *Nitraria schoberi*, clinging to a dune. He is planting the seeds near other, naked dunes. "I'm trying to accelerate the natural process," he says. He offers a berry: "Taste it." It's very salty.

In June, Sorooshian brought over a group of 10 Iranian scientists and water managers for a whirlwind tour of three saline California lakes—the Salton Sea, Mono Lake, and Owens Lake—and the Great Salt Lake. The purpose was to show them "what experiences we have gone through in the western United States. … Not to say, 'Hey, this is what you have to do,'" says Sorooshian, who is an Iranian-American. He, for one, is not ready to write Urmia's epitaph. "I'm optimistic," he says. "But we don't have much time." ■

Published by AAAS

Enzyme sensitizes plants to TNT pollution *p. 1052*

The complicated legacy of Ernest Lawrence *p. 1062* ▸



PERSPECTIVES

SUSTAINABILITY

Sustainable development agenda: 2030

Building knowledge-based societies is key to transformative technologies

By **William Colglazier**

On 25 to 27 September, United Nations member states will formally adopt the Sustainable Development Goals (SDGs) as key elements of the post-2015 development agenda (*1*), successors to the eight Millennium Development Goals (MDGs) that focused attention from 2000 to 2015. The final 2030 agenda text for adoption proposes 17 SDGs with 169 targets, to be supplemented in 2016 with numerous indicators. All of the text emphasizing science, technology, and innovation (STI) is most welcome but achieving desired outcomes by 2030 will require deep understanding of how to maximize the contributions of STI. Having had the privilege of addressing this topic to the UN High-Level Political Forum (HLPF) that will oversee the SDG effort, I discuss areas that I believe are essential to success. I focus on three issues: (i) using the Global Sustainable Development Report (GSDR) process to bridge SDGs and scientific communities, (ii) choosing targets, indicators, and roadmaps related to STI, and (iii) the imperative of building knowledge-based societies.

POLICY

BRIDGE SCIENCE AND SDGs. Science can contribute to achieving the SDGs in four general areas: what science can say about (i) challenges, (ii) actions that can make a difference, (iii) monitoring progress, and (iv) innovative solutions (see the photos). Preparatory materials for the UN Summit include an important document, the 2015 GSDR, prepared by UN staff and agencies to highlight and strengthen the "science-policy interface" (*2*). The 2015 GSDR, to be a forerunner of future editions, highlights an integrative perspective; linkages among SDGs;



Milk chiller for farmers. In Motur, Tamil Nadu, India, Promethean Power System's Rapid Milk Chiller chills milk instantly to 4°C (39°F), uses a thermal battery instead of diesel fuel, and can chill up to 1000 liters of milk per day in areas with intermittent grid power. Sorin Grama, cofounder of Promethean Power, and Karthik Chandrasekar of Sangam, an investor, are testing the first of more than 100 milk chillers placed in rural India.

PHOTO: NATIONAL INSTRUMENTS

Downloaded from www.sciencemag.org on September 5, 2015

Published by AAAS

and cross-cutting issues, such as disaster risk reduction and new data approaches for monitoring. The report also illustrates the value of in-depth assessments, e.g., a chapter on oceans with links to health and human welfare.

The focus on an integrative perspective and interconnected system of SDGs should continue in future versions of the GSDR. However, incorporating STI will require in-depth assessment of what science can contribute to each SDG, combined with periodic evaluation of progress. Chapter 5 on "Economic growth, inclusive and sustainable industrial development, and sustainable consumption and production" in the 2015 GSDR is a good start on analysis for SDG 8 (sustainable economic growth) and SDG 9 (industrialization and innovation).

The GSDR process could remain a platform for ongoing interaction between scientists and policy-makers, which would help the HLPF develop a robust "science advisory ecosystem." This ecosystem should include soliciting advice and insights from individuals and institutions, both within and beyond the UN and its member governments. More and better mechanisms are needed to capture relevant insights from civil society's institutions and the public (e.g., commission independent studies, sponsor workshops, seek crowd-sourced input).

The HLPF might consider having draft GSDR chapters crowd-sourced from respected scientific institutions at the international and national level. The UN could ask them to use their own resources and peer-review processes to produce draft chapters for the GSDR on particular issues where they have great expertise. The UN might also ask countries to prepare their own national sustainable development reports (as China has done) (*3*). Governments could ask their independent scientific institutions, such as national academies, to produce such reports. Through this process, countries will learn from each other and provide valuable input for the GSDR. The Secretary General's Scientific Advisory Board could be asked to review all input from countries and scientific institutions and to advise UN staff on how best to strengthen draft chapters and knit them together into an authoritative GSDR.

The UN should avoid making the GSDR a "one-off" exercise with people only paying attention episodically. The GSDR with its successor editions can be a learning process for countries, the scientific community, and the UN, as well as a tool for reaching out to the wider public. Implementation recommendations regarding STI for SDGs made by the Addis Ababa Action Agenda (*4*) have been adopted in the 2030 agenda, creating the Technology Facilitation Mechanism (*5*).



PHOTO: KICKSTART

Pumping for irrigation. In 2014, Beatrice Wangari Ndichu, of Kiambum, Kenya, irrigates crops with the KickStart MoneyMaker pump to lift her family from poverty. KickStart tracks the success of its pump.

This includes a new UN interagency task team, a collaborative multistakeholder forum, and an online platform—all focused on STI for SDGs. These recommendations can be integrated with the GSDR process.

The GSDR series can be useful to keep the world engaged for making progress on the SDGs. It can strengthen the science-policy interface in every country, as well as at the UN. It can help every country focus on becoming a knowledge-based society where science informs important policy decisions.

TARGETS, INDICATORS, ROADMAPS. The aspirational SDGs encompass almost every issue that can be considered relevant to sustainable development, which is both the strength and weakness of the 2030 agenda. An initial step could be to develop roadmaps for each of the 17 SDGs as plans to stimulate appropriate actions so as to achieve desired outcomes at national and international levels. Because of linkages among SDGs, each roadmap will need to take into account interdependences and trade-offs.

Each government in the 2030 agenda sets its own national targets; thus, roadmaps will first need to be developed at the national level. The task at the international level becomes how to be most helpful to countries so they can benefit from each other's experiences and knowledge. The GSDR effort and the Technology Facilitation Mechanism can become useful for advising countries on roadmaps, including providing examples for countries in special situations.

The targets for some SDGs are stronger than for others. The best, such as for SDG 3 on health, highlight relevant issues and provide a detailed guide for concrete action. Others are so general as to be less useful for stimulating focused, effective actions. Producing a detailed action plan for achieving each SDG will require deeper analysis and integration. The current targets are useful but do not encompass all relevant considerations necessary for achieving their goals.

Contributions of STI for achieving each SDG are already important components of global efforts related to SDG 2 (hunger and food security), SDG 3 (health), SDG 6 (water), SDG 7 (energy), SDG 13 (climate change), SDG 14 (oceans), and SDG 15 (terrestrial ecosystems). Insights from the social sciences have been important, particularly for SDG 4 (education), SDG 5 (gender equality), and SDG 16 (peaceful and inclusive societies). Many indicators will likely be chosen from measures already developed by natural and social sciences.

Remaining goals related to economic growth and inclusive prosperity include SDG 1 (poverty), SDG 8 (sustainable economic growth), SDG 9 (industrialization and innovation), SDG 10 (inequality), and SDG 12 (sustainable consumption and production). SDG 11 (cities) and SDG 17 (means of implementation) cut across all of the SDGs. I see eight targets among these seven SDGs that provide the best guidance to generate the greatest contribution of STI: 8.3, 9.5, 9.b and 9.c (below 9.5), 17.6, 17.8, 17.18, 17.19.

For example, targets 9.5 and 9.b should encourage countries to propose aspirational goals for national public and private investment in research and development (R&D) as a percentage of gross national product (GNP). The most innovative countries make the greatest investment in R&D as a percentage of GNP; this type of investment can be increased in most countries to produce benefits greater than their costs. (*6*) There is also substantial correlation between the most innovative countries and the least corrupt countries (*7*). Target 8.3 is focused on job creation and entrepreneurship, especially in small- and medium-sized industries. Target 9.c emphasizes information and communications technology (ICT) and universal and affordable access to the Internet. It will be important to have indicators focused here, even if countries set their own numerical targets.

Visiting Scientist and Senior Scholar, Center for Science Diplomacy, American Association for the Advancement of Science, Washington, DC 20005, USA.
E-mail: bcolglaz@aaas.org

Published by AAAS

The concept of the "global technology facilitation mechanism" in target 17.6 is explained in some detail in the 2030 agenda, but the concept of "technology bank" in target 17.8 is not defined. Rather than an unworkable and unrealistic "technology bank," focus could be instead on a "data bank" providing information and know-how combined with STI and ICT capacity-building efforts. Targets 17.18 and 17.19 emphasize support of quality data and statistics in developing countries.

Targets for SDGs 1, 10, 11, and 12 miss some of the most meaningful ways that STI can contribute. In SDGs 1 and 10, the role of STI for dealing with poverty and inequality for the least-developed countries is not highlighted in the targets. The importance of STI for achieving these goals (as seen with mobile phones in Africa) has been emphasized in the work of development agencies of several countries (e.g., Canada's International Development Research Center and U.S. Agency for International Development's Global Development Lab).

"Our greatest legacy to future generations...may be building knowledge-based societies..."

The concept of "smart cities"—maximizing STI and new data sources to enhance management of cities for economic, social, and environmental goals—is missing in targets for SDG 11. For SDG 12 on sustainable consumption and production, there is encouragement of "resource efficiency" in targets 12.2 to 12.5 (as well as in targets 8.4 and 9.4), but except for target 12.a there is little emphasis on the crucial role of STI capacity for achieving greater resource efficiency.

KNOWLEDGE-BASED SOCIETIES. The importance of STI capacity-building and wider global availability of knowledge and technologies are acknowledged in the "means of implementation" section of the 2030 agenda (*8*), but two sentences from an earlier draft should have been retained:

"We recognize the central role that science, technology, and innovation play in enabling the international community to respond to sustainable development challenges. We recognize the power of communication technologies, technical cooperation, and capacity building for sustainable development."

The fundamental principles for building STI capacity are consistent with the SDGs, but highlighting these principles would have been useful: strengthening educational systems from grade school to graduate school (SDGs 4 and 5); supporting students pursuing science and technology (SDGs 4, 5, 8, and 9); supporting and linking R&D in universities, national laboratories, and private companies, and enhancing international STI collaboration (SDGs 8 and 9 and paragraphs 67 and 68 of the 2030 agenda); strengthening government policies and investments to facilitate a competitive, "bottom-up" innovative ecosystem (SDGs 8, 9, 16 and 17); promoting the rule of law, reducing corruption, and developing effective and accountable institutions (SDG 16); and creating a robust "science advisory ecosystem" for providing scientific evidence to inform public-policy decisions (SDGs 1 to 17). Every country needs STI-competent people and institutions in order to use existing, as well as to create new, knowledge and technologies.

The landmark 1987 Bruntland Report defined Sustainable Development by stating that it "meets the needs of the present without compromising the ability of future generations to meet their own needs" [see ¶ 7 of (*9*)]. The critically important role of STI could have been signaled by a slight altering of its definition to say "meets the needs of the present *while expanding* the ability of future generations to meet their own needs." Our greatest legacy to future generations, in addition to avoiding wars and conflicts, may be building knowledge-based societies and accelerating expansion of scientific knowledge and useful technologies. The post-2015 development agenda can be as important for supporting the development of knowledge-based and innovative societies as for solving our current global challenges and making near-term progress on the 17 SDGs. ■

REFERENCES AND NOTES

1. UN, *Transforming Our World: The 2030 Agenda for Sustainable Development* (UN, New York, 2015); http://bit.ly/TransformAgendaSDG-pdf.
2. UN, *2015 Global Sustainable Development Report* (UN, New York, 2015); http://bit.ly/2015GSDR-pdf.
3. UN, China's 2012 National Report on Sustainable Development (UN, New York, 2012); http://bit.ly/ChinaSD.
4. UN, "Outcome document of the Third International Conference on Financing for Development: Addis Ababa Action Agenda" (UN, New York, 2015); www.un.org/esa/ffd/wp-content/uploads/2015/08/AAAA_Outcome.pdf.
5. See ¶ 70 of (*1*) and ¶ 114 to ¶ 124 of (*4*).
6. K. E. Maskus, "Benefits and costs of the science and technology targets for the post-2015 development agenda" (Working paper, Copenhagen Consensus, 2014); http://bit.ly/BenefitsSandTtargets-pdf.
7. A. Mungiu-Pippidi, *Nature* **518**, 295–297 (2015).
8. See ¶ 62, ¶ 63, ¶ 67, and ¶ 68 of (*1*).
9. UN, Report of the World Commission on Environment and Development: Our Common Future; www.un-documents.net/our-common-future.pdf.

ACKNOWLEDGMENTS

W.C. thanks G. Dana of the Office of the Science and Technology Adviser to the U.S. Secretary of State and D. O'Connor, R. A. Roehrl, and F. Soltau of the UN Department of Economic and Social Affairs for valuable insights.

10.1126/science.aad2333

BIOENGINEERING

Yeast cell factories on the horizon

Metabolic engineering in yeast gets increasingly more versatile

By **Jens Nielsen**[1,2,3]

For thousands of years, yeast has been used for making beer, bread, and wine. In modern times, it has become a commercial workhorse for producing fuels, chemicals, and pharmaceuticals such as insulin, human serum albumin, and vaccines against hepatitis virus and human papillomavirus. Yeast has also been engineered to make chemicals at industrial scale (e.g., succinic acid, lactic acid, resveratrol) and advanced biofuels (e.g., isobutanol) (*1*). On page 1095 of this issue, Galanie *et al.* (*2*) demonstrate that yeast can now be engineered to produce opioids (*2*), a major class of compounds used for treating severe pain. Their study represents a tour de force in the metabolic engineering of yeast, as it involved the expression of genes for more than 20 enzymatic activities from plants, mammals, bacteria, and yeast itself. It clearly represents a breakthrough advance for making complex natural products in a controlled and sustainable way.

Yeast has previously been recruited for producing complex natural products through the reconstruction of biosynthetic pathways taken from plants or animals (*3*). This is done by transferring genes that encode enzymes of the metabolic pathway, from the organism that naturally produces the chemical of interest, into yeast. A key requirement is that this heterologous metabolic pathway hooks up to endogenous yeast metabolism. As central metabolism is highly conserved between different organisms, it is generally possible to identify a metabolite in the endogenous yeast metabolism that can be used as a precursor for the heterologous pathway. Indeed, using this approach, yeast was engineered to produce hydrocortisone (a steroid used to synthesize drugs with anti-inflammatory and antiproliferative effects) by recruiting part of the endogenous yeast pathway that generates ergosterol (*4*). Several endogenous yeast enzymes were put to use, but it was still necessary to express more than 10 mammalian

Published by AAAS

The concept of the "global technology facilitation mechanism" in target 17.6 is explained in some detail in the 2030 agenda, but the concept of "technology bank" in target 17.8 is not defined. Rather than an unworkable and unrealistic "technology bank," focus could be instead on a "data bank" providing information and know-how combined with STI and ICT capacity-building efforts. Targets 17.18 and 17.19 emphasize support of quality data and statistics in developing countries.

Targets for SDGs 1, 10, 11, and 12 miss some of the most meaningful ways that STI can contribute. In SDGs 1 and 10, the role of STI for dealing with poverty and inequality for the least-developed countries is not highlighted in the targets. The importance of STI for achieving these goals (as seen with mobile phones in Africa) has been emphasized in the work of development agencies of several countries (e.g., Canada's International Development Research Center and U.S. Agency for International Development's Global Development Lab).

"Our greatest legacy to future generations...may be building knowledge-based societies..."

The concept of "smart cities"—maximizing STI and new data sources to enhance management of cities for economic, social, and environmental goals—is missing in targets for SDG 11. For SDG 12 on sustainable consumption and production, there is encouragement of "resource efficiency" in targets 12.2 to 12.5 (as well as in targets 8.4 and 9.4), but except for target 12.a there is little emphasis on the crucial role of STI capacity for achieving greater resource efficiency.

KNOWLEDGE-BASED SOCIETIES. The importance of STI capacity-building and wider global availability of knowledge and technologies are acknowledged in the "means of implementation" section of the 2030 agenda (*8*), but two sentences from an earlier draft should have been retained:

"We recognize the central role that science, technology, and innovation play in enabling the international community to respond to sustainable development challenges. We recognize the power of communication technologies, technical cooperation, and capacity building for sustainable development."

The fundamental principles for building STI capacity are consistent with the SDGs, but highlighting these principles would have been useful: strengthening educational systems from grade school to graduate school (SDGs 4 and 5); supporting students pursuing science and technology (SDGs 4, 5, 8, and 9); supporting and linking R&D in universities, national laboratories, and private companies, and enhancing international STI collaboration (SDGs 8 and 9 and paragraphs 67 and 68 of the 2030 agenda); strengthening government policies and investments to facilitate a competitive, "bottom-up" innovative ecosystem (SDGs 8, 9, 16 and 17); promoting the rule of law, reducing corruption, and developing effective and accountable institutions (SDG 16); and creating a robust "science advisory ecosystem" for providing scientific evidence to inform public-policy decisions (SDGs 1 to 17). Every country needs STI-competent people and institutions in order to use existing, as well as to create new, knowledge and technologies.

The landmark 1987 Bruntland Report defined Sustainable Development by stating that it "meets the needs of the present without compromising the ability of future generations to meet their own needs" [see ¶ 7 of (*9*)]. The critically important role of STI could have been signaled by a slight altering of its definition to say "meets the needs of the present *while expanding* the ability of future generations to meet their own needs." Our greatest legacy to future generations, in addition to avoiding wars and conflicts, may be building knowledge-based societies and accelerating expansion of scientific knowledge and useful technologies. The post-2015 development agenda can be as important for supporting the development of knowledge-based and innovative societies as for solving our current global challenges and making near-term progress on the 17 SDGs. ■

REFERENCES AND NOTES

1. UN, *Transforming Our World: The 2030 Agenda for Sustainable Development* (UN, New York, 2015); http://bit.ly/TransformAgendaSDG-pdf.
2. UN, *2015 Global Sustainable Development Report* (UN, New York, 2015); http://bit.ly/2015GSDR-pdf.
3. UN, China's 2012 National Report on Sustainable Development (UN, New York, 2012); http://bit.ly/ChinaSD.
4. UN, "Outcome document of the Third International Conference on Financing for Development: Addis Ababa Action Agenda" (UN, New York, 2015); www.un.org/esa/ffd/wp-content/uploads/2015/08/AAAA_Outcome.pdf.
5. See ¶ 70 of (*1*) and ¶ 114 to ¶ 124 of (*4*).
6. K. E. Maskus, "Benefits and costs of the science and technology targets for the post-2015 development agenda" (Working paper, Copenhagen Consensus, 2014); http://bit.ly/BenefitsSandTtargets-pdf.
7. A. Mungiu-Pippidi, *Nature* **518**, 295–297 (2015).
8. See ¶ 62, ¶ 63, ¶ 67, and ¶ 68 of (*1*).
9. UN, Report of the World Commission on Environment and Development: Our Common Future; www.un-documents.net/our-common-future.pdf.

ACKNOWLEDGMENTS

W.C. thanks G. Dana of the Office of the Science and Technology Adviser to the U.S. Secretary of State and D. O'Connor, R. A. Roehrl, and F. Soltau of the UN Department of Economic and Social Affairs for valuable insights.

10.1126/science.aad2333

BIOENGINEERING

Yeast cell factories on the horizon

Metabolic engineering in yeast gets increasingly more versatile

By **Jens Nielsen**[1,2,3]

For thousands of years, yeast has been used for making beer, bread, and wine. In modern times, it has become a commercial workhorse for producing fuels, chemicals, and pharmaceuticals such as insulin, human serum albumin, and vaccines against hepatitis virus and human papillomavirus. Yeast has also been engineered to make chemicals at industrial scale (e.g., succinic acid, lactic acid, resveratrol) and advanced biofuels (e.g., isobutanol) (*1*). On page 1095 of this issue, Galanie *et al.* (*2*) demonstrate that yeast can now be engineered to produce opioids (*2*), a major class of compounds used for treating severe pain. Their study represents a tour de force in the metabolic engineering of yeast, as it involved the expression of genes for more than 20 enzymatic activities from plants, mammals, bacteria, and yeast itself. It clearly represents a breakthrough advance for making complex natural products in a controlled and sustainable way.

Yeast has previously been recruited for producing complex natural products through the reconstruction of biosynthetic pathways taken from plants or animals (*3*). This is done by transferring genes that encode enzymes of the metabolic pathway, from the organism that naturally produces the chemical of interest, into yeast. A key requirement is that this heterologous metabolic pathway hooks up to endogenous yeast metabolism. As central metabolism is highly conserved between different organisms, it is generally possible to identify a metabolite in the endogenous yeast metabolism that can be used as a precursor for the heterologous pathway. Indeed, using this approach, yeast was engineered to produce hydrocortisone (a steroid used to synthesize drugs with anti-inflammatory and antiproliferative effects) by recruiting part of the endogenous yeast pathway that generates ergosterol (*4*). Several endogenous yeast enzymes were put to use, but it was still necessary to express more than 10 mammalian

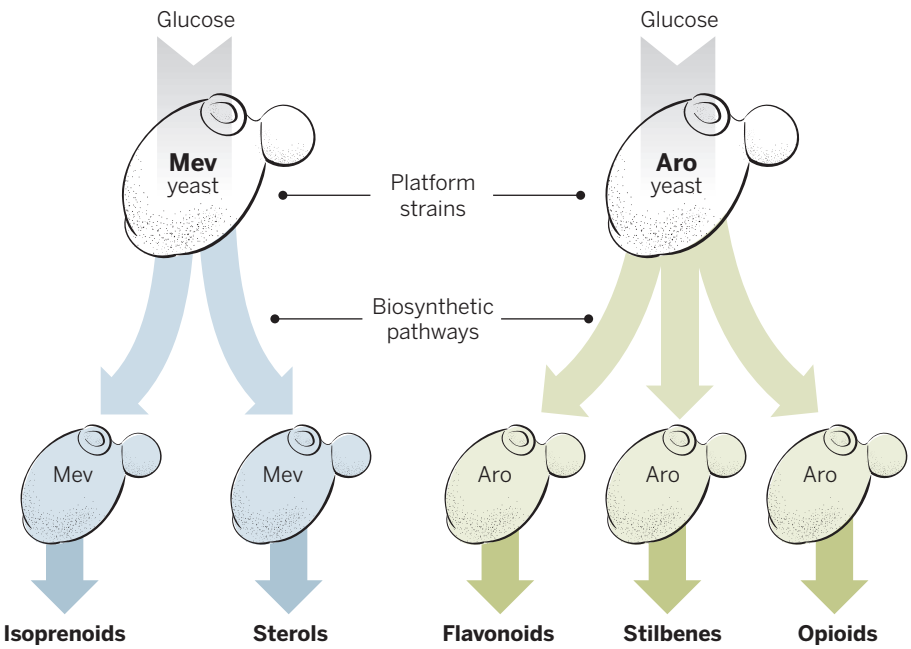
Downloaded from www.sciencemag.org on September 5, 2015

Published by AAAS

enzymes in combination with overexpressing the yeast genes to enable production of hydrocortisone from glucose. Ergosterol is synthesized via the so-called mevalonate pathway (also used for cholesterol biosynthesis in mammals), and plants use this pathway to make a wide range of isoprenoids (or terpenoids). Members of this family have a broad spectrum of applications, including food products, pharmaceuticals, cosmetics, and biofuels (*3*), and through recruitment of the mevalonate pathway, it has been possible to engineer yeast to produce compounds normally extracted from plants [such as perfumes (e.g., santalene) (*5*)]. Several companies are currently working on developing this technology to enable the production of fine chemicals through yeast fermentation, thereby providing a stable, sustainable, and scalable source of the desired compound.

The biosynthesis of perfumes typically requires the expression of only one to three plant enzymes in yeast. However, it is possible to express a multistep heterologous pathway from plants to produce artemisinic acid, which can be chemically converted to the antimalarial drug artemisinin (*6*). Again, this relied on the endogenous mevalonate pathway in yeast, and through combined engineering of this pathway and optimization of the heterologous pathway, productivity was improved to the point where it could be taken forward for commercial production of artemisinin (*7*, *8*). This process currently provides up to one-third of the global need for this antimalarial drug. Even though artemisinin can be extracted from plants, the biotech-based production ensures stable production, which is particularly important as the supply has suffered from large fluctuations in the past.

A general observation from past studies is that to ensure sufficient production of the natural products, it was necessary to boost the endogenous yeast pathway for efficient provision of precursors, such as those from the mevalonate pathway. Galanie *et al.* also relied on up-regulating the endogenous yeast pathway for providing tyrosine, the precursor for opioid biosynthesis. It is likely that the successful production of opioids from glucose rests on the initial generation of "platform" yeast strains—one platform strain for efficient production of tyrosine, and a second platform strain to efficiently produce reticuline, an intermediate in the opiod biosynthetic pathway. A general lesson therefore seems to be that successful metabolic engineering of yeast for producing complex natural products requires platform strains (*9*). Moreover, a single platform strain can be used to make a range of different natural products (see the figure).



Versatile yeast. Reconstructing heterologous biosynthesis pathways enables the recruitment of yeast endogenous metabolism to produce complex natural products. By using the mevalonate pathway (Mev), a platform yeast strain can be engineered to synthesize different isoprenoids and sterols; through recruitment of an aromatic amino acid biosynthesis pathway (Aro), such as for tyrosine, a different platform yeast strain can be engineered to produce flavonoids, stilbenes, and opioids.

The progress made by Galanie *et al.* represents an important milestone in metabolic engineering of long and complex biosynthetic pathways in yeast. Even though the titer and productivities are low, the result may ultimately lead to commercial production of opioids. Controlled production of these chemicals also will allow for contained production, with the goal of completely eliminating traditional extraction from plants. This could reduce illicit production. The question of scaling up yeast-based production of opioids is now at hand, but getting there may not be so trivial. With the current output, it would take 4400 gallons of bioengineered yeast to produce a single therapeutic dose for pain relief (*10*). Scaling up the production of artemisinin, for example, took more than 5 years of investigation and required investments exceeding $50 million. That is not to say that scaling up opioid production in yeast is not inevitable; therefore, the advance by Galanie *et al.* raises the important question of regulating access to such yeast strains.

The study of Galanie *et al.* also demonstrates how reconstruction of a plant pathway in yeast allows for enzyme discovery and screening for efficient enzymes for biosynthesis, which is of value for any metabolic engineering project. For opioid synthesis, for example, the authors identified one new enzyme required for the biosynthesis and screened more than 20 variants of a key enzyme of the pathway to increase the flux toward opioids. By demonstrating that a 23-step biosynthetic pathway can be reconstructed in yeast, the study advances the ability to ensure sustainable production of fuels, chemicals, and pharmaceuticals. Even though the 2010 market for renewable chemicals was only about 1% of the total chemical market (about $30 billion out of a total market of $3 trillion), metabolic engineering of cell factories, and especially yeast, has clear potential to increase this proportion in the future. ■

[1]*Department of Biology and Biological Engineering, Chalmers University of Technology, SE-41296 Gothenburg, Sweden.* [2]*Novo Nordisk Foundation Center for Biosustainability, Technical University of Denmark, DK-2970 Hørsholm, Denmark.* [3]*Science for Life Laboratory, Royal Institute of Technology, SE-17121 Stockholm, Sweden.*
E-mail: nielsenj@chalmers.se

REFERENCES

1. J. Nielsen, C. Larsson, A. van Maris, J. Pronk, *Curr. Opin. Biotechnol.* **24**, 398 (2013).
2. S. Galanie, K. Thodey, I. J. Trenchard, M. Filsinger Interrante, C. D. Smolke, *Science* **349**, 1095 (2015).
3. A. Krivoruchko, J. Nielsen, *Curr. Opin. Biotechnol.* **35**, 7 (2015).
4. F. M. Szczebara *et al.*, *Nat. Biotechnol.* **21**, 143 (2003).
5. G. Scalcinati *et al.*, *Microb. Cell Fact.* **11**, 117 (2012).
6. D.-K. Ro *et al.*, *Nature* **440**, 940 (2006).
7. P. J. Westfall *et al.*, *Proc. Natl. Acad. Sci. U.S.A.* **109**, E111 (2012).
8. C. J. Paddon *et al.*, *Nature* **496**, 528 (2013).
9. J. Nielsen, *MBio* **5**, e02153-14 (2014).
10. https://med.stanford.edu/news/all-news/2015/08/researchers-genetically-engineer-yeast-to-produce-opioids.html

10.1126/science.aad2081

ILLUSTRATION: K. SUTLIFF/*SCIENCE*

Published by AAAS

PLANT BIOCHEMISTRY

Lighting the fuse on toxic TNT

An enzyme that helps control reactive oxidants sensitizes plants to TNT pollution

By **Graham Noctor**

Most of the oxygen used by aerobic cells is safely converted to water, but a small part can be transformed into unstable derivatives called reactive oxygen species (ROS). Although dangerous to life, ROS are also important signaling messengers that provide information on the cellular environment. They are implicated in human diseases and in plant development and environmental responses. Cells can live with ROS and exploit them as signals because they use antioxidant systems to regulate their accumulation and so avoid the oxidative stress they can cause. Plant antioxidant networks are complex, and there is keen interest in dissecting the biological roles of the many enzymes and metabolites that may be involved. On page 1072 of this issue, Johnston *et al.* report a role for a specific member of the antioxidant enzyme family in conferring sensitivity to soil-borne pollutants, including the explosive 2,4,6-trinitrotoluene (TNT), on the model plant *Arabidopsis* (*1*).

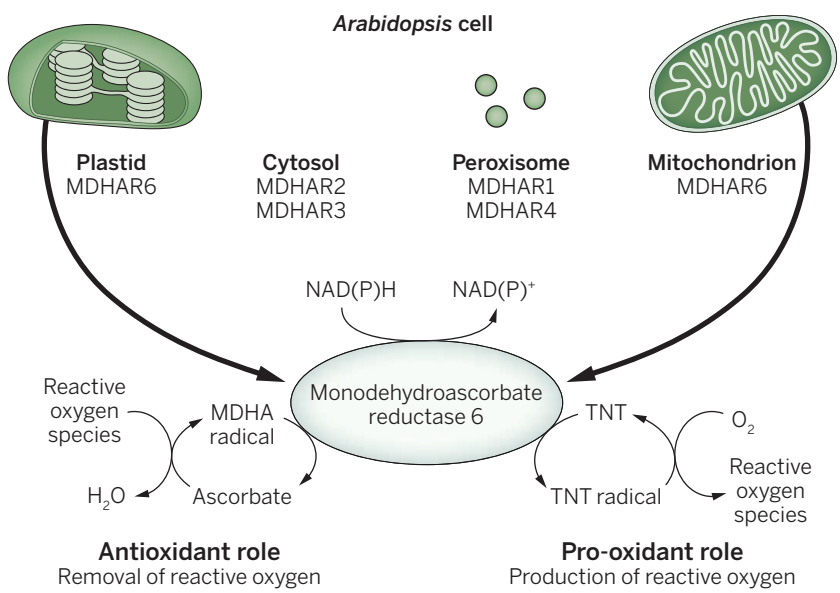
Plants produce a battery of proteins that are able to detoxify noxious pollutants, but some cell components actually potentiate the deleterious effects of foreign chemicals. Photosynthesis is not possible without the potent reducing compounds produced in chloroplasts exposed to light, but the reducing power of these compounds can be hijacked by herbicides such as paraquat, triggering massive ROS production that induces death. According to Johnston *et al.*, TNT pollution in soil negatively affects the growth of *Arabidopsis* roots. Rather than inhibiting a specific target enzyme, as do herbicides such as glyphosate, TNT affects plant growth by generating oxidative stress, catalytically promoting ROS production in a similar manner to paraquat. The effect of TNT is nonetheless genetically dependent, as loss-of-function mutants for a specific gene are much less sensitive to the explosive.

Intriguingly, the gene in question encodes a well-characterized antioxidant enzyme: monodehydroascorbate reductase (MDHAR), whose primary biological role is considered to be in the regeneration of ascorbate (vitamin C) from its initial oxidation product, and therefore in counteracting oxidative stress (*2*–*4*) (see the figure).

Although it is certainly remarkable that TNT interacts with MDHAR to harm plants in this way, other reports have underscored the two-faced nature of the plant antioxidant system. Some plants enriched in the antioxidant tripeptide glutathione show constitutive disease symptoms because of its higher levels (*5*), and glutathione can facilitate pathogenesis-related phytohormone signaling elicited by ROS such as H_2O_2 (*6*). Similarly, catalase, although a very active H_2O_2 scavenging enzyme, is a positive promoter of cell death in certain conditions (*7*), and MDHAR itself may contribute to superoxide production in the chloroplast (*8*). All these observations call attention to the intricacy of the antioxidant system, emphasize the potential importance of "side reactions" in certain conditions, and challenge simplistic views of oxidative stress that pit deleterious ROS on one side against beneficial antioxidants on the other.

The study of Johnston *et al.* reveals that a specific MDHAR sensitizes the plant to the effects of TNT. The gene in question, *MDHAR6*, is one of five thought to encode the reductase enzyme in *Arabidopsis*. *MDHAR6* is currently considered to be solely responsible for the enzyme activity in the mitochondria and chloroplasts (*4*, *9*). Two questions immediately arise for future investigation. The first relates to the nature of the factors that might explain the specificity of *MDHAR6* function in conferring toxicity. The answer may lie in biochemical differences between the different MDHARs, or in preferential accumulation of TNT or different sensitivities to ROS overproduction at various cellular and subcellular sites within the roots.

The second question concerns the role of MDHAR in regenerating ascorbate, an essential compound without which *Arabidopsis* cannot survive past the early seedling stage (*10*). Even at basal levels of ROS production, ascorbate oxidation in chloroplasts and mitochondria probably outpaces its de novo synthesis from sugar precursors. If so, the complete loss of MDHAR-dependent regenerating capacity in these two organelles might be predicted to cause some depletion of tissue ascorbate, and this should be even more evident in



Two-faced enzyme. The long-accepted antioxidant role of monodehydroascorbate reductase (MDHAR6) in regenerating ascorbate to support the removal of reactive oxygen (lower left) contrasts with its new pro-oxidant effect in mediating TNT toxicity by promoting reactive oxygen production (lower right). (Top): The subcellular locations of the proteins encoded by the five nuclear MDHAR genes in *Arabidopsis*. All MDHARs are considered to have the antioxidant function shown at lower left; the MDHAR6 located in the mitochondria seems to be particularly effective in mediating TNT toxicity in root cells through the reactions shown at lower right (*1*).

ILLUSTRATION: ADAPTED BY P. HUEY/*SCIENCE*

Institute of Plant Sciences Paris Saclay (IPS2), UMR 9213/UMR1403, Université Paris Sud, CNRS, INRA, Université d'Evry, Université Paris Diderot, Sorbonne Paris Cité, Bâtiment 630, 91405 Orsay, France. E-mail: graham.noctor@u-psud.fr

Downloaded from www.sciencemag.org on September 5, 2015

Published by AAAS

stressful conditions, when ROS production is thought to be increased. Yet Johnston *et al.* report no marked change in leaf ascorbate contents or plant phenotypes in mutants for *MDHAR6* grown without TNT. Either this enzyme plays a relatively minor role in ascorbate regeneration or, when it is no longer present, the plant engages other pathways in order to compensate for its loss. As well as ascorbate-independent antioxidant systems such as peroxiredoxins, alternative pathways include different mechanisms of ascorbate regeneration (*2*–*4*, *11*). Loss of *MDHAR6* function could be compensated in the plastids by reduction of MDHA to ascorbate by ferredoxin and, in both plastids and mitochondria, by enzyme-dependent and chemical regeneration of ascorbate from dehydroascorbate that is secondarily formed from MDHA. Ongoing studies of mutants for MDHAR and other enzymes may help to clarify the importance of specific antioxidant pathways in different growth conditions.

Military and industrial activities have led to TNT pollution at many sites throughout the world, potentially endangering human health and having a negative impact on ecological and agricultural systems. Plants could be used to clean up undesirable compounds such as TNT by extracting them from the soil and concentrating them within their tissues (phytoremediation). Depending on the nature of the resistance mechanism, plants able to thrive on polluted soils are likely to be more effective phytoremediators. Previous studies have focused on biochemical systems in plants that enhance resistance by chemically modifying TNT (*12*). This new report identifies a promising alternative strategy for making plants more resistant to this compound, by modifying or knocking out the activity of MDHAR6. Further, apart from the specific question of TNT resistance, initial observations suggest that this strategy could also be useful in conferring plant specificity to herbicides that may act through similar mechanisms (*1*). ■

REFERENCES

1. E. J. Johnston *et al.*, *Science* **349**, 1072 (2015).
2. K. Asada, *Plant Physiol.* **141**, 391 (2006).
3. C. H. Foyer, G. Noctor, *Plant Physiol.* **155**, 2 (2011).
4. N. Smirnoff, *Adv. Bot. Res.* **59**, 107 (2011).
5. G. Creissen *et al.*, *Plant Cell* **11**, 1277 (1999).
6. Y. Han *et al.*, *Antioxid. Redox Signal.* **18**, 2106 (2013).
7. T. Hackenberg *et al.*, *Plant Cell* **25**, 4616 (2013).
8. C. Miyake, U. Schreiber, H. Hormann, S. Sano, A. Kozi, *Plant Cell Physiol.* **39**, 821 (1998).
9. O. Chew, J. Whelan, A. H. Millar, *J. Biol. Chem.* **278**, 46869 (2003).
10. J. Dowdle, T. Ishikawa, S. Gatzek, S. Rolinski, N. Smirnoff, *Plant J.* **52**, 673 (2007).
11. J. Awad *et al.*, *Plant Physiol.* **167**, 1592 (2015).
12. V. Gunning *et al.*, *Plant Physiol.* **165**, 854 (2014).

10.1126/science.aad0941



PHOTO: MANUEL PRESTI/SCIENCE PHOTO LIBRARY

All about energy. In trophic terms, the lupin plant is the producer, providing energy through photosynthesis. The savannah sparrow and its insect prey are the consumers.

ECOLOGY

Energy flows in ecosystems

Relationships between predator and prey biomass are remarkably similar in different ecosystems

By **Just Cebrian**[1,2]

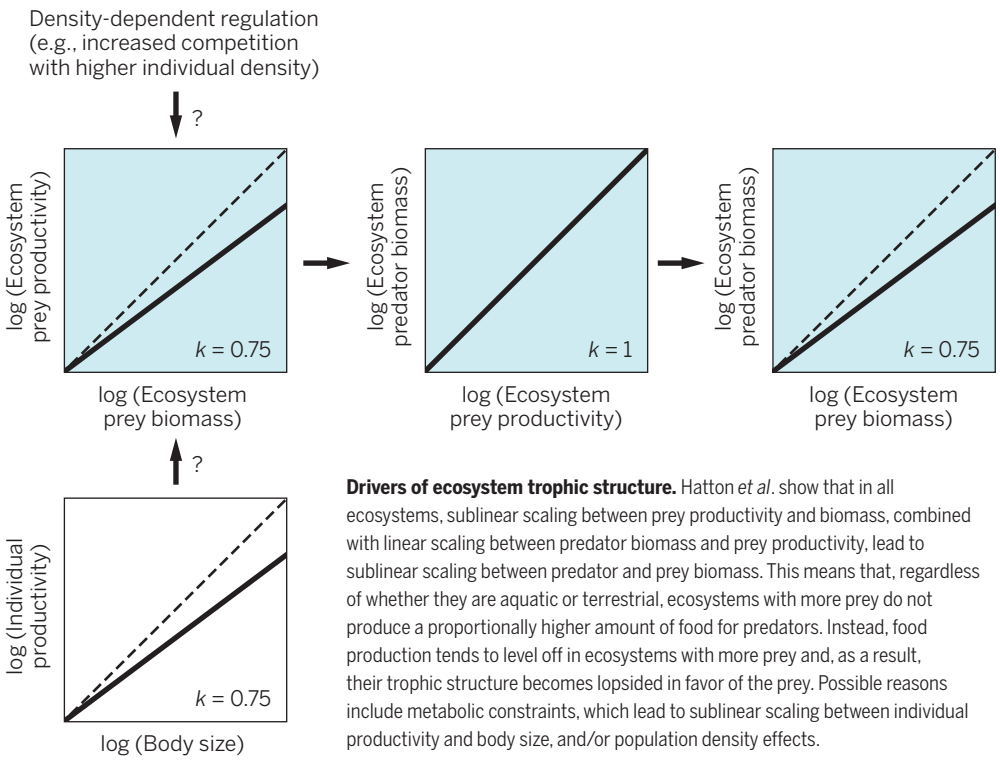
All organisms in an ecosystem can be placed on a trophic level, depending on whether they are producers or consumers of energy within the food chain (see the photo). Ecologists have long debated what regulates the trophic structure and dynamics of ecosystems (*1*). This is important because trophic structure and dynamics regulate many of the goods and services that ecosystems provide to wildlife and humankind, such as the production of harvestable food and energy, carbon sequestration and modulation of climate change, and nutrient uptake and control of global biogeochemical cycles (*2*). A study by Hatton *et al.* on page 1070 of this issue (*3*) and a recent report by Lafferty *et al.* (*4*) represent important advances toward a unified theory of trophic structure that captures observed trends across all ecosystems.

The ratio of predator-to-prey biomass is a key element of trophic structure that has been studied intensively given its importance for understanding biomass distributions and energy cycling in ecosystems. The nature and control of this ratio have been controversial, but a growing body of literature shows the ratio to be more bottom-heavy in ecosystems with higher prey biomass. In other words, as prey biomass increases, the ratio of predator-to-prey biomass decreases in ecosystems. This pattern has, however, only been demonstrated for specific types of ecosystems, such as planktonic systems (*5*), and its generality has remained uncertain. Hatton *et al.* show that this pattern—that is, a decreasing predator-to-prey biomass ratio with increasing prey biomass—applies universally in both aquatic and terrestrial ecosystems. Furthermore, they demonstrate that this universal pattern emerges from a sublinear scaling ($k = 0.75$, see the graph) that is independent of the ecosystem considered.

Where does this sublinear pattern stem from? Prior research has shown that, in

Published by AAAS

aquatic and terrestrial ecosystems, consumer biomass is linearly related to the consumption of basal resource, which in turn is linearly related to the productivity of the basal resource (*6*, *7*). Thus, predator (consumer) biomass and prey (basal resource) productivity are linearly related, and if predator biomass is sublinearly related to prey biomass, then prey productivity should also be sublinearly related to prey biomass. In a series of elegant calculations with simple trophic models and fits to empirical data, Hatton *et al.* demonstrate the universality of these processes (see the graph). Previous studies have found similar trends in some aquatic and terrestrial ecosystems (*6*–*9*), but Hatton *et al.* now generalize their occurrence in nature, thereby advancing substantially our understanding of ecosystem trophic dynamics and structure.



Drivers of ecosystem trophic structure. Hatton *et al*. show that in all ecosystems, sublinear scaling between prey productivity and biomass, combined with linear scaling between predator biomass and prey productivity, lead to sublinear scaling between predator and prey biomass. This means that, regardless of whether they are aquatic or terrestrial, ecosystems with more prey do not produce a proportionally higher amount of food for predators. Instead, food production tends to level off in ecosystems with more prey and, as a result, their trophic structure becomes lopsided in favor of the prey. Possible reasons include metabolic constraints, which lead to sublinear scaling between individual productivity and body size, and/or population density effects.

The question follows why prey productivity is scaled sublinearly to prey biomass. If we can answer this question, then we would understand the mechanisms underlying the universal trophic cascade processes shown by Hatton *et al*. The authors consider tenets of the metabolic theory of ecology. According to this theory, metabolic constraints with increasing individual size generate a sublinear scaling between individual growth (biomass production) and size (biomass), with a sublinear scaling coefficient of $k = 0.75$ (*10*). Thus, if ecosystems with higher prey biomass are also composed of larger-size prey, it follows that metabolic constraints on body size could explain the sublinear scaling between prey productivity and biomass in ecosystems. Recent evidence (*11*) has shown this to be the case across ecosystem types differing widely in individual prey size. For instance, when comparing phytoplankton communities to seagrass beds, shrublands, and forests, increasing individual prey size explains the sublinear scaling between ecosystem prey productivity and biomass.

However, when Hatton *et al.* compared communities within the same ecosystem type, they found that individual prey size does not increase with ecosystem prey biomass and, thus, cannot account for the sublinear scaling pattern. Instead, prey density was higher in ecosystems with higher prey biomass. The authors suggest that processes that depend on prey density, such as competition for resources and other negative interactions among prey species, can result in the sublinear scaling between ecosystem prey productivity and biomass (*3*). Another interesting idea is that higher ecosystem biomass, regardless of the size of the prey in the ecosystem, could be subject to the same metabolic constraints on individual body size, thereby averting the need to invoke density-dependent processes to explain the sublinear scaling.

The numerous avenues of new and exciting research opened by Hatton *et al.* are heightened by the results of Lafferty *et al.* In an impressive compilation, the authors show that all trophic models published to date, including the seminal Lotka-Volterra predator-prey equations (*12*), can be unified into a general consumer-resource population model. The general model contains several quantifiable state variables for consumers and their resources. It can thus be adapted to explain diverse trophic dynamics, ranging from classical examples where the consumer is a predator to cases where the consumer is a micropredator, parasitoid, or parasite. Trophic models that may have been regarded as disconnected and exclusive now emerge as variants of the same conceptual framework. Adaptation of the general model to specific models reveals the simplifications and assumptions that are idiosyncratic to each of them. This provides an accurate procedure to evaluate the focus, limitations, and applicability of all trophic models.

Lafferty *et al.* bring the patterns found by Hatton *et al.* to a new level of scrutiny, providing a test for whether such patterns are truly universal. The general trophic model of Lafferty *et al.* indicates that all consumers and their resources follow the same fundamental principles that govern energy transfer and trophic structure in ecosystems. Thus, the sublinear biomass scaling reported by Hatton *et al.* for predators and their prey could also apply to any other type of consumer and its resource, including micropredators and parasites. Such patterns could in turn invariably emerge from sublinear scaling between resource productivity and biomass. Confirming these hypotheses would mark a major milestone in ecosystem science. ■

[1]*Dauphin Island Sea Lab, Dauphin Island, AL, USA.* [2]*Department of Marine Sciences, University of South Alabama, Mobile, AL, USA. E-mail: jcebrian@disl.org*

REFERENCES

1. V. Volterra, *Nature* **118**, 558 (1926).
2. O. J. Schmitz *et al.*, *Ecosystems (N. Y.)* **17**, 344 (2014).
3. I. A. Hatton *et al.*, *Science* **349**, aac6284 (2015).
4. K. D. Lafferty *et al.*, *Science* **349**, 854 (2015).
5. J. M. Gasol, P. A. del Giorgio, C. M. Duarte, *Limnol. Oceanogr.* **42**, 1353 (1997).
6. J. Cebrian, J. Lartigue, *Ecol. Monogr.* **74**, 237 (2004).
7. J. Cebrian, *Ecol. Lett.* **7**, 232 (2004).
8. J. Cebrian, *Am. Nat.* **154**, 449 (1999).
9. C. M. Duarte, C. L. Chiscano, *Aquat. Bot.* **65**, 159 (1999).
10. J. H. Brown, J. F. Gillooly, A. P. Allen, V. M. Savage, G. B. West, *Ecology* **85**, 1771 (2004).
11. J. R. Schramski, A. I. Dell, J. M. Grady, R. M. Sibly, J. H. Brown, *Proc. Natl. Acad. Sci. U.S.A.* **112**, 2617 (2015).
12. A. J. Lotka, *Elements of Physical Biology* (Dover, New York, 1924).

10.1126/science.aad0684

Published by AAAS

IMMUNOLOGY

Fragmented communication between immune cells

Neutrophils blaze a trail with migratory cues for T cells to follow to sites of infection

By **E. Kiermaier** *and* **M. Sixt**

Immune cells constantly circulate in the body in search of pathogens or tissue damage. Because they move autonomously, immune cell trafficking must be tightly controlled and coordinated by extracellular cues. The main signals that guide immune cells are chemokines, small polypeptides that modulate the migratory behavior of cells. Remarkably, most chemokines are not only sensed but also secreted by immune cells, indicating that immune cells might either attract more of their own kind or trigger complex patterns of feedbacks between different cell populations. Such cascades might allow different immune cell types to orchestrate their sequential arrival at a site of infection (*1*). On page 1071 of this issue, Lim *et al.* (*2*) show that this is indeed the case with neutrophils and cytotoxic T cells, the former leaving a trail of cues for the latter to follow during the eradication of a viral infection.

> ***"Lim et al. provide a lucid example of how one immune cell type maps the route for the next one by depositing positional and/or directional landmarks."***

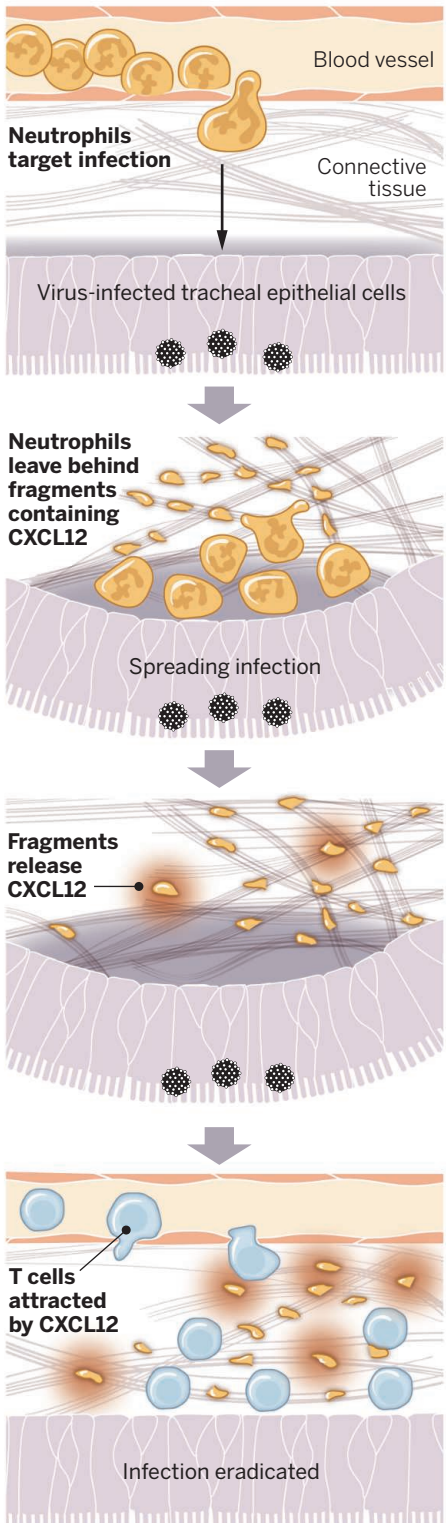
A notable example of coordination between different cell populations is the cross-talk between the cells of the innate and the adaptive immune responses (*3*). Whereas innate cells, such as neutrophils, quickly infiltrate sites of tissue damage via the blood circulation, antigen-specific adaptive immune cells, such as T cells, first need to be activated and amplified in lymphoid organs before they enter the site of infection and eradicate the pathogen.

Lim *et al.* used a mouse model of influenza virus infection to track two waves of immune cells arriving in the trachea after inhalation of the virus. A cohort of infiltrating neutrophils appeared around 3 to 4 days after infection and vanished thereafter. Antigen-specific cytotoxic T cells, which are required to ultimately clear the viral infection, peaked more than a week after infection. Despite their nonoverlapping presence, adaptive immunity depended on the innate phase because depletion of neutrophils decreased later T cell infiltration. Consequently, neutrophil-depleted mice were less effective in managing the infection. Although neutrophils can affect priming of adaptive immune responses in other model systems (*4*), Lim *et al.* noted that T cell activation was unaltered upon neutrophil depletion. Thus, the neutrophils must influence T cells at the site of infection.

Using intravital microscopy to visualize the immune cell behavior in situ, Lim *et al.* found that after neutrophil depletion, T cells were not only less abundant in the trachea but also failed to home in on their virus-infected target, the tracheal epithelial cells—even though almost no neutrophils were present in the tissue at this late stage of infection. When the authors screened for expression of factors that might mediate the innate cell–adaptive cell cross-talk, they identified chemokine (C-X-C motif) ligand 12 (CXCL12) as a potential candidate. Indeed, conditional deletion of CXCL12 from neutrophils had similar (albeit less pronounced) effects on T cell behavior to those of neutrophil depletion. The chemokine appears to be a key mediator for localizing cytotoxic T cells at the site of infection.

How does neutrophil-derived CXCL12 affect T cell behavior at time points when neutrophils have already left the infected tissue? Lim *et al.* observed that crawling neutrophils on adhesive surfaces often leave behind membrane patches that are highly enriched in CXCL12. Hence, instead of releasing CXCL12 as a solute as one would expect for a secreted polypeptide, the neutrophils deposited the chemokine wrapped in membrane. Interestingly, the membrane patches were not

Institute of Science and Technology Austria (IST Austria), 3400 Klosterneuburg, Austria. E-mail: sixt@ist.ac.at



Follow me. Chemoattractants released at the site of infection by damaged cells attract neutrophils from the blood circulation. Neutrophils, crawling through the tissue, leave behind trails of cell fragments containing the chemokine CXCL12. The fragments remain attached to connective tissue fibers and gradually release the chemokine, even after the neutrophils have left the site of infection. CXCL12 guides a next wave of infiltrating cytotoxic T cells to clear the infection.

ILLUSTRATION: K. SUTLIFF/*SCIENCE*

Downloaded from www.sciencemag.org on September 5, 2015

Published by AAAS

directly sensed by the T cells, as they did not strictly follow the paths of neutrophils when migrating together in culture dishes. Rather, the membrane patches acted as depots that slowly released CXCL12, thereby creating a promigratory and chemoattractive milieu for T cells. This buffering function might explain the delayed action of the chemokine in vivo. Lim *et al.* again used intravital microscopy to visualize infiltrating neutrophils in the virus-infected mouse model, and indeed found that they left fragments on connective tissue fibers. As with the in vitro experiments, these fragments contained CXCL12, strongly suggesting that the same mechanism holds true in vivo.

Lim *et al.* provide a lucid example of how one immune cell type maps the route for the next one by depositing positional and/or directional landmarks. Their finding might reflect an evolutionary very ancient theme, because the slime mold *Dictyostelium discoideum*, the classical model system to study chemotactic behavior, uses a very similar strategy. When *Dictyostelium* switches from the single-celled to the multicellular stage of development, cells stream together into an aggregate, which then moves as a multicellular slug to finally form a fruiting body. Single-cell migration is guided by cyclic adenosine monophosphate, a chemoattractant. During aggregation, crawling cells lay down membrane packages that release the attractant. This information relay leads to a typical head-to-tail organization of the streaming cells (*5*).

Although this mechanism might represent conserved patterns of intercellular communication in directed cell trafficking, the observed neutrophil fragments might also serve additional functions. Various types of secreted extracellular vesicles (exosomes) have been suggested as mediators of intercellular communication (*6*). The neutrophil-derived cell fragments might release not only guidance cues but also cytokines and other factors, which then influence the adaptive effector phase. ■

REFERENCES

1. A. Rot, U. H. von Andrian, *Annu. Rev. Immunol.* **22**, 891 (2004).
2. K. Lim, Y.-M. Hyun, K. Lambert-Emo, T. Capece, S. Bae, R. Miller, D. J. Topham, M. Kim, *Science* **349**, aaa4352 (2015).
3. A. Mantovani, M. A. Cassatella, C. Costantini, S. Jaillon, *Nat. Rev. Immunol.* **11**, 519 (2011).
4. F. C. Weber, T. Németh, J. Z. Csepregi, A. Dudeck, A. Roers, B. Ozsvári, L. G. Puskás, T. Jakob, A. Mócsai, S. F. Martin, *J. Exp. Med.* **212**, 15 (2015).
5. P. W. Kriebel, V. A. Barr, C. A. Parent, *Cell* **112**, 549 (2003).
6. M. Colombo, G. Raposo, C. Théry, *Annu. Rev. Cell Dev. Biol.* **30**, 255 (2014).

10.1126/science.aad0867

SELF-ORGANIZATION

Fueling connections between chemistry and biology

Chemical reactions create far-from-equilibrium materials by mastering self-assembly

By **Daan van der Zwaag** *and* **E. W. Meijer**

Many biological functions are the result of architectures that form through strong, directional interactions between subunits that constitute the cellular structure. These self-assembly processes display rich, dynamic behavior, where growth and shrinkage are carefully controlled by biochemical feedback mechanisms. One fascinating example is the guanosine triphosphate (GTP)–mediated assembly and disassembly of tubulin into microtubules (*1*). The realization of a chemically fueled synthetic mimic is a long-standing challenge in the field of supramolecular chemistry (*2*). On page 1075 of this issue, Boekhoven *et al.* (*3*) demonstrate the far-from-equilibrium self-assembly of molecular subunits driven by the consumption of a chemical fuel, leading to the transient formation of fibrous hydrogel materials. These conditions result in peculiar self-assembly processes unprecedented in synthetic systems, mimicking in part the fluctuations observed in microtubules.

Microtubules are part of the cellular cytoskeleton, a dynamic and adaptive self-assembled network that is critical for achieving compartmentalization, generating directed forces, and facilitating intracellular traffic (*4*). Individual microtubules display complex assembly dynamics, alternating between regimes of stable growth and catastrophic disassembly. This dynamic instability greatly increases the ability of the fibers to reorganize and cover large volumes of cellular space (*5*). The mechanism underlying the dynamic instability—simultaneous GTP-driven growth and guanosine diphosphate (GDP)–initiated shrinkage—relies on the critical composition of the so-called GTP-rich cap: that is, on far-from-equilibrium conditions (*6*).

Although chemists could construct responsive one-dimensional fibrous structures (*2*), the assembly-disassembly processes reported so far are all based on changing the equilibrium conditions and converting one stable aggregate state to another or to the monomer state. Illustrative examples include the enzyme-mediated self-assembly of peptide oligomers (*7*), photochemically tuned assembly and disassembly of zinc porphyrins (*8*), and the adenosine triphosphate (ATP)–induced helix inversion of chiral fibers (*9*). These processes have all been appropriately described by equilibrium models (*10*). Kinetic studies that take pathway complexity into account (*11*) have advanced our understanding of responsive synthetic fibers, despite the paucity of far-from-equilibrium systems investigated thus far.

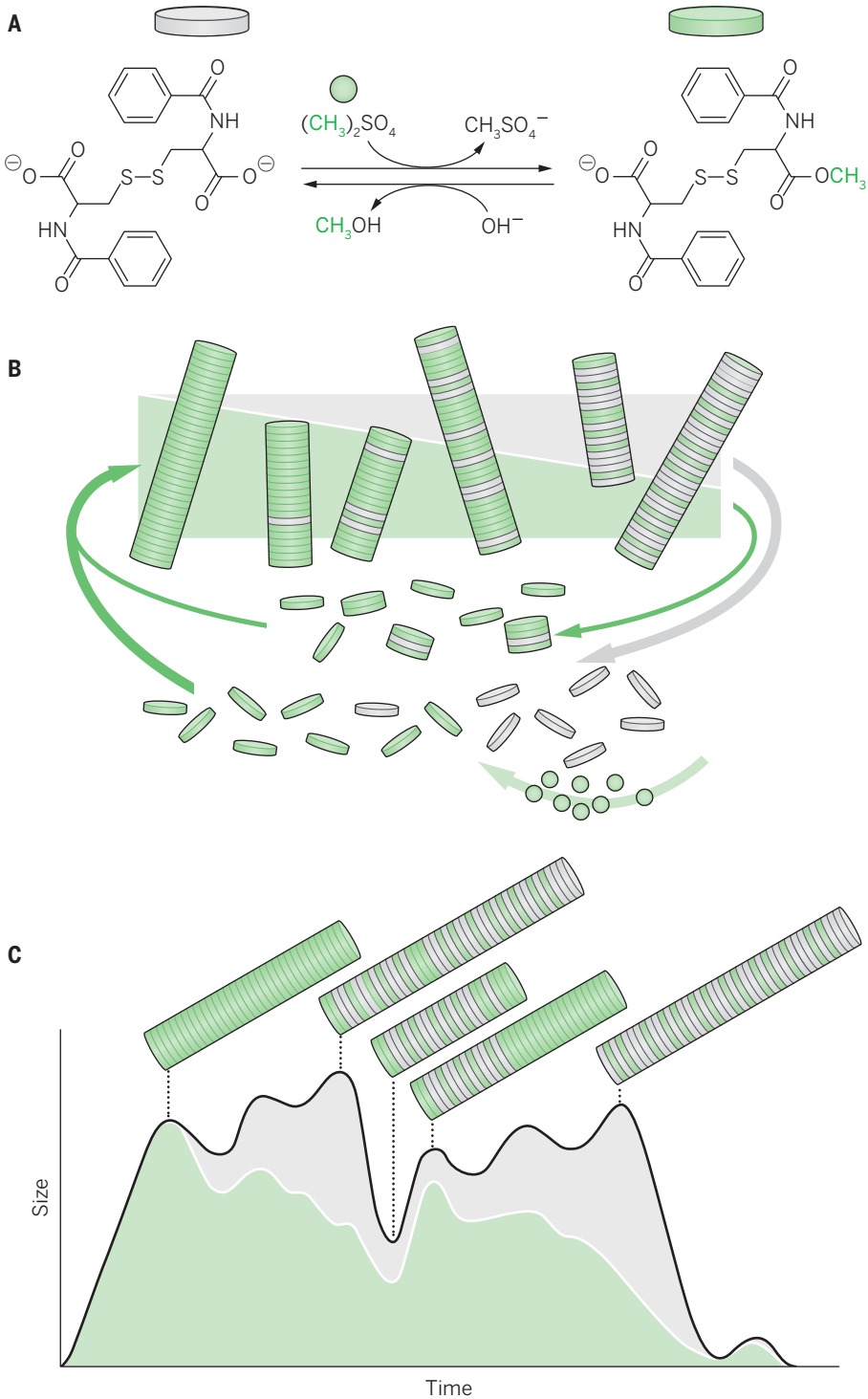
"...the far-from-equilibrium conditions allowed the authors to observe some of the more appealing characteristics of dissipative self-assembly..."

As early as 2010, Eelkema, van Esch, and collaborators disclosed initial results on the use of chemical fuels to power supramolecular polymerizations (*12*). In their strategy, a charged, inactive dicarboxylic monomer is transformed into an activated ester by alkylation, yielding a fibrous structure through aggregation. Competitive hydrolysis of the ester resulted in the eventual degradation of the supramolecular polymer. The addition of subsequent portions of alkylating agent resulted in new cycles of supramolecular polymerization followed by depolymerization.

Boekhoven *et al.* extended this concept to far-from-equilibrium conditions by increasing the rate of the reactions involved in the supramolecular cycle, leading to an increase in the concentration of fibrous filaments. This increase in turn led to the transient formation of hydrogels with storage moduli of up to 10 kPa, indicating elastic properties similar to those of other synthetic hydrogels used, for example, in tissue engineering. By independently controlling alkylation and hydrolysis, the materials' properties and

Institute of Complex Molecular Systems, Eindhoven University of Technology, Post Office Box 513, 5600 MB Eindhoven, Netherlands. E-mail: e.w.meijer@tue.nl

Published by AAAS



Fuel-driven supramolecular polymerization. (**A**) The interconversion of nonactive and active monomers. (**B**) The (dis)assembly of the subunits given in (A) into one-dimensional fibers. (**C**) The occurrence of sustained growth and catastrophic collapse in a single fiber. The black line represents the total fiber length; the white line indicates the number of active subunits in the fiber.

lifetime can be tuned. Although immediate applications of these gels are hard to foresee (because of the toxic nature of the dimethyl sulfate fuel), the far-from-equilibrium conditions allowed the authors to observe some of the more appealing characteristics of dissipative self-assembly: stochastic fiber collapse and simultaneous growth and shrinkage, both reminiscent of microtubule dynamics (see the figure).

A detailed analysis of the fibers during one chemical cycle using confocal microscopy enabled the authors to quantify the growth rate of each individual filament. This single-aggregate analysis is critical, because the average length changed gradually and did not show any characteristic signs of dissipative self-assembly. At the individual-fiber level, however, detailed insights into the assembly mechanisms emerged. Initially, fast fiber growth occurs universally because of the abundance of activated monomers. When the fuel is consumed, hydrolysis competes with activation, leading to the effects illustrated in the figure. First, catastrophic fiber collapse is observed, indicating a threshold of hydrolyzed subunits in the fiber, below which shrinkage takes place. Second, the collapse occurs solely at fiber ends and can be rescued by patches of nonhydrolyzed subunits resembling the microtubule GTP cap. Third, renewed growth after fuel depletion is facilitated by the release of activated monomers from concurrently degrading fibers. Finally, after complete hydrolysis, the remaining fibers collapse.

Although this behavior is surprisingly similar to microtubule dynamics, some facets still need to be designed and integrated in order to arrive at artificial life-like systems. Several important challenges can be set. How do we convert the responsiveness of fibrous materials to macroscopic work? How do we couple the transient growth of these materials to active networks with positive and negative feeback loops based on interacting chemistries? And finally, how are all of these components integrated? Progress in supramolecular polymerization may soon lead to the rational design of highly ordered filaments that can be used to perform mechanical action. Furthermore, recent advances in systems chemistry, combined with an increasing understanding of isolated biochemical networks, will undoubtedly allow chemists to optimize chemical networks in a holistic way. However, the true challenge lies in achieving the synchronized operation of optimized filaments with materials functionality and chemical networks. ■

REFERENCES

1. A. Desai, T. J. Mitchison, *Annu. Rev. Cell Dev. Biol.* **13**, 83 (1997).
2. T. Aida, E. W. Meijer, S. I. Stupp, *Science* **335**, 813 (2012).
3. J. Boekhoven *et al.*, *Science* **349**, 1075 (2015).
4. D. A. Fletcher, R. D. Mullins, *Nature* **463**, 485 (2010).
5. T. E. Holy, S. Leibler, *Proc. Natl. Acad. Sci. U.S.A.* **91**, 5682 (1994).
6. M. Kirschner, T. Mitchison, *Cell* **45**, 329 (1986).
7. S. Toledano, R. J. Williams, V. Jayawarna, R. V. Ulijn, *J. Am. Chem. Soc.* **128**, 1070 (2006).
8. T. Hirose, F. Helmich, E. W. Meijer, *Angew. Chem. Int. Ed.* **52**, 304 (2013).
9. M. Kumar *et al.*, *Nat. Commun.* **5**, 5793 (2014).
10. P. Jonkheijm *et al.*, *Science* **313**, 80 (2006).
11. P. A. Korevaar *et al.*, *Nature* **481**, 492 (2012).
12. J. Boekhoven *et al.*, *Angew. Chem. Int. Ed.* **49**, 4825 (2010).

10.1126/science.aad0194

Published by AAAS

MICROBIOME

Microbial growth dynamics and human disease

Examining microbial genome replication in tissues may reflect health status

By **Julia A. Segre**

How do human-associated microbial communities contribute to health and disease? To answer this, scientists have been exploring changes in the gut microbiota between individuals, and even across generations and continents (*1*, *2*). Large genome sequence data sets are producing tally sheets of bacteria in time and space throughout disease courses (*3*, *4*). One challenge has been to determine the metabolic state of these microbial communities to identify bacteria that are responding to a perturbation and/or driving disease pathogenesis (*5*, *6*). On page 1101 of this issue, Korem *et al.* (*7*) explore metagenomic DNA sequence data sets to estimate growth rates (metabolic states) of bacterial taxa in a microbial community.

Leveraging the classic understanding that genomes utilize defined origins to initiate replication, the authors discern differential proliferative states of microorganisms, even within a complex mixed community, and correlate these microbial growth dynamics with human disease states. Microbial DNA sequence data sets, which have been viewed historically as snapshots of diverse ecosystems, may now give rise to a moving picture that was unwittingly captured alongside.

Genomes replicate in an organized, molecularly defined process, and for most bacteria with a single chromosome, the bidirectional DNA fork initiates from a single fixed origin and moves toward a single terminus (*8*). Therefore, one might expect that under growth conditions, a bacterial genome would yield twice as many sequence reads surrounding the origin of replication ("peak") relative to the termini ("trough"). Although this concept has been explored in yeast and human genomes (*9*, *10*), Korem *et al.* have mined microbial data sets to glean a new understanding about metabolic states that underlie bacterial communities.

From first principles, Korem *et al.* demonstrate that nondividing stationary cultures of *Escherichia coli*, a workhorse lab bacterium, produce a relatively constant read depth across their genomes [peak-to-trough ratio (PTR) of 1], whereas rapidly growing cultures of *E. coli* produce twice as many DNA reads at loci near the origin of replication (PTR of 2). Moreover, an increased PTR precedes an increase in growth rate by about 30 min in a rapidly growing culture, thus demonstrating that PTR predicts changes in bacterial abundance. Analyzing 583 different human gut metagenomic samples that contain *E. coli*, the authors found PTRs that vary from 1 to 2.4, with a distribution that approximates the in vitro growth PTR range.

Do PTRs of *E. coli* accurately reflect the growth rates of human-associated commensals? Korem *et al.* tested *Enterococcus faecalis* and *Lactobacillus gasseri* under aerobic and anaerobic conditions, and as monocultures and as part of a mixed microbial community. They found that PTRs accurately reflect the in vitro growth rates of these commensal microbes. Moreover, the authors demonstrate that PTR values accurately reflect the in vitro growth rates for the pathogen *Citrobacter rodentium* under homeostatic conditions, and when treated with bacteriostatic or bactericidal antibiotics. Complementing these in vitro studies, Korem *et al.* found that when a mouse depleted of normal gut flora by antibiotic treatment is colonized with either virulent or nonvirulent *C. rodentium*, the PTR values in vivo correlate with virulence, mucosal adhesion, and proliferative properties of the bacteria. These results strengthen the predictive link between PTR and growth rate under many conditions, and even in a mixed defined microbial community.

The analysis of Korem *et al.* would be expected to become more complicated when applied to undefined mixed microbial communities with multiple strains of the same species, copy-number variation among genomic regions, and unannotated "dark matter," all layered on top of variable sequencing depth and coverage. However, drawing on a combination of biological insight and computational deftness, the authors performed multiple simulations to determine the robustness of binning reads into 10-kb regions, smoothing the coverage across bins, and only analyzing genomes with 60% of the 10-kb bins covered with overall median coverage greater than 0.05-fold. Data simulations show that this method was robust to the presence of multiple strains, copy-number variation of multiple 10-kb fragments, and genomes covered at only 0.05×. Notably, 0.05-fold coverage of an average 4-Mb bacterial genome requires only 200,000 reads—a number easily achieved with most metagenomic studies.

Because PTR values should peak at origins of replication, Korem *et al.* applied their computational analysis to hundreds of existing metagenomic samples and predicted the locations of the origin and terminus of replication for 187 different microbial strains. Their predictions agreed with the known replication origin of 132 strains and predicted the origin for the other 55 strains, with previously undefined origins. From existing metagenomic data sets with multiple body sites from the same individual, Korem *et al.* calculated the values of species present in both the oral cavity and stool from matched samples: *Streptococcus salivarius* has a higher PTR value in the oral cavity than in stool, whereas *Bacteroides vulgatus* has a higher PTR value in stool than in the oral cavity.

Tissue/organ "A"

In a given tissue in an individual, an abundant microbial species may not necessarily be one with high metabolic activity (PTR value).

BACTERIA	ABUNDANCE	GROWTH RATE (PTR VALUE)	METABOLIC ACTIVITY	DISEASE CORRELATION
Species "1"	Highest	1.2	Lowest	No
Species "2"	Lowest	2.0	Highest	Yes

Microbial Genomics Section, Translational and Functional Genomics Branch, National Human Genome Research Institute, National Institutes of Health, Bethesda, MD, USA. E-mail: jsegre@nhgri.nih.gov

Published by AAAS

Downloaded from www.sciencemag.org on September 5, 2015

These microbial growth differences may reflect a combination of the site's physiology, metabolic potential, and bacterial composition (see the table).

Do bacterial growth dynamics correlate with disease status? Again, exploring existing large metagenomic data sets (*3*, *11*), Korem *et al.* found associations between the mean bacterial PTR value and the occurrence of Crohn's disease and type II diabetes, as well as specific associations between eight different bacterial species and clinical parameters, such as a marker of glycemic control in diabetes. Most of the associations between species' growth dynamics and clinical parameters remained statistically significant even after correcting for relative abundance, underscoring that PTR is an independent feature reflecting gut metabolic state.

The dynamic readout derived from measuring PTRs for mixed bacterial communities offers enormous potential to detect which bacterial species or strains are rapidly responding to a therapeutic intervention in a prospective patient study. Correlating microbial growth dynamics across a longitudinal study could also discern which bacteria are modulating the response of other members of the microbial complex. Combining overall PTR values of the bacterial community, along with functional annotation of the replicating strains or species, could be harnessed within flux-balance analyses to predict the samples' metabolic state or potential (*12*, *13*). It is possible that confounding variables would complicate a "clean" interpretation of in vivo results; for example, an ileum sample with bacteria growing in a transitional aerobic-anaerobic environment would average different PTRs of the two states. But overall, computationally revealing growth dynamics from static metagenomic data sets is like hearing the actors speak in a talking movie for the first time after only viewing silent films. ■

REFERENCES

1. D. A. Relman, *N. Engl. J. Med.* **365**, 347 (2011).
2. E. A. Grice, J. A. Segre, *Annu. Rev. Genomics Hum. Genet.* **13**, 151 (2012).
3. J. Qin *et al.*, *Nature* **464**, 59 (2010).
4. Human Microbiome Project Consortium, *Nature* **486**, 207 (2012).
5. D. Kang, B. Shi, M. C. Erfe, N. Craft, H. Li, *Sci. Transl. Med.* **7**, 293ra103 (2015).
6. J. J. Faith, N. P. McNulty, F. E. Rey, J. I. Gordon, *Science* **333**, 101 (2011).
7. T. Korem *et al.*, *Science* **349**, 1101 (2015).
8. M. L. Mott, J. M. Berger, *Nat. Rev. Microbiol.* **5**, 343 (2007).
9. A. Koren *et al.*, *Cell* **159**, 1015 (2014).
10. J. Xu *et al.*, *Genome Biol.* **13**, R27 (2012).
11. H. B. Nielsen *et al.*, *Nat. Biotechnol.* **32**, 822 (2014).
12. O. Manor, R. Levy, E. Borenstein, *Cell Metab.* **20**, 742 (2014).
13. W. R. Harcombe *et al.*, *Cell Rep.* **7**, 1104 (2014).

10.1126/science.aad0781

MATERIALS SCIENCE

The mechanism of crystal deformation

Microscopy provides an atomistic view of how crystalline materials deform

By **Wayne D. Kaplan**

Modern metals and alloys (pure metals containing additives that modify the metal structure and properties) are used in almost all aspects of modern engineering. One of the unique properties of metals and alloys not shared by other materials, such as ceramics, semiconductors, and some polymers, is that they are malleable. That is, they can be plastically deformed to obtain a necessary shape. Furthermore, their degree of ductility can actually be controlled so as to define the level of malleability according to the requirements of the manufacturing process, or what is required during use. The mechanism by which metals deform is via the motion of linear defects at the atomistic scale, called dislocations (see the figure). In metals, dislocations are usually mobile, and their motion provides for the irreversible shifting of atomic planes in a process called slip, resulting in plastic deformation. Without the mechanism of moving dislocations, metals would fail under mechanical loading by brittle fracture, behaving in a manner similar to brittle semiconductors or ceramics. As a result, dislocation theory has been a critical issue from both a fundamental and applied point of view. On page 1080 of this issue, Kuzmina *et al.* (*1*) address perhaps one of the most crucial questions regarding dislocations and their properties: What is the nature of the dislocation core, and can its structure and chemistry be modified to control the properties of dislocations?

Defects in materials are usually classified as point defects, linear defects (dislocations), and planar defects. Planar defects include the planar surface of contact between crystals having the same structure and chemistry but rotated in space, or so-called grain boundaries. Planar defects also include the planar contact between crystals having a different structure and/or chemistry (so-called phase boundaries) and include the planar contact between crystals and gases or liquids, which are basically the free surfaces of materials. As the length scale of a material's microstructure is reduced (the size of crystals in a polycrystalline material), planar defects have an increased influence on material properties. As such, similar to dislocations, planar defects have been studied in detail for many years.

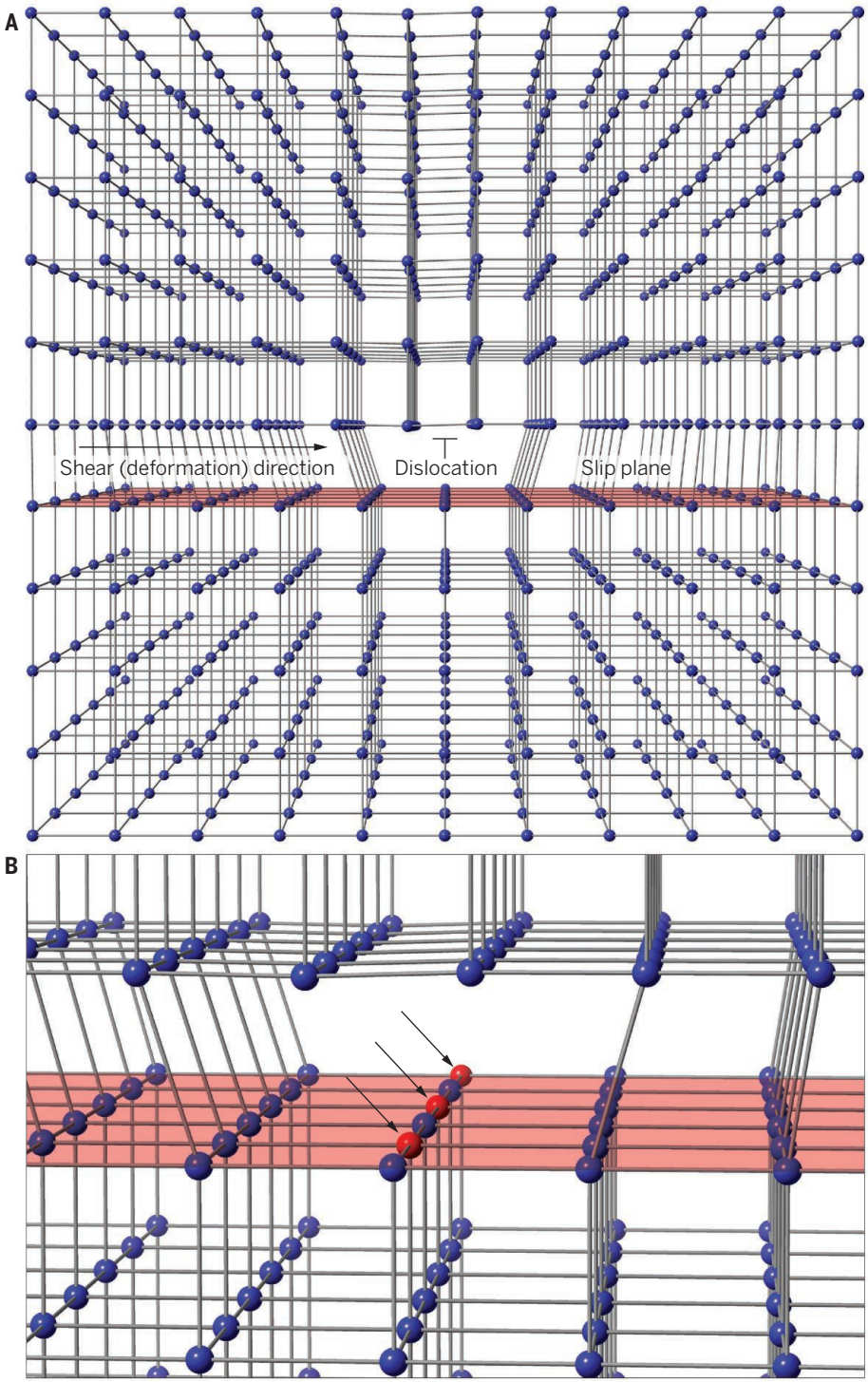
One of the most fundamental theories regarding planar defects was introduced by Gibbs in 1878 (*2*), where he defined the correlation between surface energy, the chemical activity of solute atoms in solution in a material, and the excess amount of solute (a concentration different from that in solution in the bulk) at the surface. As a system approaches equilibrium, the chemical composition of planar defects (surfaces, phase boundaries, and grain boundaries) can be very different from the chemical composition of the bulk. The concept of correlating the surface energy with surface chemistry was recently expanded to include the structural order of atoms in the plane of a surface (*3*). This has been experimentally confirmed to occur (*4*–*6*) and to minimize energy (*7*), and has been tied into properties and kinetics of surface motion (*8*) and even adhesion (*9*, *10*). Some researchers have referred to the two-dimensional (2D) equilibrium state as being a phase, but of course such surface states can only exist at the boundary between bulk phases, and certainly cannot exist at equilibrium if a bulk phase is not present. So as to prevent confusion, these 2D states are often called complexions (*11*).

> ***"The existence of complexions along dislocation lines...offers opportunities for new fields of fundamental research, together with important technological implications."***

Kuzmina *et al.* extend the concept of complexions to the equilibrium state along the

Department of Materials Science and Engineering, Technion–Israel Institute of Technology, Haifa, Israel.
E-mail: kaplan@technion.ac.il

Published by AAAS



The route to deformation. (**A**) Schematic of a dislocation in a crystal, where the dislocation line is marked with a T. The slip plane, upon which the dislocation moves in the horizontal direction and thus facilitates plastic deformation, is indicated in red. In (**B**) every other atom in the dislocation line is replaced by an atom (red) from solution, driven by the reduction in line energy of the dislocation, thereby altering the dislocation chemistry and potentially the structure, and hypothetically its mobility.

line of dislocations via experimental characterization of dislocation line chemistry and structure. They studied dislocations in an equilibrated model steel alloy of Fe containing 9 atomic percent Mn. Dislocations in a thin sharp needle of the alloy were identified by scanning transmission electron microscopy, and the chemical excess of Mn along the lines of the same dislocations was characterized by atom probe tomography, where the same needle was subjected to an electric field at such an intensity that atoms were removed from the apex of the needle (*12*). These atoms, now ions, moved through a time-of-flight detector and were then recorded on a position-sensitive detector, identifying the chemical species and even the isotope of each individual ion and the site from which it was extracted. Kuzmina *et al.* were able to experimentally demonstrate that an excess of Mn exists along the line of the dislocations. In addition, electron diffraction from the dislocation lines indicated a different atomic structural packing of the Fe and Mn atoms from that of the bulk Fe. These results indicate that linear complexions can exist, in addition to complexions at planar defects.

The existence of complexions along dislocation lines as reported by Kuzmina *et al.* offers opportunities for new fields of fundamental research, together with important technological implications. The structure and chemistry in the core of different types of dislocations in the same material should be characterized and correlated with the mobility of the dislocations (which is associated with plastic deformation). First-order complexion transitions at grain boundaries and surfaces have been identified, and similar transitions may occur along dislocations, thus potentially expanding the number of parameters available to engineers to control plasticity. It may even be possible to alter the mobility of normally immobile (sessile) dislocations in ceramics or semiconductors, thus reducing the intrinsically brittle nature of such materials. Finally, dislocations at interfaces often act as traps for charge carriers (electrons and holes), detrimentally affecting electrical mobility at semiconductor interfaces. By altering the complexion of dislocations, it may be possible to reduce charge trapping and to improve the conductivity at interfaces between dissimilar materials. ■

REFERENCES

1. M. Kuzmina, M. Herbig, D. Ponge, S. Sandlöbes, D. Raabe, *Science* **349**, 1080 (2015).
2. J. W. Gibbs, *The Scientific Papers of J. Willard Gibbs, Vol. 1* (Dover, New York, 1961), p. 219.
3. M. Tang, W. C. Carter, R. M. Cannon, *Phys. Rev. B* **73**, 024102 (2006).
4. J. V. Lauritsen *et al.*, *Phys. Rev. Lett.* **103**, 076103 (2009).
5. G. Z. Zhu, G. Radtke, G. A. Botton, *Nature* **490**, 384 (2012).
6. S. H. Oh, Y. Kauffmann, C. Scheu, W. D. Kaplan, M. Rühle, *Science* **310**, 661 (2005).
7. M. Baram, D. Chatain, W. D. Kaplan, *Science* **332**, 206 (2011).
8. S. J. Dillon, M. Tang, W. C. Carter, M. P. Harmer, *Acta Mater.* **55**, 6208 (2007).
9. E. Nussbaum, H. Meltzman, W. D. Kaplan, *J. Mater. Sci.* **47**, 1647 (2012).
10. J. Luo, H. Cheng, K. M. Asl, C. J. Kiely, M. P. Harmer, *Science* **333**, 1730 (2011).
11. W. D. Kaplan, D. Chatain, P. Wynblatt, W. C. Carter, *J. Mater. Sci.* **48**, 5681 (2013).
12. D. N. Seidman, *Annu. Rev. Mater. Res.* **37**, 127 (2007).

10.1126/science.aac9623

Published by AAAS



In *Natural Capital*, Dieter Helm advocates the inclusion of Earth's assets in economic decision-making processes.

Natural Capital
Valuing the Planet
Dieter Helm
Yale University Press, 2015. 289 pp.



ENVIRONMENTAL ECONOMICS

Banking on nature

A framework for valuing and protecting natural resources

By **Doris Capistrano**

Does economic growth have to be at the expense of nature and future generations? Lucid and compellingly argued, Dieter Helm's latest volume, *Natural Capital*, says no.

Ensuring that the present generation's growth will still permit future generations to meet their needs and grow requires a sufficient stock of natural capital assets—the renewable and nonrenewable natural resources and ecosystems that provide humans with a wide range of goods and services. A highly respected economist, Helm proposes a consistent framework and economically efficient approach to protect and enhance these assets so as to achieve sustainable growth.

The book's central argument is that only by putting the environment at the heart of the economy can there be any hope of preventing the destruction that will otherwise happen. Helm argues that because natural resources are free, their real worth is not fully valued by producers and consumers, nor are the benefits derived from them reflected in standard economic measures such as gross domestic product. Thus, they tend to be overused and receive little investment for their management and conservation.

Building on ideas from economics, ecosystems science, and public policy, Helm advocates for asset-based accounting and valuation as a first step and a policy approach defined by a simple rule: The aggregate level of natural capital should not decline. This rule allows for the substitution of different types of capital as long as the aggregate level is maintained and as long as ecological thresholds are not crossed.

Sharply written and well illustrated with examples from the United Kingdom and elsewhere, this engaging book offers a coherent package of practical solutions. Because not all natural capital assets can be saved, Helm argues that we should focus on renewable assets such as forests and fisheries, particularly those at risk, and ensure that these are not exploited beyond the limits of their capacity for self-regeneration. Nonrenewables, such as oil and gas, he argues, can be substituted for with other forms of capital, such as solar power. Renewables can also be substituted for, but only up to a threshold.

Helm calls for taxing pollution and for requiring that any physical damage to renewable natural capital be compensated for with improvements in other equivalent, renewable capital. For example, destruction of habitat for development projects can be offset with habitat creation or land restoration elsewhere. He also argues for the creation of an intergenerational fund financed by the excess profits, also called "economic rent," that can be derived from nonrenewable resources as a result of their scarcity. Such a fund would be used to restore degraded ecosystems, protect renewable assets, and compensate future generations for the depletion of nonrenewable resources. Together, the compensation payments, pollution taxes, and rents from nonrenewable resources would allow for a self-financing system. By Helm's reckoning, despite some short-term pain the resulting long-term growth path will be sustainable.

Some of the proposals Helm discusses are already being piloted. The Economics of Ecosystems and Biodiversity, for example, is a global study that was jointly initiated in 2007 by the German Federal Ministry for the Environment and the European Commission in an effort to demonstrate and capture the value of ecosystems and biodiversity. The World Bank–led Wealth Accounting and the Valuation of Ecosystem Services is another example of a partnership dedicated to incorporating natural resources into development planning and national economic accounts. More than 30 countries have begun natural capital accounting using a standard methodology adopted by the United Nations Statistical Commission in 2012, and nearly 30 influential financial institutions have pledged to incorporate the value of natural capital into their investment decisions. Payment schemes for reducing carbon emissions from deforestation and forest degradation are in varying stages of readiness in many developing countries. Helm weaves these and other market-based ideas into a comprehensive framework and lends them a fresh and powerful voice.

Considering the practicalities and politics of policy-making, Helm argues for market-based mechanisms as a first resort over regulation and other options. Market-based mechanisms have inherent advantages, Helm notes, including making lobbying and regulatory capture much harder to effect. In many countries, however, making market-based mechanisms work effectively will entail first dealing with tangled issues of power and rights, especially at the local level. Although land and natural resources may be state-owned in many developing countries, for example, diverse tenure arrangements frequently determine actual resource use. Lessons from forestry and other sectors show that securing the rights of local users—forest dwellers, fishers, or farmers—who are often best positioned to protect the resources is critical for ecosystem maintenance, long-term conservation, and livelihood improvement. Getting natural capital asset valuation right may be central to sustainable growth, but securing and protecting rights to resources is fundamental.

Natural Capital should be required reading for policy-makers, economists, environmentalists, and all those concerned about sustainable growth and development.

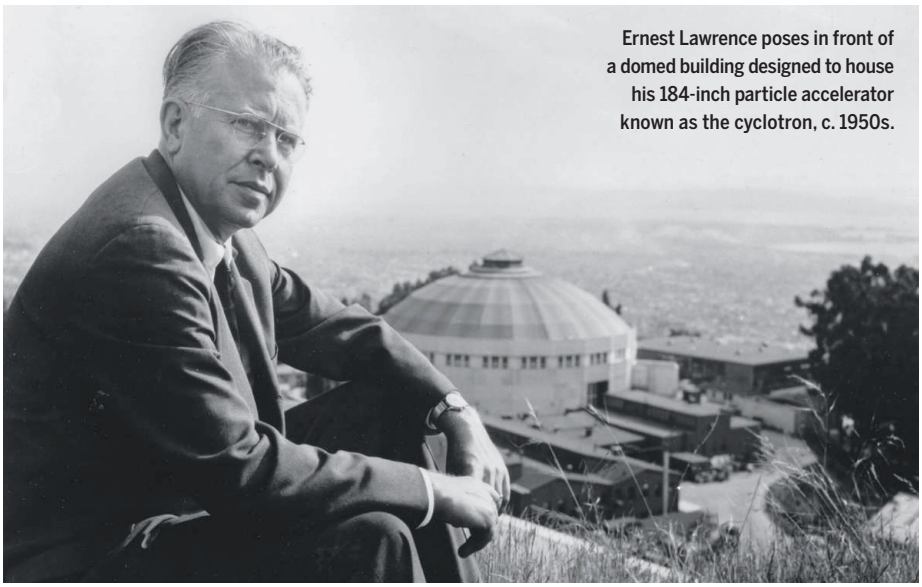
The reviewer is senior advisor of the Association of Southeast Asian Nations (ASEAN)–Swiss Partnership on Social Forestry and Climate Change, Jakarta, Indonesia.

10.1126/science.aab3400

CREDIT: © MONTY RAKUSEN/CORBIS

Downloaded from www.sciencemag.org on September 5, 2015

Published by AAAS



Ernest Lawrence poses in front of a domed building designed to house his 184-inch particle accelerator known as the cyclotron, c. 1950s.

Big Science
Ernest Lawrence and the Invention That Launched the Military-Industrial Complex
Michael Hiltzik
Simon and Schuster, 2015. 549 pp.



HISTORY OF PHYSICS

Cult of the machine

A major player in 20th-century physics, Ernest Lawrence helped usher in an era of big-budget research projects

By **Alex Wellerstein**

High above the hills of the University of California, Berkeley, sits a physics laboratory that employs more than 3000 people, boasts an association with 13 Nobel Prizes, and has a budget of over $750 million dollars. The Lawrence Berkeley Laboratory is named after its founder, the famed American physicist Ernest Orlando Lawrence. Lawrence's name also adorns the Berkeley laboratory's weapons spinoff at Livermore, a career award issued by the U.S. Department of Energy, and an element (the actinide metal "lawrencium"). By any standard, he was a giant of American physics and, arguably, the architect of the late-20th-century approach to science that required big machines, big budgets, and big staffs, known fittingly as "Big Science" (*1*).

Michael Hiltzik, a Pulitzer Prize–winning journalist, has written a new biography of Lawrence, the only such monograph published since Herbert Childs's (family-sanctioned) book *An American Genius* was released in 1968 (*2*). Hiltzik takes a less hagiographical approach than did Childs, and the book reflects a shift in society's perception of Big Science, in particular its deep historical connections to military research.

What kind of scientist was Ernest Lawrence? He was less a discoverer than an inventor, more a tool builder than a tool user. At the center of Lawrence's world was the circular particle accelerator he invented, dubbed the "cyclotron." Around this initially humble creation, Lawrence built an empire of labor and of funding and a new way of doing physics.

Lawrence's approach relied on the "remorseless exploitation of cheap graduate-student labor," as Hiltzik aptly puts it. His first cyclotron, a small device a mere six inches in diameter, was apparently constructed entirely by a graduate student named Niels Edlefsen. Lawrence was singing its successes even before it was clear that it worked—which, it turned out, it didn't. The first functioning model was developed by his next student, M. Stanley Livingston, who debugged the earlier machine and fixed its numerous faults. Even before Livingston had put the cyclotron prototype through its paces, Lawrence was hot on the trail of the money needed to build a bigger model.

Lawrence's methods were viewed with justifiable skepticism among the scientific greats of Europe. For the first decade, they failed to produce real results. His first major scientific announcement—a theory of deuteron disintegration—proved to be an embarrassing flop. Instead of describing a new phenomenon that overturned the laws of physics, Lawrence instead broadcast to the world that the Radiation Laboratory couldn't keep its samples clean.

Lawrence's problem, as diagnosed by his contemporaries, was that he was more interested in the "cult of the machine" than the scientific results. A French visitor once ridiculed the laboratory for having "a mania for gadgets or a post-infantile fascination for scientific meccano [sic] games." The number of major discoveries that the Radiation Laboratory ought to have stumbled across, had it been watching for them, is a long one: The existence of the positron and the neutron were discovered during this time by using more modest tools and staffs, for example, as were the phenomena of induced radioactivity and nuclear fission.

Yet the funding continued to pour in, in part because of what Lawrence would at one point dub "the vaudeville"—his ability to project boundless enthusiasm and confidence to nonscientific audiences. In a rare moment of candor, he once admitted that he was making the cyclotrons bigger simply because he could get the money to do so, not because he had any idea about what the bigness would let him do.

To a large degree, Lawrence's strategy worked. The cyclotron went from being a crazy venture to a common tool, earning Lawrence the Nobel Prize in 1939. Part of the reason for this was that, in the right hands, it did yield important results. Ed McMillan, Luis Alvarez, and Glenn Seaborg—all future Nobel Laureates—cut their teeth and did some of their best work in the Radiation Laboratory, finding ways to make Lawrence's chaotic fiefdom work for them. Additionally, when it became clear that cyclotrons could produce radioisotopes in quantity for other types of scientific research, Lawrence was happy to provide them to collaborators, knowing that he could only gain from their rising applicability.

The Second World War brought the ultimate patron to Lawrence's door: the U.S. military establishment. Lawrence's involvement in defense work began with radar but hit its stride with nuclear weapons. His relationship with the military would continue until the end of his life.

The reviewer is at the College of Arts and Letters, Stevens Institute of Technology, Hoboken, NJ 07030, USA. E-mail: wellerstein@gmail.com

PHOTO: EMILIO SEGRÈ VISUAL ARCHIVES, AMERICAN INSTITUTE OF PHYSICS

Downloaded from www.sciencemag.org on September 5, 2015

Published by AAAS

Lawrence was one of the loudest proponents of building the atomic bomb, largely because he claimed that he could practically pull it off single-handedly. In this, as with many things, he overpromised. The results-driven General Leslie Groves, head of the Manhattan Project, who did not accept the kinds of delays, excuses, and cost overruns that Lawrence had become accustomed to, proved a force to reckon with. Lawrence was ultimately able to generate enough highly enriched uranium for the Hiroshima bomb; however, his approach was scrapped in favor of a competitor's technology in the early postwar.

Lawrence comes off as particularly shallow and unreflective in the immediate postwar period. He complained that the scientists who participated in the discussions about the domestic control of atomic energy were "frittering away so much time and energy on political problems, when they could be devoting themselves to scientific pursuits." In response to his former colleague J. Robert Oppenheimer's expressions of unease, Lawrence glibly remarked that, "I am a physicist and I have no knowledge to lose in which physics has caused me to know sin." If one believes these sentiments were rooted in true conviction, one might be inclined to give Lawrence the benefit of the doubt. But it is all too easy to read these comments cynically, as Lawrence benefited immensely from taking such unruffled positions about the militarization of science.

Some of Lawrence's political opinions eventually caught up with him. His unwavering support for anti-Communist loyalty oaths and internal investigations, for example, led to an exodus of top-flight theoretical physicists from his laboratory in the early 1950s. He advocated strongly for the thermonuclear "super" bomb in 1949 and later lent his name, and credibility, to many questionable Cold War projects, including the development of a so-called "clean bomb." To many contemporaries, he appeared to be cheapening his reputation as a scientist in order to please his political patrons.

Lawrence's hawkish leanings were in keeping with the sentiments of many physicists involved in defense work at the time, but his politics would eventually go a step further. He played a key role in the "Oppenheimer affair," the hearing conducted by the Atomic Energy Commission that ultimately resulted in the revocation of Oppenheimer's security clearance. When questioned by the chief counsel of the review board before the hearing, Lawrence made disparaging comments about his former friend, stating at one point that Oppenheimer "should never again have anything to do with the forming of policy." Claiming illness and presumably fearing retribution, Lawrence begged out of testifying at the actual hearing at the last minute.

Lawrence's career was not without missteps. His efforts to set up the Livermore laboratory using the Radiation Laboratory as a model (cheap workers surrounding an all-powerful director) produced a string of nuclear fizzles. Funding became harder to procure when the people judging his project proposals were fellow physicists who proved less susceptible to his infectious optimism. A brief foray into private industry in the 1950s ended in a lackluster failure. The things Lawrence was good at (over-budgeted one-off technical accomplishments) were precisely the opposite of the requirement for building and manufacturing profitable consumer electronics.

Still, no one could accuse him of a lack of initiative, ambition, or energy. But the endless work appears to have taken a heavy toll—in 1958, Lawrence died from complications from stress-related ulcerative colitis.

Ultimately, it is difficult to judge Lawrence only by his legacy in physics, without considering the post–Cold War environment in which he worked. The era in which individual governments forked over huge sums of taxpayer funding to build monuments to discovery, with the vague expectation of military benefits, appears to have ended.

In the end, Hiltzik seems uncertain as to what genre the book is to belong: blushingly flattering at times, damningly critical at others, he never quite gets inside Lawrence's head. What was it that drove the man: a true devotion to science or to ego? Is he a scientific hero or a cautionary tale?

REFERENCES AND NOTES

1. P. Galison, B. Hevly, Eds., *Big Science: The Growth of Large-Scale Research* (Stanford Univ. Press, Stanford, CA, 1992).
2. H. Childs, *American Genius: The Life of Ernest O. Lawrence* (Dutton, New York, 1968).

10.1126/science.aac7351



RED POPPY
[*Ignis Ubinanae*]
Flower with
fiery plasma.

CREDIT: © VINCENT FOURNIER

BIOTECHNOLOGY

Bio Art: Altered Realities
William Myers
Thames and Hudson, 2015. 256 pp.



In *Bio Art*, writer and curator William Myers offers a timely look at the implications of new and emerging biological technologies as interpreted by more than 60 contemporary artists. Combining microorganisms with traditional media, pieces such as Julia Lohmann's *Co-Existence* (2009) probe our evolving understanding of the relationship between human and nonhuman organisms, while others, including Mara Haseltine's artificial oyster reefs (*Oyster Island*, 2010), explore how we are reinventing our roles in the earth's ecosystems. Still other works—including Eduardo Kac's transgenic petunia, which includes a gene isolated from the artist's own body (*Natural History of the Enigma*, 2008)—encourage us to reflect on the possibilities enabled by synthetic biology. Thoughtful and provocative, *Bio Art* is a compelling contribution to the biotechnology conversation.

10.1126/science.aad2616

Published by AAAS

LETTERS

Edited by **Jennifer Sills**

Hot genome leaves natural histories cold

ON 3 JUNE, the Avian Phylogenomics Consortium announced an ambitious plan to generate draft genome sequences for about 10,500 extant bird species over the next 5 years (*1*). This news has excited global ornithologists and evolutionary biologists, who long to understand how avian phylogeny, morphology, life history, ecology, behavior, and physiology have been shaped over the past billion years.

In contrast, species' natural history information—the crucial phenotypes for interpreting the patterns of genome sequences—is still poor in birds. Clutch size as a basic demographic parameter remains unknown for 50% of the 10,500 bird species on the list to be sequenced (*2*), in spite of at least 150 years of naturalists' efforts. Knowledge gaps are even bigger for other aspects of the species' natural history. Fewer than 270 species have been evaluated for genetic mating systems (*3*) and fewer than 80 species for metabolic rates in the wild (*4*). We are unlikely to learn these phenotypic data in the next 5 years.

Why is natural history research, in contrast to genomics, left out in the cold? One reason is likely the currently prevailing academic evaluation system. The fact that time-consuming natural history studies have few opportunities to get published in high–impact factor journals forces many ornithologists to turn to molecular-based studies, especially sequencing genomes (*5*). Another reason could be that many young people are losing their passion to work in such exciting places as the Tibetan plateau and Amazon rainforests due largely to an increasingly urbanized and digitalized lifestyle.

It is time to make an effort to collect species' natural history information, both to make sense of the ever-booming genome sequencing projects and to enrich human's knowledge about nature.

Xin Lu

Department of Ecology, College of Life Sciences, Institute for Advanced Studies, Wuhan University, Wuhan 430072, China.
E-mail: luxinwh@163.com

REFERENCES

1. G. Zhang, *Nature* **522**, 34 (2015).
2. W. Jetz, C. H. Sekercioglu, K. Bohning-Gaese, *PLOS Biol.* **6**, 2650 (2008).
3. C. K. Cornwallis, S. A. West, K. E. Davis, A. S. Griffin, *Nature* **466**, 969 (2010).
4. L. N. Hudson, N. J. B. Isaac, D. C. Reuman, *J. Anim. Ecol.* **82**, 1009 (2013).
5. G. Zhang, E. D. Jarvis, M. T. P. Gilbert, *Science* **346**, 1308 (2014).

Documenting rare disease data in China

RARE DISEASES HAVE benefited from increasing public awareness in China. The upcoming establishment of a Rare Diseases Prevention and Treatment Law (*1*) and the foundation of the Chinese Organization for Rare Disorders (CORD) have promoted the development of rare-disease management. However, for most rare diseases, our understanding of their etiology and pathogenesis is poor, and few effective treatment methods exist.

Many Western countries are aware of the importance of rare-disease data and have made substantial efforts to promote data sharing and consolidated data collection for rare diseases, such as the Canadian Organization for Rare Disorders and the European Reference Networks (*2*). By contrast, there is still no similar public database or cooperative platform being developed in China, although this country supports relatively abundant patient resources. Undoubtedly, this is a huge loss for rare disease research, not only in China but also worldwide.

With support from local regulatory bodies and the Ministry of Science and Technology of China Grants (973 program, 2015CB964600), a pilot project aimed at conducting clinical and translational research on congenital cataracts, Childhood Cataract Program of the Chinese Ministry of Health (CCPMOH), is being conducted at Zhongshan Ophthalmic Center, Sun Yat-sen University in Guangzhou, one of China's largest eye care facilities. Since 2011, we have included clinical data for over 1300 patients in our clinical database [the largest clinical database of congenital cataracts registered at www.clinicaltrials.gov (NCT01417819)], containing information on the entire treatment process and the follow-up records. In addition, more than 200 bio-specimens from pediatric patients have been collected and stored in our bio-bank, which can be used for future biological research.

Efforts made by a single center or an independent team are clearly insufficient. Changing this situation in China will be a win-win both for doctors and their patients with rare diseases. We hope that this model, along with those of Canada and Europe, will serve as a guide for policy-makers working to promote easier access to data exchange and integration and to construct a nationwide data-sharing platform in China.

Haotian Lin, Erping Long, Weirong Chen, Yizhi Liu*

The State Key Laboratory of Ophthalmology, Zhongshan Ophthalmic Center, Sun Yat-sen University, Guangzhou, 510060, China.

*Corresponding author. E-mail: yizhi_liu@aliyun.com

REFERENCES

1. J. J. Gao, P. P. Song, W. Tang, *Drug Discoveries Therapeut.* **7**, 126 (2013).
2. M. I. Bellgard *et al.*, *Health Pol. Technol.* **3**, 325 (2014).



The *Pipra fasciicauda* is among the many bird species with unknown natural histories.

PHOTO: © GLENN BARTLEY/ BIA/MINDEN PICTURES/CORBIS

Acknowledging AI's dark side

THE 17 JULY special section on Artificial Intelligence (AI) (p. 248), although replete with solid information and ethical concern, was biased toward optimism about the technology.

The articles concentrated on the roles that the military and government play in "advancing" AI, but did not include the opinions of any

Downloaded from www.sciencemag.org on September 5, 2015

Published by AAAS

political scientists or technology policy scholars trained to think about the unintended (and negative) consequences of governmental steering of technology. The interview with Stuart Russell touches on these concerns ("Fears of an AI pioneer," J. Bohannon, News, p. 252), but as a computer scientist, his solutions focus on improved training. Yet even the best training will not protect against market or military incentives to stay ahead of competitors.

Likewise double-edged was M. I. Jordan and T. M. Mitchell's desire "that society begin now to consider how to maximize" the benefits of AI as a transformative technology ("Machine learning: Trends, perspectives, and prospects," Reviews, p. 255). Given the grievous shortcomings of national governance and the even weaker capacities of the international system, it is dangerous to invest heavily in AI without political processes in place that allow those who support and oppose the technology to engage in a fair debate.

The section implied that we are all engaged in a common endeavor, when in fact AI is dominated by a relative handful of mostly male, mostly white and east Asian, mostly young, mostly affluent, highly educated technoscientists and entrepreneurs and their affluent customers. A majority of humanity is on the outside looking in, and it is past time for those working on AI to be frank about it.

The rhetoric was also loaded with positive terms. AI presents a risk of real harm, and any serious analysis of its potential future would do well to unflinchingly acknowledge that fact.

The question posed in the collection's introduction—"How will we ensure that the rise of the machines is entirely under human control?" ("Rise of the machines," J. Stajic *et al.*, p. 248)—is the wrong question to ask. There are no institutions adequate to "ensure" it. There are no procedures by which all humans can take part in the decision process. The more important question is this: Should we slow the pace of AI research and applications until a majority of people, representing the world's diversity, can play a meaningful role in the deliberations? Until that question is part of the debate, there is no debate worth having.

Christelle Didier,[1] Weiwen Duan,[2] Jean-Pierre Dupuy,[3] David H. Guston,[4] Yongmou Liu,[5] José Antonio López Cerezo,[6] Diane Michelfelder,[7] Carl Mitcham,[8] Daniel Sarewitz,[9] Jack Stilgoe,[10] Andrew Stirling,[11] Shannon Vallor,[12] Guoyu Wang,[13] James Wilsdon,[11] Edward J. Woodhouse[14]*

[1]Lille University, Education, Lille, 59653, France. [2]Institute of Philosophy, Chinese Academy of Social Sciences, Beijing, 100732, China. [3]Department of Philosophy, Ecole Polytechnique, Paris, 75005, France. [4]School for the Future of Innovation in Society, Arizona State University, Tempe, AZ 85287-5603, USA. [5]Department of Philosophy, Renmin University of China, Beijing, 100872, China. [6]Department of Philosophy, University of Oviedo, Oviedo, Asturias, 33003, Spain. [7]Department of Philosophy, Macalester College, Saint Paul, MN 55105, USA. [8]Liberal Arts and International Studies, Colorado School of Mines, Golden, CO 80401, USA. [9]Consortium for Science, Policy, and Outcomes, Arizona State University, Washington, DC 20009, USA. [10]Department of Science and Technology Studies, University College London, London, WC1E 6BT, UK. [11]Science Policy Research Unit, University of Sussex, Falmer, Brighton, BN1 9SL, UK. [12]Department of Philosophy, Santa Clara University, Santa Clara, CA 95053, USA. [13]Department of Philosophy, Dalian University of Technology, Dalian, 116024, China. [14]Department of Science and Technology Studies, Rensselaer Polytechnic Institute, Troy, NY 12180, USA.

*Corresponding author.
E-mail: woodhouse@rpi.edu

TECHNICAL COMMENT ABSTRACTS

Comment on "Glacial cycles drive variations in the production of oceanic crust"

John A. Goff

Crowley *et al.* (Reports, 13 March 2015, p. 1237) propose that abyssal hill topography can be generated by variations in volcanism at mid-ocean ridges modulated by Milankovitch cycle–driven changes in sea level. Published values for abyssal hill characteristic widths versus spreading rate do not generally support this hypothesis. I argue that abyssal hills are primarily fault-generated rather than volcanically generated features.

Full text at http://dx.doi.org/10.1126/science.aab2350

Response to Comment on "Glacial cycles drive variations in the production of oceanic crust"

John W. Crowley, Richard F. Katz, Peter Huybers, Charles H. Langmuir, Sung-Hyun Park

Goff comments that faulting is important for creation of abyssal hills and is the dominant process at slow-spreading ridges. We respond that faulting is indeed important but cannot alone explain the bathymetric signal predicted by our models and observed at the Australian-Antarctic Ridge. We show that for intermediate- to fast-spreading ridges, abyssal hill spacing is consistent with the periodicity of the obliquity cycle.

Full text at http://dx.doi.org/10.1126/science.aab3497

Published by AAAS

TECHNICAL COMMENT

OCEANOGRAPHY

Comment on "Glacial cycles drive variations in the production of oceanic crust"

John A. Goff

Crowley *et al*. (Reports, 13 March 2015, p. 1237) propose that abyssal hill topography can be generated by variations in volcanism at mid-ocean ridges modulated by Milankovitch cycle–driven changes in sea level. Published values for abyssal hill characteristic widths versus spreading rate do not generally support this hypothesis. I argue that abyssal hills are primarily fault-generated rather than volcanically generated features.

Crowley *et al*. (*1*) purport to show evidence that topographic profiles through abyssal hill morphology perpendicular to the spreading ridge axis exhibit periodicities that correspond well to Milankovitch cycles. The argument is that this correspondence could be explained by volcanic output at the mid-ocean ridge (MOR) modulated by the lithostatic pressure variations associated with rising and falling sea level. A contemporaneous paper by Tolstoy (*2*) reaches the same conclusion. I will refer to this argument as the "CT hypothesis." Crowley *et al*. also formulate a sophisticated numerical model to predict seafloor variations that could result from sea-level variability over the past 1.2 million years.

The CT hypothesis makes specific predictions about the variation of abyssal hill horizontal scales in the direction perpendicular to the spreading axis (the "width" of the abyssal hill) as a function of spreading rate; these predictions can be tested with existing published results. In the simplest possible case, the CT hypothesis predicts that abyssal hill width will scale linearly with spreading rate. For example, if we assume that the 100,000-year Milankovitch cycle is the dominant driver for abyssal hill formation, as suggested by Tolstoy (*2*), then abyssal hill width will be 1 km for every 1 cm/year of half-spreading rate. Thus, widths would be ~1 km at ultraslow half-spreading rates of 1 cm/year and ~7 km at ultrafast rates of 7 cm/year. The numerical modeling by Crowley *et al*., however, suggests that shorter-period Milankovitch cycles may be more dominant at faster rates. Depending on certain modeling parameters, the 41,000-year cycle might dominate at 4 cm/year half-spreading rate, and the 23,000-year cycle might dominate at 7 cm/year half-spreading rate [see figure 1 in (*1*)]. If so, this would suggest a much lower sensitivity of abyssal hill width on spreading rate, varying from ~1 km at 1 cm/year half-rate to just 1.6 km at 7 cm/year half-rate.

Institute for Geophysics, Jackson School of Geosciences, University of Texas at Austin, Austin, TX, USA.
E-mail: goff@ig.utexas.edu

Global, averaged estimates of the characteristic abyssal hill width (*3*, *4*) are presented as a function of half-spreading rate (Fig. 1). The characteristic width is formally estimated by the width of the covariance function but can also be derived with the von Kármán statistical model (*5*) from the inverse of the corner frequency of a power spectrum modeled as a band-limited fractal (*6*). The characteristic width describes the dominant visual scale (*6*). The von Kármán spectral model, being fractal in nature, does not contain periodicities. However, if this model were fit to the spectral functions modeled by Crowley *et al*. in their figure 1, the corner frequency would correspond to the periodicity with the highest amplitude, because this is where the spectrum transitions from being approximately white (flat) at low frequencies to red (fractal) at high frequencies. Therefore, the characteristic width should represent a reasonable estimate of the dominant abyssal hill width if the abyssal hills were, in fact, periodic. Under this assumption, the characteristic width values shown in Fig. 1 are incompatible with the predictions of the CT hypothesis in two important ways: (i) average widths measured at the slowest spreading rates, ~8 km, are far too large to be correlated with Milankovitch cycles, and (ii) the trend of widths with spreading rate is negative, rather than the predicted positive or flat trend, at least to half-rates of ~3.7 cm/year (or the transition from axial valley to axial high MOR morphology). The characteristic widths also exhibit a large (>2 km) downward step, independent of spreading rate, where the MOR morphology transitions from axial valley to axial high; these values were estimated on the flanks of the Southeast Indian Ridge (*3*).

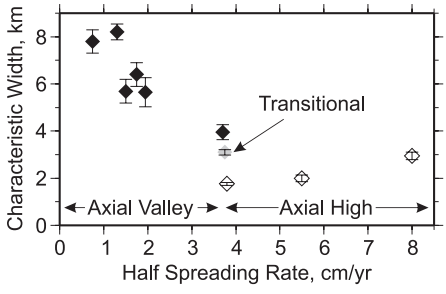


Fig. 1. Abyssal hill characteristic widths, averaged by region, plotted as a function of half-spreading rate. Error bars, mean ± 1 SD. Figure adapted from Goff *et al*. (*3*), with additional data from Sloan *et al*. (*4*). Black symbols indicate regions formed at axial valley MORs; open symbols at axial high MORs; and gray symbol at transitional MOR.

The negative trend in characteristic width with spreading rate can be seen as consistent with a faulted origin. Fault offset and spacing scale with elastic plate thickness (*7*, *8*), which is dependent on thermal structure (*9*). Thermal structure is, in turn, dependent on spreading rate (*10*). As a result of these relationships, colder lithosphere at slower spreading rates should result in larger offsets on more widely spaced faults. Faulting may also be controlled by variations in magma supply (*11*), which could explain variations in abyssal hill morphology that are independent of spreading rate, such as along the Southeast Indian Ridge (*3*). Observational studies have shown that abyssal hills are primarily fault-controlled horst-and-graben features, rather than volcanic-controlled constructs, at both fast (*12*) and slow (*13*) spreading rates. Indeed, the abyssal hills displayed by Crowley *et al*. exhibit a strikingly linear, axis-parallel morphology, which is likely most consistent with a faulted origin. Although the correlation between axial volcanism and sea-level variations is certainly plausible, it appears more likely to translate only as a secondary superposition on the primarily tectonic abyssal hill morphology (*12*).

At half-spreading rates greater than ~3.7 cm/year, where the axial high ridge morphology dominates, the trend of characteristic width with spreading rate is no longer negative and, in fact, may be slightly positive in going from ~2 km at 3.7 cm/year to ~3 km at 8 cm/year (Fig. 1). Goff *et al*. (*3*) argued that lack of sensitivity of abyssal hills to spreading rate at these higher rates could be associated with a nearly uniform presence of a weak zone in the lower crust at axial high ridges (*14*), which would decouple surface faulting from deeper strain. We cannot, however, discount the possibility that Milankovich cycle–driven volcanism is contributing, at least in part, to the increase in measured characteristic with spreading rate at axial high ridges; no other plausible explanation for this observation has been offered, to my knowledge.

REFERENCES AND NOTES

1. J. W. Crowley, R. F. Katz, P. Huybers, C. H. Langmuir, S.-H. Park, *Science* **347**, 1237–1240 (2015).
2. M. Tolstoy, *Geophys. Res. Lett.* **42**, 1346–1351 (2015).
3. J. A. Goff, Y. Ma, A. Shah, J. R. Cochran, J.-C. Sempéré, *J. Geophys. Res.* **102**, 15521–15534 (1997).
4. H. Sloan, D. Sauter, J. A. Goff, M. Cannat, *Geochem. Geophys. Geosyst.* **13**, Q0AE06 (2012).
5. J. A. Goff, A. Levander, *J. Geophys. Res.* **101**, 8489–8501 (1996).
6. J. A. Goff, T. H. Jordan, *J. Geophys. Res.* **93**, 13589–13608 (1988).
7. A. Malinverno, P. A. Cowie, *J. Geophys. Res.* **98**, 17921–17935 (1993).

Downloaded from www.sciencemag.org on September 5, 2015

8. P. R. Shaw, J. Lin, *J. Geophys. Res.* **98**, 21839–21851 (1993).
9. M. K. McNutt, *J. Geophys. Res.* **89**, 11180–11194 (1984).
10. J. Phipps Morgan, Y. J. Ghen, *Nature* **364**, 706–708 (1993).
11. W. R. Buck, L. L. Lavier, A. N. Poliakov, *Nature* **434**, 719–723 (2005).
12. K. C. Macdonald, P. J. Fox, R. T. Alexander, R. Pockalny, P. Gente, *Nature* **380**, 125–129 (1996).
13. C. Durant, V. Ballu, P. Gente, J. Dubois, *Tectonophysics* **265**, 275–297 (1996).
14. W. J. Shaw, J. Lin, *J. Geophys. Res.* **101**, 17977–17993 (1996).

ACKNOWLEDGMENTS

The author thanks G. Christeson for helpful comments on an earlier draft.

30 March 2015; accepted 24 July 2015
10.1126/science.aab2350

TECHNICAL RESPONSE

OCEANOGRAPHY

Response to Comment on "Glacial cycles drive variations in the production of oceanic crust"

John W. Crowley,[1,2]* Richard F. Katz,[1]† Peter Huybers,[2] Charles H. Langmuir,[2] Sung-Hyun Park[3]†

Goff comments that faulting is important for creation of abyssal hills and is the dominant process at slow-spreading ridges. We respond that faulting is indeed important but cannot alone explain the bathymetric signal predicted by our models and observed at the Australian-Antarctic Ridge. We show that for intermediate- to fast-spreading ridges, abyssal hill spacing is consistent with the periodicity of the obliquity cycle.

We appreciate Goff's Comment (*1*) and the opportunity to reemphasize a point that may have been lost to some readers of our paper [Crowley *et al.* (*2*)]: Faulting is an important and ubiquitous process in abyssal hill creation, particularly at slow-spreading ridges. However, our paper also shows, through modeling and observations, that sea level has a substantial effect on melt delivery to ocean ridges and an influence on the fabric of the sea floor. The greater importance of faulting at slow-spreading ridges led us to consider bathymetry at a faster-spreading ridge, where the subaxial lithosphere is thin and the magma supply is robust.

Because of the balance between faulting and magma supply, intermediate- and faster-spreading ridges offer the best opportunity to detect crustal thickness variations driven by glacial cycles. Goff's figure can be used to emphasize this point. In Fig. 1 here, we add a line to his figure 1 indicating the predominant spacing that would be produced by 40,000-year periodicity. At slow spreading rates, there is no correspondence between this line and the spacing data. At intermediate and fast spreading rates, however, both the absolute value and the relative increase in spacing are in accord with the Milankovitch periodicity. Goff also notes this slight increase. As he states, "no other plausible explanation for this observation has been offered." It would be premature, however, to rule out other speculative mechanisms that might relate fault-generated bathymetry to sea-level change.

Although we are thus in overall agreement with the Comment, it should be noted that the characteristic width determined by the von Kármán spectral model may not be an apt statistical measure of the variability in bathymetry. As noted by Goff and Jordan (*3*), the von Kármán spectral model assumes power-law scaling that rolls off to white at a corner frequency and does not provide a very good approximation in the presence of periodicities. Furthermore, our detection of excess spectral energy at Milankovitch bands involves prewhitening, which in this case systematically deemphasizes lower-frequency contributions. Those lower-frequency contributions are expected to influence characteristic width estimates and cause some disconnect between our results and Goff's results.

Finally, it should be noted that faulting may be mechanically coupled with temporal variations in magma supply. Ito and Behn (*4*) found that fault spacing depends on the periodicity of cycles between magmatic and tectonic extension at ~100,000 years and greater periods. If this is the case, the admittance structure from our paper would need to be modified. Ultimately, a more complete model is needed that consistently combines faulting, glacially induced variations in magma supply, and variations caused by other processes (e.g., mantle fertility or instabilities in the melting regime).

We are in broad agreement with Goff's Comment that faulting is dominant at slow-spreading ridges and that the hypothesis of sea-level–induced changes in magma production is currently the most plausible explanation for spectral energy at Milankovitch frequencies found in bathymetry at faster-spreading ridges.

[1]Department of Earth Sciences, University of Oxford, Oxford, UK. [2]Department of Earth and Planetary Sciences, Harvard University, Cambridge, USA. [3]Division of Polar Earth-System Sciences, Korea Polar Research Institute, Incheon, Korea. *Present address: Engineering Seismology Group Canada, Kingston, Canada. †Corresponding author. E-mail: richard.katz@earth.ox.ac.uk (R.F.K.); shpark314@kopri.re.kr (S.-H.P.)

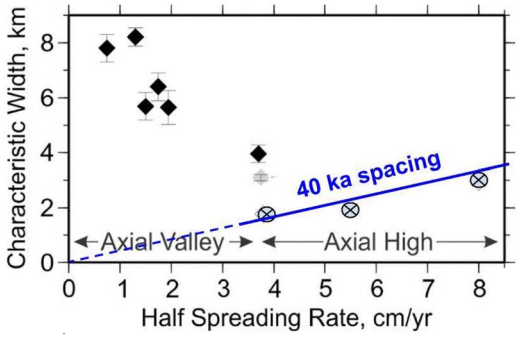


Fig. 1. Characteristic width of abyssal hills versus half-spreading rate. Adapted from figure 1 of Goff's Comment. The line indicates the predominant spacing that would be produced by a 40,000-year periodicity.

REFERENCES AND NOTES

1. J. A. Goff, *Science* **349**, 1065 (2015).
2. J. W. Crowley, R. F. Katz, P. Huybers, C. H. Langmuir, S.-H. Park, *Science* **347**, 1237–1240 (2015).
3. J. A. Goff, T. H. Jordan, *J. Geophys. Res.* **93**, 13589–13608 (1988).
4. G. Ito, M. D. Behn, *Geochem. Geophys. Geosyst.* **9**, Q09012 (2008).

ACKNOWLEDGMENTS

Funding was provided by the European Research Council (ERC) under the European Union's Seventh Framework Programme (FP7/2007–2013)/ERC grant agreement 279925, the U.S. National Science Foundation under grant 1338832, and the Korea Polar Research Institute as part of projects PP13040 and PE14050.

13 May 2015; accepted 24 July 2015
10.1126/science.aab3497

Downloaded from www.sciencemag.org on September 5, 2015

RESEARCH

Improved properties of graphene-based fibers

Xin et al., *p. 1083*



IN *SCIENCE* JOURNALS

Edited by **Stella Hurtley**



Aftermath of the 2015 Gorkha earthquake, Nepal

NATURAL HAZARDS

The bigger they are, the harder they fall

The magnitude 7.8 Gorkha earthquake hit Nepal on 25 April 2015. The earthquake killed thousands and caused great damage. Galetzka *et al.* determined how the fault that caused this earthquake ruptured. The rupture showed a smooth slip pulse 20 km wide that moved eastward along the fault over about 6 s. The nature of the rupture limited damage to regular dwellings but generated shaking that collapsed taller structures. — BG

Science, this issue p. 1091

IMMUNOLOGY

Restraining plasma cells and multiple myeloma

Plasma cells are specialized B cells that secrete antibodies. People with multiple myeloma have too many plasma cells. Mutations in the gene encoding the adaptor TRAF3 are associated with some cases of multiple myeloma. Lin *et al.* thus characterized mice that lacked TRAF3 in B cells. These mice had more plasma cells, and their B cells were more responsive to interleukin-6 (IL-6), a key cytokine for the development and survival of plasma cells. In normal mouse B cells, TRAF3 promoted the inactivation of a transcription factor downstream of the IL-6 receptor, suggesting that TRAF3 limits plasma cell numbers by inhibiting IL-6 signaling. — JFFS*Sci. Signal.* **8**, ra88 (2015).

METALLUGY

Welcoming steel's new complexion

Metals have a number of famous properties, including good strength and ductility. Controlling these properties frequently requires modifying the number and type of structural defects in a metal alloy. Kuzmina *et al.* produced a new type of defect, called a linear complexion, in magnesium-rich steel (see the Perspective by Kaplan). These complexions are chemically and structurally distinct regions located inside a linear defect and are isolated from the bulk by a layer of dislocations. The discovery suggests a new path for targeting defects and improving alloy development. — BG

Science, this issue p. 1080; see also p. 1059

GENETIC DISORDER

Mutation switches ligand specificity

Fibrodysplasia ossificans progressiva (FOP) is a rare but deadly genetic condition that causes bone growth in place of soft tissues. The causal mutation in the bone morphogenetic protein (BMP) receptor ACVR1 is thought to boost receptor activity and trigger bone formation. Now, Harsell *et al.* suggest a different mechanism. They found that the mutated receptor (mACVR1) responds to activin. Normally, activin blocks BMP from binding to ACVR1. Adult mice expressing mACVR1 developed heterotopic ossification that required stimulation by endogenous activin. Small sponges soaked with activin ossified when implanted into mACVR1 mice, and animals treated with a monoclonal antibody to activin were protected. This unusual mechanism may explain why ossification

Downloaded from www.sciencemag.org on September 5, 2015

PHOTO: HE - IMAGINECHINA

Published by AAAS

in FOP patients is triggered by tissue trauma, which induces activin. — KLK

Sci. Transl. Med. **7**, 303ra137 (2015).

SYNTHETIC BIOLOGY

Toward opioids without poppy fields

Producing opioids without having to depend on field-grown poppies would be of great benefit. Synthetic production could potentially produce more-effective drugs with fewer side effects. Now, Galanie *et al.* have engineered yeast to produce the opioid compounds thebaine and hydrocodone, starting from sugar (see the Perspective by Nielsen). The amounts produced so far are tiny compared with what would be needed commercially. Future optimization and scaleup are the next challenge. — BJ

Science, this issue p. 1095; see also p. 1050

ALLERGY

How farming protects against allergies

People who grow up on dairy farms only rarely develop asthma or allergies. This is probably because as children, they breathe air containing bacterial components, which reduce the overall reactivity of the immune system. Schuijs *et al.* chronically exposed mice to bacterial endotoxin before they received an allergic stimulus. The protocol indeed protected them from developing an allergic response. Protection relied on a particular enzyme: A20. In humans, a variant of A20 correlates with increased susceptibility to asthma and allergy in children growing up on farms. — KLM

Science, this issue p. 1106

DNA SEGREGATION

Plasmid partitioning superstructure system

Partitioning and sharing DNA between dividing cells is critical for all domains of life. Prokaryotes must share certain plasmids as well as their genomic DNA to survive. Schumacher *et al.* studied the partition system that segregates a conjugative plasmid in the prokaryote Sulfolobus. The system consists of three proteins. AspA spreads along the plasmid DNA to create a protein-DNA superhelix. The ParA motor protein is linked to the protein-DNA superhelix through the ParB protein, which has structural similarities to eukaryotic centromere segregating proteins. — GR

Science, this issue p. 1120

CATALYSIS

Iron lends power to traces of palladium

Palladium (Pd) is a mainstay of chemical catalysis. The precious metal has a knack for forging carbon-carbon (C-C) bonds. Handa *et al.* now report that when mixed in a specific preparation with iron, just parts per million of Pd suffice to catalyze the C-C bond–forming Suzuki coupling reaction. The addition of surfactants allowed the reaction to proceed in water. The protocol bodes well for conserving Pd in pharmaceutical and agrochemical synthesis. — JSY

Science, this issue p. 1087

PLANT SCIENCE

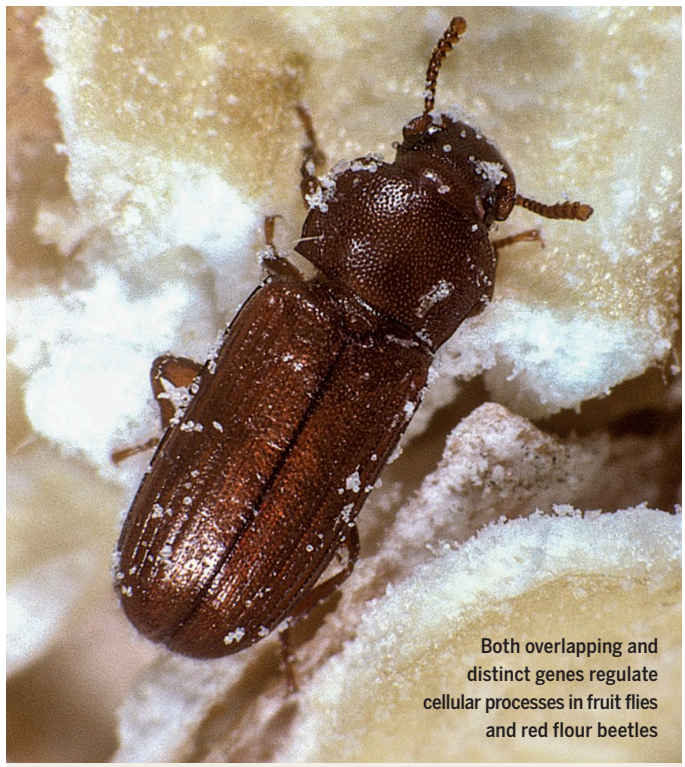
Bioremediation from disabled self-destruction

Explosives used in mining, construction, or military operations leave behind contaminated soils. Although bioremediation could help, plants do not thrive on these soils. Johnston *et al.* have now found out why (see the Perspective by Noctor). An enzyme found in plant mitochondria and chloroplasts spins out of control when given the explosive TNT, generating toxic reactive oxygen species and subverting biochemical pathways. With the key enzyme disabled, the plants are better at tolerating and accumulating TNT. These results point the way to future bioremediation and herbicide strategies. — PJH

Science, this issue p. 1072; see also p. 1052

IN OTHER JOURNALS

Edited by **Kristen Mueller** *and* **Jesse Smith**



Both overlapping and distinct genes regulate cellular processes in fruit flies and red flour beetles

GENETICS

A beetle reveals its genetic secrets

Sequencing tells us the molecular makeup of a genome, but genetic screens—an experimental technique that uses RNA interference (RNAi) or mutagenesis to select for specific phenotypes of interest—reveal gene function. Genetic screens of the *Drosophila* genome have informed scientists about how cell signaling, metabolism, and development occur in these insects. However, whether other insects exhibit similar biology remains unclear. To find out, Schmitt-Engel *et al.* performed an RNAi screen of the red flour beetle and found both similarities and differences in the genes and pathways that regulate beetle development, signaling, and physiology as compared to *Drosophila*. Broadening genetic screens to other insects may prove instrumental for understanding insect gene function. — BAP

Nat. Commun. **6**, 782 (2015)

PSYCHOLOGY

Need we think about what others think?

Imagine how everyday life would be if we were unable to represent in our own minds what others believed or intended or desired. Such a scenario would likely demand a whole new level of mental focus. Yet we enjoy rich social lives without seeming to spend much effort figuring out what others are thinking—it merely happens—in a process psychologists call automaticity. Phillips *et al.*, however, cast doubt on this hypothesis by conducting a thorough analysis of a complex experimental design used to obtain evidence in favor of automaticity; they find that

PHOTO: © NIGEL CATTLIN, /VISUALS UNLIMITED/CORBIS

Published by AAAS



Stress can lead people to make unhealthy food choices

NEUROSCIENCE

Stress reduces self-control

Everyone experiences situations in which our willpower fades, and we abandon self-control for choices that we later regret. Maier *et al.* assessed how stress affects self-control in young adults that have a healthy lifestyle but reported indulging in fast-food treats regularly. Compared to control participants, participants who were experimentally stressed preferred tastier foods more often in a two-choice taste test, regardless of whether their choice was less healthy and in disagreement with their self-imposed dietary restrictions. Brain imaging revealed more-active reward and taste circuits in stressed participants and less activity in regions associated with self-control. This suggests that stressed individuals prefer immediate reward over following a long-term goal. — LNS

Neuron **87**, 621 (2015).

a subtle error in experimental design undermines the earlier conclusions. These errors do not rule out automaticity, but highlight the need for more carefully designed research. — GJC

Psych. Sci. **26**, 10.1177/0956797614558717 (2015).

POLITICAL SCIENCE

Electing by Internet search algorithm

With more people relying on the Internet as their primary information source, how information is delivered becomes increasingly important. To determine how Internet search rankings can influence undecided voters, Epstein and Robertson performed double-blinded, randomized controlled experiments on participants in the United States and India. They found that manipulating search engine results influenced voting preferences of undecided voters in a manner that could substantially affect a close election. Study participants perceived the induced bias infrequently. Artificially increasing the ranking of candidates shifted the voting preferences of undecided voters by 20% or more. — BJ

Proc. Natl. Acad. Sci. U.S.A. 10.1073/pnas.1419828112 (2015).

GLACIOLOGY

Shaking with the flow

The flow of water beneath glaciers affects glacial motion, the transport of sediments, and water discharge into the ocean, among other things. Too little is known about the details of subglacial hydrology, however, to fully understand the full range of its impacts. Bartholomaus *et al.* report that subglacial discharge can be detected by measurement of the seismic tremor that it causes. Their observations at the edges of a half-dozen glaciers in Alaska and Greenland show that subglacial discharge is less intense in the winter than in the summer, and they demonstrate how the technique can be used to constrain important processes such as iceberg calving and submarine glacial melting. — HJS

Geophys. Res. Lett. 10.1002/2015GL064590 (2015).

ASTROCHEMISTRY

Diffuse interstellar bands in the lab

The diffuse interstellar bands (DIBs) are a set of hundreds of broad optical/near-infrared absorption features seen throughout the interstellar medium. Despite the first DIBs being discovered as long ago as 1922, none of the bands has ever been convincingly identified with a particular chemical species. Now Campbell *et al.* have obtained gas-phase lab spectroscopy of the buckminsterfullerene ion C_{60}^+ that matches two of the known DIBs, finally confirming a tentative assignment made in 1994. This is the first conclusive identification of a DIB carrier and demonstrates that fullerenes are widely distributed in space. — KTS

Nature **523**, 322 (2015).

FERROELECTRICS

Stretching ferroelectrics from within

Squeezing or stretching ferroelectric materials can strongly affect their properties. Although it is relatively easy to apply isotropic compressive stress, tensile stress is trickier. Wang *et al.* have found a way to do that in nanowires made out of the ferroelectric $PbTiO_3$. The wires initially had a tetragonal structure, but when they were exposed to air and high temperatures, they transformed into the so-called perovskite phase, which is much denser. The densification progressed from the surface of the wires inward, inflicting tensile stress and causing voids to form inside the wires. For a narrow range of wire diameters, this resulted in a deformation along the polarization axis and the enhancement of ferroelectric properties. — JS

Nat. Mat. 10.1038/nmat4365 (2015).

PHOTO: © RUTH BLACK/THE PICTURE PANTRY/CORBIS

Published by AAAS

ALSO IN *SCIENCE* JOURNALS

Edited by **Nick Wigginton**

EPIDEMIOLOGY

Bringing ecology to infection

The tools we use to investigate infectious diseases tend to focus on specific one-host–one-pathogen relationships, but pathogens often have complex life cycles involving many hosts. Johnson *et al.* review how such complexity is analyzed by community ecologists. Ecologists have the investigative tools to probe cause and effect relationships that change with spatial scale in multispecies communities. These techniques are used to monitor the ways in which communities change through time and to probe the heterogeneity that characterizes individuals, species, and assemblages—all issues that are also essential for disease specialists to understand. — CA

Science, this issue p. 1069

T CELL CHEMOTAXIS

Neutrophils lay down the tracks

T cells constantly circulate throughout the body until an invading pathogen calls them into action. Microbes often cause localized infections, so how do T cells know where to go? Lim *et al.* explore this question in a mouse model of influenza infection and find that immune cells called neutrophils help guide the way (see the Perspective by Kiermaier and Sixt). Upon infection, neutrophils quickly traffic to the trachea. There, they lay down "tracks" enriched in proteins called chemokines, especially the chemokine CXCL12, which guide $CD8^+$ T cells to the infected organ. Mice whose neutrophils could not lay down such tracks exhibited defects in $CD8^+$ T cell recruitment and viral clearance. — KLM

Science, this issue p. 1071; see also p. 1055

MICROBIOME

Estimating bacterial growth dynamics

The pattern of sequencing read coverage of bacteria in metagenomic samples reflects the growth rate. This pattern is predictive of growth because bacterial genomes are circular, with a single origin of replication. So during growth, copies of the genome accumulate at the origin. Korem *et al.* use the ratio of copy number at the origin to the copy number at the terminus to detect the actively growing species in a microbiome (see the Perspective by Segre). They could spot the difference between virulent and avirulent strains, population diurnal oscillations, species that are growing in irritable bowel disease, and what happens when a host's diet changes. Results were consistent in chemostats, in mice, and in human fecal samples. — CA

Science, this issue p. 1101; see also p. 1058

MACROECOLOGY

A general scaling law for ecology

Despite the huge diversity of ecological communities, they can have unexpected patterns in common. Hatton *et al.* describe a general scaling law that relates total predator and prey biomass in terrestrial and aquatic animal communities (see the Perspective by Cebrian). They draw on data from many thousands of population counts of animal communities ranging from plankton to large mammals, across a wide range of biomes. They find a ubiquitous pattern of biomass scaling, which may suggest an underlying organization in ecosystems. It seems that communities follow systematic changes in structure and dynamics across environmental gradients. — AMS

Science, this issue p. 1070; see also p. 1053

CHEMISTRY

Nonequilibrium transient self-assembly

In biology, the constant supply of energy can drive a system to be far from its equilibrium conditions and allow for useful work to be done. In contrast, in most synthetic systems, there is a drive toward lower energy states. Boekhoven *et al.* made a molecule that can switch between a nonassociating state and an associating state through the addition of a chemical fuel (see the Perspective by Van der Zwagg and Meijer). The lifetime, stiffness, and regenerative behavior of the self-assembled state could be controlled and tuned by the kinetics of fuel conversion. — MSL

Science, this issue p. 1075; see also p. 1056

MATERIALS SCIENCE

A superior mix of big and small

Graphene is often described as an unrolled carbon nanotube. However, although nanotubes are known for their exceptional mechanical and conductivity properties, the same is not true of graphene-based fibers. Xin *et al.* intercalated small fragments of graphene into the gaps formed by larger graphene sheets that had been coiled into fibers. Once annealed, the large sheets provided pathways for conduction, while the smaller fragments helped reinforce the fibers. The result? Superior thermal and electrical conductivity and mechanical strength. — MSL

Science, this issue p. 1083

MEMBRANE FUSION

Unravelling the SM-SNARE conundrum

So-called SNARE proteins mediate and lend specificity to the fusion between different intracellular membranes. The SM proteins are universally required for intracellular vesicle fusion, yet their mechanism of action has long been enigmatic. Baker *et al.* have solved a piece of the puzzle by "capturing" SNAREs in the process of assembling into fusogenic complexes on the surface of an SM protein. The findings suggest exactly how and why SM proteins help vesicular fusion during intracellular membrane trafficking. — SMH

Science, this issue p. 1111

RNA EDITING

RNA editing helps identify cellular RNAs

Adenosine bases in messenger RNA (mRNAs) can be enzymatically modified and changed into inosine bases. This RNA "editing" is mediated by adenosine deaminase acting on RNA (ADAR) enzymes. Liddicoat *et al.* show that the in vivo targets of the principal editing enzyme, ADAR1, are long double-stranded RNA (dsRNA) structures in noncoding portions of cellular mRNAs. ADAR1-directed editing of these cellular targets is critical to avoid activation of an immune response to dsRNA in the cytoplasm, because dsRNA is also a marker of viral infection. — GR

Science, this issue p. 1115

GENE EXPRESSION

Amalgamated regulators of gene expression

Less than 5% of the mammalian genome encodes protein-coding genes; over 95% of the genome consists of regulatory elements. These regulatory elements, which are referred to as enhancers or cis-regulatory elements, provide information that safeguards tissue- and cell type–specific expression of protein-coding genes. Bresnick *et al.* find that a single protein-coding gene can harbor multiple cis-regulatory elements. The elements are essential during development and for differentially controlling stem cell and

Published by AAAS

progenitor cell transitions. Thus, amalgamated enhancer regulatory mechanisms orchestrate the seamless execution of developmental gene expression. — ASH

Sci Adv. 10.1126/ sciadv.1500503 (2015).

Published by AAAS

REVIEW SUMMARY

EPIDEMIOLOGY

Why infectious disease research needs community ecology

Pieter T. J. Johnson,* Jacobus C. de Roode, Andy Fenton

BACKGROUND: Despite ongoing advances in biomedicine, infectious diseases remain a major threat to human health, economic sustainability, and wildlife conservation. This is in part a result of the challenges of controlling widespread or persistent infections that involve multiple hosts, vectors, and parasite species. Moreover, many contemporary disease threats involve interactions that manifest across nested scales of biological organization, from disease progression at the within-host level to emergence and spread at the regional level. For many such infections, complete eradication is unlikely to be successful, but a broader understanding of the community in which host-parasite interactions are embedded will facilitate more effective management. Recent advances in community ecology, including findings from traits-based approaches and metacommunity theory, offer the tools and concepts to address the complexities arising from multispecies, multiscale disease threats.

ADVANCES: Community ecology aims to identify the factors that govern the structure, assembly, and dynamics of ecological communities. We describe how analytical and conceptual approaches from this discipline can be used to address fundamental challenges in disease research, such as (i) managing the ecological complexity of multihost-multiparasite assemblages; (ii) identifying the drivers of heterogeneities among individuals, species, and regions; and (iii) quantifying how processes link across multiple scales of biological organization to drive disease dynamics. We show how a community ecology framework can help to determine whether infection is best controlled through "defensive" approaches that reduce host suitability or through "offensive" approaches that dampen parasite spread. Examples of defensive approaches are the strategic use of wildlife diversity to reduce host and vector transmission, and taking advantage of antagonism between symbionts to suppress within-host growth and pathology. Offensive approaches include the targeted control of superspreading hosts and the reduction of human-wildlife contact rates to mitigate spillover. By identifying the importance of parasite dispersal and establishment, a community ecology framework can offer additional insights about the scale at which disease should be controlled.

ON OUR WEB SITE

Read the full article at http://dx.doi.org/10.1126/science.1259504

OUTLOOK: Ongoing technological advances are rapidly overcoming previous barriers in data quality and quantity for complex, multispecies systems. The emerging synthesis of "disease community ecology" offers the tools and concepts necessary to interpret these data and use that understanding to inform the development of more effective disease control strategies in humans and wildlife. Looking forward, we emphasize the increasing importance of tight integration among surveillance, community ecology analyses, and public health implementation. Building from the rich legacy of whole-system manipulations in community ecology, we further highlight the value of large-scale experiments for understanding host-pathogen interactions and designing effective control measures. Through this blending of data, theory, and analytical approaches, we can understand how interactions between parasites within hosts, hosts within populations, and host species within ecological communities combine to drive disease dynamics, thereby providing new ways to manage emerging infections. ■



The community ecology of disease. (**A**) Interactions between parasites can complicate management. Among Tsimane villagers, treatment of hookworms increases infections by *Giardia lamblia*. (**B**) Similarly, understanding how ecological communities of hosts assemble can help forecast changes in disease. Biodiversity losses can promote interactions between white-footed mice and deer ticks, leading to an increase in the risk of Lyme disease from *Borrelia burgdorferi*. [Credits: (A) A. Pisor, CDC, F. Dubs; (B) J. Brunner, T. Shears, NIH]

The list of author affiliations is available in the full article online.
*Corresponding author. E-mail: pieter.johnson@colorado.edu
Cite this article as P. T. J. Johnson *et al.*, *Science* **349**, 1259504 (2015). DOI: 10.1126/science.1259504

Downloaded from www.sciencemag.org on September 5, 2015

REVIEW

EPIDEMIOLOGY

Why infectious disease research needs community ecology

Pieter T. J. Johnson,[1]* Jacobus C. de Roode,[2] Andy Fenton[3]

Infectious diseases often emerge from interactions among multiple species and across nested levels of biological organization. Threats as diverse as Ebola virus, human malaria, and bat white-nose syndrome illustrate the need for a mechanistic understanding of the ecological interactions underlying emerging infections. We describe how recent advances in community ecology can be adopted to address contemporary challenges in disease research. These analytical tools can identify the factors governing complex assemblages of multiple hosts, parasites, and vectors, and reveal how processes link across scales from individual hosts to regions. They can also determine the drivers of heterogeneities among individuals, species, and regions to aid targeting of control strategies. We provide examples where these principles have enhanced disease management and illustrate how they can be further extended.

Despite notable successes (*1*, *2*), infectious diseases remain a leading source of human morbidity and mortality (*3*) and continue to threaten wildlife conservation and food production (*4*–*6*). A common factor underlying emerging diseases is the involvement of multiple host, vector, or parasite species in complex ecological communities. Nearly 70% of emerging human infectious diseases have wildlife hosts or vectors (*7*, *8*), while several human parasites have spilled over to cause morbidity and mortality in wildlife, such as measles in mountain gorillas and tuberculosis in Asian elephants (*9*) (Fig. 1). The use of multiple hosts by parasites complicates control efforts that target particular hosts for management; for example, *Schistosoma japonicum*, the primary cause of human schistosomiasis in Asia, can infect 120 different species of mammals (*10*). Similarly, more than 20 species of triatomine bugs can transmit *Trypanosoma cruzi*, which causes Chagas disease in South America, such that efforts to control the dominant vector species alone may be inadequate to achieve elimination (*11*). Such threats continue to grow in importance as global travel and human activities increase contact with novel sources of parasites and aid their spread across the globe (*6*).

Alongside the multihost nature of many infections, interactions among co-infecting parasites can alter host pathology, parasite transmission, and virulence evolution (*12*–*14*). Parasites that disrupt immune function (Fig. 1), such as HIV, have facilitated the reemergence of drug-resistant forms of tuberculosis (*15*); co-infection with parasitic worms (helminths) such as hookworm can exacerbate malaria (*16*). Interactions between several parasite species have been similarly implicated in coral reef diseases, epidemics in plants, and marine mammal die-offs (*17*–*19*). Because many host-parasite interactions are intimately embedded within communities of organisms, management efforts are sometimes thwarted by "ecological surprises" (*20*). Recent examples include the unexpected amplification of MERS (Middle East respiratory syndrome) coronavirus in internationally traded camels, and increased contact between badgers and cattle after implementation of badger culling, ultimately leading to increased rather than decreased transmission of bovine tuberculosis in the United Kingdom (*21*–*23*). Managing the challenges of emerging infectious diseases thus requires a clear understanding of the full ecological context of infection and transmission.

Our ability to understand and control infectious diseases has much to gain from the discipline of community ecology, which has developed a range of analytical tools for addressing complexity, species interactions, and multilevel scaling (Fig. 2). These tools can be adopted to improve our understanding and management of infectious diseases, both by quantifying environmental and biological factors governing the structure of complex communities of multiple hosts, vectors, and parasites, and also by identifying the effect and source(s) of heterogeneity among individual hosts, host species, and geographic locations. These tools further offer insight into interactions and feedbacks across multiple scales of organization, from within hosts to across regions. We examine how the application of tools and concepts from community ecology can help public health efforts to manage infectious disease threats.

Community ecology as a framework to understand infectious diseases

Community ecology offers a mechanistic bridge between processes unfolding at the fine scale of individuals and populations and the ecological and evolutionary drivers of species distributions at coarser scales. Whereas some principles from community ecology have been applied to various host-parasite systems [e.g., (*24*–*27*)], the "community ecology of disease" remains in its relative infancy, with most studies focusing on interactions between a single host and parasite species, often at a single scale. Data availability and quality are increasing rapidly, partly through advances in sequencing technology, underscoring both the need for and the opportunity to implement new methods to study infection dynamics in complex natural systems.

Community ecology theory tells us that, in parallel to the processes underlying population genetics theory (i.e., gene flow, selection, drift, and mutation), the diversity, abundance, and composition of species within a community can be understood in terms of dispersal, ecological selection, ecological drift, and speciation (*28*). After dispersal from the regional species pool, a species' success within a habitat is filtered by both niche-based and stochastic processes (*29*, *30*). Within this framework, what needs to be understood is the degree to which community structure is built predictably from niche-based effects associated with interactions among species and the environment, or whether it arises through stochastic processes such as historical legacy, demographic stochasticity, and environmental fluctuations (Fig. 3).

Within their niche, parasites are affected by host condition, immune responses, the abiotic environment, and interactions with co-infecting symbionts or associated free-living organisms. If the assembly of parasite communities is predominantly deterministic, then the richness and composition of parasite species will vary according to measurable characteristics of the host and the environment, and will therefore be predictable (Fig. 3). However, stochastic events and dispersal will also influence parasite colonization-extinction dynamics. In some systems, for instance, the outcome of parasite interactions depends strongly on the order of arrival within the host (*14*, *31*). For example, long-term sampling of wild field vole (*Microtus agrestis*) populations revealed that infection with the protozoan *Babesia microti* reduced the probability that a host subsequently became infected with the bacteria *Bartonella* spp.; however, if *Bartonella* established first, then *B. microti* was only 25% as likely to invade (*14*). Similarly, high propagule dispersal by parasites can overcome niche effects related to host susceptibility (*32*). For instance, although humans are dead-end hosts with no onward transmission for many zoonotic infections, high exposure to such parasites can have serious consequences for public health, such as West Nile encephalitis and late-stage Lyme disease. Quantifying the relative contributions of niche-based and dispersal-based processes in determining parasite community structure and individual infection risk offers an ecological foundation for guiding resource investment into either defensive strategies, which focus on altering niches to inhibit parasite

[1]Ecology and Evolutionary Biology, University of Colorado, Boulder, CO 80309, USA. [2]Department of Biology, Emory University, Atlanta, GA 30322, USA. [3]Institute of Integrative Biology, University of Liverpool, Liverpool L69 7ZB, UK.
*Corresponding author. E-mail: pieter.johnson@colorado.edu

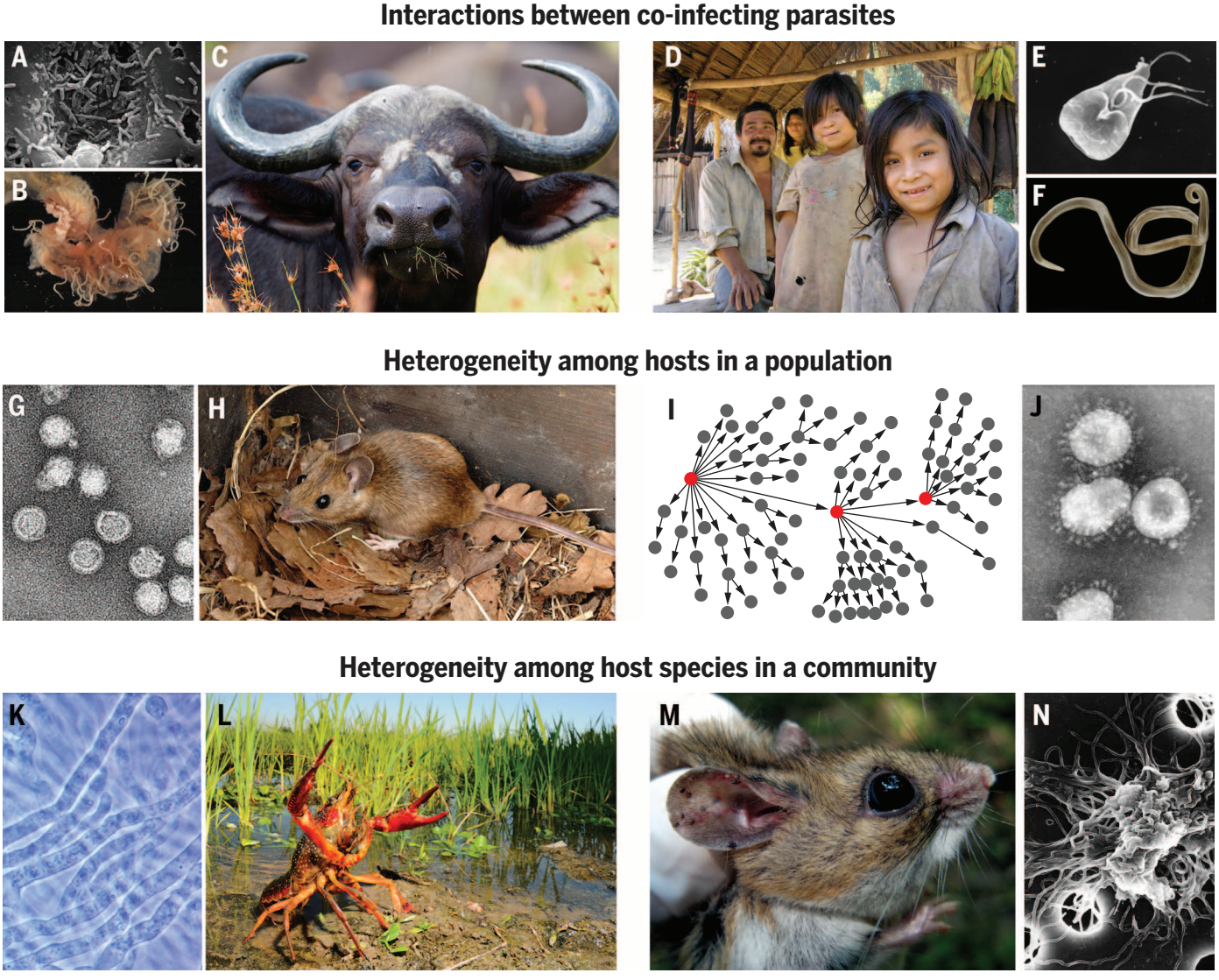


Fig. 1. The community ecology of infectious disease. (**A** to **C**) Co-infection by nematodes (A) increases host mortality due to bovine TB (B) among African buffalo (C) (*63*). (**D** to **F**) Tsimane villagers in Bolivia (D) reveal negative correlations between *Giardia lamblia* (E) and *Ascaris lumbricoides* (F), where deworming increased *Giardia* (*99*). (**G** and **H**) For tick-borne encephalitis (G), 93% of transmission events involve large-bodied, male yellow-necked mice (H), which constitute <20% of the population (*53*). (**I** and **J**) For humans, disproportionate contact among individuals (I) led to "superspreading events" for SARS (J) (*50*). (**K** to **N**) Among-species heterogeneities can alter community-wide transmission. Crayfish plague (K) introduced to Europe with highly susceptible red swamp crayfish (L) led to native crayfish declines; biodiversity losses tend to promote interactions between ticks and white-footed mice (M), which are highly competent hosts for *Borrelia burgdorferi* (N) and influence production of infected ticks that transmit Lyme borreliosis (*65*). [Image credits: [(A), (E), (I), (J)] CDC, (B) R. Grencis, (C) Y. Krishnappa, (D) A. Pisor, (F) F. Dubs, (G) (*100*) (H) V. Dostál, (K) T. Vrålstad, (L) F. Pupin, (M) J. Brunner, (N) NIH]

establishment, or offensive strategies, which focus on limiting dispersal (Fig. 4).

Approaches for understanding multilevel infection processes

Parasite metacommunities and assembly theory

Metacommunity theory provides a valuable toolkit for understanding the relative importance of niche-based effects and dispersal-based effects in regulating the structure of parasite communities (*24*, *33*). By recognizing that landscapes support a series of ecological communities connected through dispersal, metacommunity theory links interactions across local and regional scales (*32*). For parasites, this framework is relevant to communities of parasites dispersing among host individuals or across disjunct landscapes. Although rarely applied to parasite communities, metacommunity-based approaches offer the potential to explore the interactive roles of evolutionary history, dispersal limitation, host community composition, and the abiotic environment in driving parasite distributions (*34*) (Fig. 2). In a long-term study of 65 parasite species from 15 species of desert rodents, for instance, Dallas and Presley (*35*) found that parasite community structure was driven by niche effects associated with the "patch quality" of host species, including host traits such as body size, longevity, and abundance, rather than by characteristics related to dispersal opportunities, such as host diet breadth, home range size, or evolutionary history. In a study of plant parasites, Parker *et al.* (*36*) recently showed that spillover risk in field experiments could be predicted by knowing the abundance of the host and its phylogenetic relationships with other hosts in the community. In contrast to free-living communities, parasite metacommunities do incur some unique analytical challenges, including the potential for infections to sicken or kill individual hosts and thereby alter the availability of habitat "patches" for dispersal (*26*). Likewise, because parasites also interact with each other, the

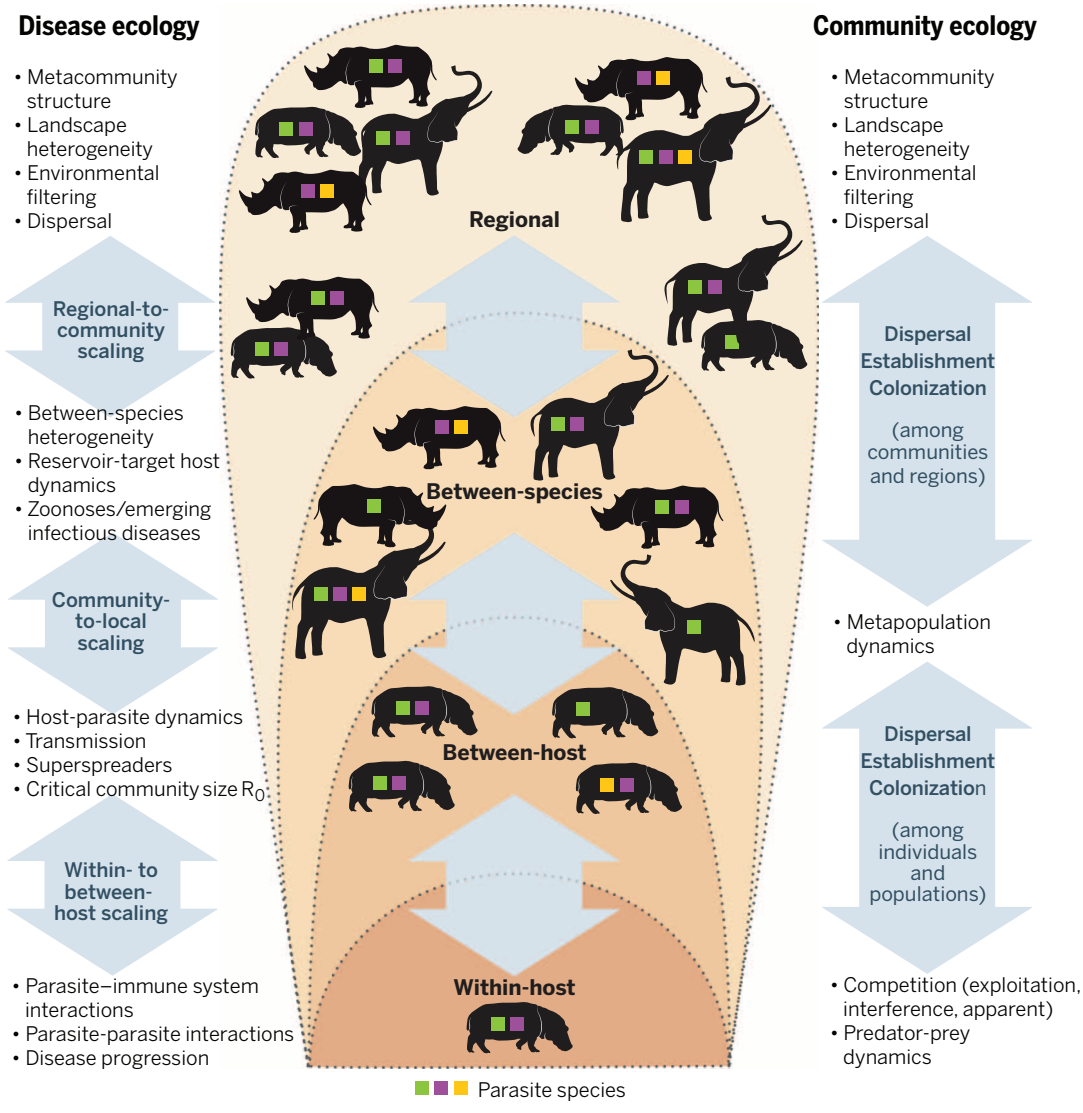


Fig. 2. Ecological hierarchies applied to host-parasite interactions and analogous processes in community ecology. The range of scales includes within-host ("parasite infracommunity," often dominated by parasite-parasite and parasite-immune system interactions); between-host ("parasite component community," population biology); among species ("parasite supracommunity," community ecology); and across regions (macroecology and disease biogeography). The different colored squares represent different parasite species; the text at the right and left highlights the relevant processes from community ecology and disease ecology, respectively. The potential importance for interactions and feedback across these scales represents an essential research frontier in the field of disease community ecology.

co-assembly of host and parasite communities needs to be examined concurrently (*37*), and an extra nested scale (i.e., for the within-host dynamics) often needs to be included in analyses (Fig. 2).

Tools from network theory can be additionally valuable for understanding how interactions between entire host and parasite communities vary over space and time (*38*). For instance, Griffiths *et al.* (*39*) used network approaches to show that co-infecting parasites of humans were organized into dense clusters around distinct locations in the body (e.g., organs) and tended to interact with each other via shared resources within the host, rather than via the immune system. Similar approaches have been applied across other scales of organization—for example, to define contact pathways for transmission among individual hosts (*40*, *41*) and to identify the role of parasites in structuring ecological food webs (*42*). Although the focus of network approaches thus far has often been on the patterns of links among species, emerging tools allow for more explicit examination of interaction strengths, which will help to forecast dynamic changes in the system (*43*).

Infection heterogeneity and traits-based approaches

Community ecology emphasizes the importance of understanding individual and species-level functional traits, thereby offering greater mechanistic and predictive power relative to simple taxonomic classifications (*44*, *45*). Predicting the specific identities of species within an assemblage is made difficult by stochastic factors such as historical legacy, whereas the composition and frequency of functional traits may be more deterministic (*46*). Thus, although hosts and parasites are typically defined in taxonomic terms, it may be more useful to classify them in terms of functional traits that influence performance. For parasites, such traits include transmission mode, site of infection, and resource use; for hosts, they include body size, dispersal ability, and immune competence. For instance, Han *et al.* (*47*) identified "trait profiles" of known reservoir species and used these to forecast candidate rodents likely to act as reservoirs for future zoonotic infections. Their analysis revealed the importance of "fast-paced" species that reproduce early and often; by contrast, taxonomic labels did a relatively poor job of classifying reservoir host status.

Trait-based analyses align with the long-standing recognition in disease ecology of the disproportionate influence of superspreader individuals, amplification or reservoir host species, or "hotspot" locations in driving transmission (*22*, *48*, *49*). Superspreading events have been recorded for both wildlife and human diseases, including typhoid fever, HIV-1, SARS, and tuberculosis (*22*, *50*, *51*), and can sometimes be linked to measurable variation in traits such as host immunity, behavior, age, diet, and sex (*52*–*54*). For example, Perkins *et al.* (*53*) found that large-bodied, sexually active male mice contribute 93% of potential transmission events for tick-borne encephalitis virus, despite representing only ~20% of the host population (Fig. 1). Methods to partition the contributions of particular hosts, species, or locations to parasite transmission are beginning to be developed (*48*, *55*). For example, Rudge *et al.* (*10*) quantified host

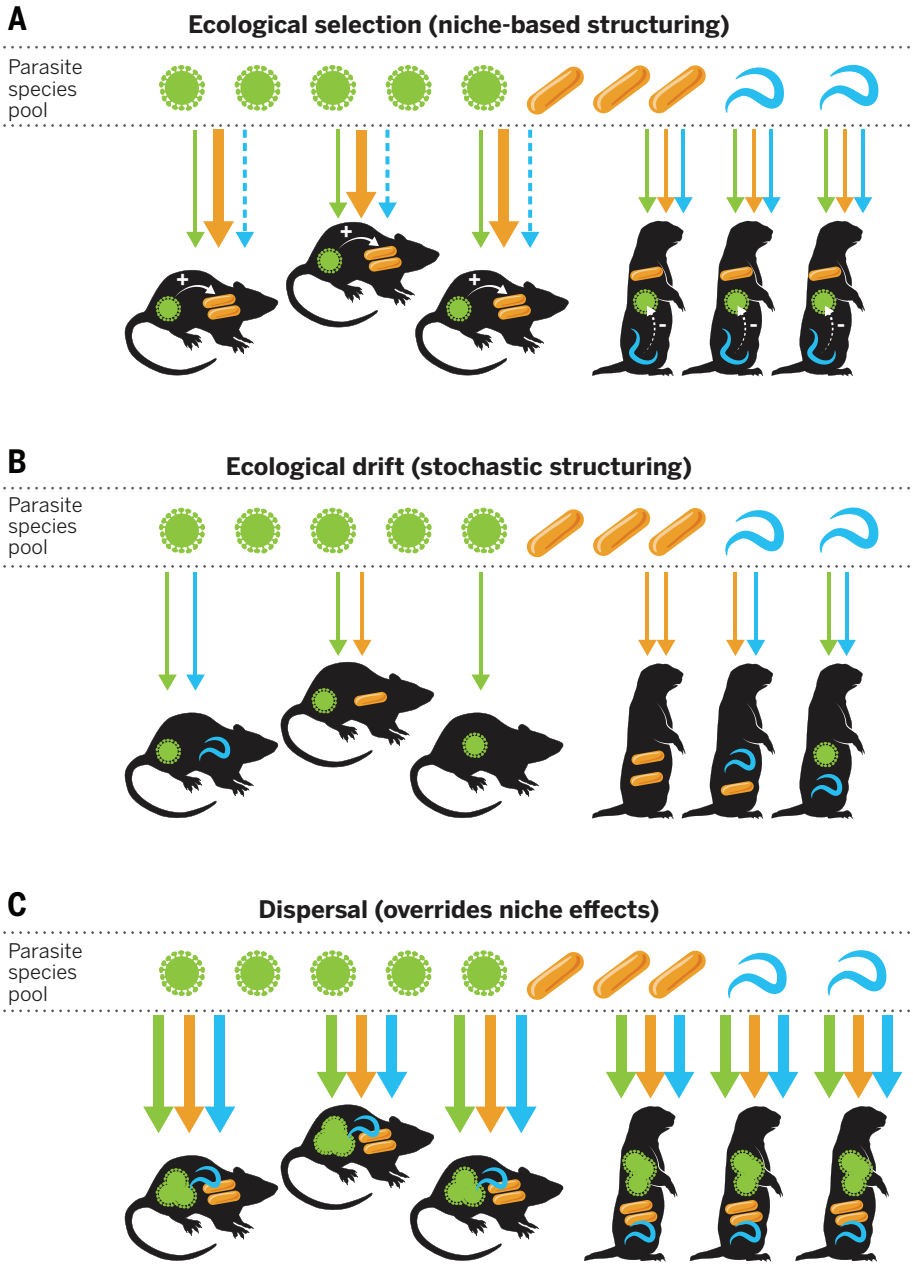


Fig. 3. Parasite community assembly depends on a combination of ecological selection, ecological drift, and dispersal. (**A**) After input via dispersal (indicated as arrows from the parasite regional pool), parasite establishment depends on ecological selection: different species (mice versus prairie dogs) select for different parasites according to genetics, behavior, immune status, and other host properties (including vaccination status or drug presence). Dashed arrows indicate failed infection. Deterministic, within-host parasite interactions (indicated by + and − signs) are an additional niche-based influence on parasite communities; positive parasite interactions (facilitation) are indicated by solid arrows; negative interactions are indicated by dashed arrows. (**B**) Parasite community assembly is also influenced by ecological drift (stochasticity), particularly when colonizing populations are small or the outcome of parasite interactions depends on their order of arrival ("priority effects"). As a result, parasite communities can appear random with respect to host species or type, even if strongly affected by species interactions. (**C**) High rates of dispersal can swamp niche effects and overwhelm stochasticity, resulting in more similar parasite communities across hosts, regardless of host species. For simplicity, no feedback loops are shown from the individual hosts back to the parasite pool, although understanding such feedbacks represents an important research priority (Fig. 2).

species contributions to the number of cases generated (R_0) of *S. japonicum* in China, for which more than 120 host species have been identified. They showed that bovids maintain infection in marshlands, whereas rodents are the main source of transmission in hilly areas, which suggests that different control strategies are needed in the two habitats. The key challenge for management is to identify how much of this heterogeneity is linked to measurable traits, and is therefore predictable (niche-based), or whether it arises stochastically through unpredictable temporal or spatial heterogeneity in exposure (*56*).

Moving across scales

A core principle of community ecology is the importance of scale in affecting the strength and form of species interactions not only with each other but also with the environment (*57*) (Fig. 2). Research in disease ecology often falls into one of three distinct levels: (i) within-host, which is concerned with interactions with the host immune system and other parasites (*13*, *58*); (ii) between-host, which is focused on parasite spread through host populations (*59*, *60*) or, less often, through host communities; or (iii) on regional or biogeographical scales, which use comparative methods from macroecology to explore the drivers of parasite distributions and diversity (*61*).

Studies focused on one scale often ignore, or treat as phenomenological black boxes, the dynamics occurring at higher and lower scales; in reality, it appears that dynamic interactions occur in both directions (*41*, *57*). For instance, interactions among co-infecting parasites within hosts can cause individual variation in susceptibility, infectiousness, behavior, and survival (*14*, *62*, *63*), potentially with counterintuitive consequences for transmission at the population level (*64*). African buffalo co-infected with gastrointestinal nematodes and bovine tuberculosis (bTB) exhibit increased mortality (Fig. 1), such that treating animals to reduce their worm burdens improves individual survival but, by enabling infected hosts to live longer, is predicted to increase population-level spread of bTB (*63*). Reciprocally, variation in host community composition within a region can affect infection risk and spread at the individual and population levels (*10*, *55*). For vector-borne infections such as Lyme disease, wildlife species vary considerably in their tendency to amplify the bacterium responsible and transmit it to suitable tick vectors, such that regional variation in host species diversity is hypothesized to be a major determinant of local infection risk for humans (*65*) (Box 1). However, such cross-scale processes are hard to infer from observational data alone, and experimental perturbations are often needed to definitively assess how processes at one scale affect those at another (*66*). In parallel with the rich legacy of system manipulations from community ecology (*67*), disease ecologists have increasingly used experimental approaches involving natural systems—for example, through antiparasite drug treatments (*68*), hormone manipulation (*69*), nutrient supplementation (*70*), and diversity manipulations (*71*, *72*). Although these experiments have often focused on single host–single parasite systems, implementing such experiments in more complex natural communities and at larger scales is increasingly important for testing hypotheses about parasite transmission, impact, and control.

How community ecology can help manage infectious diseases

We suggest that disease control strategies would benefit by incorporating community ecology

theory and approaches to explicitly account for the joint influences of dispersal and environmental filters. Specifically, the "offensive" versus "defensive" concept developed for invasive species can be applied to disease management [Fig. 4; see also (*73*)]. Offensive strategies allocate resources to limit the dispersal of an invader from established sites, whereas defensive efforts reduce the vulnerability of uninvaded habitats to colonization (*74*). Although this concept parallels existing epidemiological emphasis on prevention versus control, its successful application requires deeper insights into whether a parasite community is dispersal-limited, niche-based, or random in its assembly (Fig. 3). This approach can be used to strengthen current methods of infectious disease management across the gamut of multihost parasites, multisymbiont communities, and infection heterogeneities across scales (Fig. 2).

Managing multihost parasites

A current pressing question is how ongoing changes in biodiversity will affect the spread and severity of infectious diseases (*66*, *75*). When diverse communities also support species that interfere with transmission, such as the presence

Box 1. The role of simple theory in disease ecology and its extension to complex communities.

The pioneering work of Anderson and May (*60*, *101*) formalized our understanding of parasite dynamics by highlighting the importance of the basic reproductive number (R_0) as a measure of whether a parasite will spread through a population ($R_0 > 1$) or die out ($R_0 < 1$). The fundamental principles of these basic models—initially developed for single host–single parasite systems—can provide insight into infection dynamics in more complex ecological systems. For example, parasites often face a diverse community of potential host species that differ in abundance, susceptibility, and infectiousness. Simple extensions of basic disease ecology theory can determine the conditions under which one host species amplifies or dilutes infection risk for other species in the community. For directly transmitted parasites, or even those transmitted via infective stages in the environment, theory shows that the parasite's overall basic reproductive number among the available host community ($R_{0,TOT}$) can simply be proportional to the sum of the R_0 for each host species alone, provided there is equal mixing within and between host species (although other relationships between the individual-level and community-level R_0 values may occur if mixing is not equal) (*10*, *102*). Hence, there is a clear connection between this more complex scenario and the classical single-host theory.

This theory can be extended further for vector-borne parasites, which become complicated to model when hosts differ in their relative competencies for the parasite and the vector. For example, tick-borne parasites may involve a mammalian host species that is parasite-competent but cannot support tick reproduction, as well as another mammalian species that is noncompetent for the parasite but essential for tick reproduction, as shown in the figure. Here, there are three possible outcomes: (i) tick and parasite exclusion, (ii) tick persistence but parasite exclusion, and (iii) tick and parasite persistence, depending on different combinations of the R_0 values for the parasite ($R_{0,parasite}$) and the tick ($R_{0,tick}$). Ultimately, this results in outcomes that are nonlinearly related to the density of the noncompetent host; initial increases in noncompetent host abundance (N) can cause vector amplification, leading to increased parasite R_0, whereas high N dilutes transmission through "wasted" bites on the noncompetent host (*103*–*105*).

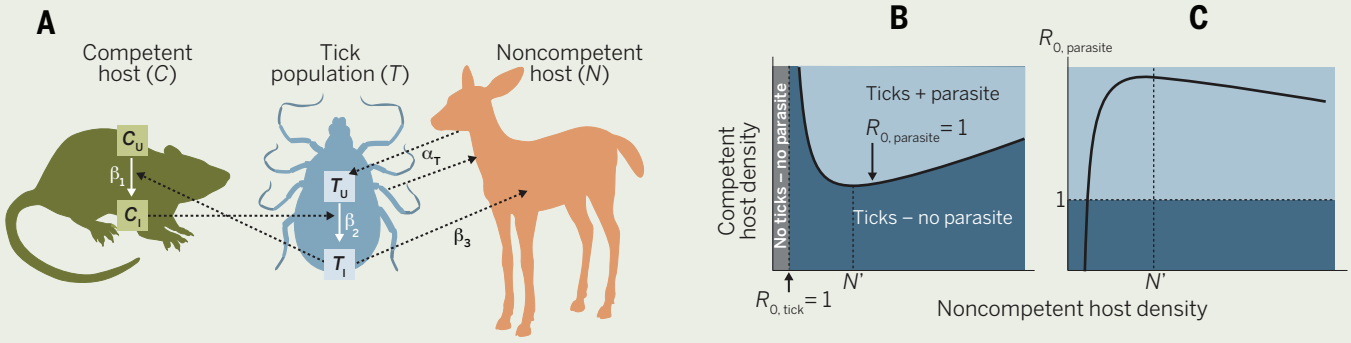
The figure shows a model of a tick-borne parasite system with two host species, showing potential for both amplification and dilution within the same system. (**A**) Schematic diagram of the model, where one host species (C) is parasite-competent but cannot support tick reproduction, and the other (N) is noncompetent but essential for tick reproduction. This system can be described by the following equations [modified from (*103*–*105*)]:

$$dC_P/dt = (1 - C_P)\beta_1 T_I - \delta_C C_P$$

$$dT/dt = (\alpha_T - s_T T)T\beta_3 N - \delta_T T$$

$$dT_I/dt = (T - T_I)\beta_2 C C_P - \delta_T T_I - T_I \beta_3 N$$

where T is the total number of ticks (T_U in the figure is the number of uninfected ticks; T_I is the number of infected ticks), C_P is parasite prevalence within C (C_U in the figure is the number of uninfected hosts; C_I is the number of infected hosts), β_1 is the tick → C transmission rate of the parasite, β_2 is the C → tick transmission rate of the parasite, β_3 is the tick → N biting rate, δ_C and δ_T are the respective mortality rates of competent hosts and ticks, a_T is the tick reproduction rate, and s_T is the strength of tick density dependence. (**B**) Phase plot of competent host (C) and noncompetent host (N) densities, showing the three regions of dynamical outcome separated by the boundaries of $R_{0,tick} = 1$ and $R_{0,parasite} = 1$, where $R_{0,tick} = \alpha_T\beta_3 N/\delta_T$ and $R_{0,parasite} = [C\beta_1\beta_2(\alpha_T\beta_3 N - \delta_T)]/[s_T\beta_3 N\delta_C(\delta_T + \beta_3 N)]$. (**C**) $R_{0,parasite}$ as a function of noncompetent host density, showing that low host densities facilitate parasite transmission due to vector amplification, whereas high host densities reduce parasite transmission through wasted tick bites. The vertical line marked N' (given by the value of N at which $R_{0,tick} = 1 + \sqrt{1 + \alpha_T}$) shows the noncompetent host density at which the effect on the parasite switches from amplification to dilution.



of low-susceptibility hosts, predators, or symbionts, community structure can be manipulated defensively to manage infections by limiting niche suitability (*37*). For example, zooprophylaxis (in which livestock are used as bait to divert blood-feeding arthropod vectors away from people) has been proposed as a control strategy for vector-borne diseases for more than a century, but has had limited success in some settings because increased livestock density can also increase vector abundance. However, recent models on malaria and zoonotic cutaneous leishmaniasis indicate that carefully chosen livestock densities coupled with insecticide treatment can effectively reduce parasite transmission to humans (*76*, *77*). Similar approaches, such as intercropping and crop rotation, have been used successfully to reduce plant pests and parasites in agricultural systems (*78*). Although evidence for such dilution effects continues to grow (*79*), the degree to which biodiversity will regulate infection by a particular parasite depends on the degree to which host assembly is deterministic, whether the parasite is niche- or dispersal-limited, and how increases in richness affect host and vector abundance (*66*).

Managing host communities is also crucial to mitigating the risk of spillover events from animal reservoirs to humans. To minimize spillover, there are several potential offensive and defensive approaches (Fig. 4), the choice of which will depend on the specific biology of the hosts and vectors involved. The first option is to reduce infection in reservoir hosts. For instance, vaccine baits have successfully eliminated rabies from several European countries through their protective effects on nonhuman hosts (*80*). The second approach is to limit contacts between wildlife and humans—for example, by reducing bushmeat consumption and its potential to introduce novel infections (*81*). In West Africa, increasing the use of alternative protein sources such as marine fish could relieve pressure on the bushmeat trade (*82*). Such approaches require tight coordination among many parties, including medical scientists, anthropologists, and governments. Similarly, the

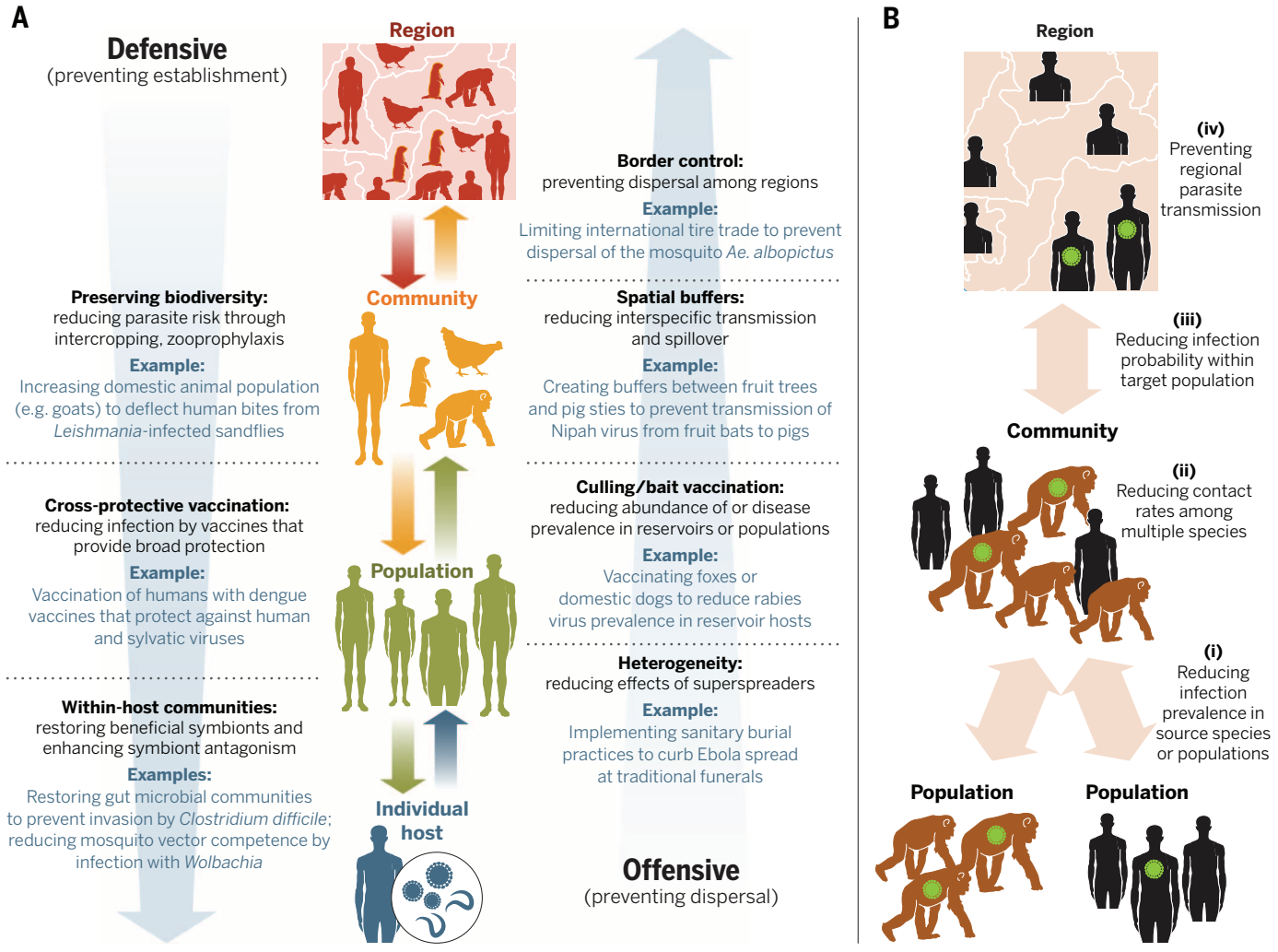


Fig. 4. How community ecology can inform infectious disease management. (**A**) Using community ecology–based management strategies for infectious disease. Levels of ecological organization are shown in the middle, and colored arrows indicate the ecological processes that connect these levels. Parasite dispersal connects scales going up through the hierarchy; parasite establishment connects scales moving down the hierarchy. Blue arrows indicate the relative importance of offensive strategies (preventing parasite dispersal) and defensive strategies (preventing parasite establishment), with darker shades reflecting greater importance. (**B**) Management strategies focused on reducing spillover from wildlife to humans (zoonosis) and from humans to wildlife (anthronosis or reverse zoonosis). Probability of spillover and subsequent spread of infection can be reduced through four major strategies: (i) Control may focus on reducing disease prevalence in reservoir hosts; for instance, vaccine baits have been successfully used to eliminate rabies from several European countries (*80*). (ii) Contact rates can be reduced between humans and wild animals (*8*); for example, limiting the proximity between humans and wildlife can reduce spillover of human illnesses such as measles, tuberculosis, and MRSA to wildlife. (iii) Zoonotic risk can be reduced by lowering the probability of infection when contact is unavoidable or unpredictable. For instance, some human dengue vaccine candidates provide cross-protection against sylvatic dengue viruses, which naturally circulate in nonhuman primates (*85*). (iv) When spillover does occur, regional control strategies—including isolation of infected populations, dispatching of medical personnel and aid, and enhanced border control—can be used to prevent disease transmission across borders.

use of transmission barriers can help to limit contact between wildlife reservoirs and domestic animals (*83*, *84*). The third approach is to reduce the probability of infection when contact is unavoidable or unpredictable. Ongoing yet unpredictable spillovers of dengue viruses from nonhuman primates, for instance, complicate the control of human disease in Southeast Asia and Africa. One approach to control such infections is through the implementation of cross-reactive vaccines, which are currently under development (*85*). When vaccines are not yet available, as was the case for Ebola virus during most of the 2014–2015 epidemic, reducing human-human transmission through contact tracing and subsequent quarantine and treatment can help to limit epidemic spread (*86*).

Managing symbiont communities

Interactions among co-infecting parasites or symbionts can also be used as niche-based management tools (Fig. 4). For example, treating patients suffering from lymphatic filariasis with the antibiotic doxycycline eliminates essential symbiotic bacteria required by filarial worms, ultimately leading to worm sterility and death (*87*). Restoration or augmentation of the microbial community within the host can also provide protection against parasite invasion. For example, transferring human-microbial communities by fecal transplants often leads to clinical resolution of intestinal pathology associated with *Clostridium difficile* infection (*88*). Finally, interactions among co-infecting parasites, parasite strains, or other symbionts can be manipulated to reduce the spread of disease-causing organisms. Long-lived parasites, such as helminths, may exacerbate disease caused by co-infecting parasites, leading to calls to incorporate deworming to improve management of HIV, malaria, and TB (*16*, *89*). In other cases, antagonistic interactions between parasites or other symbionts may be used to benefit the host. For instance, trials are under development to reduce the vector competence of mosquitoes by infecting them with the bacterium *Wolbachia*, which inhibits dengue virus and filarial worm survival and transmission through a combination of immune activation, competition for cellular components, and shortened mosquito lifespan (*90*, *91*). These examples emphasize the importance of understanding and predicting the outcome of multiple infections, for which community ecology approaches focused on parasite traits and resource use have already offered added insights (*92*).

Heterogeneity and scale

The disproportionate roles of particular locations, particular host species, and particular individual hosts in driving epidemics or epizootics raise the tantalizing promise of highly efficient targeted control and treatment (*22*, *48*, *50*). In the Serengeti, for example, where rabies can infect up to 12 carnivore species, domestic dogs are responsible for more than 70% of transmission events to humans (*93*). Annual vaccination of 60% of dogs is projected to control the virus, a target that is logistically and economically feasible (*94*). During the recent Ebola epidemic in West Africa, close contact between deceased patients and family or friends during traditional burials functioned as superspreading events (*95*), and implementation of "sanitary burials" that reduced such contacts helped to curb the epidemic. Thus, targeting superspreading hosts or events is feasible when transmission heterogeneities are deterministic and can be linked to measurable traits or characteristics.

Ultimately, the efficacy of offensive and defensive approaches will depend on whether the scale of application is local or regional, the transmission and dispersal characteristics of the parasite involved, and the point in the epidemic when the intervention is initiated (*73*). Defensive, niche-based management strategies, ranging from vaccination and prophylaxis to ecological competition by probiotic symbionts, are more likely to be effective when parasite dispersal is high, for parasites with high or unpredictable propagule pressure, and for epidemics already under way (Fig. 4). In contrast, offensive strategies that focus on reducing dispersal are more likely to succeed at community and regional scales than at individual and population scales, because parasite dispersal between individuals within a host population is often harder to control than dispersal between sites. For instance, established populations of the Asian tiger mosquito *Aedes albopictus*, recently linked to a large outbreak of the viral disease chikungunya on the Indian Ocean island La Réunion (*96*), are almost impossible to eliminate; however, because most introductions of this vector have occurred through the shipment of used tires, focused efforts to limit this trade offer the best potential for containing future spread of the vector (*96*).

Outlook

The disciplines of epidemiology and community ecology have developed largely independently of one another. Nonetheless, the multispecies nature of many contemporary disease threats demands a community-scale approach to complement more traditional biomedical treatments. The proposed synthesis of "disease community ecology" offers a theoretical framework and the analytical tools to move beyond the historical emphasis on particular host-parasite interactions and consider the full suite of species that influence infection dynamics. We have emphasized approaches from community ecology that can advance our ability to manage infections by (i) identifying the factors that govern the structure and dynamics of communities composed of multiple hosts, vectors, and symbionts; (ii) isolating the drivers of heterogeneity; and (iii) understanding how processes and patterns link across multiple scales of biological organization. For many emerging infections, complete eradication is unlikely to be successful, but a broader understanding of the ecological communities in which host-parasite interactions are embedded will facilitate more effective management.

Transforming this broader understanding into practical disease management requires tight integration of surveillance, community ecology analysis, and public health implementation (*97*) (Fig. 4). Ongoing technological advances are rapidly overcoming previous barriers in data quality and quantity, highlighting emerging opportunities to incorporate approaches from community ecology into existing disease research and to evaluate the factors driving the structure and dynamics of natural disease systems. Combining analyses of these high-resolution data with modeling approaches and large-scale manipulations of host-parasite interactions—similar to the foundational experiments from community ecology (*67*)—offers excellent opportunities for developing a deeper understanding of the processes underlying disease emergence and control. To date, there have been some practical successes that follow this broad approach. For example, following the observation of five dead howler monkeys—a key host for yellow fever virus—a collaborative effort between the U.S. Agency for International Development (USAID) PREDICT program and the Bolivian government led to rapid implementation of human vaccination and mosquito control in the affected area (*98*). Similarly, increased use of buffer zones between fruit trees and livestock housing has been effectively used in Malaysia to reduce Nipah virus transmission into pigs and the risks of human outbreaks (*83*), while electrified fences in Kruger National Park have helped limit contact between bovine TB–infected wildlife and cattle in surrounding areas (*84*). Such scenarios demonstrate how a broader appreciation for the epidemiological links among humans, domestic animals, and wildlife can promote disease community ecology as a discipline and result in more effective control of disease risk in ecological communities.

REFERENCES AND NOTES

1. B. Jasny, L. Roberts, M. Enserink, O. Smith, What works [introduction to Global Health special issue]. *Science* **345**, 1256–1257 (2014). doi: 10.1126/science.345.6202.1256; pmid: 25214599
2. J. Sepúlveda, C. Murray, The state of global health in 2014. *Science* **345**, 1275–1278 (2014). pmid: 25214611
3. World Health Organization, *The Top 10 Causes of Death* (2014); www.who.int/mediacentre/factsheets/fs310/en.
4. M. C. Fisher *et al*., Emerging fungal threats to animal, plant and ecosystem health. *Nature* **484**, 186–194 (2012). doi: 10.1038/nature10947; pmid: 22498624
5. B. V. Purse *et al*., Climate change and the recent emergence of bluetongue in Europe. *Nat. Rev. Microbiol.* **3**, 171–181 (2005). doi: 10.1038/nrmicro1090; pmid: 15685226
6. K. F. Smith *et al*., Global rise in human infectious disease outbreaks. *J. R. Soc. Interface* **11**, 20140950 (2014). doi: 10.1098/rsif.2014.0950; pmid: 25401184
7. K. E. Jones *et al*., Global trends in emerging infectious diseases. *Nature* **451**, 990–993 (2008). doi: 10.1038/nature06536; pmid: 18288193
8. J. O. Lloyd-Smith *et al*., Epidemic dynamics at the human-animal interface. *Science* **326**, 1362–1367 (2009). doi: 10.1126/science.1177345; pmid: 19965751
9. A. M. Messenger, A. N. Barnes, G. C. Gray, Reverse zoonotic disease transmission (zooanthroponosis): A systematic review of seldom-documented human biological threats to animals. *PLOS ONE* **9**, e89055 (2014). doi: 10.1371/journal.pone.0089055; pmid: 24586500
10. J. W. Rudge *et al*., Identifying host species driving transmission of schistosomiasis japonica, a multihost parasite system, in China. *Proc. Natl. Acad. Sci. U.S.A.* **110**, 11457–11462 (2013). doi: 10.1073/pnas.1221509110; pmid: 23798418
11. J. E. Rabinovich *et al*., Ecological patterns of blood-feeding by kissing-bugs (Hemiptera: Reduviidae: Triatominae). *Mem. Inst. Oswaldo Cruz* **106**, 479–494 (2011). doi: 10.1590/S0074-02762011000400016; pmid: 21739038

12. S. Alizon, J. C. de Roode, Y. Michalakis, Multiple infections and the evolution of virulence. *Ecol. Lett.* **16**, 556–567 (2013). doi: 10.1111/ele.12076; pmid: 23347009
13. A. B. Pedersen, A. Fenton, Emphasizing the ecology in parasite community ecology. *Trends Ecol. Evol.* **22**, 133–139 (2007). doi: 10.1016/j.tree.2006.11.005; pmid: 17137676
14. S. Telfer *et al.*, Species interactions in a parasite community drive infection risk in a wildlife population. *Science* **330**, 243–246 (2010). doi: 10.1126/science.1190333; pmid: 20929776
15. C. K. Kwan, J. D. Ernst, HIV and tuberculosis: A deadly human syndemic. *Clin. Microbiol. Rev.* **24**, 351–376 (2011). doi: 10.1128/CMR.00042-10; pmid: 21482729
16. P. Druilhe, A. Tall, C. Sokhna, Worms can worsen malaria: Towards a new means to roll back malaria? *Trends Parasitol.* **21**, 359–362 (2005). doi: 10.1016/j.pt.2005.06.011; pmid: 15967721
17. A. K. Gibson *et al.*, Polyparasitism is associated with increased disease severity in *Toxoplasma gondii*-infected marine sentinel species. *PLOS Negl. Trop. Dis.* **5**, e1142 (2011). doi: 10.1371/journal.pntd.0001142; pmid: 21629726
18. J. D. Voss, D. K. Mills, J. L. Myers, E. R. Remily, L. L. Richardson, Black band disease microbial community variation on corals in three regions of the wider Caribbean. *Microb. Ecol.* **54**, 730–739 (2007). doi: 10.1007/s00248-007-9234-1; pmid: 17393054
19. H. Susi, B. Barrès, P. F. Vale, A. L. Laine, Co-infection alters population dynamics of infectious disease. *Nat. Commun.* **6**, 5975 (2015). doi: 10.1038/ncomms6975; pmid: 25569306
20. D. F. Doak *et al.*, Understanding and predicting ecological dynamics: Are major surprises inevitable? *Ecology* **89**, 952–961 (2008). doi: 10.1890/07-0965.1; pmid: 18481520
21. J. A. Al-Tawfiq, Z. A. Memish, Middle East respiratory syndrome coronavirus: Transmission and phylogenetic evolution. *Trends Microbiol.* **22**, 573–579 (2014). pmid: 25178651
22. P. J. Hudson, S. E. Perkins, I. M. Cattadori, in *Infectious Disease Ecology: Effects of Ecosystems on Disease and of Disease on Ecosystems*, R. S. Ostfeld, F. Keesing, V. T. Eviner, Eds. (Princeton Univ. Press, Princeton, NJ, 2008), pp. 347–367.
23. R. Woodroffe *et al.*, Culling and cattle controls influence tuberculosis risk for badgers. *Proc. Natl. Acad. Sci. U.S.A.* **103**, 14713–14717 (2006). doi: 10.1073/pnas.0606251103; pmid: 17015843
24. J. R. Mihaljevic, Linking metacommunity theory and symbiont evolutionary ecology. *Trends Ecol. Evol.* **27**, 323–329 (2012). doi: 10.1016/j.tree.2012.01.011; pmid: 22341499
25. E. C. Rynkiewicz, A. B. Pedersen, A. Fenton, An ecosystem approach to understanding and managing within-host parasite community dynamics. *Trends Parasitol.* **31**, 212–221 (2015). doi: 10.1016/j.pt.2015.02.005; pmid: 25814004
26. E. W. Seabloom *et al.*, The community ecology of pathogens: Coinfection, coexistence and community composition. *Ecol. Lett.* **18**, 401–415 (2015). doi: 10.1111/ele.12418; pmid: 25728488
27. R. D. Holt, A. Dobson, in *Disease Ecology: Community Structure and Pathogen Dynamics*, S. K. Collinge, C. Ray, Eds. (Oxford Univ. Press, Oxford, 2006), pp. 6–27.
28. M. Vellend, Conceptual synthesis in community ecology. *Q. Rev. Biol.* **85**, 183–206 (2010). doi: 10.1086/652373; pmid: 20565040
29. P. B. Adler, J. HilleRisLambers, J. M. Levine, A niche for neutrality. *Ecol. Lett.* **10**, 95–104 (2007). doi: 10.1111/j.1461-0248.2006.00996.x; pmid: 17257097
30. J. M. Chase, Drought mediates the importance of stochastic community assembly. *Proc. Natl. Acad. Sci. U.S.A.* **104**, 17430–17434 (2007). doi: 10.1073/pnas.0704350104; pmid: 17942690
31. A. F. Read, L. H. Taylor, The ecology of genetically diverse infections. *Science* **292**, 1099–1102 (2001). doi: 10.1126/science.1059410; pmid: 11352063
32. M. A. Leibold *et al.*, The metacommunity concept: A framework for multi-scale community ecology. *Ecol. Lett.* **7**, 601–613 (2004). doi: 10.1111/j.1461-0248.2004.00608.x
33. S. J. Presley, C. L. Higgins, M. R. Willig, A comprehensive framework for the evaluation of metacommunity structure. *Oikos* **119**, 908–917 (2010). doi: 10.1111/j.1600-0706.2010.18544.x
34. G. Suzán *et al.*, Metacommunity and phylogenetic structure determine wildlife and zoonotic infectious disease patterns in time and space. *Ecol. Evol.* **5**, 865–873 (2015). doi: 10.1002/ece3.1404; pmid: 25750713
35. T. Dallas, S. J. Presley, Relative importance of host environment, transmission potential and host phylogeny to the structure of parasite metacommunities. *Oikos* **123**, 866–874 (2014). doi: 10.1111/oik.00707
36. I. M. Parker *et al.*, Phylogenetic structure and host abundance drive disease pressure in communities. *Nature* **520**, 542–544 (2015). doi: 10.1038/nature14372; pmid: 25903634
37. P. T. J. Johnson, D. L. Preston, J. T. Hoverman, B. E. LaFonte, Host and parasite diversity jointly control disease risk in complex communities. *Proc. Natl. Acad. Sci. U.S.A.* **110**, 16916–16921 (2013). doi: 10.1073/pnas.1310557110; pmid: 24082092
38. R. Poulin, Network analysis shining light on parasite ecology and diversity. *Trends Parasitol.* **26**, 492–498 (2010). doi: 10.1016/j.pt.2010.05.008; pmid: 20561821
39. E. C. Griffiths, A. B. Pedersen, A. Fenton, O. L. Petchey, Analysis of a summary network of co-infection in humans reveals that parasites interact most via shared resources. *Proc. R. Soc. B* **281**, 20132286 (2014). doi: 10.1098/rspb.2013.2286; pmid: 24619434
40. S. Davis, B. Abbasi, S. Shah, S. Telfer, M. Begon, Spatial analyses of wildlife contact networks. *J. R. Soc. Interface* **12**, 20141004 (2014). doi: 10.1098/rsif.2014.1004; pmid: 25411407
41. D. M. Tompkins, A. M. Dunn, M. J. Smith, S. Telfer, Wildlife diseases: From individuals to ecosystems. *J. Anim. Ecol.* **80**, 19–38 (2011). doi: 10.1111/j.1365-2656.2010.01742.x; pmid: 20735792
42. A. R. Cirtwill, D. B. Stouffer, Concomitant predation on parasites is highly variable but constrains the ways in which parasites contribute to food web structure. *J. Anim. Ecol.* **84**, 734–744 (2015). doi: 10.1111/1365-2656.12323; pmid: 25418425
43. T. Poisot, E. Canard, D. Mouillot, N. Mouquet, D. Gravel, The dissimilarity of species interaction networks. *Ecol. Lett.* **15**, 1353–1361 (2012). doi: 10.1111/ele.12002; pmid: 22994257
44. B. J. McGill, B. J. Enquist, E. Weiher, M. Westoby, Rebuilding community ecology from functional traits. *Trends Ecol. Evol.* **21**, 178–185 (2006). doi: 10.1016/j.tree.2006.02.002; pmid: 16701083
45. C. T. Webb, J. A. Hoeting, G. M. Ames, M. I. Pyne, N. LeRoy Poff, A structured and dynamic framework to advance traits-based theory and prediction in ecology. *Ecol. Lett.* **13**, 267–283 (2010). doi: 10.1111/j.1461-0248.2010.01444.x; pmid: 20455917
46. E. Weiher *et al.*, Advances, challenges and a developing synthesis of ecological community assembly theory. *Philos. Trans. R. Soc. B* **366**, 2403–2413 (2011). doi: 10.1098/rstb.2011.0056; pmid: 21768155
47. B. A. Han, J. P. Schmidt, S. E. Bowden, J. M. Drake, Rodent reservoirs of future zoonotic diseases. *Proc. Natl. Acad. Sci. U.S.A.* **112**, 7039–7044 (2015). doi: 10.1073/pnas.1501598112; pmid: 26038558
48. S. H. Paull *et al.*, From superspreaders to disease hotspots: Linking transmission across hosts and space. *Front. Ecol. Environ.* **10**, 75–82 (2012). doi: 10.1890/110111; pmid: 23482675
49. D. G. Streicker, A. Fenton, A. B. Pedersen, Differential sources of host species heterogeneity influence the transmission and control of multihost parasites. *Ecol. Lett.* **16**, 975–984 (2013). doi: 10.1111/ele.12122; pmid: 23714379
50. J. O. Lloyd-Smith, S. J. Schreiber, P. E. Kopp, W. M. Getz, Superspreading and the effect of individual variation on disease emergence. *Nature* **438**, 355–359 (2005). doi: 10.1038/nature04153; pmid: 16292310
51. Z. Shen *et al.*, Superspreading SARS events, Beijing, 2003. *Emerg. Infect. Dis.* **10**, 256–260 (2004). doi: 10.3201/eid1002.030732; pmid: 15030693
52. A. L. Graham *et al.*, Fitness correlates of heritable variation in antibody responsiveness in a wild mammal. *Science* **330**, 662–665 (2010). doi: 10.1126/science.1194878; pmid: 21030656
53. S. E. Perkins, I. M. Cattadori, V. Tagliapietra, A. P. Rizzoli, P. J. Hudson, Empirical evidence for key hosts in persistence of a tick-borne disease. *Int. J. Parasitol.* **33**, 909–917 (2003). doi: 10.1016/S0020-7519(03)00128-0; pmid: 12906875
54. W. E. Stutz, O. L. Lau, D. I. Bolnick, Contrasting patterns of phenotype-dependent parasitism within and among populations of threespine stickleback. *Am. Nat.* **183**, 810–825 (2014). doi: 10.1086/676005; pmid: 24823824
55. D. G. Streicker, A. Fenton, A. B. Pedersen, Differential sources of host species heterogeneity influence the transmission and control of multihost parasites. *Ecol. Lett.* **16**, 975–984 (2013). doi: 10.1111/ele.12122; pmid: 23714379
56. J. M. Calabrese, J. L. Brunner, R. S. Ostfeld, Partitioning the aggregation of parasites on hosts into intrinsic and extrinsic components via an extended Poisson-gamma mixture model. *PLOS ONE* **6**, e29215 (2011). doi: 10.1371/journal.pone.0029215; pmid: 22216216
57. P. Chesson, Scale transition theory: Its aims, motivations and predictions. *Ecol. Complex.* **10**, 52–68 (2012). doi: 10.1016/j.ecocom.2011.11.002
58. A. Fenton, S. E. Perkins, Applying predator-prey theory to modelling immune-mediated, within-host interspecific parasite interactions. *Parasitology* **137**, 1027–1038 (2010). doi: 10.1017/S0031182009991788; pmid: 20152061
59. R. M. Anderson, R. M. May, Regulation and stability of host-parasite population interactions. I. Regulatory processes. *J. Anim. Ecol.* **47**, 219–247 (1978). doi: 10.2307/3933
60. R. M. Anderson, R. M. May, The population dynamics of microparasites and their invertebrate hosts. *Philos. Trans. R. Soc. London Ser. B* **291**, 451–524 (1981). doi: 10.1098/rstb.1981.0005
61. R. R. Dunn, T. J. Davies, N. C. Harris, M. C. Gavin, Global drivers of human pathogen richness and prevalence. *Proc. R. Soc. B* **277**, 2587–2595 (2010). doi: 10.1098/rspb.2010.0340; pmid: 20392728
62. S. C. L. Knowles *et al.*, Stability of within-host-parasite communities in a wild mammal system. *Proc. R. Soc. B* **280**, 20130598 (2013). doi: 10.1098/rspb.2013.0598; pmid: 23677343
63. V. O. Ezenwa, A. E. Jolles, Opposite effects of anthelmintic treatment on microbial infection at individual versus population scales. *Science* **347**, 175–177 (2015). doi: 10.1126/science.1261714; pmid: 25574023
64. A. Fenton, Dances with worms: The ecological and evolutionary impacts of deworming on coinfecting pathogens. *Parasitology* **140**, 1119–1132 (2013). doi: 10.1017/S0031182013000590; pmid: 23714427
65. R. S. Ostfeld, F. Keesing, Effects of host diversity on infectious disease. *Annu. Rev. Ecol. Evol. Syst.* **43**, 157–182 (2012). doi: 10.1146/annurev-ecolsys-102710-145022
66. P. T. J. Johnson, R. S. Ostfeld, F. Keesing, Frontiers in research on biodiversity and disease. *Ecol. Lett.* (2015). doi: 10.1111/ele.12479
67. D. W. Schindler, Replication versus realism: The need for ecosystem-scale experiments. *Ecosystems* **1**, 323–334 (1998). doi: 10.1007/s100219900026
68. A. B. Pedersen, A. Fenton, The role of antiparasite treatment experiments in assessing the impact of parasites on wildlife. *Trends Parasitol.* **31**, 200–211 (2015). doi: 10.1016/j.pt.2015.02.004; pmid: 25778845
69. D. A. Grear, S. E. Perkins, P. J. Hudson, Does elevated testosterone result in increased exposure and transmission of parasites? *Ecol. Lett.* **12**, 528–537 (2009). doi: 10.1111/j.1461-0248.2009.01306.x; pmid: 19392718
70. A. B. Pedersen, T. J. Greives, The interaction of parasites and resources cause crashes in a wild mouse population. *J. Anim. Ecol.* **77**, 370–377 (2008). doi: 10.1111/j.1365-2656.2007.01321.x; pmid: 18028357
71. P. T. J. Johnson, D. L. Preston, J. T. Hoverman, K. L. D. Richgels, Biodiversity decreases disease through predictable changes in host community competence. *Nature* **494**, 230–233 (2013). doi: 10.1038/nature11883; pmid: 23407539
72. G. Suzán *et al.*, Experimental evidence for reduced rodent diversity causing increased hantavirus prevalence. *PLOS ONE* **4**, e5461 (2009). pmid: 19421313
73. K. E. Langwig *et al.*, Context-dependent conservation responses to emerging wildlife diseases. *Front. Ecol. Environ.* **13**, 195–202 (2015). doi: 10.1890/140241
74. K. L. S. Drury, J. D. Rothlisberger, Offense and defense in landscape-level invasion control. *Oikos* **117**, 182–190 (2008). doi: 10.1111/j.2007.0030-1299.16081.x
75. F. Keesing *et al.*, Impacts of biodiversity on the emergence and transmission of infectious diseases. *Nature* **468**, 647–652 (2010). doi: 10.1038/nature09575; pmid: 21124449
76. A. O. Franco, M. G. M. Gomes, M. Rowland, P. G. Coleman, C. R. Davies, Controlling malaria using livestock-based interventions: A one health approach. *PLOS ONE* **9**, e101699 (2014). doi: 10.1371/journal.pone.0101699; pmid: 25050703
77. B. Kaabi, S. B. Ahmed, Assessing the effect of zooprophylaxis on zoonotic cutaneous leishmaniasis transmission: A system dynamics approach. *Biosystems* **114**, 253–260 (2013). doi: 10.1016/j.biosystems.2013.10.003; pmid: 24157699
78. Y. Zhu *et al.*, Genetic diversity and disease control in rice. *Nature* **406**, 718–722 (2000). doi: 10.1038/35021046; pmid: 10963595
79. D. J. Civitello *et al.*, Biodiversity inhibits parasites: Broad evidence for the dilution effect. *Proc. Natl. Acad. Sci. U.S.A.*

112, 8667–8671 (2015). doi: 10.1016/j.biosystems.2013.10.003; pmid: 24157699
80. P. Mähl *et al*., Twenty year experience of the oral rabies vaccine SAG2 in wildlife: A global review. *Vet. Res.* **45**, 77 (2014). doi: 10.1186/s13567-014-0077-8; pmid: 25106552
81. N. D. Wolfe *et al*., Emergence of unique primate T-lymphotropic viruses among central African bushmeat hunters. *Proc. Natl. Acad. Sci. U.S.A.* **102**, 7994–7999 (2005). doi: 10.1073/pnas.0501734102; pmid: 15911757
82. J. S. Brashares *et al*., Bushmeat hunting, wildlife declines, and fish supply in West Africa. *Science* **306**, 1180–1183 (2004). doi: 10.1126/science.1102425; pmid: 15539602
83. P. Daszak, R. Plowright, J. Epstein, J. Pulliam, S. Abdul Rahman, H. Field, C. Smith, K. Olival, S. Luby, K. Halpin, A. D. Hyatt, A. A. Cunningham, in *Disease Ecology: Community Structure and Pathogen Dynamics*, S. K. Collinge, C. Ray, Eds. (Oxford Univ. Press, Oxford, 2006), pp. 186–201.
84. A. R. Renwick, P. C. L. White, R. G. Bengis, Bovine tuberculosis in southern African wildlife: A multi-species host-pathogen system. *Epidemiol. Infect.* **135**, 529–540 (2007). doi: 10.1017/S0950268806007205; pmid: 16959052
85. A. P. Durbin *et al*., Emergence potential of sylvatic dengue virus type 4 in the urban transmission cycle is restrained by vaccination and homotypic immunity. *Virology* **439**, 34–41 (2013). doi: 10.1016/j.virol.2013.01.018; pmid: 23485373
86. J. M. Drake *et al*., Ebola cases and health system demand in Liberia. *PLOS Biol.* **13**, e1002056 (2015). doi: 10.1371/journal.pbio.1002056; pmid: 25585384
87. M. J. Taylor, A. Hoerauf, M. Bockarie, Lymphatic filariasis and onchocerciasis. *Lancet* **376**, 1175–1185 (2010). doi: 10.1016/S0140-6736(10)60586-7; pmid: 20739055
88. E. van Nood *et al*., Duodenal infusion of donor feces for recurrent *Clostridium difficile*. *N. Engl. J. Med.* **368**, 407–415 (2013). doi: 10.1056/NEJMoa1205037; pmid: 23323867
89. G. Harms, H. Feldmeier, HIV infection and tropical parasitic diseases - deleterious interactions in both directions? *Trop. Med. Int. Health* **7**, 479–488 (2002). doi: 10.1046/j.1365-3156.2002.00893.x; pmid: 12031069
90. A. A. Hoffmann *et al*., Successful establishment of *Wolbachia* in *Aedes* populations to suppress dengue transmission. *Nature* **476**, 454–457 (2011). doi: 10.1038/nature10356; pmid: 21866160
91. Z. Kambris, P. E. Cook, H. K. Phuc, S. P. Sinkins, Immune activation by life-shortening *Wolbachia* and reduced filarial competence in mosquitoes. *Science* **326**, 134–136 (2009). doi: 10.1126/science.1177531; pmid: 19797660
92. A. L. Graham, Ecological rules governing helminth-microparasite coinfection. *Proc. Natl. Acad. Sci. U.S.A.* **105**, 566–570 (2008). doi: 10.1073/pnas.0707221105; pmid: 18182496
93. T. Lembo *et al*., Exploring reservoir dynamics: A case study of rabies in the Serengeti ecosystem. *J. Appl. Ecol.* **45**, 1246–1257 (2008). doi: 10.1111/j.1365-2664.2008.01468.x; pmid: 22427710
94. K. Hampson *et al*., Transmission dynamics and prospects for the elimination of canine rabies. *PLOS Biol.* **7**, e53 (2009). pmid: 19278295
95. A. Pandey *et al*., Strategies for containing Ebola in West Africa. *Science* **346**, 991–995 (2014). doi: 10.1126/science.1260612; pmid: 25414312
96. E. J. Scholte, F. Schaffner, in *Emerging Pests and Vector-Borne Diseases in Europe*, W. Takken, B. G. J. Knols, Eds. (Wageningen Academic, Wageningen, Netherlands, 2007), pp. 241–260.
97. S. S. Morse *et al*., Prediction and prevention of the next pandemic zoonosis. *Lancet* **380**, 1956–1965 (2012). doi: 10.1016/S0140-6736(12)61684-5; pmid: 23200504
98. "PREDICT success: Yellow fever discovered in Bolivian howler monkeys" (One Health Institute, 2014); www.vetmed.ucdavis.edu/ohi/predict/news/bolivia-success-howler-monkeys.cfm.
99. A. D. Blackwell, M. Martin, H. Kaplan, M. Gurven, Antagonism between two intestinal parasites in humans: The importance of co-infection for infection risk and recovery dynamics. *Proc. R. Soc. B* **280**, 20131671 (2013). doi: 10.1098/rspb.2013.1671; pmid: 23986108
100. K. Stiasny *et al*., Characterization of a structural intermediate of flavivirus membrane fusion. *PLOS Pathog.* **3**, e20 (2007). doi: 10.1371/journal.ppat.0030020
101. R. M. Anderson, R. M. May, Population biology of infectious diseases: Part I. *Nature* **280**, 361–367 (1979). doi: 10.1038/280361a0; pmid: 460412
102. A. Dobson, Population dynamics of pathogens with multiple host species. *Am. Nat.* **164** (suppl. 5), S64–S78 (2004). doi: 10.1086/424681; pmid: 15540143
103. L. Gilbert, R. Norman, K. M. Laurenson, H. W. Reid, P. J. Hudson, Disease persistence and apparent competition in a three-host community: An empirical and analytical study of large-scale, wild populations. *J. Anim. Ecol.* **70**, 1053–1061 (2001). doi: 10.1046/j.0021-8790.2001.00558.x
104. R. Norman, R. G. Bowers, M. Begon, P. J. Hudson, Persistence of tick-borne virus in the presence of multiple host species: Tick reservoirs and parasite mediated competition. *J. Theor. Biol.* **200**, 111–118 (1999). doi: 10.1006/jtbi.1999.0982; pmid: 10479543
105. C. L. Wood, K. D. Lafferty, Biodiversity and disease: A synthesis of ecological perspectives on Lyme disease transmission. *Trends Ecol. Evol.* **28**, 239–247 (2013). doi: 10.1016/j.tree.2012.10.011; pmid: 23182683

ACKNOWLEDGMENTS

For discussions and feedback helpful in shaping the manuscript, we thank S. Altizer, D. Calhoun, G. Devevey, I. Doron, S. Haas, K. Hoang, B. Hoye, M. Joseph, J. Koprivnikar, T. McDevitt-Galles, J. Mihaljevic, A. Pedersen, O. Petchey, A. Pierce, D. Preston, Y. Springer, W. Stutz, L. Tao, S. White, and members of the Macroecology of Infectious Disease Research Coordination Network (funded by NSF/NIH/USDA DEB 131223). Supported by NSF grant DEB-1149308 and NIH grant R01GM109499 (P.T.J.J.), NSF grant DEB-1257160 and NIH grant R01GM109501 (J.C.d.R.), and UK Natural Environment Research Council grants NE/G006830/1
and NE/I024038/1 (A.F.).

SUPPLEMENTARY MATERIALS

www.sciencemag.org/content/349/6252/1259504/suppl/DC1
Supplementary Text

10.1126/science.1259504

RESEARCH ARTICLE SUMMARY

MACROECOLOGY

The predator-prey power law: Biomass scaling across terrestrial and aquatic biomes

Ian A. Hatton,* Kevin S. McCann, John M. Fryxell, T. Jonathan Davies, Matteo Smerlak, Anthony R. E. Sinclair, Michel Loreau

INTRODUCTION: A surprisingly general pattern at very large scales casts light on the link between ecosystem structure and function. We show a robust scaling law that emerges uniquely at the level of whole ecosystems and is conserved across terrestrial and aquatic biomes worldwide. This pattern describes the changing structure and productivity of the predator-prey biomass pyramid, which represents the biomass of communities at different levels of the food chain. Scaling exponents of the relation between predator versus prey biomass and community production versus biomass are often near ¾, which indicates that very different communities of species exhibit similar high-level structure and function. This recurrent community growth pattern is remarkably similar to individual growth patterns and may hint at a basic process that reemerges across levels of organization.

RATIONALE: We assembled a global data set for community biomass and production across 2260 large mammal, invertebrate, plant, and plankton communities. These data reveal two ecosystem-level power law scaling relations: (i) predator biomass versus prey biomass, which indicates how the biomass pyramid changes shape, and (ii) community production versus community biomass, which indicates how per capita productivity changes at a given level in the pyramid. Both relations span a wide range of ecosystems along large-scale biomass gradients. These relations can be linked theoretically to show how pyramid shape depends on flux rates into and out of predator-prey communities. In order to link community-level patterns to individual processes, we examined community size structure and, particularly, how the mean body mass of a community relates to its biomass.

RESULTS: Across ecosystems globally, pyramid structure becomes consistently more bottom-heavy, and per capita production declines with increasing biomass. These two ecosystem-level patterns both follow power laws with near ¾ exponents and are shown to be robust to different methods and assumptions. These structural and functional relations are linked theoretically, suggesting that a common community-growth pattern influences predator-prey interactions and underpins pyramid shape. Several of these patterns are highly regular (R^2 > 0.80) and yet are unexpected from classic theories or from empirical relations at the population or individual level. By examining community size structure, we show these patterns emerge distinctly at the ecosystem level and independently from individual near ¾ body-mass allometries.

ON OUR WEB SITE

Read the full article at http://dx.doi.org/10.1126/science.aac6284

CONCLUSION: Systematic changes in biomass and production across trophic communities link fundamental aspects of ecosystem structure and function. The striking similarities that are observed across different kinds of systems imply a process that does not depend on system details. The regularity of many of these relations allows large-scale predictions and suggests high-level organization. This community-level growth pattern suggests a systematic form of density-dependent growth and is intriguing given the parallels it exhibits to growth scaling at the individual level, both of which independently follow near ¾ exponents. Although we can make ecosystem-level predictions from individual-level data, we have yet to fully understand this similarity, which may offer insight into growth processes in physiology and ecology across the tree of life. ■



African large-mammal communities are highly structured. In lush savanna, there are three times more prey per predator than in dry desert, a pattern that is unexpected and systematic. [Photo: Amaury Laporte]

The list of author affiliations is available in the full article online.
*Corresponding author. E-mail: i.a.hatton@gmail.com
Cite this paper as I. A. Hatton *et al.*, *Science* 349, aac6284 (2015).
DOI: 10.1126/science.aac6284

Downloaded from www.sciencemag.org on September 5, 2015

RESEARCH ARTICLE

MACROECOLOGY

The predator-prey power law: Biomass scaling across terrestrial and aquatic biomes

Ian A. Hatton,[1]* Kevin S. McCann,[2] John M. Fryxell,[2] T. Jonathan Davies,[1] Matteo Smerlak,[3] Anthony R. E. Sinclair,[4,5] Michel Loreau[6]

Ecosystems exhibit surprising regularities in structure and function across terrestrial and aquatic biomes worldwide. We assembled a global data set for 2260 communities of large mammals, invertebrates, plants, and plankton. We find that predator and prey biomass follow a general scaling law with exponents consistently near ¾. This pervasive pattern implies that the structure of the biomass pyramid becomes increasingly bottom-heavy at higher biomass. Similar exponents are obtained for community production-biomass relations, suggesting conserved links between ecosystem structure and function. These exponents are similar to many body mass allometries, and yet ecosystem scaling emerges independently from individual-level scaling, which is not fully understood. These patterns suggest a greater degree of ecosystem-level organization than previously recognized and a more predictive approach to ecological theory.

Many large-scale patterns in nature follow simple mathematical functions, indicating a basic process with the potential for deeper understanding (*1*). When the same pattern recurs in different kinds of systems, it urges consideration of their shared properties and provides the opportunity for synthesis across systems (*2*). Ecology has increasingly observed patterns over very large scales and across levels of organization, from individuals and populations to communities and whole ecosystems (*3*–*8*). These patterns depict the boundaries in which life exists and are often highly conserved across taxa and types of communities. This points either to intrinsic characteristics of the individual, such as shared ancestry or energetic constraints (*5*, *6*), or else extrinsic factors, such as the way that many individuals are aggregated, grow, and interact (*1*, *7*). The challenge in ecology, as in many fields, is to link large-scale patterns to finer-grain processes (*1*, *4*).

Here, we present a pattern that follows a simple function and recurs across a variety of ecosystem types in different biomes worldwide. The pattern is only observed over large aggregations of individuals and appears to emerge uniquely at the ecosystem level. We do not know why this pattern occurs, because it is not predicted by current theoretical models and, as far as we can detect, is unexpected from lower-level structure. What is surprising is that the same pattern recurs systematically in different places, including grasslands, forests, lakes, and oceans. Our analysis has its basis in empirical data drawn from more than 1000 published studies, many of which are cross-system meta-analyses (*9*–*33*) (materials and methods, section M1, A to C). In total, we bring together biomass and production measurements for tens of thousands of populations over 2260 ecosystems in 1512 distinct locations globally. Our approach is similar to a number of other large-scale cross-system meta-analyses (*10*, *19*–*21*, *29*–*42*), allowing comparisons to previous work.

We began by considering the predator-prey biomass power law in African savanna, shown in Fig. 1, which serves to identify key properties of this more general phenomenon. The pattern describes relative changes in the shape of the "Eltonian" pyramid of biomass, which represents how total biomass is distributed across communities at different trophic levels in the food chain (*43*–*45*). In any given environment, the pyramid often exhibits a consistent shape, called the trophic structure, but in different environments, the same communities of species may be in quite different relative proportions (*39*–*42*). That is, pyramid shape may change with size, which can be described by the predator-prey power law exponent k.

Power laws are simple functions of the form $y = cx^k$, where c is the coefficient (y value at $x = 1$) and k is the dimensionless scaling exponent (*1*, *2*). On logarithmic axes, power laws follow a straight line with slope k but on ordinary axes may curve up ($k > 1$) or down ($k < 1$). The slope k of the relation of the log of predator biomass versus the log of prey biomass identifies the relative change in the shape of the pyramid (Fig. 2). An exponent $k > 1$ means that the pyramid becomes relatively more top-heavy at higher biomass and is predicted by top-down control of predators on prey (*41*, *42*, *46*–*48*) (appendix S1). An exponent $k = 1$ indicates that pyramid shape remains constant and is predicted by bottom-up control, whereby a constant fraction of biomass is produced and transferred to each successively higher trophic level (*8*, *41*, *42*, *49*) (appendix S1). Last, $k < 1$ indicates that the pyramid becomes relatively more bottom-heavy at higher biomass (Fig. 2).

We show that the shape of the predator-prey biomass pyramid becomes systematically more bottom-heavy as pyramid size increases along a biomass gradient. Similar changes are also observed for per capita productivity with biomass, suggesting a basic link between aspects of ecological structure and function. Our findings thus reveal highly conserved patterns in pyramid size, shape, and growth across different kinds of ecosystems. In particular, community production-biomass scaling is commonly near $k = ¾$ across

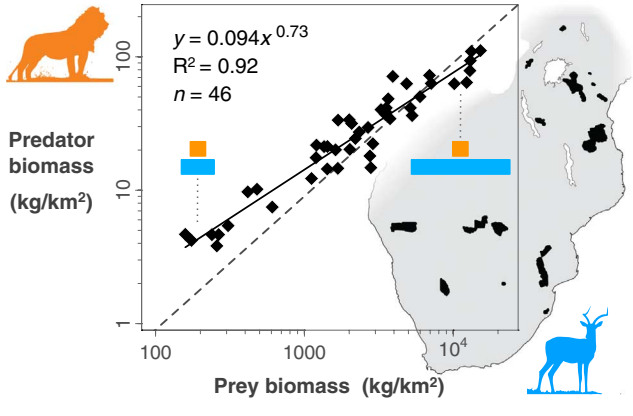


Fig. 1. African predator-prey communities exhibit systematic changes in ecosystem structure. Predators include lion, hyena, and other large carnivores (20 to 140 kg), which compete for large herbivore prey from dik-dik to buffalo (5 to 500 kg). Each point is a protected area, across which the biomass pyramid becomes three times more bottom-heavy at higher biomass. This near ¾ scaling law is found to recur across ecosystems globally.

[1]Department of Biology, McGill University, Montréal, Québec H3A 1B1, Canada. [2]Department of Integrative Biology, University of Guelph, Guelph, Ontario N1G 2W1, Canada. [3]Perimeter Institute for Theoretical Physics, Waterloo, Ontario N2L 2Y5, Canada. [4]Biodiversity Research Centre, University of British Columbia, Vancouver, British Columbia V6T 1Z4, Canada. [5]Tanzania Wildlife Research Institute, P.O. Box 661, Arusha, United Republic of Tanzania. [6]Centre for Biodiversity Theory and Modeling, Experimental Ecology Station, CNRS, 09200 Moulis, France.
*Corresponding author. E-mail: i.a.hatton@gmail.com

different types of ecosystems and is thus curiously similar to individual production-body mass allometry. This may suggest a similar process recurs across levels of organization.

Why are there not more lions?

Across African savanna ecosystems (Fig. 1), the total biomass of large carnivores follows a consistent relation to the total biomass of their herbivore prey. The exponent is $k = 0.73$, which is sublinear ($k < 1$), and indicates that the trophic pyramid becomes relatively more bottom-heavy at higher biomass. From the dry Kalahari desert to the teeming Ngorongoro Crater, there are threefold fewer predators per pound of prey, which leads to the question: where prey are abundant, why are there not more lions?

Trophic structure in African savanna

The African predator-prey pattern is remarkably systematic given how it is constituted (R^2 =

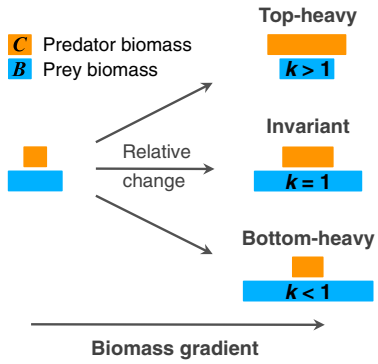


Fig. 2. The predator-prey power law exponent *k* describes relative changes in pyramid shape. The slope k (from $\log C = k \log B + \log c$) identifies how the predator-prey ratio changes along a biomass gradient. Top-heavy and bottom-heavy refer to relative tendencies at higher biomass.

0.92; Fig. 1). Data derive from 190 studies that reported population density in 23 protected areas at different points in time (section M2A). These counts cover the dominant species of large carnivores (wild dog, cheetah, leopard, hyena, and lion) and their characteristic herbivore prey [5 to 500 kg; 27 species (*50*, *51*)]. The population density (numbers of individuals per unit area) of these species vary over 3 to 4 orders of magnitude (Fig. 3A), but, when aggregated into trophic communities within their respective ecosystems, the variability collapses along a highly regular power law (Fig. 1). The observed change in pyramid shape is unexpected given that trophic communities maintain a near constant size structure. The mean body mass, which is the total biomass divided by the total numerical density (*52*), averages over all individuals and provides an indication of community size structure. Both carnivore and herbivore mean body mass scale with biomass near exponents $k = 0.03$ (Fig. 3B), indicating that size structure is nearly invariant and that both the pyramids of biomass and the pyramid of numbers (numerical density) change in similar ways (section M2B) (*43*–*45*). Both the diversity and the frequency of different size classes are also nearly invariant, so that most species have similar relative frequencies across the biomass gradient (histograms in Fig. 3B). The carnivore-to-herbivore body mass ratio is thus constant even as their biomass ratio declines dramatically (Fig. 3C).

Declines in the predator-prey biomass ratio can be tested by comparing the relation to the null hypothesis of an invariant pyramid shape ($k = 1$). The dashed line in Fig. 1 is the prediction that 1 kg of predator varies with every 111 kg of prey (*53*). This implies some form of bottom-up control, whereby as prey double, we expect predators to double. In Fig. 3C, the y axis is transformed to the predator-prey biomass ratio, giving a null exponent $k = 0$. In contrast to the null hypothesis, the observed predator-prey biomass ratio exhibits highly significant declines (P value $< 10^{-9}$), a pattern that has been observed independently in separate studies (*9*–*12*) and is robust to a variety of assumptions (section M2B). This pattern, however, cannot be predicted from population or community structure (Fig. 3, A and B), and, as far as we are aware, there is no current theoretical basis for expecting such changes in trophic structure (appendix S1). Large-mammal time series over the past 50 years in several of these systems show that communities are near steady state, even as component populations fluctuate and largely compensate with one another, for a more regular central tendency at the community level (section M2C). The predator-prey pattern thus appears to emerge uniquely at the ecosystem level by aggregating over large numbers of individuals.

Linking trophic structure and function

If we cannot predict this pattern from lower-level structure, what high-level function might be operating? What flux rates into or out of each trophic community may be shaping trophic structure? For systems near steady state, flux in and out should balance, but flux rates may not be proportional to standing biomass. To investigate the relation between pyramid shape and trophic flux, we consider a simple predator-prey model (Fig. 4). Predator biomass C and prey biomass B can be thought to depend on two functions: prey produced $P(B)$ and prey consumed by predators $Q(B, C)$. This model framework includes models going back to Lotka-Volterra, depending on how P and Q functions are specified (*8*, *41*, *42*, *46*–*49*, *54*–*57*). The model can thus be adapted to different trophic levels in different kinds of systems (appendix S1). Because

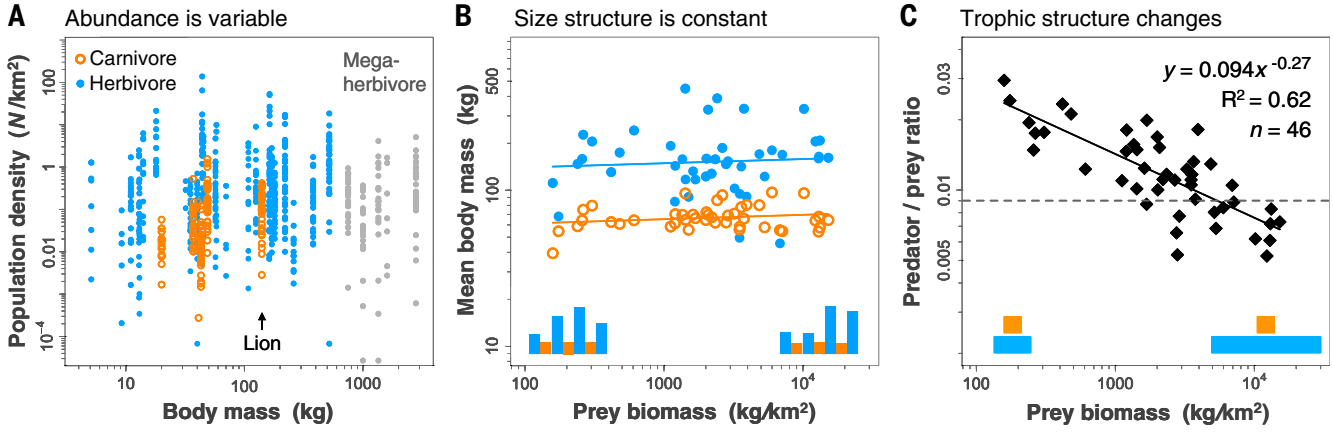


Fig. 3. Emergent trophic structure in African savanna. Large mammal abundance is aggregated across systems to show size structure and trophic structure. Trophic structure follows a regular pattern that is not evident from lower-level structure. These data are also shown in Fig. 1 and Fig. 5, A and B. Further details are in section M2. (**A**) African large mammals vary greatly in density, estimated for 38 species in 23 protected areas at different times. (**B**) Size structure of predator and prey communities is nearly constant across the biomass gradient. Populations from (A) are aggregated into their respective predator and prey communities, so that each point is an ecosystem. Mean body mass averages over all individuals in each community (both slopes are $k = 0.03$ and are not significant). Relative frequencies of different size classes are also near constant, as shown by histograms (bars sum to 1). (**C**) Carnivore-to-herbivore biomass ratios show significant declines at greater prey biomass (P value $< 10^{-9}$). Data are as in Fig. 1 but show the predator/prey ratio, which changes threefold across the biomass gradient.

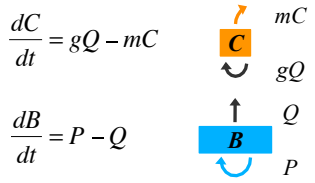


Fig. 4. A predator-prey model (*C*, *B*) with two functions (*P*, *Q*). Different models are specified based on the functions for prey production $P(B)$ and prey consumption by predators, $Q(B,C)$. Predator production, gQ, depends on the growth efficiency g in converting consumption into offspring. Predator loss is mC, where m is mortality rate.

we believe African large mammal communities to be near steady state (C^*, B^*), the predator-prey power law can be expressed as

$$C^* = cB^{*k}$$

where c is the predator-prey coefficient (in Fig. 1, $c = 0.094\ \mathrm{kg}^{1-k}$ and $k = 0.73$). We thus seek P and Q functions that give rise to this structural pattern. At equilibrium, both equations in Fig. 4 can be set to zero, and we can substitute the prey equation ($Q^* = P^*$) into the predator equation ($C^* = gQ^*/m$) (where g is the predator growth efficiency and m is the predator mortality rate), giving $C^* = gP^*/m$. To obtain $C^* = cB^{*k}$ above, prey production may scale in the same way with prey biomass, which can be expressed as

$$P = rB^k$$

Here r is the prey production coefficient (units kg^{1-k}/time), and k is assumed to be 0.73. The predator-prey coefficient is thus

$$c = rg/m$$

Regardless of how consumption Q is specified, trophic structure should depend on lower trophic productivity, P, according to a simple relation of flux rates. On the left of the equality is the predator-prey coefficient c, which influences pyramid shape, whereas on the right are parameters for flux rates into and out of each trophic community. Clearly, the dynamic interactions of five carnivore species and many more species of prey across vast areas of the continent cannot be captured by two differential equations. This coarse-grained description, however, focuses on a few key flux rates and brings dynamical perspective to the question of what is shaping trophic structure. We have tested this theoretical prediction ($c = rg/m$) for African large mammals, estimating their community rate parameters (r, g, and m) independently from the fitted coefficient in Fig. 1, and find close correspondence (appendix S2). This suggests a link between trophic structure and the production function. Specifically, where prey are abundant, they appear to reproduce at consistently lower rates, which in turn influences the biomass of predators. Lion abundance, for example, appears to depend on the productivity of the prey community, which exhibits a systematic form of density dependence, but also on the densities of other predators, with which lions are compensatory. The regularity of this pattern suggests high-level organization and possibly complex regulatory pathways, which only more detailed study can elaborate. But how general are these structural and functional patterns across other kinds of ecosystems?

Biomass scaling globally

Predator-prey biomass scaling is not unique to the African savanna and is found to recur across a variety of other kinds of ecosystems. Our model suggests this pattern is underpinned by similar production-biomass scaling (Fig. 4). Although data are not available for the same ecosystems to test this connection directly, these two scaling relations exhibit similar exponents near $k = \frac{3}{4}$ across terrestrial and aquatic ecosystems. This suggests that a common community growth pattern may be shaping biomass pyramids across distinct ecosystem types.

Empirical findings

Predator and prey biomass follow a power law with a sublinear exponent ($k < 1$) across several terrestrial and aquatic biomass gradients. Tiger and wolf biomass over their respective continents both scale to prey biomass with exponents near $k = \frac{3}{4}$ (Fig. 5, C and D) (*13*–*17*). These carnivores represent a dominant part of the large predator community, comparable to lion and hyena populations (Fig. 5, A and B). Similarly, zooplankton and phytoplankton biomass follow near ¾ scaling patterns across lakes and oceans and through time (Fig. 5, E to H) (*18*–*22*). A number of studies have reported the same qualitative declines in predator-prey ratios across diverse environments (*14*, *17*, *19*–*22*, *38*, *40*–*42*, *58*–*64*) (section M3), suggesting a widespread phenomenon.

Similar scaling is also observed for community production-biomass relations in grasslands (*23*–*25*), broadleaf and coniferous forests (*26*–*28*), seagrass beds (*29*), and algal (*18*) and invertebrate communities (*30*) (Fig. 5, I to O; section M3, I to O; and table S1). Exceptions to this pattern exist where multiple trophic groups are combined. Fish (Fig. 5P), for example, combine benthivores and planktivores, as well as piscivores, at a higher trophic level (*31*, *32*). Although data are few, when these trophic groups are considered separately, lower-trophic groups scale sublinearly [k ranges from 0.74 to 0.81 (*33*)], whereas piscivores exhibit near-linear scaling ($k = 1.1$; section M3P). It is possible that piscivores are dominating the pattern in Fig. 5P, although data among higher trophic levels are generally limited.

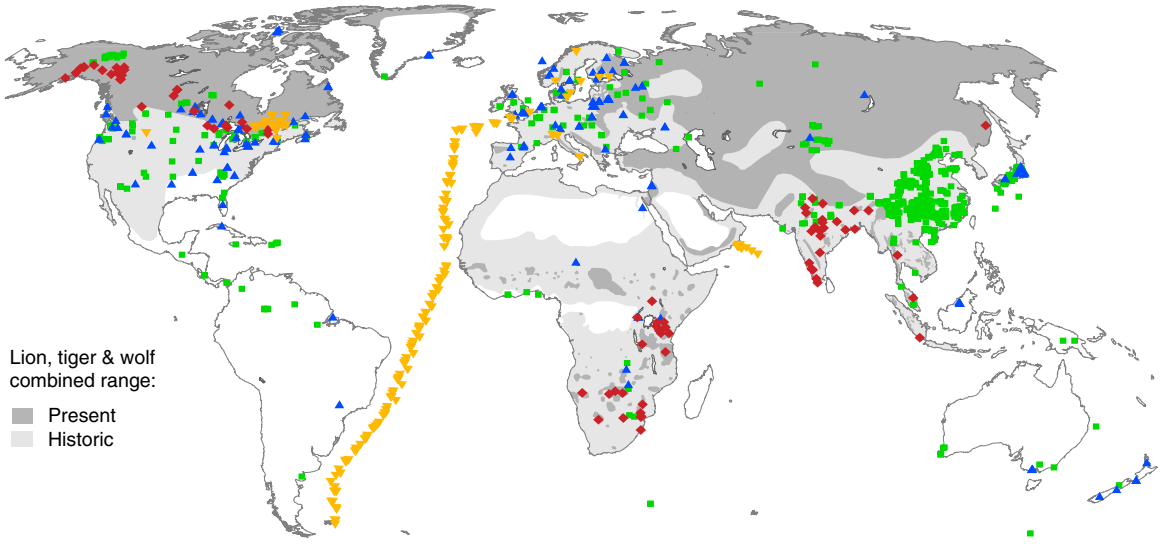
This pattern is largely robust to regression methods and is validated by independent data sources. Previous cross-system studies have reported exponents fit by ordinary least squares (*10*, *19*–*21*, *29*–*42*). As far as we can determine, this is the least biased regression method for the data that we report (section M1D). Although least squares exponents are increasingly underestimated with increasing error, alternative methods (e.g., type II) tend to overestimate the exponent (section M1D) and yet are also sublinear ($k < 1$) for all plots, except where data are highly dispersed [Fig. 5, F, G, and L; $R^2 < 0.5$; k near 1; section M3; (*65*)]. Nonetheless, we cannot be certain of the exponent value, and even the best-studied ecosystem types do not extend much beyond a two order of magnitude biomass gradient, which may be insufficient to establish power law behavior. Currently available data also do not permit highly standardized community level measurements, so that different biomes may represent different levels of sampling and taxonomic resolution. Despite these limitations, however, declines in y/x versus x are highly significant for all variables in Fig. 5, A to O (all P values < 0.01). Similar scaling is also obtained for each of 25 published cross-system data sets (*9*–*30*, *66*, *67*); $k_{avg} = 0.72$; $n_{tot} = 2950$ ecosystems; section M3; table S2), providing independent validation of the pattern. Across terrestrial and aquatic ecosystems, therefore, the predator-prey ratio and per capita production decline significantly at higher biomass, both following similar scaling.

Theoretical implications

Several cross-system meta-analyses, using similar methods to our own, have shown that herbivore consumption scales near linear ($k = 1$) to primary production (*34*–*37*) (section M3Q and table S5). This implies that flux rates into and out of basal communities are roughly proportional across productivity gradients, which may be expected for systems near steady state. Together with these earlier studies (*34*–*37*), our empirical findings have implications for ecological theory.

1) Predator-prey scaling is sublinear (Fig. 5, A to H), which indicates that trophic structure is more bottom-heavy at higher biomass. At steady state, this can be expressed as $C^* = cB^{*k}$, where c is the predator-prey coefficient and $k < 1$. This equilibrium solution is at odds with common models that assume that prey production P follows logistic density dependence. These models are often classed as top-down or bottom-up control according to how Q is specified and predict more top-heavy ($k > 1$) or invariant ($k = 1$) pyramid structures with increasing biomass (*8*, *41*, *42*, *46*–*49*) (appendix S1). Classic models can be reconciled with data by introducing the production function described below (2).

2) Production-biomass scaling is sublinear (Fig. 5, I to O) and indicates that per capita growth declines at higher biomass. For prey, this can be expressed as $P = rB^k$, where r is the production coefficient and $k < 1$. This production function theoretically yields observed predator-prey scaling (Fig. 4) and implies that, in the absence of predators, prey increase if food is available, but with an ever-diminishing tendency. This is a weaker form of density dependence than logistic, but systematic and possibly scale-free. Model stability is thus found to be extensive in parameter space for different Q functions

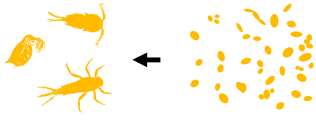


Predator-prey scaling



- Top-carnivore biomass vs total herbivore prey biomass

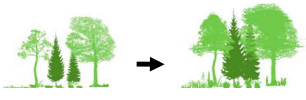
***k* = 0.74** (0.68, 0.81), *n* = 184



- Zooplankton biomass vs total algal community biomass

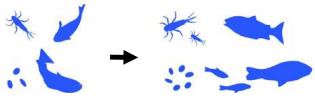
***k* = 0.71** (0.65, 0.76), *n* = 667

Production-biomass scaling



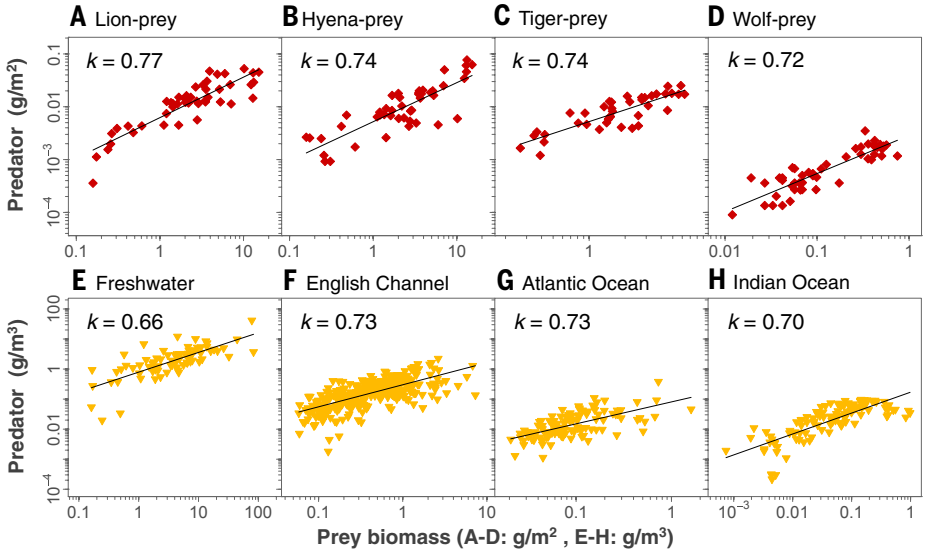
- Plant community production vs total foliage biomass

***k* = 0.67** (0.64, 0.71), *n* = 1153



- Aquatic trophic community production vs total biomass

***k* = 0.76** (0.68, 0.83), *n* = 256



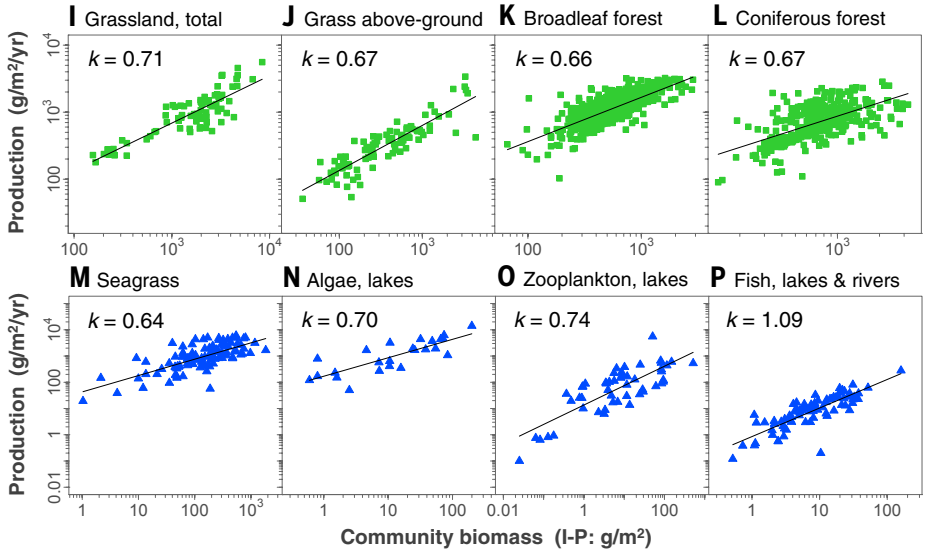


Fig. 5. Similar scaling links trophic structure and production. Each point is an ecosystem at a period in time (n = 2260 total from 1512 locations) along a biomass gradient. (**A** to **P**) An exponent k in bold (with 95% CI) is the least squares slope fit to all points n in each row of plots. Further details are in section M3 and table S1.

(see supplementary text), suggesting that this growth pattern may help to balance trophic interactions across large-scale gradients.

3) The similarity of predator-prey (item 1) and production-biomass (item 2) scaling implies a broadly conserved link between these structural and functional variables. Although our model (Fig. 4) is only a phenomenological description of trophic dynamics, it may provide a first approximation for the link between these two power law coefficients ($c = rg/m$), allowing variables in Fig. 5 to be reformulated in terms of one another for more extensive predictions (e.g., appendix S2). Theory and data thus point to a general community growth pattern that shapes trophic structure in terrestrial and aquatic systems.

But where does this growth pattern originate? Although we cannot be certain of the exponent value, ecosystem-level scaling is often near $k = ¾$ and evokes a link to individual-level body mass allometry. Many vital characteristics of an individual scale with body mass near $k = ¾$ (*68*), including metabolism (*5*, *6*), production (*69*–*72*), and consumption (*9*, *52*, *57*). This means that, as a body enlarges within a species or across taxa, these rates decline on a per mass basis. Near ¾ body mass exponents appear to be physiologically linked and are widely thought to be energetically constrained (*5*–*7*, *71*–*76*). Here, however, we are considering aggregations of many individuals across separate ecosystems, and so it is not clear how the same energetic constraints would apply. Unlike the similarity between predator-prey and production-biomass scaling, which has some theoretical basis (implication 3, above), the similarity between ecosystem and individual scaling does not.

Links to lower levels

Community production and biomass represents the total individual production and total body mass summed over all individuals within the community, and so we consider the individual production allometry. From microscopic algae up to elephant, maximum individual production exhibits highly robust near ¾ scaling with body mass (Fig. 6 and section M4) (*5*, *6*, *68*–*76*). Individual and community production scaling are thus notably similar, and although there are important exceptions, such as for individual protists (*77*), this parallel tends to hold across major taxa (Fig. 7) (tables S1 to S3). But maximum individual growth is not the actual individual growth within a community, and so this apparent similarity may be misleading.

Deductions from size structure

To connect ecosystem- to individual-level processes, we examine community size structure (Fig. 8) and specifically mean body mass versus total biomass (*52*) (section M5). As in African ecosystems (Fig. 3B), we find that size structure shows few systematic changes across large mammal and forest biomass gradients (Fig. 8, A to C) (*13*–*16*, *26*, *27*). In contrast, at higher aquatic biomass, mean size increases in plankton communities, especially among algae (Fig. 8, D to F) (*22*, *31*, *32*, *52*). For biomass scaling to be the direct result of body mass allometry, we expect mean body mass to scale with biomass near $k = 1$. Changes in plankton size structure, therefore, are not sufficient to account for changes in trophic structure or per capita productivity. We can thus deduce the following (which only partly holds for plankton communities).

1) Ecosystem and individual near ¾ exponents appear to arise independent of changes in size structure. Mean body mass is poorly correlated to community biomass, indicating that their mass exponents are not directly related.

2) Increases in community biomass along a biomass gradient are largely due to increases in population density. Increases in biomass may also be due to increases in diversity but are never solely due to changes in body size.

3) Per capita declines in community production are largely due to density-dependent declines in individual productivity from their maximum potential, shown in Fig. 6.

Size structure thus suggests that the scaling of individual maximum production is independent from that of community production. Instead, individual production appears to systematically decline from its maximum (Fig. 6), with increases in the density of the community in which it resides. We therefore expect to observe maximum individual production only at very low densities, where we can make predictions for community production from individual data. At higher densities, however, community production will likely be overestimated unless density dependent declines in individual production are accounted for. Assuming a biomass exponent

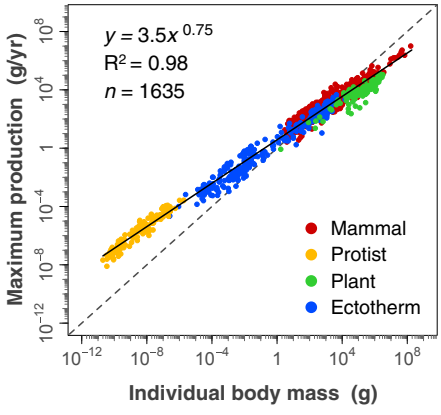


Fig. 6. Individual production to body mass exhibits near ¾ scaling across taxa. Maximum individual production includes somatic growth and offspring production. Each point is an individual, representing 1098 species over 127 taxonomic orders. Further details are in section M4 and table S3.

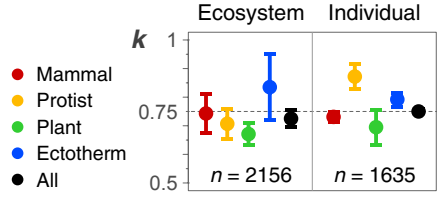


Fig. 7. Ecosystem and individual growth patterns are similar. Least squares exponents k (and 95% CI) for production-mass across ecosystems (from Fig. 5) and individuals (from Fig. 6) are often near $k = ¾$. Each exponent estimate is for $n > 100$ data points. Seagrass data ($n = 104$; Fig. 5M) were excluded. Further details are in section M4.

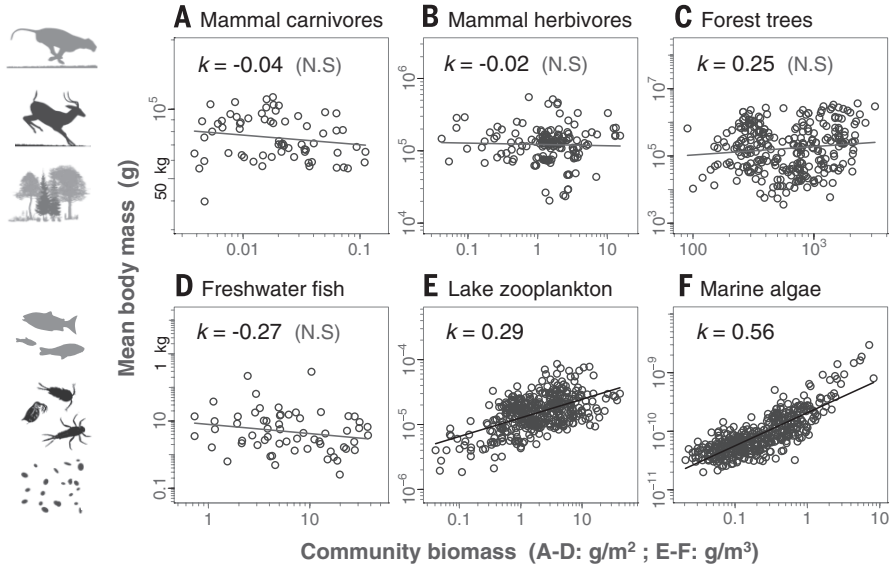


Fig. 8. Mean body mass is poorly correlated to community biomass except in plankton. Points are mostly the same as those in Fig. 5. Mean body mass averages over all individuals in a community. The slopes k in (**A**) to (**D**) are not significant (N.S; all $R^2 < 0.05$), but plankton size structure varies positively with biomass (**E** and **F**). Mammal systems (A and B) include data from Fig. 3B. Further details are in section M5 and table S4.

near k = ¾ allows community-level predictions from individual-level data across a biomass gradient (appendix S2).

Outlook

Size-structure suggests unique emergence of growth scaling at the community and individual levels, and, although we can make high-level predictions from lower-level function, we do not know why growth patterns at different levels are so markedly similar. Models for individual growth scaling going back to the well-known Bertalanffy model assume a dependence on metabolic scaling (*73*–*76*). Although our model for prey community growth (Fig. 4) resembles these ontogenetic growth models, we cannot assume the same metabolic rationale. Community growth scaling arises over large aggregations of individuals that often change little in their size structure, which leads us to wonder not only what underpins this pattern in different ecosystems, but how might it recur across levels of organization.

Density-dependent growth has been observed over thousands of populations in diverse taxa (*78*, *79*) and is qualitatively consistent with this growth pattern. Population density is known to influence physiology, community composition, and competition for space. Density-dependent factors can alter reproductive behavior, life history, and metabolism (*80*, *81*); promote self-shading and self-thinning (*82*, *83*); cause changes in size structure and nutritional quality (*36*–*41*, *84*–*86*); and trigger interference and territorial aggression (*87*, *88*). What is not known is whether these factors can account for observed scaling exponents, and whether these different factors may have similar effects when aggregated across whole communities. The generality of community-level scaling suggests a process that operates in regular ways and independently of system details. A theory for growth-mass scaling encompassing both individual and ecosystem levels would efficiently unite basic aspects of physiology and ecology.

Conclusion

Ecosystems exhibit emergent regularities in trophic structure and production dynamics across terrestrial and aquatic biomes of the world (Fig. 5). The predator-prey ratio and per capita community production both significantly decline at higher biomass. Both of these relations follow similar power law scaling, which suggests a conserved link between ecosystem structure and function across diverse systems. Often these patterns are highly regular (e.g., Fig. 1), implying a greater degree of ecosystem-level organization than previously recognized and raising questions about the processes that regulate abundance in ecological communities. We show how sublinear growth scaling tends to stabilize predator-prey interactions (supplementary text), but further work is needed to understand how specific factors operate in different systems.

Perhaps the most intriguing aspect of these findings is that community and individual growth patterns both follow near ¾ scaling laws (Fig. 7). Community growth scaling emerges over large numbers of individuals and size structure is often near constant, indicating that similar growth dynamics at the community and individual levels arise independently (Fig. 8). This may point to basic processes that reemerge across systems and levels of organization.

Materials and methods

A description of our empirical approach and data (Figs. 1 to 5) is outlined below (sections M1 to M5). Materials and methods are supplemented with regression tables S1 to S5 and appendices S1 and S2 (supplementary materials file), as well as raw data and original sources in the data file (database S1), and are available at *Science* Online.

M1. Empirical approach

A. Criteria for inclusion in the database

This study focuses on how ecological structure and dynamics change across ecosystems made of similar species assemblages. This requires data gathered consistently by different studies across large-scale biomass gradients. We focused on relatively distinct trophic communities, rather than ecosystems with more complex feeding relationships. This restricted the kinds of ecosystems that could be considered to currently available data on large mammals, plants, and basal aquatic communities.

All data were sourced from peer-reviewed publications and met the following criteria: (i) Ecosystems were relatively free of human influence or disturbance and were thus representative of natural conditions. (ii) Ecosystems were surveyed over a much larger area than the largest animal home range, so that density estimates were not biased because of local aggregation. (iii) Communities comprised the majority of dominant species and were thus representative of whole trophic communities. Noted exceptions include predator communities in Southeast Asia and North America, represented by a single top-predator population (Fig. 5, C and D, tiger and wolf), and zooplankton communities in the Atlantic and the Indian Ocean, represented only by micro-zooplankton (Fig. 5, G and H). These predators are reported to be the dominant consumers of prey biomass in their respective ecosystems (*14*, *17*, *22*).

B. Conversion of raw data into standard units

Many of the meta-analyses that were combined for this study reported data in different units. Conversion into standard units required particular care, especially among aquatic systems, where mass variables may be reported in fresh or dry mass (picograms to tons) and density may be reported in areal or volumetric units. We avoided changing density dimensions (e.g., area to volume) in all but one case (one of four meta-analyses used in Fig. 5E), where the authors made clear how the data were estimated and provided mean lake depth, allowing conversion of mass per unit area into mass per unit volume (*18*).

Biomass density was converted to kg/km^2 for Figs. 1 and 3 and to g/m^2 or g/m^3 for Figs. 5 and 8. Changing units for all data in a plot in a consistent way has no effect on the scaling exponent but will alter the coefficient. However, the use of different conversion factors for different meta-analyses combined in the same plot can affect both the exponent and the coefficient. For example, each of Fig. 5, E, I, and J, combines multiple meta-analyses, some of which are reported in fresh mass, whereas others are in dry mass. We used conversion factors reported in the original studies to normalize data to a consistent set of units. Where conversion factors were not reported, we converted all dry mass or mass of carbon to fresh mass by multiplying by a factor of 10 (*68*). In these instances, we tested whether each meta-analysis yielded similar exponents in isolation; all of them were found to be within 0.1 of exponents from combined meta-analyses. Exponents reported in Fig. 5 are thus representative of the individual studies they comprise (table S2).

C. Methods for estimating biomass and production

Community biomass is the total mass density summed over all individuals in a given trophic level community (e.g., g/m^2). Production is the total increase in biomass per unit time (e.g., g/m^2 per year), in the absence of consumption, which has the same units. Methods for estimating community biomass and production are not equivalent across ecosystem types, nor are they always equivalent across biomass gradients of similar species (Fig. 5). The same is true for body mass and individual production across the size spectrum (Fig. 6). Details of methods can be found in the original studies and summarized in the relevant places cited in database S1. A summary of methods for biomass and production measurements at the ecosystem level can be found in Cebrian and Lartigue (*37*) and at the individual level in Ernest *et al.* (*71*).

Despite attempts of different studies to estimate the same variables in standardized convertible units, combining data obtained through very different methods can cause inaccuracies in the scaling exponent. This is particularly true if there are any systematic biases across a biomass gradient. Many inaccuracies will likely be relatively small compared with the near two orders of magnitude over which many relations extend. Nonetheless, this was an important consideration for treating ecosystem types separately, where the most substantial divergences in methodology exist.

D. Regression method

Ordinary least squares (OLS) was used for all fits to log-transformed data, consistent with a number of other published cross-ecosystem meta-analyses (*10*, *19*–*21*, *29*–*42*). However, there is ongoing debate about which regression methods are least biased depending on the distribution of error between x- and y-axis variables (*65*, *89*–*96*). OLS (type I) is the standard

approach in fitting bivariate power laws in biology (68, 95), but it assumes all error is in the y variable and thus tends to underestimate k as error in x increases. Type II regression methods, such as reduced major axis (RMA) and major axis (MA), partition error to both axes but can overestimate k as the error in y increases relative to x (65, 91, 93–96).

We assumed OLS to be the least biased slope estimator for the specific data that we report, given the greater fraction of error associated with y-axis variables compared with x-axis variables. Mammal predators, such as lion, hyena, tiger and wolf (y axis, Fig. 5, A to D), are considerably more difficult to census than their prey (x axis) because of their often nocturnal habits and relatively low densities, which cause greater potential for estimation error (14, 60, 97, 98). Top carnivores were also enumerated as single populations that are likely compensatory with other dominant guild members. The African savanna data shown in Fig. 1 are an exception because they estimate the entire community of large predators. Here, the exponent remains nearly unchanged from OLS (k = 0.73) to MA (k = 0.75) and RMA (k = 0.76), but for individual lion and hyena to prey (Fig. 5, A and B), type II methods give exponents near k = 0.88. Similarly, zooplankton community biomass (y axis, Fig. 5, E to H) tends to be less well estimated than that of phytoplankton (x axis), because zooplankton aggregate and migrate in the water column (99). Estimating their biomass requires separate techniques for different components of the community [e.g., crustacean, rotifer, and protozoan (22, 100)], whereas phytoplankton measurements tend to converge on similar values (99, 101, 102). For the Atlantic and Indian Ocean (Fig. 5, G and H), macrozooplankton data were not available, and so the y-axis variable is also a partially incomplete community measure.

Error is thus likely greater in the y axis for predator-prey relations (Fig. 5, A to H), and the same is true for production-biomass relations (Fig. 5, I to P). As a dynamic variable, production has the additional dimension of time over standing stock biomass and should control or account for consumption and decomposition between time intervals (44). Moreover, production measurements often use a variety of techniques that can give significantly diverging values [grasslands (103), forests (104, 105), aquatic invertebrates (106)]. For data in Fig. 5, the majority of measurement error is in the y-axis variable, and therefore exponents derived from OLS are expected to provide the most robust predictions of the three regression approaches.

The precise distribution of error among axes remains difficult to ascertain. Reported k values likely underestimate the exponent, and all the more so as error increases. An RMA exponent can be estimated by dividing the OLS k value by the square root of the coefficient of determination ($\sqrt{R^2}$) (65, 91). These statistics are listed in tables S1 to S5. The vast majority of analyzed data sets exhibit sublinear biomass scaling exponents under all three methods. Exponent values obtained by using RMA and MA are discussed further in section M3.

The relations shown here are bivariate, so that much of the statistical literature on power law fitting of univariate rank-frequency distributions may be less relevant (107, 108). Each axis variable was gathered independent of the other, often using different methodologies, and so there is no possibility that the strength of these patterns is due to indirectly regressing a variable against some proxy of itself (109).

M2. African savanna data (Figs. 1 and 3)

The African savanna data set includes complete large mammal abundance estimates assembled across whole ecosystems. Most systems were censused over the entire extent of the protected area, which were only included in the database if all dominant large mammals (>5 kg) were counted. Data were checked against other published estimates, particularly for carnivore counts, where errors can most influence the fit (section M1D). On average, 22 species from a pool of 40 were estimated in each system, for a total of 1000 large mammal abundance estimates drawn from 190 published sources (Fig. 3A).

A. African ecosystem attributes

The distribution of African protected areas span the savanna rainfall gradient, from Kalahari desert to Ngorongoro Crater (Fig. 9). The relationship of log rainfall to log herbivore biomass has been shown to yield significant slopes between k = 1.5 and 2.0 (10, 110, 111). Our data include a large proportion of ecosystems where other sources of water dominate, which obscures the rainfall-to-herbivore relationship [Lake Manyara National Park (NP), Tarangire NP, the Okavango Delta, Amboseli NP, and the area around Sabie River in Kruger]. The 23 analyzed regions range in area from 100 to 40,000 km^2, totaling more than 150,000 km^2, over which census counts were made. Protected area map boundaries are from (112), and lion range from (113).

The relation of mammal abundance to body mass is highly variable across and within African protected areas (Fig. 3A). Mammal population density has previously been shown to scale with body mass by a negative exponent between k = −1 to −½ [also known as Damuth's law, or size-density scaling (5, 56, 68, 114)]. This size-density scaling relation extends over six orders of magnitude in body mass and also reveals that individuals of all size classes typically range in density over about three orders of magnitude. This high residual variation results in insignificant size-density correlations over a limited range in body size, as in Fig. 3A, even compensating for possible undercounting smaller animals [e.g., a factor of 10; page 91 of (115)].

Populations in Fig. 3A were aggregated into their respective ecosystems to study the size structure of each trophic community across different ecosystems. Mean body mass is described further below, in section M5. The histograms in Fig. 3B show the frequency of different size classes, averaged for the six systems with lowest and highest prey biomass. The four herbivore size classes are 5 to 20, 20 to 50, 50 to 200, and 200 to 500 kg. The three carnivore size classes are the three smallest carnivores combined (wild dog, leopard, and cheetah; 20 to 40 kg), hyena (50 kg), and lion (125 kg). The slight change in some herbivore size classes is small relative to the changes in trophic structure shown in Figs. 1 and 3C.

The predator-prey biomass scaling pattern shown in Fig. 1 and their ratio in Fig. 3C includes the five dominant African carnivores (lion, spotted hyena, leopard, cheetah, and wild dog), which compete for prey ranging from 5 to 500 kg (50, 51). In the Savuti region of Chobe NP, mega-herbivores (>750 kg) are frequently preyed upon by lions in the dry season (116) and were included as prey in this ecosystem (Fig. 9). We excluded the migrant population biomass of wildebeest, zebra, and gazelle in regions such as the Serengeti ecosystem and Masai Mara GR, which are known to largely escape predators, but nonetheless provide important prey subsidies to carnivores (117). Excluding migrant biomass, Serengeti and Masai Mara become the largest outliers above the best fit line (Fig. 9), possibly because of the exclusion of these subsidies. The largest outlier below the line is in Katavi NP (Fig. 9), where previous research has also reported relatively few predators (118).

B. Robustness of the African predator-prey pattern

The African predator-prey pattern appears to be robust to the following: (i) how ecosystems are replicated at different time periods, (ii) what species are included in predator and prey communities, (iii) variations in species body mass, (iv) possible systematic bias in sampling, and (v) alternative regression approaches. These considerations are elaborated further below.

1) Predator and prey biomass were fit to 23 protected areas, some of which were sampled in different decades for a total of n = 46 ecosystem time periods. Replicate time periods are averaged in Fig. 9 (and Fig. 10A) to give equal weighting to each area. Tarangire NP is the only system not averaged given large biomass fluctuations between wet and dry seasons in 1962 and 2000. The resultant fit is very similar to Fig. 1 (k = 0.75; n = 25 protected ecosystems R^2 = 0.93), suggesting there are no biases from possible pseudoreplication.

2) The pattern holds under alternative assumptions about the breadth of the prey community. We excluded mega-herbivores from the prey community, although carnivores will consume juveniles and carcasses of mega-herbivores, such as giraffe and elephant. Including mega-herbivores as prey in all ecosystems slightly reduces the exponent and goodness of fit but is otherwise quite similar (k = 0.66; R^2 = 0.65; Fig. 10C).

3) The pattern is robust to variations in species body mass. Given that community composition is largely invariant across the prey biomass gradient (Fig. 3B), the sublinear scaling evident between total predator and prey biomass is also evident for numerical density (Fig. 10B; k = 0.63; R^2 = 0.86) and implies that the pattern is largely robust to

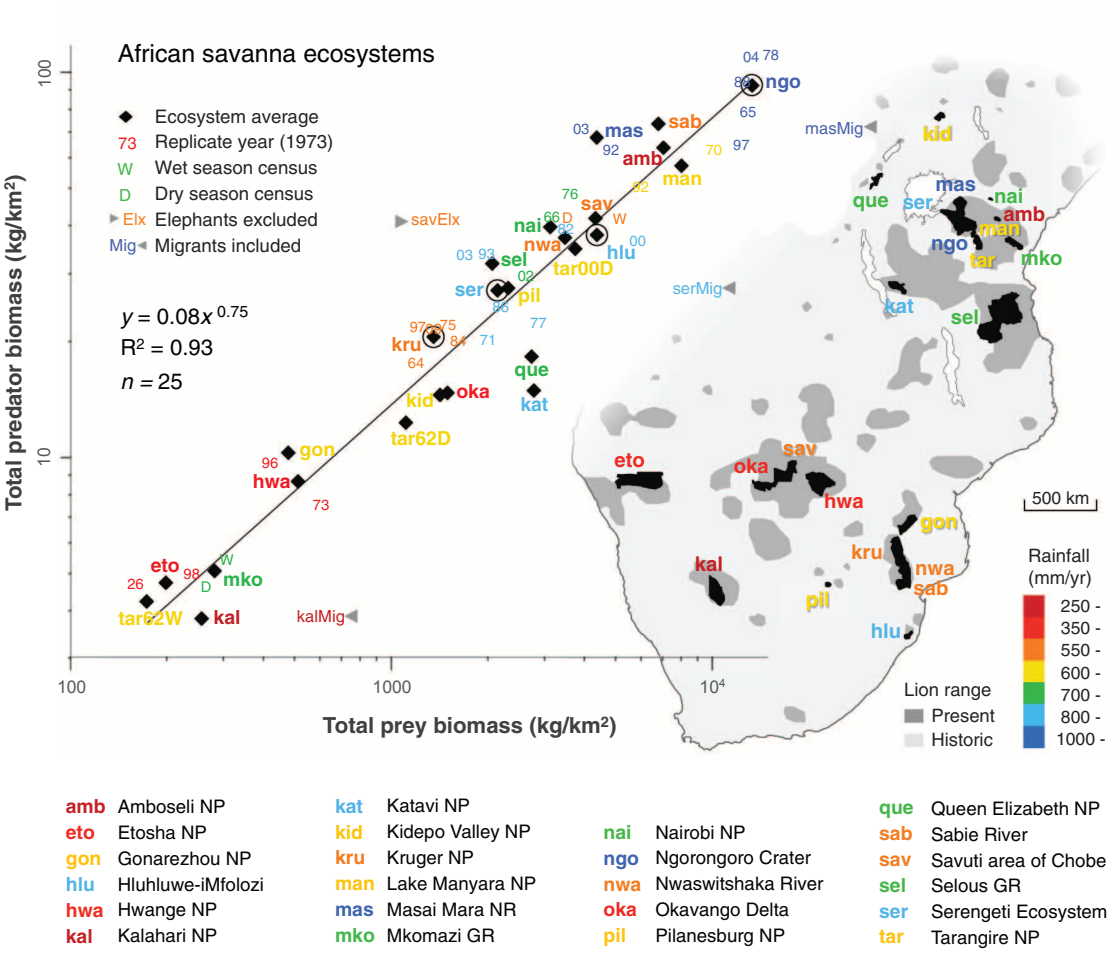


Fig. 9. African savanna ecosystem characteristics. These data are shown in Fig. 1, but here abundance in different time periods are averaged to give equal weight to each protected area (k = 0.75 ; 95% CI = 0.66, 0.83; n = 23). We excluded migrant biomass in Serengeti and Masai Mara, which include the largest three outliers above the line (ser and mas). Mega-herbivores were excluded as prey in all but the Savuti region of Chobe NP (sav), where lions prey on elephants (*116*). When excluded from Savuti, the point becomes a notable outlier (savElx). The largest outlier below the line is Katavi NP (kat), where previous research has reported relatively few predators (*118*). Tarangire (tar) is not averaged due to large biomass fluctuations. Black circles are the ecosystems in which time series data are shown in Fig. 10D.

assumptions about species body mass. Systematic changes in average species body mass exhibited by some mammals across ecosystems are never more than a factor of two and thus not sufficient to account for these sublinear scaling patterns.

4) Although it is possible that there are systematic biases of sampling one or both trophic groups at high or low densities, this seems unlikely. The linear prediction of Carbone and Gittleman (*53*) is shown by the dotted line in Fig. 1 and Fig. 3C, which predicts that 111 kg of prey are needed for every 1 kg of predator. The ecosystems that most distinguish the predator-prey scaling relation from this prediction lie at the far left of the regression. Among these, five whole-ecosystem censuses of all predators and prey were estimated by the same authors: Hwange (*119*), Mkomazi wet and dry season (*120*), Tarangire wet season (*121*), and Kalahari (*122*). This suggests that similar censusing methods were applied to both predators and prey communities and that the deviation from a linear prediction is unlikely a result of bias. More generally, at least four independent meta-analyses of a similar nature have been conducted across African ecosystems, all of which yield similar sublinear patterns (*9*–*12*) (k ranges 0.67 to 0.80; Fig. 11A and table S2.1-4).

5) Last, the scaling pattern is robust to alternative regression methods such as type II, which yield exponents well within the confidence interval (CI) of the least squares fit (95% CI = 0.66 to 0.79; major axis k = 0.75 and reduced major axis k = 0.76; see section M1D).

C. Population compensation in space and time

African mammal populations appear to be compensatory in space and time, which allows greater regularity to emerge among whole communities than among individual populations. For example, the community-level predator-prey pattern shown in Fig. 1 is not evident because fewer species are aggregated into the community. Although the relations of lion and hyena to total prey biomass give robust scaling patterns, they exhibit greater dispersion (Fig. 5A, R^2 = 0.77, and Fig. 5B, R^2 = 0.69) than the whole predator community pattern (Fig. 1, R^2=0.92). In ecosystems where lion are above the line, hyena tend to be below, and vice versa (Fig. 5, A and B). Given this compensation among predator populations, higher R^2 is obtained when lion and hyena are summed together and highest by further aggregating the large carnivore biomass of leopard, cheetah, and wild dog populations, all of which compete for similar prey (*50*, *51*).

Prey populations are also compensatory relative to predators. When fewer populations are included in the prey community, the predator-prey pattern exhibits greater dispersion, so that even dominant populations, such as lion versus zebra or hyena versus impala, exhibit little or no pattern (all R^2 < 0.4 for population-level predator-prey relations). Prey also exhibit compensation within any given ecosystem in time. Population biomass time series for lion and the six most dominant African prey species were assembled across four large protected areas (Kruger NP, Hluhluwe-iMfolozi NP, Serengeti ecosystem, and Ngorongoro Crater; Fig. 10D). In nearly all cases the coefficient of variation (standard deviation divided by mean) is lower, indicating less fluctuation, for total prey community biomass than it is for the populations it comprises. This implies that populations are compensatory in time (Fig. 10D), which is consistent with the emergence of the predator-prey pattern at the ecosystem-level.

M3. Global community data (Fig. 5)

Community-level data aggregate many thousands of population counts across 2260 ecosystems globally and are drawn from over 850 published sources, some of which include meta-analyses of additional studies. Units were converted to g/m^2 for all terrestrial biomass data (Fig. 5, A to D and I to L). Aquatic predator-prey data (Fig. 5, E to H) were originally reported in various volumetric units and converted to g/m^3. All production-biomass data, including aquatic studies (Fig. 5, I

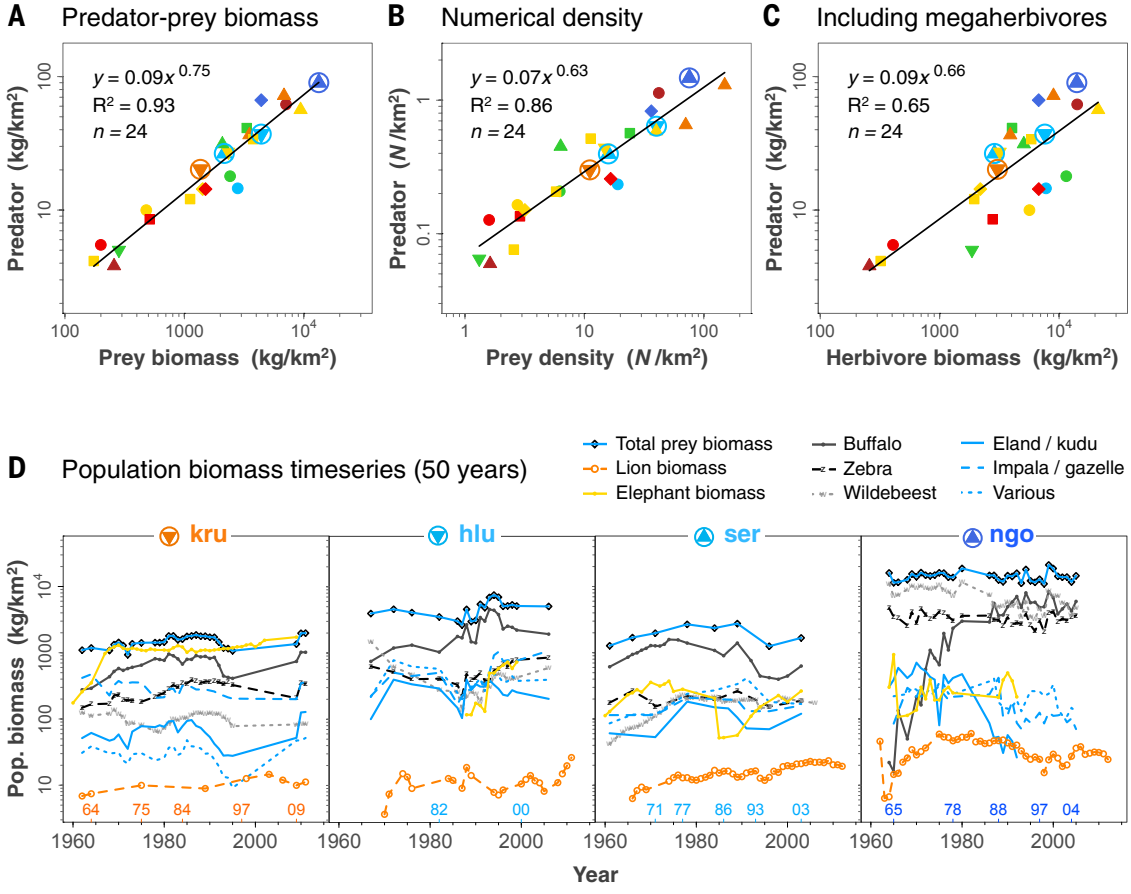


Fig. 10. African mammal biomass, numerical density relations, and population time series. (**A**) This relation duplicates Fig. 9 (colored according to rainfall) to allow comparisons to the pyramid of numbers (B) and prey biomass including megaherbivores (C). Note that Savuti is excluded and Tarangire is not averaged for reasons outlined in Fig. 9. (**B**) Predator-prey total numerical density shows a similar pattern because of the near invariance of mean body mass with community biomass (Fig. 3B). The lower exponent is driven largely by two areas of Kruger NP (sab and nwa; orange triangles) with high densities of impala. The exponent for all ecosystem time periods, omitting sab and nwa, is $k = 0.70$ ($n = 42$; $R^2 = 0.90$). (**C**) Predator to total herbivore biomass, including all the prey in (A) plus all mega-herbivores (giraffe to elephant). The exponent for all ecosystem-time periods is $k = 0.70$ ($n = 44$; $R^2 = 0.67$). (**D**) Population biomass time series for dominant species in each of four protected areas with complete ecosystem censuses. Replicate years used in Fig. 1 are labeled in color and chosen on the basis of available census data for all species. Total prey biomass has a consistently lower coefficient of variation (standard deviation divided by mean; CV) than the population biomass it comprises for all but two populations in Serengeti (ser), where data are sparse. The CV for total prey biomass is as follows (with min. and max. CV for the six dominant herbivore populations): kru—0.196 (0.20, 0.40); hlu—0.29 (0.32, 0.69); ser—0.30 (0.20, 0.53); ngo—0.16 (0.19, 0.73).

to P), were originally reported in areal units and converted to g/m^2 (section M1B). The principal meta-analyses contributing to the data in Fig. 5 are summarized in Fig. 11 and tables S1 and S2.

We used OLS for all fits to data, which are believed to provide the least biased predictions of available methods (see section M1D). We considered two alternative regression methods to fit the data in Fig. 5, using the 'smatr' library package in R (*123*): RMA and MA. Excluding fish (Fig. 5P) for the reasons stated in section M3P, type II regression approaches (RMA and MA) yield sublinear exponents for all plots in Fig. 5, except where data are highly dispersed ($R^2 < 0.5$, k near 1; Fig. 5, F, G and L). The same is also true for published cross-system meta-analyses summarized in Fig. 11 and table S2.

Predator-prey scaling (Fig. 5 A to H)

A and B. Lion and hyena to prey

Data are shown aggregated with other predators in Figs. 1 and 3 (see also Fig. 9). These data derive from 190 publications and are described further in section M2. Four meta-analyses reveal sublinear scaling in isolation [Farlow (*9*), East (*10*), Hemson (*11*), and Grange and Duncan (*12*): k ranges 0.66 to 0.80; Fig. 11A and table S2.1-4]

C. Tiger to prey

Data are from averages of 829 large mammal population censuses in India from Project Tiger combined with 22 other studies undertaken throughout Southeast Asia. Three of these studies are large-scale meta-analyses that each reveals sublinear scaling in isolation [Project Tiger (*13*), Karanth *et al.* (*14*), and Kawanishi and Sunquist (*15*): k ranges 0.62 to 0.79; Fig. 11B and table S2.5-7].

D. Wolf to prey

Data are from two meta-analyses: Fuller (*16*) and Messier (*17*). Messier lists only moose as prey, claiming they represent at least 75% of all prey in the ecosystems studied. Six sites with reported heavy wolf exploitation were removed. Both studies alone each reveal sublinear scaling (k ranges 0.72 to 0.87; Fig. 11C; table S2.8-9).

E. Freshwater zooplankton to algae

Data are from four meta-analyses: Cyr and Peters (*18*) (average estimates from the International Biological Program, converted from areal to volumetric units on the basis of reported mean lake depth); McCauley and Kalff (*19*) (averages of 207 plankton community estimates); del Giorgio and Gasol (*20*); and del Giorgio *et al.* (*21*). All studies reveal sublinear scaling in isolation (k ranges 0.64 to 0.72; Fig. 11, D and E, and table S2.10-14).

F to H. Marine zooplankton to algae

Data are from Irigoien *et al.* (*22*). English Channel (F) data include multiple stations at various time periods, which estimate total zooplankton and phytoplankton community biomass. Atlantic (G) and Indian (H) ocean data include only microzooplankton, which the authors claim are the main consumers of algae in oceans. One extreme Atlantic point is removed ($k = 0.67$ with point included). When all microzooplankton to algae are combined across Atlantic, Indian, and a number of other marine areas ($n = 547$), the exponent k equals 0.54 (Fig. 11F and table S2.15).

Production-biomass scaling (Fig. 5, I to P)

I. and J. Grassland P-B

Data are from six meta-analyses from the International Biological Program, notably Coupland (*23*), Sims *et al.* (*24*), and Sims and Singh (*25*).

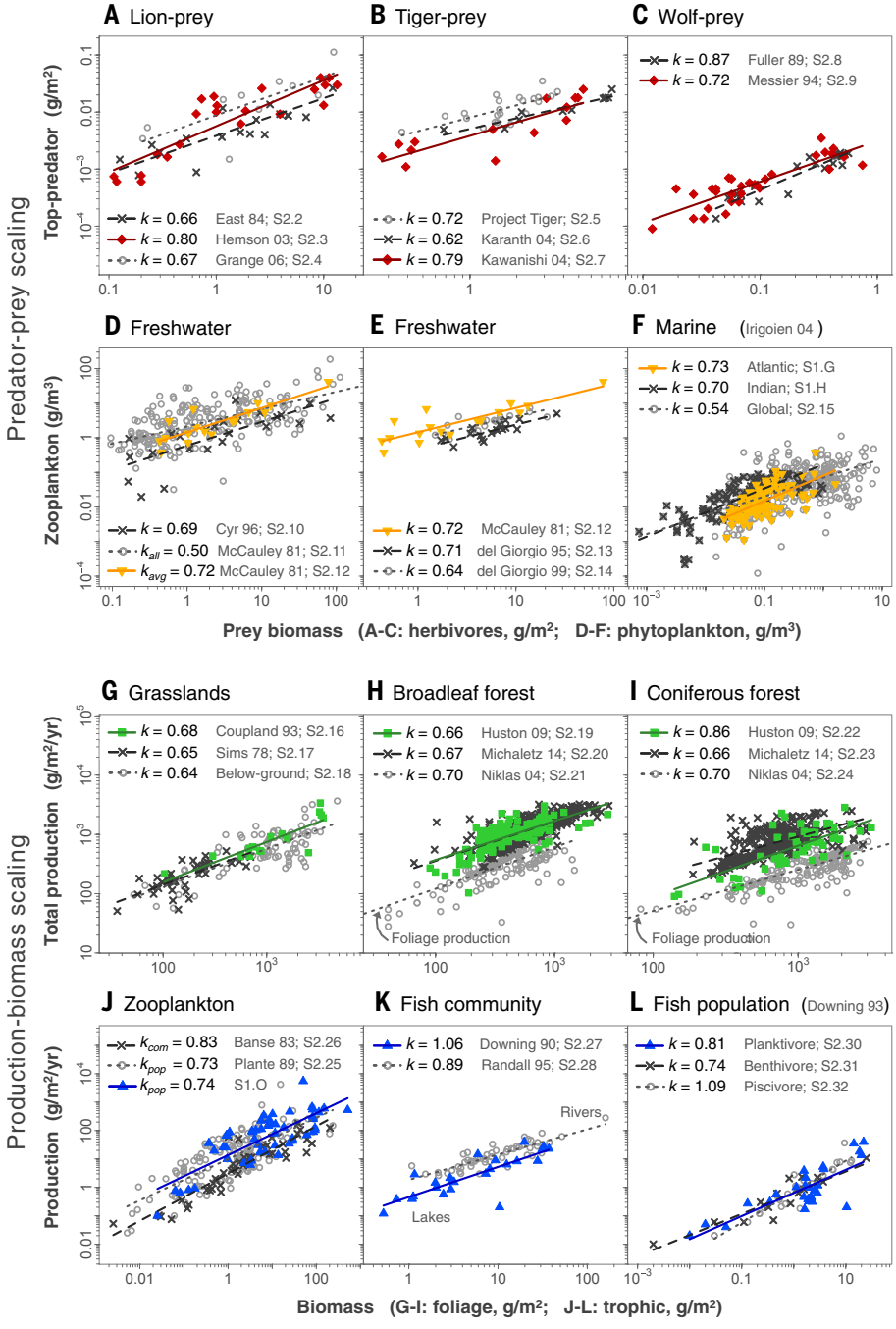


Fig. 11. Published cross-system meta-analyses contributing to regressions in Fig. 5. (**A** to **L**) These plots each derive from a single source and show similar scaling to combined plots in Fig. 5 (table S2).

These three studies yield sublinear scaling in isolation for both total and above-ground *P-B* [(*23*–*25*); k ranges 0.64 to 0.68; Fig. 11G and table S2.16-18].

K and L. Forest P-B

Total production to foliage biomass data are from two large meta-analyses: Huston and Wolverton (*26*), which includes global data digitized from Cannell (*27*), and Michaletz *et al.* (*28*), with sites mostly in China, most of which derive from Luo (*124*), described in Ni *et al.* (*125*). Foliage biomass (x axis) excludes all stem, branch, and root material, representing the most photosynthetically active biomass, whereas total production includes all forest growth. Similar exponent values are obtained for foliage production to foliage biomass from the Niklas and Enquist data set (*66*), which is also from Cannell (*27*). We removed all sites with reported growing seasons less than 6 months in order to better compare annual production across sites. Relaxing this assumption has no effect on exponent values for forests from Cannell (*27*) but lowers exponents for needleleaf sites from Michaletz *et al.* (*28*). One extreme point was removed from each of broadleaf and coniferous forests, as noted in the data set. All three studies reveal sublinear scaling in isolation [(*26*, *28*, *66*); k ranges 0.66 to 0.86; Fig. 11, H to I, and table S2.19-24].

M. Seagrass bed P-B

Data were digitized from Duarte and Chiscano (*29*), authors' figure 2. Original data and geocoordinates are not available. These data are not mapped in Fig. 5 and are excluded from Fig. 7. Original statistics are reproduced from authors' page 170.

N. Algae P-B

Data from International Biological Program were compiled and averaged in Cyr and Peters (*18*). These data are for 24 of the same lakes as in Fig. 5E, providing one of the few direct comparisons between predator-prey and production-biomass scaling across the same ecosystems.

O. Zooplankton P-B

Data were from Plante and Downing (*30*). These data were originally reported at the population level but were aggregated into community measures in Fig. 5O. The authors reported a similar production-biomass exponent at the population level (k = 0.73; n = 164 populations; table S2.25). A somewhat higher exponent (k = 0.83; n = 43 populations) is reported for invertebrate population production-biomass by Banse and Mosher (*67*) (Fig. 11J and table S2.26).

P. Fish P-B

Data from two meta-analyses of Downing and Plante [(*31*); lakes; n = 25] and Randall [(*32*); rivers; n = 51]. Each study reveals similar scaling in isolation (k ranges 0.89 to 1.06; Fig. 11K and table S2.27-28). The fish community is composed of multiple trophic groups, and it is possible that lower trophic levels exhibit sublinear scaling. The meta-analysis of Downing and Plante (*33*) is at the population level for lake fish and shows that benthivores and planktivores scale as k = 0.74 and k = 0.81, whereas piscivores scale as k = 1.09 (Fig. 11L and table S2.29-32). The near-linear (k = 1) scaling of the higher level piscivores may be dominating the whole fish community relation shown in Fig. 5P.

Flux of primary production (Fig. 12)

Q. Consumption and primary production

In both terrestrial and aquatic systems globally, herbivore consumption and decomposition have been shown to scale near linearly (k near 1) with primary production (*36*, *37*). This suggests that there are no systematic changes in the proportion of primary production transferred to herbivores or decomposers as production increases. Data from these meta-analyses are reproduced in Fig. 12; regressions are summarized in table S5 and are broadly similar to the original analyses by Cebrian (*36*, *37*). Scaling exponents tend to

range from near k = 0.9 to just above 1 for consumption (n = 247) and near 1 or slightly above for decomposition (n = 232 ecosystems). However, terrestrial herbivore biomass to primary production tends to be closer to k = 1.2 or 1.3, which is not fully understood and is hindered by data limitations. Linear consumption and decomposition scaling with primary production is consistent with the link between trophic structure and production. It implies a general steady state, whereby production into the plant community is matched by similar ratios of consumption out of the community.

M4. Individual production data (Figs. 6 and 7)

At the individual level, a great variety of vital rates scale with body mass near k = ¾ (*5*, *68*). Individual maximum whole-organism annual production to adult body mass is notable for exhibiting k = ¾ across all eukaryotes without large discrete shifts between major taxa, as there are, for example, among metabolic allometries across this same size spectrum (*69*, *126*). Whole-organism production is measured differently for different species but seeks to estimate the total biomass added in a standard unit of time that can be attributed to a single individual. This combines both somatic and reproductive growth, as detailed in Ernest *et al.* (*71*) for different taxa. Figure 6 excludes prokaryotes and birds, because these taxa are not represented at the ecosystem level in Fig. 5.

The individual production allometry (n = 1635 estimates from 1098 species) derives from 362 published sources and principally from the following meta-analyses: multiple taxa—Ernest *et al.* (*71*) and Savage *et al.* (*127*); mammals—Duncan *et al.* (*128*), Fagan *et al.* (*129*), and Pereira and Daily (*130*); protists—DeLong *et al.* (*77*); land plants—Niklas and Enquist (*66*), after Cannell (*27*); ectotherms—Plante and Downing (*30*), invertebrates, and Downing and Plante (*31*), fish. Regressions of the full data set (n = 1705 estimates; 1283 species spanning 146 taxonomic orders and 276 families) reveal equivalent scaling across 21 orders of magnitude (table S3.1-3). Regression statistics at more detailed taxonomic resolution are shown in table S3. Bacteria appear to have steeper scaling (k > 1) than other taxa (*77*). Note that exponents for prokaryotes and protists are OLS derived and thus differ from RMA-derived slopes reported in DeLong *et al.* (*77*).

Figure 7 compares production-mass exponents at the ecosystem level (Fig. 5) with the individual level (Fig. 6). Ecosystem-level exponents were obtained by fitting a single slope and multiple categorical variables (one for each plot) to the relevant data in Fig. 5. Each colored taxonomic group for the individual data in Fig. 6 was fit to a single slope. Data at the ecosystem level (Fig. 5) and individual level (Fig. 6) are as follows: mammal—Fig. 5, A to D (n = 184 data points) and Fig. 6 in red (n = 1061); protist—Fig. 5, E to H and N (n = 691) and Fig. 6 in yellow (n = 137); plant—Fig. 5, I to L (n = 1153) and Fig. 6 in green (n = 132); ectotherm—Fig. 5, O and P (n = 127) and Fig. 6 in blue (n = 305). Seagrass beds (Fig. 5M) were excluded from the comparison because the original data are not available (section M3M) and no data for individual seagrass production and plant mass are available. We repeated this comparison only with plots with R^2 > 0.5 (thus excluding Fig. 5, F, G, and L) and found no discernible difference to the scaling exponents or confidence intervals. More detailed comparison can be made from tables S1 to S3.

M5. Mean body mass data (Fig. 8)

Community data from Fig. 5 were decomposed into population-level values to calculate mean body mass (b) plotted against community biomass (B). The plots in Fig. 8 combine ecosystems from multiple plots in Fig. 5, A to D, F to H, K to L, and O and P. Similar poor correlations between these variables are observed for distinct ecosystem types, as shown by detailed regressions in table S4. No individual size data were available for grasslands or seagrass beds (Fig. 5, I, J, and M), and so these community types are not included in Fig. 8. Mean body mass is the sum of the abundance (N) of each species (j) in a trophic community multiplied by the unit body mass for the population (b_j) and divided by the sum of all organisms in the ecosystem. This is equivalent to total biomass divided by total numerical density for a trophic community.

$$\overline{b} = \frac{\sum N_j b_j}{\sum N_j}$$

A. Large mammal carnivores

Mean body mass to carnivore community biomass combines systems from Africa (lion, spotted, hyena, leopard, cheetah, and wild dog) and Asia [tiger, leopard, striped hyena, wolf, and dhole; from Project Tiger (*13*)]. Carnivore mean body mass tends to be higher in Asia than in Africa because of the larger-bodied tigers (table S4.3-5). This plot includes data shown in Fig. 3B. Note that in Fig. 3B, African mean carnivore size is plotted against herbivore prey biomass, whereas in Fig. 8A it is plotted against carnivore biomass (and combined with Indian carnivores).

B. Large mammal herbivores

Mean body mass to herbivore biomass data combines all the African, Asian, and North American ecosystems in Fig. 5, A to D (table S4.2, 6-7). This plot includes data shown in Fig. 3B.

C. Broadleaf and coniferous forest

Body mass includes all wood, branch, and foliage mass per tree, whereas biomass includes only foliage biomass per unit area (as in Fig. 5, K and L). Mean tree size to foliage biomass combines data in Fig. 5, K and L, from Huston and Wolverton (*26*), digitized from Cannell (*27*). The number of stems per site was not available in Michaletz *et al.* (*28*), and so sites in China are not included. The lack of any systematic size structure relation is also evident in the Niklas and Enquist data set (*27*, *66*). These regressions tend to be influenced by a few extreme points, but most are not significant with low R^2 values. (table S4.8-13).

D. Fish

Mean body mass to biomass is for the same ecosystems as shown in Fig. 5P {Downing *et al.* [lakes (*31*)] and Randall [rivers (*32*)]}. The slightly negative relation is due to the combination of lake and river fish, the former of which has larger mean size and lower community biomass. None of these relations in isolation is significant (table S4.14-16).

E. Lake zooplankton (g/m^3)

Digitized from Cyr and Pace (*52*), combining authors' figure 4, A and B, each of which are

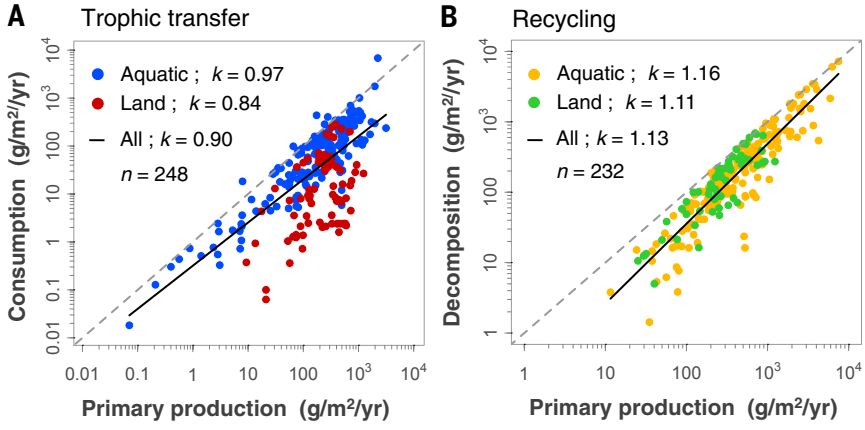


Fig. 12. A near-constant fraction of primary production is transferred to herbivores and decomposers. Data show near-linear (k = 1) scaling in the fraction of primary production (**A**) transferred to herbivore consumption and (**B**) recycled to decomposers, across global productivity gradients. This suggests few systematic changes in the ratios of flux rates. These data and regressions are reported in Cebrian and Cebrian and Lartigue (*36*, *37*), combining 196 original published sources. Further details are available in the original studies (*36*, *37*) and table S5.

also significant relations with exponents ranging from k = 0.26 to 0.41. These ecosystems are not the same as shown in Fig. 5, E or O, although there is likely overlap for lakes in Québec. Data were originally presented as zooplankton biomass on the y axis and mean body mass on the x axis, which are reversed in Fig. 8E (table S4.17-19). The data shown in Fig. 8E are approximate.

F. Marine algae (g/m^3)

Digitized from Irigoien *et al.* (*22*), authors' figure 3a. Mean algal cell size to biomass data are for the English Channel, the Atlantic, and the Indian Ocean (Fig. 5, F to H; table S4.20-24). The authors reported k = 0.44 for their global data set, which includes numerous additional sites. The data shown in Fig. 8F are approximate.

REFERENCES AND NOTES

1. S. A. Frank, The common patterns of nature. *J. Evol. Biol.* **22**, 1563–1585 (2009). doi: 10.1111/j.1420-9101.2009.01775.x; pmid: 19538344
2. P. A. Marquet *et al.*, Scaling and power-laws in ecological systems. *J. Exp. Biol.* **208**, 1749–1769 (2005). doi: 10.1242/jeb.01588; pmid: 15855405
3. J. H. Brown, B. A. Maurer, Macroecology: The division of food and space among species on continents. *Science* **243**, 1145–1150 (1989). doi: 10.1126/science.243.4895.1145; pmid: 17799895
4. S. A. Levin, The problem of pattern and scale in ecology: The Robert H. MacArthur award lecture. *Ecology* **73**, 1943–1967 (1992). doi: 10.2307/1941447
5. J. H. Brown, J. F. Gillooly, A. P. Allen, V. M. Savage, G. B. West, Toward a metabolic theory of ecology. *Ecology* **85**, 1771–1789 (2004). doi: 10.1890/03-9000
6. R. M. Sibly, J. H. Brown, A. Kodric-Brown, *Metabolic Ecology: A Scaling Approach* (Wiley, New York, 2012).
7. J. Harte, *Maximum Entropy and Ecology: A Theory of Abundance, Distribution, and Energetics* (Oxford Univ. Press, Oxford, 2011).
8. M. Loreau, *From Populations to Ecosystems: Theoretical Foundations for a New Ecological Synthesis (MPB-46)* (Princeton Univ. Press, Princeton, NJ, 2010).
9. J. O. Farlow, A consideration of the trophic dynamics of a Late Cretaceous large-dinosaur community (Oldman Formation). *Ecology* **57**, 841–857 (1976). doi: 10.2307/1941052
10. R. East, Rainfall, soil nutrient status and biomass of large African savanna mammals. *Afr. J. Ecol.* **22**, 245–270 (1984). doi: 10.1111/j.1365-2028.1984.tb00700.x
11. G. Hemson, thesis, University of Oxford, Oxford, UK (2003).
12. S. Grange, P. Duncan, Bottom-up and top-down processes in African ungulate communities: Resources and predation acting on the relative abundance of zebra and grazing bovids. *Ecography* **29**, 899–907 (2006). doi: 10.1111/j.2006.0906-7590.04684.x
13. Project Tiger Directorate, Reserve Guide: Project Tiger Reserves in India, *Project Tiger India*, projecttiger.nic.in/map.htm.
14. K. U. Karanth, J. D. Nichols, N. S. Kumar, W. A. Link, J. E. Hines, Tigers and their prey: Predicting carnivore densities from prey abundance. *Proc. Natl. Acad. Sci. U.S.A.* **101**, 4854–4858 (2004). doi: 10.1073/pnas.0306210101; pmid: 15041746
15. K. Kawanishi, M. E. Sunquist, Conservation status of tigers in a primary rainforest of Peninsular Malaysia. *Biol. Conserv.* **120**, 329–344 (2004). doi: 10.1016/j.biocon.2004.03.005
16. T. K. Fuller, Population dynamics of wolves in North-Central Minnesota. *Wildl. Monogr.* **105**, 1–41 (1989).
17. F. Messier, Ungulate population models with predation: A case study with the North American moose. *Ecology* **75**, 478–488 (1994). doi: 10.2307/1939551
18. H. Cyr, R. H. Peters, Biomass-size spectra and the prediction of fish biomass in lakes. *Can. J. Fish. Aquat. Sci.* **53**, 994–1006 (1996). doi: 10.1139/f96-033
19. E. McCauley, J. Kalff, Empirical relationships between phytoplankton and zooplankton biomass in lakes. *Can. J. Fish. Aquat. Sci.* **38**, 458–463 (1981). doi: 10.1139/f81-063
20. P. A. del Giorgio, J. M. Gasol, Biomass distribution in freshwater plankton communities. *Am. Nat.* **146**, 135–152 (1995). doi: 10.1086/285790
21. P. A. del Giorgio, J. J. Cole, N. F. Caraco, R. H. Peters, Linking planktonic biomass and metabolism to net gas fluxes in northern temperate lakes. *Ecology* **80**, 1422–1431 (1999). doi: 10.1890/0012-9658(1999)080[1422:LPBAMT]2.0.CO;2
22. X. Irigoien, J. Huisman, R. P. Harris, Global biodiversity patterns of marine phytoplankton and zooplankton. *Nature* **429**, 863–867 (2004). doi: 10.1038/nature02593; pmid: 15215862
23. R. T. Coupland, *Natural Grasslands: Eastern Hemisphere and Résumé* (Elsevier, Amsterdam, ed. 1, 1993), vol. 8B.
24. P. L. Sims, J. S. Singh, W. K. Lauenroth, The structure and function of ten Western North American grasslands: I. Abiotic and vegetational characteristics. *J. Ecol.* **66**, 251–285 (1978). doi: 10.2307/2259192
25. P. L. Sims, J. S. Singh, The structure and function of ten Western North American grasslands: III. Net primary production, turnover and efficiencies of energy capture and water use. *J. Ecol.* **66**, 573–597 (1978). doi: 10.2307/2259152
26. M. A. Huston, S. Wolverton, The global distribution of net primary production: Resolving the paradox. *Ecol. Monogr.* **79**, 343–377 (2009). doi: 10.1890/08-0588.1
27. M. G. R. Cannell, *World Forest Biomass and Primary Production Data* (Academic Press, London, 1982).
28. S. T. Michaletz, D. Cheng, A. J. Kerkhoff, B. J. Enquist, Convergence of terrestrial plant production across global climate gradients. *Nature* **512**, 39–43 (2014). pmid: 25043056
29. C. M. Duarte, C. L. Chiscano, Seagrass biomass and production: A reassessment. *Aquat. Bot.* **65**, 159–174 (1999). doi: 10.1016/S0304-3770(99)00038-8
30. C. Plante, J. A. Downing, Production of freshwater invertebrate populations in lakes. *Can. J. Fish. Aquat. Sci.* **46**, 1489–1498 (1989). doi: 10.1139/f89-191
31. J. A. Downing, C. Plante, S. Lalonde, Fish production correlated with primary productivity, not the morphoedaphic index. *Can. J. Fish. Aquat. Sci.* **47**, 1929–1936 (1990). doi: 10.1139/f90-217
32. R. G. Randall, C. K. Minns, J. R. M. Kelso, Fish production in freshwaters: Are rivers more productive than lakes? *Can. J. Fish. Aquat. Sci.* **52**, 631–643 (1995). doi: 10.1139/f95-063
33. J. A. Downing, C. Plante, Production of fish populations in lakes. *Can. J. Fish. Aquat. Sci.* **50**, 110–120 (1993). doi: 10.1139/f93-013
34. S. J. McNaughton, M. Oesterheld, D. A. Frank, K. J. Williams, Ecosystem-level patterns of primary productivity and herbivory in terrestrial habitats. *Nature* **341**, 142–144 (1989). doi: 10.1038/341142a0; pmid: 2779651
35. H. Cyr, M. L. Pace, Magnitude and patterns of herbivory in aquatic and terrestrial ecosystems. *Nature* **361**, 148–150 (1993). doi: 10.1038/361148a0
36. J. Cebrian, Patterns in the fate of production in plant communities. *Am. Nat.* **154**, 449–468 (1999). doi: 10.1086/303244; pmid: 10523491
37. J. Cebrian, J. Lartigue, Patterns of herbivory and decomposition in aquatic and terrestrial ecosystems. *Ecol. Monogr.* **74**, 237–259 (2004). doi: 10.1890/03-4019
38. J. M. Gasol, P. A. del Giorgio, C. M. Duarte, Biomass distribution in marine planktonic communities. *Limnol. Oceanogr.* **42**, 1353–1363 (1997). doi: 10.4319/lo.1997.42.6.1353
39. J. Cebrian, C. M. Duarte, The dependence of herbivory on growth rate in natural plant communities. *Funct. Ecol.* **8**, 518–525 (1994). doi: 10.2307/2390077
40. J. Cebrian *et al.*, Producer nutritional quality controls ecosystem trophic structure. *PLOS ONE* **4**, e4929 (2009). pmid: 19300514
41. M. A. Leibold, J. M. Chase, J. B. Shurin, A. L. Downing, Species turnover and the regulation of trophic structure. *Annu. Rev. Ecol. Syst.* **28**, 467–494 (1997). doi: 10.1146/annurev.ecolsys.28.1.467
42. J. M. Chase, M. A. Leibold, A. L. Downing, J. B. Shurin, The effects of productivity, herbivory, and plant species turnover in grassland food webs. *Ecology* **81**, 2485–2497 (2000). doi: 10.1890/0012-9658(2000)081[2485:TEOPHA]2.0.CO;2
43. C. S. Elton, *Animal Ecology* (Univ. of Chicago Press, Chicago, IL, 1927).
44. E. P. Odum, *Fundamentals of Ecology* (Saunders, Philadelphia, ed. 3, 1971).
45. R. Trebilco, J. K. Baum, A. K. Salomon, N. K. Dulvy, Ecosystem ecology: Size-based constraints on the pyramids of life. *Trends Ecol. Evol.* **28**, 423–431 (2013). doi: 10.1016/j.tree.2013.03.008; pmid: 23623003
46. M. L. Rosenzweig, Paradox of enrichment: Destabilization of exploitation ecosystems in ecological time. *Science* **171**, 385–387 (1971). doi: 10.1126/science.171.3969.385; pmid: 5538935
47. L. Oksanen, T. Oksanen, The logic and realism of the hypothesis of exploitation ecosystems. *Am. Nat.* **155**, 703–723 (2000). doi: 10.1086/303354; pmid: 10805639
48. K. S. McCann, *Food Webs (MPB-50)* (Princeton Univ. Press, Princeton, NJ, 2011).
49. R. Arditi, L. Ginzburg, *How Species Interact: Altering the Standard View on Trophic Ecology* (Oxford Univ. Press, Oxford, 2012).
50. A. R. E. Sinclair, S. Mduma, J. S. Brashares, Patterns of predation in a diverse predator-prey system. *Nature* **425**, 288–290 (2003). doi: 10.1038/nature01934; pmid: 13679915
51. N. Owen-Smith, M. G. L. Mills, Predator-prey size relationships in an African large-mammal food web. *J. Anim. Ecol.* **77**, 173–183 (2008). doi: 10.1111/j.1365-2656.2007.01314.x; pmid: 18177336
52. H. Cyr, M. L. Pace, Allometric theory: Extrapolations from individuals to communities. *Ecology* **74**, 1234–1245 (1993). doi: 10.2307/1940493
53. C. Carbone, J. L. Gittleman, A common rule for the scaling of carnivore density. *Science* **295**, 2273–2276 (2002). doi: 10.1126/science.1067994; pmid: 11910114
54. A. J. Lotka, *Elements of Physical Biology* (Dover, New York, 1924).
55. V. Volterra, Fluctuations in the abundance of a species considered mathematically. *Nature* **118**, 558–560 (1926). doi: 10.1038/118558a0
56. J. P. DeLong, D. A. Vasseur, A dynamic explanation of size-density scaling in carnivores. *Ecology* **93**, 470–476 (2012). doi: 10.1890/11-1138.1; pmid: 22624202
57. S. Pawar, A. I. Dell, V. M. Savage, Dimensionality of consumer search space drives trophic interaction strengths. *Nature* **486**, 485–489 (2012). pmid: 22722834
58. C. Melis *et al.*, Predation has a greater impact in less productive environments: Variation in roe deer, *Capreolus capreolus*, population density across Europe. *Glob. Ecol. Biogeogr.* **18**, 724–734 (2009). doi: 10.1111/j.1466-8238.2009.00480.x
59. G. Wang *et al.*, Density dependence in northern ungulates: Interactions with predation and resources. *Popul. Ecol.* **51**, 123–132 (2009). doi: 10.1007/s10144-008-0095-3
60. A. Treves, A. J. Plumptre, L. T. B. Hunter, J. Ziwa, Identifying a potential lion Panthera leo stronghold in Queen Elizabeth National Park, Uganda, and Parc National des Virunga, Democratic Republic of Congo. *Oryx* **43**, 60–66 (2009). doi: 10.1017/S003060530700124X
61. C. Carbone, N. Pettorelli, P. A. Stephens, The bigger they come, the harder they fall: Body size and prey abundance influence predator-prey ratios. *Biol. Lett.* **7**, 312–315 (2011). doi: 10.1098/rsbl.2010.0996; pmid: 21106569
62. B. Jedrzejewska, W. Jedrzejewski, *Predation in Vertebrate Communities: The Bialowieza Primeval Forest as a Case Study* (Springer, Berlin, 1998), vol. 135.
63. E. Jeppesen, J. Peder Jensen, M. Søndergaard, T. Lauridsen, F. Landkildehus, Trophic structure, species richness and biodiversity in Danish lakes: Changes along a phosphorus gradient. *Freshw. Biol.* **45**, 201–218 (2000). doi: 10.1046/j.1365-2427.2000.00675.x
64. Q. Dortch, T. T. Packard, Differences in biomass structure between oligotrophic and eutrophic marine ecosystems. *Deep-Sea Res. A, Oceanogr. Res. Pap.* **36**, 223–240 (1989). doi: 10.1016/0198-0149(89)90135-0
65. P. Legendre, L. F. Legendre, *Numerical Ecology* (Elsevier, Amsterdam, 2012), vol. 24.
66. K. J. Niklas, B. J. Enquist, Biomass allocation and growth data of seeded plants data set, Oak Ridge National Laboratory Distributed Active Archive Center, Oak Ridge, TN (2004), www. daac. ornl. gov.
67. K. Banse, S. Mosher, Adult body mass and annual production/ biomass relationships of field populations. *Ecol. Monogr.* **50**, 355–379 (1980). doi: 10.2307/2937256
68. R. H. Peters, *The Ecological Implications of Body Size* (Cambridge Studies in Ecology, Cambridge Univ. Press, Cambridge, ed. 1, 1983).
69. T. Fenchel, Intrinsic rate of natural increase: The relationship with body size. *Oecologia* **14**, 317–326 (1974). doi: 10.1007/BF00384576
70. T. J. Case, On the evolution and adaptive significance of postnatal growth rates in the terrestrial vertebrates. *Q. Rev. Biol.* **53**, 243–282 (1978). doi: 10.1086/410622; pmid: 362471

71. S. K. M. Ernest *et al*., Thermodynamic and metabolic effects on the scaling of production and population energy use. *Ecol. Lett.* **6**, 990–995 (2003). doi: 10.1046/j.1461-0248.2003.00526.x
72. J. M. Grady, B. J. Enquist, E. Dettweiler-Robinson, N. A. Wright, F. A. Smith, Evidence for mesothermy in dinosaurs. *Science* **344**, 1268–1272 (2014). pmid: 24926017
73. L. von Bertalanffy, Quantitative laws in metabolism and growth. *Q. Rev. Biol.* **32**, 217–231 (1957). doi: 10.1086/401873; pmid: 13485376
74. G. B. West, J. H. Brown, B. J. Enquist, A general model for ontogenetic growth. *Nature* **413**, 628–631 (2001). doi: 10.1038/35098076; pmid: 11675785
75. A. M. Makarieva, V. G. Gorshkov, B.-L. Li, Ontogenetic growth: Models and theory. *Ecol. Modell.* **176**, 15–26 (2004). doi: 10.1016/j.ecolmodel.2003.09.037
76. C. Hou *et al*., Energy uptake and allocation during ontogeny. *Science* **322**, 736–739 (2008). doi: 10.1126/science.1162302; pmid: 18974352
77. J. P. DeLong, J. G. Okie, M. E. Moses, R. M. Sibly, J. H. Brown, Shifts in metabolic scaling, production, and efficiency across major evolutionary transitions of life. *Proc. Natl. Acad. Sci. U.S.A.* **107**, 12941–12945 (2010). doi: 10.1073/pnas.1007783107; pmid: 20616006
78. R. M. Sibly, D. Barker, M. C. Denham, J. Hone, M. Pagel, On the regulation of populations of mammals, birds, fish, and insects. *Science* **309**, 607–610 (2005). doi: 10.1126/science.1110760; pmid: 16040705
79. B. W. Brook, C. J. Bradshaw, Strength of evidence for density dependence in abundance time series of 1198 species. *Ecology* **87**, 1445–1451 (2006). doi: 10.1890/0012-9658(2006)87[1445:SOEFDD]2.0.CO;2; pmid: 16869419
80. N. B. Goodwin, A. Grant, A. L. Perry, N. K. Dulvy, J. D. Reynolds, Life history correlates of density-dependent recruitment in marine fishes. *Can. J. Fish. Aquat. Sci.* **63**, 494–509 (2006). doi: 10.1139/f05-234
81. J. P. DeLong, T. C. Hanley, D. A. Vasseur, Competition and the density dependence of metabolic rates. *J. Anim. Ecol.* **83**, 51–58 (2014). doi: 10.1111/1365-2656.12065; pmid: 23565624
82. R. A. Duursma *et al*., Self-shading affects allometric scaling in trees. *Funct. Ecol.* **24**, 723–730 (2010). doi: 10.1111/j.1365-2435.2010.01690.x
83. G. B. West, B. J. Enquist, J. H. Brown, A general quantitative theory of forest structure and dynamics. *Proc. Natl. Acad. Sci. U.S.A.* **106**, 7040–7045 (2009). doi: 10.1073/pnas.0812294106; pmid: 19363160
84. N. G. Hairston Jr., N. G. Hairston Sr., Cause-effect relationships in energy flow, trophic structure, and interspecific interactions. *Am. Nat.* **142**, 379–411 (1993). doi: 10.1086/285546
85. A. J. Kerkhoff, B. J. Enquist, Ecosystem allometry: The scaling of nutrient stocks and primary productivity across plant communities. *Ecol. Lett.* **9**, 419–427 (2006). doi: 10.1111/j.1461-0248.2006.00888.x; pmid: 16623727
86. S. Watson, E. McCauley, Contrasting patterns of net-and nanoplankton production and biomass among lakes. *Can. J. Fish. Aquat. Sci.* **45**, 915–920 (1988). doi: 10.1139/f88-112
87. C. Packer *et al*., Ecological change, group territoriality, and population dynamics in Serengeti lions. *Science* **307**, 390–393 (2005). doi: 10.1126/science.1105122; pmid: 15662005
88. J. M. Fryxell, A. Mosser, A. R. E. Sinclair, C. Packer, Group formation stabilizes predator-prey dynamics. *Nature* **449**, 1041–1043 (2007). doi: 10.1038/nature06177; pmid: 17960242
89. W. E. Ricker, Linear regressions in fishery research. *J. Fish. Board Can.***30**, 409–434 (1973). doi: 10.1139/f73-072
90. B. H. McArdle, The structural relationship: Regression in biology. *Can. J. Zool.* **66**, 2329–2339 (1988). doi: 10.1139/z88-348
91. R. R. Sokal, F. J. Rohlf, *Biometry* (Freeman, New York, ed. 3, 1995).
92. P. Jolicoeur, Bivariate allometry: Interval estimation of the slopes of the ordinary and standardized normal major axes and structural relationship. *J. Theor. Biol.* **144**, 275–285 (1990). doi: 10.1016/S0022-5193(05)80326-1
93. D. I. Warton, I. J. Wright, D. S. Falster, M. Westoby, Bivariate line-fitting methods for allometry. *Biol. Rev. Camb. Philos. Soc.* **81**, 259–291 (2006). doi: 10.1017/S1464793106007007; pmid: 16573844
94. R. J. Smith, Use and misuse of the reduced major axis for line-fitting. *Am. J. Phys. Anthropol.* **140**, 476–486 (2009). doi: 10.1002/ajpa.21090; pmid: 19425097
95. E. P. White, X. Xiao, N. J. Isaac, R. M. Sibly, "Methodological tools," in *Metabolic Ecology: A Scaling Approach*, (2012), pp. 7–20.
96. C. R. White, Allometric estimation of metabolic rates in animals. *Comp. Biochem. Physiol. A Mol. Integr. Physiol.* **158**, 346–357 (2011). doi: 10.1016/j.cbpa.2010.10.004; pmid: 20937406
97. K. Nowell, P. Jackson, *Wild Cats: Status Survey and Conservation Action Plan* (IUCN/SSC Cat Specialist Group, Gland, Switzerland, 1996).
98. P. M. Gros, M. J. Kelly, T. M. Caro, Estimating carnivore densities for conservation purposes: Indirect methods compared to baseline demographic data. *Oikos* **77**, 197 (1996). doi: 10.2307/3546058
99. J. Kalff, *Limnology: Inland Water Ecosystems* (Prentice Hall, Upper Saddle River, NJ, 2002), vol. 592.
100. E. McCauley, in *A Manual on Methods for the Assessment of Secondary Productivity in Fresh Waters* (Blackwell Scientific, Oxford, 1984), pp. 228–265.
101. G. Harris, *Phytoplankton Ecology-Structure, Function and Fluctuation* (Chapman and Hall, New York, 1986).
102. N. Billington, A comparison of three methods of measuring phytoplankton biomass on a daily and seasonal basis. *Hydrobiologia* **226**, 1–15 (1991). doi: 10.1007/BF00007775
103. J. S. Singh, W. K. Lauenroth, R. K. Steinhorst, Review and assessment of various techniques for estimating net aerial primary production in grasslands from harvest data. *Bot. Rev.* **41**, 181–232 (1975). doi: 10.1007/BF02860829
104. D. A. Clark *et al*., Measuring net primary production in forests: Concepts and field methods. *Ecol. Appl.* **11**, 356–370 (2001). doi: 10.1890/1051-0761(2001)011[0356:MNPPIF]2.0.CO;2
105. S. P. Long, P. R. Hutchin, Primary production in grasslands and coniferous forests with climate change: An overview. *Ecol. Appl.* **1**, 139–156 (1991). doi: 10.2307/1941807
106. C. Plante, J. A. Downing, Empirical evidence for differences among methods for calculating secondary production. *J. N. Am. Benthol. Soc.* **9**, 9–16 (1990). doi: 10.2307/1467929
107. E. P. White, B. J. Enquist, J. L. Green, On estimating the exponent of power-law frequency distributions. *Ecology* **89**, 905–912 (2008). doi: 10.1890/07-1288.1; pmid: 18481513
108. A. Clauset, C. R. Shalizi, M. E. Newman, Power-law distributions in empirical data. *SIAM Rev.* **51**, 661–703 (2009). doi: 10.1137/070710111
109. S. Nee, N. Colegrave, S. A. West, A. Grafen, The illusion of invariant quantities in life histories. *Science* **309**, 1236–1239 (2005). doi: 10.1126/science.1114488; pmid: 16109879
110. M. J. Coe, D. H. Cumming, J. Phillipson, Biomass and production of large African herbivores in relation to rainfall and primary production. *Oecologia* **22**, 341–354 (1976). doi: 10.1007/BF00345312
111. H. Fritz, P. Duncan, On the carrying capacity for large ungulates of African savanna ecosystems. *Proc. R. Soc. London Ser. B* **256**, 77–82 (1994). doi: 10.1098/rspb.1994.0052; pmid: 8008761
112. MAPA Project, MAPA Project, (2011), www.mapaproject.org/.
113. ALERT, African Lion and Environmental Research Trust (2011), www.lionalert.org.
114. J. Damuth, Interspecific allometry of population density in mammals and other animals: The independence of body mass and population energy-use. *Biol. J. Linn. Soc. Lond.* **31**, 193–246 (1987). doi: 10.1111/j.1095-8312.1987.tb01990.x
115. R. East, IUCN/SSC Antelope Specialist Group, *African Antelope Database 1998* (IUCN, Gland, Switzerland, and Cambridge, UK, 1999).
116. R. J. Power, R. X. Shem Compion, Lion predation on elephants in the Savuti, Chobe National Park, Botswana. *Afr. Zool.* **44**, 36–44 (2009). doi: 10.3377/004.044.0104
117. J. M. Fryxell, J. Greever, A. R. E. Sinclair, Why are migratory ungulates so abundant? *Am. Nat.* **131**, 781–798 (1988). doi: 10.1086/284822
118. C. Kiffner, B. Meyer, M. Muhlenberg, M. Waltert, Plenty of prey, few predators: What limits lions Panthera Leo in Katavi National Park, Western Tanzania? *Oryx* **43**, 52–59 (2009). doi: 10.1017/S0030605307002335
119. V. J. Wilson, *Mammals of the Wankie National Park, Rhodesia* (Trustees of the National Museums and Monuments of Rhodesia, Salisbury, Rhodesia, 1975).
120. L. D. Harris, "An ecological description of a semi-arid East African ecosystem," *Range Science Department Science Series* (11, Colorado State University, Fort Collins, CO, 1972).
121. H. F. Lamprey, The Tarangire game reserve. *Tanganyika Not. Record.* **60**, 10–22 (1963).
122. M. G. L. Mills, *Kalahari Hyenas: Comparative Behavioral Ecology of Two Species* (Blackburn, Caldwell, NJ, 1990).
123. D. I. Warton, R. A. Duursma, D. S. Falster, S. Taskinen, smatr 3–an R package for estimation and inference about allometric lines. *Methods Ecol. Evol.* **3**, 257–259 (2012). doi: 10.1111/j.2041-210X.2011.00153.x
124. T. X. Luo, thesis, Chinese Academy of Sciences, Beijing, China (1996).
125. J. Ni, X.-S. Zhang, J. M. Scurlock, Synthesis and analysis of biomass and net primary productivity in Chinese forests. *Ann. For. Sci.* **58**, 351–384 (2001). doi: 10.1051/forest:2001131
126. A. M. Makarieva *et al*., Mean mass-specific metabolic rates are strikingly similar across life's major domains: Evidence for life's metabolic optimum. *Proc. Natl. Acad. Sci. U.S.A.* **105**, 16994–16999 (2008). doi: 10.1073/pnas.0802148105; pmid: 18952839
127. V. M. Savage, J. F. Gillooly, J. H. Brown, G. B. West, E. L. Charnov, Effects of body size and temperature on population growth. *Am. Nat.* **163**, 429–441 (2004). doi: 10.1086/381872; pmid: 15026978
128. R. P. Duncan, D. M. Forsyth, J. Hone, Testing the metabolic theory of ecology: Allometric scaling exponents in mammals. *Ecology* **88**, 324–333 (2007). doi: 10.1890/0012-9658(2007)88[324:TTMTOE]2.0.CO;2; pmid: 17479751
129. W. F. Fagan, H. J. Lynch, B. R. Noon, Pitfalls and challenges of estimating population growth rate from empirical data: Consequences for allometric scaling relations. *Oikos* **119**, 455–464 (2010). doi: 10.1111/j.1600-0706.2009.18002.x
130. H. M. Pereira, G. C. Daily, Modeling biodiversity dynamics in countryside landscapes. *Ecology* **87**, 1877–1885 (2006). doi: 10.1890/0012-9658(2006)87[1877:MBDICL]2.0.CO;2; pmid: 16937624

ACKNOWLEDGMENTS

We thank N. Owen-Smith, L. Glass, J. H. Brown, V. M. Savage, J. P. Lessard, J. P. DeLong, J. M. Grady, and three anonymous reviewers for helpful comments on earlier drafts; X. Irigoien, S. K. M. Ernest, and H. Cyr for providing data; S. N. Driscoll for mapping assistance; and C. Miki for database assistance. I.A.H. was supported by a Natural Sciences and Engineering Research Council of Canada CGS-D fellowship. M.L. was supported by the TULIP Laboratory of Excellence (ANR-10-LABX-41). Research at Perimeter Institute was supported by the Government of Canada through Industry Canada and by the Province of Ontario through the Ministry of Research and Innovation. Data are available in the supplementary materials at *Science* Online.

SUPPLEMENTARY MATERIALS

www.sciencemag.org/content/349/6252/aac6284/suppl/DC1
Supplementary Text
Tables S1 to S5
Appendices S1 and S2
References (*131*–*144*)
Database S1

21 May 2015; accepted 3 August 2015
10.1126/science.aac6284

RESEARCH ARTICLE SUMMARY

T CELL CHEMOTAXIS

Neutrophil trails guide influenza-specific CD8$^+$ T cells in the airways

Kihong Lim, Young-Min Hyun, Kris Lambert-Emo, Tara Capece, Seyeon Bae, Richard Miller, David J. Topham, Minsoo Kim*

INTRODUCTION: Influenza virus infects the epithelial cells that line the respiratory tract. Therefore, cytotoxic CD8$^+$ T cells must traffic to this site to eliminate infected cells. The functions of antiviral CD8$^+$ T cell effector at tissue sites require a successful and early innate immune response. Neutrophils are an immune cell subset that helps organs initiate and maintain immune reactions and shapes the overall immune response by signaling to multiple immune cell types, including T cells. Under most inflammatory conditions, neutrophils are the first cell type that crosses the blood vessel endothelium into the tissue, often preceding a subsequent wave of effector T cells. Although neutrophils are known to recruit T cells into infected sites during both bacterial and viral infections and in chronic inflammatory diseases, the molecular mechanisms that link neutrophil and T cell migration remain unknown.

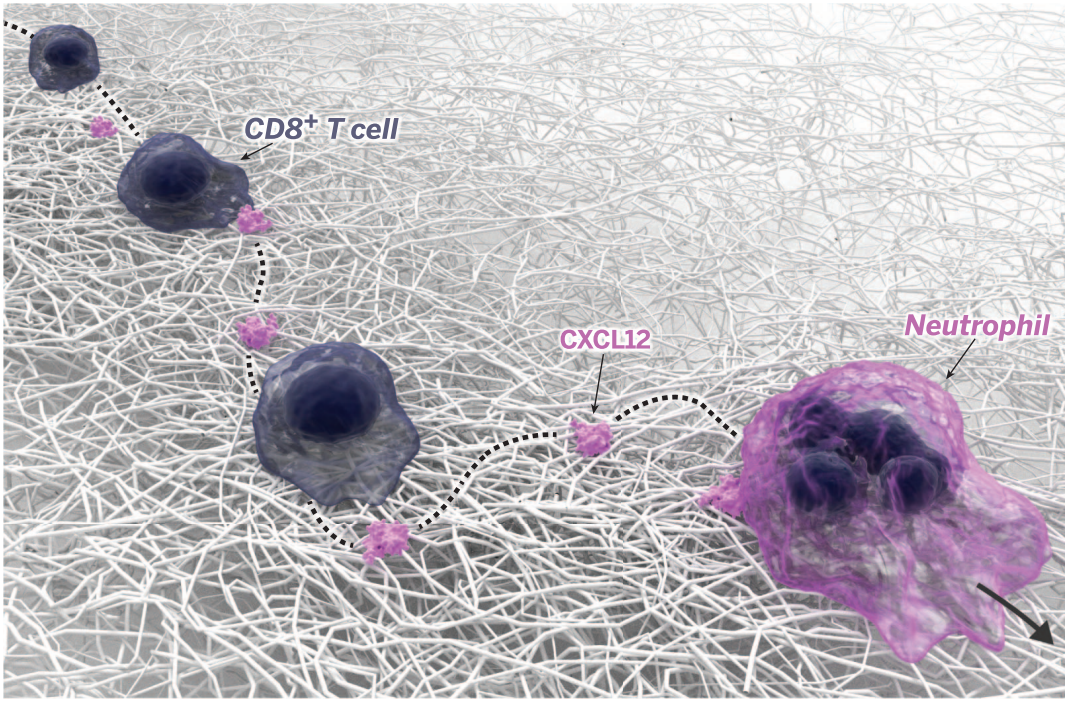
RATIONALE: The chemokine receptor family is the most potent tissue-specific family of homing receptors for T cells and is subset-selective. Therefore, it is widely assumed that the distinct migratory properties and distribution patterns of different subsets of specialized T cells result from the differential expression of the chemokines and their receptors. Although this idea has been verified experimentally in some settings, multiple chemokine receptors expressed on the effector T cells and the redundancy in their signaling pathways suggest the presence of a more complex mechanism that can confer specificity and selectivity to T cell recruitment. Furthermore, less is known about how chemokines released from newly recruited leukocytes act together with the local chemokines produced within the inflamed tissue. To address this, we performed intravital multiphoton microscopy imaging of the influenza-infected mouse trachea and explored how neutrophil-derived chemokines cooperate with the tissue-specific inflammatory cues to finely control the recruitment of CD8$^+$ T cells to the influenza-infected trachea.

ON OUR WEB SITE

Read the full article at http://dx.doi.org/10.1126/science.aaa4352

RESULTS: Here, we show that optimal CD8$^+$ T cell–mediated immune protection requires the early recruitment of neutrophils into influenza-infected trachea. In particular, the relative motility of virus-specific CD8$^+$ T cells in the trachea was determined by their localization to the epithelium, which was governed by the presence of neutrophils during early infection. Both in vitro and in vivo imaging showed that migrating neutrophils leave behind long-lasting trails from their elongated uropods (a protrusion at the rear of a cell) that are prominently enriched in the chemokine CXCL12. We observed that CXCL12 derived from the epithelial cells remained close to the epithelium, whereas CXCL12 derived from neutrophils was the main source of CXCL12 in the tissue interstitium during infection. Experiments with granulocyte-specific CXCL12 conditionally depleted (knockout) mice and a CXCR4 antagonist revealed that CXCL12 derived from neutrophil trails is critical for virus-specific CD8$^+$ T cell recruitment and antiviral effector functions.

CONCLUSION: The data presented here demonstrate that migrating neutrophils leave behind chemoattractant-containing trails, which result in the local accumulation of neutrophil-derived chemoattractant signals in inflamed tissues. As chemokines are small, diffusible molecules, perhaps these trails function to package the chemoattractant so that it can be preserved and survive severe mechanical perturbation during inflammation. Otherwise, the chemoattractant would be present only transiently, or it would immediately diffuse away from the site. ■



Neutrophils trails guide virus-specific CD8$^+$ T cell migration. In the influenza-infected trachea, tissue-infiltrating neutrophils (pink) deposit chemokine (CXCL12)–containing trails, which may serve like breadcrumbs or long-lasting chemokine depots to provide both chemotactic and haptotactic cues for efficient virus-specific CD8$^+$ T cell migration and localization in the infected tissues.

The list of author affiliations is available in the full article online.
*Corresponding author. E-mail: minsoo_kim@urmc.rochester.edu
Cite this paper as K. Lim *et al.*, *Science* **349**, aaa4352 (2015).
DOI: 10.1126/science.aaa4352

Downloaded from www.sciencemag.org on September 5, 2015

RESEARCH ARTICLE

T CELL CHEMOTAXIS

Neutrophil trails guide influenza-specific CD8$^+$ T cells in the airways

Kihong Lim,[1]* Young-Min Hyun,[1]* Kris Lambert-Emo,[1] Tara Capece,[1] Seyeon Bae,[1] Richard Miller,[2] David J. Topham,[1] Minsoo Kim[1]†

During viral infections, chemokines guide activated effector T cells to infection sites. However, the cells responsible for producing these chemokines and how such chemokines recruit T cells are unknown. Here, we show that the early recruitment of neutrophils into influenza-infected trachea is essential for CD8$^+$ T cell–mediated immune protection in mice. We observed that migrating neutrophils leave behind long-lasting trails that are enriched in the chemokine CXCL12. Experiments with granulocyte-specific CXCL12 conditionally depleted mice and a CXCR4 antagonist revealed that CXCL12 derived from neutrophil trails is critical for virus-specific CD8$^+$ T cell recruitment and effector functions. Collectively, these results suggest that neutrophils deposit long-lasting, chemokine-containing trails, which may provide both chemotactic and haptotactic cues for efficient CD8$^+$ T cell migration and localization in influenza-infected tissues.

Precise trafficking of activated effector T cells to infection sites is key to their protective functions against a virus. Infected tissues often harbor an array of diverse inflammation-induced chemokines that guide effector T cell migration and retention. The predominant view in the field is that effector T cells home to the infection sites by following the prepatterned tissue-specific chemokine gradients created by the target cells (*1*–*4*). However, many of these chemokines are derived from newly recruited innate immune cells during the initial infection (*1*, *5*–*7*) and little is known about how these innate immune-derived chemotactic signals are present in the tissue microenvironment and how they act to recruit T cells (*8*). Note that an early innate immune response that is local and successful is critical for elicitation of T cell effector functions at the peripheral tissue sites (*9*). Therefore, it is likely that the type of innate cells, mode of early innate responses, and associated local inflammatory mediators will all affect the molecular mechanisms by which effector T cells successfully move into the inflamed tissues.

The maintenance of homeostatic immune surveillance and the development of effective adaptive immune responses require that T cells cross tissue barriers and move throughout the body as they migrate in and out of the bone marrow and lymphoid and nonlymphoid tissues, under normal, infected, or inflamed conditions (*8*). Activated effector T cells must traffic efficiently into peripheral nonlymphoid tissues to protect the host from infection.

[1]Department of Microbiology and Immunology, David H. Smith Center for Vaccine Biology and Immunology, University of Rochester, Rochester, NY, USA. [2]Department of Pharmacology, Northwestern University, Chicago, IL, USA. *These authors contributed equally to this work. †Corresponding author. E-mail: minsoo_kim@urmc.rochester.edu

Neutrophils are key players that help organs initiate and maintain immune reactions (*10*) and that shape the overall immune response by signaling to dendritic cells, monocytes, and T cells. Under most inflammatory conditions, neutrophils are the first cell type that crosses the blood vessel endothelium into the tissue, often preceding a subsequent wave of effector T cells (*11*, *12*). Although neutrophil-mediated recruitment of T cells into infected sites has been documented in both bacterial and viral infections and in chronic inflammatory diseases (*13*–*18*), the molecular mechanisms that link neutrophil and T cell migration remain unknown.

Results

Reduced CD8$^+$ T cell response in the influenza-infected trachea of neutropenic mice

To investigate the role of neutrophil recruitment in shaping CD8$^+$ T cell responses during influenza infection, we first measured the kinetics of neutrophil and CD8$^+$ T cell responses in the trachea of C57BL/6 mice infected with influenza A virus. Infection of mice with 3×10^4 plaque-forming units of HKx31 influenza virus resulted in the rapid, but transient, infiltration of neutrophils into the trachea, with increases in cell number peaking on day 4, followed by the subsequent recruitment of CD8$^+$ T cells between days 6 and 8 (Fig. 1, A and B). We then established highly selective and near-complete (> 95%) neutrophil depletion using the Ly6G-specific monoclonal antibody (mAb) 1A8 (fig. S1, A and B). Examination of trachea tissue on day 7 postinfection revealed that the depletion of neutrophils during infection elicited a significant delay in influenza virus clearance (Fig. 1C). This delay in virus clearance did not promote a more robust antiviral CD8$^+$ T cell response (fig. S1, C and D); instead, neutrophil depletion after the primary infection of C57BL/6 mice with HKx31 reduced the total CD8$^+$ T cell response and significantly decreased the number of CD8$^+$ T cells specific for the nucleoprotein-derived epitope of the influenza A virus presented by H2-Db (D^bNP_{366}) (Fig. 1D).

Upon resolution, local tissue-resident memory T cells normally provide protection during lethal secondary virus challenge (*19*, *20*). The number of memory T cells in both the lung and trachea, but not lymphoid memory T cells, was significantly lower when neutrophils were depleted during the primary infection (Fig. 1E). As shown previously (*21*), similar numbers of total D^bNP_{366}-specific CD8$^+$ T cells were recovered from draining lymph nodes of immunoglobulin G (IgG)–treated versus mAb 1A8-treated mice during the primary infection (fig. S1, C and D), which suggested that the absence of neutrophils reduced the magnitude of the influenza-specific CD8$^+$ T cell response, as well as its memory, without altering T cell priming and expansion.

The observed difference in CD8$^+$ T cell homing after neutrophil depletion was further examined by whole-mount immunostaining of CD8$^+$ T cells within the HKx31-infected trachea. CD8$^+$ T cells were visible strictly in the subepithelium, whereas many T cells remained in the interstitium and more distal to the epithelium after neutrophil depletion (Fig. 2A). To further examine the dynamics of influenza-specific CD8$^+$ T cells in the trachea, we transferred 2×10^6 splenocytes from a transgenic mouse that had a naïve green fluorescent protein (GFP)–expressing OT-I T cell receptor (TCR) [that is, OT-I^{GFP} mice in which the OT-I TCR recognizes a peptide fragment of chicken ovalbumin (OVA)]. The splenocytes were introduced into the recipient mice 1 day before inoculation with HKx31-OVA virus (*22*). We then performed intravital two-photon microscopy (IV-TPM) on the surgically cannulated trachea (fig. S2). On day 7 postinfection, we found a large number of GFP-positive CD8$^+$ T cells actively migrating throughout the trachea (Fig. 2B). As a substantial number of cells accumulated along the infected epithelium, the T cells became less motile, with a lower mean velocity and displacement (Fig. 2, B and C, and movie S1). Furthermore, T cell migration appeared to be random, with confined motion for the imaging periods (movie S1). Similar to our observations using whole-mount immunostaining, fewer T cells were found to be localized within the vicinity of the epithelium of the influenza-infected mouse trachea after neutrophil depletion (Fig. 2B and movie S2). Additionally, the movement of CD8$^+$ T cells occurred at a higher mean velocity and displacement in the parenchyma upon neutrophil depletion (Fig. 2C). This significant change in CD8$^+$ T cell speed and displacement after neutrophil depletion was observed in all examined mice and did not depend on the local T cell abundance. These results suggest that the relative motility of virus-specific CD8$^+$ T cells in the trachea is determined by their localization to

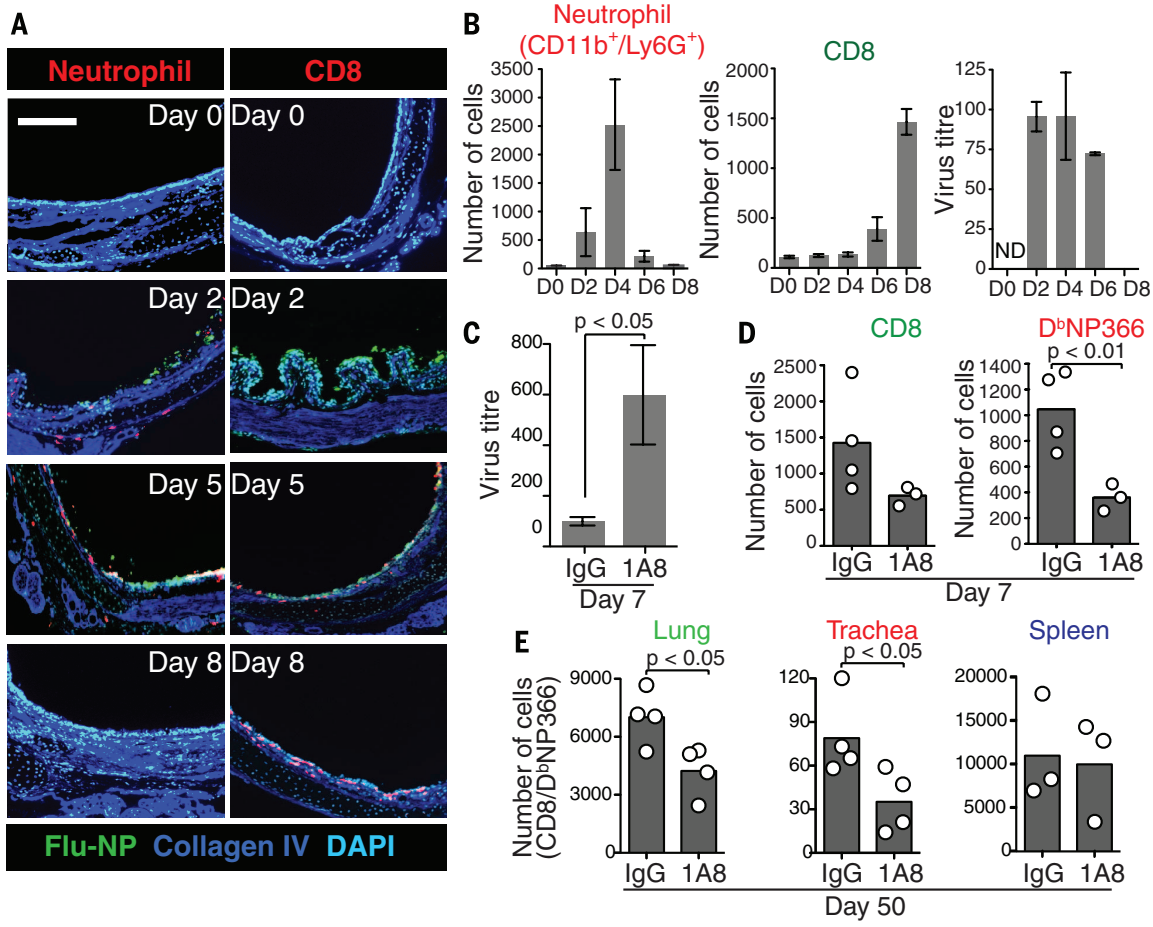


Fig. 1. Reduced CD8$^+$ T cell response in the neutropenic mice. (**A**) Immunofluorescence images of trachea sections from influenza virus–infected mice on the indicated days postinfection. Red, neutrophils or CD8$^+$ T cells; green, viral NP; blue, collagen IV; cyan, nuclear staining with DAPI. Each panel shows one representative image from three repeated experiments. Scale bar, 200 μm. (**B**) Flow cytometric analysis of neutrophils (left) and CD8$^+$ T lymphocytes (middle) in the trachea after influenza infection (mean ± SEM, $n \geq 3$ mice per group). Viral NP mRNA levels (right) normalized by cellular actin mRNA (as a percentage) in the trachea by using qRT-PCR (at day 2 postinfection, mean ± SEM, $n = 3$ mice per group). ND, not detected. (**C**) Neutrophils were depleted by intraperitoneal injection of Ly6G Ab (1A8) on day –1, +1, +3, and +5 postinfection, and viral loads were measured on day 7 [percentage of isotype control IgG-treated group (IgG), mean ± SEM, $n \geq 6$ mice per group]. (**D**) Total or virus (D^bNP_{366})-specific CD8$^+$ T cell numbers were counted from 1A8- or IgG-injected mice by using flow cytometry on day 7 after infection. (**E**) Numbers of virus-specific memory CD8$^+$ T cells in the indicated tissues of mice with or without neutrophil depletion were measured on day 50 postinfection. (D) and (E) Points indicate data from individual mice. Statistical differences in (C), (D), and (E) were assessed by using Student's *t* test.

the epithelium, which is governed by the presence of neutrophils during early infection.

Neutrophil-derived chemokine induces CD8$^+$ T cell migration

Under inflammatory conditions, neutrophils release matrix metalloproteases (MMP-2 and -9), which are capable of remodeling the extracellular matrix (ECM) by cleaving type IV collagen present in the basement membrane (*23*, *24*). Therefore, we used MMP-2/9 inhibitor I (*25*) to assess whether ECM modification by neutrophil-derived MMPs is an important part of CD8$^+$ T cell homing during influenza infection. Treatment of influenza-infected mice with the inhibitor did not have significant effects on T cell, which suggested that neutrophil-derived MMPs have a minimal impact on the initial T cell homing to influenza-infected trachea (fig. S3).

In addition to proteolytic enzymes, neutrophils release a variety of cytokines, which can lead to the amplification of many T cell functions during infection. The finding that the initial infiltration of neutrophils directly correlates with virus-specific CD8$^+$ T cell recruitment to the infected trachea suggests that neutrophils may be a major source of chemokines during influenza infection or may be mediators of chemoattractant release from infected cells. To examine chemokine production by murine neutrophils, we first screened 21 mouse chemokines and detected nine chemokines in neutrophil lysates prepared from both naïve and influenza-infected mice on day 4 after infection (Fig. 3A). The activated CD8$^+$ T cells were found to express receptors that could recognize at least six of the nine detected chemokines (fig. S4) (*26*, *27*). Two known neutrophil chemokines, CXCL1 and CXCL2, were excluded from the analysis because of the lack of receptor expression on CD8$^+$ T cells (fig. S4). Among the six chemokines tested for CD8$^+$ T cell migration, only CXCL12 significantly induced cell migration in vitro (Fig. 3B), and this effect was completely abolished by the CXCR4 antagonist AMD3100 (Fig. 3C). The changes in CD8$^+$ T cell recruitment and location after neutrophil depletion in vivo were recapitulated by treating mice with AMD3100 (Fig. 3, D and E), which suggested that the CD8$^+$ T cell response during influenza infection is dependent on CXCL12 signals.

Although CXCL12 expression by nonhematopoietic cells in multiple tissues and its pleiotropic functions both in organ development and in the peripheral immune system are well established (*28*), relatively little is known regarding the CXCL12 that is released by newly infiltrating immune cells during infections. To visualize the local expression of CXCL12 after influenza infection, we infected CXCL12-reporter mice [the gene expressing $CXCL12^{DsRed}$ is inserted into these "knock-in" mice, which express DsRed under the endogenous *Cxcl12* promoter (*29*)] with HKx31 virus. Consistent with previous reports (*29*, *30*), CXCL12 was primarily expressed by endothelial and perivascular stromal cells, as well as by epithelial cells of the naïve trachea (movie S3). Furthermore, the CXCL12 expression patterns in these nonmotile cells were similar, irrespective of virus infection. On day 2 postinfection, we detected additional CXCL12$^+$ cells that actively migrated throughout the interstitium of the trachea, and more than 95% of these CXCL12$^+$ motile cells were Ly6G-positive (Fig. 3F and movie S4). Thus, identifying CXCL12 reporter cells allowed us to observe that, among the innate immune cells that are recruited during early influenza infection, neutrophils are the main producers of local CXCL12 signals in the trachea. To

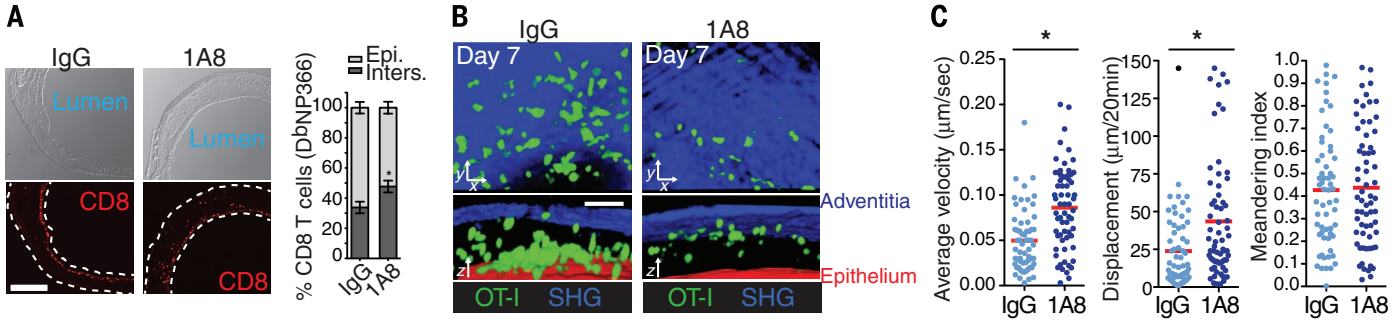


Fig. 2. Location and migration of CD8$^+$ T cells in the neutropenic mice. (**A**) Immunofluorescence images of the trachea sections from virus-infected mice with or without neutrophil depletion. (Top) Bright-field microscopy images; (bottom) CD8$^+$ T cells (red). The dotted line indicates tracheal tissue borders. (Graph) The ratio (percentage of total) of the numbers of CD8$^+$ T cells in the epithelium or the interstitium ($n \geq 3$ sections from a mouse, $N \geq 3$ mice per group). *$P < 0.05$ compared with IgG. Epi., epithelium; Inters., interstitium. Scale bar, 200 μm. (**B**) (Top) *x*,*y* plane and (bottom) *z*-stacks from a representative IV-TPM of OT-I^{GFP} CD8$^+$ T cells in HKx31-OVA virus-infected trachea on day 7 postinfection with or without neutrophil depletion. OVA-specific CD8$^+$ T cells (green), adventitia (blue), and the tracheal lumen (red) are shown. Scale bar, 50 μm. (**C**) Mean velocity, displacement, and meandering index of OT-I^{GFP} CD8$^+$ T cells in HKx31-OVA–infected trachea. Points, individual cells pooled from three mice per each group. *$P < 0.001$ compared with IgG. Statistical differences in (A) and (C) were assessed with nonparametric Mann-Whitney test.

further confirm that the neutrophil-derived, local CXCL12 signal is critical for CD8$^+$ T cell recruitment, we generated a granulocyte-specific CXCL12 conditionally depleted (knockout) mouse (CXCL12 cKO) by crossing CXCL12^{flox} + Ela2^{Cre} mice (fig. S5, A and B). Deletion of CXCL12 in neutrophils resulted in a significant delay in D^{b}NP$_{366}$-specific CD8$^+$ T cell recruitment and disrupted localization in the trachea compared with the control CXCL12-floxed mice after influenza infection (Fig. 3G and fig. S6). Virus titers at the peak were identical in all strains of mice, although the CXCL12-deficient mice had slightly delayed virus clearance, similar to that of neutrophil-depleted mice (Fig. 3H). This decrease in T cell response was likely due to the reduced total CXCL12 level in the trachea, as measured by total CXCL12 immunofluorescence intensity after day 7 of infection (Fig. 3I).

Neutrophil leaves chemokine-containing trails

Although neutrophils produce a wide range of cytokines and chemokines, little is known about their release. Even with high concentrations of inflammatory stimuli, such as tumor necrosis factor–α (TNFα) (Fig. 4A and fig. S7) or formyl-methionyl-leucyl-phenylalanine (fMLP), we failed to detect a substantial release of soluble CXCL12 from neutrophils, whereas stimulation with phorbol 12-myristate 13-acetate (PMA) caused the dramatic secretion of CXCL12. To assess whether inflammatory signals that induce active neutrophil migration predispose neutrophils to release more CXCL12 and, thus, successfully induce CD8$^+$ T cell migration, we collected supernatant from actively migrating neutrophils and measured the CXCL12 level and its impact on CD8$^+$ T cell migration. Again, we could not detect a marked amount of CXCL12 in the supernatant, nor did it induce CD8$^+$ T cell chemokinesis (Fig. 4B). To test whether the minimum amount of CXCL12 released from migrating neutrophils could bind to glycosaminoglycan-coated surfaces and could induce haptotactic CD8$^+$ T cell migration (*31*, *32*), we incubated heparan sulfate (HS)–coated coverslips with the neutrophil supernatant and subsequently measured CD8$^+$ T cell migration. Even after prolonged incubation with the supernatant, coverslips coated with HS and intercellular adhesion molecule 1 (ICAM-1) (HS+ICAM-1) failed to induce CD8$^+$ T cell migration (Fig. 4B). To further test our hypothesis that migrating neutrophils release CXCL12 in a highly confined proximal area to guide only closely adjacent CD8$^+$ T cell chemotaxis in a chase-and-run fashion, we coincubated neutrophils and CD8$^+$ T cells on ICAM-1–coated plates. fMLP was used to induce cell migration only in neutrophils (fig. S8), and the migration of each CD8$^+$ T cell was tracked beginning with its first physical encounter with a migrating neutrophil. The spontaneous CD8$^+$ T cell migration was carried out in a random fashion, without any sizable positive correlation with the neutrophil migration tracks (Fig. 4C).

To screen for potential chemotactic signals for CD8$^+$ T cells that could be generated during neutrophil migration, we next turned our attention to neutrophil-experienced assay coverslips and measured cell migration on the neutrophil-experienced surface, after the migrating neutrophils were completely removed by extensive washing of the glass surface. To our surprise, the migration of activated CD8$^+$ T cells was most significantly enhanced in the absence of any additional exogenous chemotactic signals, whereas other cell types (CD4$^+$ T cells, neutrophils, and monocytes) showed no or minimally enhanced migration (Fig. 4D). The inhibition of CXCR4 with AMD3100 completely abolished this CD8$^+$ T cell migration, which suggested that the CD8$^+$ T cell migration on neutrophil-experienced coverslips depended on CXCL12 signals (Fig. 4E). First, we reasoned that a few damaged neutrophils had remained on the coverslip after washing and had released CXCL12 during the assay. We therefore used a fluorescently labeled Ly6G Ab to visualize any remaining neutrophils on the coverslip after our extensive washings. Unlike our prediction, we could not detect any remaining neutrophil cell bodies on the glass surface, but we did observe a substantial amount of membrane particles that were deposited on the coverslip (fig. S9). To determine whether the membrane particles were parts of damaged neutrophils that had been left behind during detachment or if the particles had been actively deposited along the membrane trail during migration by neutrophils, neutrophils labeled with fluorescein isothiocyanate (FITC)–conjugated Ly6G antibody (Ab) were allowed to migrate on the coverslip. Live fluorescence imaging showed that the neutrophils formed long membrane tethers during migration and subsequently left behind membranous trails (Fig. 4F and movie S5). Scanning electron microscopy (EM) of the migrating neutrophils further confirmed the ultrastructure of these neutrophil trails (Fig. 4G). Similar neutrophil trails were observed on ICAM-1–coated surfaces under both static and shear (1 dyne/cm^2) conditions (Fig. 4H). Moreover, the formation of neutrophil trails was inhibited by an antibody on ICAM-1 that blocked a specific leukocyte function–associated antigen–1 (LFA-1) and by an antibody that blocked a macrophage-1 antigen (Mac-1) on a fibronectin (FN)–coated surface (Fig. 4I), which suggested an important role for integrins in the formation of neutrophil trails.

In *Dictyostelium*, which responds to adenosine 3′,5′-monophosphate (cAMP) for chemotaxis, the enzyme that generates cAMP is highly enriched in the membrane vesicles that are deposited behind migrating cells (*33*). cAMP is released from these vesicles to prompt fellow cells to align and generate their head-to-tail streaming migration patterns. We hypothesized that similar membrane shedding and chemotactic signal compartmentalization exist for neutrophils during normal immune responses (*34*). To test this hypothesis, we characterized the chemokine composition of neutrophil-derived membrane trails. The mouse chemokine Ab array data showed that among the more than 50 cytokines and/or chemokines that were screened, only CXCL12 was preferentially enriched in the trails generated from the uropods of migrating neutrophils (Fig. 5A). We also detected abundant CXCL12 in many scattered vesicles inside the elongated neutrophil

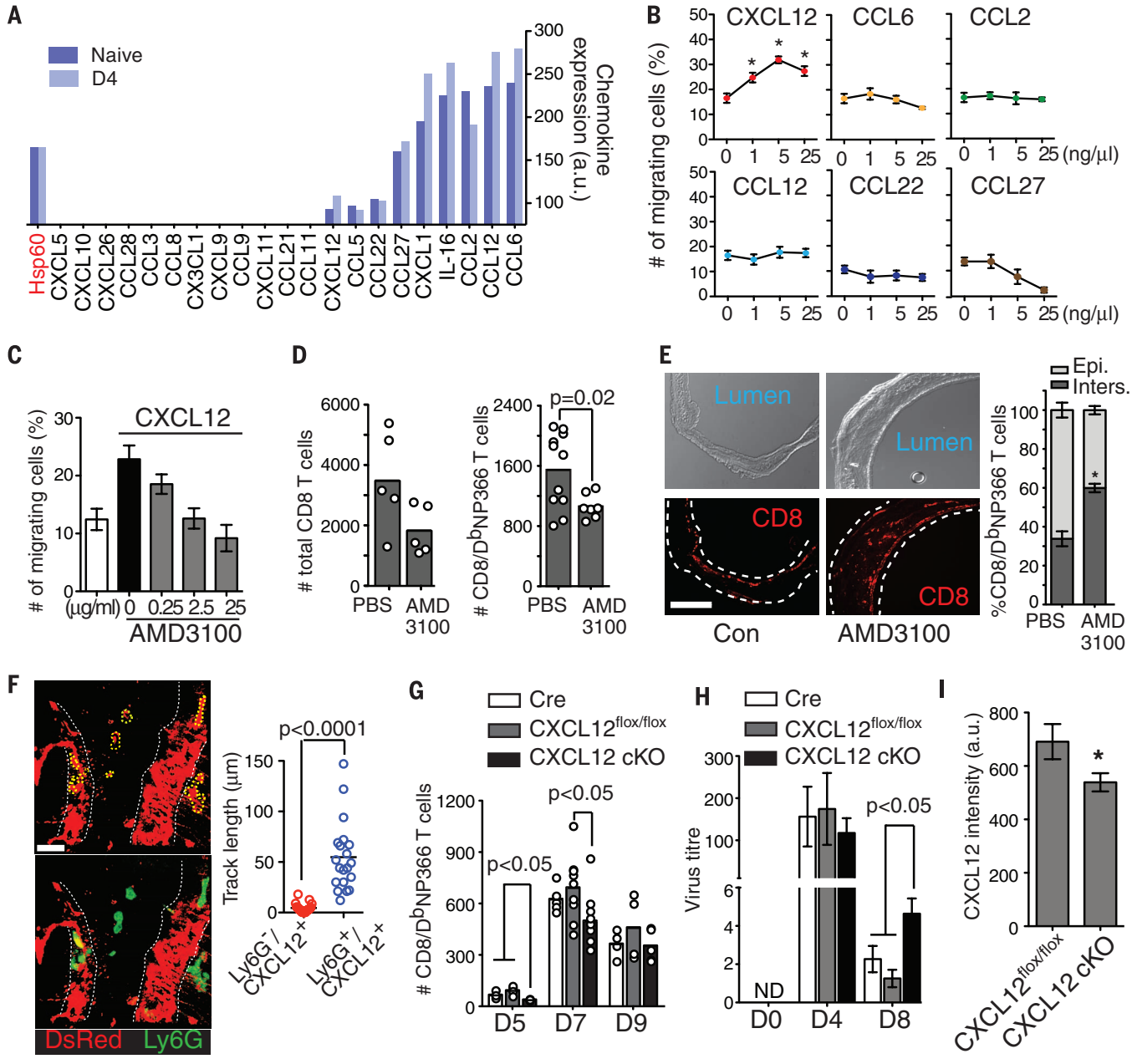


Fig. 3. Neutrophil-derived CXCL12 induces CD8$^+$ T cell migration. (**A**) Chemokine microarray with total lysates of bone marrow–derived neutrophils from naïve or influenza-infected mice on day 4 postinfection (n = 2 mice per group). Chemokine expression levels were expressed as an arbitrary unit measured by densitometry. (**B**) CD3/CD28-activated CD8$^+$ T cell migration on ICAM-1 with the indicated chemokines. The ratio of the number of cells crawling more than 50 µm for 15 min (percentage of total) in a field of view was presented. A single assay analyzed at least 10 cells (n = 3 assays per group). *P < 0.05 compared with control. (**C**) CD8$^+$ T cell migration assay on ICAM-1 and CXCL12 in the presence or absence of AMD3100, a CXCR4 antagonist (n = 3 assays per group). (**D**) The number of total (left) or D^{b}NP$_{366}$-specific (right) CD8$^+$ T cells in the trachea on day 7 postinfection with or without AMD3100 (n = 5 to 11 per group). (**E**) Immunofluorescent microscopy of tissue sections from the virus-infected trachea with or without AMD3100 treatment. (Top) Bright-field microscopy images; (bottom) CD8$^+$ T cells (red). The dotted lines indicate tracheal tissue borders. (Graph) The ratio (percentage of total) of CD8$^+$ T cell number in the epithelium and the interstitium (n ≥ 3 sections per mouse, N ≥ 3 mice per group, *P < 0.05 compared with PBS). Scale bar, 250 µm. Epi., epithelium; Inters., interstitium. (**F**) Representative images from IV-TPM of Ly6G$^+$DsRed$^+$ neutrophils in the trachea of CXCL12^{DsRed} mouse infected with influenza virus. (Top) DsRed in red; (Bottom) Ly6G in green + DsRed in red. White dotted line, blood vessel; yellow dotted area, neutrophil. Scale bar, 20 µm. (Graph) Track lengths of Ly6G$^-$DsRed$^+$ and Ly6G$^+$DsRed$^+$ cells for 15 min (n = 3 mice per group). (**G**) Cre (*Ela2*$^{Cre/+}$), *CXCL12*$^{flox/flox}$, and CXCL12 cKO mice were infected, and D^{b}NP$_{366}$-specific CD8$^+$ T cells in the trachea were measured by flow cytometry on the indicated days (n = 3 to 8 per group). (**H**) Cre (*Ela2*$^{Cre/+}$), *CXCL12*$^{flox/flox}$, and CXCL12 cKO mice were infected, and viral loads in the trachea were measured on the indicated days (percentage of CXCL12 cKO on day 4, n = 4 to 8 per group). (**I**) Total CXCL12 intensity of tissue sections of the whole trachea was measured by fluorescent microscopy (n ≥ 3 sections per mouse and N = 6 mice per group, *P < 0.05 compared with *CXCL12*$^{flox/flox}$). (D), (F), and (G) Points indicate data from individual mice. (B), (G), and (H) Data were analyzed with Kruskal-Wallis followed by Dunn's posttest, (D), (E), (F), (G, day 7), and (I) Data were analyzed with Student's t test.

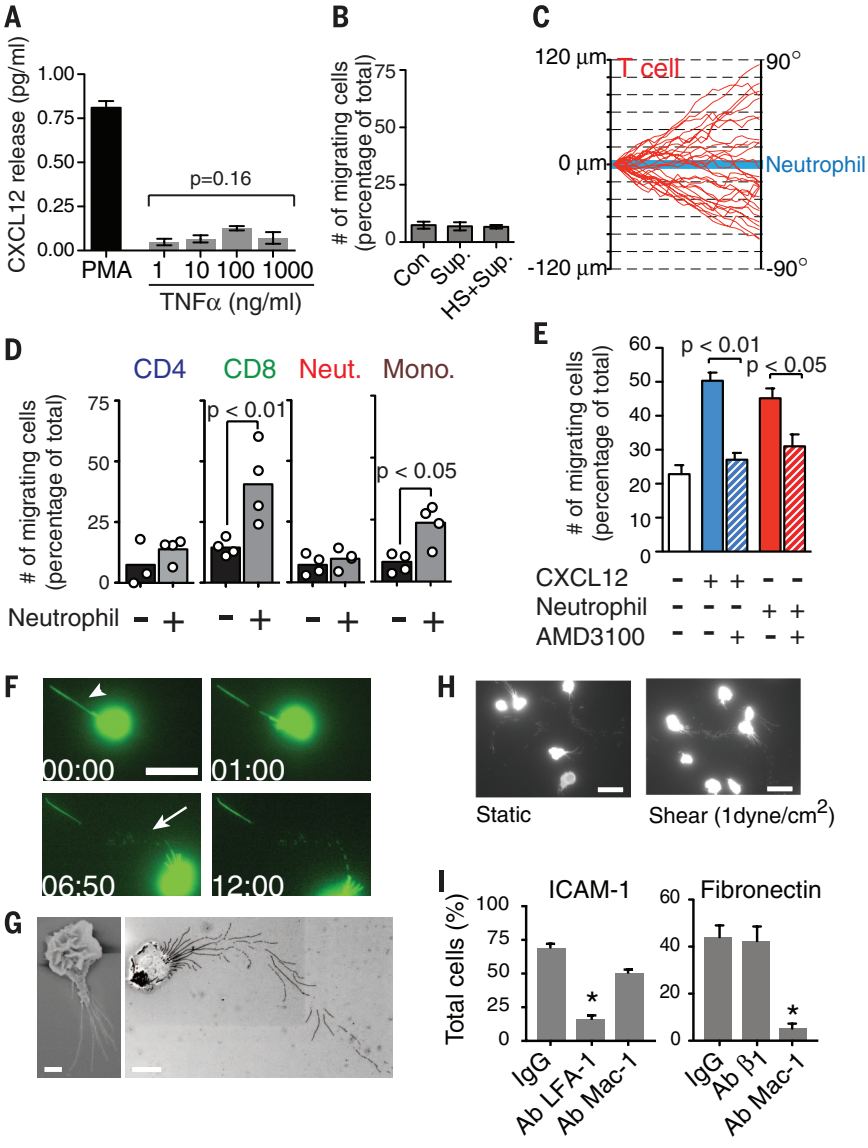


Fig. 4. Neutrophil trails induce CD8$^+$ T cell migration. (**A**) CXCL12 secretion from neutrophils in response to PMA (100 ng/ml) or the indicated concentration of TNFα (n = 3). (**B**) Activated CD8$^+$ T cell migration on a chamber coated with ICAM-1 alone or with ICAM-1 + HS preincubated with or without the supernatant from migrating neutrophils stimulated by fMLP (n = 3 assays per group). Sup., supernatant. (**C**) Tracking of single CD8$^+$ T cell migration (red) versus neutrophil tracks (blue). The shortest distance of a CD8$^+$ T cell from a neutrophil track was measured at each time point of migration and plotted every 15 s from t = 0 to t = 6 min (total 30 cells from three independent assays). (**D**) Migration of indicated cells on neutrophil-experienced (+) or nonexperienced (−) ICAM-1–coated surface. The ratio (percentage of total) of cells migrating ≥ 50 μm (CD4$^+$, CD8$^+$, neutrophil) or ≥ 25 μm (monocyte) for 15 min in a field of view was presented. (**E**) CD3/CD28-activated CD8$^+$ T cell migration on ICAM-1 coated with CXCL12 or neutrophil trails in the presence or absence of AMD3100 (n ≥ 3 assays per group). Points indicate data from individual experiments (average). (**F**) Time-lapse images from a representative movie showing a Ly6G-stained (green) neutrophil crawling on ICAM-1–coated surface in the presence of fMLP. Arrowhead and arrow indicate neutrophil trails. Scale bars, 20 μm. (**G**) Scanning EM of neutrophil trails on ICAM-1. Scale bar, 2 μm (left) and 10 μm (right). (**H**) Immunofluorescence images of Ly6G-stained migrating neutrophils under a static condition or shear flow. Scale bars, 20 μm. (**I**) Integrin-dependent trail formation. Migrating neutrophils with trails were counted (percentage of total) on ICAM-1 or fibronectin in the presence of the indicated blocking antibodies (n = 3 assays per group). *P < 0.05 compared with IgG. (A) CXCL12 secretion was analyzed with Kruskal-Wallis followed by Dunn's posttest. (D), (E), and (I) Cell migration was analyzed with Student's t test.

uropods, using a highly specific Ab against mouse CXCL12 (Fig. 5B and fig. S10). Immunohistologic examination of mouse neutrophils suggests that CXCL12 is stored within organelles lacking myeloperoxidase (primary granule), lactoferrin (secondary granule), and MMP-9 (tertiary granule); these organelles may be secretory vesicles (fig. S11) (*35*). To further determine whether the enhanced CD8$^+$ T cell migration on the neutrophil-experienced coverslip was directly mediated by CXCL12 derived from neutrophil trails, we used the granulocyte-specific CXCL12 cKO mouse (CXCL12 cKO). First, we allowed CXCL12 cKO neutrophils to migrate on an ICAM-1–coated glass surface in the presence of fMLP. After we confirmed the generation of neutrophil trails on the glass surface, the neutrophil cell bodies were removed, with minimal detachment of their trails. Subsequently, CD8$^+$ T cells were added, and their migration was analyzed. Unlike CD8$^+$ T cell migration on the coverslips preconditioned with wild-type (WT) neutrophil, T cell migration on the coverslips that had been treated with CXCL12 cKO was not significantly increased (Fig. 5C).

Unlike neutrophils, which often show highly coordinated directional chemotaxis in tissues, T cells migrating in both lymphoid and nonlymphoid tissues have been observed to migrate by chemokine-mediated random or generalized Lévy walks (*36*, *37*). The neutrophil trail did not directly induce the chemotaxis of adjacent CD8$^+$ T cells in a chase-and-run fashion (Fig. 4C), which indicated that the trails might function as a slow-release CXCL12 depot or as a haptotactic CXCL12 signal that directly enhances CD8$^+$ T cell migration upon contact. To further dissect this, we performed a microchamber chemotaxis assay (Fig. 5D). Neutrophils were first placed in the left-side well ("neutrophil zone") and were then allowed to migrate on an ICAM-1– or fibronectin-coated surface in the presence of fMLP, which permitted them to deposit trails in the neutrophil zone. After removing the neutrophils from the neutrophil zone, CD8$^+$ T cells were placed in the right-side well ("T cell zone"); the separation wall (500 μm in width) was then removed, and the T cells were followed by video microscopy. Within 5 to 10 min after the onset of migration, the CD8$^+$ T cells in the T cell zone began to move toward the neutrophil zone, whereas the CD8$^+$ T cells that were placed next to the neutrophil zone preconditioned with non-neutrophils or CXCL12 cKO neutrophils were unresponsive (Fig. 5D). These observations suggested that neutrophil trails indeed release a soluble factor that attracts CD8$^+$ T cells from a long distance (>500 μm).

Neutrophil leaves CXCL12-containing trails in the tissues

Previously, we and others reported extreme uropod elongation during neutrophil extravasation in vivo (*38*–*40*). We observed that neutrophil uropods became elongated, and they left behind membrane trails during extravasation and interstitial migration in influenza-infected trachea (Fig. 6, A to C, and movie S6 to S8). Indeed, many neutrophils appeared to be crawling in directional patterns

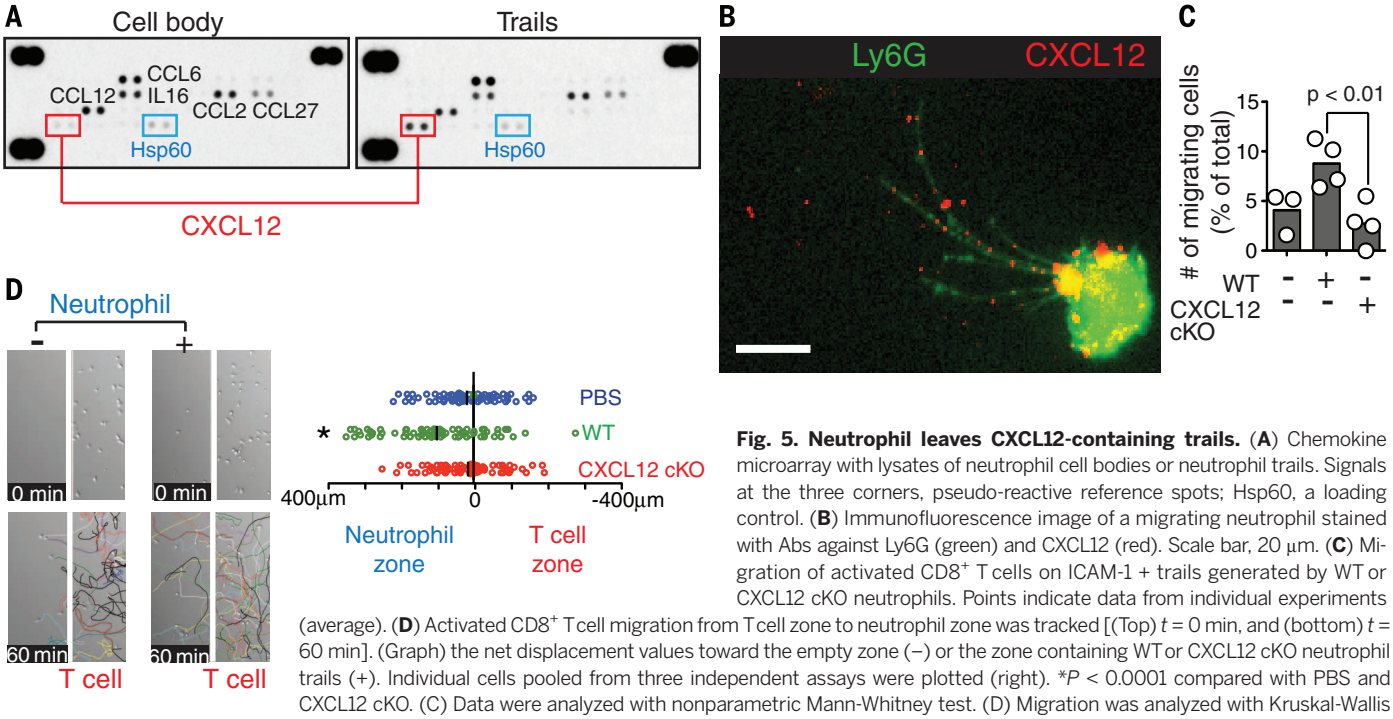


Fig. 5. Neutrophil leaves CXCL12-containing trails. (**A**) Chemokine microarray with lysates of neutrophil cell bodies or neutrophil trails. Signals at the three corners, pseudo-reactive reference spots; Hsp60, a loading control. (**B**) Immunofluorescence image of a migrating neutrophil stained with Abs against Ly6G (green) and CXCL12 (red). Scale bar, 20 μm. (**C**) Migration of activated CD8$^+$ T cells on ICAM-1 + trails generated by WT or CXCL12 cKO neutrophils. Points indicate data from individual experiments (average). (**D**) Activated CD8$^+$ T cell migration from T cell zone to neutrophil zone was tracked [(Top) t = 0 min, and (bottom) t = 60 min]. (Graph) the net displacement values toward the empty zone (−) or the zone containing WT or CXCL12 cKO neutrophil trails (+). Individual cells pooled from three independent assays were plotted (right). *P < 0.0001 compared with PBS and CXCL12 cKO. (C) Data were analyzed with nonparametric Mann-Whitney test. (D) Migration was analyzed with Kruskal-Wallis followed by Dunn's posttest.

that closely followed the local collagen fibers as seen by second-harmonic generation (SHG) signals. Using mice expressing monomer red fluorescent protein (mRFP)–tagged CXCL12 (*41*), we further confirmed that CXCL12-containing neutrophil trails were preferentially deposited along the SHG fibers in vivo (Fig. 6D, fig. S12, and movie S9). Note that many CD8$^+$ T cells migrated in close contact with the local collagen structures (*42*) and made serial contacts with the neutrophil trails (Fig. 6E and movie S10). The frequency of the direct contact between neutrophil trails and CD8$^+$ T cells during migration was significantly decreased in the presence of AMD3100 (Fig. 6F), which suggested that the interaction is dependent on CXCL12 signals.

To determine how long these neutrophil trails remain in the tissue, we first treated influenza-infected trachea with collagenase and removed all intact cells by slow-speed centrifugation (fig. S13A). The trails deposited in the tissue were then measured by Western blot analysis of Ly6G signals in the digested trachea. The result showed that Ly6G-containing trails were persistent in the infected trachea during the infection (Fig. 7A). The prolonged retention of CXCL12-containing Ly6G$^+$ trails was further confirmed by isolating the micro-sized trail particles using ultracentrifugation (*43*, *44*) and by immunostaining (fig. S13, B and C). These data demonstrated that the signature of deposited neutrophil trails (Ly6G) remained in the tissue until the host cleared an infection. That led us to hypothesize that the trails could provide prolonged local CXCL12 signals, even after the early marginated neutrophil pools were cleared from the infected trachea (Fig. 1B). To test this hypothesis, we measured the CXCL12 levels within the trachea. Whole-mount immunostainings of previously fixed and permeabilized mouse trachea cross sections revealed a lining of CXCL12 staining that was exclusively associated with the epithelium [day 0 (D0) in Fig. 7D], which suggested that the main source of CXCL12 production in the noninfected trachea is the epithelium (*30*). Upon influenza infection, the overall intensity of the CXCL12 signal was significantly increased in the WT trachea but not in the CXCL12 cKO mice (Fig. 7B). Data integration from multiple trachea sections revealed that the increase in CXCL12 signal during infection mainly occurred in the interstitial area (Fig. 7C). We calculated the colocalization coefficient to estimate how well the detected CXCL12 signals complied with the distribution of CXCL12-producing cells (CXCL12^{DsRed}) within the trachea during infection and found that the CXCL12 and CXCL12^{DsRed} signals were closely localized within the naïve trachea (D0 in Fig. 7, D and E), which suggested that the CXCL12 produced by epithelial cells remains in close proximity to the epithelium. However, the colocalization coefficient was dramatically decreased during influenza infection, although the total CXCL12 intensity increased (D4 and D8 in Fig. 7, D and E). These results indicate that either epithelial cell–derived CXCL12 diffuses widely in a tissue or that newly infiltrated migratory cells release and deposit CXCL12 in the interstitium. The depletion of neutrophils during infection prevented a decrease in the colocalization coefficient and abolished the increase in total CXCL12 intensity in the trachea (Fig. 7F). These findings suggested that newly recruited neutrophils during influenza infection are a main source of CXCL12.

Discussion

Recruiting leukocyte subtypes into peripheral tissues occurs in cascades, with the movement of one cell type following the remodeling of the local tissue environment, which induces and regulates the recruitment of the next wave of immune cells (*45*). Given the complexity and multifaceted pathophysiology of influenza infection and the high degree of redundancy of the homing receptors on the T cell surface, we hypothesized that specific combinations of local tissue milieus created by early innate responses regulate chemoattractant signals to control the recruitment of effector T cells to the infected sites. Indeed, influenza infection causes rapid expression of high levels of inflammatory chemokines, including CCL2, CCL3, CCL5, and CXCL10 (*46*). Furthermore, the newly activated effector CD8$^+$ T cells released from lymphoid organs express diverse inflammatory chemokine receptors, such as CCR2, CCR5, and CXCR3 (*47*). Therefore, it is possible that multiple chemokines cooperate temporally and spatially to finely control the movement of T cells and to prioritize their responses to the different chemokines present in the inflamed tissues. Alternatively, a hierarchy of chemokine response may exist, in which certain chemokines initially dominate other local chemokine signals; this signal is then desensitized, and the T cells follow a new gradient of local chemokines in a sequential manner. In both cases, inhibition of any single chemokine would cause a profound effect on T cell trafficking, as we have seen with CXCL12 inhibition.

The data presented here demonstrate that migrating neutrophils leave behind chemoattractant-containing trails, which result in the local accumulation of neutrophil-derived chemoattractant signals in inflamed tissues. As chemokines are small, diffusible molecules, perhaps these trails serve to package the chemoattractant so that it can be preserved and can survive severe

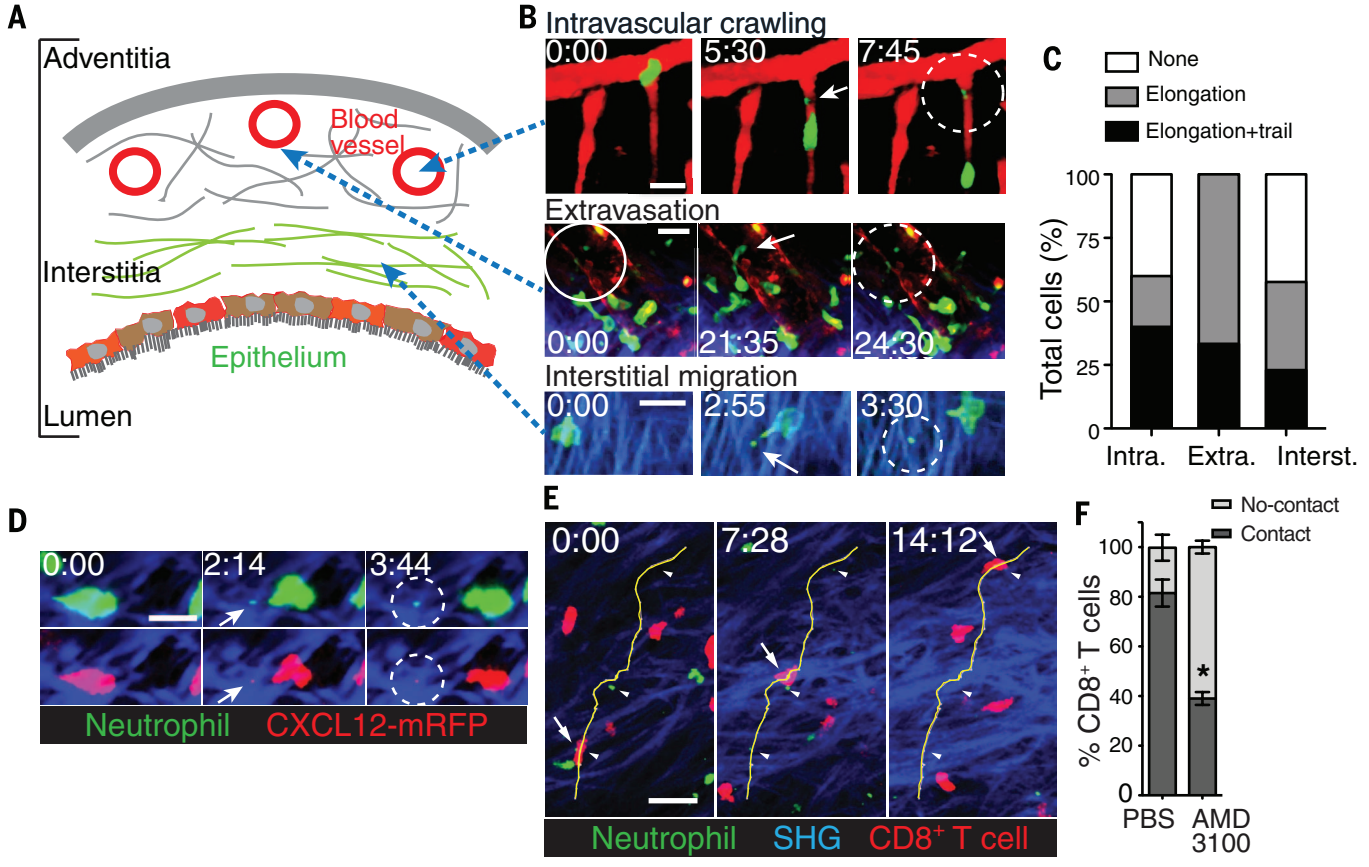


Fig. 6. Neutrophils leave CXCL12-trails in the infected trachea. (**A**) A cartoon illustrating trachea tissue structure. (**B**) Time-lapse images from IV-TPM showing neutrophils migrating in the vessel (top), during extravasation (middle), and in the interstitial space (bottom) of the influenza-infected trachea. Green, Ly6G-stained neutrophils; red, blood vessel (Texas Red dextran); blue, SHG. White arrows and circles indicate trail formations. Scale bar, 25 μm. (**C**) Neutrophils were analyzed to quantify trail generation in the each step of migration, including intravascular crawling (Intra.), extravasation (Extra.), and interstitial migration (Interst.). (**D**) Time-lapse images from IV-TPM showing $CXCL12^+$ trail generation during neutrophil migration in the mouse ear. Green, Gr1-stained neutrophils; red, CXCL12-mRFP; blue, SHG. White arrows and circles indicate trail formations. Scale bar, 20 μm. (**E**) Time-lapse images from IV-TPM showing $CD8^+$ T cell migration following neutrophil trails. $CD8^+$ T cells (red) and neutrophils (green) were intradermally transferred to the mouse ear 3 hours before imaging. A representative of time-lapse images was shown from five independent experiments. Yellow line indicates T cell migration track. Blue, SHG. Scale bar, 30 μm. (**F**) The percentage of total $CD8^+$ T cells that make at least one contact with a neutrophil trail during each imaging (>20 min) was quantified. $CD8^+$ T cells were pretreated with or without AMD3100 before imaging (n = 5 mice, $^*P < 0.01$ compared with PBS, Mann-Whitney test).

mechanical perturbation during inflammation (*48*); otherwise, it would be present only transiently on cell surfaces and tissue matrix or immediately diffuse away from the site.

Both $CD8^+$ T cell recruitment and virus clearance were affected in the CXCL12 cKO mice in spite of the presence of epithelial cell–derived CXCL12, which indicates that this is not the relevant source of the chemokine during the infection. On the basis of our data, we concluded that CXCL12 derived from the epithelial cells remained close to the epithelium, whereas CXCL12 derived from neutrophils was the main source of CXCL12 in the tissue interstitium during infection. It is interesting that CXCL12 expressed by the epithelial cells remains in close proximity to the epithelium and does not diffuse widely to the interstitium. This may be due, at least in part, to high expression of CXCR7 (another high-affinity receptor for CXCL12) in epithelial cells (*49*). CXCR7 acts as a scavenger receptor for CXCL12 by sequestering and reducing the level of CXCL12 at tissues to maintain a chemotactic gradient (*50*, *51*).

Unlike the observations in our in vitro study, we saw that neutrophil trails were sparsely distributed and rather rarely shown in the in vivo imaging. We previously showed that microparticles generated from neutrophil trails had multiple spherical shapes ranging from 100 to 500 nm in diameter (*38*). At present, it is not possible to detect small microparticles (<0.5 μm) in vivo because of the resolution limit of multiphoton intravital microscopy. Therefore, it is tempting to speculate that we only show big neutrophil microparticles (bigger than 500 nm in diameter) in our in vivo images, whereas small, undetected particles still can guide $CD8^+$ T cell migration.

Neutrophils can express and/or produce numerous cytokines (including interferon-γ) that can alter local $CD8^+$ T cell activation. Indeed, the virus-specific $CD8^+$ T cells in the influenza-infected airway displayed impaired cytokine production and cytotoxic effector function in the absence of neutrophils without significant changes in influenza virus–specific antigen presentation or $CD8^+$ T cell priming in the secondary lymphoid organs (*21*). Together with our results, these data strongly suggest that the absence of neutrophils not only impairs the establishment of a sustained $CD8^+$ T cell population at the site of infection through altered $CD8^+$ T cell traffic and localization, but it also greatly diminished the effector function of the remaining $CD8^+$ T cells. Now, however, a causal relation between neutrophil-mediated $CD8^+$ T cells migration and activation of local $CD8^+$ T cell effector functions is unknown.

Materials and methods

Antibodies and reagents

Recombinant mouse proteins (ICAM-1, CXCL12, CCL2, CCL6, CCL12, CCL22, CCL27, and TNFα) and carboxyfluorescein (CFS)–, phycoerythrin (PE)–, or allophycoerythrin (APC)–conjugated CXCL12-specific Ab (79018), APC-conjugated CCR1-specific Ab (643854), APC-conjugated CCR2-specific Ab (475301), APC-conjugated CXCR2-specific Ab (242216), and Ab against myeloperoxidase (392105) were purchased from R&D systems. PE-conjugated

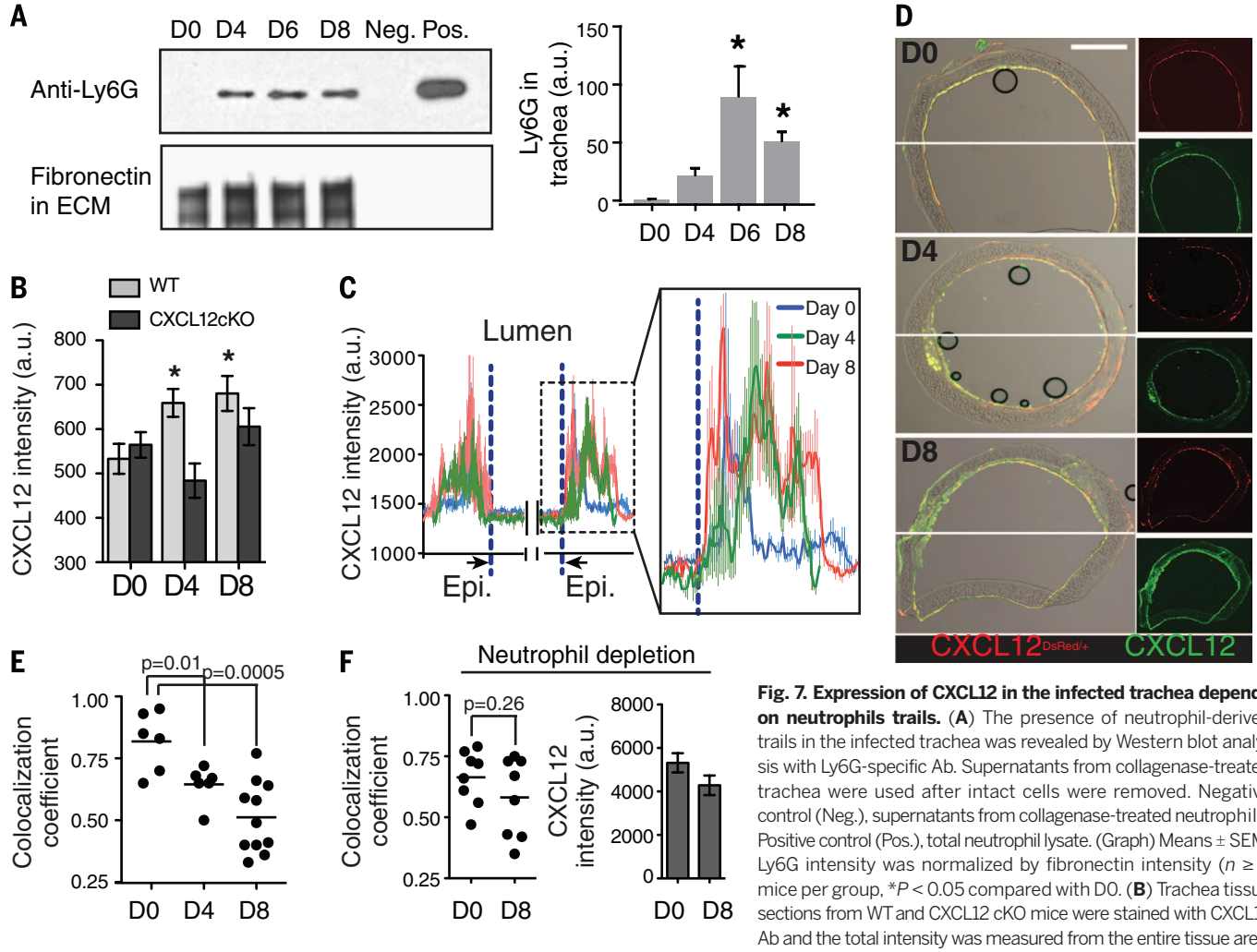


Fig. 7. Expression of CXCL12 in the infected trachea depends on neutrophils trails. (**A**) The presence of neutrophil-derived trails in the infected trachea was revealed by Western blot analysis with Ly6G-specific Ab. Supernatants from collagenase-treated trachea were used after intact cells were removed. Negative control (Neg.), supernatants from collagenase-treated neutrophils. Positive control (Pos.), total neutrophil lysate. (Graph) Means ± SEM. Ly6G intensity was normalized by fibronectin intensity ($n \geq 3$ mice per group, $^*P < 0.05$ compared with D0. (**B**) Trachea tissue sections from WT and CXCL12 cKO mice were stained with CXCL12 Ab and the total intensity was measured from the entire tissue area. (Graph) The mean fluorescent intensities [arbitrary units (a.u.)/μm^2, means ± SEM) of CXCL12 from each tissue section ($n \geq 2$ sections per mouse, $N = 3$ to 5 mice per group, $^*P < 0.05$ compared with D0). (**C**) CXCL12 line intensity profiles across the trachea were obtained (white lines in Fig. 7D) and plotted (*y* axis, CXCL12 intensity; *x* axis, line distance; Epi, epithelium; means ± SEM; $n \geq 2$ sections per mouse, $N = 3$ to 5 mice per group). (**D** and **E**) CXCL12 immunostaining (green) of $CXCL12^{DsRed}$ (red) trachea sections on the indicated days postinfection (D) and colocalization (Pearson's coefficient) of CXCL12 (green) and $CXCL12^{DsRed}$ cells (red) (E) ($n \geq 2$ sections per mouse, $n = 3$ mice per group). Scale bar, 200 μm. (**F**) (Left) Colocalization of CXCL12 (green) and $CXCL12^{DsRed}$ cells (red) and (right) the total CXCL12 intensity from the trachea sections on D0 and D8 postinfection with neutrophil depletion ($n = 2$ sections per mouse, $n = 4$ mice per group). (A) and (B) Ly6G in trachea and CXCL12 intensity, respectively, were analyzed with Kruskal-Wallis followed by Dunn's posttest. (E) and (F) Colocalization coefficients were analyzed with nonparametric Mann-Whitney test.

CXCR4-specific Ab (2B11) and Alexa Fluor 647–conjugated CD8-specific Ab (53-6.7) were purchased from eBioscience. FITC-conjugated, APC-conjugated, or unconjugated Ly6G-specific Ab (1A8), FITC- or Alexa Fluor 647–conjugated Gr1-specific Ab (RB6-8C5), PE-conjugated CCL2-specific Ab (2H5), Ab against CD11a integrin (M17/4), Ab against CD11b integrin (M1/70), Ab against β1 integrin (HMB1-1), rat IgG2a, and rat IgG2b antibodies were purchased from Biolegend. Ab against Ly6G (1A8) for neutrophil depletion and rat IgG2a control Ab (2A3) were purchased from BioXcell. Abs against fibronectin (96-23750) and against CXCR1 (ab10400) were from Abcam. Alexa Fluor 488– or Alexa Fluor 647–conjugated F4/80-specific Ab (BM8) were purchased from Invitrogen. CD3e-specific Ab (145-2C11), CD28-specific Ab (37.51) and FITC-conjugated CD45-specific Ab (553772) were purchased from BD Bioscience. Ab against type IV collagen (1340-01) was purchased from Southern Biotechnology. The Ab to influenza A virus nucleoprotein (NP) conjugated with FITC was purchased from ViroStat. Ab against CXCL12 (C-19), Ab against matrix metalloproteinase 9 (sc-6841), and Ab against lactoferrin (sc-25622) were from Santa Cruz Biotechnology. Horseradish peroxidase–conjugated Abs against mouse IgG or rat IgG, and Cy3-conjugated Ab against goat IgG antibodies were from Jackson ImmunoResearch. Heparan sulfate; 4′,6′-diamidino-2-phenylindole (DAPI); Texas Red–conjugated dextran; fMLP; and saponin were purchased from Sigma Aldrich. AMD3100 was purchased from Tocris. MMP-2/9 inhibitor I was from Calbiochem (*25*). A chemiluminescent reagent (Supersignal West Pico) was from Thermo Scientific.

Mice

C57BL/6, $Tyr^{c\text{-}2J/c\text{-}2J}$ (B6-Albino), and $CXCL12^{flox/flox}$ mice were purchased from the Jackson Laboratory. The $CXCL12^{DsRed}$ mouse was the gift from Morrison (*29*). OT-I TCR transgenic mouse was crossed with *C57BL/6-Tg(CAG-EGFP)1Osb/J* (Jackson Laboratory) for enhanced green fluorescent protein–expressing OT-1 strain ($OT\text{-}1^{GFP}$). $CXCL12^{flox/flox}$ was crossed with elastase2 ($Ela)^{Cre/+}$ for granulocyte-specific knockout of CXCL12, and $CXCL12^{flox/flox}Ela^{Cre/+}$ mice were used for experiments with their littermates $CXCL12^{flox/flox}Ela^{+/+}$ or $Ela^{Cre/+}$ as a control group. Genotyping for each strain was performed according to the corresponding reference (*29*). All mice were maintained in a pathogen-free environment of the University of Rochester animal facility, and the animal experiments were approved by the University Committee on Animal Resources at the University of Rochester (Rochester, NY, USA).

Influenza virus and neutrophil depletion

Male mice 8 to 12 weeks old were anesthetized using Avertin (2,2,2-tribromoethanol) and

intranasally inoculated with 30 μl of influenza A virus suspension (HKx31, 3×10^4 plaque-forming units and HKx31-OVA, $3 \times 10^{3.25}$ of the 50% effective egg-infective dose). For neutrophil depletion, 500 μg of Ly6G Ab (1A8) was intraperitoneally injected into a mouse a day before infection and on day +1, +3, and +5 postinfection, and isotype control IgG (rat IgG2a) was similarly injected into a control group. For $CD8^+$ T cell imaging in vivo, splenocytes (2 million) from $OT\text{-}1^{GFP}$ mouse were injected into a recipient mouse via tail vein 24 hours before infection with HKx31-OVA virus.

Viral nucleoprotein mRNA levels in trachea

Total RNA from trachea was prepared using RNeasy kit (Qiagen), and the first-strand cDNA was synthesized using Moloney murine leukemia virus reverse transcriptase (Promega) and oligo-$(dT)_{18}$. Quantitative reverse transcription polymerase chain reaction (qRT-PCR) was performed using SYBR green reagent (BioRad) and the following primers: viral nucleoprotein gene, forward 5′-TTTTCTAGCACGGTCTGCACTCATATTG-3′ and reverse 5′-CTTGGCTGTTTTGAAGCAGTCTGAAAG-3′, and β-actin, forward 5′-GTCCCTCACCCTCCCAAAG-3′ and reverse 5′-GCTGCCTCAACACCTCAACC-3′. The levels of viral nucleoprotein mRNA were normalized by those of the actin mRNA.

Leukocytes preparation

Neutrophils were freshly prepared from mouse bone marrow using EasySep Neutrophil enrichment kit (STEMCELL Technologies). $CD4^+$ and $CD8^+$ T lymphocytes from spleen and lymph node were isolated using a negative selection method and activated by culturing them on a CD3 (10 μg/ml) Ab-coated dish in the presence of CD28 (2 μg/ml) and 10 unit/ml interleukin-2 (IL-2). F4/80-positive mouse monocytes were isolated from blood with fluorescence-activated cell sorting (FACS).

In vitro migration

Cell migration chambers (Millicell EZ slide eight-well glass from Millipore or Delta T dish from Biotech) were prepared by coating their glass bottoms with 10 μg/ml recombinant mouse ICAM-1 or mouse fibronectin in phosphate-buffered saline (PBS) with or without indicated chemokines. For in vitro live cell imaging, leukocytes were placed in L15 medium (Invitrogen) in the chamber at 37°C, and video microscopy was conducted using TE2000-U microscope (Nikon). Images were acquired using a ×10, ×20, or ×60 magnification objective with the appropriate filters. Migration analysis and image processes were performed using NIS (Nikon) or Volocity software (PerkinElmer). For integrin blocking, neutrophils were preincubated with the indicated blocking antibodies (10 μg/ml) for 10 min and allowed to crawl in the presence of the same Ab. For migration under shear, fMLP-stimulated neutrophils stained with FITC-Ly6G were allowed to crawl in ICAM-1 coated μ-Slide I 0.8 Luer flow chamber (Ibidi), and flow was created by a syringe pump. For chemotaxis assay, the chamber (Millicell EZ slide four-well glass, Millipore) was coated with 5 μg/ml fibronectin and 0.25 μg/ml ICAM-1 overnight. Next day, the chamber was washed, and the culture insert from a wound-healing dish (30 μ-Dish culture insert, Ibidi) was placed. fMLP-stimulated neutrophils were allowed to crawl in the left well and washed after 20 min. $CD8^+$ T cells were then added to the right well and allowed to adhere for 10 min. Then, the insert was removed and T cell migration was tracked for 1 hour.

For transwell assay, 1×10^4/100 μl of T cells were added in 5-μm pore size, polycarbonate 24-well tissue culture inserts (Costar, Cambridge, MA), and 600 μl of medium with or without a chemoattractant (CXCL12 or fMLP) was added to the lower well. After 3 hours, counting beads were added to the lower chamber and collected for flow cytometric analysis. Cell number was determined relative to the number of beads collected. All points were performed in triplicate for multiple mice ($n \geq 3$).

Immunofluorescence microscopy

For immunofluorescence microscopy of trachea, frozen trachea sections of 10-μm thickness were prepared and stained with the indicated antibodies. Superblock (Thermo Scientific) was used as a blocker. Quantitative analysis of fluorescent signals was performed using NIS (Nikon) or Autoquant X software (MediaCybernetics). For immunofluorescence microscopy of neutrophils, cells were fixed with 2% paraformaldehyde and stained with the indicated antibodies in the presence of 0.025% saponin.

Flow cytometry

The trachea was digested with 1 mg/ml collagenase II (Gibco) for 1 hour at 37°C with frequent agitation, and the digests were filtered through 70-μm strainer (BD Falcon). Single-cell populations from lymph nodes, spleen, or lung were obtained by squeezing the tissue through a 40-μm strainer, followed by lysis of red blood cells. The isolated cells were stained with the indicated antibodies or APC-conjugated NP tetramer (NIH Tetramer Core Facility) and analyzed with FACS Caliber (BD biosciences). For intracellular staining, cells were fixed and 0.1% Tween 20 was included during the staining and washing.

IV-TPM

Each mouse was anesthetized by intraperitoneally injecting pentobarbital sodium salt [65 mg per kg of body weight (mg/kg)]. The trachea was exteriorized, and a small cut was made on the frontal wall to insert an 18G blunt-end cannula. To discern the border of epithelium in the luminal side, the cannula was painted red. Ly6G-FITC Ab (20 μg) and Texas Red–conjugated dextran (20 mg/kg) were injected via femoral vein to stain the neutrophils and blood vessels, respectively. The mouse was subsequently placed on a custom-designed platform for imaging (fig. S2). For IV-TPM of the mouse ear, 5×10^4 neutrophils with or without 5×10^4 $CD8^+$ T cells in 5 μl PBS were intradermally injected into $Tyr^{c\text{-}2J/c\text{-}2J}$ (B6-Albino) mouse 3 hours before imaging. For the control, cells (1×10^7 cells/ml PBS) were treated with AMD3100 (25 μM) for 30 min before intradermal injection. To visualize $CD8^+$ T cells and neutrophils simultaneously, $CD8^+$ T cells were prepared from *C57BL/6-Tg(CAG-EGFP)1Osb/J* mouse, and WT neutrophils were stained with red dye (CMTPX, Life Technologies). The anesthetized mouse was laid in a lateral recumbent position on a custom-designed platform to expose the ventral side of the ear pinna for imaging. Further anesthesia was maintained with isoflurane for restraint and to avoid psychological stress and pain to the animal during imaging. The mouse was imaged with FV1000-AOM multiphoton system using ×25 NA1.05 objective (Olympus). During imaging, both mouse body and the objective were maintained at 37°C. For whole-mount tissue imaging, the trachea was fixed with paraformaldehyde, blocked, and permeabilized with Superblock (Thermo Scientific) containing 0.1% Tween 20. CXCL12 was stained with 0.5 μg/ml CXCL12-specific Ab (C-19; Santa Cruz Biotechnology) overnight at 4°C. Imaging data were processed using Volocity (PerkinElmer) and Image J.

Scanning EM

Neutrophils migrating on ICAM-1–coated glass were fixed with 2.5% glutaraldehyde and processed further for scanning EM in the Electron Microscope Research Core at the University of Rochester.

Chemokine microarray

To collect neutrophil trails, neutrophils were allowed to migrate on ICAM-1–coated glass in the presence of 2 μM fMLP for 1 hour. Then, neutrophil cell bodies were removed, and the remaining trails were lysed by adding 1% Triton-containing PBS supplemented with 1 mM EDTA and protease inhibitor cocktail (Roche). The whole-cell neutrophil lysate was prepared in the same lysis buffer. The amount and quality of extracted proteins were checked by NanoDrop (Thermo Scientific) and silver staining after gel electrophoresis of proteins. The microarray was carried out using Proteome Profiler Mouse chemokine and cytokine array (R&D systems) according to the manufacturer's instruction. This Ab array detects CCL11, CCL12, CCL2, CCL21, CCL22, CCL27, CCL28, CCL3/4, CCL5, CCL6, CCL8, CCL9, chemerin, complement component C5, CX3CL1, CXCL1, CXCL10, CXCL11, CXCL12, CXCL13, CXCL16, CXCL2, LIX, CXCL9, and IL-16.

Western blot analysis of trails

The trachea was digested with collagenase, and intact cells were removed by centrifugation at 1000*g* for 30 min before Western blot analysis. To collect neutrophil trails directly from the trachea, the supernatant was further centrifuged at 18,000*g* for 1 hour. For Western blotting, the membrane was blocked with a blocker (3% bovine serum albumin, 0.1% Tween 20 in PBS) for 30 min after proteins were transfer from a gel and incubated with 0.5 μg/ml of 1A8 Ab for 1 hour at room temperature. Then, the membrane was incubated with horseradish peroxidase–conjugated rat IgG–specific Ab (0.4 μg/ml) for 1 hour, and

the protein was detected using a chemiluminescent reagent. The intensity of Ly6G protein band was normalized by that of fibronectin.

Enzyme-linked immunosorbent assay (ELISA)

Neutrophils (5×10^6 cells) were stimulated by incubating them in L15 medium containing indicated concentrations of TNFα or PMA at 37°C for 1 hour. The amount of CXCL12 in the supernatants was measured using Quantikine ELISA (R&D systems).

REFERENCES AND NOTES

1. J. W. Griffith, C. L. Sokol, A. D. Luster, Chemokines and chemokine receptors: Positioning cells for host defense and immunity. *Annu. Rev. Immunol.* **32**, 659–702 (2014). doi: 10.1146/annurev-immunol-032713-120145; pmid: 24655300
2. W. W. Agace, Tissue-tropic effector T cells: Generation and targeting opportunities. *Nat. Rev. Immunol.* **6**, 682–692 (2006). doi: 10.1038/nri1869; pmid: 16932753
3. S. G. Ward, F. M. Marelli-Berg, Mechanisms of chemokine and antigen-dependent T-lymphocyte navigation. *Biochem. J.* **418**, 13–27 (2009). doi: 10.1042/BJ20081969; pmid: 19159344
4. I. C. Schneider, J. M. Haugh, Mechanisms of gradient sensing and chemotaxis: Conserved pathways, diverse regulation. *Cell Cycle* **5**, 1130–1134 (2006). doi: 10.4161/cc.5.11.2770; pmid: 16760661
5. P. Scapini *et al*., The neutrophil as a cellular source of chemokines. *Immunol. Rev.* **177**, 195–203 (2000). doi: 10.1034/j.1600-065X.2000.17706.x; pmid: 11138776
6. A. D. Luster, The role of chemokines in linking innate and adaptive immunity. *Curr. Opin. Immunol.* **14**, 129–135 (2002). doi: 10.1016/S0952-7915(01)00308-9; pmid: 11790543
7. J. R. Groom *et al*., CXCR3 chemokine receptor-ligand interactions in the lymph node optimize CD4+ T helper 1 cell differentiation. *Immunity* **37**, 1091–1103 (2012). doi: 10.1016/j.immuni.2012.08.016; pmid: 23123063
8. A. D. Luster, R. Alon, U. H. von Andrian, Immune cell migration in inflammation: Present and future therapeutic targets. *Nat. Immunol.* **6**, 1182–1190 (2005). doi: 10.1038/ni1275; pmid: 16369557
9. S. J. Galli, N. Borregaard, T. A. Wynn, Phenotypic and functional plasticity of cells of innate immunity: Macrophages, mast cells and neutrophils. *Nat. Immunol.* **12**, 1035–1044 (2011). doi: 10.1038/ni.2109; pmid: 22012443
10. C. Nathan, Neutrophils and immunity: Challenges and opportunities. *Nat. Rev. Immunol.* **6**, 173–182 (2006). doi: 10.1038/nri1785; pmid: 16498448
11. A. Mantovani, M. A. Cassatella, C. Costantini, S. Jaillon, Neutrophils in the activation and regulation of innate and adaptive immunity. *Natl. Rev.* **11**, 519–531 (2011). doi: 10.1038/nri3024; pmid: 21785456
12. C. Summers *et al*., Neutrophil kinetics in health and disease. *Trends Immunol.* **31**, 318–324 (2010). doi: 10.1016/j.it.2010.05.006; pmid: 20620114
13. N. Borregaard, O. E. Sørensen, K. Theilgaard-Mönch, Neutrophil granules: A library of innate immunity proteins. *Trends Immunol.* **28**, 340–345 (2007). doi: 10.1016/j.it.2007.06.002; pmid: 17627888
14. T. S. Olson, K. Ley, Chemokines and chemokine receptors in leukocyte trafficking. *Am. J. Physiol. Regul. Integr. Comp. Physiol.* **283**, R7–R28 (2002). doi: 10.1152/ajpregu.00738.2001; pmid: 12069927
15. M. Pelletier *et al*., Evidence for a cross-talk between human neutrophils and Th17 cells. *Blood* **115**, 335–343 (2010). doi: 10.1182/blood-2009-04-216085; pmid: 19890092
16. N. Grabie *et al*., Neutrophils sustain pathogenic CD8+ T cell responses in the heart. *Am. J. Pathol.* **163**, 2413–2420 (2003). doi: 10.1016/S0002-9440(10)63596-1; pmid: 14633613
17. R. M. de Oca *et al*., Polymorphonuclear neutrophils are necessary for the recruitment of CD8(+) T cells in the liver in a pregnant mouse model of *Chlamydophila abortus* (*Chlamydia psittaci* serotype 1) infection. *Infect. Immun.* **68**, 1746–1751 (2000). doi: 10.1128/IAI.68.3.1746-1751.2000; pmid: 10679002
18. T. Engeman, A. V. Gorbachev, D. D. Kish, R. L. Fairchild, The intensity of neutrophil infiltration controls the number of antigen-primed CD8 T cells recruited into cutaneous antigen challenge sites. *J. Leukoc. Biol.* **76**, 941–949 (2004). doi: 10.1189/jlb.0304193; pmid: 15328335
19. S. J. Ray *et al*., The collagen binding alpha1beta1 integrin VLA-1 regulates CD8 T cell-mediated immune protection against heterologous influenza infection. *Immunity* **20**, 167–179 (2004). doi: 10.1016/S1074-7613(04)00021-4; pmid: 14975239
20. T. Gebhardt *et al*., Memory T cells in nonlymphoid tissue that provide enhanced local immunity during infection with herpes simplex virus. *Nat. Immunol.* **10**, 524–530 (2009). doi: 10.1038/ni.1718; pmid: 19305395
21. M. D. Tate, A. G. Brooks, P. C. Reading, J. D. Mintern, Neutrophils sustain effective CD8(+) T-cell responses in the respiratory tract following influenza infection. *Immunol. Cell Biol.* **90**, 197–205 (2012). doi: 10.1038/icb.2011.26; pmid: 21483446
22. P. G. Thomas *et al*., An unexpected antibody response to an engineered influenza virus modifies CD8+ T cell responses. *Proc. Natl. Acad. Sci. U.S.A.* **103**, 2764–2769 (2006). doi: 10.1073/pnas.0511185103; pmid: 16473934
23. S. Chakrabarti, K. D. Patel, Matrix metalloproteinase-2 (MMP-2) and MMP-9 in pulmonary pathology. *Exp. Lung Res.* **31**, 599–621 (2005). doi: 10.1080/01902149044232; pmid: 16019990
24. L. M. Bradley, M. F. Douglass, D. Chatterjee, S. Akira, B. J. Baaten, Matrix metalloprotease 9 mediates neutrophil migration into the airways in response to influenza virus-induced toll-like receptor signaling. *PLOS Pathog.* **8**, e1002641 (2012). doi: 10.1371/journal.ppat.1002641; pmid: 22496659
25. Y. Tamura *et al*., Highly selective and orally active inhibitors of type IV collagenase (MMP-9 and MMP-2): *N*-Sulfonylamino acid derivatives. *J. Med. Chem.* **41**, 640–649 (1998). doi: 10.1021/jm9707582; pmid: 9484512
26. A. Gehad *et al*., Differing requirements for CCR4, E-selectin, and $\alpha_4\beta_1$ for the migration of memory CD4 and activated T cells to dermal inflammation. *J. Immunol.* **189**, 337–346 (2012). doi: 10.4049/jimmunol.1102315; pmid: 22664869
27. S. Hudak *et al*., Immune surveillance and effector functions of CCR10(+) skin homing T cells. *J. Immunol.* **169**, 1189–1196 (2002). doi: 10.4049/jimmunol.169.3.1189; pmid: 12133939
28. M. Kucia *et al*., CXCR4-SDF-1 signalling, locomotion, chemotaxis and adhesion. *J. Mol. Histol.* **35**, 233–245 (2004). doi: 10.1023/B:HIJO.0000032355.66152.b8; pmid: 15339043
29. L. Ding, S. J. Morrison, Haematopoietic stem cells and early lymphoid progenitors occupy distinct bone marrow niches. *Nature* **495**, 231–235 (2013). doi: 10.1038/nature11885; pmid: 23434755
30. B. N. Gomperts *et al*., Circulating progenitor epithelial cells traffic via CXCR4/CXCL12 in response to airway injury. *J. Immunol.* **176**, 1916–1927 (2006). doi: 10.4049/jimmunol.176.3.1916; pmid: 16424223
31. G. S. Campanella *et al*., Oligomerization of CXCL10 is necessary for endothelial cell presentation and in vivo activity. *J. Immunol.* **177**, 6991–6998 (2006). doi: 10.4049/jimmunol.177.10.6991; pmid: 17082614
32. M. Weber *et al*., Interstitial dendritic cell guidance by haptotactic chemokine gradients. *Science* **339**, 328–332 (2013). doi: 10.1126/science.1228456; pmid: 23329049
33. P. W. Kriebel, V. A. Barr, E. C. Rericha, G. Zhang, C. A. Parent, Collective cell migration requires vesicular trafficking for chemoattractant delivery at the trailing edge. *J. Cell Biol.* **183**, 949–961 (2008). pmid: 19047467
34. M. Pruenster *et al*., The Duffy antigen receptor for chemokines transports chemokines and supports their promigratory activity. *Nat. Immunol.* **10**, 101–108 (2009). pmid: 19060902
35. O. Soehnlein, A. Zernecke, C. Weber, Neutrophils launch monocyte extravasation by release of granule proteins. *Thromb. Haemost.* **102**, 198–205 (2009). pmid: 19652869
36. S. N. Mueller, Effector T-cell responses in non-lymphoid tissues: Insights from in vivo imaging. *Immunol. Cell Biol.* **91**, 290–296 (2013). doi: 10.1038/icb.2012.75; pmid: 23295362
37. T. H. Harris *et al*., Generalized Lévy walks and the role of chemokines in migration of effector CD8+ T cells. *Nature* **486**, 545–548 (2012). pmid: 22722867
38. Y. M. Hyun *et al*., Uropod elongation is a common final step in leukocyte extravasation through inflamed vessels. *J. Exp. Med.* **209**, 1349–1362 (2012). doi: 10.1084/jem.20111426; pmid: 22711877
39. M. Sperandio *et al*., P-selectin glycoprotein ligand-1 mediates L-selectin-dependent leukocyte rolling in venules. *J. Exp. Med.* **197**, 1355–1363 (2003). doi: 10.1084/jem.20021854; pmid: 12756271
40. N. C. Peters *et al*., In vivo imaging reveals an essential role for neutrophils in leishmaniasis transmitted by sand flies. *Science* **321**, 970–974 (2008). doi: 10.1126/science.1159194; pmid: 18703742
41. D. S. Mithal, D. Ren, R. J. Miller, CXCR4 signaling regulates radial glial morphology and cell fate during embryonic spinal cord development. *Glia* **61**, 1288–1305 (2013). doi: 10.1002/glia.22515; pmid: 23828719
42. M. G. Overstreet *et al*., Inflammation-induced interstitial migration of effector CD4□ T cells is dependent on integrin α_V. *Nat. Immunol.* **14**, 949–958 (2013). doi: 10.1038/ni.2682; pmid: 23933892
43. J. Dalli *et al*., Annexin 1 mediates the rapid anti-inflammatory effects of neutrophil-derived microparticles. *Blood* **112**, 2512–2519 (2008). doi: 10.1182/blood-2008-02-140533; pmid: 18594025
44. E. Pluskota *et al*., Expression, activation, and function of integrin $\text{alpha}_M\text{beta}_2$ (Mac-1) on neutrophil-derived microparticles. *Blood* **112**, 2327–2335 (2008). doi: 10.1182/blood-2007-12-127183; pmid: 18509085
45. C. D. Sadik, A. D. Luster, Lipid-cytokine-chemokine cascades orchestrate leukocyte recruitment in inflammation. *J. Leukoc. Biol.* **91**, 207–215 (2012). doi: 10.1189/jlb.0811402; pmid: 22058421
46. D. Damjanovic, C.-L. Small, M. Jeyanathan, S. McCormick, Z. Xing, Immunopathology in influenza virus infection: Uncoupling the friend from foe. *Clin. Immunol.* **144**, 57–69 (2012). doi: 10.1016/j.clim.2012.05.005; pmid: 22673491
47. S. K. Bromley, T. R. Mempel, A. D. Luster, Orchestrating the orchestrators: Chemokines in control of T cell traffic. *Nat. Immunol.* **9**, 970–980 (2008). doi: 10.1038/ni.f.213; pmid: 18711434
48. R. Majumdar, M. Sixt, C. A. Parent, New paradigms in the establishment and maintenance of gradients during directed cell migration. *Curr. Opin. Cell Biol.* **30**, 33–40 (2014). doi: 10.1016/j.ceb.2014.05.010; pmid: 24959970
49. K. Balabanian *et al*., The chemokine SDF-1/CXCL12 binds to and signals through the orphan receptor RDC1 in T lymphocytes. *J. Biol. Chem.* **280**, 35760–35766 (2005). doi: 10.1074/jbc.M508234200; pmid: 16107333
50. B. Boldajipour *et al*., Control of chemokine-guided cell migration by ligand sequestration. *Cell* **132**, 463–473 (2008). doi: 10.1016/j.cell.2007.12.034; pmid: 18267076
51. C. Dambly-Chaudière, N. Cubedo, A. Ghysen, Control of cell migration in the development of the posterior lateral line: Antagonistic interactions between the chemokine receptors CXCR4 and CXCR7/RDC1. *BMC Dev. Biol.* **7**, 23 (2007). doi: 10.1186/1471-213X-7-23; pmid: 17394634

ACKNOWLEDGMENTS

We thank A. Gaylo, Y. Xu, B. Walling, J. Wong, N. Laniewski, H. Yang, and U. Sivagnanalingam for their technical assistance and comments on manuscript, and thank S. Morrison for $\text{CXCL12}^{\text{DsRed}}$ mouse. The data presented in this manuscript are tabulated in the main paper and in the supplementary materials. K.L. conducted most of the experiments and performed most of the statistical analysis of the data; Y.-M.H. and K.L.-E. designed the mouse trachea IV-TPM protocol and Y.-M.H. performed in vivo imaging and helped in the data analysis; K.L.-E., T.C., and S.B. helped in the virus infection and mouse T cell preparations. T.C. performed the transwell assay. R.M. provided CXCL12-mRFP expressing mice. D.J.T. designed the influenza-infection model of mouse trachea. M.K. conceived, designed, and directed the study. K.L. and M.K. wrote the manuscript with suggestions from all authors. This project was financially supported through grants from the NIH (HL087088 to M.K. and AI102851 to M.K. and D.J.T., and HHSN272201400005C to D.J.T.), WCU Neurocytomics Program grant, Seoul National University Graduate School, Seoul, South Korea to M.K., and the American Heart Association (11SDG7520018 to Y-M.H.). The authors have no conflicting financial interests.

SUPPLEMENTARY MATERIALS

www.sciencemag.org/content/349/6252/aaa4352/suppl/DC1
Figs. S1 to S13
Movies S1 to S10

5 December 2014; accepted 30 June 2015
10.1126/science.aaa4352

RESEARCH ARTICLE

PLANT SCIENCE

Monodehydroascorbate reductase mediates TNT toxicity in plants

Emily J. Johnston,[1]* Elizabeth L. Rylott,[1]*† Emily Beynon,[1] Astrid Lorenz,[1] Victor Chechik,[2] Neil C. Bruce[1]†

The explosive 2,4,6-trinitrotoluene (TNT) is a highly toxic and persistent environmental pollutant. Due to the scale of affected areas, one of the most cost-effective and environmentally friendly means of removing explosives pollution could be the use of plants. However, mechanisms of TNT phytotoxicity have been elusive. Here, we reveal that phytotoxicity is caused by reduction of TNT in the mitochondria, forming a nitro radical that reacts with atmospheric oxygen, generating reactive superoxide. The reaction is catalyzed by monodehydroascorbate reductase 6 (MDHAR6), with *Arabidopsis* deficient in MDHAR6 displaying enhanced TNT tolerance. This discovery will contribute toward the remediation of contaminated sites. Moreover, in an environment of increasing herbicide resistance, with a shortage in new herbicide classes, our findings reveal MDHAR6 as a valuable plant-specific target.

Recalcitrant to degradation, 2,4,6-trinitrotoluene (TNT) is a worldwide pollutant, contaminating manufacturing waste sites, mines, current and former conflict zones, and military land (*1*); the U.S. Department of Defense has an estimated 10 million hectares of operational ranges contaminated with munitions constituents (*2*). Rated a class C carcinogen by the Environmental Protection Agency, TNT has toxic effects on all living organisms: in animals, causing hepatitis, anemia, hyperplasia of bone marrow, and cataracts (*3*), and in soil, severely affecting microbial diversity (*4*) and the establishment of vegetation (*5*). In plants, the majority of TNT remains in the roots (*6*), where growth and development is inhibited, reducing overall biomass (*5*).

Despite these inhibitory effects, TNT can be detoxified by plants to a limited extent (*7*–*9*), and there is great interest in the development of plant-based explosives remediation (*10*). Seeking to identify plant TNT-detoxifying enzymes, we screened Weigel activation–tagged *Arabidopsis thaliana* plant lines (*11*) for greater root growth in the presence of TNT and isolated a mutant with enhanced TNT tolerance. Through outcrossing with single-nucleotide polymorphism analysis, bulk segregant analysis, and sequencing of candidate genes, this phenotype was mapped to *mdhar6-1* (At1g63940) (fig. S1). The *mdhar6-1* mutant was found to have a thymine deletion 2181 bases from the start codon, introducing a frame shift and an early stop codon and predicted to truncate over a third of the protein. Two further *mdhar6* mutant lines were sourced (Fig. 1, A and B, and fig. S1), and all three had enhanced shoot and root biomass when grown in TNT-treated soil (Fig. 1, A and B, and fig. S2).

[1]Centre for Novel Agricultural Products, Department of Biology, University of York, York YO10 5DD, UK. [2]Department of Chemistry, University of York, York YO10 5DD, UK.
*These authors contributed equally to this work. †Corresponding author. E-mail: liz.rylott@york.ac.uk (E.L.R.); neil.bruce@york.ac.uk (N.C.B.)

The role of monodehydroascorbate reductase (MDHAR)

The finding that the TNT tolerant line had a frame shift in *MDHAR6*, rather than overexpression of a TNT-detoxifying enzyme, was surprising, because MDHARs are considered to protect plants from oxidative stress by recycling the antioxidant ascorbic acid; MDHARs are flavin adenine dinucleotide–dependent oxidoreductases that reduce monodehydroascorbate (MDA), the free radical oxidation product of ascorbic acid (*12*, *13*). Analysis of the *Arabidopsis* genome has revealed five MDHARs; MDHAR1 (At3g52880) and 4 (At3g27820) are targeted to peroxisome matrices and membranes, respectively, whereas MDHAR2 (At5g03630) and 3 (At3g09940) are cytosolic (*14*). MDHAR6 is targeted to mitochondria or plastids, depending on the transcription start site used (fig. S1) (*15*), and is expressed highly in all tissues and developmental stages (*16*).

To confirm whether MDHAR6 deficiency increases TNT tolerance, binary vectors expressing mitochondria or plastid-targeted *MDHAR6* were stably transformed into *mdhar6-1* and the Col7 background line. Plastidial *MDHAR6* partially restored TNT toxicity, and expression of the mitochondrial form completely restored TNT toxicity (Fig. 2 and figs. S3 and S4).

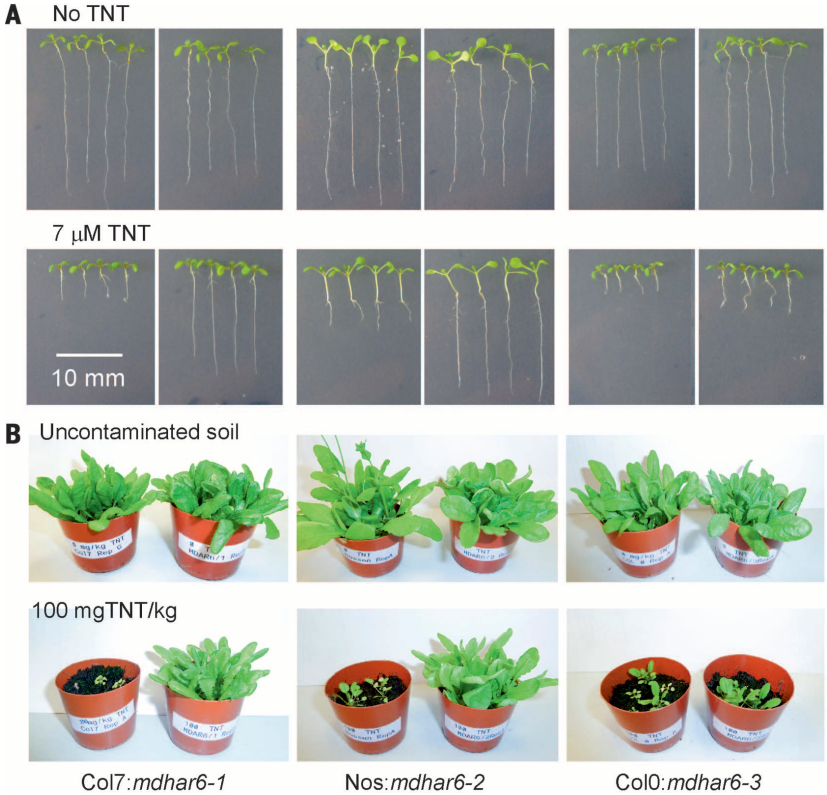


Fig. 1. Plants deficient in *MDHAR6* are more tolerant to TNT. (**A**) Seven-day-old *mdhar6* mutant and WT seedlings germinated on 0 or 7 μM TNT ½ Murashige-Skoog agar. (**B**) Appearance of 6-week-old *mdhar6* plants (right) adjacent to WT backgrounds (left), which were transferred to TNT-treated or untreated soil at 5 days of age.

Downloaded from www.sciencemag.org on September 5, 2015

To investigate whether the enhanced tolerance was due to reduced TNT uptake, seedlings were transferred to liquid media, which was dosed with TNT, and the media was sampled over 3 days. The mutants removed TNT from the media at equivalent rates to their wild-type (WT) backgrounds, indicating that the TNT tolerance is not due to reduction in TNT uptake (fig. S2).

Uptake of TNT from soil by Col7 and *mdhar6-1* was also tested; TNT binds strongly to humic fractions of soil, and on artillery ranges reaches concentrations over 100 mg TNT/kg soil (*17*). When young *Arabidopsis* seedlings were transferred to 100 mg TNT/kg soil and grown for 5 weeks, 40% more TNT was recoverable from soil treated with Col7 plants compared with *mdhar6-1* (table S1).

Stress tolerance of *mdhar6* mutants is specific to TNT

To investigate whether MDHAR6 deficiency confers resistance to other stresses, Col7 and *mdhar6-1* were germinated on media supplemented with NaCl, sorbitol, methyl viologen (Paraquat), or hydrogen peroxide up to lethal concentrations, and root lengths were measured. No enhanced tolerance in *mdhar6-1* was identified (fig. S5), indicating that the tolerance to TNT is not due to enhanced general defenses.

Considering that MDHAR6 is the only mitochondria and plastid-targeted MDHAR in *Arabidopsis*, it is surprising that plants carrying mutations in MDHAR6 were not more susceptible to environmental stresses. The *mdhar6-1* plants are indistinguishable from the wild type throughout development and are as robust as the wild type when grown in uncontaminated soil. This raises new questions as to the role of plastidial and mitochondrial MDHAR6 in protecting plants from oxidative stress. Ascorbate deficiency could be complemented by other antioxidant and/or enzyme activity, including dehydroascorbate reductase, which reduces dehydroascorbate, using glutathione as the electron donor (*18*).

Conjugation of reduced glutathione to TNT serves to detoxify the pollutant (*9*). Because ascorbate and glutathione are coupled antioxidants (*18*), we investigated the effect of MDHAR6 deficiency on ascorbate and glutathione levels. There were no differences between Col7 and *mdhar6-1* seedling leaves; however, *mdhar6-1* roots contained 26% more glutathione than WT roots, with no difference in percentage of oxidation (fig. S6). When whole seedlings were grown in the already more stressful conditions of liquid culture, and treated with TNT or a control treatment, we found no significant differences between Col7 and *mdhar6-1* ascorbate and glutathione levels and percentage of oxidation (fig. S6), suggesting that differences in glutathione levels do not account for the increase in TNT tolerance.

To further investigate whether the increased glutathione level observed in *mdhar6-1* roots (fig. S6) is involved in promoting TNT tolerance, studies

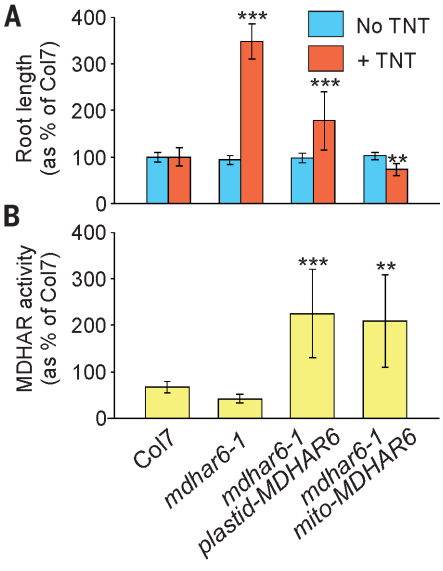


Fig. 2. Complementation of *mdhar6-1* by constitutively expressed plastidial (*plastid-MDHAR6*) and mitochondrial (*mito-MDHAR6*) transcripts. (**A**) Root length of seedlings on solid agar with and without 7 μM TNT (n = 6 biological replicates ± SD; $^{**}P < 0.01$, $^{***}P < 0.01$, Student's t test compared to Col7). (**B**) Rosette leaf MDHAR activity, with MDA as substrate (n = 5 biological replicates ± SD).

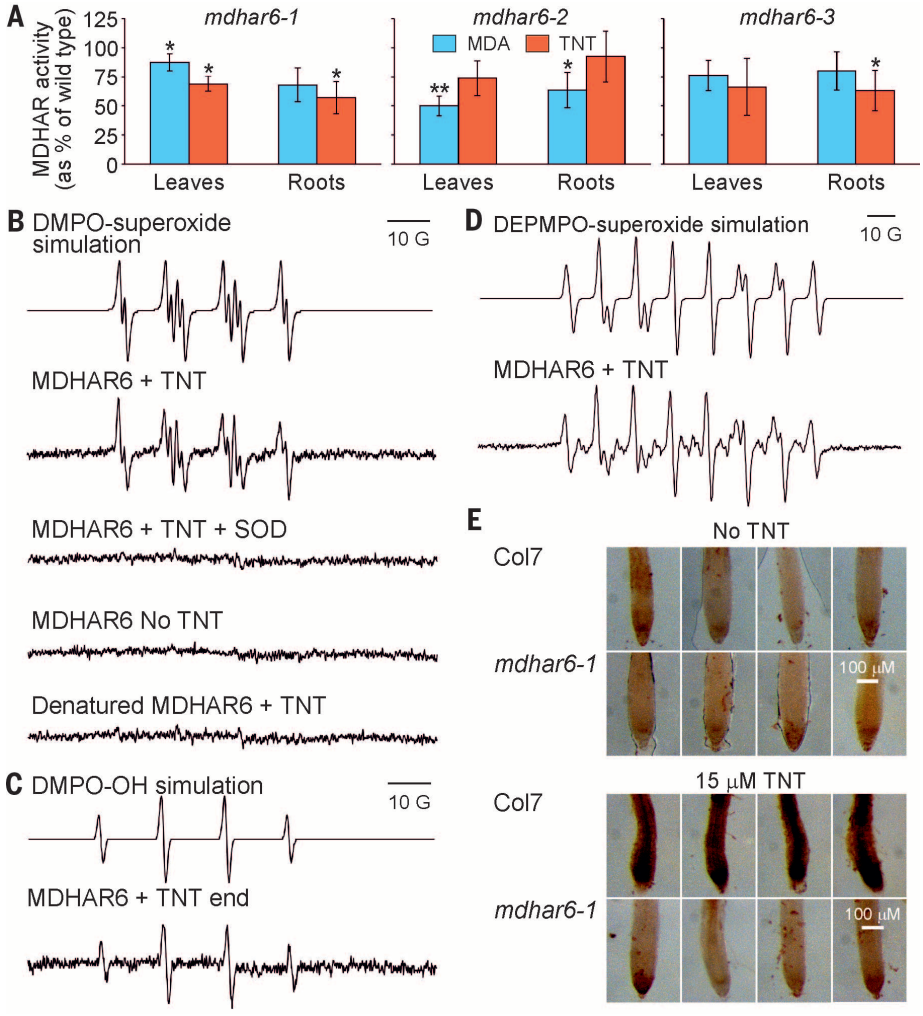


Fig. 3. Purified MDHAR6 reduces TNT, forming a nitro radical that subsequently generates superoxide. (**A**) Crude protein extract activity toward MDA and TNT, as a percentage of activity from WT tissue extract (n = 5 ± SD, Student's t test between *mdhar6* and corresponding ecotype background; $^{*}P < 0.05$, $^{**}P < 0.01$, Student's t test compared to wild type). (**B** to **D**) Simulated and experimental EPR spectra of ROS adducts with spin traps. (B) Simulated EPR spectrum of the DMPO-superoxide adduct followed by experimental spectra observed when MDHAR6 reacts with TNT in the presence of DMPO, when superoxide dismutase (SOD) is included, when TNT is omitted, and when heat-denatured MDHAR6 is used. (C) Simulated spectrum of the DMPO-superoxide degradation product DMPO-OH (*28*), followed by experimental spectrum observed when NADH in the assay is depleted. (D) Simulated spectrum of DEPMPO-superoxide adduct, followed by experimental spectrum observed when MDHAR6 reacts with TNT in the presence of DEPMPO. (**E**) Seven-day-old seedlings grown on agar plates in the presence or absence of 15 μM TNT, stained with DAB.

using the glutathione synthesis blocker buthionine sulfoximine (BSO), which inhibits γ-glutamylcysteine synthetase (*19*), were performed. Seedlings were grown for 7 days on agar plates containing increasing levels of BSO in the presence or absence of TNT. In plates containing 250 μM BSO, *mdhar6-1* seedlings remained more tolerant to 7 μM TNT than Col7 (fig. S7), indicating that the tolerance of *mdhar6-1* to TNT is not coupled to a glutathione detoxification system. We also observed that *mdhar6-1* seedlings had enhanced tolerance to BSO compared with Col7 seedlings, in the absence of TNT, indicating that the *mdhar6-1* mutation causes additional subcellular effects.

While phenotyping our mutant lines, we assayed the activity of crude protein extract toward the endogenous substrate MDA and toward TNT. Crude extract MDHAR activity differed between the WT lines (in roots, Col7 659 μmol min^{-1} mg^{-1}, Nossen 505 μmol min^{-1} mg^{-1}, and Col0 353 μmol min^{-1} mg^{-1}) and was reduced in the mutants (Fig. 3A). The decrease in crude extract MDHAR activity from the roots of *mdhar6-1* and *mdhar6-2* (209 and 198 μmol min^{-1} mg^{-1}, respectively) was far greater than the decrease in activity for *mdhar6-3* (70 μmol min^{-1} mg^{-1}), respectively, which corresponds with the degree of enhanced TNT tolerance in the different mutants. The *mdhar6-3* line contains a transferred DNA insert 76 base pairs upstream of the MDHAR6 start ATG and is likely to be a weaker allele, explaining why it is not so tolerant to TNT toxicity. The reduced form of nicotinamide adenine dinucleotide (NADH)–dependent activity in crude extracts toward TNT in the mutants indicated that MDHAR6 could have activity toward TNT.

MDHAR6 generates superoxide from TNT

To investigate MDHAR6 activity toward TNT and whether it could account for TNT phytotoxicity, we expressed *MDHAR6* recombinantly in *Escherichia coli* and purified the protein by affinity chromatography (fig. S8). Oxidation of cofactor NADH in the presence of TNT confirmed that MDHAR6 has activity toward TNT. Kinetics analysis of this activity gave Michaelis constant and maximal velocity values for MDA of 4.1 ± 1 μM and 109 ± 1.7 mmol min^{-1} mg^{-1} and for TNT of 522 ± 57 μM and 0.143 ± 0.0067 mmol min^{-1} mg^{-1}, respectively (fig. S8).

MDHAR6 activity toward TNT did not result in a decrease in TNT concentration when measured by high-performance liquid chromatography (HPLC) (fig. S8). Electron paramagnetic resonance (EPR) spectrometry was therefore used to determine whether the reaction is a one-electron reduction of TNT to produce a nitro radical, which would then autoxidize generating reactive superoxide. This cyclic reaction would explain why no decrease in TNT concentration was observed by HPLC. Reactive oxygen species (ROS) generation has previously been hypothesized as the cause of TNT-induced cataracts when catalyzed by zeta-crystallin (*20*) and neuronal damage when catalyzed by neuronal nitric oxide synthase (*21*).

Analyzing this hypothesis, we used EPR spectrometry with either spin trap 5,5-dimethyl-pyrroline N-oxide (DMPO) or 5-diethoxyphosphoryl-5-methyl-1-pyrroline-N-oxide (DEPMPO), and spectra correlating with superoxide production were observed (Fig. 3, B to D). The DMPO-superoxide spectrum was not observed in the presence of superoxide dismutase, or when TNT was omitted, or when denatured MDHAR6 was used. These results unambiguously confirm superoxide production during reduction of TNT by MDHAR6. To confirm that this process *in planta* leads to oxidative stress, we used 3,3′-diaminobenzidine (DAB) to visualize H_2O_2 generation. In seedlings grown on agar plates containing 15 μM TNT, the intensity of color (due to DAB oxidation by peroxide) was much higher in WT roots than in *mdhar6-1* roots (Fig. 3E). This finding is indicative of superoxide production by MDHAR6 activity with TNT.

Because *mdhar6* plants show enhanced tolerance to TNT but not to other stresses, we propose that production of superoxide by MDHAR6 with TNT as a substrate is the main mechanism for TNT toxicity in plants. The cyclic nature of the reaction is such that only catalytic amounts of TNT are needed to generate damaging levels of ROS within the mitochondria and plastids (Fig. 4). The reaction also requires NADH, use of which could induce an energy deficit, impeding adenosine triphosphate generation in the mitochondria and subsequent plant growth. The results presented (Fig. 1B and fig. S4) demonstrate that MDHAR6 contributes to the majority of TNT toxicity in *Arabidopsis*. Further toxicity could derive from reduction of TNT by one or more of the remaining four members of the MDHAR family. However, the biochemical environment of the peroxisome, which contains high levels of catalase, would be predicted to ameliorate the production of ROS. While in the cytosol, it is predicted that conjugation to glutathione and glucose would mitigate toxicity by reducing TNT availability (*7*, *9*).

Protein sequence alignment (*22*) against the National Center for Biotechnology Information database indicates that MDHAR6 is specific to plants (table S2). MDHAR6 has homologs with high sequence similarity among monocots and dicots, and in *Amborella trichopoda* at the base

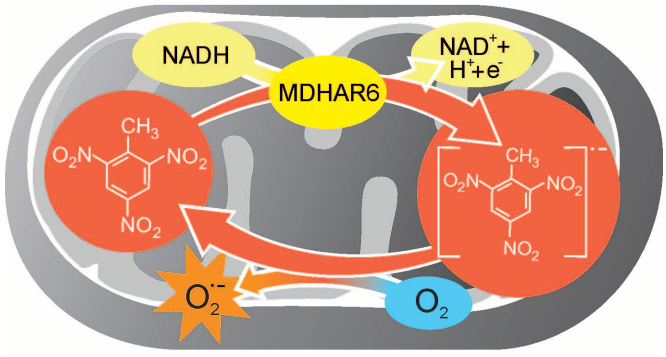


Fig. 4. A schematic drawing of the catalytic activity of mitochondrial MDHAR6 toward TNT.

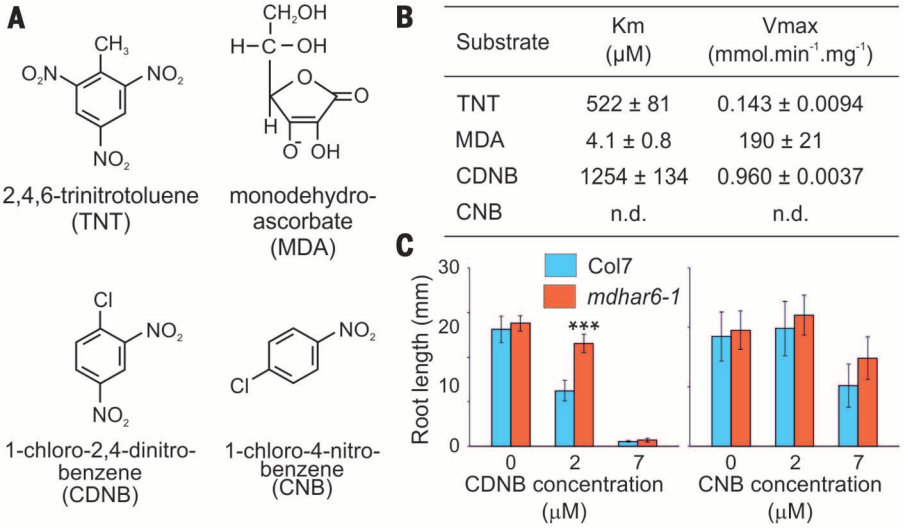


Fig. 5. Enzymatic activity of MDHAR6. (**A**) Structures of substrates tested against purified MDHAR6. (**B**) Kinetics of MDHAR6 activity with substrates, as measured by rates of NADH depletion (n.d., not detected; *n* = 3 technical replicates ± SD). (**C**) Root lengths of 7-day-old Col7 and *mdhar6-1* seedlings germinated on agar containing increasing concentrations of CDNB or CNB (*n* = 30 biological replicates ± SD; Student's *t* test compared to Col7 in same treatment, ***$P < 0.001$).

of the Angiosperm lineage. There are homologs with less similarity in lower plants and algae, and similarity with proteins outside of the Plantae is very low.

Applications

Although herbicide resistance has been increasing steadily since the 1970s (*23*), no new herbicide mode of action has been commercialized since the 1980s (*24*). The toxic effect of the plant-specific MDHAR6 reaction with TNT could be leveraged to develop environmentally acceptable substrates for MDHAR6 as a new class of herbicide. We therefore investigated activity of MDHAR6 toward two additional nitro-group–containing chemicals, 1-chloro-2,4-dinitrobenzene (CDNB) and 1-chloro-4-nitro-benzene (CNB), shown in Fig. 5A. Activity of purified MDHAR6, measured by following NADH oxidation, was detected toward CDNB but not CNB (Fig. 5B and fig. S8F). Measurement using HPLC demonstrated that CDNB was not depleted in assay mixtures (Fig. 5C). As observed for TNT, CDNB inhibited seedling root growth in WT Col7 seedlings on agar plates containing CDNB, with *mdhar6-1* seedlings exhibiting significantly longer roots than the wild type (Fig. 5D). These results demonstrate that MDHAR6 can reduce CDNB, with toxic effect to *Arabidopsis*, further supporting the idea that herbicidal substrates could be developed. Whereas WT seedling root lengths were reduced by ~50% in the presence of 2 μM CDNB, root lengths on 2 μM CNB were unaffected, demonstrating that CNB is significantly less phytotoxic. Alongside this result, we were unable to detect activity toward CNB using recombinant protein (Fig. 5). These results are in agreement with our hypothesis that formation of a nitro radical is the major cause of TNT toxicity in plants.

Although TNT binds to the organic and clay fractions of soil, and is thus not readily mobile in water, a common copollutant in sites contaminated with explosives is royal demolition explosive (hexahydro-1,3,5-trinitro-1,3,5-triazine) (RDX), which is highly mobile in soils and readily contaminates water supplies (*25*). Future work on effective bioremediation of explosives contamination will need both existing RDX-degrading capabilities (*26*, *27*) and resistance to the toxic copollutant TNT. Our findings explain the acute toxicity of TNT to plants and also provide an avenue by which MDHAR6 deficiency can be exploited to increase plant biomass in the presence of TNT, permitting greater rates of remediation for both TNT and RDX. Molecular breeding approaches could be used to identify deletions in *MDHAR6* orthologs, potentially enhancing TNT tolerance in relevant plant species such as switchgrass (*Panicum virgatum*), thus enabling revegetation and remediation of explosives-contaminated sites.

REFERENCES AND NOTES

1. J. Pichtel, *Appl. Environ. Soil Sci.* **2012**, 617236 (2012).
2. U.S. General Accountability Office, *Department of Defense Operational Ranges: More Reliable Cleanup Cost Estimates and a Proactive Approach to Identifying Contamination Are Needed* (GAO Publication GAO-04-601, 2004); www.gao.gov/products/GAO-04-601.
3. U.S. Agency for Toxic Substances and Disease Registry, Toxicological profile for 2,4,6-trinitrotoluene (TNT), ATSDR publication CAS 118-96-7 (ATSDR, Atlanta, 1995); www.atsdr.cdc.gov/toxprofiles/tp.asp?id=677&tid=125.
4. E. R. Travis *et al.*, *Environ. Sci. Technol.* **41**, 5854–5861 (2007).
5. E. R. Travis, N. C. Bruce, S. J. Rosser, *Environ. Pollut.* **153**, 119–126 (2008).
6. L. B. Brentner, S. T. Mukherji, S. A. Walsh, J. L. Schnoor, *Environ. Pollut.* **158**, 470–475 (2010).
7. F. Gandia-Herrero *et al.*, *Plant J.* **56**, 963–974 l(2008).
8. E. R. Beynon *et al.*, *Plant Physiol.* **151**, 253–261 (2009).
9. V. Gunning *et al.*, *Plant Physiol.* **165**, 854–865 (2014).
10. E. L. Rylott, A. Lorenz, N. C. Bruce, *Curr. Opin. Biotechnol.* **22**, 434–440 (2011).
11. D. Weigel *et al.*, *Plant Physiol.* **122**, 1003–1014 (2000).
12. O. Arrigoni, S. Dipierro, G. Borraccino, *FEBS Lett.* **125**, 242–244 (1981).
13. M. A. Hossain, K. Asada, *J. Biol. Chem.* **260**, 12920–12926 (1985).
14. C. S. Lisenbee, M. J. Lingard, R. N. Trelease, *Plant J.* **43**, 900–914 (2005).
15. K. Obara, K. Sumi, H. Fukuda, *Plant Cell Physiol.* **43**, 697–705 (2002).
16. T. Hruz *et al.*, *Adv. Bioinformatics* **2008**, 420747 (2008).
17. T. F. Jenkins *et al.*, *Chemosphere* **63**, 1280–1290 (2006).
18. C. H. Foyer, G. Noctor, *Plant Physiol.* **155**, 2–18 (2011).
19. O. W. Griffith, A. Meister, *J. Biol. Chem.* **254**, 7558–7560 (1979).
20. Y. Kumagai *et al.*, *FEBS Lett.* **478**, 295–298 (2000).
21. Y. Kumagai, M. Kikushima, Y. Nakai, N. Shimojo, M. Kunimoto, *Free Radic. Biol. Med.* **37**, 350–357 (2004).
22. S. F. Altschul, W. Gish, W. Miller, E. W. Myers, D. J. Lipman, *J. Mol. Biol.* **215**, 403–410 (1990).
23. I. Heap, The International Survey of Herbicide Resistant Weeds (1993–2015); available at www.weedscience.org.
24. S. O. Duke, *Pest Manag. Sci.* **68**, 505–512 (2012).
25. J. Clausen, J. Robb, D. Curry, N. Korte, *Environ. Pollut.* **129**, 13–21 (2004).
26. E. L. Rylott *et al.*, *Nat. Biotechnol.* **24**, 216–219 (2006).
27. R. G. Jackson, E. L. Rylott, D. Fournier, J. Hawari, N. C. Bruce, *Proc. Natl. Acad. Sci. U.S.A.* **104**, 16822–16827 (2007).
28. E. Finkelstein, G. M. Rosen, E. J. Rauckman, *Mol. Pharmacol.* **21**, 262–265 (1982).

ACKNOWLEDGMENTS

The authors acknowledge the assistance of M. V. Budarina for technical support. E.J.J., E.B., and A.L. were supported by Ph.D. studentships from the Biotechnology and Biological Sciences Research Council, the Burgess family, and the Garfield Weston Foundation, respectively. This work was supported by funding from the Strategic Environmental Research and Development Program of the U.S. Department of Defense to E.L.R and N.C.B. The supplementary materials contain additional data.

SUPPLEMENTARY MATERIALS

www.sciencemag.org/content/349/6252/1072/suppl/DC1
Materials and Methods
Figs. S1 to S8
Tables S1 and S2
References (*29*–*37*)

14 April 2015; accepted 22 July 2015
10.1126/science.aab3472

REPORTS

CHEMISTRY

Transient assembly of active materials fueled by a chemical reaction

Job Boekhoven,[1]*† Wouter E. Hendriksen,[1]† Ger J. M. Koper,[1] Rienk Eelkema,[1,2]‡ Jan H. van Esch[1,2]‡

Fuel-driven self-assembly of actin filaments and microtubules is a key component of cellular organization. Continuous energy supply maintains these transient biomolecular assemblies far from thermodynamic equilibrium, unlike typical synthetic systems that spontaneously assemble at thermodynamic equilibrium. Here, we report the transient self-assembly of synthetic molecules into active materials, driven by the consumption of a chemical fuel. In these materials, reaction rates and fuel levels, instead of equilibrium composition, determine properties such as lifetime, stiffness, and self-regeneration capability. Fibers exhibit strongly nonlinear behavior including stochastic collapse and simultaneous growth and shrinkage, reminiscent of microtubule dynamics.

Active self-assembly driven by chemical fuels is at the basis of many processes in living organisms, including cellular transport, cell motility, proliferation, and morphogenesis (*1*). Active self-assembled structures such as actin networks and microtubules (*2*) distinguish themselves from equilibrium self-assembled systems and materials (*3*) by their ability to use the free energy provided by the conversion of the fuel to achieve transient structure formation and to carry out work (*4*, *5*); in addition, their behavior is controlled by the kinetics of fuel consumption instead of by thermodynamic stability. The realization of artificial active materials created through a fuel-driven self-assembly process would further the understanding of kinetically

controlled dynamic behavior and associated spatiotemporal organization. It would also open opportunities for further developments in active separation and drug delivery, self-healing and adaptive materials, and autonomous control of chemical processes (*6*). The few artificial, chemically fueled, active self-assembling systems that have been reported typically use biological components such as DNA (*7*), enzymes (*8*, *9*), or protein building blocks (*2*, *10*, *11*), or they exploit an oscillating reaction to periodically shift the equilibrium of self-assembling (nano)particles (*12*). The need for complex biological components and oscillating reactions makes these systems expensive, complicated to use, and applicable to a limited range of working conditions. A molecular fuel-driven self-assembly process recently developed in our laboratory (*13*) showed the formation of dispersed fibrous structures with very slow dynamics, inhibiting the formation of true artificial active materials. It remains a challenge to achieve the formation of active materials where temporal material properties are controlled by fuel-conversion kinetics.

We report a general approach toward synthetic, transient, self-assembling molecular materials, driven by the consumption of chemical energy, and in which lifetime, stiffness, and regenerative behavior are controlled and can be tuned by the kinetics of fuel conversion. The system consists of simple synthetic chemicals that are commercially available on a multigram scale, and it can operate in water at room temperature, on time scales of hours to days. These active materials display nonlinear fiber dynamics, reminiscent of the dynamic instability observed in microtubules.

To arrive at a chemical fuel–driven active material, we coupled a switchable self-assembling system to a chemical reaction cycle, using the following design elements: (i) a molecule that can be switched between a nonassociating state and an associating state by the removal and reinstallment of a repulsive ionic charge; (ii) a chemical "activation" reaction between the self-assembling molecule and a sacrificial reactant (i.e., the fuel) that removes the repulsive ionic charge of the self-assembling molecule, thereby activating the self-assembling building block; (iii) a chemical "deactivation" reaction that restores the charge and returns the original charged self-assembling molecule; and (iv) different pathways for the activating and deactivating chemical reactions to form a reaction cycle, driven by the consumption of the fuel. If the activating and deactivating reactions run along the same path, adding a reactant would merely shift the chemical equilibrium, as is typically observed in triggered self-assembly processes (*14*, *15*).

Self-assembling molecules containing anionic carboxylate groups, in combination with an ester-forming carboxylate alkylation reaction (as the activating reaction) and an ester hydrolysis reaction (as the deactivating reaction), can fulfill the abovementioned requirements. The carboxylate carries a negative charge that can be removed by reaction with an alkylating electrophile fuel to form a neutral ester function. Esters can undergo spontaneous hydrolysis in aqueous environments, leading to the formation of a charged carboxylate and an alcohol waste product. As such, a carboxylate function can be used to control the molecular assembly process by changing the net charge on the molecule through kinetically controlled alkylation and hydrolysis (Fig. 1).

Kinetic analysis of the alkylation of carboxylates to drive supramolecular assembly has revealed that a substantial acceleration of the reaction kinetics (as compared with our previous study) is key to the formation of an active gel state (*13*). To reach this goal, we selected a more reactive alkylating agent and adjusted pH levels by means of a buffer to enable the formation and decay of supramolecular structures on time scales of hours, instead of 5 to 15 days (*13*). Increasing buffer concentrations resulted in a system capable of autonomously forming soft molecular materials without continuous pH adjustment and in a switch to monocarboxylates as the active gelators.

Using this system, we tested several molecular gelators (**1** to **3** in Fig. 1) containing two or three carboxylate moieties for the formation of active materials. These bis- and tris-carboxylate gelators formed isotropic aqueous solutions above the pK_a of their carboxylates (~4.5, where K_a is the acid dissociation constant). Active hydrogel materials were obtained during reaction cycles of gelators **2** or **3** with dimethyl sulfate [DMS, $(CH_3)_2SO_4$], a commercially available strong methylating agent, under hydrolytic (basic) conditions (Fig. 1). In a typical reaction cycle, the batchwise addition of DMS to buffered solutions of **1a**, **2a**, and **3a** resulted in its transient methylation, yielding methyl esters **1b**, **2b**, and **3b** (Fig. 1, A and B, and figs. S1 and S2) (*16*). Under these conditions, gelator **1** formed a

[1]Department of Chemical Engineering, Delft University of Technology, Julianalaan 136, 2628 BL Delft, Netherlands. [2]Delft Process Technology Institute, Delft University of Technology, Leeghwaterstraat 39, 2628 CB Delft, Netherlands.
*Present address: Institute for Advanced Study and Department of Chemistry, Technische Universität München, Lichtenbergstrasse 2A, 85748 Garching near Munich, Germany. †These authors contributed equally to this work. ‡**Corresponding author. E-mail: r.eelkema@tudelft.nl (R.E.); j.h.vanesch@tudelft.nl (J.H.V.E.)**

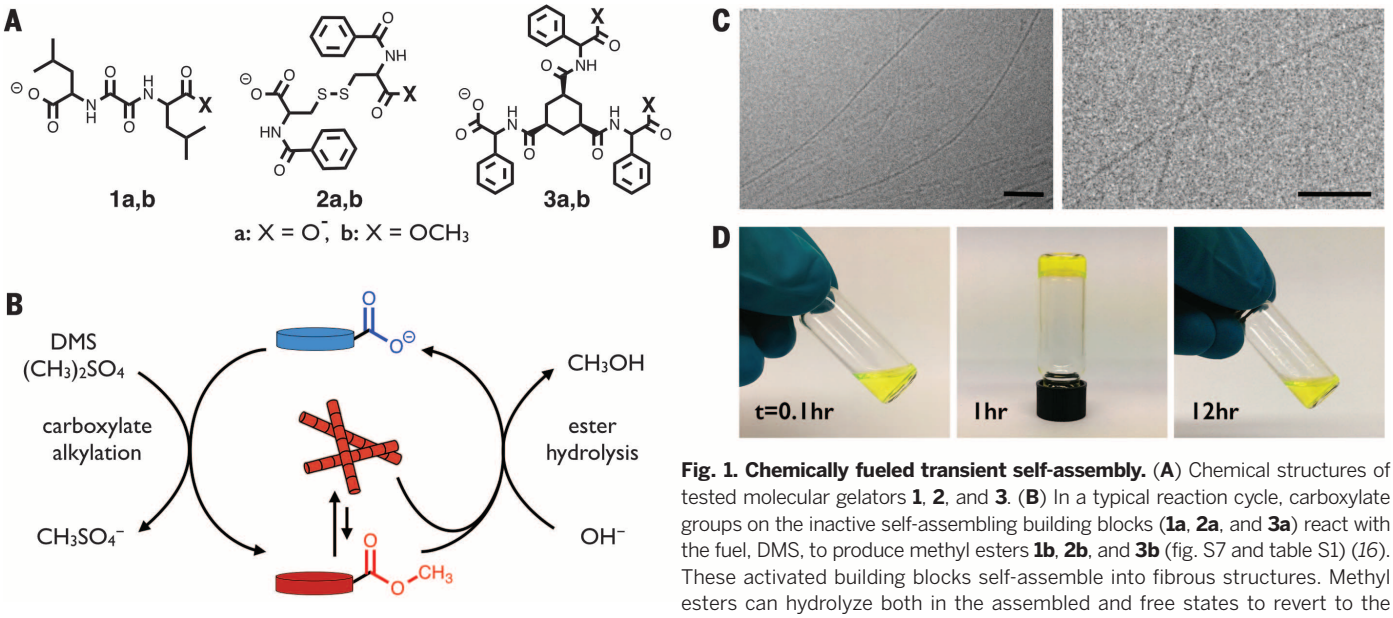


Fig. 1. Chemically fueled transient self-assembly. (**A**) Chemical structures of tested molecular gelators **1**, **2**, and **3**. (**B**) In a typical reaction cycle, carboxylate groups on the inactive self-assembling building blocks (**1a**, **2a**, and **3a**) react with the fuel, DMS, to produce methyl esters **1b**, **2b**, and **3b** (fig. S7 and table S1) (*16*). These activated building blocks self-assemble into fibrous structures. Methyl esters can hydrolyze both in the assembled and free states to revert to the original inactive building block. One full cycle produces CH_3OH (methanol) and $CH_3SO_4^-$ (MMS) as waste products. (**C**) Cryogenic transmission electron microscopy (cryo-TEM) micrographs of a gel of **2** at t = 120 min (pH 9, $[\mathbf{2a}]_0$ = 50 mM, $[DMS]_0$ = 100 mM, scale bar = 100 nm). (**D**) A typical sample in a reaction cycle (pH 11, $[\mathbf{2a}]_0$ = 50 mM, $[DMS]_0$ = 200 mM) at t = 0.1, 1, and 12 hours, with 1 μM of fluorescein added for coloring.

gelatinous precipitate but failed to form a hydrogel. We found that hydrogels of **2** and ***3*** consisted of bundles of fibers over a micrometer in length at high buffer concentrations, with individual fiber diameters of 8 and 10 nm, respectively (Figs. 1C and 4B and fig. S2) (*16*).

Focusing on gelator **2**, more detailed kinetic investigations showed that **2b** reached a critical gelation concentration typically 20 min after the addition of fuel, at which the formation of fibers resulted in macroscopic semitransparent gel materials (Fig. 1D). The critical gelation concentration of **2b** was estimated from inverted tube tests and rheology experiments to be between 0.1 and 2.8 mM, but it could not be determined accurately because of the dynamic nature of the material (tables S4 and S5) (*16*). Over time, **2b** hydrolyzed back to **2a** (Fig. 1), leading to the breakdown of the fibers and the dissolution of the gels. In a reaction cycle at the relatively low pH value of 9, the hydrolysis reaction took place at a slow rate, producing gels that persisted for weeks. Running a reaction cycle at higher pH values increased the rate of hydrolysis; as a result, the concentration of **2b** reached a maximum value, after which it decreased to zero on a time scale of hours. For instance, a gel formed at pH 11 had a lifetime of around 10 hours (*17*). Likewise, reducing the amount of fuel added at pH 11 resulted in a change in gel lifetime from 10 hours (initial fuel concentration, $[DMS]_0$ = 200 mM) to less than 4 ($[DMS]_0$ = 175 mM).

The time scales of gel formation and dissolution thus depend strongly on the reaction conditions employed. Moreover, the material properties and their time dependence change with changing reaction conditions. Hence, the reaction cycle started by gelator **2a** and DMS constitutes a fuel-driven self-assembling system that can operate autonomously, at reaction-cycle

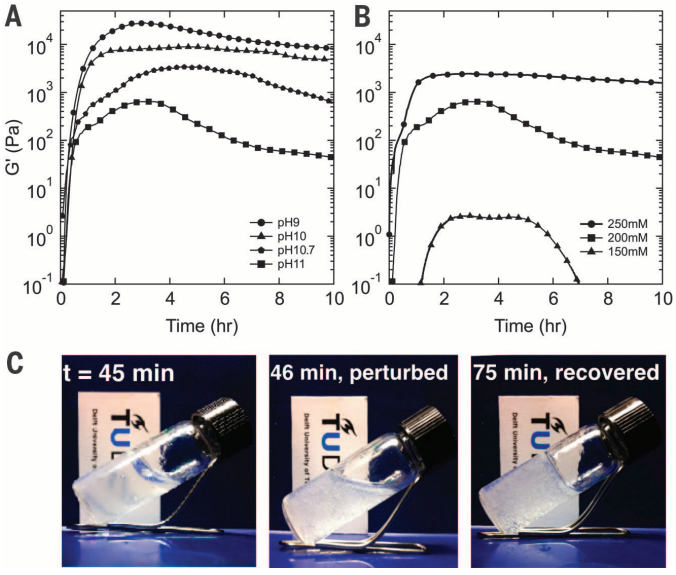


Fig. 2. Macroscopic mechanical behavior of the active material. (**A**) Rheology time sweeps of solutions of **2** during a reaction cycle at varying pH ($[DMS]_0$ = 200 mM, pH 9 to 11) and (**B**) at varying DMS concentrations ($[DMS]_0$ = 150 to 250 mM, pH 11). (**C**) Fuel-driven gel regeneration: photographs of an active gel of **2** before, immediately after, and 30 min after mechanical perturbation of the gel. In all experiments, $[\mathbf{2a}]_0$ = 50 mM.

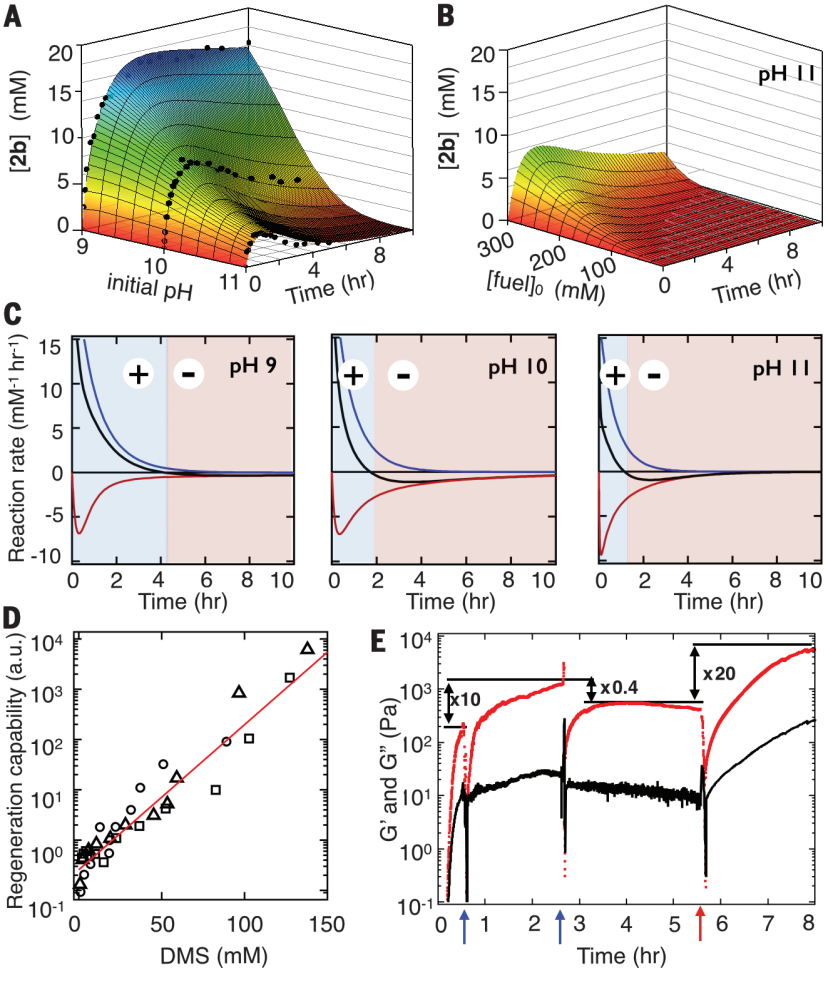


Fig. 3. Kinetics of transient gelator formation and gel regeneration. (**A** and **B**) The influence of reaction conditions on the concentration of **2b** over time. The black markers depict data points obtained from HPLC. The surface plots depict the kinetic model obtained at (A) different initial pH, with a constant initial DMS concentration, and (B) an initial pH of 11, with different initial DMS concentrations. (**C**) Rates of alkylation of **2a** (blue lines), hydrolysis of **2b** (red lines), and net formation of **2b** (black lines) against time at pH 9, 10, and 11 ($[\mathbf{2a}]_0$ = 50 mM, $[DMS]_0$ = 200 mM). Blue areas indicate net alkylation (+); red areas indicate net hydrolysis (−). (**D**) The relative regeneration of the gels, as determined by rheology, versus the concentration of remaining fuel at the moment of perturbation (square, pH 9; triangle, pH 10; circle, pH 11; $[\mathbf{2a}]_0$ = 50 mM, $[DMS]_0$ = 200 mM) (figs. S12 to S15) (*16*). (**E**) The mechanical response of a gel after perturbation and addition of new fuel (*G*', red; *G*'', black). Blue arrows at 0.5 and 2.7 hours indicate perturbation by applying strain; the red arrow at 5.5 hours indicates a perturbation and addition of 200 mM of DMS. Values between horizontal black lines indicate relative regeneration ratios.

time scales of 4 to 10 hours, and that provides access to the active gel state.

The rheology of **2**- and **3**-based active materials showed the formation of gels and a rapid increase in gel stiffness after the addition of fuel (Fig. 2A and figs. S3 to S5) (*16*). At pH 9, the near absence of a deactivating hydrolysis reaction resulted in stiff gels with persistent storage moduli (G') in the 10-kPa range and a loss factor (tan δ) of ~0.03 for **2**; for **3**, it resulted in a G' of 0.4 kPa with a tan δ of ~0.5. G' and G'' (the loss modulus) were constant over a wide frequency range, which is typical behavior for soft fibrillar gels formed from supramolecular gelators (*18*). Higher pH values resulted in less stiff gels, and, over time, a declining storage modulus was observed, with a decay rate that increased with pH. Changing the initial concentration of the fuel changed both the lifetime and the maximum stiffness of the gels, with results ranging, for instance, from short-lived, very weak gels at $[DMS]_0$ = 150 mM to much stronger gels with lifetimes of multiple days at $[DMS]_0$ = 250 mM (Fig. 2B). The observed strong dependence on fuel concentrations and pH was confirmed by a kinetic reaction model for **2**.

These materials also showed fuel-driven self-regenerating behavior after destructive mechanical perturbation. When destroyed during the first hours after the addition of fuel, gels of **2** quickly regained and surpassed the stiffness obtained before destruction (Figs. 2C, 3D, and 3E and figs. S12 to S15) (*16*). This behavior is generally not observed in conventional low–molecular weight gels near thermodynamic equilibrium. If perturbed late in the reaction cycle when the fuel was depleted, the regeneration capability dropped below one and eventually was lost completely. Thus, the mechanical and regenerative behavior of these active materials is strongly dependent on the progression of the reaction cycle. We also showed that the system can operate under continuous-flow conditions with a continuous supply of fuel, prolonging the lifetime of the material (fig. S22) (*16*).

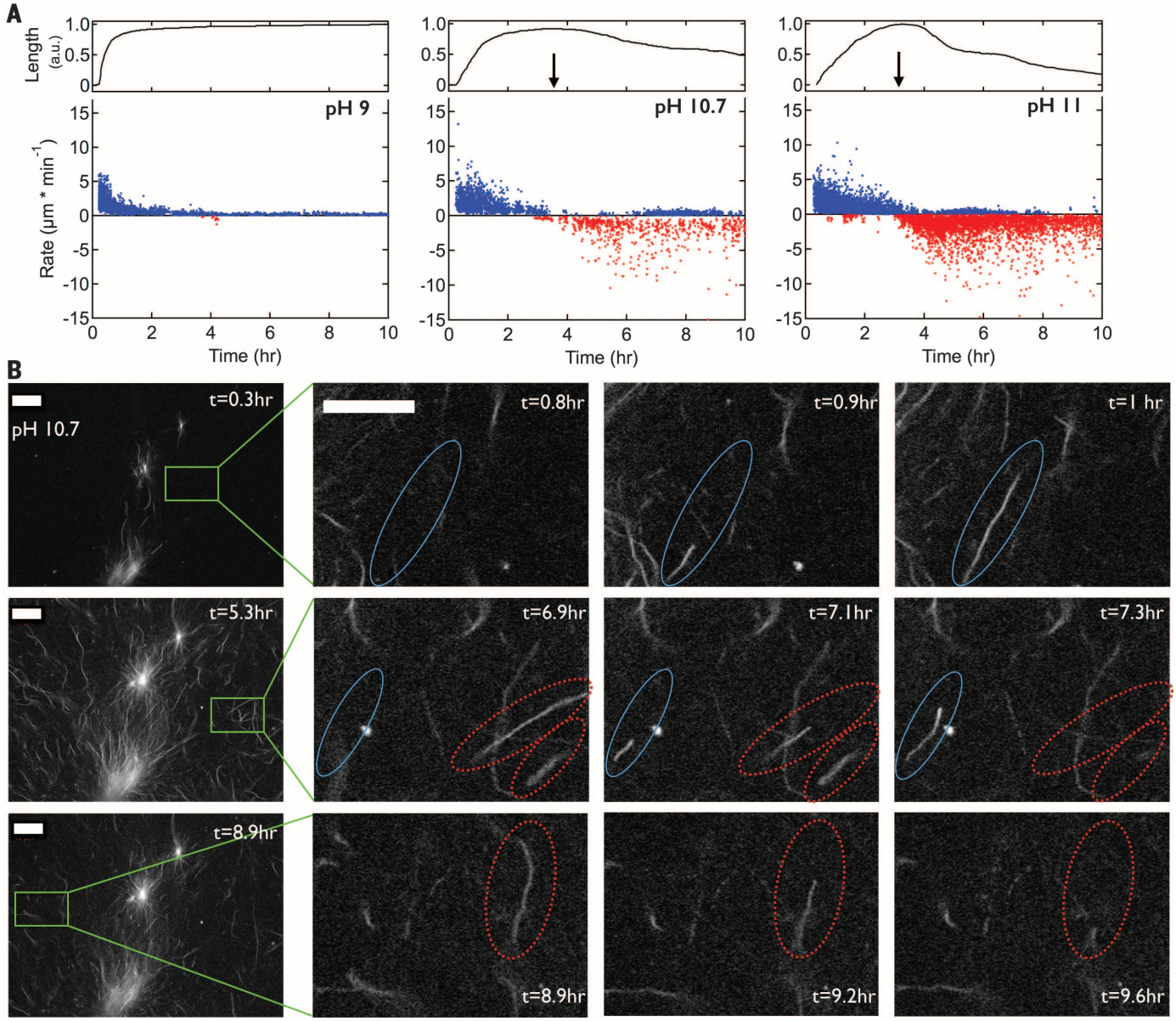


Fig. 4. Microscopic analysis of fiber dynamics. (**A**) Upper panel: normalized total fiber length against time in the reaction cycle. Arrows indicate the reaction-cycle time where G' reaches its maximum value (Fig. 2A). Lower panel: rates of fiber growth (blue) and fiber shrinkage (red), at various pH's. (**B**) Confocal micrographs over time, showing distinct fiber growth, shrinkage, and overlapping periods during a reaction cycle. Growing fibers are indicated in blue circles, and shrinking fibers are indicated in red circles. All samples were prepared with $[\mathbf{2a}]_0$ = 50 mM, $[DMS]_0$ = 200 mM, and pH 10.7. The scale bar is 10 μm.

To link the observed macroscopic behavior to the molecular-scale reactions, we performed a kinetic analysis of the active materials from gelator **2**. Starting from the pronounced dependence of gel lifetimes on fuel concentration and pH, we developed a simple kinetic model based on two competing chemical reactions: the forward alkylation of **2a** to **2b** by DMS and the reverse hydrolysis of **2b** to **2a** (Fig. 1B). The direct hydrolysis of DMS to monomethyl sulfate (MMS) was also taken into account as a separate background reaction. Using kinetic data from high-performance liquid chromatography (HPLC) and proton nuclear magnetic resonance (^{1}H-NMR) spectroscopy measurements, we determined the rate constants of all relevant reactions, allowing the construction of a kinetic model for the formation of **2b** (Fig. 3 and figs. S6 to S11) (*16*). We found that the rate of alkylation, k_1[**2a**][DMS], with k_1 = 2.5 M^{-1} $hour^{-1}$ at pH 10, followed a linear decay until all DMS had been depleted and showed a marginal variation with the pH. By contrast, the rate of hydrolysis, k_2[**2b**][OH^-], with $k_2 = 5.6 \times 10^4$ M^{-1} $hour^{-1}$ at pH 10 (table S3) (*16*), was exponentially dependent on pH. Subtracting the hydrolysis rate from the alkylation rate gives the net rate of formation of **2b** (Fig. 3C).

Using these rates, we defined two regimes through which the active gels progress. At first, the system is in a growth regime where the alkylation of **2a** is the dominant reaction. Subsequently, the system moves to the decay regime, in which hydrolysis is the dominant reaction. We then applied this model to analyze the relationship between the behavior of the system and the governing chemical reactions over time. The model showed that, unlike systems assembling near thermodynamic equilibrium, the behavior of these fueled systems evolves over time and is strongly dependent on the various reaction parameters, especially fuel levels and pH. The lifetimes of these active gels are globally connected to the period where [**2b**] is high, which is controlled by the initial reaction parameters (pH, $[\mathbf{2a}]_0$, $[DMS]_0$) and can be predicted with the kinetic model (Fig. 3, A and B). However, we observed a delay between the concentration of **2b** over time ($[\mathbf{2b}]_t$) (Fig. 3A) and the rheological behavior (Fig. 2A). This effect may indicate a nucleated growth mechanism of gel fiber formation and was not accounted for in the kinetic model.

We also observed that the gel state persisted for periods extending far beyond the time when reasonable concentrations of **2b** were present. For instance, the pH-11 system still contained a gel with G' > 50 Pa after 10 hours of reaction, even though [**2b**] had dropped below 0.6 mM after 5 hours. The dependence on reaction parameters and the transient character of the system indicates kinetically controlled states that do not reside at the thermodynamic minimum.

Using the model, we estimated the fuel concentration at any given time in the regeneration experiments. The regeneration capability (*19*) of these materials had an exponential dependence on the fuel concentration at the moment of perturbation (Fig. 3D), but it appeared to be independent of the pH, showing that this behavior is fuel-driven and is not significantly influenced by the hydrolysis rate (figs. S12 to S15) (*16*). When $[DMS]_t$ was less than 20 mM, the gels were no longer able to fully regenerate, indicating that the rate of formation of **2b**, needed for network repair, became too small. That the regeneration is fuel-driven implies that it can be restored at any time by the addition of new fuel. Indeed, the addition of fuel to a gel that was unable to regenerate restored its regeneration capability (Fig. 3E).

To gain more insight into the divergence between the time scales of the macroscopic behavior and the underlying chemical reaction network, we investigated the fiber dynamics of active gels from **2** with low and high hydrolysis rates (pH 9 to 11) using confocal microscopy (Fig. 4, figs. S16 to S21, and movies S1 to S4) (*16*). In all cases, after the addition of fuel, fiber growth was observed after a short lag period, coinciding with a rapid increase in gel stiffness (Figs. 4A and 2A). At pH 9, a rapid increase in the total fiber length was initially observed until the growth leveled off, and only a few shrinking fibers were observed (Fig. 4A). The active gels with higher hydrolysis rates (pH 10.7 to 11) also showed this rapid increase, but they reached a clear maximum, after which the fibers entered a shrinking regime and the total fiber length decreased. The transition between these two regimes coincided with the moment when the gels reached their maximum storage moduli. Both the moment of transition between regimes and the rate of decrease in the total fiber length depended on the pH and matched with the evolution of the storage moduli of the gels (Figs. 4A and 2A). Although fiber lengths decreased, a significant total fiber length persisted late in the reaction cycle, despite a negligible concentration of **2b**. All gels showed their highest level of structure (total fiber length, gel stiffness) midway through the reaction cycle.

At the microscopic level, several other unexpected observations were made (Fig. 4B). Instead of a gradual and simultaneous shrinking of all fibers, the assemblies tended to collapse stochastically with rates up to 15 μm/min (Fig. 4A). The fibers shrunk only at their tips and did not fracture or dissolve along their lengths. Also, for a certain period, both growing and shrinking fibers were observed in proximity to each other, randomly distributed throughout the microscope focal plane (Fig. 4B and figs. S18 to S21) (*16*). These observations are inconsistent with fiber dissolution driven by a decrease in [**2b**]. Instead, these findings point to hydrolysis of **2b** taking place both in the solution and within the fibers. The hydrolysis rate depends on the total concentration of **2b**, irrespective of the fraction bound in fibers (*20*). The observed fast stochastic collapse of fibers suggests that they become unstable above a certain critical hydrolysis level of **2b**, at which moment they rapidly dissolve, which may account for the discrepancies between molecular reaction rates and the macroscopic and microscopic behaviors. These observations show surprising similarities to the behavior of microtubule (de)polymerization, such as nonlinear fiber dynamics and dynamic instability, which are key ingredients in achieving out-of-equilibrium self-organization.

This work demonstrates the far-from-equilibrium self-assembly of molecular building blocks driven by a chemical fuel, leading to the transient formation of an active material. In these far-from-equilibrium materials, properties such as lifetime, stiffness, and self-regeneration capability are determined by reaction kinetics and fuel levels, rather than by equilibrium composition. These materials show nonlinear fiber dynamics reminiscent of microtubule behavior, and they constitute a key step in the development of synthetic self-organizing in out-of-equilibrium systems.

REFERENCES AND NOTES

1. E. Karsenti, *Nat. Rev. Mol. Cell Biol.* **9**, 255–262 (2008).
2. F. J. Nédélec, T. Surrey, A. C. Maggs, S. Leibler, *Nature* **389**, 305–308 (1997).
3. T. Aida, E. W. Meijer, S. I. Stupp, *Science* **335**, 813–817 (2012).
4. A. Desai, T. J. Mitchison, *Annu. Rev. Cell Dev. Biol.* **13**, 83–117 (1997).
5. G. M. Whitesides, B. Grzybowski, *Science* **295**, 2418–2421 (2002).
6. M. Fialkowski *et al.*, *J. Phys. Chem. B* **110**, 2482–2496 (2006).
7. D. Y. Zhang, R. F. Hariadi, H. M. T. Choi, E. Winfree, *Nat. Commun.* **4**, 1965 (2013).
8. S. Debnath, S. Roy, R. V. Ulijn, *J. Am. Chem. Soc.* **135**, 16789–16792 (2013).
9. C. G. Pappas, I. R. Sasselli, R. V. Ulijn, *Angew. Chem. Int. Ed.* **54**, 8119–8123 (2015).
10. F. C. Keber *et al.*, *Science* **345**, 1135–1139 (2014).
11. G. von Maltzahn *et al.*, *Adv. Mater.* **19**, 3579–3583 (2007).
12. I. Lagzi, B. Kowalczyk, D. Wang, B. A. Grzybowski, *Angew. Chem. Int. Ed.* **49**, 8616–8619 (2010).
13. J. Boekhoven *et al.*, *Angew. Chem. Int. Ed.* **49**, 4825–4828 (2010).
14. A. R. Hirst *et al.*, *Nat. Chem.* **2**, 1089–1094 (2010).
15. Y. Gao, J. Shi, D. Yuan, B. Xu, *Nat. Commun.* **3**, 1033 (2012).
16. Materials and methods are available as supporting materials on *Science* Online.
17. All pH values denote initial pH values. The pH decreases as the cycle proceeds as a result of the release of protons. The drift in pH is taken into account in the kinetic model.
18. R. G. Weiss, P. Terech, Eds., *Molecular Gels: Materials with Self-Assembled Fibrillar Networks* (Springer, Dordrecht, Netherlands, 2006).
19. The regeneration capability is defined as the ratio between the storage modulus (G') just before a strain sweep and the recovered maximum storage modulus, as determined by rheology (see the supplementary materials).
20. K. J. C. van Bommel, M. C. A. Stuart, B. L. Feringa, J. van Esch, *Org. Biomol. Chem.* **3**, 2917–2920 (2005).

ACKNOWLEDGMENTS

This work was supported by the Netherlands Organization for Scientific Research through a Vici grant (J.B. and J.H.v.E.) and a Complexity program grant (W.E.H., G.J.M.K., R.E., and J.H.v.E.). We thank E. Mendes for stimulating discussions, M. C. A. Stuart (University of Groningen) for carrying out initial cryo-TEM experiments, B. Norder for the initial rheology experiments, M. Bus for the atomic force microscopy measurements, and L. Palmer (Northwestern University) for proofreading the manuscript. The authors have no competing interests. Full data are in the supplementary materials.

SUPPLEMENTARY MATERIALS

www.sciencemag.org/content/349/6252/1075/suppl/DC1
Materials and Methods
Supplementary Text
Figs. S1 to S22
Tables S1 to S5
References (*21*–*25*)
Movies S1 to S4

19 May 2015; accepted 17 July 2015
10.1126/science.aac6103

METALLURGY

Linear complexions: Confined chemical and structural states at dislocations

M. Kuzmina, M. Herbig, D. Ponge, S. Sandlöbes, D. Raabe*

For 5000 years, metals have been mankind's most essential materials owing to their ductility and strength. Linear defects called dislocations carry atomic shear steps, enabling their formability. We report chemical and structural states confined at dislocations. In a body-centered cubic Fe–9 atomic percent Mn alloy, we found Mn segregation at dislocation cores during heating, followed by formation of face-centered cubic regions but no further growth. The regions are in equilibrium with the matrix and remain confined to the dislocation cores with coherent interfaces. The phenomenon resembles interface-stabilized structural states called complexions. A cubic meter of strained alloy contains up to a light year of dislocation length, suggesting that linear complexions could provide opportunities to nanostructure alloys via segregation and confined structural states.

Structural defects such as interfaces or dislocations in crystalline solid solutions are disturbed regions and attract solute segregation when diffusion is enabled (*1*–*5*). According to the Gibbs isotherm, the driving force is the reduction of the system's energy. Extending this concept also to nonisostructural cases suggests that local structural transformations can occur if the chemical composition and stress at a defect reach a level sufficient for stabilizing a state different from that of the matrix (*6*, *7*). The concept of interface complexions (*8*–*17*) extends the classical isotherm to interface-stabilized states that have a structure and composition different from that of the matrix and remain confined in the region where they form. We observed such a phenomenon also at linear defects—edge dislocations—in a binary Fe–9 atomic % Mn model alloy in which a stable face-centered cubic (fcc; austenitic) confined structure forms in an otherwise body-centered cubic (bcc; martensitic) crystal. This is a phenomenological one-dimensional (1D) analog of the previously observed complexions that were observed at planar defects (*8*).

We homogenized the Fe–9 atomic % Mn alloy at 1100°C and then quenched and cold-rolled it to 50% reduction for increasing the dislocation density. Subsequent annealing at (i) 400°C for 336 hours (2 weeks); (ii) 450°C for 6 hours, 18 hours, and 336 hours; and (iii) 540°C for 6 hours enabled Mn diffusion (*18*). To characterize structure and composition at the same positions, we conducted correlative scanning transmission electron microscopy–atom probe tomography (STEM-APT) analysis (*19*–*23*). We identified structural defects using STEM and cross-correlated it with solute decoration observed with APT (Fig. 1). Two grain boundaries and a single dislocation line are highlighted in Fig. 1 by blue arrows in the STEM micrograph and in the 3D atom map, in which they are visible as Mn-enriched regions. The correlative STEM experiments clearly identify the linear Mn-enriched features in the APT volumes as dislocations. As evident from the STEM micrograph, not all dislocations attract solute segregation high enough to be detectable with APT (Fig. 1A, red arrow "1").

We obtained 1D compositional profiles along cylindrical regions with 1 nm diameter at individual locations (Fig. 1E). Profile 1 shows a concentration of 25 ± 2 atomic % Mn at the dislocation core, which corresponds to an enrichment factor of 2.7 compared with the matrix concentration of Mn (9.1 atomic %). The average thickness of the Mn-enriched zone is ~1 nm. Besides the high Mn content at the dislocation cores, the composition along the dislocation line (profile 2) reveals periodic Mn changes—enriched and depleted zones alternating with a spacing of ~5 nm, resembling a nano-sized pearl necklace.

Sufficient segregation in conjunction with local elastic distortion at the defect may promote formation of confined structural states. This phenomenon has been observed at grain boundaries in Fe-Mn alloys and was explained in terms of a conventional phase transformation model (*6*, *7*). The huge segregation level observed here at some of the dislocations reveals similar features, reaching up to 25 atomic % Mn. This is in excellent agreement with the equilibrium concentration of Mn in the fcc phase (austenite) in the bcc-fcc two-phase region of the binary Fe-Mn system at the given annealing temperature (450°C), indicating an austenitic state of the dislocation core region. We conducted experiments on three samples, exposed to different annealing temperatures (400°C, 450°C, and 540°C) to study this further. We quantified the average compositional profiles around all probed dislocations observed in all individual APT data sets using proximity histograms ("proxigrams") (Fig. 2) (*24*). For all temperatures, we found an excellent agreement of the thermodynamically predicted equilibrium Mn concentrations (*18*) in austenite (dashed lines), with the experimentally observed local chemical compositions within 0.5 to 1 nm distance from the dislocation core.

As a third approach to prove that the dislocation cores transform from bcc to fcc, we performed transmission electron microscopy (TEM) to reveal the local crystallographic structures at the Mn-enriched dislocation sections. The investigations were done on martensite grains tilted a few degrees away from the [001] zone axis. Because of the small volume of the Mn-enriched dislocation core regions with respect to the surrounding matrix, no fcc reflections are visible in the diffraction patterns (Fig. 3A). Nevertheless, the measured area contains fcc regions that fulfill a Kurdjumov-Sachs (K-S) or Nishiyama-Wassermann (N-W) orientation relationship with the parent bcc grain, as we demonstrated by means of dark-field imaging. Shown in Fig. 3A is the diffraction pattern taken from a region containing a small-angle grain boundary (Fig. 3B). The diffraction pattern is indexed as $[001]_{bcc}$; the positions of the fcc diffraction spots for a N-W orientation relationship are also plotted into the same image. Austenite with a K-S orientation relationship is rotated by 5.26° around $[011]_{bcc}$, and the corresponding reflections are within the yellow circle in Fig. 3A. For better clarity, only one N-W fcc variant is shown, but the symmetric relationship applies for all possible variants. The bright-field TEM micrographs (Fig. 3B) show a mixed-type small-angle grain boundary containing edge and screw dislocations. When performing dark-field imaging using the yellow region in Fig. 3A, only the edge dislocations produce contrast. As clearly visible from the diffraction pattern (Fig. 3A), bcc dislocations would not give contrast under these dark-field diffraction conditions. These TEM results are a direct proof of the presence of a confined zone, with fcc structure having a K-S or N-W orientation relationship with respect to the martensitic matrix at edge dislocations.

Although these experiments give proof of austenitic states at the edge dislocation cores, to our surprise we did not detect any further growth of these regions into the martensite matrix, even during extended annealing treatments (*18*). In classical nucleation theory, a newly formed phase will grow once it has overcome the nucleation barrier. However, the analysis of samples annealed even for 2 weeks (336 hours) at 450°C in the two-phase region of the phase diagram revealed no change in size or composition of the austenitic dislocation cores as compared with those of the samples annealed for 6 hours at 450°C (*18*). This result indicates that these austenitic states are not viable outside of the dislocation core regions, hence matching the confinement characteristic of a complexion.

We further analyzed this phenomenon by use of a thermodynamic energy balance model (*25*).

Max-Planck Institut für Eisenforschung, Max-Planck-Straße 1, D-40237 Düsseldorf, Germany.
*Corresponding author. E-mail: raabe@mpie.de

Downloaded from www.sciencemag.org on September 5, 2015

We considered two cases: (i) an incoherent fcc-bcc interface formed by a diffusive transformation and (ii) a coherent interface formed by an athermal reversed Bain transformation from bcc to fcc (displacive transformation) (*26*). For the second case, the newly formed fcc zone (austenite) should hold an orientation relationship, for which the maximum misfit direction is nearly parallel to the Burgers vector of the dislocation (*27*, *28*). For the case of the incoherent fcc-bcc interface, we considered as an upper bound the removal of the dislocation's strain energy (*25*); the formation of a new incoherent interface; and a free-energy term associated with the transition from the bcc into the fcc state. For the special case of a coherent, athermal transformation, we added an additional energy penalty term for the misfit distortion associated with the reverse transformation. Including these contributions, we calculated the free energy per unit length of a cylinder surrounding an infinite straight dislocation

$$F = -A\log(r/R) + 2\pi\gamma r - \pi f r^2 \left[+B\pi r^2\right] \quad (1)$$

where r is the spatial coordinate perpendicular to the dislocation line, R is the inner cut-off radius for the dislocation core ($\sim b$), $A = [Gb^2/4\pi(1-v)]$ is the energy of an edge dislocation (G, shear modulus; b, Burgers vector; and v, Poisson ratio), γ is the interfacial energy between the newly formed confined fcc zone and the bcc matrix, $f = \Delta F_v$ is the bcc-fcc transformation energy, and $B = Gs^2(2-v)/8(1-v)$ is the distortion energy for the special case of a displacive transformation (s, net shear in a plane). The latter term is in brackets because it applies only in the case of a diffusionless transformation from bcc to fcc. The transformation free energy ΔF_v was taken from (*18*, *29*). For the fcc-bcc interface energy (γ), we used values ranging from 0.2 Jm^{-2} for a coherent interface with a specific orientation match, which is expected for the case of a displacive transformation, up to 1.2 Jm^{-2} for a less ordered one, which is expected for a diffusive transformation (Fig. 4) (*30*).

Indications for either a diffusive or displacive transformation mechanism exist. The pronounced partitioning of Mn suggests at first view a diffusional mechanism. However, the initial segregation occurs before the transformation, and the partitioning could go on after a displacive transformation. The crystallographic coherency between the two structures (matrix, bcc; dislocation core, fcc) observed in TEM seems to support a displacive transformation mechanism; however, K-S relationships can occur for diffusive transformations, too.

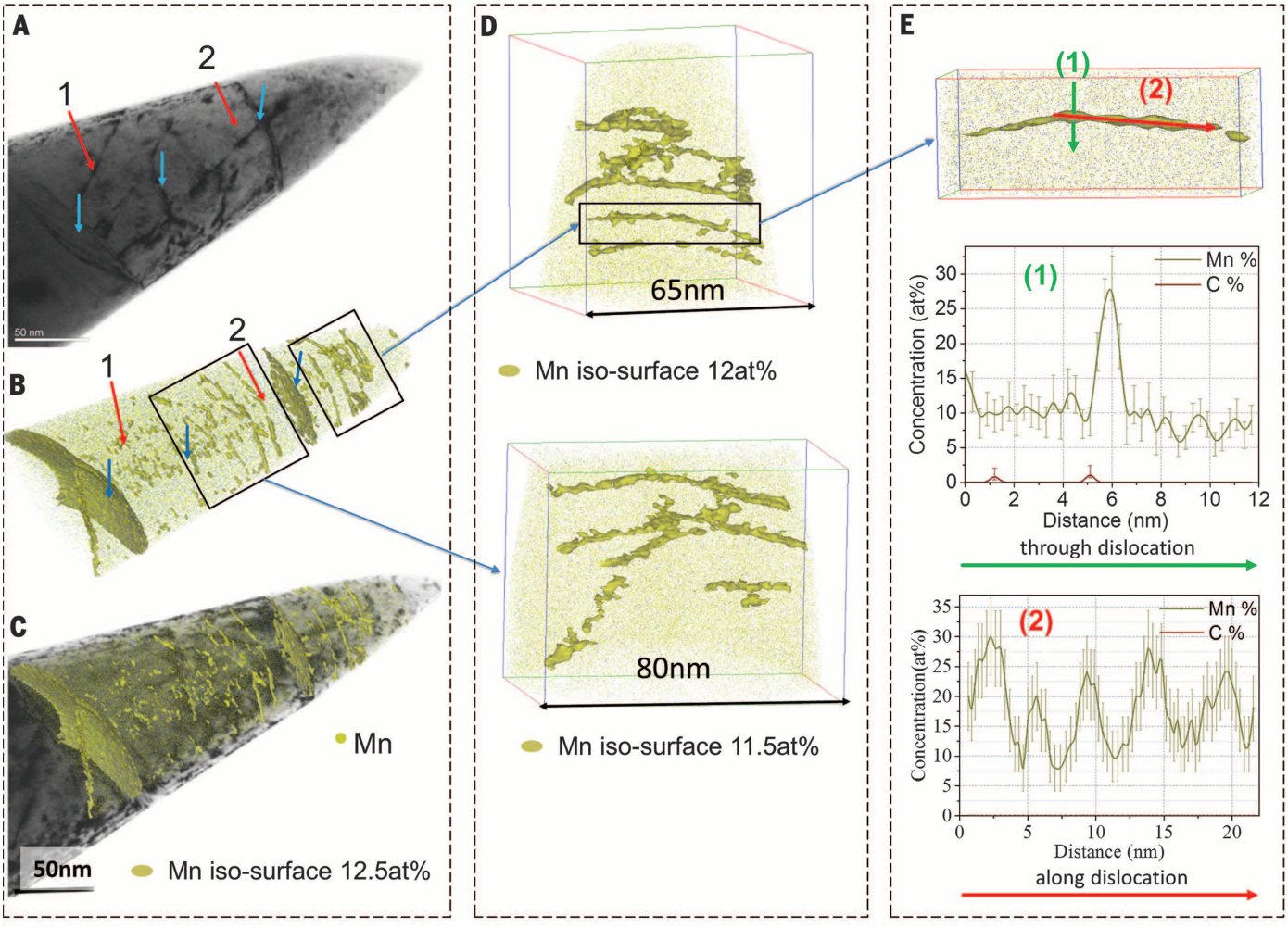


Fig. 1. Fe–9 atomic % Mn solid solution, 50% cold-rolled and annealed at 450°C for 6 hours to trigger Mn segregation. (**A**) Bright-field STEM image. (**B**) Correlative atom probe tomography results of the same tip shown in (A) using 12.5 atomic % Mn isoconcentration surfaces (12.5 atomic % Mn was chosen as a threshold value to highlight Mn-enriched regions). The blue arrows mark grain boundaries and dislocation lines that are visible in both the STEM micrograph and the atom probe tomography map. Not all dislocations visible in STEM are also visible in the atom probe data and vice versa (red arrows). (**C**) Overlay of (A) and (B). (**D**) Magnification of two subregions taken from (B). (**E**) 1D compositional profiles along 1 (perpendicular to dislocation line) and 2 (along dislocation line).

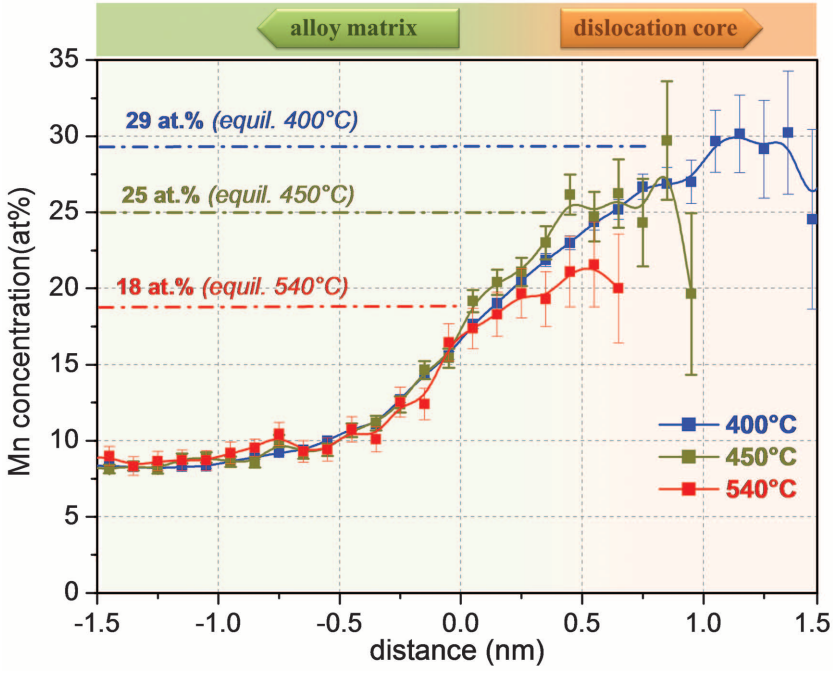


Fig. 2. Partitioning of Mn among the matrix and the dislocation cores. Proxigram of the local Mn concentration at dislocation lines in the binary Fe–9 atomic % Mn model alloy, annealed at 400°C for 336 hours (2 weeks) (blue line), 450°C for 6 hours (black line), and 540°C for 6 hours (red line). The parameters used for the isoconcentration surface values and for the proxigram calculations (*18*) were identical for all data sets (delocalization, 2 nm; voxel size, 0.7 nm; Mn isoconcentration value, 14 atomic % as threshold value). The thermodynamically predicted equilibrium concentrations of Mn in austenite at the respective annealing temperatures are marked by dashed lines (*18*).

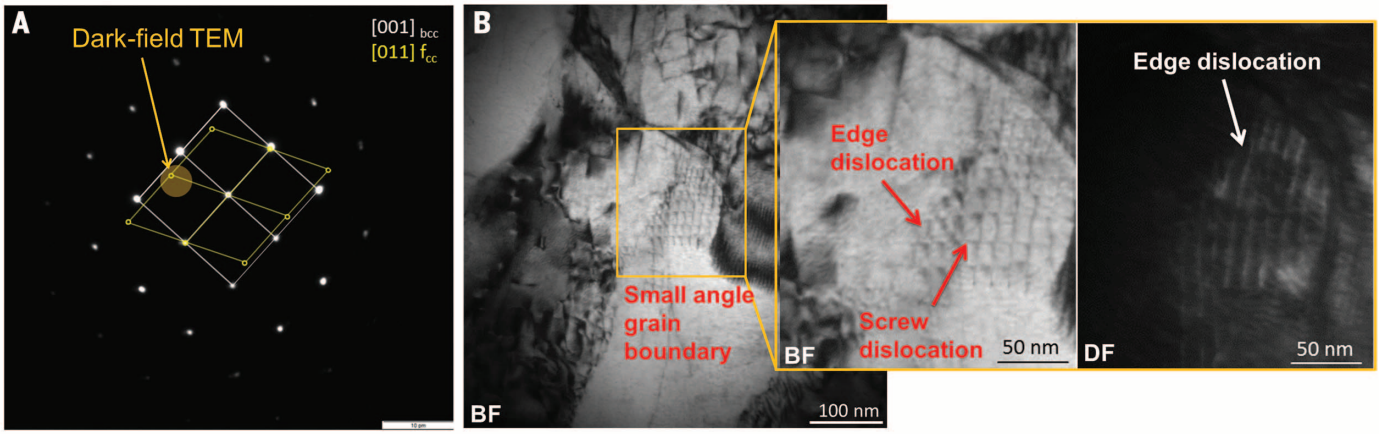


Fig. 3. Confined austenitic states at dislocation segments in a martensitic matrix imaged with TEM. (**A**) Selected area diffraction pattern (SADP) from the enlarged region shown in (B). The diffraction patterns are indexed as $[001]_{bcc}$; the positions of fcc diffraction spots for a N-W orientation relationship are drawn into the image. (**B**) BF-TEM and dark-field (DF)–TEM micrographs of a small-angle grain boundary. The DF micrograph was taken from the region marked by the yellow circle in (A), indicating austenitic edge dislocation core regions.

For the case of a displacive confined transformation at a dislocation in conjunction with a coherent fcc-bcc low-energy interface, the energy balance reaches a steep local minimum at an austenite size of ~0.4 nm. We interpret this as a stable austenitic state that remains confined to the defect.

The colored curves indicate solutions for a diffusive mechanism in conjunction with an incoherent interface by using different fcc-bcc interface energies. Both types of scenarios could in principal explain our observations (Fig. 4). The activation barrier for such a linear structure to be turned into a conventional phase, when in a two-phase region of the phase diagram, is rather small for the diffusive cases or—for interface energies <1 J/m^2—even absent. In such cases, a spontaneous (pseudospinodal) phase formation could occur (*31*). The coherency between the matrix and the austenitic dislocation core and the fact that these fcc zones remain strictly confined at the defects without any temporal changes in size or composition (*18*) are the reasons why we use the term "linear complexions" to describe the current phenomena.

We also observed that the segregation of Mn forms alternating regions of high and low Mn concentration along a dislocation line (Fig. 1E). We attribute this necklace-like arrangement of the transformation zones to a Rayleigh instability, which is driven by the minimization of the interface area and occurs if their wavelength exceeds their circumference, as observed in the present case.

Our results confirm confined austenitic states at martensitic dislocation cores. The observations rest on atomic-scale structural and chemical analysis, thermodynamic calculations, and an analytical model that accounts for the free-energy gain obtained when rendering dislocation cores into undistorted spatially confined austenite zones. We suggest extending the recently introduced planar complexion concept phenomenologically to the linear case. The effect observed fulfills all characteristics of a linear

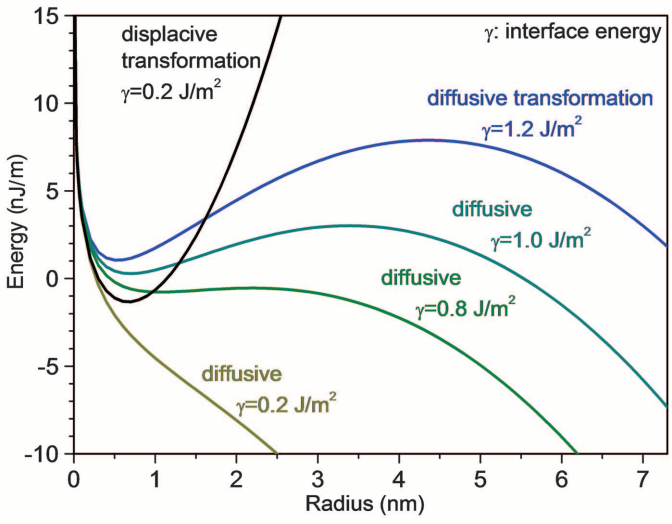


Fig. 4. Modeling supports a confined austenitic state at a dislocation core in martensite. Free energy per unit length of an austenitic (fcc) cylinder in a surrounding Fe–9 atomic % Mn martensite (bcc) matrix formed along an infinite straight-edge dislocation line, calculated for a range of interface energies between 1.2 and 0.2 J/m^2 for the case of a diffusive and a displacive confined transformation, respectively, at a temperature of 450°C. The black line applies to a displacive transformation at a dislocation in conjunction with a coherent fcc-bcc low-energy interface, and the colored curves indicate solutions for a diffusive transformation in conjunction with an incoherent fcc-bcc interface by using different interface energies. The local minima in several of these curves indicate the size of a confined austenitic (fcc) state.

complexion (*8*)—namely, equilibrium structural and chemical states through defect stabilization, geometrical confinement to the defect region, individual structural and compositional state, as well as dimensional and compositional stability. The thermodynamic driving forces for the formation of planar and linear complexions may be different, though, owing to the associated differences in structure and distortion of the underlying lattice defects. The discovery of linear complexions provides opportunities to nanostructure alloys via targeted segregation and confined structural states of dislocations.

REFERENCES AND NOTES

1. P. Lejcek, *Grain Boundary Segregation in Metals* (Springer, Berlin, Heidelberg, 2010).
2. I. J. Langmuir, *Am. Chem. Soc.* **40**, 1361–1403 (1918).
3. M. P. Seah, *Surf. Sci.* **53**, 168–212 (1975).
4. D. McLean, *Grain Boundaries in Metals* (Oxford Univ. Press, Oxford, UK, 1957).
5. R. Kirchheim, *Acta Mater.* **55**, 5129–5138 (2007).
6. D. Raabe *et al.*, *Acta Mater.* **61**, 6132–6152 (2013).
7. D. Raabe *et al.*, *Curr. Opin. Solid State Mater. Sci.* **18**, 253–261 (2014).
8. M. Tang, W. C. Carter, R. M. Cannon, *Phys. Rev. Lett.* **97**, 075502 (2006).
9. M. Tang, W. C. Carter, R. M. Cannon, *Phys. Rev. B* **73**, 024102 (2006).
10. S. J. Dillon, M. Harmer, *Acta Mater.* **55**, 5247–5254 (2007).
11. S. J. Dillon, M. Tang, W. C. Carter, M. P. Harmer, *Acta Mater.* **55**, 6208–6218 (2007).
12. M. P. Harmer, *Science* **332**, 182–183 (2011).
13. M. Baram, D. Chatain, W. D. Kaplan, *Science* **332**, 206–209 (2011).
14. W. Kaplan, D. Chatain, P. Wynblatt, W. C. Carter, *J. Mater. Sci.* **48**, 5681–5717 (2013).
15. T. Frolov, D. L. Olmsted, M. Asta, Y. Mishin, *Nat. Commun.* **4**, 1899 (2013).
16. T. Frolov, S. V. Divinski, M. Asta, Y. Mishin, *Phys. Rev. Lett.* **110**, 255502 (2013).
17. P. R. Cantwell *et al.*, *Acta Mater.* **62**, 1–48 (2014).
18. Materials and methods are available as supplementary materials on *Science* Online
19. M. Herbig *et al.*, *Phys. Rev. Lett.* **112**, 126103 (2014).
20. W. Guo *et al.*, *Phys. Rev. Lett.* **113**, 035501 (2014).
21. M. Herbig, P. Choi, D. Raabe, *Ultramicroscopy* **153**, 32–39 (2015).
22. L. Rigutti *et al.*, *Nano Lett.* **14**, 107–114 (2014).
23. I. Arslan, E. A. Marquis, M. Homer, M. A. Hekmaty, N. C. Bartelt, *Ultramicroscopy* **108**, 1579–1585 (2008).
24. O. C. Hellman, J. A. Vandenbroucke, J. Rüsing, D. Isheim, D. N. Seidman, *Microsc. Microanal.* **6**, 437–444 (2000).
25. J. W. Cahn, *Acta Metall.* **5**, 169–172 (1957).
26. K. E. Easterling, A. R. Thölén, *Acta Metall.* **24**, 333–341 (1975).
27. R. Bullough, B. A. Bilby, *Proc. Phys. Soc. B* **69**, 1276–1286 (1956).
28. T. Furuhara, T. Maki, *Mater. Sci. Eng. A* **312**, 145–154 (2001).
29. Thermo-Calc Software AB, TCFE7_TCS steels/Fe-Alloys Database, Version 7.1 (Thermo-Calc Software AB, Stockholm).
30. N. Nakada, T. Tsuchiyama, S. Takaki, N. Miyano, *ISIJ Int.* **51**, 299–304 (2011).
31. S. Nag *et al.*, *Acta Mater.* **60**, 6247–6256 (2012).

ACKNOWLEDGMENTS

The authors gratefully acknowledge funding by the European Union, provided under the 7th Framework Programme through the European Research Council Advanced Grant SMARTMET. M.H. is grateful to the German Research Foundation [Deutsche Forschungsgemeinschaft (DFG)] for funding through SFB 761 "Steel Ab Initio." Data are available in the main text and the supplementary materials.

SUPPLEMENTARY MATERIALS

www.sciencemag.org/content/349/6252/1080/suppl/DC1
Materials and Methods
Figs. S1 and S2
Table S1

1 April 2015; accepted 8 July 2015
10.1126/science.aab2633

MATERIALS SCIENCE

Highly thermally conductive and mechanically strong graphene fibers

Guoqing Xin,[1] Tiankai Yao,[1] Hongtao Sun,[1] Spencer Michael Scott,[1] Dali Shao,[2] Gongkai Wang,[1] Jie Lian[1]*

Graphene, a single layer of carbon atoms bonded in a hexagonal lattice, is the thinnest, strongest, and stiffest known material and an excellent conductor of heat and electricity. However, these superior properties have yet to be realized for graphene-derived macroscopic structures such as graphene fibers. We report the fabrication of graphene fibers with high thermal and electrical conductivity and enhanced mechanical strength. The inner fiber structure consists of large-sized graphene sheets forming a highly ordered arrangement intercalated with small-sized graphene sheets filling the space and microvoids. The graphene fibers exhibit a submicrometer crystallite domain size through high-temperature treatment, achieving an enhanced thermal conductivity up to 1290 watts per meter per kelvin. The tensile strength of the graphene fiber reaches 1080 megapascals.

As one of carbon's allotropes, single-layer graphene has the highest thermal conductivity ever reported, up to ~5000 W m^{-1} K^{-1} at room temperature (*1*–*3*); it also has the highest Young's modulus (~1100 GPa) (*4*), fracture strength (130 GPa) (*4*), and mobility of charge carriers (200,000 cm^2 V^{-1} s^{-1}) (*5*). However, such remarkable properties of single-layer graphene are on a molecular level and have not been achieved when processed into fibers. Macroscopic graphene oxide (GO) fibers can be assembled from a dispersion of GO in aqueous media, with graphene fibers produced upon reduction of the GO fibers (*6*, *7*). The anisotropic liquid crystalline behavior of the GO sheets can lead to a prealigned orientation, which can further be directed under shear flow to form an ordered assembly in a macroscopic fiber structure

[1]Department of Mechanical, Aerospace and Nuclear Engineering, Rensselaer Polytechnic Institute, 110, 8th Street, Troy, NY 12180, USA. [2]Department of Electrical, Computer, and Systems Engineering, Rensselaer Polytechnic Institute, 110, 8th Street, Troy, NY 12180, USA.
*Corresponding author. E-mail: lianj@rpi.edu

via a simple and cost-effective wet-spinning process (*6*, *7*). Improvement of the mechanical properties of the GO fibers and graphene fibers is achieved by introducing metal ion cross-linking bonds between graphene or GO sheets (*8*) or forming graphene or GO–based composite fibers—e.g., by adding carbon nanotubes (*9*, *10*) (see a summary in table S1). A tensile strength of 652 MPa was observed for a GO-hyperbranched polyglycerol-glutaraldehyde composite fiber (*11*), and for pure graphene fibers fabricated from large-sized GO sheets as the building block, a tensile strength of 501 MPa with 11.2-GPa Young's modulus was reported (*8*). GO fibers are typically electrically insulating. Electrical conductivity can be recovered on the order of 10^4 S/cm upon thermal or chemical reductions (*12*, *13*) and can be further increased to 9.3×10^4 S/m through doping with silver nanowires (*13*). The reported mechanical and electrical properties of graphene fibers are orders magnitudes lower than those of single-layer graphene (*4*) and substantially inferior to commercialized carbon fibers and carbon nanotube fibers (*14*–*17*).

It is difficult to realize simultaneously high mechanical and superior thermal and electrical properties. Highly aligned sp^2 graphene sheets are required for high thermal and electrical transport in which the mechanical strength is thus primarily limited by the van der Waals interaction between graphene sheets (*6*–*8*, *18*). However, heterogeneous structures, including functional groups and sp^3 bonds in cross-linked graphene nanosheets needed to improve mechanical strength, behave as effective phonon- and electron-scattering centers, thus reducing the electrical and thermal conductivities (*18*).

In contrast to the conventional approach, in which only large-sized GO (LGGO) is believed to be favorable for electrical and mechanical properties (because of its greater aspect ratio) (*8*, *19*, *20*), we adopt a strategy of using small-sized GO (SMGO) (average size of 0.8 μm, fig. S1A) and LGGO (average size of ~23 μm, fig. S1B) to form an intercalated and compact fiber structure (Fig. 1A-1) (*21*). LGGO sheets form a highly aligned backbone, whereas SMGO sheets fill the space and voids between LGGO sheets without altering the high degree of sheet orientation and alignment. By varying the content of SMGO sheets occupying the voids between LGGO sheets, an optimal balance between compactness and sheet alignment can be reached. Upon thermal reduction and high-temperature annealing, the as-spun insulating GO fibers transform to ordered, highly thermally and electrically conductive, and mechanically strong graphene fibers (Fig. 1A-2). The optimized graphene fiber with the addition of 30 weight % (wt %) SMGOs, subjected to thermal annealing at 2850°C, achieves thermal and electrical conductivities up to 1290 ± 53 W m^{-1} K^{-1} and 2.21 (±0.06) ×10^5 S m^{-1}, respectively.

The optimized graphene fiber shows excellent heat transport performance, superior to that of the graphene fiber from pure LGGOs and copper wire (Fig. 1B). The optimized graphene fibers also outperform commercially available thermally conductive mesophase pitch-based carbon fibers (typically thermal conductivities of 600 to 1000 W m^{-1} K^{-1}) (*14*, *22*–*24*) and are more cost effective owing to low-cost raw materials, simple preparation, and a lower annealing temperature. Mechanically, the graphene fibers from pure LGGOs achieve tensile strength of 940 ± 62 MPa (best value 1005 MPa; Fig. 1C); the optimization of graphene sheet alignment and compactness by intercalating SMGOs further improves the strength of the graphene fiber to 1080 ± 61 MPa (best value 1150 MPa; Fig. 1C).

The alignment of graphene sheets, the compactness of the fiber structure, and the crystalline graphitic domain size ultimately determine the mechanical properties, and the phonon and electron transport behaviors, of the graphene fiber. Liquid crystals with larger domains can yield macroscopic materials with a higher microstructural order (*8*, *19*, *20*). Initially, LGGO dispersed in aqueous solution with large liquid crystalline domains is spun into a highly aligned fiber structure, as evidenced by sectional scanning electron microscope (SEM) images and surface morphology of the GO fibers (fig. S2). Upon annealing and reduction at 1800°C, the graphene

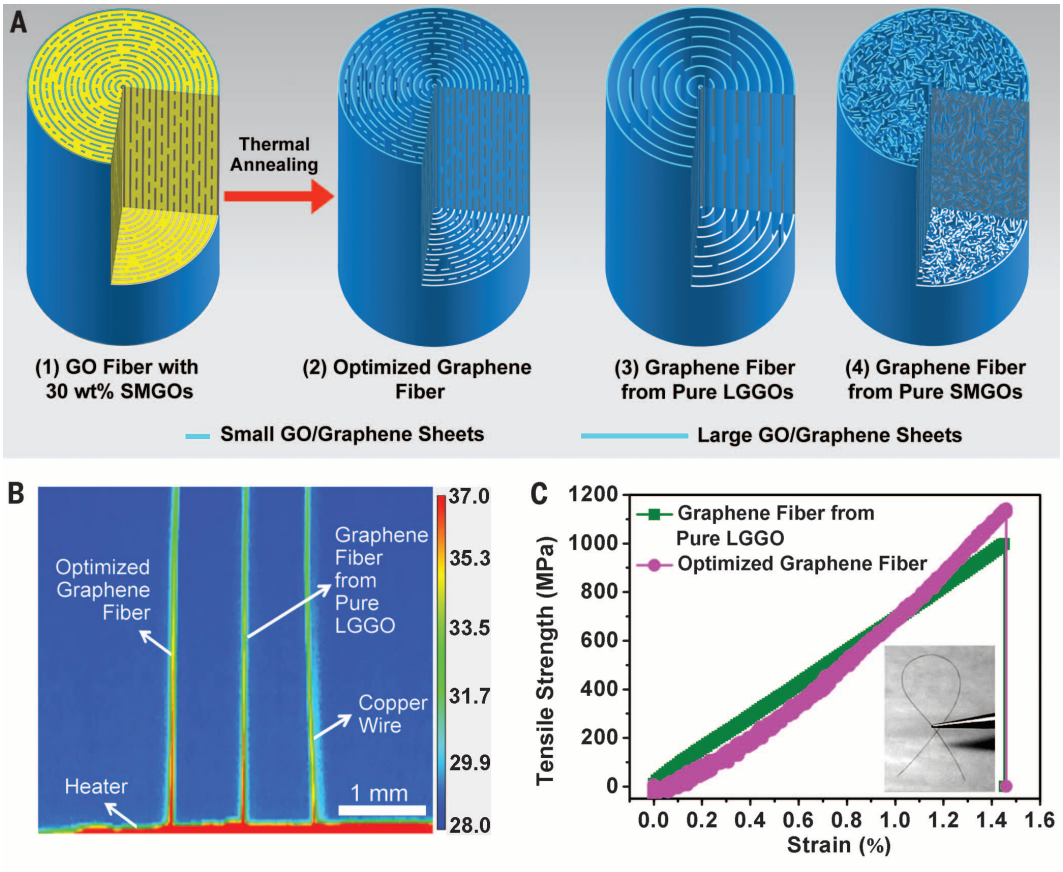


Fig. 1. Highly thermally conductive and mechanically strong graphene fibers with an "intercalated" structure of large and small-sized graphene sheets. (**A**) Schematics of the "intercalated" structure of the GO fibers and graphene fibers: (1) GO fiber with optimized LGGO and SMGO loadings; (2) optimized graphene fiber with a highly ordered and compact structure with 30 wt % SMGOs filling into the microvoids; (3) graphene fiber from pure LGGOs showing a highly ordered but less dense structure; and (4) graphene fiber from pure SMGOs showing a random sheet alignment. (**B**) A thermal image showing rapid heat transport on the optimized graphene fiber and comparison with graphene fiber from pure LGGOs and copper wire. All of the fibers and the copper wire have a diameter of 50 μm and are attached vertically on a microheater. The histogram on right indicates the color scale according to temperature (unit: °C). (**C**) Exceptional mechanical strength as revealed by typical stress-strain curves of graphene fiber from pure LGGO (annealed at 1600°C) and optimized graphene fiber (annealed at 1800°C). The inset shows a highly flexible optimized graphene fiber.

fibers display well-maintained graphene sheet alignment as determined by small-angle x-ray scattering (SAXS) (*25*–*28*). The graphene fiber from LGGO shows a strong equatorial streak scattering pattern, indicating slit-shaped microvoids with a high aspect ratio, well-aligned with the fiber axis (Fig. 2A) (*25*–*28*). The microvoids are primarily induced by graphene sheet restacking and the removal of oxygen functional groups as gaseous H_2O, CO, and CO_2 during the thermal annealing process (*29*, *30*). Low density and high porosity are observed in the graphene fibers upon thermal reduction of the GO fibers (Fig. 2C), resulting in inferior thermal and mechanical properties. The filling of microvoids with SMGOs leads to a deformation of the equatorial streak from strong anisotropic patterns to more isotropic ellipse patterns, suggesting a random distribution of the slit-shaped microvoids (Fig. 2A) (*25*–*28*). The misalignment angle (shown in Fig. 2B and the calculation in supplementary materials) increases with the addition of SMGOs, suggesting a reduction in the degree of graphene orientation with respect to the fiber axis (*25*–*28*). The addition of SMGOs with a low aspect ratio disrupts the large liquid crystalline domains during spinning, resulting in a less oriented microstructure, unfavorable for the physical properties of graphene fibers. By contrast, the addition of SMGO sheets increases the physical density of the graphene fibers and reduces the porosity monotonically (Fig. 2C), and the graphene fiber becomes more compact.

An optimized balance between graphene sheet alignment and compactness should be achieved to improve thermal and electrical properties. At a low weight percent of SMGOs, the thermal and electrical conductivities increase with the addition of SMGOs until 30 wt %. The measured peak thermal and electrical conductivities are up to 607 ± 25 W m^{-1} K^{-1} and $1.11(\pm0.05) \times 10^5$ S m^{-1}, representing improvements of 35.8 and 31.6%, respectively, as compared to those of the fibers from pure LGGOs (Fig. 2, D and E). Further increase in the fraction of SMGOs beyond a 30 wt % threshold leads to a reduction in the thermal and electrical conductivities despite the continuous reduction in the fiber porosity. The graphene sheet alignment is disrupted and the increase in defective boundaries results in a degradation of the graphene fibers' physical properties.

The inner fiber structures of the graphene fibers are revealed by SEM (Fig. 3 and fig. S4). The highly aligned structure in GO fibers from pure LGGO sheets is well maintained in the graphene fibers, and the annealed graphene sheets stack into a layer-by-layer structure throughout the transverse section (Fig. 3, A and B), extending continuously along the longitudinal direction (Fig. 3C). However, microvoids are generated between graphene sheets during thermal annealing, resulting in a higher porosity (Fig. 2C and Fig. 3B). With the addition of 30 wt % SMGOs, the high degree of orientation has been well maintained inside the GO fibers (fig. S2) and the annealed graphene fibers (Fig. 3, D to F). Meanwhile, a more dense structure as compared with the fibers from pure LGGOs has been created inside GO fibers (fig. S2) and annealed graphene fibers (Fig. 3E) by intercalating small-sized graphene sheets into large-sized graphene sheets (fig. S5). The pure SMGO fibers show the most compact structure; however no alignment of graphene sheets can be observed in both transverse and longitudinal sections (Fig. 3, G to I). The small aspect ratio and random distribution of small-sized graphene sheets inside graphene fibers induce high resistance for phonon and electron transport and low thermal and electrical conductivities (Fig. 2, D and E).

The thermal and electrical properties of the graphene fibers can be markedly improved by eliminating oxygen functional groups and residual defects (Fig. 4 and fig. S6) and continuously increased graphene sheet alignment and compactness (fig. S7) upon thermal annealing. The as-spun GO fibers are essentially poor electrical and thermal conductors (*7*, *13*, *18*). For pure LGGO graphene fibers annealed at 2850°C, thermal and electrical conductivities reach 1025 ± 40 W m^{-1} K^{-1} and $1.79(\pm0.06) \times 10^5$ S m^{-1}, respectively. The highest thermal and electrical conductivities achieved for the optimized graphene fibers annealed at 2850°C are 1290 ± 53 W m^{-1} K^{-1} and $2.21(\pm0.06) \times 10^5$ S m^{-1}. Lower-temperature annealing at 2000° and 2200°C can be applied to improve the cost effectiveness, and the thermal conductivity (800 to 1030 W m^{-1} K^{-1}) achieved for the optimized graphene fibers is comparable with that of the best mesophase pitch-based carbon fibers (*14*, *22*–*24*).

The annealed graphene fibers also show exceptional mechanical properties as measured by tensile testing (Fig. 4, C and D). The tensile strength of the as-spun GO fibers from pure LGGOs is 231 ± 30 MPa (Fig. 4C), comparable with previous reports (*8*, *19*), and the addition of 30 wt % SMGOs increases the tensile strength of the GO fibers to 308 ± 32 MPa. The tensile strength of the graphene fibers from pure LGGOs annealed at 1400° and 1600°C increases to 756 ± 35 and 940 ± 62 Mpa, respectively, and then decreases to the range of 616 to 823 MPa at greater annealing temperatures (above 1800°C). The optimized graphene fibers show an increase in tensile strength from 614 ± 35 MPa at an annealing temperature of 1400°C to 1080 ± 61 MPa at 1800°C, then decreases to 705 to 820 MPa at annealing temperatures above 2000°C. The Young's modulus of the optimized graphene fibers monotonically increases with annealing temperatures and approaches 135 ± 8 GPa when annealed at 2850°C.

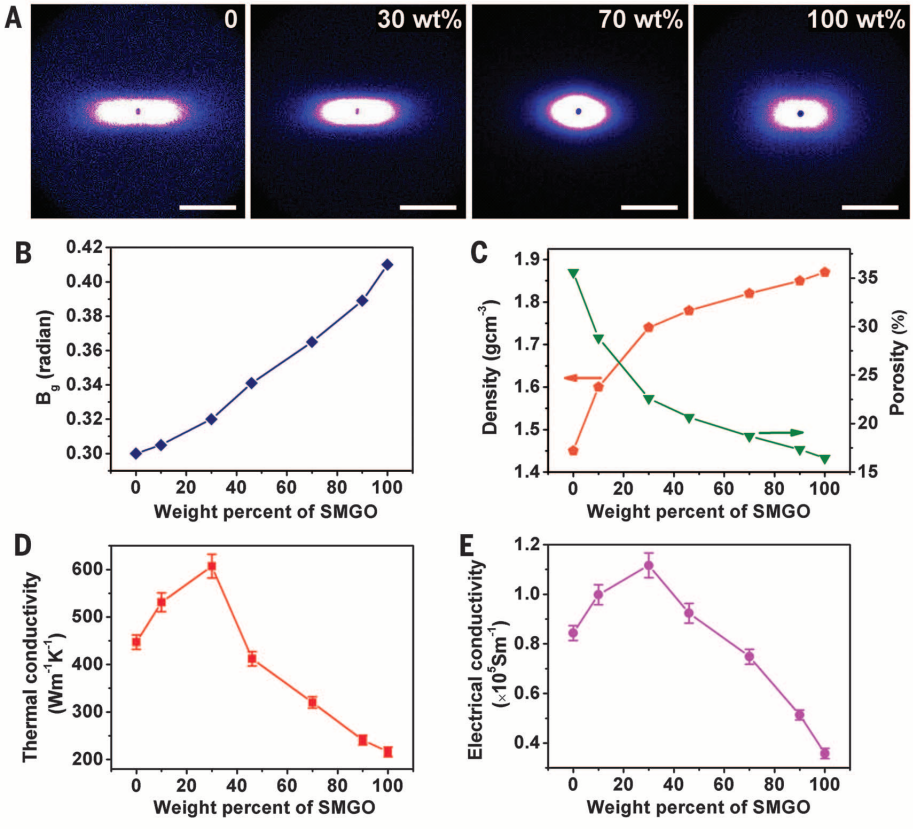


Fig. 2. Graphene sheet alignment and physical, thermal, and electrical properties of the graphene fibers annealed at 1800°C. (**A**) Small-angle x-ray scattering patterns of the fibers with a different wt % of SMGO (the fiber axis is vertical in all measurements; scale bar: 1 nm^{-1}); (**B**) misalignment angle B_g; (**C**) density and porosity; and (**D**) thermal and (**E**) electrical conductivities of the graphene fibers. The uncertainties of the thermal and electrical conductivities are based on a standard deviation of seven to nine measurements.

The graphene sheet alignment and compactness (see fig. S7) and the cross-link between adjacent graphene sheets eventually determine the tensile strength of the graphene fibers. The increased tensile strength of the graphene fibers upon lower-temperature annealing can be attributed to the enhancement in the alignment and densification. Substantial oxygen functional cross-links still remain upon annealing below 1800°C (fig. S6), and new C-C cross-links between neighboring graphene sheets may be created during the release of decomposing components of the chemical groups upon thermal reduction of GOs, further opposing the gliding between graphene faces (*15*). When the annealing temperature exceeds 2000°C, almost all of the cross-links are removed (see Raman and x-ray photoelectron spectroscopy spectra in fig. S6), leading to a reduction of the tensile strength. At higher annealing temperatures, the interlayer graphene sliding is primarily dominated by the van der Waals force interaction between adjacent graphene sheets (*15*, *22*), and no obvious variation in tensile strength is observed. The trend of monotonically increased Young's modulus of the graphene fibers is consistent with the previously reported polyacrylonitrile (PAN) and mesophase pitch-based carbon fibers (*12*, *15*) and can be primarily attributed to the improvement of the graphene sheet alignment (figs. S6 and S7) and increased dimension of crystallite domains as evidenced by greater Raman graphite band and defect band I_G/I_D intensity ratios along both transverse and longitudinal directions (fig. S8) (*15*, *31*, *32*). The intercalation of the small- and large-sized graphene sheets leads to greater tensile strength and Young's modulus for the optimized graphene fibers.

The tensile strength (1080 ± 61 MPa) and Young's modulus (135 ± 8 GPa) of the optimized graphene fibers are still much lower than these of carbon fibers (5.69 GPa and 0.94 TPa) (*15*, *16*) and carbon nanotube fibers (1~4.3 GPa and 120 GPa) (*17*, *33*). The inferior mechanical properties of the graphene fibers can be attributed to the intrinsic limit of the van der Waals interaction between graphene sheets within the macroscopic fiber structure upon reassembly of

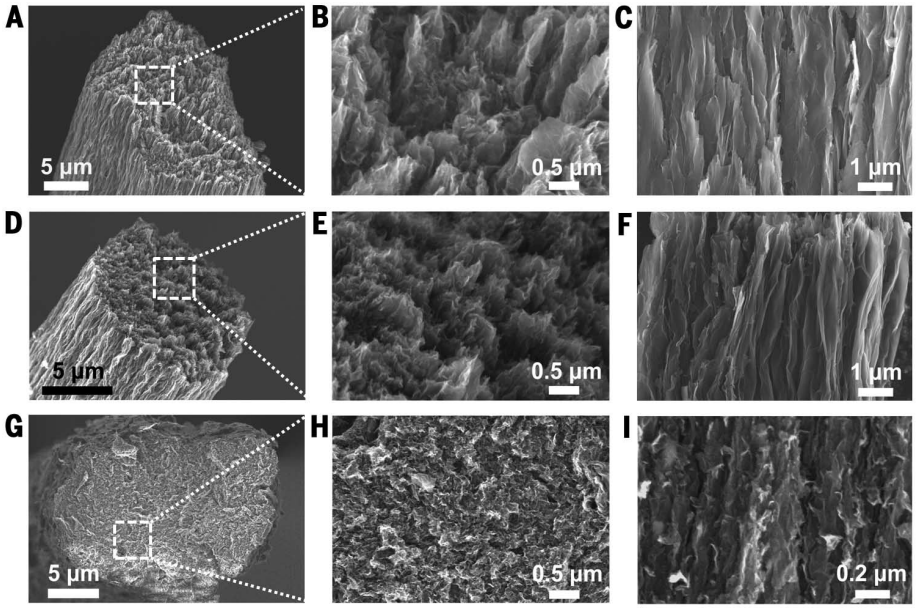


Fig. 3. SEM images showing morphology and inner structure of the graphene fibers (annealed at 1800°C). (**A** to **C**) tilted (A), transverse (B), and longitudinal section view (C) of the graphene fibers from pure LGGOs; (**D** to **F**) tilted (D), transverse (E), and longitudinal section view (F) of the optimized graphene fiber with 30 wt % SMGOs; (**G** to **I**) transverse section (G and H) and longitudinal section view (I) of the graphene fibers from pure SMGOs.

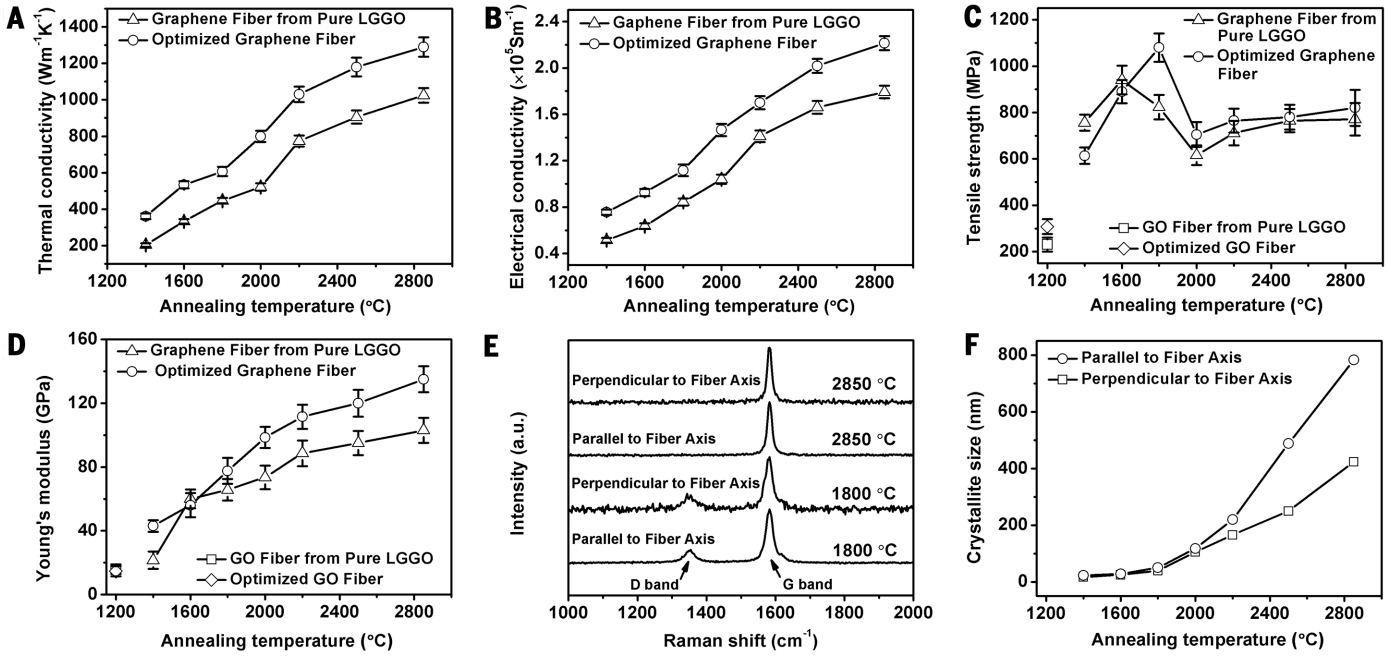


Fig. 4. Thermal, electrical, and mechanical properties of graphene fibers and the growth of crystallites upon thermal annealing. (**A**) Thermal conductivity of graphene fibers; (**B**) electrical conductivity of graphene fibers; (**C** and **D**) tensile strength and Young's modulus of GO fibers and graphene fibers; (**E**) polarized Raman spectra from the optimized graphene fibers in different directions; and (**F**) crystallite sizes in perpendicular and parallel directions to the fiber axis. The uncertainties are evaluated by the standard deviation of seven to nine measurements.

two-dimensinal individual GO sheets (*15*, *18*). The physical entanglement and strong covalent cross-links between graphitic planes may strongly improve the mechanical properties of conventional PAN-based carbon fibers and carbon nanotube fibers (*15*–*17*). Additionally, high-performance carbon fibers and carbon nanotube fibers can achieve more compact and more dense structures (e.g., up to a theoretical density of 2.2 g/cm^3 for carbon fibers and thus minimized voids and defects) (*15*, *16*, *33*).

High-performance carbon fibers are typically categorized into high-strength PAN-based fibers and high-modulus mesophase pitch-based carbon fibers (*15*, *16*, *22*). Thermal conductivity is typically lower for PAN-based carbon fibers because cross-linking atoms behave as scattering centers to reduce phonon transport (*15*). A strong correlation among the tensile strength, Young's modulus, and thermal and electrical conductivities was identified for mesophase pitch-based carbon fibers (*22*). High-temperature carbonization allows the development and growth of the crystalline graphitic domains and thus enables simultaneously high modulus and high conductivities for mesophase pitch-based carbon fibers (*15*, *22*, *24*). The superior thermal conductivity but lower modulus of the optimized graphene fibers as compared with mesophase pitch-based carbon fibers is unexpected and could be attributed to the unique fiber structure by intercalating large- and small-sized graphene sheets and substantially larger crystalline domain sizes in both transverse and longitudinal directions.

For graphene-based materials, heat conduction is dominated by phonon transport from lattice vibrations of the covalent sp^2 bonding network, and the electron transport is largely determined by the delocalized π-bond over the whole graphene sheet (*1*, *3*, *18*, *30*). The lattice vacancies and the residual functional groups on graphene sheets upon thermal reduction create substantial numbers of phonon- and electron-scattering centers, significantly degrading the thermal and electrical properties (*1*, *3*, *18*, *30*). High-temperature annealing heals defects in the lattice structure and removes oxygen functional groups and significantly increases the size of the sp^2 domains (fig. S6). The crystallite sizes (Fig. 4F) in parallel and perpendicular directions to the fiber axis have been calculated from the integrated intensity ratios of the D-band (1350 cm^{-1}) and the G-band (1581 cm^{-1}) based on polarized Raman spectra of the optimized graphene fibers annealed at different temperatures (Fig. 4E and fig. S8) (*31*, *32*). At lower annealing temperatures (e.g., 1800°C), graphene fibers demonstrate smaller-sized sp^2 domains (40 to 50 nm) with residual defects. The domain sizes of the optimized graphene fibers in both longitudinal and transverse directions increase substantially with the annealing temperature (Fig. 4F) and approach 783 and 423 nm, respectively, upon annealing at 2850°C. This is further evidenced by the submicrometer-sized crystalline domains along the fiber axis for the high temperature–treated fibers as observed in the bright-field transmission electron microscope images (fig. S6). These are orders of magnitude larger than the nanocrystalline graphitic domains (several tens of nanometers) inside the mesophase pitch-based and PAN-based carbon fibers (*15*, *22*, *32*). Despite the relatively lower density, the reduced phonon scattering from the boundary and interface due to the larger-sized crystalline domains enables more efficient phonon transport and, thus, enhanced thermal conductivity. The highly thermally conductive and mechanically strong graphene fibers with intercalated large- and small-sized graphene sheets have potential for thermal management materials in high-power electronics and reinforcing components for high-performance composite materials.

REFERENCES AND NOTES

1. A. A. Balandin, *Nat. Mater.* **10**, 569–581 (2011).
2. W. Jang, Z. Chen, W. Bao, C. N. Lau, C. Dames, *Nano Lett.* **10**, 3909–3913 (2010).
3. J. H. Seol *et al.*, *Science* **328**, 213–216 (2010).
4. C. Lee, X. Wei, J. W. Kysar, J. Hone, *Science* **321**, 385–388 (2008).
5. X. Du, I. Skachko, A. Barker, E. Y. Andrei, *Nat. Nanotechnol.* **3**, 491–495 (2008).
6. Z. Xu, C. Gao, *Nat. Commun.* **2**, 571 (2011).
7. Z. Xu, C. Gao, *Acc. Chem. Res.* **47**, 1267–1276 (2014).
8. Z. Xu, H. Sun, X. Zhao, C. Gao, *Adv. Mater.* **25**, 188–193 (2013).
9. H.-P. Cong, X.-C. Ren, P. Wang, S.-H. Yu, *Sci. Rep.* **2**, 613 (2012).
10. M. K. Shin *et al.*, *Nat. Commun.* **3**, 650 (2012).
11. X. Hu, Z. Xu, Z. Liu, C. Gao, *Sci. Rep.* **3**, 2374 (2013).
12. C. Xiang *et al.*, *ACS Nano* **7**, 1628–1637 (2013).
13. Z. Xu, Z. Liu, H. Sun, C. Gao, *Adv. Mater.* **25**, 3249–3253 (2013).
14. P. M. Adams, H. A. Katzman, G. S. Rellick, G. W. Stupian, *Carbon* **36**, 233–245 (1998).
15. X. Qin, Y. Lu, H. Xiao, Y. Wen, T. Yu, *Carbon* **50**, 4459–4469 (2012).
16. K. Naito, Y. Tanaka, J.-M. Yang, Y. Kagawa, *Carbon* **46**, 189–195 (2008).
17. N. Behabtu *et al.*, *Science* **339**, 182–186 (2013).
18. G. Xin *et al.*, *Adv. Mater.* **26**, 4521–4526 (2014).
19. C. Xiang *et al.*, *Adv. Mater.* **25**, 4592–4597 (2013).
20. L. Chen *et al.*, *Nanoscale* **5**, 5809–5815 (2013).
21. Materials and methods are available as supplementary materials on *Science* Online.
22. F. G. Emmerich, *Carbon* **79**, 274–293 (2014).
23. J.- Wang, M. Gu, W.- Ma, X. Zhang, Y. Song, *New Carbon Mater.* **23**, 259–263 (2008).
24. N. C. Gallego *et al.*, *Carbon* **38**, 1003–1010 (2000).
25. A. F. Thünemann, W. Ruland, *Macromolecules* **33**, 1848–1852 (2000).
26. A. Gupta, I. R. Harrison, J. Lahijani, *J. Appl. Cryst.* **27**, 627–636 (1994).
27. C. Zhu *et al.*, *Carbon* **50**, 235–243 (2012).
28. S. Zhang *et al.*, *Nat. Mater.* **9**, 594–601 (2010).
29. L. Song *et al.*, *Carbon* **52**, 608–612 (2013).
30. S. Pei, H.-M. Cheng, *Carbon* **50**, 3210–3228 (2012).
31. L. G. Cançado *et al.*, *Appl. Phys. Lett.* **88**, 163106 (2006).
32. M. Endo *et al.*, *Phys. Rev. B* **58**, 8991–8996 (1998).
33. J. N. Wang, X. G. Luo, T. Wu, Y. Chen, *Nat. Commun.* **5**, 3848 (2014).

ACKNOWLEDGMENTS

This work is financially supported by the U.S. National Science Foundation under awards DMR 1151028 and CMMI 1463083.

SUPPLEMENTARY MATERIALS

www.sciencemag.org/content/349/6252/1083/suppl/DC1
Materials and Methods
Supplementary Text
Figs. S1 to S8
Table S1
References (*34*–*40*)

8 January 2015; accepted 30 July 2015
10.1126/science.aaa6502

CATALYSIS

Sustainable Fe–ppm Pd nanoparticle catalysis of Suzuki-Miyaura cross-couplings in water

Sachin Handa,[1] Ye Wang,[1] Fabrice Gallou,[2] Bruce H. Lipshutz[1]*

Most of today's use of transition metal–catalyzed cross-coupling chemistry relies on expensive quantities of palladium (Pd). Here we report that nanoparticles formed from inexpensive $FeCl_3$ that naturally contains parts-per-million (ppm) levels of Pd can catalyze Suzuki-Miyaura reactions, including cases that involve highly challenging reaction partners. Nanomicelles are employed to both solubilize and deliver the reaction partners to the Fe–ppm Pd catalyst, resulting in carbon-carbon bond formation. The newly formed catalyst can be isolated and stored at ambient temperatures. Aqueous reaction mixtures containing both the surfactant and the catalyst can be recycled.

Precious metal catalysis has been and continues to be a predominant means of C-C, C-H, and C-heteroatom bond construction in organic synthesis. In particular, palladium-catalyzed Suzuki-Miyaura, Heck, and Negishi couplings are indispensable, as recognized by the 2010 Nobel Prize (*1*, *2*). However, economically accessible supplies of Pd and other precious metals are dwindling, thus raising concerns about the sustainability of this chemistry (*3*).

To circumvent this situation, alternative metals such as nickel (*4*, *5*) and copper (*6*, *7*) have been studied, especially as applied to the heavily used, Pd-catalyzed Suzuki-Miyaura reactions (*8*, *9*). Despite varying degrees of success, Pd remains, by

[1]Department of Chemistry and Biochemistry, University of California–Santa Barbara, Santa Barbara, CA 93106, USA. [2]Novartis Pharma, Basel, Switzerland.
***Corresponding author. E-mail: lipshutz@chem.ucsb.edu**

far, the most effective metal for such reactions. In trace levels, perhaps as impurities in salts of less expensive metals, Pd could ultimately prove to be both natural and sustainable for use in catalysis. Here we disclose such a discovery: a technique that takes a readily available commercial salt derived from Earth-abundant iron—which naturally contains parts-per-million (ppm) levels of Pd—and processes it, in a single step, into highly active nanoparticles capable of mediating Suzuki-Miyaura cross-couplings in recyclable water as the reaction medium.

At the heart of this advance lies the confluence of several reaction variables: the origin and source of the iron salt, the presence of ppm levels of Pd, the manner through which these are converted to nanoparticles, and the use of aqueous micellar conditions for catalysis. The catalyst preparation calls for the use of inexpensive (97% purity) $FeCl_3$ containing ppm levels of Pd, admixed with a ligand and dissolved specifically in tetrahydrofuran (THF). Treatment of this solution at room temperature with two equivalents of a Grignard reagent, also in THF, quickly affords nanoparticles that, after solvent removal in vacuo, can be used directly in Suzuki-Miyaura reactions. The in situ generation of 5 mole percent (mol %) of these Fe–ppm Pd nanoparticles was found empirically to be sufficient. Next, an aqueous solution containing 2 weight percent (wt %) of our commercially available designer surfactant TPGS-750-M (*10*) and a base ($K_3PO_4 \cdot H_2O$, 1.5 to 2.0 equivalents) is added to the nanoparticles. Reaction partners **1** and **2** as model substrates are then introduced, leading to biaryl product **3** (Fig. 1). The choice of ligand is crucial (Fig. 1), with SPhos (2-dicyclohexylphosphino-2′,6′-dimethoxybiphenyl) and XPhos (2-dicyclohexylphosphino-2′,4′,6′-triisopropylbiphenyl) affording the best results. Vigorous stirring at temperatures between ambient and 45°C, depending upon the extent of crystallinity of the reaction partners, is sufficient to drive couplings to completion, typically in the 12- to 24-hour time frame (at a global concentration of 0.5 M).

We examined the scope of this technology and found that many representative cases afford good-to-excellent isolated yields (Fig. 2). A broad variety of aromatic and heteroaromatic arrays, with either partner being the aryl halide or boron derivative, can be tolerated. Functional groups including CF_3, amines, acetals, amides, aldehydes, esters, ketones, phosphate esters, nitro groups, polyaromatics, sulfonamides, and carbamates are represented among these examples. Several types of heteroaromatic arrays are also amenable, including nitrogen-containing moieties that might present complications as competing ligands for Pd. Both bromides and iodides are excellent educts, and the boron species involved can be any of those commonly employed: boronic acids, Bpin (boronic acid pinacol ester) (*11*) or *N*-methyliminodiacetic acid (MIDA) boronates (*12*, *13*), and BF_3K salts (*14*, *15*).

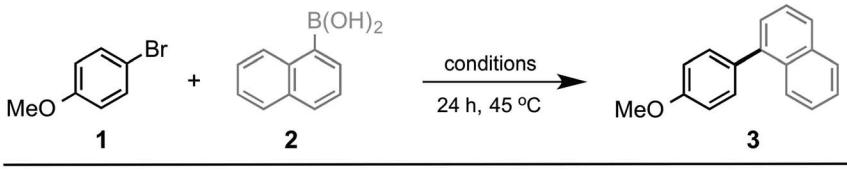
The composition of the iron salt plays a role in the activity of the resulting nanoparticles, as does the manner in which the salt is reduced. Attempts to use $Fe(acac)_3$ (acac, acetylacetonate) and iron pyrophosphate [$Fe_4(P_2O_7)_3$], as well as several other salts (table S2), led to a far less reactive catalyst (also formed in situ) than that derived from $FeCl_3$. Analysis of $FeCl_3$ from a commercially available source by inductively coupled plasma (ICP) atomic absorption spectrometry showed that ~300 to 350 ppm Pd was present. Sources that contained less precious metal (*16*, *17*) led to incomplete reactions under otherwise identical conditions. Doping alternative sources of $FeCl_3$ (≥97% purity) with 350 ppm $Pd(OAc)_2$ (OAc, acetate) yielded nanoparticles of identical activity, as assessed by using the model reaction that produced **3** (table S14) (*17*–*20*). However, attempts to use these ppm levels of Pd in the absence of preformed iron-based nanoparticles led to virtually no reaction, suggesting that the release of Pd into the aqueous medium is not responsible for the catalysis observed. Although the use of Grignard reagents MeMgX (X = Cl or Br) and *i*-PrMgCl yielded material of comparable activity, both PhMgCl and *n*-hexyl-MgBr, among other reductants (e.g., $NaBH_4$, polymethylhydrosiloxane), led to nanoparticles of inferior quality (table S4).

Successful couplings require the presence of both Fe and Pd within these nanocomposites, as determined by several control reactions (Fig. 3). Reactions that were attempted using 400 ppm $Pd(OAc)_2$, with SPhos as a ligand in various ratios, did not lead to product formation. The use of 5 mol % pure $FeCl_3$ with 400 ppm $Pd(OAc)_2$ and 500 ppm SPhos, without prior treatment with MeMgCl, afforded none of the biaryl product. However, upon reduction of 5 mol % pure $FeCl_3$ with 10 mol % MeMgCl in the presence of 320 ppm $Pd(OAc)_2$ and 5 mol % SPhos, a highly active nanocatalyst was generated that mediated the desired coupling to deliver pure product in a 95% isolated yield.

Doping pure $FeCl_3$ with 500 ppm of other metals, such as $NiCl_2$, $Ni(acac)_2$, $CoCl_3$, $MnCl_2$, $Cu(OAc)_2$, or $CuBr_2$, led to catalysts that produced variable levels of product formation. In all cases, the yields were ≤38%, as compared with 95% obtained in the presence of added $Pd(OAc)_2$ (table S5).

Solid iron nanoparticles formed from $FeCl_3$ and MeMgCl were collected and analyzed by transmission electron microscopy (TEM) and x-ray photoelectron spectroscopy (XPS) (figs. S8 to S11). As illustrated in fig. S11, XPS analysis revealed that most of this nanomaterial is raft-shaped; composed of large amounts of carbon (57.4%), oxygen (23.6%), magnesium (6.5%), and chlorine (9.8%); and characterized by an essentially 1:1 ratio between iron (1.4%) and phosphorus (in SPhos; 1.3%). The high levels of carbon and oxygen are associated with residual solvent (THF) integrated within these clusters; the C-O signal appears as a shoulder in the C1s spectrum (286.5 eV) (figs. S9 to S11). Only 1.4% iron, in the form of iron oxides (Fe $2p_3$, 710.86 eV), was present in the nanoparticles produced via reduction of $FeCl_3$ with MeMgCl in THF.

Cryogenic TEM (cryo-TEM) analysis revealed the aggregation of rafts of metal nanoparticles, either inside or around the nanomicellar surface (Fig. 4, A to C). Scanning electron microscopy (SEM), together with energy-dispersive x-ray (EDX) analyses, showed the presence of hybrid nanoparticles containing both iron and ligand (Fig. 4, D and E, and figs. S12 to S14). Further analyses by atomic force microscopy (AFM)



entry	ligand	yield **3** (%)*	entry	ligand	yield **3** (%)*
1	none	-	8	IPr	70
2	PPh_3	28	**9**	**SPhos**	**98**
3	dppf	70	10	*t*-BuSPhos	92
4	dtbpf	75	11	XPhos	94
5	Bidime	81	12	*t*-BuXPhos	89
6	Tangphos	69	13	BrettPhos	44
7	IMes	50	14	*t*-BuBrettPhos	40

Fig. 1. Ligand optimization for Fe–ppm Pd catalysis of Suzuki-Miyaura cross-couplings. Conditions were as follows: 4-bromoanisole (0.5 mmol), naphthalene-1-boronic acid (0.75 mmol), 5 mol % Fe–ppm Pd nanoparticles, $K_3PO_4 \cdot H_2O$ (0.75 mmol), 2 wt % TPGS-750-M (1 ml). Asterisks indicate yields based on gas chromatography–mass spectrometry (GC-MS).

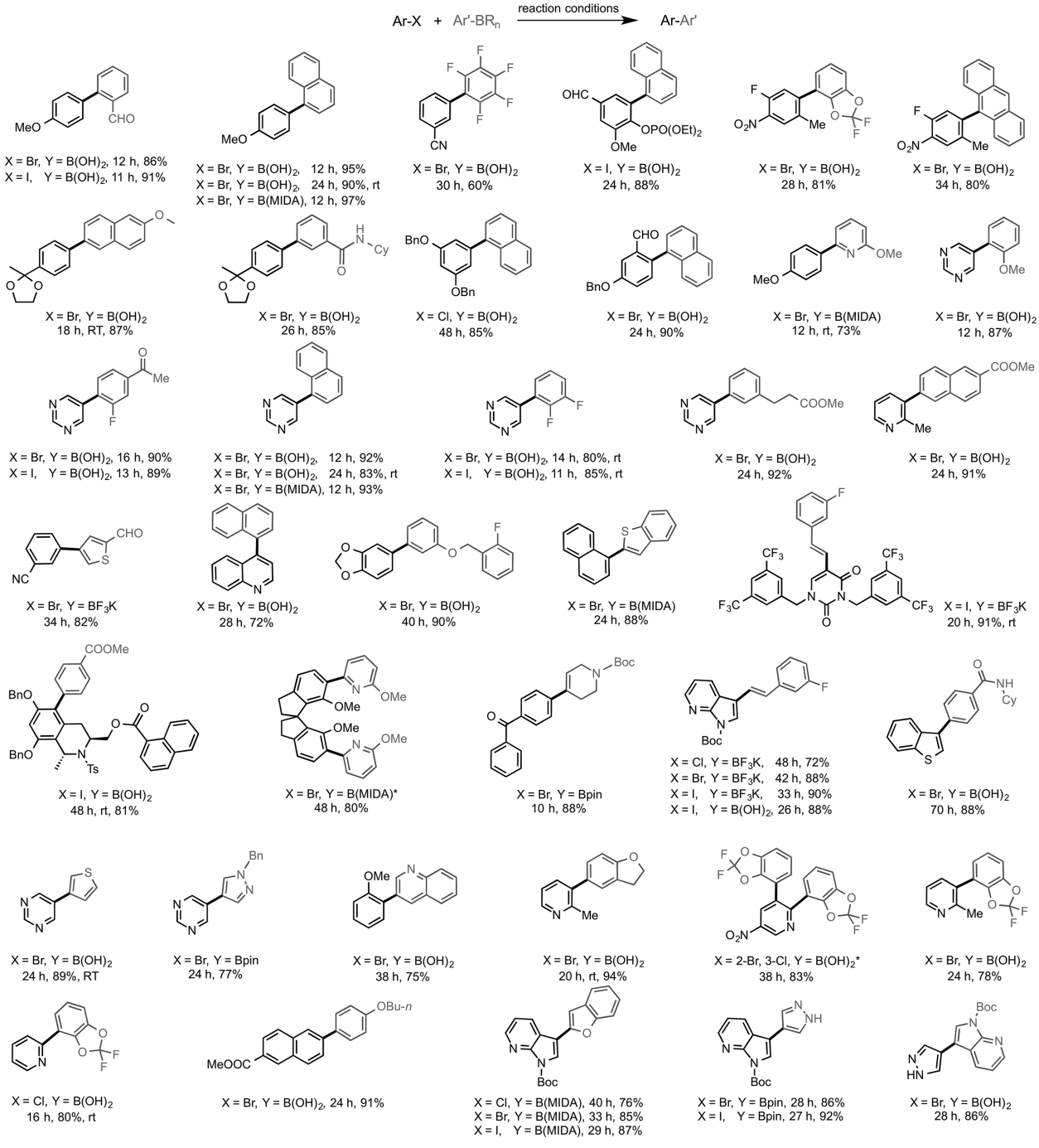


Fig. 2. Couplings between aryl halides (Ar-X) and aryl (Ar') or alkenyl boron derivatives. Unless otherwise noted, conditions for these couplings were as follows: Ar-X (0.5 mmol), Ar'-BRn (0.6 mmol), $FeCl_3$ (5 mol %), SPhos (5 mol %), MeMgCl (10 mol %), K_3PO_4•H_2O (0.75 mmol), TPGS-750-M (2 wt %, 1 ml), 45°C. Room temperature, rt. Asterisks indicate the use of Ar-$B(OH)_2$ or Ar-B(MIDA) (1.2 mmol) and K_3PO_4•H_2O (1.5 mmol). Reported yields are for isolated, chromatographically purified materials. 320 ppm Pd is required (the general procedure is described in detail in the supplementary materials).

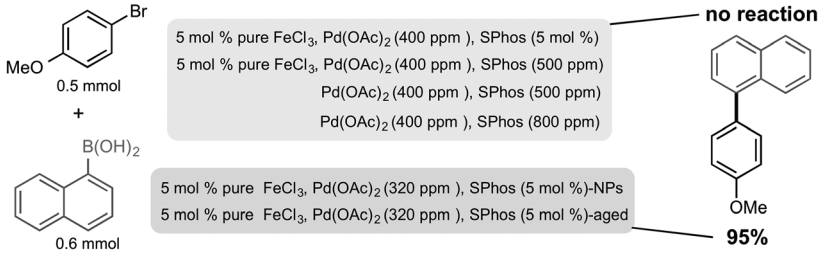


Fig. 3. Control reactions documenting the importance of both Fe and Pd in catalyst formation. Details are provided in the supplementary materials.

(Fig. 4F) revealed an atypical arrangement of iron atoms intermixed mainly with Mg. These particles have a long shelf life (≥1 month at room temperature) and are virtually identical in catalytic activity to those prepared and used in situ.

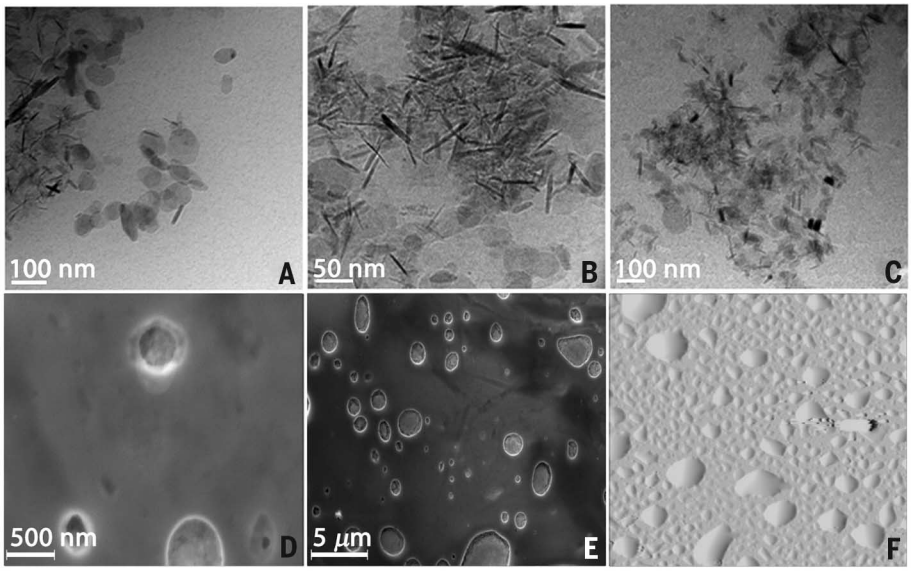


Fig. 4. Catalyst characterization. (**A** to **C**) Cryo-TEM images of Fe-Pd nanorods in aqueous TPGS-750-M. (**D** and **E**) SEM images of the solid nanomaterial. (**F**) AFM image of the solid nanomaterial.

Thermogravimetric analysis (TGA) of nanomaterial revealed about a 40% total drop in weight between 60° and 145°C, corresponding to the loss of THF bound within the catalyst. Material heated beyond 145°C was stable up to 380°C. However, when the catalyst was preheated at 80°C under a vacuum for 12 hours (fig. S6), a loss of catalytic activity was observed, indicating the importance of THF in maintaining the nanocage structure.

Upon completion of a Suzuki-Miyaura coupling, in-flask extraction with a single organic solvent (e.g., ethyl acetate or methyl *tert*-butyl ether) at ambient temperatures produces crude material that can be further purified by standard means (fig. S2). The remaining aqueous mixture containing both nanomicelles and nanoparticles of iron can then be recycled, with a modest augmentation of Pd [i.e., 160 ppm $Pd(OAc)_2$] at every other recycling to compensate for losses during extraction. Although the external addition of this Pd salt extends the catalyst activity, the manner in which it is reduced to active Pd(0) and how it is incorporated into the Fe nanoparticles remain unclear. Either the same or different educts can be used in these couplings, indicating the robustness of the process. Alternatively, with solid products, dilution with water could be followed by simple filtration to produce the targeted material

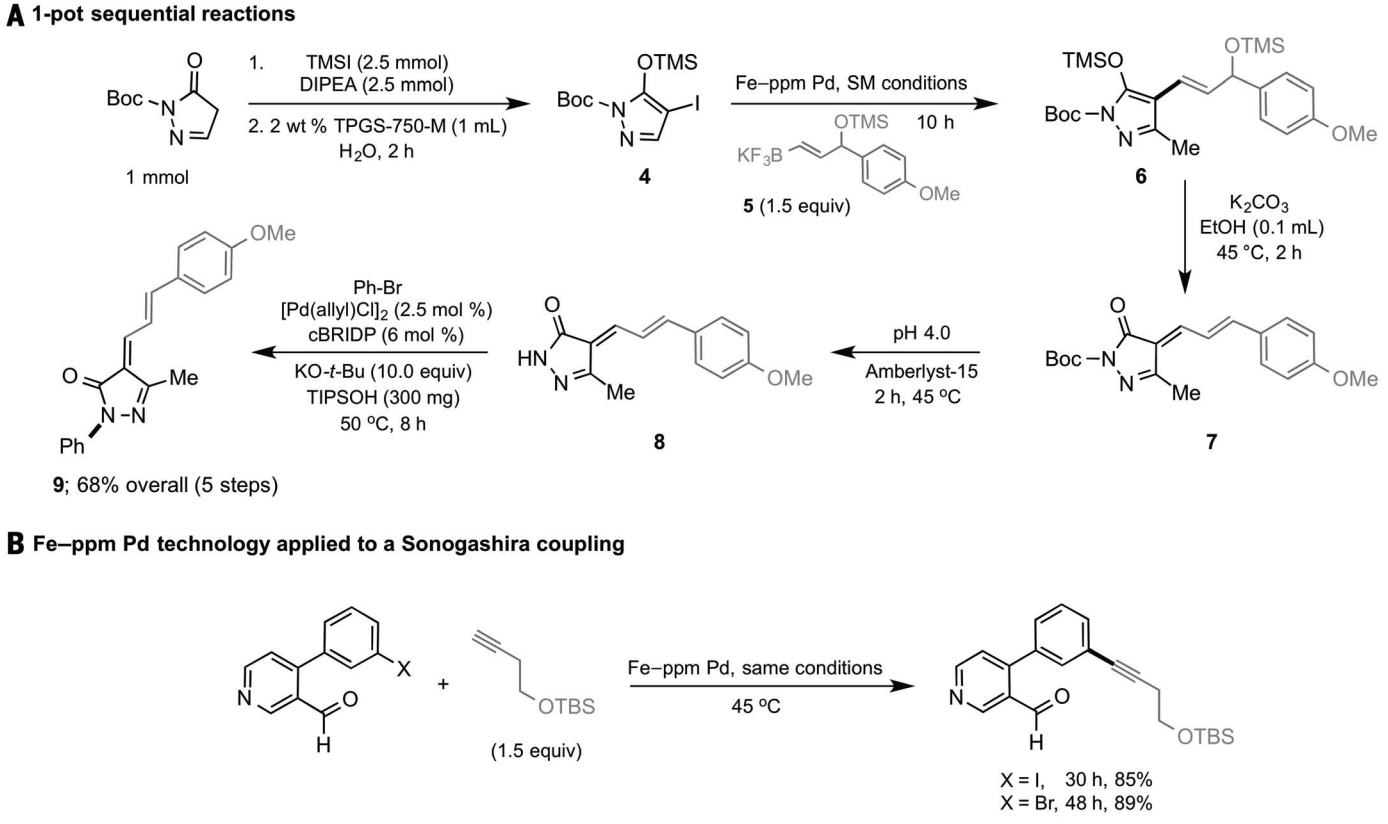


Fig. 5. Further applications of Fe–ppm Pd–catalyzed couplings. (**A**) Sequential reactions, including a Suzuki-Miyaura coupling using Fe–ppm Pd nanoparticles as the catalyst (TMSI, TMS iodide; DIPEA, diisopropylethylamine; cBRIDP, di-*t*-butyl(2,2-diphenyl-1-methyl-1-cyclopropyl)phosphine; KO-*t*-Bu, potassium *t*-butoxide; TIPSOH, triisopropylsilyl alcohol). (**B**) A representative example suggestive of the extension of this approach to Sonogashira couplings (OTBS, *t*-butyldimethylsilyloxy).

directly. The diluted filtrate could be augmented with TPGS-750-M to the original level (2 wt %) and reused, thereby creating little to no wastewater stream. The environmental factor (E factor) (*21*), a metric of "greenness" that has previously been applied to micellar catalysis (*22*), is very low (E factor = 3).

We used ICP to analyze the palladium content (<10 ppm) of a product formed via the technology presented here, and we compared the result with that quantified following a traditional Suzuki-Miyaura coupling in organic solvent (fig. S4). Residual palladium in the product derived from a standard coupling in dioxane was far higher than that observed using our nanoparticle approach.

Prospects for incorporating this water-based nanomicelle-nanometal technology into a one-pot sequence of reactions are shown in Fig. 5A. Heteroaryl iodide **4**, containing carbamate and trimethylsilyl (TMS) protecting groups, was generated in situ and then subjected to cross-coupling with alkenyl tetrafluoroborate salt **5**, using the Fe–ppm Pd nanoparticle protocol. The coupling product **6** was then exposed to aqueous base to remove the TMS groups and effect elimination to **7**, followed by butoxycarbonyl (Boc) deprotection to **8**. Final aryl amination with bromobenzene to **9** provided entry to the bioactive class of 2,4,5-substituted pyrazol-3-one compounds in a one-pot sequence with an overall isolated yield of 68% (*23*).

In addition, testing the potential for this mixed-metal catalyst system to effect other important Pd-catalyzed reactions, such as Sonogashira couplings, was carried out (in the absence of added copper), following the example illustrated in Fig. 5B. The prognosis for a similar outcome is good.

REFERENCES AND NOTES

1. C. C. C. Johansson Seechurn, M. O. Kitching, T. J. Colacot, V. Snieckus, *Angew. Chem. Int. Ed.* **51**, 5062–5085 (2012).
2. H. Li, C. C. C. Johansson Seechurn, T. J. Colacot, *ACS Catal.* **2**, 1147–1164 (2012).
3. J. Kooroshy, C. Meindersma, R. Podkolinski, M. Rademaker, T. Sweijs, A. Diederen, M. Beerthuizen, S. de Goede, *Scarcity of Minerals: A Strategic Security Issue* (No. 02/01/10, The Hague Center for Strategic Studies, The Hague, Netherlands, 2009).
4. F.-S. Han, *Chem. Soc. Rev.* **42**, 5270–5298 (2013).
5. J. C. Tellis, D. N. Primer, G. A. Molander, *Science* **345**, 433–436 (2014).
6. S. K. Gurung, S. Thapa, A. Kafle, D. A. Dickie, R. Giri, *Org. Lett.* **16**, 1264–1267 (2014).
7. Y. Zhou, W. You, K. B. Smith, M. K. Brown, *Angew. Chem. Int. Ed.* **126**, 3543–3547 (2014).
8. M. R. Netherton, G. C. Fu, *Adv. Synth. Catal.* **346**, 1525–1532 (2004).
9. G. D. Allred, L. S. Liebeskind, *J. Am. Chem. Soc.* **118**, 2748–2749 (1996).
10. B. H. Lipshutz *et al.*, *J. Org. Chem.* **76**, 4379–4391 (2011).
11. A. J. J. Lennox, G. C. Lloyd-Jones, *Chem. Soc. Rev.* **43**, 412–443 (2014).
12. N. A. Isley, F. Gallou, B. H. Lipshutz, *J. Am. Chem. Soc.* **135**, 17707–17710 (2013).
13. S. J. Lee, T. M. Anderson, M. D. Burke, *Angew. Chem. Int. Ed.* **49**, 8860–8863 (2010).
14. G. A. Molander, Y. Yokoyama, *J. Org. Chem.* **71**, 2493–2498 (2006).
15. S. Darses, J.-P. Genet, *Chem. Rev.* **108**, 288–325 (2008).
16. T. H. Bointon *et al.*, *Nano Lett.* **14**, 1751–1755 (2014).
17. S. L. Buchwald, C. Bolm, *Angew. Chem. Int. Ed.* **48**, 5586–5587 (2009).
18. C. L. Chun, D. R. Baer, D. W. Matson, J. E. Amonette, R. L. Penn, *Environ. Sci. Technol.* **44**, 5079–5085 (2010).
19. Y.-P. Sun, X. Q. Li, J. Cao, W.-X. Zhang, H. P. Wang, *Adv. Colloid Interface Sci.* **120**, 47–56 (2006).
20. I. Thomé, A. Nijs, C. Bolm, *Chem. Soc. Rev.* **41**, 979–987 (2012).
21. R. A. Sheldon, *Green Chem.* **9**, 1273 (2007).
22. B. H. Lipshutz, N. A. Isley, J. C. Fennewald, E. D. Slack, *Angew. Chem. Int. Ed.* **52**, 10952–10958 (2013).
23. P. N. Dube *et al.*, *Chem. Biol. Drug Des.* **84**, 409–419 (2014).

ACKNOWLEDGMENTS

We thank Novartis for financial support; J. Feng for technical assistance; M. Cornish for acquisition of the AFM images; S. Kraemer for obtaining the cryo-TEM, SEM, and EDX data; and J. Matthey for providing Pd salts. Parts of this work were carried out in the Characterization Facility, University of Minnesota, which receives partial support from NSF through the Materials Research Science and Engineering Center (MRSEC) program. This work also made use of the University of California–Santa Barbara (UCSB) Materials Research Laboratory Central Facilities, supported by NSF's MRSEC program under award no. DMR-1121053. ICP-MS analyses were provided by J. Reilly (Novartis, Cambridge, MA). We also acknowledge support from NIH in the form of a Shared Instrument Grant to UCSB(1S10OD012077-01A1). A preliminary patent covering this chemistry has been filed by the University of California–Santa Barbara. The experimental data reported in this paper are available in the supplementary materials.

SUPPLEMENTARY MATERIALS

www.sciencemag.org/content/349/6252/1087/suppl/DC1
Materials and Methods
Figs. S1 to S18
Tables S1 to S15
References (*24*–*34*)

13 June 2015; accepted 30 July 2015
10.1126/science.aac6936

NATURAL HAZARDS

Slip pulse and resonance of the Kathmandu basin during the 2015 Gorkha earthquake, Nepal

J. Galetzka,[1]* D. Melgar,[2] J. F. Genrich,[1] J. Geng,[3] S. Owen,[4] E. O. Lindsey,[3] X. Xu,[3] Y. Bock,[3] J.-P. Avouac,[5,1]† L. B. Adhikari,[6] B. N. Upreti,[7] B. Pratt-Sitaula,[8] T. N. Bhattarai,[9] B. P. Sitaula,[9] A. Moore,[4] K. W. Hudnut,[10] W. Szeliga,[11] J. Normandeau,[12] M. Fend,[12] M. Flouzat,[13] L. Bollinger,[13] P. Shrestha,[6] B. Koirala,[6] U. Gautam,[6] M. Bhatterai,[6] R. Gupta,[6] T. Kandel,[6] C. Timsina,[6] S. N. Sapkota,[6] S. Rajaure,[6] N. Maharjan[6]

Detailed geodetic imaging of earthquake ruptures enhances our understanding of earthquake physics and associated ground shaking. The 25 April 2015 moment magnitude 7.8 earthquake in Gorkha, Nepal was the first large continental megathrust rupture to have occurred beneath a high-rate (5-hertz) Global Positioning System (GPS) network. We used GPS and interferometric synthetic aperture radar data to model the earthquake rupture as a slip pulse ~20 kilometers in width, ~6 seconds in duration, and with a peak sliding velocity of 1.1 meters per second, which propagated toward the Kathmandu basin at ~3.3 kilometers per second over ~140 kilometers. The smooth slip onset, indicating a large (~5-meter) slip-weakening distance, caused moderate ground shaking at high frequencies (>1 hertz; peak ground acceleration, ~16% of Earth's gravity) and minimized damage to vernacular dwellings. Whole-basin resonance at a period of 4 to 5 seconds caused the collapse of tall structures, including cultural artifacts.

The shape of the slip-rate time function (STF) during a seismic rupture provides critical insight into the constitutive fault properties. The abruptness of the slip onset determines the high-frequency content of the STF, and hence the intensity of the near-field ground motion (*1*), whereas the tail, which discriminates pulse-like and crack-like ruptures (*2*), has a low-frequency signature. Therefore, resolving the STF with band-limited strong-motion records is difficult. Combining high-rate Global Positioning System (GPS) waveforms (*3*, *4*), which capture both dynamic and permanent deformation, overcomes this limitation.

The 25 April 2015 moment magnitude (M_w) 7.8 earthquake in Gorkha, Nepal resulted from the unzipping of the lower edge of the locked portion of the Main Himalayan Thrust (MHT) fault, along which the Himalayan wedge is thrust over India (*5*). The earthquake nucleated ~80 km northwest of Kathmandu and ruptured a 140-km-long segment of the fault (Fig. 1A), with a hypocentral depth of ~15 km and a dip angle of 7° to 12° (*5*, *6*). The MHT accommodates most of the convergence between India and southern Tibet, with a convergence rate between 17 and 21 mm/year (*7*). For the 2015 event, which resulted in over 8000 deaths (mostly in Kathmandu and adjacent districts), modified Mercalli intensities (MMIs) reported by the National Society for Earthquake Technology–Nepal (NSET) (*8*) reached up to IX (violent shaking) and exceeded VI (strong shaking) over an area 170 km by 40 km. Kathmandu has been struck by repeated earthquakes in the past, with major destruction [MMI > X (extreme shaking)] in the years 1255, 1344, 1408, 1681, 1833, and 1934 (*9*–*11*). These earthquakes all occurred close to Kathmandu and have been

assigned magnitudes between M_w 7.5 and 8.4. During the Gorkha earthquake, damages in the Kathmandu basin were probably amplified by site effects, as has happened in past events (*12*, *13*). The basin is filled with 500 to 600 m of fluviolacustrine sediments resting on a metamorphic basement (*14*).

The damage to the most vulnerable vernacular dwellings in Kathmandu, which rarely exceed four stories, was much less than expected in view of the 2015 earthquake's magnitude and its proximity to Kathmandu. In contrast, some taller structures were more severely affected, such as the 60-m-tall Dharahara tower, which collapsed even though it had partially survived an M_w 8.1 to 8.4 earthquake in 1934. The 1934 event caused much more extensive destruction to vernacular dwellings in Kathmandu than the 2015 event did: 20% of the buildings in Kathmandu were destroyed in 1934 versus less than 1% in 2015 (*15*). These observations reflect the combined effects of the earthquake source characteristics and local geological conditions, in addition to the evolution of building practices.

The 2015 Gorkha earthquake ruptured a subhorizontal portion of the MHT that lies directly beneath a network (*16*) of continuous GPS (cGPS) stations, which record data at a high rate of five samples per second, and one accelerometer station (*17*) (Fig. 1A). In addition, surface displacements were measured with interferometric synthetic aperture radar [InSAR (*18*, *19*)] (fig. S1). Although a number of recent earthquakes have been documented with similar techniques (*20*, *21*), the Gorkha event is the first occurrence of a large continental thrust earthquake to be recorded by high-rate cGPS stations very close to and completely encompassing the rupture area. The combination of these measurements provides the opportunity to image the kinematics of the source process and the strong ground motion that led to the particular pattern of structural damage observed during this earthquake.

The records of seismic displacements and accelerations (Fig. 2 and fig. S2) show southward motion of up to 2 m, with a rise time on the order of 6 s. The pulse is particularly clear at cGPS station KKN4, located on bedrock just north of Kathmandu and only ~13 km above the fault. The displacement at this station started about 25 s after the onset of the rupture, corresponding to 15 s after the *P*-wave arrival (Fig. 2); it reached its final static value by about 32 s, based on the origin time of 06:11:26.270 UTC determined by the U.S. Geological Survey (USGS) from the arrival of radiated direct *P* waves (*6*). The records indicate a pulse-like rupture (*22*), with slip on any given portion of the fault occurring over a short fraction of the total ~70-s earthquake source duration (*5*). Given the ~78-km distance of KKN4 from the epicenter, the pulse must have propagated at ~3 km/s, a value consistent with waveform modeling and back projection of high-frequency seismic waves recorded at teleseismic distances (*5*). Surface velocities reached values of ~0.7 m/s. In addition to the pulse recorded at KKN4, the cGPS station NAST within the Kathmandu basin detected strong oscillations of about 3- to 4-s periods lasting for ~20 s (Fig. 2 and Fig. 3A). The Gorkha earthquake

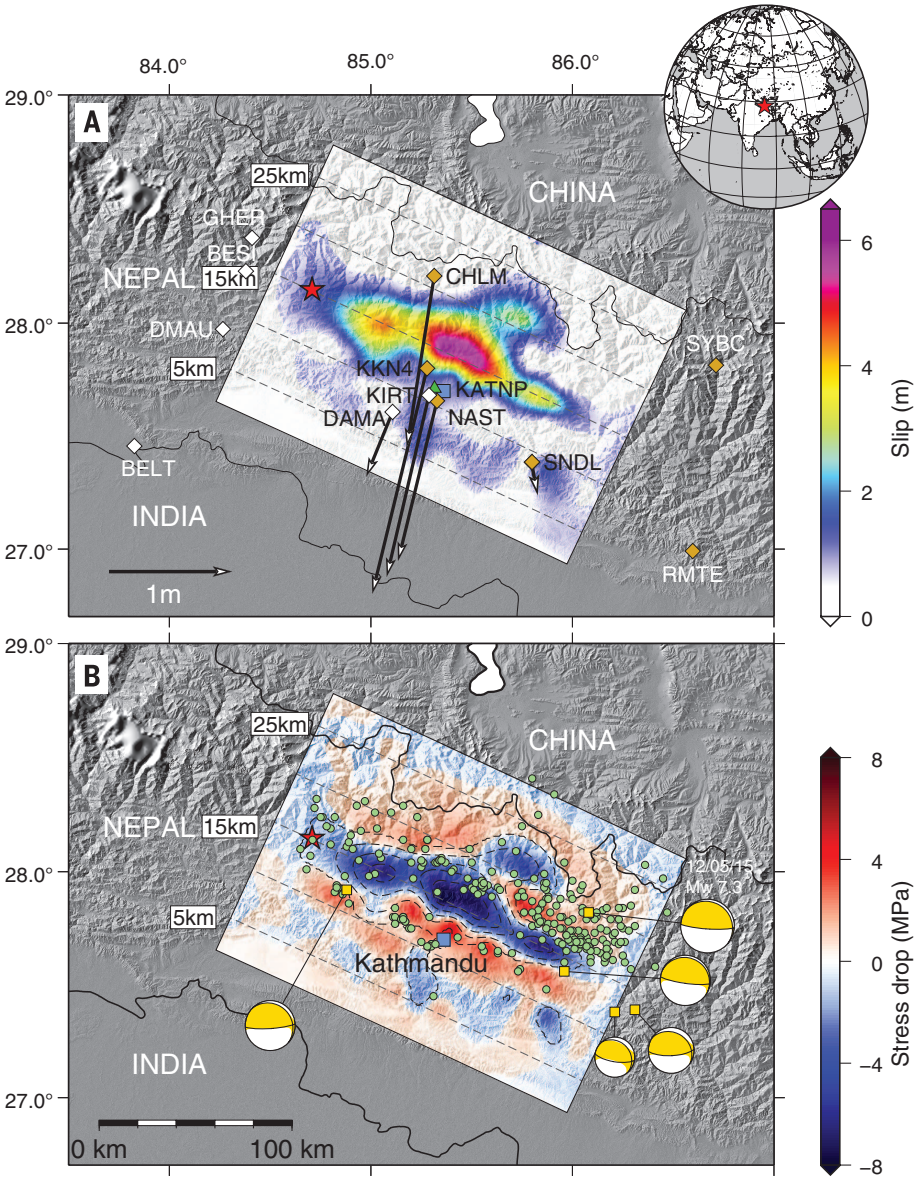


Fig. 1. Cumulative slip distribution of and static stress drop due to the Gorkha earthquake. (**A**) Slip inversion results for the M_w 7.8 Gorkha event. The red star is the hypocenter. Dashed contours are depths to the fault. Orange diamonds are 5-Hz cGPS stations, and white diamonds are low-rate (1/30-Hz) stations. The green triangle is the strong-motion station. Kathmandu is represented by the blue square. The black arrows indicate the coseismic offsets measured at the sites (the values and uncertainties are given in table S1). Vectors with less than 10 cm of displacement are not shown. (**B**) Static stress drop predicted by the model of Fig. 1A. Green circles are aftershocks with local magnitudes greater than four, recorded and located by the Nepal National Seismic Center. Focal mechanisms (yellow and white circles) represent the global centroid-moment tensor solutions for aftershocks with magnitudes greater than six.

[1]Department of Geology and Planetary Sciences, California Institute of Technology (Caltech), Pasadena, CA 91125, USA. [2]Berkeley Seismological Laboratory, University of California (UC)–Berkeley, Berkeley, CA 94720, USA. [3]Cecil H. and Ida M. Green Institute of Geophysics and Planetary Physics, Scripps Institution of Oceanography, UC–San Diego, La Jolla, CA 92037, USA. [4]Jet Propulsion Laboratory (JPL), Caltech, Pasadena, CA 91109, USA. [5]Department of Earth Sciences, University of Cambridge, Cambridge CB2 3EQ, UK. [6]Department of Mines and Geology, Lainchour, Kathmandu, Nepal. [7]Nepal Academy of Science and Technology, Khumaltar, Lalitpur, Nepal. [8]Department of Geological Sciences, Central Washington University (CWU), Ellensberg, WA 98926, USA. [9]Tri-Chandra Campus, Tribhuvan University, Ghantaghar, Kathmandu, Nepal. [10]U.S. Geological Survey (USGS), Pasadena, CA 91106, USA. [11]Pacific Northwest Geodetic Array and Department of Geological Sciences, CWU, Ellensberg, WA 98926, USA. [12]UNAVCO, Boulder, CO 80301, USA. [13]Département Analyse et Sureveillance de l'Environnement (DASE), Commissariat à l'Energie Atomique (CEA), 91297 Bruyères-le-Châtel, Arpajon, France.
*Present address: UNAVCO, Boulder, CO 80301, USA.
†Corresponding author. E-mail: avouac@gps.caltech.edu

must have excited a resonance of the Kathmandu basin as a whole. The resonance is evident in the response spectra from these stations and in data from the accelerometer station, KATNP (Fig. 3, G to I).

To determine the kinematics of the seismic rupture, we carried out a formal inversion of time-dependent slip on the fault (*23*, *24*) and compared the recorded waveforms with forward predictions, assuming a propagating slip pulse with varied characteristics. We assumed a planar fault geometry with a strike of 295° and a dip of 11°, in accordance with the teleseismic W-phase moment tensor solution calculated by the USGS (*6*). We tested shallower dips up to 7° but found that 11° provided a better fit to the data. The fault was discretized into 10 km by 10 km subfault segments. We jointly inverted the three-component 5-Hz GPS–derived velocity waveforms, the GPS static offsets, and the InSAR line of sight (LOS) static displacements measured between 22 February and 3 May (fig. S1). The GPS displacement time series shows large postseismic motion at only one station (CHLM), with a magnitude of less than 2 cm in both the horizontal and vertical directions over the week after the earthquake. Therefore, we neglected the contribution of postseismic deformation to the LOS displacements. The model fits both data sets closely (Fig. 1A), with an 86% reduction in variance for the InSAR and GPS coseismic displacements and a 74% reduction in variance for the GPS velocity waveforms (figs. S2 and S4). The model indicates a predominantly unilateral rupture to the southeast, with a peak slip of ~6.5 m on a large asperity to the north of Kathmandu. The event duration was 65 s (fig. S4), with the peak moment release at 23 s when the slip pulse was less than 10 km north of Kathmandu (movie S1); the peak slip rate was 1.1 m/s. Most of the slip was concentrated within a narrow region between the 10- and 20-km fault-depth contours. We found a large asperity with 3.0 m of slip, located east of the main asperity and between 20 and 23 km below the surface. The rupture velocity of the propagating slip pulse, indicated by the onset of slip in our best-fitting model, was ~3.2 km/s and had a maximum allowed velocity of 3.3 km/s (fig. S4). This velocity corresponds to ~95% of the shear wave speed at the depth where the majority of the slip occurred (15 km), according to the local velocity model used to calculate the Green's functions (table S2), which indicates a very fast rupture propagation. The slip tapered at 17 to 20 km depth along the edge of the locked zone of the MHT.

The inversion that we performed includes a large number of parameters, which would allow for a relatively complex rupture history. However, the resulting model is simple, with essentially a single propagating slip pulse. The spatiotemporal evolution of the slip pulse matches well with the location of the sources of high-frequency seismic waves (0.5 to 2 Hz) derived from back projection of the teleseismic waveforms (*5*) (movie S1).

We calculated the static stress change on the fault plane due to the earthquake (Fig. 1B). This

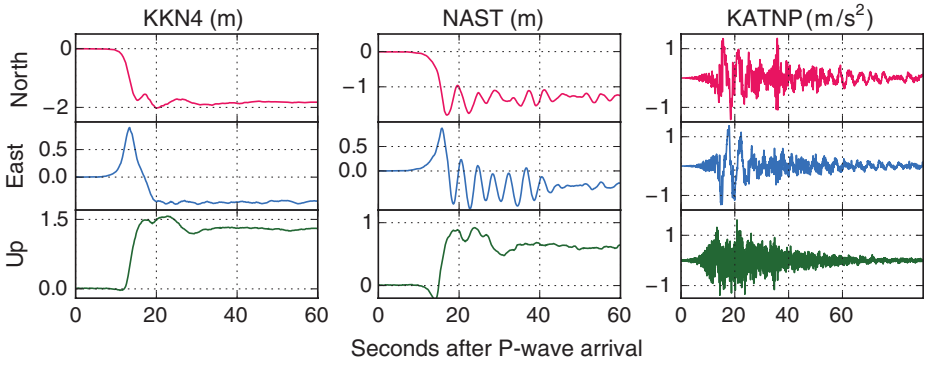


Fig. 2. Records of ground displacements and accelerations during the Gorkha earthquake. Shown are displacement waveforms at cGPS stations KKN4 and NAST (five samples per second) and acceleration waveforms at strong-motion station KATNP (Fig. 1).

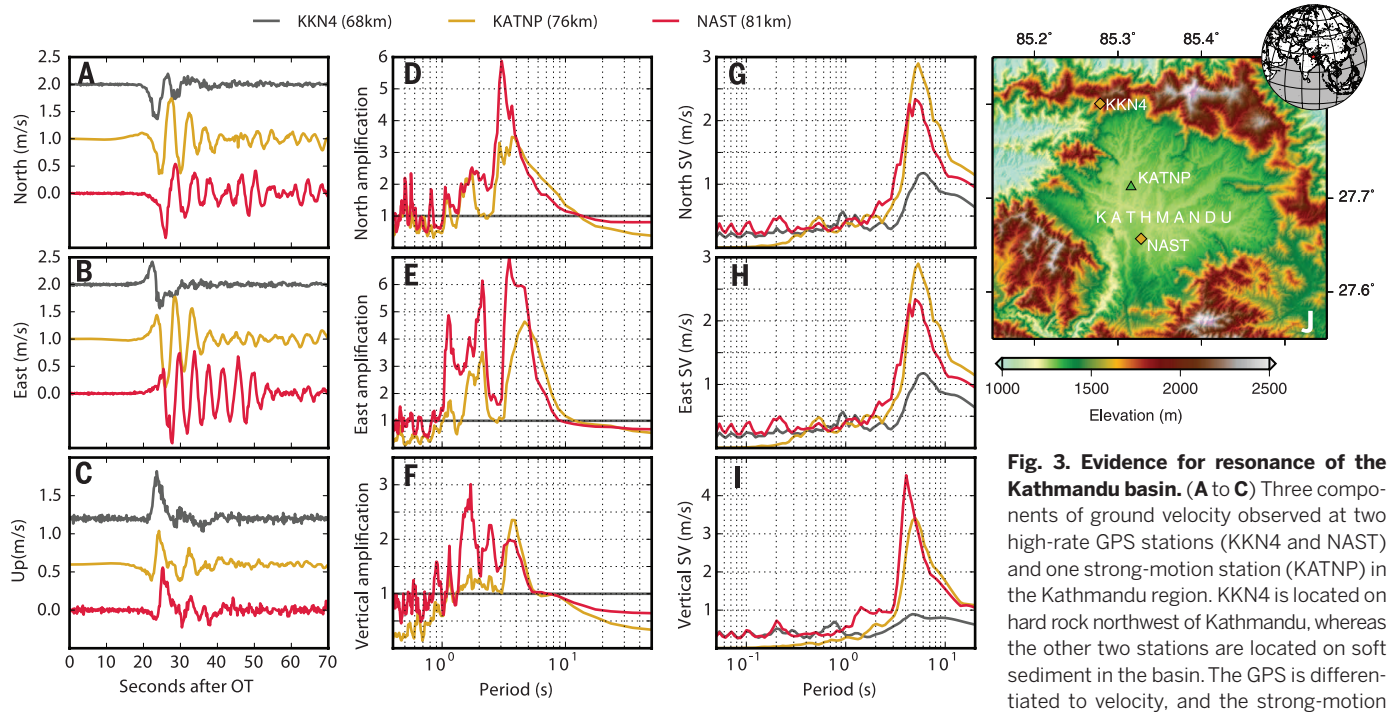


Fig. 3. Evidence for resonance of the Kathmandu basin. (**A** to **C**) Three components of ground velocity observed at two high-rate GPS stations (KKN4 and NAST) and one strong-motion station (KATNP) in the Kathmandu region. KKN4 is located on hard rock northwest of Kathmandu, whereas the other two stations are located on soft sediment in the basin. The GPS is differentiated to velocity, and the strong-motion data are integrated after high-pass filtering at 0.02 Hz. (**D** to **F**) Ground-motion amplification observed at the two basin stations. Plotted is the ratio of the amplitude spectra of the basin stations to the amplitude spectra of the reference bedrock station, KKN4. (**G** to **I**) Five-percent damped velocity response spectra for all three stations. (**J**) Close-up map showing the location of the basin and bedrock stations.

calculation showed loading of the fault around the main asperity where most of the aftershocks occurred, including the M_w 7.3 aftershock of 12 May, as expected for aftershocks triggered by coseismic stress transfer (*25*). The model predicted a pattern of uplift in the Kathmandu basin and subsidence at the front of the high range (fig. S4), approximately opposite to the pattern observed in the interseismic period, as expected from simple models of the seismic cycle on the MHT (*26*, *27*).

The record at station KKN4 should be a close representation of the STF, as it lies only about 13 km above the propagating slip pulse and is not affected by the site effects observed at the stations in the Kathmandu basin. We conducted synthetic tests with the same Earth structure model used in the inversion (table S1) to assess the distortion and smoothing introduced by the elastic half-space response (fig. S5). We found a vertical velocity amplitude of about 70% of the peak slip rate on the fault directly beneath the station, along with a well-preserved temporal shape. Furthermore, the tests demonstrated that the smooth onset of slip is not an artifact of the transfer through the elastic medium, represented by the elastodynamic Green's functions. The shape of the slip pulse can also be retrieved from the GPS records at NAST and the strong-motion vertical records at KATNP, which are less affected by site effects than the horizontal records (Fig. 1). All three records indicate a pulse ~6 s in duration. The shape of the pulse fits the regularized Yoffe function (*28*), yielding a smooth rise, with an acceleration time to the peak slip rate of τ_s = 1.7 s, a rise time of τ_R = 3.3 s, and a total effective duration of τ_{eff} = 6.7 s. The slip-rate pulse derived from the inversion also fits well, using the same values of τ_s and τ_R and peak slip-rate of ~0.9 m/s (Fig. 4). We compared the recorded waveforms with predictions from a suite of forward models to test the robustness of our results. We used the static slip model in these tests, deduced from the inversion of the GPS static and InSAR measurements (fig. S7). We assumed a propagating slip pulse and a regularized Yoffe STF with varying characteristics. We varied the rupture velocity between 2.8 and 3.6 km/s and the rise time between 2 and 10 s (fig. S8). By inverting synthetics calculated from forward modeling, we also tested the resolution power of the inversion and the limited bias introduced by the regularization applied to the inversion (*24*) (figs. S10 and S11). Together, these tests demonstrated that the duration of the slip pulse was probably less than 10 s, the time to the peak slip rate could not have been shorter than 1 s (we would otherwise have observed a much larger amplitude at high frequencies), and the average propagation rate of the slip pulse was not less than ~3.0 km/s over the first 30 s (until KKN4, NAST, and KATNP recorded a pulse signal).

Tinti *et al.* (*28*) analyzed how the shape of the STF relates to the characteristics of the friction law that governs the dynamics of the rupture. Based on this rationale (their equations 6 and 11), we estimated the slip-weakening distance to be ~5 m (for a peak slip of 6.5 m). This distance is large compared with those estimated from kinematic and dynamic modeling of seismic ruptures (*29*, *30*), which tend to be overestimated (*1*) and are typically on the order of 0.5 to 1 m. The large value we obtained is possibly related to the earthquake's having occurred close to the brittle-ductile transition at the lower edge of the locked portion of the MHT. The modeled smooth onset of the STF and the related large slip-weakening distance provide an explanation of the relatively low amplitude of shaking at frequencies above 1 Hz. The observed slip-weakening behavior does not require the slip-weakening friction law to be in effect: A fault obeying the rate-and-state friction law can show an apparent slip-weakening behavior with an effective critical distance that is several orders of magnitude larger than the critical distance entering the friction law (*31*). Aspects of the rupture kinematics and ground strong motion observed during the Gorkha event may also be due to hanging wall effects, the importance of which could be assessed through dynamic modeling of the rupture (*32*, *33*).

Our study provides insight into the main factors that determined the damage sustained during the Gorkha earthquake. Although the hypocenter was ~80 km away from the city, the main asperity that radiated most of the energy was much closer, just north of the basin and at a relatively shallow depth. Comparison of the waveforms recorded within the sedimentary basin at NAST and KATNP (Fig. 3) with the bedrock records at KKN4 shows prominent differences, even though the stations are less than 13 km apart. The waveforms recorded at the bedrock station KKN4 were simple, mostly dominated by the single pulse, whereas within the basin, peak horizontal ground velocities of 0.5 to 0.8 m/s [considered severe to violent (*34*)] were sustained for 20 s at KATNP and 40 s at NAST. The ratio of the amplitude spectra of the basin waveforms to those recorded at the bedrock station (Fig. 3, D to F) indicates an amplification of long-period energy between 1 and 9 s, with horizontal-direction amplitudes in the basin six to seven times as large as those at the bedrock station. The response spectra (Fig. 3, G to I) show that, within this amplified period band, the 4-s-period shaking was the strongest at the basin stations.

The 4-s peak in the response spectra agrees with the observation that the source time function beneath Kathmandu had a duration of ~6 to 7 s. The net effect of this long source duration with a slow onset time was to produce radiated energy depleted in the high-frequency component (fig. S11). This explains why vernacular dwellings with only a few stories were not severely affected, despite the anticipated short-period site effects from microzoning (*13*). Furthermore, high-frequency intensity measures such as peak ground accelerations (Fig. 2) were modest (~1.6 m/s^2, MMI = VI), whereas longer-period intensity measures such as peak ground velocity (Fig. 3) were very large (80 cm/s, MMI = IX). Kathmandu was faced with a combination of source and site effects. The rupture directivity focused radiated seismic energy toward the city; the smooth onset and 6- to 7-s duration of the pulse excited a resonance of the Kathmandu basin, producing a protracted duration of violent shaking at a period of around 4 s.

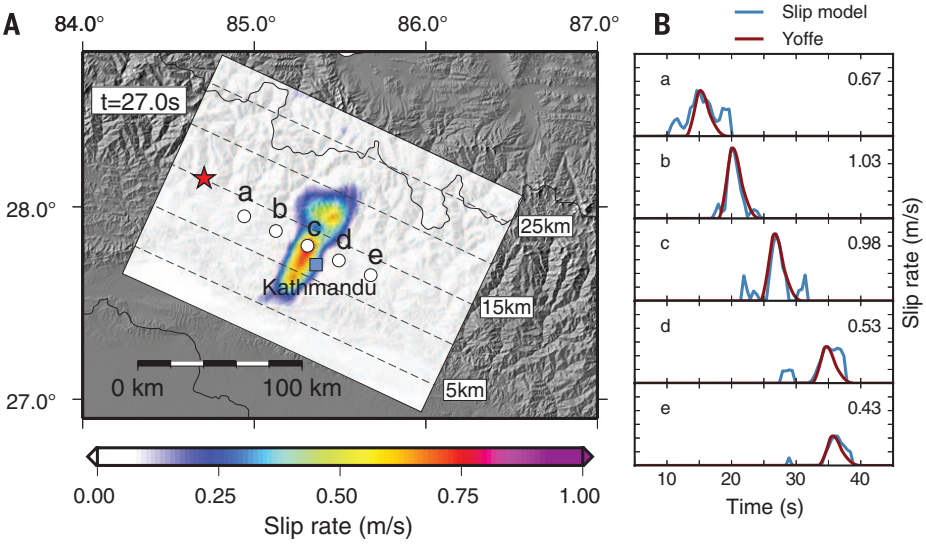


Fig. 4. Slip-pulse kinematics during the Gorkha earthquake. (**A**) Snapshot of the slip rate on the MTH at 27 s after the origin time, during propagation of the seismic rupture from the model in Fig. 1. The red star is the hypocenter, and dashed contours represent the depth to the fault. The white circles are the centers of five subfaults used to compare against theoretical regularized Yoffe source time functions (*28*). (**B**) STFs at the five locations from (A). Plotted are the inverted slip rates and the regularized Yoffe functions measured from the vertical velocity at KKN4, scaled to the maximum observed slip rate at each point, which is indicated numerically. Time is relative to the hypocentral origin (28.147°N, 84.708°E; 25 April 2015, 06:11:26.270 UTC).

REFERENCES AND NOTES

1. M. Guatteri, P. Spudich, *Bull. Seismol. Soc. Am.* **90**, 98–116 (2000).
2. X. Lu, N. Lapusta, A. J. Rosakis, *Proc. Natl. Acad. Sci. U.S.A.* **104**, 18931–18936 (2007).
3. R. M. Nikolaidis *et al*., *J. Geophys. Res. Solid Earth* **106**, 21897–21916 (2001).
4. G. L. Emore, J. S. Haase, K. Choi, K. A. Larson, A. Yamagiwa, *Bull. Seismol. Soc. Am.* **97**, 357–378 (2007).
5. J.-P. Avouac, L. Meng, S. Wei, W. Wang, J.-P. Ampuero, *Nat. Geosci.* (2015).
6. USGS, *M7.8 - 36km E of Khudi, Nepal* (2015); http://earthquake.usgs.gov/earthquakes/eventpage/us20002926.
7. T. Ader *et al*., *J. Geophys. Res. Solid Earth* **117**, B04403 (2012).
8. NSET, *Gorkha Earthquake: Intensity Maps* (2015); www.nset.org.np/eq2015/intensity_maps.php.
9. J. L. Mugnier, P. Huyghe, A. P. Gajurel, B. N. Upreti, F. Jouanne, *Tectonophysics* **509**, 33–49 (2011).
10. R. Bilham, *Curr. Sci.* **69**, 101–128 (1995).
11. M. R. Pant, *Ādarśa* **2**, 29–60 (2002).
12. Kathamandu Valley Earthquake Risk Management Project, *The Kathmandu Valley Earthquake Risk Management Action Plan* (NSET, Lalitpur, Nepal, 1998); www.preventionweb.net/english/professional/publications/v.php?id=1496.
13. Y. R. Paudyal, R. Yatabe, N. P. Bhandary, R. K. Dahal, *Earthq. Eng. Eng. Vib.* **11**, 257–268 (2012).
14. S. Moribayashi, Y. Maruo, *J. Jap. Soc. Eng. Geol.* **21**, 80–87 (1980).
15. B. S. J. B. Rana, *Nepal Ko Maha Bhukampa (1990 Sala) Nepal's Great Earthquake* (Sahyogi Prakashan, Kathmandu, 1935).
16. The Nepal Geodetic Array (www.tectonics.caltech.edu/resources/kmlnepal.html) was deployed through a collaboration between the Caltech Tectonics Observatory (USA), the Department of Mines and Geology (Nepal), and the Department Analyse et Surveillance de l'Environnement (CEA, France).
17. USGS, *NetQuakes: Station KATNP_NQ_01*, 25 April 2015; http://earthquake.usgs.gov/monitoring/netquakes/station/KATNP_NQ_01/20150425061138/.
18. E. Lindsey *et al*., *Nepal Earthquake: Line of Sight Deformation from ALOS-2 Interferometry*, 7 May 2015; http://topex.ucsd.edu/nepal.
19. European Space Agency, *Nepal Earthquake: Sentinel-1 InSAR Analysis*, April 2015; http://insarap.org/.
20. C. Ji, K. M. Larson, Y. Tan, K. W. Hudnut, K. H. Choi, *Geophys. Res. Lett.* **31**, L17608 (2004).
21. H. Yue *et al*., *J. Geophys. Res. Solid Earth* **118**, 5453–5466 (2013).
22. T. H. Heaton, *Phys. Earth Planet. Inter.* **64**, 1–20 (1990).
23. D. Melgar, Y. Bock, *J. Geophys. Res. Solid Earth* **120**, 3324–3349 (2015).
24. Materials and methods are available as supplementary materials on *Science* Online.
25. R. S. Stein, *Nature* **402**, 605–609 (1999).
26. R. Bilham, K. Larson, J. Freymueller, *Nature* **386**, 61–64 (1997).
27. R. Cattin, J.-P. Avouac, *J. Geophys. Res. Solid Earth* **105**, 13389–13407 (2000).
28. E. Tinti, E. Fukuyama, A. Piatanesi, M. Cocco, *Bull. Seismol. Soc. Am.* **95**, 1211–1223 (2005).
29. S. Ide, M. Takeo, *J. Geophys. Res. Solid Earth* **102**, 27379–27391 (1997).
30. T. Mikumo, K. B. Olsen, E. Fukuyama, Y. Yagi, *Bull. Seismol. Soc. Am.* **93**, 264–282 (2003).
31. A. Bizzarri, M. Cocco, *J. Geophys. Res. Solid Earth* **108**, 2373 (2003).
32. J. E. Kozdon, E. M. Dunham, *Bull. Seismol. Soc. Am.* **103**, 1275–1289 (2013).
33. D. D. Oglesby, R. J. Archuleta, S. B. Nielsen, *Science* **280**, 1055–1059 (1998).
34. C. B. Worden, M. C. Gerstenberger, D. A. Rhoades, D. J. Wald, *Bull. Seismol. Soc. Am.* **102**, 204–221 (2012).

ACKNOWLEDGMENTS

The GPS data are available from the UNAVCO website. The InSAR data are available at http://topex.ucsd.edu/nepal/. The Nepal Geodetic Array was funded by Caltech and DASE (to J.-P.A.) and by the Gordon and Betty Moore Foundation, through grant GBMF 423.01 to the Caltech Tectonics Observatory; support was maintained by NSF grant EAR-1345136. A. Miner and the Pacific Northwest Geodetic Array (PANGA) at CWU are thanked for technical assistance with the construction and operation of the Tribhuvan University (TU)–CWU network. Additional funding for the TU-CWU network came from the United Nations Development Programme and the Nepal Academy for Science and Technology. The high-rate data were recovered thanks to (i) a rapid intervention funded by NASA (USA) and the Department of Foreign International Development (UK) and (ii) engineering services provided by UNAVCO via the GAGE (Geodesy Advancing Geosciences and EarthScope) Facility, with support from NSF and NASA under NSF Cooperative Agreement no. EAR-1261833. We also thank Trimble Navigation and the Vaidya family for supporting the rapid response. The accelerometer record at KATNP was provided by USGS. We thank A. Nathan (U.S. Embassy in Kathmandu), S. Hough, D. Given, I. Flores, and J. Luetgert for contributions to the installation of this station. Research at UC–Berkeley was funded by the Gordon and Betty Moore Foundation through grant GBMF 3024. A portion of this work was carried out at JPL under a contract with the NASA. The GPS data were processed by the Advanced Rapid Imaging and Analysis Center for Natural Hazards (JPL) and the Scripps Orbit and Permanent Array Center. The effort at the Scripps Institution of Oceanography was funded by NASA grants NNX14AQ53G and NNX14AT33G. Advanced Land Observing Satellite–2 data were provided by the Japan Aerospace Exploration Agency under investigations 1148 and 1413. J.-P.A. thanks the Royal Society for support. We thank D. Dreger for discussion and W. Mooney for comments. J.-P.A led the study and wrote the article. D.M. performed the kinematic modeling and wrote the article. Y.B. supervised the high-rate data processing and wrote the article. J.Ga. led the field operations. J.Ge. conducted the high-rate data processing. S.O., A.M., W.S., and J.F.G. conducted the low-rate data analysis to estimate coseismic offsets. E.O.L. and X.X. conducted the InSAR data processing. L.B. helped to organize the field operations. All other authors contributed to building and servicing the GPS stations and to the post-earthquake data recovery. All authors edited the article.

SUPPLEMENTARY MATERIALS

www.sciencemag.org/content/349/6252/1091/suppl/DC1
Materials and Methods
Figs. S1 to S11
Tables S1 and S2
Movie S1
References (*35*–*45*)

25 May 2015; accepted 29 July 2015
Published online 6 August 2015
10.1126/science.aac6383

SYNTHETIC BIOLOGY

Complete biosynthesis of opioids in yeast

Stephanie Galanie,[1] Kate Thodey,[2] Isis J. Trenchard,[2] Maria Filsinger Interrante,[2] Christina D. Smolke[2]*

Opioids are the primary drugs used in Western medicine for pain management and palliative care. Farming of opium poppies remains the sole source of these essential medicines, despite diverse market demands and uncertainty in crop yields due to weather, climate change, and pests. We engineered yeast to produce the selected opioid compounds thebaine and hydrocodone starting from sugar. All work was conducted in a laboratory that is permitted and secured for work with controlled substances. We combined enzyme discovery, enzyme engineering, and pathway and strain optimization to realize full opiate biosynthesis in yeast. The resulting opioid biosynthesis strains required the expression of 21 (thebaine) and 23 (hydrocodone) enzyme activities from plants, mammals, bacteria, and yeast itself. This is a proof of principle, and major hurdles remain before optimization and scale-up could be achieved. Open discussions of options for governing this technology are also needed in order to responsibly realize alternative supplies for these medically relevant compounds.

Opioids are an important class of medicines that include the analgesic morphine and the antitussive codeine. The World Health Organization (WHO) classifies these compounds as essential medicines because of their utility in treating severe pain, in pain management, and in palliative care (*1*). In the developing world, there are shortages of painkillers; the WHO has estimated that 5.5 billion people have "low to nonexistent access to treatment for moderate or severe pain" (*2*).

All natural opiates (e.g., morphine and codeine) and semisynthetic opioids (e.g., oxycodone, hydrocodone, and hydromorphone) are currently derived from the opium poppy (*Papaver somniferum*). Approximately 100,000 ha of opium poppy are cultivated annually to yield poppy straw containing more than 800 tons of opiates, primarily morphine and thebaine, to meet licit medical and scientific demand (*3*). The majority of poppy-derived morphine and thebaine is chemically converted into higher-value compounds, including codeine, oxycodone, and hydrocodone. Industrial poppy farming is susceptible to environmental factors such as pests, disease, and climate, which can introduce instability and variability into this geographically concentrated supply chain, resulting in pressure to diversify supply (*4*). Despite diverse market demands and increasing supply risks, poppy farming remains the sole source of opioids, in part because chemical synthesis of these complex molecules is not commercially competitive. Approximately 30 chemical syntheses

[1]Department of Chemistry, Stanford University, Stanford, CA 94305, USA. [2]Department of Bioengineering, Stanford University, Stanford, CA 94305, USA.
***Corresponding author. E-mail: csmolke@stanford.edu**

of morphine and derivatives have been reported (*5*), but none are feasible for large-scale production.

A microbial-based manufacturing process for opioids or opioid precursors, which are part of the larger class of benzylisoquinoline alkaloids (BIAs), has the potential to address many of the challenges associated with the poppy-based supply chain. Industrial cultivation of microorganisms, such as the baker's yeast *Saccharomyces cerevisiae*, occurs over days, whereas poppies are annuals. Also, because microbes are grown in closed fermentation vessels, the production process is not susceptible to external environmental factors and could provide greater consistency in product composition and impurity profiles across batches.

In recent years, researchers have engineered yeast to produce a variety of plant-based natural products (*6*), most notably artemisinic acid, a precursor to the antimalarial drug artemisinin (*7*). Semisynthetic production of artemisinin has now reached the market, meeting up to one-third of global need (*8*, *9*). Yeast-based production of artemisinic acid required the introduction of three to six heterologous plant genes and numerous genetic modifications to increase productivity (*7*, *9*). Although advances in synthetic biology have increased the complexity of plant pathways that can be reconstructed (*6*), all efforts to engineer yeast to produce BIAs downstream of (*S*)-reticuline, including morphinans, have relied on an external supply of BIA precursors (*10*–*15*). *Escherichia coli* (*16*) and, very recently, yeast (*17*, *18*) have been engineered to produce early BIA intermediates de novo; these accomplishments suggest that yeast might be capable of synthesizing opioids from simple carbon and nitrogen sources. We and others engineered the first part of the biosynthetic pathway, from tyrosine to (*S*)-reticuline (*17*, *18*). Separately, we engineered a second part of the pathway, from thebaine to morphine (*13*); others later engineered

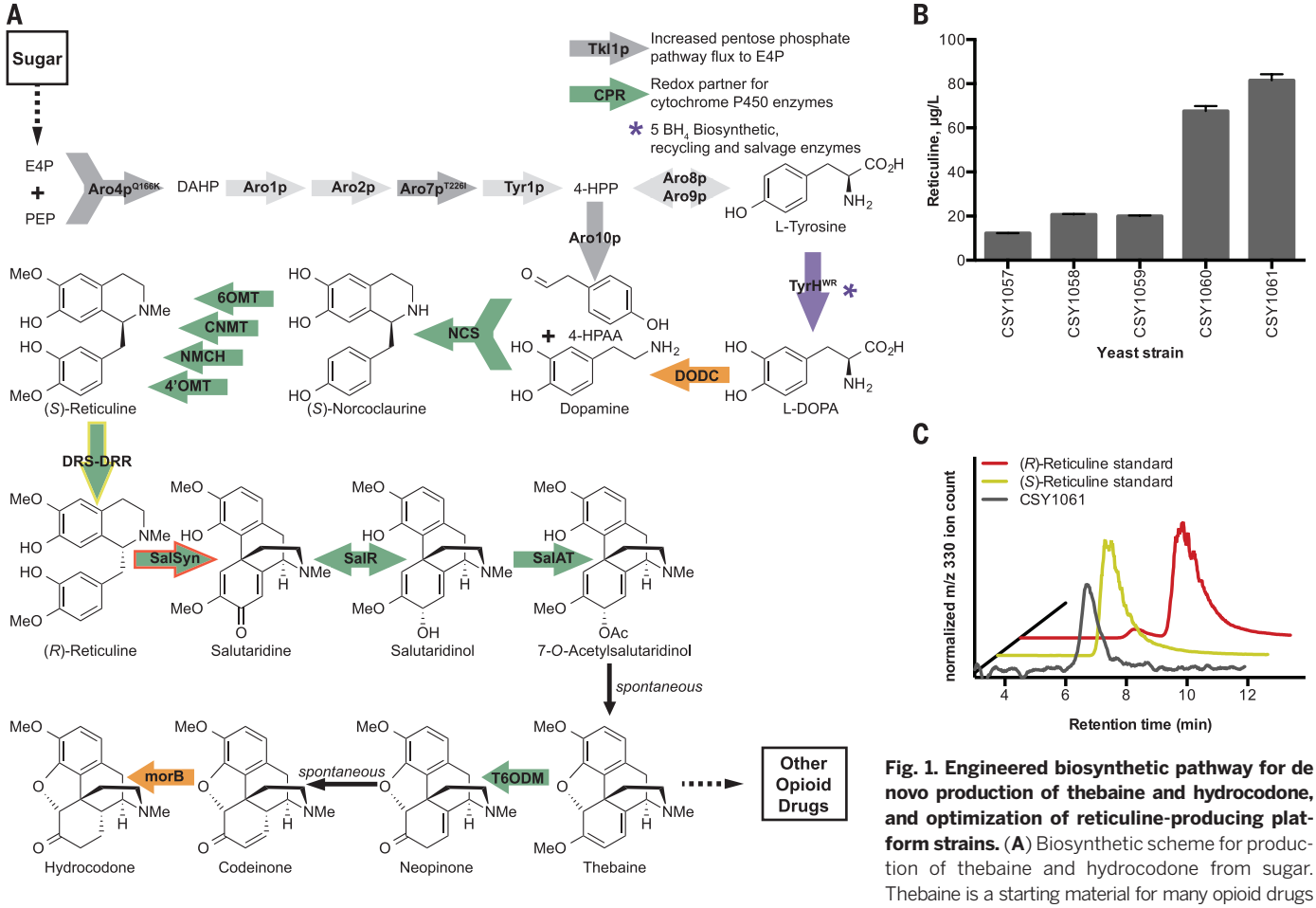


Fig. 1. Engineered biosynthetic pathway for de novo production of thebaine and hydrocodone, and optimization of reticuline-producing platform strains. (**A**) Biosynthetic scheme for production of thebaine and hydrocodone from sugar. Thebaine is a starting material for many opioid drugs through biosynthetic and semisynthetic routes. Block arrows indicate enzyme-catalyzed steps. Light gray arrows, unmodified yeast enzymes; dark gray arrows, overexpressed and modified yeast enzymes; purple arrows, mammalian (*Rattus norvegicus*) enzymes; orange arrows, bacterial (*Pseudomonas putida*) enzymes; green arrows, plant (*Papaver somniferum*, *P. bracteatum*, *Coptis japonica*, *Eschscholzia californica*) enzymes. Yellow outline highlights DRS-DRR; red outline highlights engineered SalSyn. E4P, erythrose 4-phosphate; PEP, phosphoenolpyruvate; DAHP, 3-deoxy-D-*arabino*-2-heptulosonic acid 7-phosphate; 4-HPP, 4-hydroxyphenylpyruvate; 4-HPAA, 4-hydroxyphenylacetaldehyde; BH_4, 5,6,7,8-tetrahydrobiopterin; Tkl1p, transketolase; CPR, cytochrome P450 reductase; Aro4p^{Q166K}, DAHP synthase; Aro1p, pentafunctional *arom* enzyme; Aro2p, bifunctional chorismate synthase and flavin reductase; Aro7p^{T226I}, chorismate mutase; Tyr1p, prephenate dehydrogenase; Aro8p, aromatic aminotransferase I; Aro9p, aromatic aminotransferase II; Aro10p, phenylpyruvate decarboxylase; TyrH^{WR}, feedback inhibition–resistant tyrosine hydroxylase (mutations R37E, R38E, W166Y); DODC, L-DOPA decarboxylase; NCS, (*S*)-norcoclaurine synthase; 6OMT, norcoclaurine 6-*O*-methyltransferase; CNMT, coclaurine *N*-methyltransferase; NMCH, *N*-methylcoclaurine hydroxylase; 4′OMT, 3′-hydroxy-*N*-methylcoclaurine 4′-*O*-methyltransferase; DRS-DRR, 1,2-dehydroreticuline synthase-1,2-dehydroreticuline reductase; SalSyn, salutaridine synthase; SalR, salutaridine reductase; SalAT, salutaridinol 7-*O*-acetyltransferase; T6ODM, thebaine 6-*O*-demethylase; morB, morphinone reductase. See figs. S1 and S2 for details of the BH_4 biosynthesis, recycling, and salvage pathway, conversion of (*S*)-norcoclaurine to (*S*)-reticuline, and genetic pathway modules. (**B**) Optimization of the reticuline-producing platform strain through pathway and strain engineering. Reticuline in the growth media was analyzed by LC-MS/MS multiple reaction monitoring (MRM) and quantified with an external standard curve. Error bars represent SD of three biological replicates. (**C**) Chiral analysis of reticuline produced by the platform strain. Reticuline was isolated from the growth medium of strain CSY1061 and separated on a chiral column. This chromatogram is one of two similar traces from replicate yeast cultures and was smoothed using a 7-point boxcar moving average.

a pathway from (*R*)-reticuline to codeine (*15*). However, functionally expressing the more than 20 heterologous genes required for complete biosynthesis of these complex molecules has been challenging because of the decreases in titer observed with each additional enzymatic step. Also, the key enzyme that epimerizes the (*S*)-benzylisoquinoline scaffold to the (*R*)-enantiomer, which is the biosynthetic precursor of the promorphinan and morphinan scaffolds, has remained unknown even after decades of study until recently identified by two groups (*19*, *20*) and by our team, as described below.

A decade ago, when we began work to realize total biosynthesis of opioids in yeast, we were motivated by the many foreseeable benefits yet mindful of potential negative impacts. Specifically, we were and remain concerned that a yeast-based opioid supply might contribute to opioid abuse (*21*, *22*). Thus, before starting this project, we sought and received permission to carry it out via Stanford University's institutional research registration with the U.S. Drug Enforcement Agency (DEA). Gaining permission required (i) background screening for researchers handling Schedule II compounds or yeast strains capable of making such compounds; (ii) detailed protocols limiting fermentation volumes and compound concentrations and including provisions for culture and product destruction and disposal immediately after experiments; (iii) increased physical containment for the strains and controlled compounds; (iv) increased laboratory security; and (v) explicit management and reporting. Taken together, these requirements reduce the chance that any compounds or strains generated in our research would directly enable individuals to abuse opioids.

We first built a yeast strain to produce (*S*)-reticuline, a key biosynthetic intermediate to many downstream BIAs including the morphinans. This strain was built with a new modular genetic design that incorporated modifications designed to divert greater carbon flux through tyrosine to (*S*)-reticuline. The reticuline biosynthetic pathway was split into four genetic modules that contain the coding sequences for 17 biosynthetic enzymes (Fig. 1A, figs. S1 and S2, and table S1). We selected chromosomal regions from which we expected no growth defect and active expression as integration loci (*23*–*25*). A precursor overproduction module (I) designed to increase accumulation of L-tyrosine and 4-hydroxyphenylacetaldehyde (4-HPAA) encoded the overexpression of three or four yeast proteins—mutants of 3-deoxy-D-*arabino*-2-heptulosonic acid 7-phosphate (DAHP) synthase and chorismate mutase ($Aro4p^{Q166K}$, $Aro7p^{T226I}$) that are less inhibited by L-tyrosine, and transketolase (Tkl1p); additionally, phenylpyruvate decarboxylase (Aro10p) was included in a second version of this module (fig. S2). A tetrahydrobiopterin (BH_4) module (II) designed to synthesize and recycle this mammalian redox cofactor encoded the expression of four proteins from *Rattus norvegicus*: sepiapterin reductase (SepR), 6-pyruvoyl tetrahydrobiopterin synthase (PTPS), quinonoid dihydropteridine reductase (QDHPR), and pterin carbinolamine dehydratase (PCD). An (*S*)-norcoclaurine module (III) designed to synthesize the first BIA backbone molecule encoded the expression of four proteins: a mutant of tyrosine hydroxylase ($TyrH^{WR}$; mutations R37E, R38E, W166Y) that is less inhibited by L-tyrosine and catecholamines, from *R. norvegicus*; the BH_4 salvage enzyme dihydrofolate reductase (DHFR), also from *R. norvegicus*; DOPA decarboxylase (DoDC) from the bacteria *Pseudomonas putida*; and norcoclaurine synthase (NCS) from the plant *Coptis japonica*. An (*S*)-reticuline module (IV) designed to synthesize the key BIA branchpoint molecule encoded the expression of five plant proteins, four from *P. somniferum*—norcoclaurine 6-*O*-methyltransferase (6OMT), coclaurine-*N*-methyltransferase (CNMT), 4′-*O*-methyltransferase (4′OMT), and cytochrome P450 reductase (CPR)—as well as *N*-methylcoclaurine hydroxylase (NMCH) from *Eschscholzia californica*. The enzyme variants were selected on the basis of examined activities in engineered yeast (*11*, *18*) and incorporated the addition of several new activities (i.e., Aro10p, DHFR) to increase flux to reticuline biosynthesis.

The BIA modules were integrated into a wild-type haploid CEN.PK2 strain. We assayed reticuline production by growing yeast strains in minimal synthetic complete media supplemented with ascorbic acid without ammonium sulfate for 72 hours (fig. S3) and analyzing the growth media for BIA molecules by liquid chromatography coupled with tandem mass spectrometry (LC-MS/MS) (table S2). A minimal reticuline-producing strain (CSY1057; table S3), which incorporated modules II to IV, produced reticuline with a titer of 12.3 μg/liter (Fig. 1B, fig. S4A, and table S4). The addition of module I to the strain, increasing BIA precursor supply, resulted in a factor of 1.6 improvement in reticuline accumulation, with or without Aro10p (CSY1059, 20.0 μg/liter; CSY1058, 20.7 μg/liter). We observed nearly complete consumption of L-DOPA (90 μg/liter; fig. S4B and table S4), substantial accumulation of dopamine (10 mg/liter; fig. S4C), and accumulation of 3′-hydroxy-*N*-methylcoclaurine (fig. S4, D and E) by LC-MS/MS for the strain harboring modules I to IV (CSY1059). We hypothesized that (i) increased expression of NCS

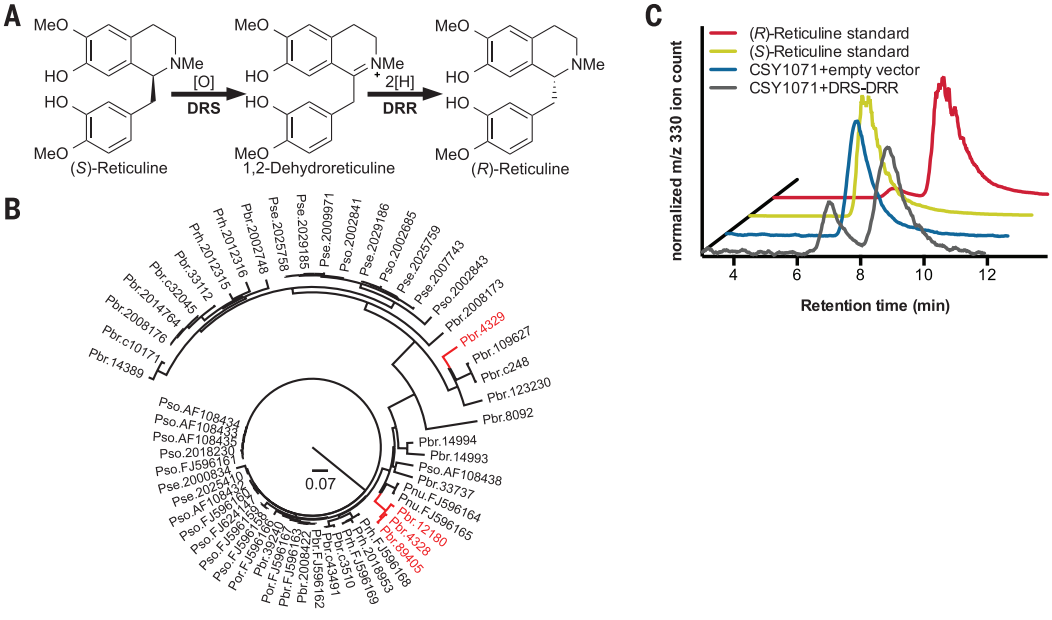


Fig. 2. DRS-DRR converts (*S*)-reticuline to (*R*)-reticuline. (**A**) Biosynthetic scheme for the reaction catalyzed by DRS-DRR; Me, methyl. (**B**) Identification of DRS-DRR via bioinformatic analysis of COR-like sequences. Bioinformatic query was COR VIGS sequence. Subject sequences were the *P. bracteatum* PhytoMetaSyn transcriptome; *P. bracteatum*, *P. setigerum*, *P. somniferum*, and *P. rhoeas* transcriptomes from the 1000 Plants Project; and all deposited sequences in GenBank belonging to *Papaveraceae*. The scale bar indicates amount of genetic change in amino acid substitutions per site. Branches highlighted in red indicate sequences containing both CYP and COR-like domains. Phylogenetic tree was generated using ClustalX bootstrap neighbor-joining tree with 1000 trials. (**C**) Chiral analysis of reticuline produced by yeast strains expressing and not expressing the enzyme DRS-DRR. Chiral analysis of reticuline accumulated in the growth media of strain CSY1071 with empty vector or DRS-DRR (pCS3301) was performed as described in Fig. 1C. This chromatogram is one of two similar traces from replicate yeast cultures and was smoothed using a 7-point boxcar moving average.

would increase conversion of dopamine and the native yeast metabolite 4-HPAA to norcoclaurine and downstream products, (ii) increased expression of TyrH^{WR} would replenish the supply of dopamine, and (iii) increased expression of 4´OMT would reduce accumulation of 3´-hydroxy-*N*-methylcoclaurine and increase flux to reticuline. Thus, we designed a bottleneck module (V), which encoded the overexpression of three proteins—TyrH^{WR}, 4´OMT, and NCS—by incorporation of additional gene copies. The module was integrated into CSY1059 and designed to knock out the native *ZWF1* gene (*zwf1*Δ; CSY1061) or to integrate into a separate locus (CSY1060). A yeast platform strain with the addition of module V into the *zwf1* locus resulted in a further factor of 4 improvement in reticuline accumulation (82 μg/liter; Fig. 1B and table S4) and a corresponding factor of 2 decrease in accumulated 3´-hydroxy-*N*-methylcoclaurine relative to CSY1059 (fig. S4D).

Reticuline produced by the yeast platform strain CSY1061 was isolated by reverse-phase high-performance liquid chromatography and analyzed by chiral LC-MS. The chiral analysis indicated that the majority of the reticuline produced is the (*S*)-enantiomer (Fig. 1C), as was expected because of the stereospecificity of the NCS-catalyzed condensation. The production of primarily the (*S*)-enantiomer in our platform strain corroborates similar observations from other bacteria and yeast engineered with the three methyltransferase enzymes, even when fed racemic substrates (*10*, *15*–*17*). Opium poppy has the unique ability to convert (*S*)-reticuline to (*R*)-reticuline, from which the morphinan alkaloids are derived (*26*, *27*). Although extensive isotope feeding and biochemical studies have indicated that the epimerase activity proceeds via oxidation to a Schiff base intermediate and stereospecific reduction (Fig. 2A), the 1,2-dehydroreticuline synthase (DRS) and 1,2-dehydroreticuline reductase (DRR) enzyme(s) had not been isolated and sequenced when we began our study (*27*–*29*). While we were preparing this manuscript for submission, one group reported the discovery of this enzyme in *P. somniferum* by characterizing mutant alleles from chemically mutagenized opium poppy plants (*19*). While our manuscript was under review, another group reported using plant transcriptome databases to identify candidates and then cloned the gene from *P. somniferum* cDNA (*20*). Our approach instead leveraged plant transcriptome databases, DNA synthesis, and the engineered (*S*)-reticuline–producing yeast strains, thus not requiring access to physical plant material.

More specifically, we noted that two independent plant gene-silencing studies found that codeinone reductase (COR) knockdown results in reticuline accumulation, and in one case specifically (*S*)-reticuline accumulation (*30*, *31*). We hypothesized that a COR-like enzyme may catalyze the stereospecific reduction and used the published virus-induced gene silencing (VIGS) sequence as a BLAST query against *Papaver* species in the 1000 Plants Project (*32*) and PhytoMetaSyn (*33*, *34*) transcriptome databases. Hit identity was determined by a reverse BLAST search against sequences deposited in GenBank. Of the 38 COR-like sequences identified that were also greater than 300 nucleotides in length, four had a cytochrome P450 oxidase (CYP) 82Y1-like domain and a COR-like domain in a single open reading frame (DRS-DRR; Fig. 2B). We considered that this natural fusion protein could catalyze both the oxidation and reduction necessary for (*S*)-reticuline epimerization. We propose that the oxidation to 1,2-dehydroreticuline may occur via either a carbinolamine or enamine intermediate, and that 1,2-dehydroreticuline is then stereospecifically reduced to (*R*)-reticuline by the COR-like DRR domain (fig. S5).

To identify additional variants of this coding sequence and determine how widespread it is in nature, we used the amino acid sequence from *P. bracteatum* DRS-DRR (Pbr.89405) to search both databases by translated BLAST nucleotides (tBLASTn). A search of all sequences in the PhytoMetaSyn database (67 plant species) and the 1000 Plants Project transcriptome database (1328 assemblies derived from a few hundred plant species) identified a total of five apparent full-length and 10 partial unique sequences that harbored both domains (fig. S6), which originated from *P. somniferum* (opium poppy), *P. setigerum* (poppy of Troy), *P. bracteatum* (Iranian poppy), or *Chelidonium majus* (greater celandine). From this secondary search (fig. S6), we identified a *P. somniferum* DRS-DRR sequence of interest, Pso.2062398, which was a full-length sequence that had consensus with several individual transcriptome hits.

To determine whether the identified DRS-DRR enzyme possesses epimerase activity, we characterized the DRS-DRR enzyme in the context of a yeast strain engineered to produce (*S*)-reticuline from fed *rac*-norlaudanosoline (CSY1071; fig. S1C) (*11*). In preliminary experiments, we screened the three variants from *P. bracteatum* that clustered together in the initial search—Pbr.89405, Pbr.12180, and Pbr.4328—in strain CSY1071 with low-copy plasmids harboring expression cassettes for yeast codon–optimized DRS-DRR and yeast codon–optimized *P. somniferum* salutaridine synthase (yPsSalSyn). Codon optimization of all synthetic genes was performed by Life Technologies (*35*). When fed 1 mM norlaudanosoline, only the strain encoding DRS-DRR variant Pbr.89405 produced substantial salutaridine. We cultured strain CSY1071 containing the low-copy plasmid harboring this *DRS-DRR* (Pbr.89405, pCS3301) with 1 mM *rac*-norlaudanosoline for 72 hours, and isolated reticuline from the growth media for chiral LC-MS analysis. In strains expressing the DRS-DRR, more than half of the reticuline produced was the (*R*)-enantiomer, whereas exclusively (*S*)-reticuline was detected in strains lacking the DRS-DRR gene (Fig. 2C).

We next examined the activity of DRS-DRR enzyme variants in the context of the downstream conversion steps to thebaine, the first morphinan alkaloid in opiate biosynthesis. In preliminary experiments, yeast codon–optimized salutaridine reductase (SalR) variants from *P. bracteatum* and *P. somniferum* and site-directed mutants that were reported to reduce substrate inhibition and

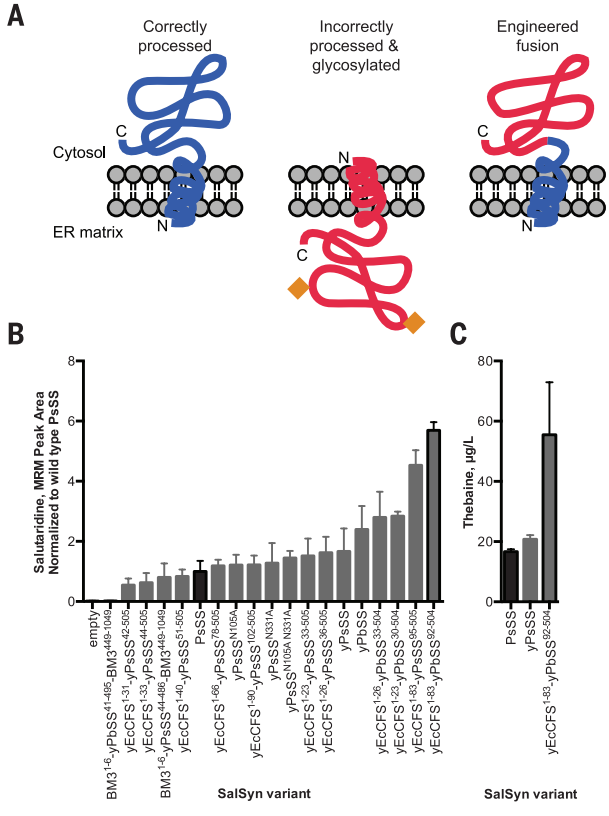


Fig. 3. Engineered SalSyn chimeras improve conversion of (*R*)-reticuline to salutaridine. (**A**) Schematic of the chimeric SalSyn engineering strategy to address incorrect processing and glycosylation of the wild-type SalSyn in yeast. Orange diamonds represent glycosylation. (**B**) Comparison of salutaridine produced from SalSyn variants, site-directed glycosylation mutants, and engineered fusions in yeast. Yeast strains expressing the indicated SalSyn variant were fed 10 μM (*R*)-reticuline, and the growth medium was analyzed by LC-MS/MS MRM. Peak areas were normalized to wild-type SalSyn (black). (**C**) Comparison of thebaine produced from SalSyn variants in yeast. Yeast strains were fed 1 mM *rac*-norlaudanosoline, and thebaine in the growth medium was quantified by LC-MS/MS MRM with an external standard curve. Bars outlined in black denote wild-type and best engineered variant. Error bars are SD of at least three biological replicates.

increase the maximum rate of reaction V_{max} (*36*, *37*) were examined for their ability to catalyze conversion of salutaridine to thebaine with yeast codon–optimized salutaridinol acetyltransferase (SalAT) variants from *P. somniferum*, *P. bracteatum*, and *P. orientale*. The *P. bracteatum* SalR (PbSalR) and *P. somniferum* SalAT (PsSalAT) enzymes exhibited the highest activities in yeast (fig. S7, A and B). A yeast artificial chromosome (YAC, pCS3308) encoding expression cassettes for yPsSalSyn, PbSalR, and PsSalAT was assembled into strain CSY1071, and DRS-DRR variants were expressed from low-copy plasmids (pCS3300–3305). The resulting strains were assayed by feeding 1 mM *rac*-norlaudanosoline for 72 hours, and the growth medium was analyzed for thebaine production. *P. bracteatum* and *P. somniferum* DRS-DRR enzymes (Pbr.89405, Pso.2062398) resulted in similar thebaine production (fig. S7C), and the *P. bracteatum* DRS-DRR (PbDRS-DRR) was used in subsequent experiments. Expression cassettes for the four genes were assembled into a YAC (pCS3309) in strain CSY1071, and the resulting strain was assayed for thebaine production from fed *rac*-norlaudanosoline. This strain produced thebaine at a concentration of 17 μg/liter when cultured with 1 mM *rac*-norlaudanosoline for 96 hours (Fig. 3C and table S5). However, substantial accumulation of the intermediate reticuline (~660 μg/liter) was observed.

Because DRS-DRR is fairly efficient in the conversion of (*S*)- to (*R*)-reticuline (Fig. 2C), the accumulation of reticuline indicated that the conversion of (*R*)-reticuline to salutaridine, catalyzed by SalSyn, warranted further optimization. Western blot analysis indicated that yeast-expressed SalSyn protein was present as three forms that could be distinguished by apparent molecular weight, whereas SalSyn transiently expressed in *Nicotiana benthamiana* (tobacco) was present primarily at the lowest of these three apparent molecular weights (fig. S8A). Site-directed mutagenesis of three potential N-linked glycosylation sites [Asn-X-Thr/Ser (N-X-T/S)] indicated that the three bands arose from glycosylation of the protein at two sites, Asn^{105} and Asn^{331}. N-linked glycosylation in yeast is indicative of incorrect N-terminal sorting of the nascent SalSyn polypeptide to the lumen of the endoplasmic reticulum (ER), where it is N-glycosylated rather than anchoring the N terminus in the outer ER membrane and maintaining the catalytic domain in the cytosol, as is typical of microsomal CYPs (Fig. 3A and fig. S8B) (*38*, *39*). We hypothesized that this misprocessing reduced SalSyn activity in yeast. However, modifying the glycosylation pattern of SalSyn by mutating the glycosylation sites reduced conversion of (*R*)-reticuline to salutaridine relative to the wild-type yeast codon–optimized enzyme (Fig. 3B).

We performed protein engineering to correct N-terminal sorting of the nascent SalSyn polypeptide, prevent N-linked glycosylation, and improve the enzyme's activity in yeast. Cheilanthifoline synthase (CFS) is a plant cytochrome P450 that is 61 to 68% identical to SalSyn, exhibits high activity when expressed in yeast (*14*), and is not glycosylated in yeast despite having one N-X-T/S site identical to the SalSyn sequence (fig. S8C). We designed yeast codon–optimized coding sequences for chimeric proteins with one or more N-terminal α helices from CFS replacing those of SalSyn variants from *P. somniferum* and *P. bracteatum*, with junction points for the fusions selected on the basis of amino acid alignments and/or protein secondary structure motifs. Western blot analysis of the chimeric proteins indicated that several of the engineered SalSyn enzymes were present as a single band in yeast, similar to the expression pattern observed for the plant-expressed parent enzyme (fig. S8D). The data indicated that the misprocessing of the nascent protein in yeast that resulted in N-linked glycosylation was repaired by the engineered fusions. As an alternative strategy, the coding sequence for the SalSyn CYP domain was cloned in place of the CYP domain in the cytosolic *Bacillus megaterium* P450 monooxygenase CYP102A1 (BM3), resulting in a chimeric protein with fused CYP and cytochrome P450 reductase domains. The chimeric SalSyn proteins were expressed from a low-copy plasmid in CSY1071 and assayed for salutaridine production from fed (*R*)-reticuline. Several of the engineered SalSyn variants exhibited improved activity relative to both the wild-type and codon-optimized enzymes, with the engineered *P. bracteatum* variant $yEcCFS^{1\text{-}83}$-$yPbSalSyn^{92\text{-}504}$ exhibiting greater conversion of (*R*)-reticuline to salutaridine by a factor of ~6 (Fig. 3B) and greater conversion of *rac*-norlaudanosoline to thebaine by a factor of >3 (55 μg/liter; Fig. 3C and table S5) relative to wild-type PsSalSyn.

To engineer a yeast strain that produces thebaine from simple carbon and nitrogen sources, we designed a thebaine module (VI) that encodes the expression of the best enzyme variants identified in our work—PbDRS-DRR, $yEcCFS^{1\text{-}83}$-$yPbSalSyn^{92\text{-}504}$, PbSalR, and PsSalAT—to convert (*S*)-reticuline to the morphinan alkaloid thebaine. Thebaine is extracted from opium poppy for use in semisynthesis of a number of opioids. This module was added to the reticuline-producing platform strain (CSY1060) as a chromosomal integration (CSY1064). The resulting strains were cultured in minimal media for 120 hours and the growth media assayed for thebaine (Fig. 4, A and B). These strains—containing 24 heterologous expression cassettes, 21 new enzyme activities, overexpression of two native enzymes, and inactivation of one native enzyme—produced thebaine at concentrations of 6.4 ± 0.3 μg/liter (table S6). We further extended the reconstructed biosynthetic pathway to a downstream opioid drug, hydrocodone (Fig. 1A), which is a main component in the second most dispensed prescription medicine in the United States (*40*). A hydrocodone module (VII), which encodes the expression of thebaine 6-*O*-demethylase (T6ODM) from *P. somniferum* and morphine reductase (morB) from *P. putida M10* (*13*), was introduced as a YAC (pCS2765) into the thebaine-producing strain CSY1064. The resulting strain was cultured in minimal media with 50 mM 2-oxoglutarate to support T6ODM activity for 120 hours and the growth media assayed for opioid compounds (Fig. 4, C and D, and table S6). The engineered yeast were able to produce low levels of hydrocodone, ~0.3 μg/liter. Thus, we have demonstrated the feasibility of extending the pathway to compounds of interest through a biosynthetic

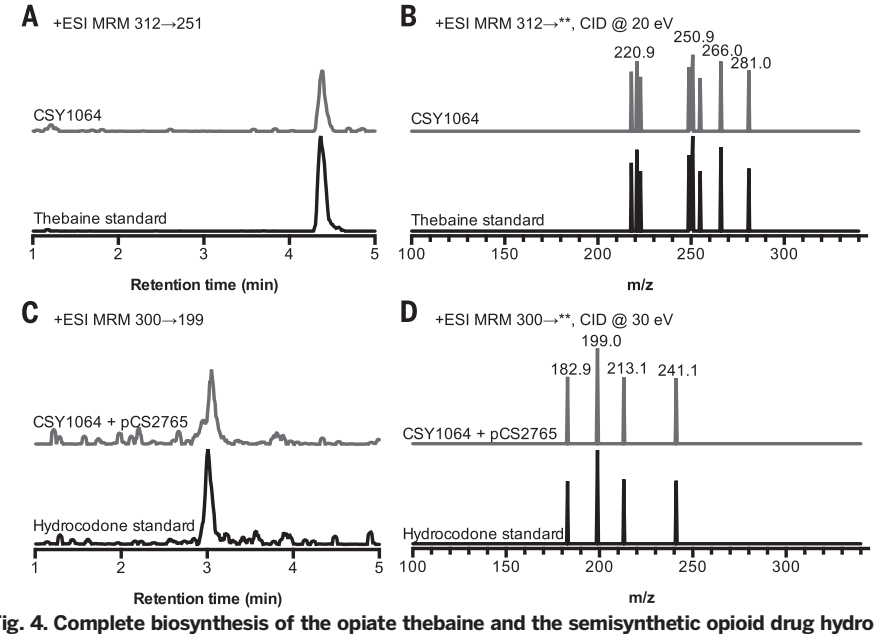


Fig. 4. Complete biosynthesis of the opiate thebaine and the semisynthetic opioid drug hydrocodone in yeast. (**A**) Chromatograms of thebaine detected in CSY1064 media and in a thebaine standard (7.8 μg/liter, 25 nM). (**B**) Spectra of eight MRM transitions of thebaine produced by engineered yeast and the thebaine standard. (**C**) Chromatograms of hydrocodone detected in CSY1064+pCS2765 media and in a hydrocodone standard (0.3 μg/liter, 1 nM). (**D**) Spectra of four MRM transitions of hydrocodone produced by engineered yeast and the hydrocodone standard. Growth medium was analyzed for opioids by LC-MS/MS MRM. Traces are representative of four biological replicates.

route that is not present in the native opium poppy without having to incorporate downstream chemical synthesis.

This work represents the complete biosynthesis of opiates in a heterologous host starting from central metabolism. Through our synthetic approach, we validated the capability of DRS-DDR variants from different plants to catalyze the (*S*)- to (*R*)-epimerization of reticuline in the context of the heterologous opiate biosynthetic pathway. The engineering of yeast able to convert central metabolites to the complex pentacyclic morphinan scaffold required enzyme engineering to correct the processing and increase the activity of the key pathway cytochrome P450 leading to the promorphinan scaffold (SalSyn), as well as pathway and strain optimization, including the expression of 21 heterologous enzymes from plants, mammals, bacteria, and yeast, overexpression of two native yeast enzymes, and deletion of one native yeast gene. The current report represents a proof of principle for generating morphinan scaffolds de novo in yeast, and opens the possibility of derivatizing these and other molecules by new biosynthetic or semisynthetic routes to improve their therapeutic properties.

Fermentation titers of ~5 g/liter would be required for yeast-based production of opioids to be a feasible alternative to poppy farming for commercial production. As this represents a yield increase of more than five orders of magnitude, the strains reported here would not be suitable for commercial scale-up. Future engineering efforts could take advantage of the pathway's role as an electron sink for fermentative production to direct greater electron and carbon flux to the opiates rather than to ethanol or other fermentation products. At commercial productivities, ~5 ml of yeast grown over several days would provide one dose of pain medication, which is currently sourced from 0.2 m^2 of poppy field land over the course of a year; sourcing opiates from sugar and yeast instead of opium poppy could decrease the overall land area required for production by a factor of >500.

There is some concern that biosynthesis of opioids in yeast may soon lead to "home brew" opiates (*41*). The production levels achieved here under controlled fermentation conditions do not enable home brew of these drugs and also are not economically competitive with poppy farming for supplying either licit or illicit markets. Specifically, at the titers reported here (<1 μg/liter), a single dose of hydrocodone, as used in Vicodin (5 mg), would require thousands of liters of fermentation broth, which no home brewer would reasonably pursue. Such improvements are not merely a matter of fermentation scale-up and would require additional research to achieve the necessary strain and pathway improvements. Thus, the work reported here does not provide a "recipe" for making opioid drugs in a manner that directly undermines public health or security. Nonetheless, as a safeguard of future public health, our yeast strains only produce opioids (e.g., hydrocodone, thebaine) with reduced potential for diversion to illicit markets due to the added steps and cost of chemically converting these specific compounds to heroin. Although such strains could potentially be further engineered to produce morphine directly, prior work to convert thebaine to morphine realized only a 1.5% yield (*13*). Thus, as a rough estimate, a strain that converts sugar to morphine would require an improvement in overall yield by a factor of ~7×10^6 relative to the work reported here.

Despite this precaution, substantially improved production of opioids via yeast should be expected in the next several years. More broadly, our work highlights the potential of yeast as a chassis for bio-based production of many complex chemicals and materials. Synthetic biology is poised to replace or supplement many supply chains with advanced bio-based manufacturing. A greatly expanded capacity to build with biology will contribute to changes in land and natural resource use, employment, and policy. Practical strategies that address concerns while enabling innovation and the realization of benefits must be developed now in order to secure our future bioeconomy. Given the complexity and diversity of both the potential concerns and possible benefits, we would strongly endorse an open deliberative process that develops options for the governance (*42*) of medicinal compound biosynthesis before economically competitive processes are realized.

REFERENCES AND NOTES

1. World Health Organization, "18th WHO essential medicines list" (Geneva, Switzerland, 2013).
2. M. J. Seya, S. F. Gelders, O. U. Achara, B. Milani, W. K. Scholten, *J. Pain Palliat. Care Pharmacother.* **25**, 6–18 (2011).
3. International Narcotics Control Board, "Narcotic drugs: Estimated world requirements for 2015—statistics for 2013" (2014).
4. K. Bradsher, "Shake-up on opium island." *New York Times* (20 July 2014); www.nytimes.com/2014/07/20/business/international/tasmania-big-supplier-to-drug-companies-faces-changes.html.
5. J. W. Reed, T. Hudlicky, *Acc. Chem. Res.* **48**, 674–687 (2015).
6. M. S. Siddiqui, K. Thodey, I. Trenchard, C. D. Smolke, *FEMS Yeast Res.* **12**, 144–170 (2012).
7. D. K. Ro *et al*., *Nature* **440**, 940–943 (2006).
8. PATH, "Stabilizing the antimalarial drug supply: Semisynthetic artemisinin could meet up to one-third of global need" (2014); www.path.org/publications/detail.php?i=2438.
9. C. J. Paddon, J. D. Keasling, *Nat. Rev. Microbiol.* **12**, 355–367 (2014).
10. H. Minami *et al*., *Proc. Natl. Acad. Sci. U.S.A.* **105**, 7393–7398 (2008).
11. K. M. Hawkins, C. D. Smolke, *Nat. Chem. Biol.* **4**, 564–573 (2008).
12. E. Fossati *et al*., *Nat. Commun.* **5**, 3283 (2014).
13. K. Thodey, S. Galanie, C. D. Smolke, *Nat. Chem. Biol.* **10**, 837–844 (2014).
14. I. J. Trenchard, C. D. Smolke, *Metab. Eng.* **30**, 96–104 (2015).
15. E. Fossati, L. Narcross, A. Ekins, J. P. Falgueyret, V. J. Martin, *PLOS ONE* **10**, e0124459 (2015).
16. A. Nakagawa *et al*., *Nat. Commun.* **2**, 326 (2011).
17. W. C. DeLoache *et al*., *Nat. Chem. Biol.* **11**, 465–471 (2015).
18. I. J. Trenchard, M. S. Siddiqui, K. Thodey, C. D. Smolke, *Metab. Eng.* **31**, 74–83 (2015).
19. T. Winzer *et al*., *Science* **349**, 309–312 (2015).
20. S. C. Farrow, J. M. Hagel, G. A. W. Beaudoin, D. C. Burns, P. J. Facchini, *Nat. Chem. Biol.* 10.1038/nchembio.1879 (2015).
21. T. Gomes *et al*., *Addiction* **109**, 1482–1488 (2014).
22. D. B. Reuben *et al*., *Ann. Intern. Med.* **162**, 295–300 (2015).
23. E. J. Dean, J. C. Davis, R. W. Davis, D. A. Petrov, *PLOS Genet.* **4**, e1000113 (2008).
24. I. Nogae, M. Johnston, *Gene* **96**, 161–169 (1990).
25. D. Bai Flagfeldt, V. Siewers, L. Huang, J. Nielsen, *Yeast* **26**, 545–551 (2009).
26. A. R. Battersby, D. M. Foulkes, R. Binks, *J. Chem. Soc.* **33**, 3323–3332 (1965).
27. K. Hirata, C. Poeaknapo, J. Schmidt, M. H. Zenk, *Phytochemistry* **65**, 1039–1046 (2004).
28. G. A. Beaudoin, P. J. Facchini, *Planta* **240**, 19–32 (2014).
29. W. DeEknamkul, M. H. Zenk, *Phytochemistry* **31**, 813–821 (1992).
30. R. S. Allen *et al*., *Nat. Biotechnol.* **22**, 1559–1566 (2004).
31. C. P. Wijekoon, P. J. Facchini, *Plant J.* **69**, 1052–1063 (2012).
32. N. Matasci *et al*., *Gigascience* **3**, 17 (2014).
33. P. J. Facchini *et al*., *Trends Biotechnol.* **30**, 127–131 (2012).
34. M. Xiao *et al*., *J. Biotechnol.* **166**, 122–134 (2013).
35. S. Fath *et al*., *PLOS ONE* **6**, e17596 (2011).
36. J. Ziegler, W. Brandt, R. Geissler, P. J. Facchini, *J. Biol. Chem.* **284**, 26758–26767 (2009).
37. Y. Higashi, T. M. Kutchan, T. J. Smith, *J. Biol. Chem.* **286**, 6532–6541 (2011).
38. V. Goder, M. Spiess, *FEBS Lett.* **504**, 87–93 (2001).
39. M. Higy, T. Junne, M. Spiess, *Biochemistry* **43**, 12716–12722 (2004).
40. IMS Institute for Healthcare Informatics, "Medicines use and spending shifts: A review of the use of medicines in the U.S. in 2014" (2015); www.imshealth.com/portal/site/imshealth/menuitem.762a961826aad98f53c753c71ad8c22a/?vgnextoid=3f140a4331e8c410VgnVCM1000000e2e2ca2RCRD.
41. K. A. Oye, J. C. Lawson, T. Bubela, *Nature* **521**, 281–283 (2015).
42. M. S. Garfinkel, D. Endy, G. L. Epstein, R. M. Friedman, *Biosecur. Bioterror.* **5**, 359–362 (2007).
43. S. Alberti, A. D. Gitler, S. Lindquist, *Yeast* **24**, 913–919 (2007).
44. R. D. Gietz, R. H. Schiestl, *Nat. Protoc.* **2**, 31–34 (2007).
45. D. G. Gibson *et al*., *Nat. Methods* **6**, 343–345 (2009).
46. G. Chao *et al*., *Nat. Protoc.* **1**, 755–768 (2006).
47. J. H. Hegemann, U. Güldener, G. J. Köhler, *Methods Mol. Biol.* **313**, 129–144 (2006).
48. Z. Shao, H. Zhao, H. Zhao, *Nucleic Acids Res.* **37**, e16 (2009).
49. T. J. Kwiatkowski Jr., H. Y. Zoghbi, S. A. Ledbetter, K. A. Ellison, A. C. Chinault, *Nucleic Acids Res.* **18**, 7191–7192 (1990).
50. F. Sainsbury, E. C. Thuenemann, G. P. Lomonossoff, *Plant Biotechnol. J.* **7**, 682–693 (2009).
51. A. Gesell *et al*., *J. Biol. Chem.* **284**, 24432–24442 (2009).
52. A. Nakagawa *et al*., *Sci. Rep.* **4**, 6695 (2014).
53. S. Valent, M. Tóth, *Int. J. Biochem. Cell Biol.* **36**, 1266–1280 (2004).
54. L. A. Hazelwood, J. M. Daran, A. J. van Maris, J. T. Pronk, J. R. Dickinson, *Appl. Environ. Microbiol.* **74**, 2259–2266 (2008).
55. J. M. Hagel, P. J. Facchini, *Nat. Chem. Biol.* **6**, 273–275 (2010).
56. W. Li, D. T. Rossi, S. T. Fountain, *J. Pharm. Biomed. Anal.* **24**, 325–333 (2000).
57. J. Schmidt, K. Raith, C. Boettcher, M. H. Zenk, *Eur. J. Mass Spectrom.* **11**, 325–333 (2005).
58. K. Raith *et al*., *J. Am. Soc. Mass Spectrom.* **14**, 1262–1269 (2003).
59. V. V. Kushnirov, *Yeast* **16**, 857–860 (2000).
60. K. Fukuda, K. Asano, K. Ouchi, S. Takasawa, *J. Ferment. Bioeng.* **74**, 117–119 (1992).
61. T. Schmidheini, P. Sperisen, G. Paravicini, R. Hütter, G. Braus, *J. Bacteriol.* **171**, 1245–1253 (1989).
62. C. Taxis, M. Knop, *Biotechniques* **40**, 73–78 (2006).
63. U. Gueldener, J. Heinisch, G. J. Koehler, D. Voss, J. H. Hegemann, *Nucleic Acids Res.* **30**, e23 (2002).
64. S. C. Daubner *et al*., *J. Mol. Biol.* **359**, 299–307 (2006).
65. K. Hawkins, thesis, California Institute of Technology (2008).
66. R. S. Sikorski, P. Hieter, *Genetics* **122**, 19–27 (1989).

ACKNOWLEDGMENTS

We thank Stanford Cell Sciences Imaging Facility for providing fluorescence microscopy access (Leica SP5, NIH grant SIG 1S10RR02557401) and training; Agilent Technologies for an award through their Global Academic Research Support Program; T. Kutchan and P. Facchini for contributing *Papaver* samples to the 1KP and PMS transcriptome projects, respectively; W. Lau of the Sattely laboratory for training, growing plants, and helpful discussions regarding plant experiments; and Y. Li, Y.-H. Wang, A. P. Klein, D. Endy for valuable feedback in the preparation of the manuscript. Supported by NIH grant AT007886 (C.D.S.), a NSF fellowship (S.G., I.J.T.), an ARCS Foundation fellowship (I.J.T.), a Stanford University fellowship (S.G.), and a Stanford Research Experiences for Undergraduates fellowship (M.F.I.). Strains making controlled substances (e.g., thebaine, hydrocodone) can only be provided to laboratories/institutions that have the appropriate approvals and licenses (e.g., DEA permits). Stanford University has a pending patent application on this work on which S.G., K.T., I.J.T., and C.D.S. are inventors. C.D.S., K.T., and I.J.T. are co-founders of Antheia Inc.

SUPPLEMENTARY MATERIALS

www.sciencemag.org/content/349/6252/1095/suppl/DC1
Materials and Methods
Figs. S1 to S8
Tables S1 to S8
References (*43*–*66*)

1 July 2015; accepted 5 August 2015
Published online 13 August 2015
10.1126/science.aac9373

MICROBIOME

Growth dynamics of gut microbiota in health and disease inferred from single metagenomic samples

Tal Korem,[1,2]* David Zeevi,[1,2]* Jotham Suez,[3]* Adina Weinberger,[1,2]* Tali Avnit-Sagi,[1,2] Maya Pompan-Lotan,[1,2] Elad Matot,[1,2] Ghil Jona,[4] Alon Harmelin,[5] Nadav Cohen,[1,2] Alexandra Sirota-Madi,[6] Christoph A. Thaiss,[3] Meirav Pevsner-Fischer,[3] Rotem Sorek,[7] Ramnik J. Xavier,[6] Eran Elinav,[3]† Eran Segal[1,2]†

Metagenomic sequencing increased our understanding of the role of the microbiome in health and disease, yet it only provides a snapshot of a highly dynamic ecosystem. Here, we show that the pattern of metagenomic sequencing read coverage for different microbial genomes contains a single trough and a single peak, the latter coinciding with the bacterial origin of replication. Furthermore, the ratio of sequencing coverage between the peak and trough provides a quantitative measure of a species' growth rate. We demonstrate this in vitro and in vivo, under different growth conditions, and in complex bacterial communities. For several bacterial species, peak-to-trough coverage ratios, but not relative abundances, correlated with the manifestation of inflammatory bowel disease and type II diabetes.

Characterization of microbiome composition and function through shotgun sequencing has provided many insights into its roles in health and disease. Gene calling (*1*, *2*), functional/pathway analysis (*3*–*6*), metagenomic-wide association studies (*7*, *8*), genome assembly (*9*, *10*), and metagenomic single-nucleotide polymorphism (SNP) detection (*11*) have all shown associations between microbiome configurations and susceptibility to several diseases, including obesity (*4*, *12*), type II diabetes (*7*), auto-inflammatory disorders (*1*, *13*), metabolic disease (*12*, *14*), and cancer (*15*, *16*). However, these approaches, which only examine a static snapshot of the microbiome at the point of collection, cannot be used to observe the highly dynamic nature of the microbiota and the differential activity of its microbial members.

Here, we asked whether microbiota growth dynamics could be probed from a single metagenomic sample by examining the pattern of sequencing read coverage across bacterial genomes. Apart from a few examples (*17*), most bacteria harbor a single circular chromosome, which replicates bidirectionally from a single fixed origin toward a single terminus (*18*) (Fig. 1A). Thus, during DNA replication, regions that have already been passed by the replication fork will have two copies, whereas the yet unreplicated regions will have a single copy.

This concept was previously used to detect the location of the replication origin in synchronized yeast colonies (*19*) but also holds true in an asynchronous bacterial population in which every cell may be at a different stage of replication. Summed across the population, the copy number of a DNA region will be higher the closer that region is to the replication origin and, conversely, lower the closer that region is to the terminus (*20*, *21*). Hence, the ratio between DNA copy number near the replication origin and that near the terminus, which we term peak-to-trough ratio (PTR), should reflect the growth rate of the bacterial population. At higher growth rates, a larger fraction of cells undergo DNA replication and more active replication forks are present in each cell (*22*). This results in a ratio higher than 1:1 between near-origin DNA and near-terminus DNA, thereby providing a quantitative readout of the population growth rate (*21*).

We grew in vitro cultures of *Escherichia coli* (K-12 strain) and sequenced them at multiple time points during late lag phase, exponential phase, and early stationary phase (*23*). During stationary phase, when most of the cells in the culture are not growing and thus have a single copy of their genome, we found uniform coverage across the genome (Fig. 1, A to C). In contrast, during exponential growth, when each bacterial cell may be at a different stage of DNA replication, the coverage pattern exhibited a single trough and a single peak, and the peak coincided with the known (*24*) replication origin (Fig. 1, A to C).

Similar patterns to those seen in vitro were also found for *E. coli* in 583 publicly available (*3*, *7*, *9*) human metagenomic fecal samples (Fig. 1B). PTRs extracted from these samples varied across individuals, in the range of 1 to 2.4, resembling the 1 to 2.6 range of ratios measured in vitro (Fig. 1B). Ratios higher than 2 are indicative of multifork replication, previously documented for *E. coli* (*18*, *22*).

To examine whether PTRs provide a quantitative measure of growth rate, we calculated the temporal growth rate of *E. coli* at different times during its growth experiment as the derivative of its abundance across time (*23*). PTRs were correlated with the measured growth rate, preceding it by 30 min ($R = 0.95$, $P < 10^{-4}$) (Fig. 1D), indicating that PTR predicts the change in abundance. To determine whether PTRs accurately reflect steady-state growth rates (as opposed to temporal growth), we grew *E. coli* in an aerobic chemostat in which steady growth rates were controlled by changing the dilution rate of the system to induce a 16-fold range (*23*) and found excellent correlation ($R = 0.996$, $P < 0.001$) (fig. S1A) between the calculated PTRs and the measured growth rates. According to theoretical models (*21*), $PTR = 2^{C/G}$, where C is the replication time (C-period), and G is the generation time, and thus $1/\log_2(PTR)$ is proportional to G/C. This transformation was correlated with measured bacterial generation time ($R = 0.96$, $P < 0.01$) (fig. S1B), confirming PTR as its proxy, even when the replication time is unknown.

The relationship between PTR and growth rate extends to other commensal strains, as we found that PTR and temporal measured growth rate were significantly correlated in similar cell growth experiments performed on *Lactobacillus gasseri* and *Enterococcus faecalis* under anaerobic conditions (*L. gasseri*, $R = 0.74$, $P < 0.001$; *E. faecalis*, $R = 0.57$, $P < 0.05$) (fig. S2, A and B). PTR also detects changes in growth rate mediated by changes in growth conditions, as PTRs and measured growth rate were correlated in additional cell growth experiments performed on *E. faecalis* in aerobic conditions and on *E. coli* in restricted growth conditions (*23*) (*E. coli*, $R = 0.92$, $P < 0.001$; *E. faecalis*, $R = 0.78$, $P < 10^{-4}$) (fig. S2, C and D). *L. gasseri* exhibited no growth in aerobic conditions, and accordingly we observed no change in PTRs (fig. S2E). PTRs for *L. gasseri* and *E. faecalis* were significantly different between aerobic and anaerobic conditions (*E. faecalis*, $P < 0.05$; *L. gasseri*, $P < 0.001$, Mann-Whitney *U* test) (fig. S2E).

To examine whether PTRs can be used to detect clinically relevant changes in culture conditions, we treated an in vitro culture of early log-phase nalidixic acid-resistant *Citrobacter rodentium* with the bacteriostatic antibiotic erythromycin. Because bacteriostatic antibiotics halt bacterial growth, and thus indirectly inhibit replication, we postulated that erythromycin treatment would decrease PTRs. As a control, cultures were treated with nalidixic acid, with the bactericidal antibiotic kanamycin, or left untreated. Indeed, erythromycin treatment lowered the PTR compared with controls (Mann-Whitney $P < 0.001$ and $P < 10^{-4}$ for untreated control or nalidixic acid treated control, respectively) (Fig. 2, A and B). PTR reduction

[1]Department of Computer Science and Applied Mathematics, Weizmann Institute of Science, Rehovot, Israel. [2]Department of Molecular Cell Biology, Weizmann Institute of Science, Rehovot, Israel. [3]Immunology Department, Weizmann Institute of Science, Rehovot, Israel. [4]Department of Biological services, Weizmann Institute of Science, Rehovot, Israel. [5]Department of Veterinary Resources, Weizmann Institute of Science, Rehovot, Israel. [6]Center for Computational and Integrative Biology, Massachusetts General Hospital, Harvard Medical School and Broad Institute, Cambridge, MA, USA. [7]Department of Molecular Genetics, Weizmann Institute of Science, Rehovot, Israel.
*These authors contributed equally to this work. †Corresponding authors. E-mail: eran.elinav@weizmann.ac.il (E.E.); eran.segal@weizmann.ac.il (E.S.)

Downloaded from www.sciencemag.org on September 5, 2015

under erythromycin was evident within 30 min after administration and preceded the halt in exponential growth that was detected only 60 min after erythromycin treatment (Fig. 2, A to C). During antibiotic recovery, obtained by washing the cultures after 2.5 hours and removing the antibiotics (*23*), PTRs increased, consistent with the rise in abundance (Mann-Whitney $P < 0.001$) (Fig. 2, A and B).

Next, we grew *L. gasseri* within a mixture of six commensal bacterial strains (*23*) and observed a rise in its PTR corresponding with the rise in abundance, with PTR and temporal growth being correlated ($R = 0.64$, $P < 0.001$) (Fig. 2D).

Together, the in vitro experiments show that PTRs precede and predict changes in abundance even in the more complex setting of a mixed bacterial community, thereby establishing the link between PTRs and growth rate.

To investigate whether PTRs remained accurate predictors of bacterial activity in a disease setting, we compared the proliferative behavior of virulent and nonvirulent (*tir*-mutant) strains of *C. rodentium*, which we used to infect C57BL/6 mice previously depleted of their native microbiota by wide-spectrum antibiotic treatment (*23*). We compared the in vivo abundance of both strains with PTRs and found that both showed similar behaviors 1 to 5 days post-infection (p.i.), with counts steadily rising from ~10^4 to 10^5 CFU/ml at day 1 to ~10^8 CFU/ml by day 5 (fig. S3). However, at 6 to 9 days p.i., the virulent strain displayed significantly higher counts (Mann-Whitney $P < 0.05$) (fig. S3) and PTRs (Mann-Whitney $P < 0.001$) (Fig. 3A) than the nonvirulent strain, likely reflecting preferential mucosal adhesion and proliferation (*25*). Whereas PTRs of the virulent strain were higher at days 6 to 9 p.i. compared with days 1 to 5 p.i. (Mann-Whitney $P < 0.001$) (Fig. 3A), PTRs of the nonvirulent strain 6 to 9 days p.i. were even lower than those of in vitro cultures of *C. rodentium*

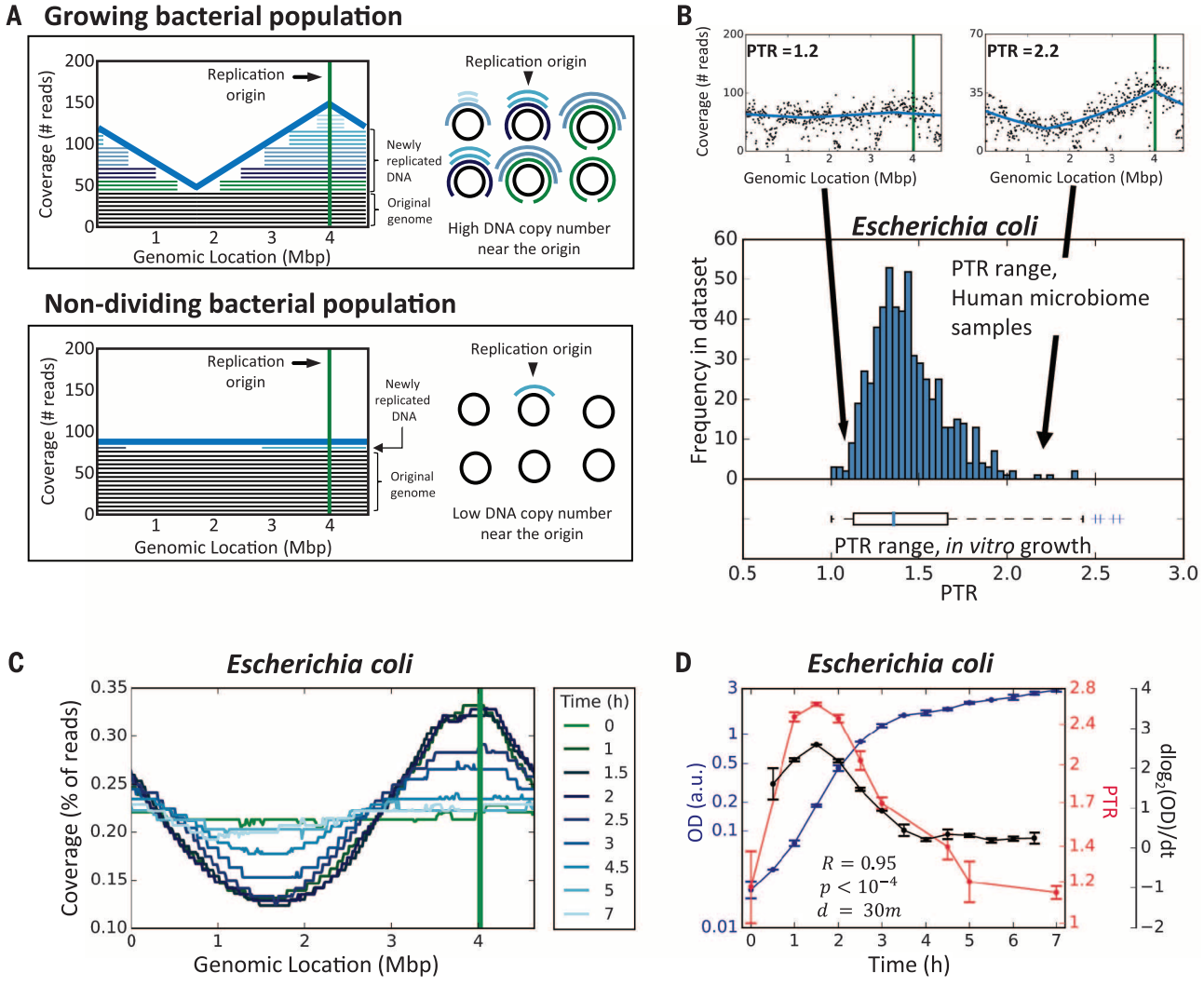


Fig. 1. PTR accurately measures in vitro growth rates of *E. coli*. (**A**) Sequenced reads are mapped to complete bacterial genomes, and the sequencing coverage across the genome is plotted. Each bacteria cell in a growing population (top) will be at a different stage of DNA replication, generating a coverage pattern that peaks near the known replication origin (green vertical line in graph), and thus produces a prototypical sequencing coverage pattern with a single peak and a single trough. Bacteria from a nondividing population (bottom) have a single copy of the genome, producing a flat sequencing coverage pattern across the genome. (**B**) (Top) Sequencing coverage patterns of a nonreplicating (left) and actively replicating (right) *E. coli* from two human gut metagenomic samples. (Bottom) Distribution of PTRs of *E. coli* across 583 different human gut metagenomic samples (*3*, *7*, *9*) (histogram) and 58 in vitro samples from four growth experiments (box plot). (**C**) Genome coverage plots of *E. coli*, measured at different times during an in vitro cell growth experiment, showing that PTRs are highest during exponential growth (time points 1 to 2.5) and lowest in lag (time point 0) and stationary (time points 3 to 7) phases. (**D**) PTRs (red line) correlate ($R = 0.95$, $P < 10^{-4}$) with the growth rate (black line), measured as the derivative of the logged abundance curve [abundance is measured as optical density of the culture (OD); blue line] in the subsequent 30 min (*23*). $N = 2$ repeats. Symbols, mean; error bars, mean ± SEM.

in stationary phase (Mann-Whitney $P < 0.001$) (Fig. 3A).

To explore the utility of the PTR measure within the complex metagenomic setting, we devised a computational pipeline that extracts PTRs for multiple samples within large metagenomic cohorts (supplementary text and fig. S4). In devising this pipeline, we took care to address (i) genomic differences between strains of a certain species; (ii) copy number variation of different genomic regions, and (iii) variable coverage levels stemming from sequencing depth. We show that our method is robust to these drivers of noise (fig. S5 to S8 and supplementary text), attributed to our examination of coverage across the entire genome, as opposed to comparing the coverage of origin and terminus regions directly.

Examining the full length of the genome also allows us to predict the replication origin location in different bacteria. We verified that coverage peak locations coincided with known locations of origins of replication. To this end, we applied our pipeline to 759 metagenomic stool samples from Chinese and European cohorts (*7*, *9*) and predicted the location of the origin and terminus of replication for 187 different microbial strains. Indeed, these predictions, computed solely based on our analysis of the bacterial genome coverage patterns, agreed with the known replication origins of 132 different strains (*24*) ($R^2 = 0.98$, $P < 10^{-30}$) (fig. S8), and for 55 strains whose replication origin location is unknown our method generated novel predictions (fig. S9).

To determine whether PTRs can uncover a possible interplay between host genetics and gut microbiome growth dynamics we collected fecal samples from three mouse strains (Swiss Webster, BALB/c, and C57BL/6) (*23*) grown under identical environmental conditions. Microbiota growth dynamics, as estimated by PTRs, differed significantly across the different mouse strains. In BALB/c mice, PTRs were lower overall compared with C57BL/6 and Swiss Webster mice ($P < 0.05$) (fig. S10A). The reduction in growth in the BALB/c mice was driven by *Parabacteroides distasonis*, which displayed consistently lower PTR than in other mouse strains (fig. S10, B to D), indicating that host genetics may affect the growth dynamics of this bacterium.

Another example of the utility of PTRs in assessing physiological microbiome growth patterns is provided in microbiome diurnal oscillation patterns, which we recently linked to host susceptibility to obesity and glucose intolerance (*26*). Examining PTRs of fecal microbiomes collected from a human volunteer every 6 hours for four consecutive days, we identified two species, out of four that passed our PTR pipeline filters, that showed abundance levels cycling with a 24-hour periodicity (*23*). For both species, the PTRs also exhibited 24-hour oscillatory patterns ($P < 0.05$) (*23*) (Fig. 3B and fig. S11), suggesting that diurnal changes in the abundance of some bacteria were reflected in their PTRs.

To investigate the effect of an extreme dietary change on bacterial growth rates, two healthy human volunteers underwent an acute dietary change, in which they shifted their normal diet to one that contained only boiled white rice for 1 week, after which they reverted back to their regular dietary habits. In both participants, we observed a global change in gut bacterial growth dynamics between dietary regimens, as reflected in statistically significant differences in the PTRs of all bacteria between the days in which rice was consumed and the days in which the participant's regular diet was followed ($P < 0.005$ for each participant) (Fig. 3, C and D).

We also examined body site–specific microbial growth rates in a metagenomic cohort (*3*) and found significantly higher PTRs in 229 tongue dorsum (1.36 ± 0.006) and 193 buccal mucosa (1.37 ± 0.007) samples, as compared with 325 stool samples (1.16 ± 0.002; $P < 10^{-50}$ in both cases) (fig. S12A). Six species were present in both the oral cavity and stool with sufficient coverage to calculate PTRs, with three featuring significantly different PTRs between sites [false discovery rate (FDR)–corrected Mann-Whitney $P < 0.1$] (fig. S12, B to G), indicating that intersite differences stem not only from distinct bacterial compositions but also from site-specific differences in growth dynamics.

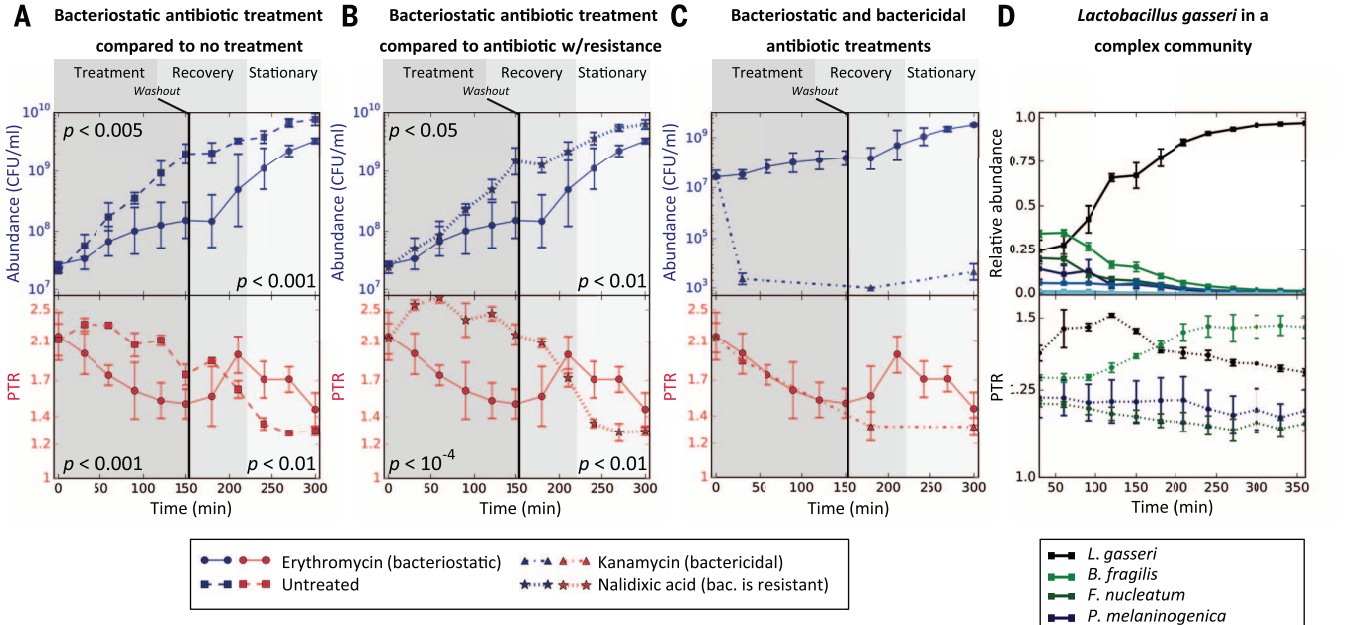


Fig. 2. PTR accurately measures in vitro growth rates in multiple conditions. (**A** to **C**) Absolute abundance levels [colony-forming units per ml (CFU/ml)] (top *y* axis, blue) and PTR (bottom *y* axis, red) as a function of time (minutes) of an *in vitro* culture of *C. rodentium* treated with erythromycin (bacteriostatic antibiotic in this setting; $N = 2$ repeats), compared to those of (A) an untreated control culture ($N = 3$ repeats); (B) a culture treated with nalidixic acid, a drug to which *C. rodentium* is resistant ($N = 3$ repeats); and (C) a culture treated with kanamycin, a bactericidal drug in this setting ($N = 3$ repeats). Background color indicates the treatment period (dark gray, left), recovery period (gray, middle), and early stationary phase (light gray, right). The black vertical line denotes antibiotic washout. PTR changes precede changes in growth. *P* values are Mann-Whitney *U* test between abundance (top) or PTR (bottom) of the two different cultures at times 30 to 150 min (left) or times 210 to 300 min (right). (**D**) Bacterial abundances (CFU/ml; top) and PTR (bottom) of *L. gasseri* and a mixture of six additional bacterial strains that inhabit the human gut. $N = 4$ repeats. Symbols, mean; error bars, mean ± SEM.

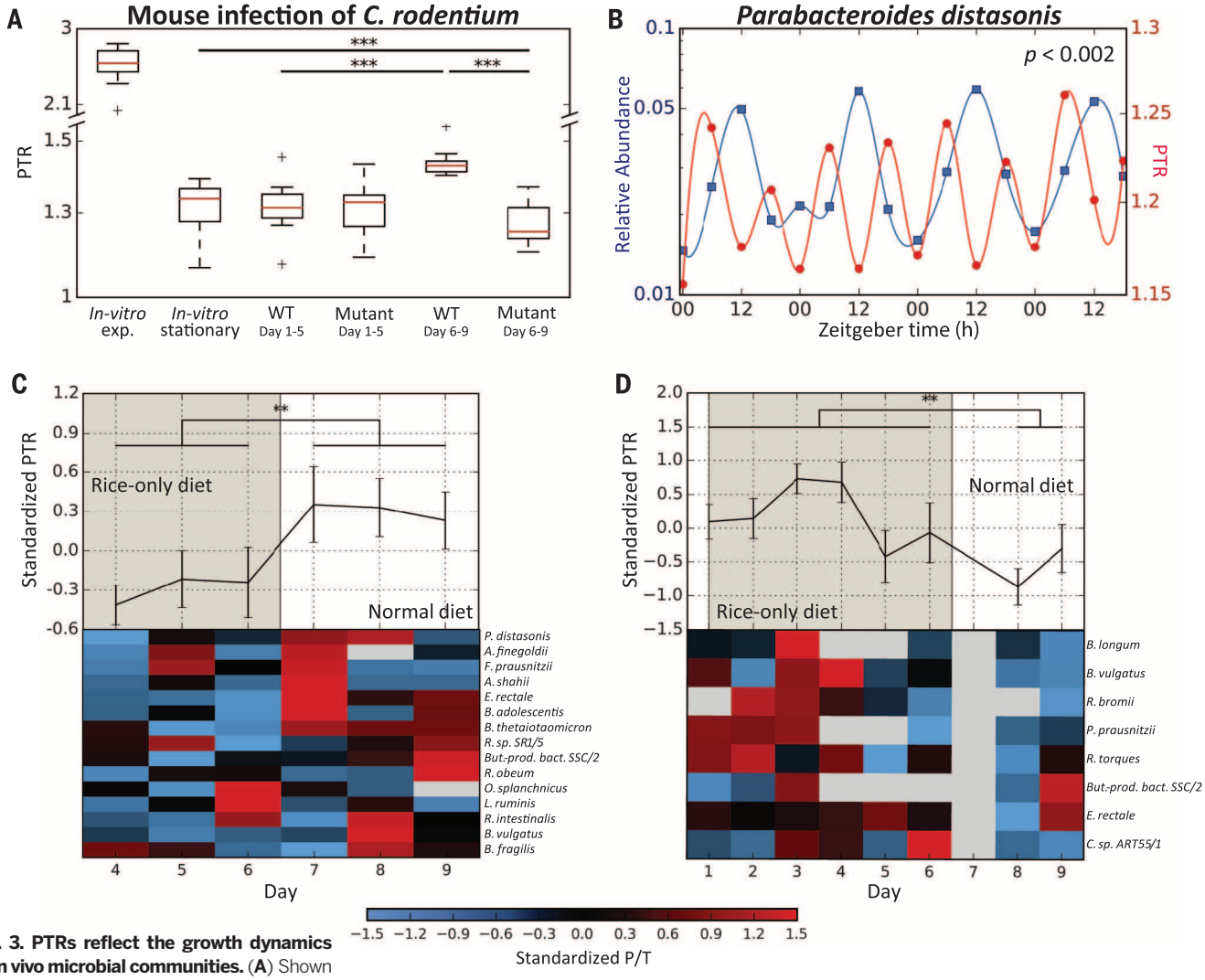


Fig. 3. PTRs reflect the growth dynamics of in vivo microbial communities. (**A**) Shown are PTRs of virulent [icc169; wild-type (WT); $N = 3$ mice] and nonvirulent (*tir* mutant; $N = 3$ mice) *C. rodentium* 1 to 5 or 6 to 9 days p.i. of C57BL/6 mice previously depleted of their native microbiota. PTRs of stationary and exponential in vitro *C. rodentium* cultures are shown for reference. *P* values are Mann-Whitney *U* test. See fig. S3 for the corresponding measured abundances. (**B**) Relative abundance (left *y* axis, blue) and PTRs (right *y* axis, red) of *Parabacteroides distasonis* from fecal metagenomic samples obtained approximately every 6 hours from one human individual on 4 consecutive days (*26*). Plotted lines are spline interpolations using the displayed data points. Time is with respect to light cycles (Zeitgeber time, horizontal axis). *P* value is for 24-hour oscillations (*23*). (**C** and **D**) Shown are standardized PTRs (top graphs, mean ± SEM) and specific PTRs for species present in the sample (bottom heat maps), belonging to two human subjects that underwent a radical dietary change. Compared are days in which only white boiled rice was consumed (gray area) and days of normal diet (white area). A global change in bacterial growth dynamics was observed between dietary regimens (**Mann-Whitney $P < 0.005$, ***$P < 0.001$).

Overall, these results provide examples of functional insights that are not achievable using traditional metagenomics analysis methods and indicate that microbiome growth dynamics vary across diverse physiological conditions and locations.

To determine whether bacterial PTRs are associated with disease and different clinical parameters, we generated PTRs for every species in samples from European ($N = 396$) (*9*) and Chinese ($N = 363$) (*7*) cohorts. In both data sets, we found large variation in PTRs across samples (Fig. 4). Notably, we found statistically significant associations between the PTRs of 20 different bacteria and multiple clinical parameters, including significant correlations between the PTR of *Bifidobacterium longum* and occurrence of Crohn's disease in the Spanish nationals of the European cohort (*9*) (FDR-corrected Mann-Whitney $P < 0.005$), and between the PTRs of 12 different bacteria and the occurrence of type II diabetes in the Chinese cohort (Fig. 4) (*7*). We also found significant correlations between PTRs and the occurrence of ulcerative colitis, body-mass index, the fraction of glycated hemoglobin (HbA1c%, a common marker of long-term glycemic control) (*27*), fasting serum insulin, and fasting blood glucose levels (Fig. 4).

These associations are independent of—and unobtainable by examining—bacterial abundances, because (i) in correlating PTRs with clinical parameters, we only used samples in which that bacteria was present, thereby withholding information about the presence or absence of the examined bacteria (*23*); (ii) in only 5 of the 38 statistically significant correlations were the abundance levels of the species also correlated with the same clinical parameter; and (iii) 36 of the 38 significant associations of PTR remained significant after correcting them for relative abundance levels. The PTRs of some species were correlated with clinical parameters only after correction for relative abundance, including *Eubacterium rectale* and the occurrence of Crohn's disease (FDR-corrected Mann-Whitney $P < 10^{-4}$).

As a global measure of the growth dynamics of the entire microbiota, for every sample we

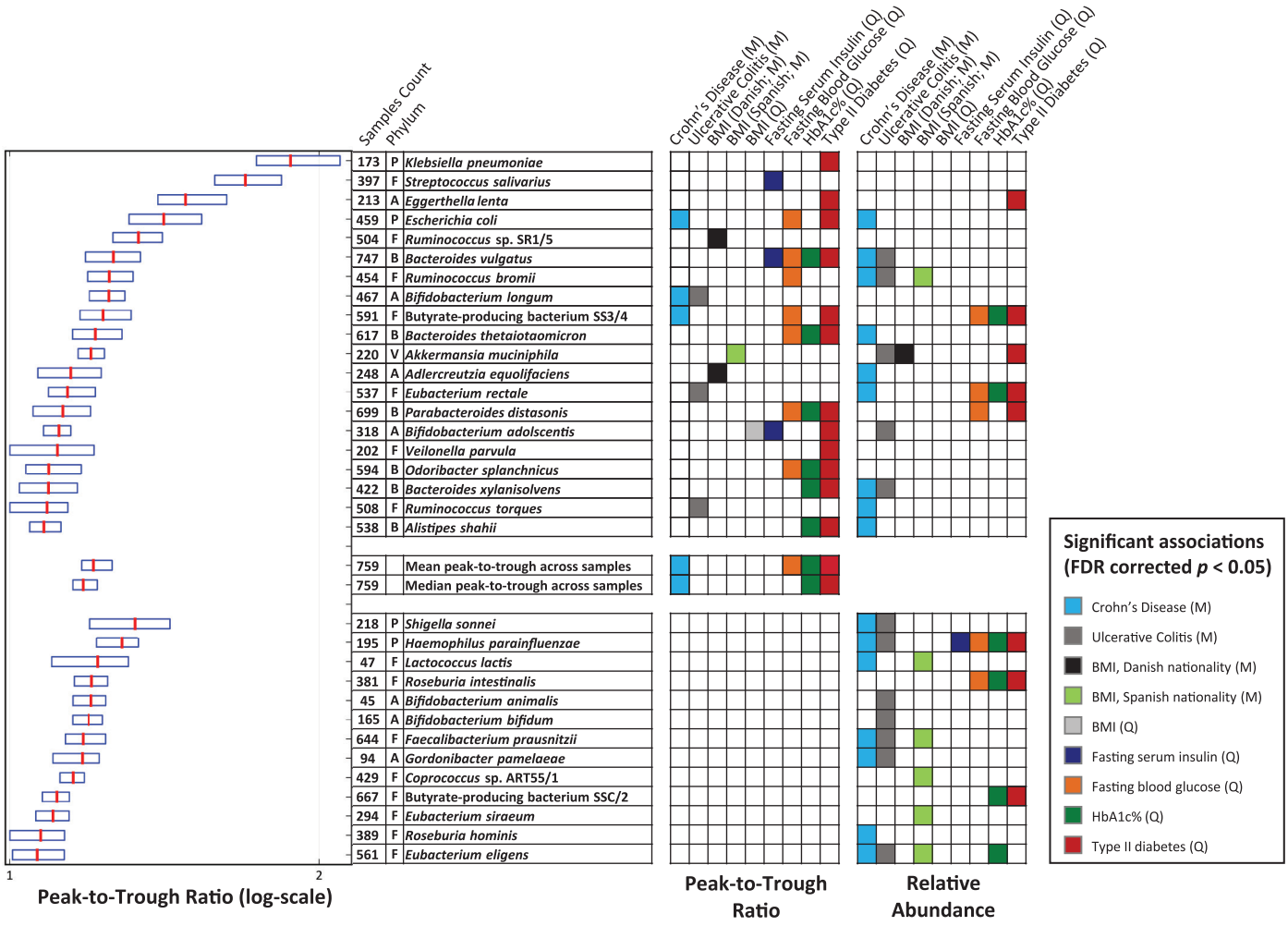


Fig. 4. Bacterial dynamics correlate with several diseases and metabolic disorders. PTRs of species from Chinese (*7*) [*N* = 363 samples (Q)] and European (*9*) [*N* = 396 samples (M)] cohorts are shown (box plots, left; red, median; boundaries, 25th to 75th percentiles) if their relative abundances or PTRs were significantly associated with clinical parameters. Shown are phylum membership; the number of samples for which PTRs were calculated; and a row with colored entries for each statistically significant (FDR-corrected $P < 0.05$) association between clinical parameters and its PTR (left column block) or relative abundance (right column block). Mann-Whitney *U* test and Spearman correlations were used for binary and continuous clinical parameters, respectively. (Top block) Species with significant associations between PTR and clinical parameters. (Bottom block) Species with significant associations only between relative abundance and clinical parameters. A, *Actinobacteria*; B, *Bacteroidetes*; F, *Firmicutes*; P, *Proteobacteria*; V, *Verrucomicrobia*; BMI, body-mass index.

calculated both the mean and the median of the PTRs of all the bacteria present. This global measure correlated with fasting blood glucose and HbA1c% levels and with the occurrence of Crohn's disease and type II diabetes, indicating that global microbiome growth dynamics also associate with disease (Fig. 4).

A preliminary analysis of 40 samples from the Prospective Registry in Inflammatory Bowel Disease (IBD) Study at Massachusetts General Hospital (MGH) (PRISM) cohort (*23*) showed that only four bacteria passed our stringent pipeline filters for PTR calculation in more than half of the samples. Notwithstanding, *Eggerthella lenta* presented significantly different PTRs between patients with active Crohn's disease and patients in remission (FDR-corrected Mann-Whitney $P < 0.1$). Neither the abundance of *E. lenta* nor of the other three species differed between active and quiescent Crohn's patients, highlighting the fact that PTRs reflect an independent feature of the effect of the gut microbiome on its host.

Overall, we present a new type of metagenomic data analysis that provides an accurate quantitative estimate of the growth dynamics of the microbiota from a single snapshot sample. These estimates have clinical relevance and correspond to changes in absolute abundances, which are masked by and unobtainable through relative abundances.

Using PTRs to "fish out" microbial kinetic behavior in a complex microbiome population could extend our understanding of how flexibly the microbiota responds functionally to environmental signals. We may be able to identify active "driver" and "modulator" species, distinguish them from bystander commensal species, and pinpoint disease-causing or disease-modulating microbes that contribute to multifactorial diseases whose activities may be masked by other bacteria. Furthermore, our method may be able to detect, follow, and assess therapeutic responsiveness of pathogenic or probiotic species introduced into the microbiome.

REFERENCES AND NOTES

1. J. Qin *et al.*, *Nature* **464**, 59–65 (2010).
2. M. Rho, H. Tang, Y. Ye, *Nucleic Acids Res.* **38**, e191 (2010).
3. Human Microbiome Project Consortium, *Nature* **486**, 207–214 (2012).
4. P. J. Turnbaugh *et al.*, *Nature* **457**, 480–484 (2009).
5. V. M. Markowitz *et al.*, *PLOS ONE* **7**, e40151 (2012).
6. F. Meyer *et al.*, *BMC Bioinformatics* **9**, 386 (2008).
7. J. Qin *et al.*, *Nature* **490**, 55–60 (2012).
8. F. H. Karlsson *et al.*, *Nature* **498**, 99–103 (2013).
9. H. B. Nielsen *et al.*, *Nat. Biotechnol.* **32**, 822–828 (2014).
10. J. Oh *et al.*, *Nature* **514**, 59–64 (2014).
11. S. Schloissnig *et al.*, *Nature* **493**, 45–50 (2013).
12. E. Le Chatelier *et al.*, *Nature* **500**, 541–546 (2013).
13. C. Manichanh *et al.*, *Gut* **55**, 205–211 (2006).

14. F. Karlsson, V. Tremaroli, J. Nielsen, F. Bäckhed, *Diabetes* **62**, 3341–3349 (2013).
15. J. Ahn *et al.*, *J. Natl. Cancer Inst.* **105**, 1907–1911 (2013).
16. S. Yoshimoto *et al.*, *Nature* **499**, 97–101 (2013).
17. J. Hinnebusch, K. Tilly, *Mol. Microbiol.* **10**, 917–922 (1993).
18. J. D. Wang, P. A. Levin, *Nat. Rev. Microbiol.* **7**, 822–827 (2009).
19. J. Xu *et al.*, *Genome Biol.* **13**, R27 (2012).
20. O. Skovgaard, M. Bak, A. Løbner-Olesen, N. Tommerup, *Genome Res.* **21**, 1388–1393 (2011).
21. H. Bremer, G. Churchward, *J. Theor. Biol.* **69**, 645–654 (1977).
22. S. Cooper, C. E. Helmstetter, *J. Mol. Biol.* **31**, 519–540 (1968).
23. See the supplementary materials on *Science* Online for details.
24F. Gao, H. Luo, C.-T. Zhang, *Nucleic Acids Res.* **41**, D90–D93 (2013).
25. S. Wiles *et al.*, *Cell. Microbiol.* **6**, 963–972 (2004).
26. C. A. Thaiss *et al.*, *Cell* **159**, 514–529 (2014).
27. R. J. Koenig *et al.*, *N. Engl. J. Med.* **295**, 417–420 (1976).

ACKNOWLEDGMENTS

We thank the members of the Segal and Elinav laboratories for fruitful discussions. T.K. and D.Z. are supported by the Ministry of Science, Technology, and Space, Israel. T.K. is the recipient of the Strauss Institute fellowship for nutritional research. C.A.T. is the recipient of a Boehringer Ingelheim Fonds Ph.D. Fellowship. E.E. is supported by Yael and Rami Ungar, Israel; Leona M. and Harry B. Helmsley Charitable Trust; the Gurwin Family Fund for Scientific Research; Crown Endowment Fund for Immunological Research; estate of Jack Gitlitz; estate of Lydia Hershkovich; the Benoziyo Endowment Fund for the Advancement of Science; Adelis Foundation; John L. and Vera Schwartz, Pacific Palisades; Alan Markovitz, Canada; Cynthia Adelson, Canada; CNRS (Centre National de la Recherche Scientifique); estate of Samuel and Alwyn J. Weber; Mr. and Mrs. Donald L. Schwarz, Sherman Oaks; grants funded by the European Research Council; the German-Israel Binational foundation; the Israel Science Foundation (ISF); the Minerva Foundation; and the Rising Tide foundation. E.E. is the incumbent of the Rina Gudinski Career Development Chair. This work was supported by grants from the European Research Council (ERC) and the ISF to E.S. The European Nucleotide Archive (ENA) accession number for the microbial shotgun sequences is PRJEB9718. The pipeline tool will be made publicly available at http://genie.weizmann.ac.il/software/bac_growth.html. All human studies were approved by the Tel Aviv Sourasky Medical Center Institutional Review Board, approval numbers TLV-0658-12, TLV-0050-13, and TLV-0522-10, and the Weizmann Institute of Science Bioethics and Embryonic Stem Cell Research oversight (ESCRO) committee. The trial was reported to https://clinicaltrials.gov, identifier NCT01892956. The study did not necessitate or involve randomization. Author contributions: T.K. and D.Z. conceived the project, designed and conducted the analyses, interpreted the results, and wrote the manuscript. J.S. devised and performed all experiments in mice, anaerobic, and pathogenic bacteria. A.W. directed some of the experiments and the production of libraries and sequencing from samples collected in this study and provided critical insights to the manuscript. T.K., D.Z., J.S., and A.W. equally contributed to this work. T.A.-S., M.P.-L., and E.M. performed experiments and extraction and sequencing of samples. M.P.-F. performed experiments. G.J. performed chemostat experiments. A.H. supervised germ-free mouse experiments. N.C. aided in the design of the computational pipeline and in conducting the analyses. A.S.-M. and R.J.X. directed the PRISM cohort. C.A.T. and E.E. directed the circadian experiments. R.S. and E.S. directed the dietary intervention study. E.E. and E.S. conceived and directed the project and analyses, designed experiments, interpreted the results, and wrote the manuscript.

SUPPLEMENTARY MATERIALS

www.sciencemag.org/content/349/6252/1101/suppl/DC1
Supplementary Text
Materials and Methods
Figs. S1 to S13
Table S1
References (*28*–*37*)

1 May 2015; accepted 16 July 2015
Published online 30 July 2015
10.1126/science.aac4812

ALLERGY

Farm dust and endotoxin protect against allergy through A20 induction in lung epithelial cells

Martijn J. Schuijs,[1,2]* Monique A. Willart,[1,2]* Karl Vergote,[1,2] Delphine Gras,[3] Kim Deswarte,[1,2] Markus J. Ege,[4] Filipe Branco Madeira,[1,2] Rudi Beyaert,[5,6] Geert van Loo,[5,6] Franz Bracher,[7] Erika von Mutius,[4] Pascal Chanez,[3] Bart N. Lambrecht,[1,2,8]†‡ Hamida Hammad[1,2]†‡

Growing up on a dairy farm protects children from allergy, hay fever, and asthma. A mechanism linking exposure to this endotoxin (bacterial lipopolysaccharide)–rich environment with protection has remained elusive. Here we show that chronic exposure to low-dose endotoxin or farm dust protects mice from developing house dust mite (HDM)–induced asthma. Endotoxin reduced epithelial cell cytokines that activate dendritic cells (DCs), thus suppressing type 2 immunity to HDMs. Loss of the ubiquitin-modifying enzyme A20 in lung epithelium abolished the protective effect. A single-nucleotide polymorphism in the gene encoding A20 was associated with allergy and asthma risk in children growing up on farms. Thus, the farming environment protects from allergy by modifying the communication between barrier epithelial cells and DCs through A20 induction.

Allergic asthma is characterized by eosinophilic airway inflammation, goblet cell metaplasia, and bronchial hyperreactivity (BHR) and is controlled by innate and adaptive immune responses to inhaled allergens such as house dust mites (HDMs), pollen, and fungal spores that signal via pattern recognition receptors (PRRs) on barrier epithelial cells (ECs) and dendritic cells (DCs) (*1*, *2*). In children, allergic sensitization and asthma are strongly influenced by genes and the environment. A dairy farm is one of the strongest protective environments (*3*–*6*). On farms, there is high-level exposure to endotoxin [lipopolysaccharide (LPS)], a cell wall component of Gram-negative bacteria. The protective effect that high levels of environmental endotoxin demonstrate against allergy has also been noticed in nonfarming households, where exposure was measured in dust collected from mattresses or kitchen floors (*7*–*9*). Protection in these environments is influenced by genetic polymorphisms in key PRRs that recognize endotoxin (*10*). A clear mechanism encompassing the complex interactions between a protective environment, genetics, and the immune response to allergens has been lacking.

[1]Laboratory of Immunoregulation, VIB Inflammation Research Center, Ghent, Belgium. [2]Department of Internal Medicine, Ghent University, Ghent, Belgium. [3]Department of Respiratory Medicine, Assistance Publique Hopitaux de Marseille, UMR INSERM U1067 CNRS 7333, Aix Marseille University, Marseille, France. [4]Dr. von Hauner Children's Hospital, Ludwig-Maximilians-Universität, Munich, Germany. [5]Unit of Molecular Signal Transduction, VIB Inflammation Research Center, Ghent, Belgium. [6]Department of Biomedical Molecular Biology, Ghent University, Ghent, Belgium. [7]Center for Drug Research, Department of Pharmacy, Ludwig Maximilians University, Butenandtstrasse 5-13, D-81377 Munich, Germany. [8]Department of Pulmonary Medicine, Erasmus Medical Center, Rotterdam, Netherlands.
*These authors contributed equally to this work. †These authors contributed equally to this work. ‡Corresponding author. E-mail: hamida.hammad@ugent.be (H.H.); bart.lambrecht@ugent.be (B.N.L.)

To address whether exposure to environmental endotoxin and protection from allergy are causally related, we exposed mice every other day for 2 weeks to a low dose (100 ng) of LPS or to control phosphate-buffered saline (PBS) before HDM sensitization and challenge (Fig. 1A) (see supplementary materials and methods). Sham-protected mice exhibited strong airway eosinophilia and lymphocytosis (Fig. 1B), T helper 2 (T_H2)–dependent HDM allergen–specific immunoglobulin E (IgE) (Fig. 1C), and BHR to methacholine (Fig. 1D). However, mice pretreated with LPS failed to develop all of these canonical asthma features. Protective LPS led to reduced production of the type 2 cytokines interleukin (IL)–5 and IL-13 in mediastinal lymph node (MLN) cells (Fig. 1E), without a shift to T_H1- or T_H17-associated cytokines or to T_H1-dependent serum immunoglobulin G2a (IgG2a) antibodies (Fig. 1, C and E). All of the key asthma features were also suppressed when a single high dose (1 μg) of LPS was given as a preventive regimen 14 days before sensitization (fig. S1, A to E), as well as when chronic low-dose LPS was given before and throughout the entire HDM sensitization and challenge period (fig. S1, F to I).

Sensitization to HDMs depends on various DC subsets that migrate to the MLNs to prime CD4 T cell responses (*11*, *12*). When PBS-treated control mice were exposed to a single dose of HDM, $CD11b^+$ conventional DCs (cDCs), $CD103^+$ cDCs, and monocyte-derived DCs (moDCs) were recruited to the lungs and MLNs (Fig. 2A). In mice receiving preventive LPS, there was less HDM-induced recruitment of both subsets of cDCs, whereas moDCs were unaffected (Fig. 2A). cDCs that migrate to the MLN cells induce T_H2 polarization in HDM-reactive naïve T cells (*12*). To study the primary immune response to HDMs, we adoptively transferred $CD4^+$ HDM-specific 1-DER T cells [that express a transgenic T cell receptor

specific for the Der p $1_{WAFSGVAAT}$ peptide from HDMs (*12*)], followed by a single administration of HDMs. Prior 2-week treatment with LPS suppressed the proliferation of 1-DER T cells in the MLN cells (Fig. 2B), along with their differentiation into IL-5– and IL-13–secreting T_H2 cells (Fig. 2C).

The recruitment of lung DCs after allergen exposure depends on the chemokine CCL20, as well as their maturation on granulocyte-macrophage colony-stimulating factor (GM-CSF) (*2*, *12*–*14*), which programs DCs to induce T_H2 cell polarization (*2*, *15*). After receiving protective LPS in vivo, the lung levels of GM-CSF and CCL20 protein induced by HDMs were reduced (Fig. 2D). As ECs are the predominant source of these cytokines (*2*, *13*, *15*), we flow-sorted $EpCAM^+CD31^-Sca1^-CD45^-$ bronchial ECs 2 hours after they received HDMs in vivo. In the PBS pretreated group, HDM induced the mRNA of GM-CSF and of CCL20, yet this response was strongly blunted in the LPS-protected group (Fig. 2E). Similar data were found for IL-33 mRNA, another pro-T_H2 cytokine made by ECs in response to HDMs (fig. S2) (*2*, *15*).

These findings demonstrate that LPS protection blunts the innate immune response to HDMs, which we and others previously found to be driven by Toll-like receptor 4 (TLR4) on ECs (*2*, *15*, *16*). TLR4 signaling in ECs leads to nuclear translocation of NF-κB, inducing not only proinflammatory genes but also attenuators of signaling such as A20 (encoded by *Tnfaip3*). A20 is a ubiquitin-modifying enzyme that attenuates NF-κB activation by deubiquitinating key signaling intermediates downstream of TLR, IL-1 receptor, and tumor necrosis factor–family receptors (*17*–*19*). The mRNA for *Tnfaip3* was induced in sorted lung ECs 2 hours after in vivo exposure to a single HDM or LPS injection, and the effect was more pronounced for LPS (Fig. 3A). To address whether A20 mediated the protective effects of LPS, we generated mice lacking A20 selectively in lung ECs by crossing *Tnfaip3*$^{fl/fl}$ mice with mice that displayed lung-specific Cre recombinase expression under the tetracycline-inducible control of the *Ccsp* promoter (*Ccsp*-rtTA × Tet_{O7}Cre mice, referred to as *Tnfaip3*$^{EC\text{-}KO}$ mice) (*20*, *21*). We treated these mice with doxycycline from birth onward (fig. S3, A and B) and observed accelerated nuclear translocation of the p65 subunit of NF-κB in lung ECs 2 hours after HDM exposure in vivo, as compared with control *Tnfaip* $^{fl/fl}$ *Ccsp*Cre^- mice (*Tnfaip3*$^{EC\text{-}WT}$) (fig. S3C). Whereas LPS suppressed the salient features of asthma in *Tnfaip3*$^{EC\text{-}WT}$ mice, this effect was completely lost in *Tnfaip3*$^{EC\text{-}KO}$ mice (Fig. 3, B to D). The suppression of lung CCL20 and GM-CSF protein was less effective in *Tnfaip3*$^{EC\text{-}KO}$ mice receiving LPS (Fig. 3E) yet was still present to some extent, suggesting the existence of other molecular mechanisms by which LPS suppresses asthma. However, the HDM-induced recruitment of DCs to the lungs and MLNs was no longer inhibited by low-dose LPS treatment in *Tnfaip3*$^{EC\text{-}KO}$ mice (Fig. 3F), and asthma was no longer suppressed, which suggests that A20 is an important player in LPS-mediated protection.

In the absence of allergen exposure, baseline production of GM-CSF did not differ between *Tnfaip3*$^{EC\text{-}KO}$ and *Tnfaip3*$^{EC\text{-}WT}$ mice (Fig. 3E). However, the production of GM-CSF after HDM injection was much higher in *Tnfaip3*$^{EC\text{-}KO}$ mice. Recently, GM-CSF was found to be a crucial determinant of allergen recognition threshold in the lung (*14*). To address whether the loss of A20 would alter the allergen recognition threshold, we lowered the dose of sensitizing HDM by a factor of 10, in the absence of preventive LPS (fig. S4A). Whereas a 100-ng dose of HDM extract did not induce asthma features in *Tnfaip3*$^{EC\text{-}WT}$ mice, it did so in *Tnfaip3*$^{EC\text{-}KO}$ mice (fig. S4, B to F). Thus, in the induced absence of A20, sensitivity to inhaled HDM allergen is increased, and asthma runs a more severe course.

In addition to LPS, dust from dairy farms also contains peptidoglycan components of the wall of Gram-positive bacteria, extracellular polysaccharides from fungi, cowshed-derived bacteria such as *Acinetobacter Iwoffii* F78, and plant-derived polysaccharides (*5*). We therefore also performed

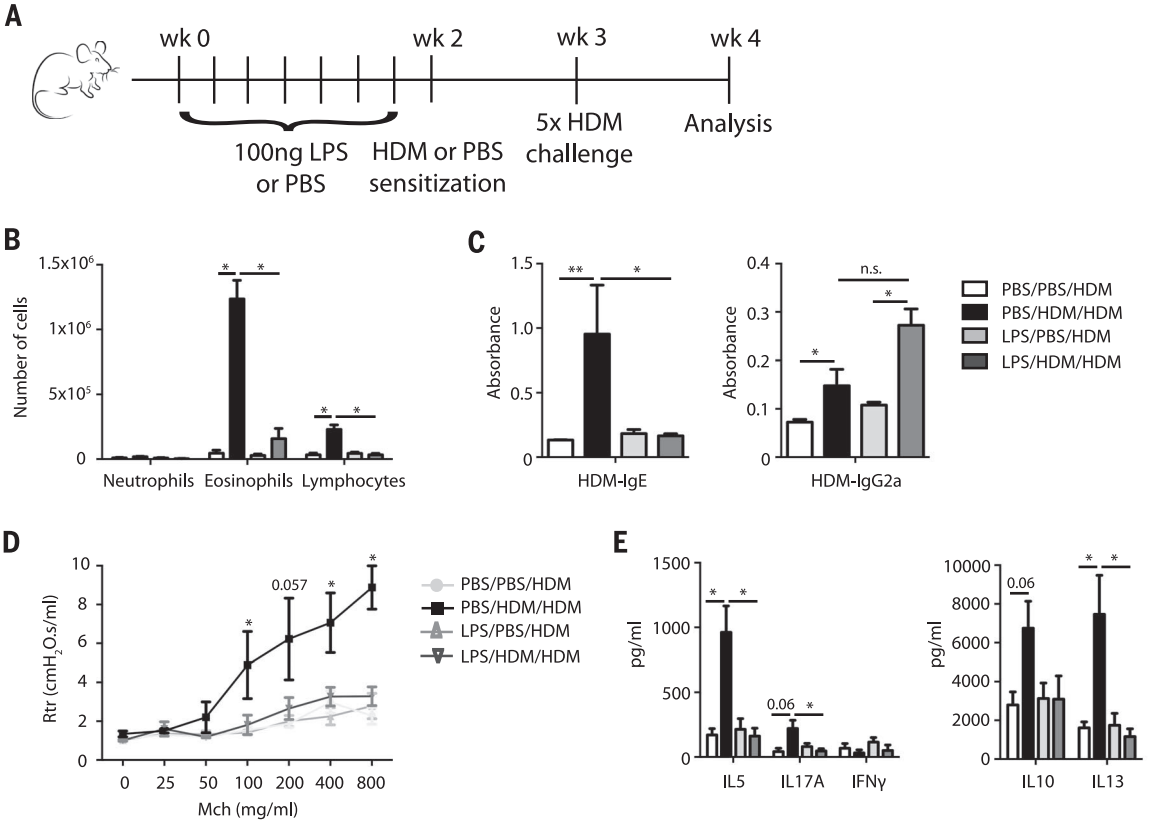


Fig. 1. Chronic LPS preexposure protects mice from asthma development. (**A**) Experimental setup illustrating the dosing regimen of LPS and the various controls. (**B**) Bronchoalveolar lavage differential cell counts of mice that received a chronic low dose of LPS or control PBS before sensitization and challenge with HDMs. To control for sensitization to HDMs, some mice were sham-sensitized to PBS. (**C**) Serum levels of HDM-specific IgE and IgG2a. (**D**) Bronchial hyperreactivity was measured after exposure to increasing doses of methacholine (Mch) using flexiVent (SCIREQ). (**E**) Cytokine production by MLN cells restimulated with HDMs for 3 days ex vivo. Data are representative of three independent experiments, with at least $n = 5$ mice per group. IFNγ, interferon-γ. In (B) to (E), error bars indicate SEM. *P* values reflect the Mann-Whitney *U* test: $^*P < 0.05$, $^{**}P < 0.01$. n.s., not significant.

experiments using dust samples collected from farms in Germany (*22*). A low dose of farm dust extract (100 ng) was given prophylactically every other day for 2 weeks before induction of HDM asthma in wild-type (WT) mice. As in the prophylactic treatment with LPS, farm dust extracts suppressed the salient features of asthma (fig. S5, A to D). The farm dust suppressed the levels of HDM-induced GM-CSF mRNA in sorted lung ECs (fig. S5E). Whereas farm dust suppressed asthma features in *Tnfaip3*$^{EC\text{-}WT}$ mice (Fig. 3G), this was not the case in *Tnfaip3*$^{EC\text{-}KO}$ mice (Fig. 3H), demonstrating that farm dust also mediates protection via epithelial A20.

We next validated our findings in humans. Normal human bronchial ECs (NHBECs) were grown to confluence and differentiated in air-liquid interface (ALI) cultures. In vitro pre-exposure of NHBECs to LPS suppressed the HDM-induced production of IL-1α and GM-CSF (Fig. 4A). We also collected endobronchial biopsies from healthy controls and patients with moderate to severe asthma (table S1 lists the clinical characteristics). Primary bronchial ECs were grown to confluence and then differentiated to ALI cultures. The ALI cultures of selected asthmatic patients (n = 3) were stimulated for 1 week with 100 ng of LPS or control PBS added every other day to the apical side of the ALI culture. In the PBS-treated group, HDM induced the production of GM-CSF and IL-1α on the basolateral side of the culture, and this was significantly reduced by LPS pretreatment (Fig. 4B). The mRNA levels of A20 were measured by quantitative reverse transcriptase polymerase chain reaction (qRT-PCR) and were significantly reduced in ALI-cultured ECs of mild (n = 12) and severe asthmatics (n = 14) compared with healthy controls (n = 12) (Fig. 4C). These effects were confirmed on protein levels (Fig. 4D). Thus, levels of A20 are lower in the barrier ECs of asthmatics, as compared with healthy controls.

We finally studied whether well-known polymorphisms in the human *TNFAIP3* gene (located at position 6q23 in the genome) were associated with various allergic diseases in the population of the GABRIELA study (table S2), a cross-sectional,

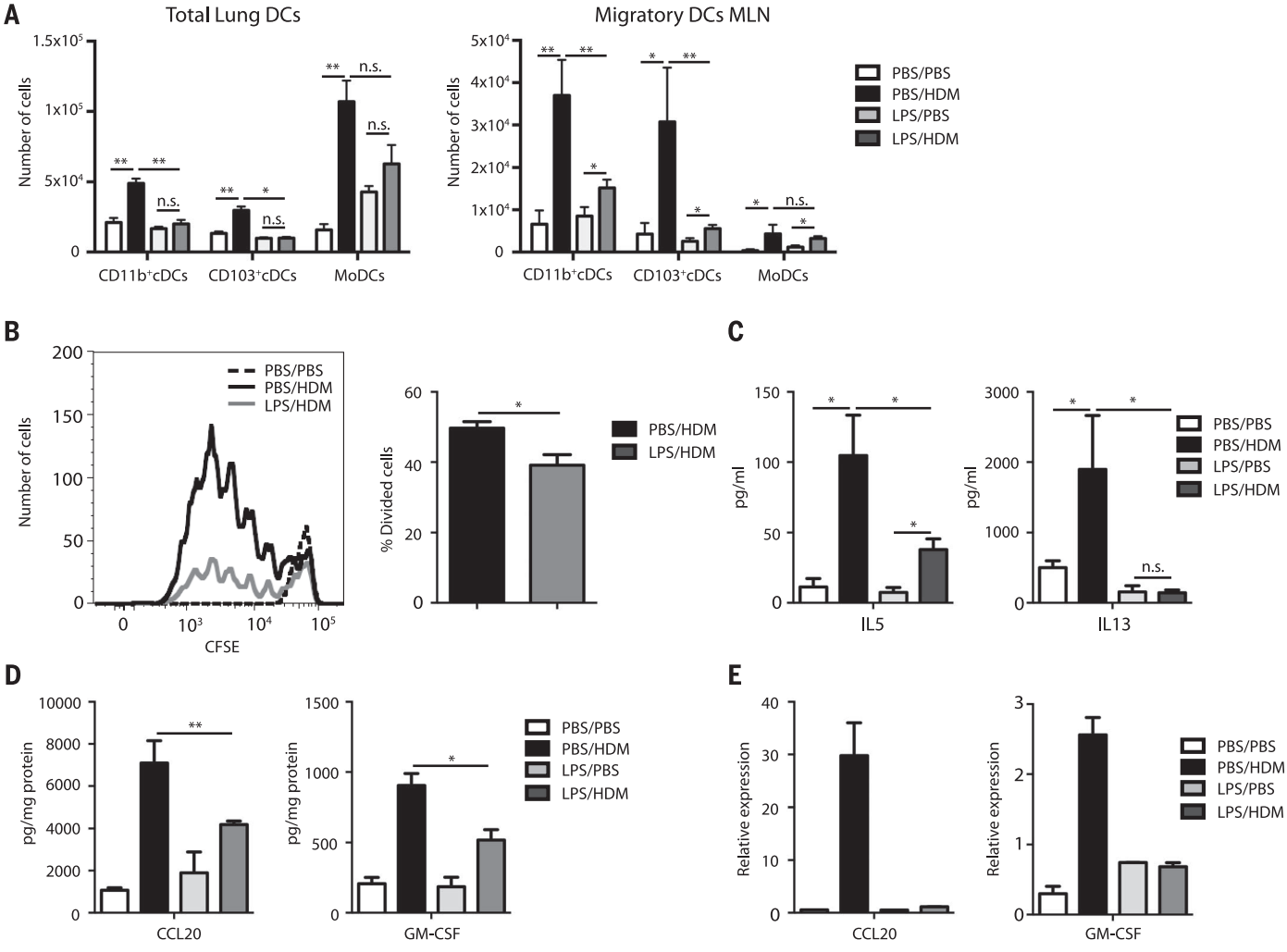


Fig. 2. Mechanism of suppression of asthma by chronic low-dose LPS inhalation. Mice received a chronic low dose of LPS or control PBS before sensitization to HDM extract. Some mice were sham-sensitized to PBS. (**A**) Recruitment of DC subsets was measured in the lungs and draining MLNs 24 hours after administration of HDM extract. (**B**) Proliferation of adoptively transferred 1-DER T cells labeled with carboxyfluorescein diacetate succinimidyl ester (CFSE), measured 3 days after a single injection of HDM. Some mice received protective low-dose LPS or control PBS, and some were sham-sensitized. (**C**) Cytokine production from the MLNs of mice receiving 1-DER T cells, collected 3 days after HDM injection. (**D**) Chemokine and cytokine levels measured in lung homogenates taken 2 hours after HDM sensitization. Some mice received protective low-dose LPS or control PBS, and some mice were sham-sensitized. (**E**) mRNA levels of the same chemokines and cytokines measured in epithelial cell adhesion molecule (EpCAM$^+$) lung ECs sorted 2 hours after HDM sensitization. Mice were treated as described in (D). Data are representative of two [(A) to (D)] and four (E) independent experiments with n = 5 mice per group [(A) to (D)] and n = 6 to 8 mice per group (E). In all panels, error bars indicate SEM. P values reflect the Mann-Whitney U test: *P < 0.05, **P < 0.01. n.s., not significant.

multiphase, population-based survey of the farm effect on asthma and allergic disease in children aged 6 to 12 years in four central European countries. Detailed data on asthma, farming exposure, and specific IgE levels have been collected from a random sample of 1707 children. From a previous genome-wide association study (GWAS), the exonic single-nucleotide polymorphism (SNP) rs2230926 and the intronic SNP rs610604 were available (*23*). We found that SNP rs2230926 (T>G), which resulted in a phenylalanine-to-cysteine switch at amino acid position 127 (Phe^{127}→Cys^{127}) in exon 3 of *TNFAIP3*, was associated with increased risk of asthma [odds ratio (OR) = 1.76] and eczema (OR = 2.18) across the entire sample population. We also noticed that there was a gene-by-environment interaction for this SNP with farming: the protective effect that growing up on a farm exerted against asthma was much stronger in children with the G allele [adjusted OR = 0.14 (0.05 to 0.39)] as compared to those with the T allele [OR = 0.73 (0.66 to 0.80); *P* for interaction = 0.030]. The rs2230926 SNP causes a mutation in the functional DUB domain in A20 and has been linked to several autoimmune disorders, such as systemic lupus erythematosus (*24*, *25*). The intronic SNP rs610604 was unrelated to the health outcomes.

The hygiene hypothesis states that the rise in allergy and asthma that has been observed in affluent countries since the Second World War is caused by reduced "infectious pressure" from the Western lifestyle environment (*26*). The mechanism behind this association has been linked to an imbalance in the immune system, favoring pathogenic T_H2 immunity (*27*, *28*) in the absence of counterbalancing T_H1 immunity, natural killer T cells, or regulatory T cells that are often induced by infections (*26*, *29*). We have provided evidence that environmental protective factors can also influence the threshold for allergen recognition, by suppressing the activation of ECs and DCs via induction of the ubiquitin-modifying enzyme A20. This regulatory mechanism is also seen in the gut, where colonizing microbiota induce the expression of A20 shortly after birth, thus dampening overt

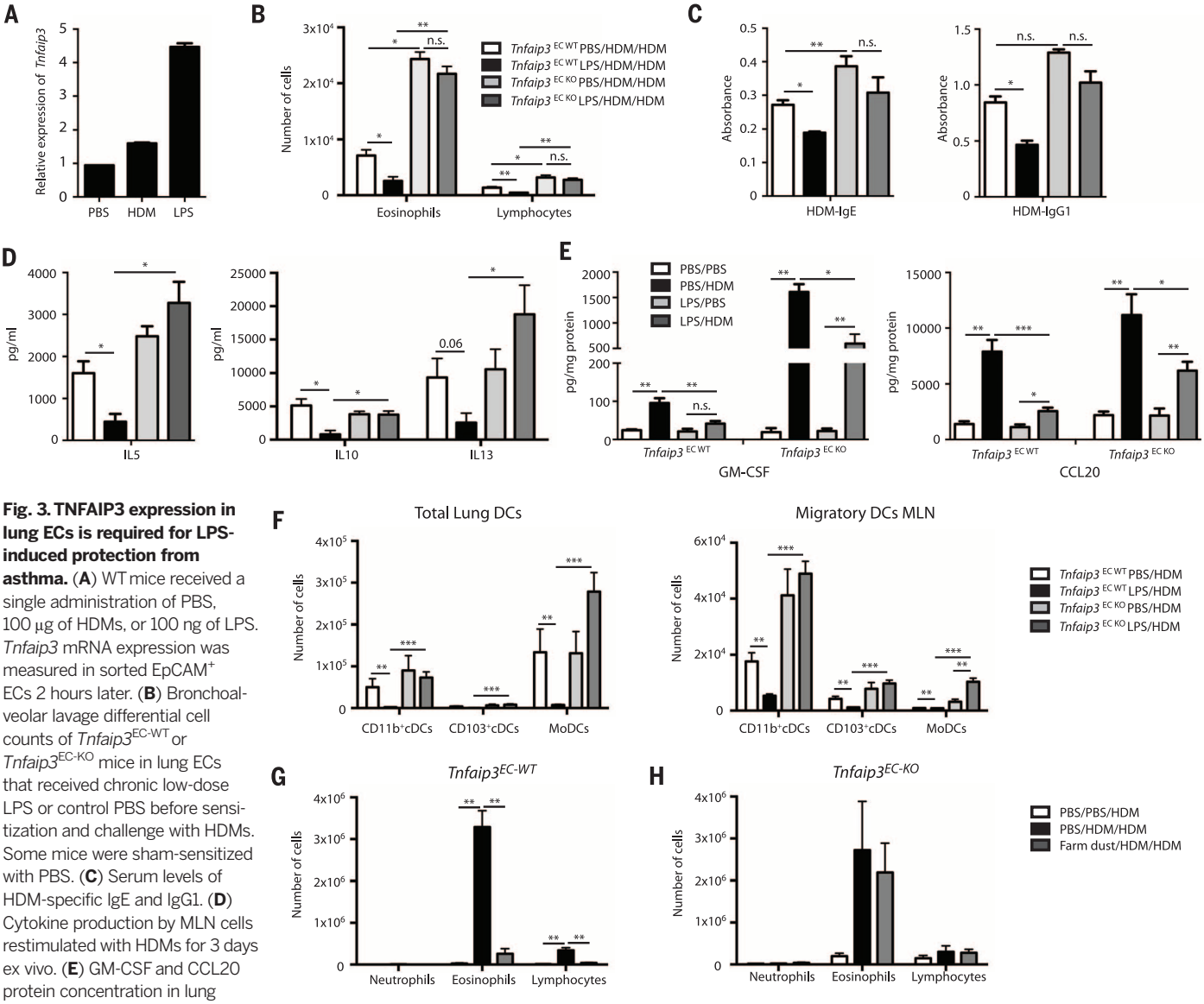


Fig. 3. TNFAIP3 expression in lung ECs is required for LPS-induced protection from asthma. (**A**) WT mice received a single administration of PBS, 100 μg of HDMs, or 100 ng of LPS. *Tnfaip3* mRNA expression was measured in sorted $EpCAM^+$ ECs 2 hours later. (**B**) Bronchoalveolar lavage differential cell counts of $Tnfaip3^{EC\text{-}WT}$ or $Tnfaip3^{EC\text{-}KO}$ mice in lung ECs that received chronic low-dose LPS or control PBS before sensitization and challenge with HDMs. Some mice were sham-sensitized with PBS. (**C**) Serum levels of HDM-specific IgE and IgG1. (**D**) Cytokine production by MLN cells restimulated with HDMs for 3 days ex vivo. (**E**) GM-CSF and CCL20 protein concentration in lung homogenates of mice preexposed to chronic LPS 14 days before a single HDM inhalation. (**F**) Mice received a chronic low dose of LPS or control PBS before sensitization to HDM extract. Some mice were sham-sensitized to PBS. Recruitment of DC subsets was measured in the lungs and draining MLNs 24 hours after the HDM extract was administered. (**G** and **H**) Bronchoalveolar lavage differential cell counts for $Tnfaip3^{EC\text{-}WT}$ (G) or $Tnfaip3^{EC\text{-}KO}$ (H) mice that received chronic low-dose farm dust or control PBS before sensitization and challenge with HDMs. Data are representative of two independent experiments with five to eight mice per group. In all panels, error bars indicate SEM. *P* values reflect the Mann-Whitney *U* test: $*P < 0.05$, $**P < 0.01$, $***P < 0.001$. n.s., not significant.

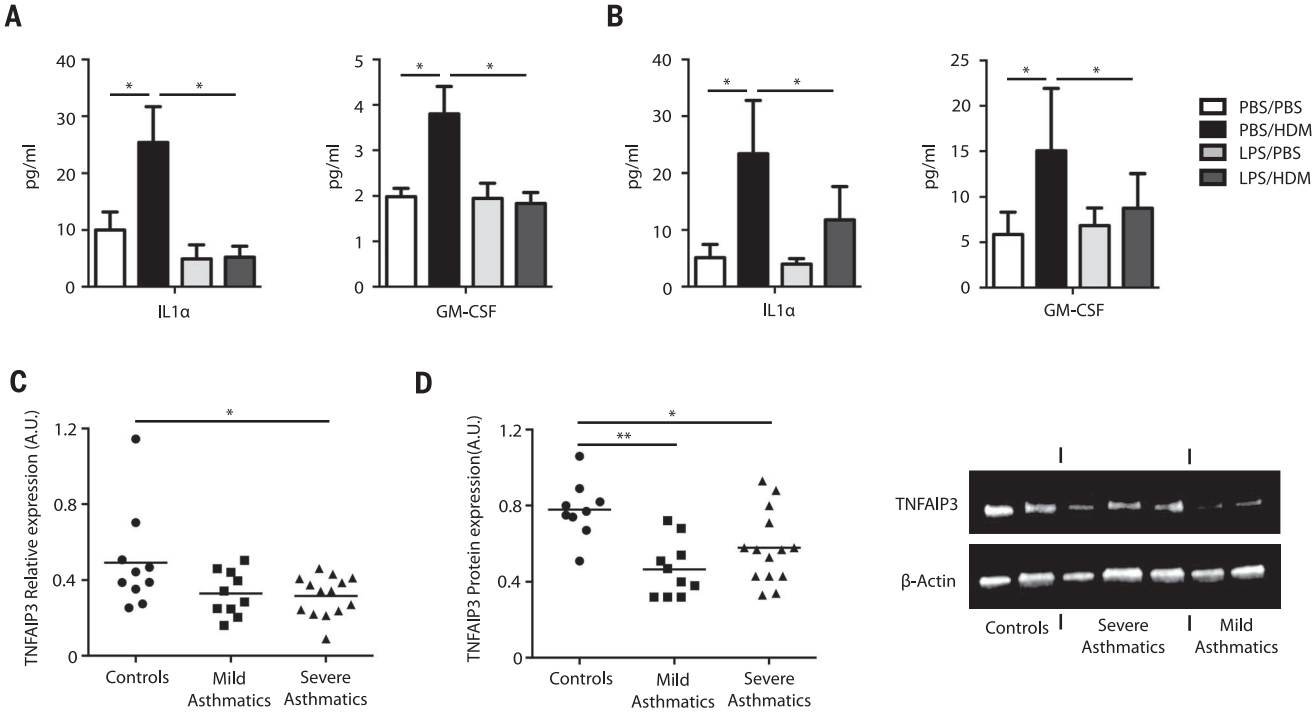


Fig. 4. Role of TNFAIP3 in human asthma. (**A**) Human IL-1α and GM-CSF concentrations were measured in ALI cultures set up from normal human bronchial ECs. Cells were exposed overnight to 100 ng of LPS or PBS. After 2 weeks, cells were stimulated with HDM extract or PBS, and cytokines were measured 24 hours later. (**B**) ALI cultures were also set up from ECs obtained by bronchial brushing of human asthmatics. These cultures were exposed to 100 ng of LPS for 1 week before stimulation with HDMs or PBS. Cytokines were measured 24 hours later. (**C** and **D**) Endobronchial biopsies were collected from healthy controls and from patients suffering from mild or severe asthma. Bronchial ECs were grown in ALI cultures, and mRNA levels of *TNFAIP3* were measured by qRT-PCR (C) and Western blot (D). A.U., arbitrary units. In (A) and (B), error bars indicate SEM. *P* values reflect the Mann-Whitney *U* test (A), the Friedman test with Dunn's post-test (B), and the Kruskall-Wallis test with Dunn's post-test [(C) and (D)]: $*P < 0.05$, $**P < 0.01$.

inflammation to commensals (*30*). Combined with the fact that a recent GWAS identified several SNPs in the TNFAIP3 interacting protein (TNIP-1) as associated with asthma, our finding that *TNFAIP3* SNPs are linked to asthma in children growing up on farms lends further support to the importance of this protective pathway (*31*, *32*). Future studies on the mechanism of the hygiene hypothesis should incorporate the effects of the environment on the activation threshold of structural cells of the airways, as they are often the drivers of innate immunity to allergens (*33*).

REFERENCES AND NOTES

1. B. N. Lambrecht, H. Hammad, *Nat. Immunol.* **16**, 45–56 (2015).
2. H. Hammad *et al.*, *Nat. Med.* **15**, 410–416 (2009).
3. J. Riedler *et al.*, *Lancet* **358**, 1129–1133 (2001).
4. M. J. Ege *et al.*, *N. Engl. J. Med.* **364**, 701–709 (2011).
5. E. von Mutius, D. Vercelli, *Nat. Rev. Immunol.* **10**, 861–868 (2010).
6. S. Illi *et al.*, *J. Allergy Clin. Immunol.* **129**, 1470–1477 (2012).
7. C. Braun-Fahrländer *et al.*, *N. Engl. J. Med.* **347**, 869–877 (2002).
8. R. P. Lauener *et al.*, *Lancet* **360**, 465–466 (2002).
9. A. Simpson *et al.*, *Am. J. Respir. Crit. Care Med.* **174**, 386–392 (2006).
10. M. J. Ege *et al.*, *J. Allergy Clin. Immunol.* **119**, 1140–1147 (2007).
11. H. Hammad *et al.*, *J. Exp. Med.* **207**, 2097–2111 (2010).
12. M. Plantinga *et al.*, *Immunity* **38**, 322–335 (2013).
13. A. T. Nathan, E. A. Peterson, J. Chakir, M. Wills-Karp, *J. Allergy Clin. Immunol.* **123**, 612–618 (2009).
14. A. Llop-Guevara *et al.*, *PLOS ONE* **9**, e88714 (2014).
15. M. A. Willart *et al.*, *J. Exp. Med.* **209**, 1505–1517 (2012).
16. J. W. McAlees *et al.*, *Mucosal Immunol.* **8**, 863–873 (2015).
17. L. Vereecke, R. Beyaert, G. van Loo, *Trends Immunol.* **30**, 383–391 (2009).
18. D. L. Boone *et al.*, *Nat. Immunol.* **5**, 1052–1060 (2004).
19. E. G. Lee *et al.*, *Science* **289**, 2350–2354 (2000).
20. L. Vereecke *et al.*, *J. Exp. Med.* **207**, 1513–1523 (2010).
21. A. K. Perl *et al.*, *Am. J. Respir. Cell Mol. Biol.* **33**, 455–462 (2005).
22. M. Peters *et al.*, *Thorax* **61**, 134–139 (2006).
23. M. J. Ege *et al.*, *J. Allergy Clin. Immunol.* **127**, 138–144 (2011).
24. S. L. Musone *et al.*, *Nat. Genet.* **40**, 1062–1064 (2008).
25. K. Kadota *et al.*, *PLOS ONE* **8**, e72551 (2013).
26. M. Yazdanbakhsh, P. G. Kremsner, R. van Ree, *Science* **296**, 490–494 (2002).
27. W. Eder, M. J. Ege, E. von Mutius, *N. Engl. J. Med.* **355**, 2226–2235 (2006).
28. N. Pearce *et al.*, *Lancet Respir Med* **1**, 96–98 (2013).
29. Y.-J. Chang *et al.*, *J. Clin. Invest.* **121**, 57–69 (2011).
30. J. Wang, Y. Ouyang, Y. Guner, H. R. Ford, A. V. Grishin, *J. Immunol.* **183**, 1384–1392 (2009).
31. X. Li *et al.*, *J. Allergy Clin. Immunol.* **130**, 861–868 (2012).
32. K. El Bakkouri, A. Wullaert, M. Haegman, K. Heyninck, R. Beyaert, *J. Biol. Chem.* **280**, 17938–17944 (2005).
33. H. Hammad, B. N. Lambrecht, *Immunity* **43**, 29–40 (2015).

ACKNOWLEDGMENTS

The data reported in this manuscript are tabulated in the main paper and in the supplementary materials. M.J.E. and E.v.M have filed patent applications (EP000002361632B1, EP000001964570B1, and US020080305089A1) that relate to identifying microorganisms and derived substances in farm dust that induce protection from several inflammatory diseases. This research was supported by European Union FP7 grant "MedALL" (Mechanisms in Development of Allergy) and by a European Union Innovative Medicines Initiative grant "EUBIOPRED." H.H. and B.N.L. are recipients of several Flanders Organization for Scientific Research (FWO) program grants. B.N.L. is a recipient of a European Research Council Consolidator grant and a Ghent University Multidisciplinary Research Platform grant (Group-ID). D.G. and P.C. are supported by grants from ARARD, Fonds de Recherche en Santé Respiratoire, and ANR "Mucocil." Population analyses were supported by two European Union research grants (GABRIEL: LSHB-CT-2006-018996, HERA: ERC2009-AdG_20090506_250268). E.v.M is supported by a Gottfried-Wilhelm-Leibniz award from the German Research Council. M.J.E. and E.v.M. are members of the German Center for Lung Research (DZL).

SUPPLEMENTARY MATERIALS

www.sciencemag.org/content/349/6252/1106/suppl/DC1
Materials and Methods
Figs. S1 to S5
Tables S1 and S2

27 May 2015; accepted 27 July 2015
10.1126/science.aac6623

MEMBRANE FUSION

A direct role for the Sec1/Munc18-family protein Vps33 as a template for SNARE assembly

Richard W. Baker,[1] Philip D. Jeffrey,[1] Michael Zick,[2] Ben P. Phillips,[1]* William T. Wickner,[2] Frederick M. Hughson[1]†

Fusion of intracellular transport vesicles requires soluble *N*-ethylmaleimide–sensitive factor attachment protein receptors (SNAREs) and Sec1/Munc18-family (SM) proteins. Membrane-bridging SNARE complexes are critical for fusion, but their spontaneous assembly is inefficient and may require SM proteins in vivo. We report x-ray structures of Vps33, the SM subunit of the yeast homotypic fusion and vacuole protein–sorting (HOPS) complex, bound to two individual SNAREs. The two SNAREs, one from each membrane, are held in the correct orientation and register for subsequent complex assembly. Vps33 and potentially other SM proteins could thus act as templates for generating partially zipped SNARE assembly intermediates. HOPS was essential to mediate SNARE complex assembly at physiological SNARE concentrations. Thus, Vps33 appears to catalyze SNARE complex assembly through specific SNARE motif recognition.

Soluble *N*-ethylmaleimide–sensitive factor attachment protein receptor (SNARE) proteins are essential for intracellular membrane fusion (*1*). They contain a 60- to 70-residue SNARE motif capable of assembling with three other SNARE motifs to form a parallel four-helical bundle (fig. S1). Most SNAREs also contain a C-terminal transmembrane anchor adjacent to their SNARE motif. The assembly of "trans" SNARE complexes—those that include SNAREs anchored in two apposed membranes—brings the C-terminal anchors into close proximity and promotes membrane fusion. In addition to their C-terminal anchors and adjacent SNARE motifs, many SNAREs contain N-terminal domains that regulate SNARE assembly and/or recruit additional proteins to the sites of membrane fusion (Fig. 1A).

SNAREs are classified by their position within the four-helix bundle and the residue that they contribute to the so-called "zero layer" at the bundle's midpoint (fig. S1) (*2*). R-SNAREs contribute an arginine to the zero layer, whereas Qa-, Qb-, and Qc-SNAREs each contribute glutamines. Polar interactions among the four zero-layer residues within the otherwise hydrophobic core of the four-helix bundle ensure that the SNAREs assemble in the proper register (fig. S1).

Membrane fusion also requires Rab guanosine triphosphatases (GTPases), tethering factors, and Sec1/Munc18 (SM) proteins. SM proteins interact with individual SNARE motifs as well as with partial (Qabc) and complete (RQabc) SNARE complexes, suggesting that they participate in SNARE complex assembly (*3*–*6*). Yet paradoxically, the first structure of a SM-SNARE complex revealed the SM protein bound to an auto-inhibited conformation of a Qa-SNARE (Fig. 1E) (*7*, *8*). Without other structures containing a SM protein and SNARE motifs, the question of how—or even whether—SM proteins promote SNARE assembly remains unresolved.

[1]Department of Molecular Biology, Princeton University, Princeton, NJ 08544, USA. [2]Department of Biochemistry, Geisel School of Medicine at Dartmouth, Hanover, NH 03755, USA.
*Present address: Medical Research Council (MRC) Laboratory of Molecular Biology, Francis Crick Avenue, Cambridge Biomedical Campus, Cambridge CB2 0QH, UK. †Corresponding author.
E-mail: hughson@princeton.edu

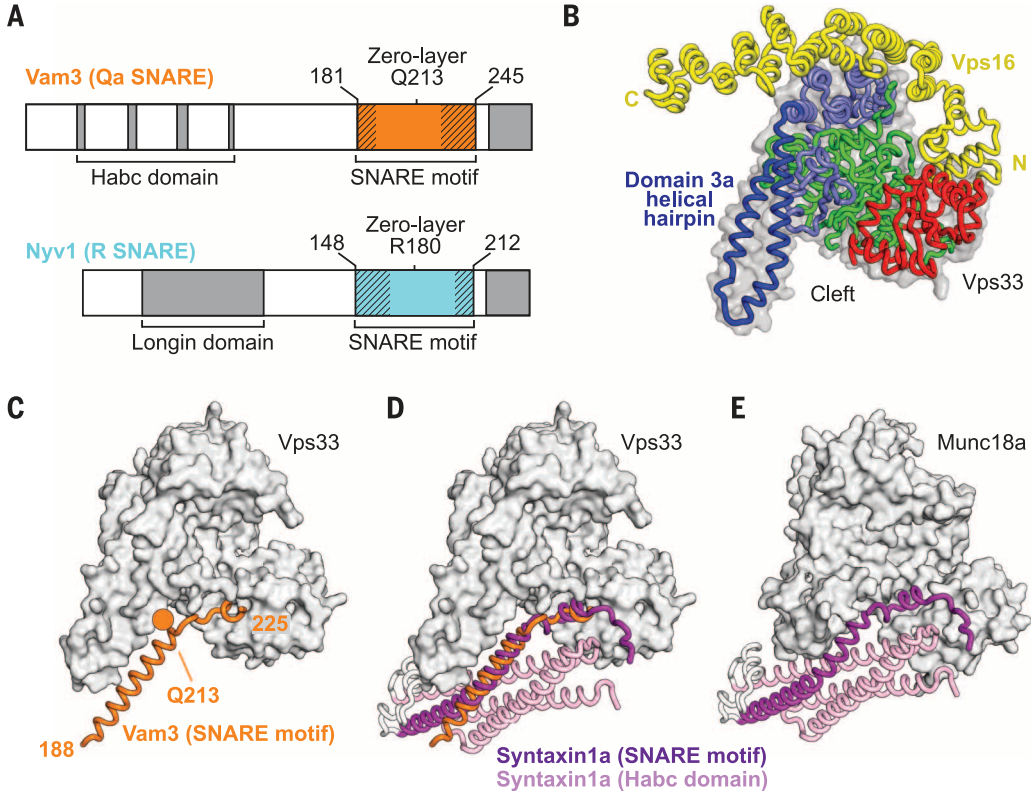


Fig. 1. Structure of the Qa-SNARE Vam3 bound to the SM protein Vps33. (**A**) *C. thermophilum* SNAREs whose SNARE motifs were cocrystallized with Vps33–Vps16. Cross-hatching indicates regions that were disordered in the resulting crystal structures (Fig. 2). TMD, transmembrane domain. Single-letter abbreviations for the amino acid residues are as follows: A, Ala; C, Cys; D, Asp; E, Glu; F, Phe; G, Gly; H, His; I, Ile; K, Lys; L, Leu; M, Met; N, Asn; P, Pro; Q, Gln; R, Arg; S, Ser; T, Thr; V, Val; W, Trp; and Y, Tyr. (**B**) Vps33–Vps16 crystal structure, highlighting domains 1 (red), 2 (green), and 3 (blue). (**C**) Complex containing the Vam3 SNARE motif (fig. S2). The zero-layer Q is highlighted. Vps16 is present in this structure but is omitted for clarity. (**D** and **E**) Comparison between Vps33–Vam3 and Munc18a–syntaxin1a (PDB code 3C98) complexes (fig. S4).

Downloaded from www.sciencemag.org on September 5, 2015

The SM protein Vps33 is a stable subunit of the heterohexameric homotypic fusion and vacuole protein-sorting (HOPS) complex, a tethering factor required for the fusion of yeast vacuoles (*9*). Vps33 binds to the SNARE motifs of two vacuolar SNAREs, the R-SNARE Nyv1 and the Qa-SNARE Vam3, as well as to the complete vacuolar SNARE complex (*4*, *5*, *10*). We generated x-ray structures of Vps33 bound to the SNARE motifs of Nyv1 and Vam3 (figs. S2 and S3, table S1). Both structures also contained a second HOPS subunit, Vps16 (Fig. 1B) (*11*–*13*). All proteins were from the thermophilic fungus *Chaetomium thermophilum*.

The SNARE motif of the Qa-SNARE Vam3 binds within the cleft formed by the arch-shaped Vps33 (Fig. 1C and fig. S2). The well-ordered portion of Vam3 closely resembles the corresponding region of the autoinhibited Qa-SNARE syntaxin1a bound to the SM protein Munc18a (Fig. 1, D and E, and figs. S2 and S4) (*7*, *8*, *14*). The SNARE motif of the R-SNARE Nyv1 binds in a nonoverlapping site, outside the cleft, on Vps33 (Fig. 2A and fig. S3). It fills the entire length of the groove formed between the antiparallel α-helices of the domain 3a helical hairpin (Fig. 1B). The Nyv1-binding groove represents the largest conserved region on the surface of Vps33; moreover, an analogous highly conserved groove is observed on the surface of Munc18 (Fig. 2B). The two ordered regions of Nyv1 are separated by a short region for which well-defined electron density is lacking; this region flanks the zero-layer arginine, R180. Nyv1 appears to be anchored in position by the layer +6 core residue, F201 (fig. S1), whose aromatic side chain inserts into a conserved hydrophobic pocket (Fig. 2A, inset). F201 itself is also widely conserved (as either phenylalanine or tyrosine) among R-SNAREs.

Vam3 and Nyv1 SNARE motifs can bind to Vps33 simultaneously (Fig. 2C and fig. S5). Overlaying the corresponding structures revealed a striking resemblance to a half-zippered SNARE complex (Fig. 2D). Vam3 and Nyv1 bind to Vps33 in the same orientation (N-to-C) and with approximately the same register—that is, with their zero-layer residues in close proximity. This complex may represent an intermediate that links apposed membranes via the templated folding of two complementary SNAREs on the surface of the SM protein Vps33.

Single-residue substitutions along the length of the Nyv1-binding groove (Fig. 2A) reduced binding of Nyv1 (fig. S6). Conversely, deleting the C-terminal region of Nyv1, or substituting the conserved residue F201 with alanine, reduced binding to Vps33 (fig S7). We also prepared an internal deletion mutant, Vps33(Δ337-359), which removed the region that interacts with the N-terminal portions of both the Nyv1 and Vam3 SNARE motifs (Fig. 2A and fig. S6B). This mutant was stably folded, bound Vps16, and was incorporated

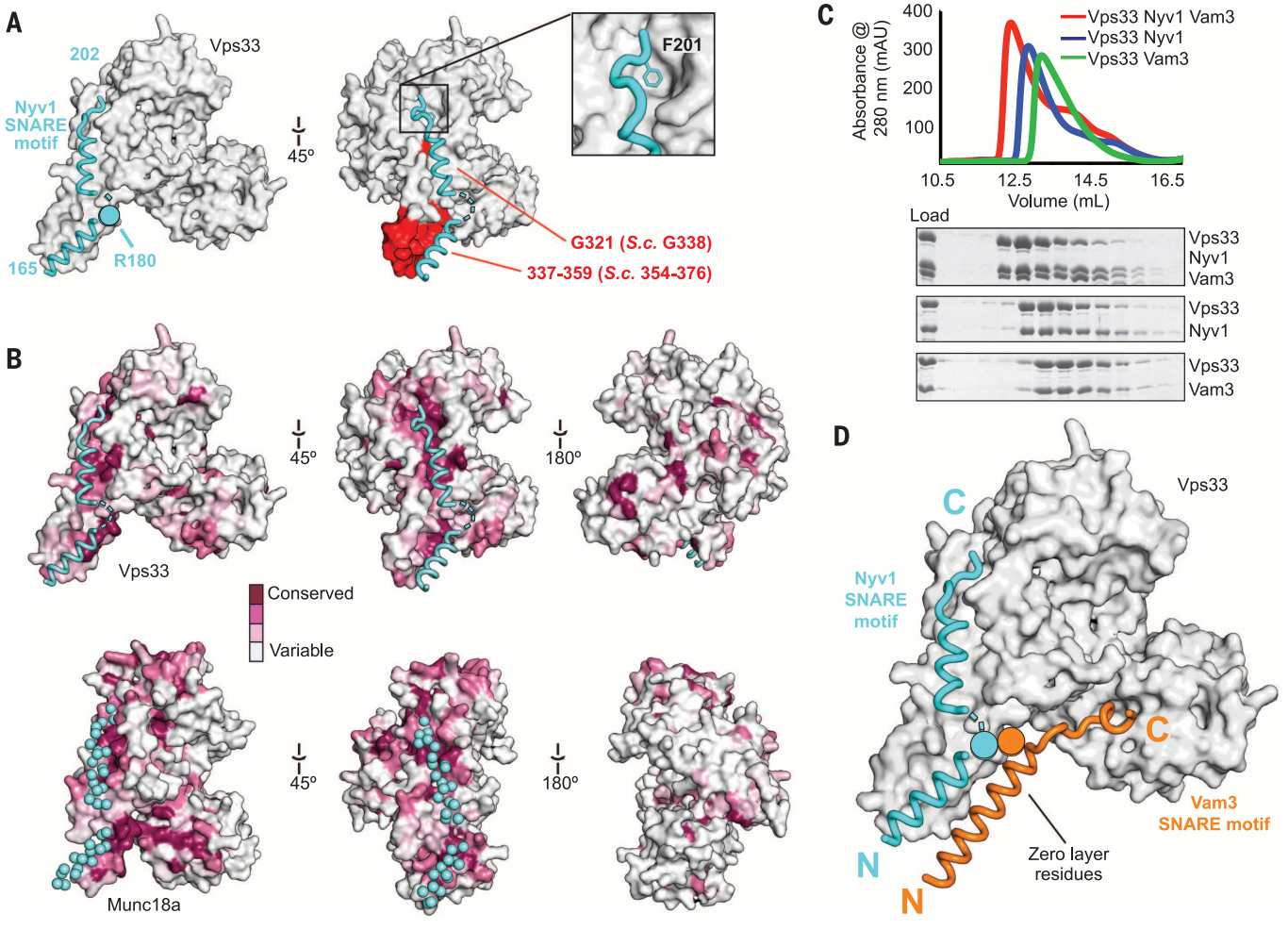


Fig. 2. Binding to a conserved surface groove on Vps33 orients and aligns the R-SNARE Nyv1 for assembly. (**A**) Vps33–Nyv1 crystal structure [Vps16 omitted for clarity (fig. S3)]. Red indicates mutations used in Fig. 3. (**B**) The Nyv1 binding site is conserved [as calculated with ConSurf (*30*)] among Vps33 homologs. The same site, indicated with light blue spheres, is conserved among Munc18 homologs (shown is 3PUJ). (**C**) Vps33, Nyv1, and Vam3 form a ternary complex as judged by means of size exclusion chromatography. Nyv1 and Vam3 SNARE motifs contain an N-terminal maltose-binding protein tag. (**D**) Model showing both SNARE domains binding simultaneously to Vps33.

into HOPS complexes but did not bind to either Nyv1 or Vam3 (fig. S6, K and L).

Next, we used *Saccharomyces cerevisiae* to examine the functional relevance of interactions between Vps33 and the Nyv1/Vam3 SNARE motifs in vivo. Wild-type yeast has one to three large vacuoles per cell (*15*). We examined two Vps33 mutants (Fig. 2A), one that selectively destabilized binding to Nyv1 (G338E, in which Gly at position 338 was replaced with Glu) and one that displayed little or no binding to either Nyv1 or Vam3 (Δ354-376) (fig. S6). Vps33 (G338E) cells often displayed 5 to 20 vacuoles per cell (Fig. 3A and fig. S8), whereas Vps33 (Δ354-376) cells resembled Δvps33 cells in having

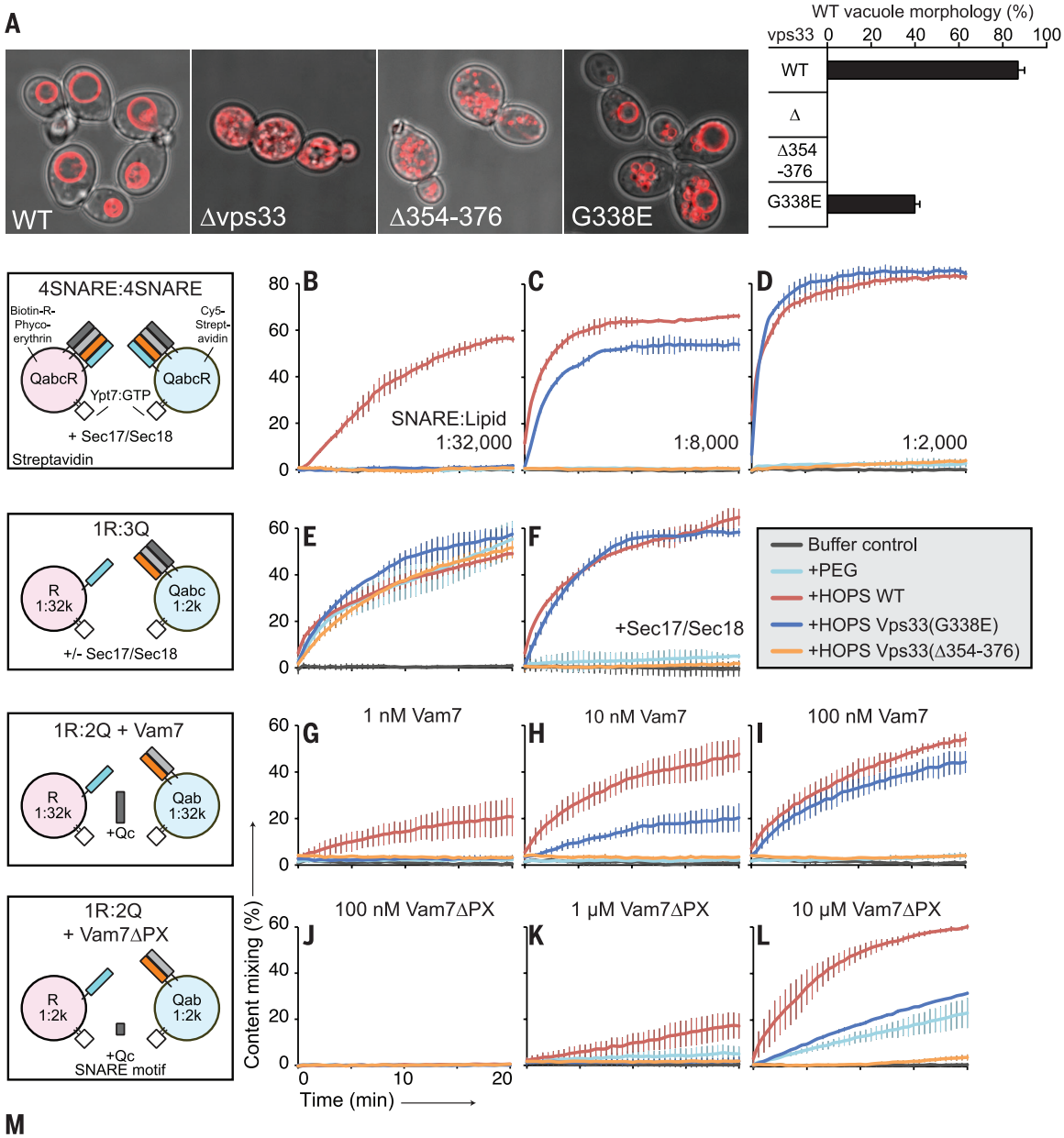


Fig. 3. Functional consequences of disrupting R-SNARE binding. (**A**) Yeast vacuolar morphology as visualized by means of FM4-64 staining (fig. S8). Cells containing one to three vacuoles were classified as having wild-type morphology. All error bars in this figure represent mean ± SD for three independent experiments. (**B** to **L**) In vitro fusion assay by use of purified HOPS containing wild-type or mutant Vps33. Proteoliposomes show an increase in FRET signal upon fusion and mixing of their luminal contents. Control experiments use PEG as an artificial tethering factor. In (B) to (D), Vps33(G338E) HOPS is fusion-deficient at low SNARE concentrations. In (E) and (F), wild-type and mutant HOPS support membrane tethering. In (G) to (L), Vps33(G338E) HOPS is compromised in recruiting [(G) to (I)] full-length Vam7 and [(J) to (L)] Vam7ΔPX into fusogenic trans-SNARE complexes. (**M**) Model showing the Vps33-templated initiation of trans-SNARE complex assembly. Numbers refer to SNARE complex core layers (fig. S1). The remaining subunits of the HOPS complex, as well as Ypt7, are omitted for clarity. Further experiments are needed to clarify whether the fully zippered SNAREs remain associated with HOPS.

no discernible vacuolar structures. Thus, both the Vps33–R-SNARE interaction and the helical hairpin of domain 3a are important for vacuolar fusion.

To substantiate that Vps33 guides SNARE complex assembly, we purified *S. cerevisiae* Vps33 (G338E)– and Vps33(Δ354-376)–containing HOPS for use in in vitro fusion reactions (*16*). Briefly, this assay uses proteoliposomes of defined lipid and protein composition, with a lumenally deposited FRET pair separated in different liposome populations; upon fusion, lumenal contents are mixed, and an increase in FRET signal is observed. To recapitulate the conditions present on vacuoles, we first analyzed proteoliposomes bearing the Rab protein Ypt7 and all four vacuolar SNAREs (R, Qa, Qb, and Qc). Fusion of these proteoliposomes requires (in addition to HOPS) that the SNAREs be liberated from "cis" complexes by the disassembly activity of Sec17/Sec18. At low SNARE:lipid ratios (1:32,000), wild-type HOPS supported membrane fusion, whereas neither of the mutant HOPS complexes did (Fig. 3B). The defect manifested by Vps33(G338E) HOPS was fully rescued at unphysiologically high (1:2000) SNARE:lipid ratios (Fig. 3D). The increased importance of Vps33–R-SNARE binding when SNARE concentrations are limiting supports a key role for this interaction in promoting SNARE assembly.

Before trans-SNARE complex assembly, membranes are tethered by large complexes such as HOPS (*17*). To test whether the deficiency of mutant HOPS in supporting membrane fusion stems from a tethering defect, we used proteoliposomes bearing either the R-SNARE or the preassembled Qabc-SNARE complex. Under this specific condition, with high Qabc-SNARE concentrations to drive spontaneous SNARE complex formation, fusion can be achieved even with a nonspecific tethering agent such as polyethylene glycol (PEG) (*18*). Mutant HOPS complexes were as effective as wild-type HOPS in stimulating this reaction, establishing that they support membrane tethering (Fig. 3E). Addition of Sec17/Sec18 under these conditions did not disrupt reactions containing wild-type or Vps33(G338E) HOPS but rendered Vps33(Δ354-376) HOPS unable to support fusion (Fig. 3F). This suggests that the distal portion of Vps33 domain 3a may help protect trans-SNARE complexes from premature disassembly by Sec17/Sec18 (*19*).

HOPS recruits the Qc-SNARE Vam7, which naturally lacks a transmembrane anchor, into fusogenic trans-SNARE complexes (*18*). The direct affinity of HOPS for Vam7's PX domain (*4*, *5*, *20*) likely contributes to this recruitment, but Vps33 might also assist by presenting a partially assembled SNARE complex. To test this idea, we performed fusion reactions in which Vam7 recruitment is rate-limiting—that is, in which the Qabc-SNARE complex is not preassembled (*18*). At low nanomolar concentrations of full-length Vam7, the fusion activity of mutant HOPS was greatly reduced relative to that of wild type (Fig. 3G), although higher Vam7 concentrations rescued the defect caused by Vps33(G338E) (Fig. 3, H and I). When Vam7 lacking an alternative recruitment mechanism (Vam7ΔPX) was used in place of the full-length protein, the mutant HOPS complexes had little activity beyond membrane tethering (Fig. 3, J to L) (*21*). Vam7ΔPX recruitment thus appears to depend on the partially zipped R-SNARE–Qa-SNARE complex presented by Vps33. Taken together, our findings support a direct role for Vps33 binding to Nyv1 (and Vam3) in promoting the assembly of fusogenic SNARE complexes.

Binding to R-SNAREs, although less studied than binding to Qa-SNAREs, is widely conserved among SM proteins (*4*, *22*, *23*). Our work highlights the role of an R-SNARE binding groove that lies outside the SM cleft and is lined by conserved residues in the domain 3a helical hairpin. Analogous conserved grooves are found in other SM proteins, including Munc18 (Fig. 2B) and Sly1 (fig. S9A), and may likewise be used for R-SNARE binding. Consistent with this idea, a mutation (L348R) in the proposed R-SNARE binding groove of Munc18a disrupted binding to the R-SNARE VAMP2 (*24*). Conversely, mutations directly flanking the VAMP2 phenylalanine residue equivalent to Nyv1 F201 (Fig. 2A) compromised Munc18-stimulated proteoliposome fusion (*25*).

Comparisons with other SM proteins also suggest that access to the R-SNARE binding site may be regulated. The first SM protein structure revealed an autoinhibited syntaxin and a bent hairpin conformation for Munc18a domain 3a (Fig. 1E and fig. S4) (*8*). The bent hairpin is incompatible with the R-SNARE binding mode observed for Vps33. Thus, "opening" of syntaxin, perhaps promoted by Munc13 (*26*), would relieve the steric blockade on R-SNARE binding. A second example is yeast Sly1, which contains an insertion that forms a "lid" over the presumptive R-SNARE binding site (fig. S9A) (*27*). A dominant gain-of-function allele (*SLY1-20*) contains a single residue substitution (E532K) (*28*) predicted to open the lid (*27*), exposing the R-SNARE binding site beneath. Other lid mutations, including the deletion of an entire α-helix, display the same dominant phenotype, bypassing otherwise essential components of the ER–Golgi transport machinery (*29*). These components may therefore regulate fusion by controlling access to the R-SNARE binding site on the SM protein.

Our work reveals a likely early intermediate in Vps33-mediated SNARE complex assembly, with the SNARE motifs of Vam3 and Nyv1 oriented and in register for further assembly (Fig. 3M). Although the N-terminal helices of Nyv1 and Vam3 appear poised for four-helix bundle formation, they would need to move somewhat closer together and rotate around their long axes to complete the process. These adjustments may be facilitated by the flexibility of the distal portion of the domain 3a helical hairpin. Last, full zippering of the four-helix bundle, and the attendant close membrane apposition, will require dislodging the C-terminal portions of the R- and Qa-SNAREs from the SM template.

REFERENCES AND NOTES

1. T. C. Südhof, J. E. Rothman, *Science* **323**, 474–477 (2009).
2. D. Fasshauer, R. B. Sutton, A. T. Brunger, R. Jahn, *Proc. Natl. Acad. Sci. U.S.A.* **95**, 15781–15786 (1998).
3. J. Rizo, T. C. Südhof, *Annu. Rev. Cell Dev. Biol.* **28**, 279–308 (2012).
4. B. T. Lobingier, A. J. Merz, *Mol. Biol. Cell* **23**, 4611–4622 (2012).
5. L. Krämer, C. Ungermann, *Mol. Biol. Cell* **22**, 2601–2611 (2011).
6. I. Dulubova *et al*., *Proc. Natl. Acad. Sci. U.S.A.* **104**, 2697–2702 (2007).
7. P. Burkhardt, D. A. Hattendorf, W. I. Weis, D. Fasshauer, *EMBO J.* **27**, 923–933 (2008).
8. K. M. Misura, R. H. Scheller, W. I. Weis, *Nature* **404**, 355–362 (2000).
9. W. Wickner, *Annu. Rev. Cell Dev. Biol.* **26**, 115–136 (2010).
10. I. Dulubova, T. Yamaguchi, Y. Wang, T. C. Südhof, J. Rizo, *Nat. Struct. Biol.* **8**, 258–264 (2001).
11. R. W. Baker, P. D. Jeffrey, F. M. Hughson, *PLOS ONE* **8**, e67409 (2013).
12. S. C. Graham *et al*., *Proc. Natl. Acad. Sci. U.S.A.* **110**, 13345–13350 (2013).
13. C. Bröcker *et al*., *Proc. Natl. Acad. Sci. U.S.A.* **109**, 1991–1996 (2012).
14. S. H. Hu *et al*., *Proc. Natl. Acad. Sci. U.S.A.* **108**, 1040–1045 (2011).
15. L. M. Banta, J. S. Robinson, D. J. Klionsky, S. D. Emr, *J. Cell Biol.* **107**, 1369–1383 (1988).
16. P. C. Zucchi, M. Zick, *Mol. Biol. Cell* **22**, 4635–4646 (2011).
17. I. M. Yu, F. M. Hughson, *Annu. Rev. Cell Dev. Biol.* **26**, 137–156 (2010).
18. M. Zick, W. Wickner, *Mol. Biol. Cell* **24**, 3746–3753 (2013).
19. H. Xu, Y. Jun, J. Thompson, J. Yates, W. Wickner, *EMBO J.* **29**, 1948–1960 (2010).
20. C. Stroupe, K. M. Collins, R. A. Fratti, W. Wickner, *EMBO J.* **25**, 1579–1589 (2006).
21. S. M. Dennison, M. E. Bowen, A. T. Brunger, B. R. Lentz, *Biophys. J.* **90**, 1661–1675 (2006).
22. Y. Xu, L. Su, J. Rizo, *Biochemistry* **49**, 1568–1576 (2010).
23. L. N. Carpp, L. F. Ciufo, S. G. Shanks, A. Boyd, N. J. Bryant, *J. Cell Biol.* **173**, 927–936 (2006).
24. D. Parisotto *et al*., *J. Biol. Chem.* **289**, 9639–9650 (2014).
25. J. Shen, D. C. Tareste, F. Paumet, J. E. Rothman, T. J. Melia, *Cell* **128**, 183–195 (2007).
26. C. Ma, L. Su, A. B. Seven, Y. Xu, J. Rizo, *Science* **339**, 421–425 (2013).
27. A. Bracher, W. Weissenhorn, *EMBO J.* **21**, 6114–6124 (2002).
28. C. Dascher, R. Ossig, D. Gallwitz, H. D. Schmitt, *Mol. Cell. Biol.* **11**, 872–885 (1991).
29. Y. Li, H. D. Schmitt, D. Gallwitz, R. W. Peng, *FEBS Lett.* **581**, 5698–5702 (2007).
30. H. Ashkenazy, E. Erez, E. Martz, T. Pupko, N. Ben-Tal, *Nucleic Acids Res.* **38**, W529–W533 (2010).

ACKNOWLEDGMENTS

We thank H. Robinson and the staff of National Synchrotron Light Source beamline X29 for assistance with data collection and A. Merz, M. Rose, and members of our laboratories for reagents, discussion, and critical comments on the manuscript. This work was funded by NIH (GM071574 to F.M.H. and GM23377 to W.T.W.) and a predoctoral fellowship from NSF (R.W.B.). The atomic coordinates and structure factors are deposited in the Protein Data Bank with accession codes 5BV1 (Vps33/Vps16), 5BUZ (Vps33/Vps16/Vam3), and 5BV0 (Vps33/Vps16/Nyv1).

SUPPLEMENTARY MATERIALS

www.sciencemag.org/content/349/6252/1111/suppl/DC1
Materials and Methods
Figs. S1 to S9
Table S1
References (*31*–*44*)

12 June 2015; accepted 24 July 2015
10.1126/science.aac7906

RNA EDITING

RNA editing by ADAR1 prevents MDA5 sensing of endogenous dsRNA as nonself

Brian J. Liddicoat,[1,2] Robert Piskol,[3] Alistair M. Chalk,[1,2] Gokul Ramaswami,[3] Miyoko Higuchi,[4] Jochen C. Hartner,[5] Jin Billy Li,[3]* Peter H. Seeburg,[4]* Carl R. Walkley[1,2]*†

Adenosine-to-inosine (A-to-I) editing is a highly prevalent posttranscriptional modification of RNA, mediated by ADAR (adenosine deaminase acting on RNA) enzymes. In addition to RNA editing, additional functions have been proposed for ADAR1. To determine the specific role of RNA editing by ADAR1, we generated mice with an editing-deficient knock-in mutation (*Adar1*^{E861A}, where E861A denotes Glu^{861}→Ala^{861}). *Adar1*$^{E861A/E861A}$ embryos died at ~E13.5 (embryonic day 13.5), with activated interferon and double-stranded RNA (dsRNA)–sensing pathways. Genome-wide analysis of the in vivo substrates of ADAR1 identified clustered hyperediting within long dsRNA stem loops within 3′ untranslated regions of endogenous transcripts. Finally, embryonic death and phenotypes of *Adar1*$^{E861A/E861A}$ were rescued by concurrent deletion of the cytosolic sensor of dsRNA, MDA5. A-to-I editing of endogenous dsRNA is the essential function of ADAR1, preventing the activation of the cytosolic dsRNA response by endogenous transcripts.

Adenosine-to-inosine (A-to-I) editing is the most prevalent form of RNA base modification in mammals. Hundreds of thousands of A-to-I editing events have been reported in the human transcriptome (*1*–*3*). A-to-I editing is catalyzed by ADAR (adenosine deaminase acting on RNA) enzymes, which deaminate genomically encoded A-to-I in double-stranded RNA (dsRNA). A-to-I editing predominantly occurs in noncoding, repetitive elements such as inverted Alus and short interspersed nuclear elements (SINEs) (*3*, *4*). There are three mammalian ADAR proteins: ADAR1, -2, and -3. ADAR1 is widely expressed during embryonic and postnatal development and is present as a predominantly nuclear, constitutive ADAR1p110 isoform expressed in all tissues and an additional interferon (IFN)–inducible ADAR1p150 isoform that is found in both the nucleus and the cytoplasm (*5*). *Adar1*$^{-/-}$ (null for both isoforms) and *Adar1p150*$^{-/-}$ mice die in utero at E11.5 (embryonic day 11.5) to E12.5, due to failed erythropoiesis and fetal liver (FL) disintegration (*6*–*8*).

Only ADAR1 and ADAR2 demonstrate editing activity in vitro. The AMPA receptor GluA2 premRNA is edited by ADAR2 in the brain, converting a glutamine residue to an arginine in a functionally critical position (*9*). *Adar2*$^{-/-}$ mice die from seizures and were rescued by the genomic substitution of the single edited adenosine for guanosine, mimicking editing of the transcript (*10*). In contrast to this elegant single-substrate paradigm that describes the *Adar2*$^{-/-}$ phenotype, no such editing site(s) described to date have resolved the physiological requirement for ADAR1.

To directly determine the contribution of A-to-I editing to ADAR1's biological function, we generated a constitutive knock-in of an editing-deficient ADAR1 allele in mice (*Adar1*^{E861A}, where E861A denotes Glu^{861}→Ala^{861}) (Fig. 1A and fig. S1A), homologous to the human ADAR1^{E912A} allele, which is catalytically inactive in vitro (*11*) (also see supplementary materials and methods). In E12.5 whole embryos, ADAR1p110 protein was detected in *Adar1*$^{E861A/E861A}$ samples at comparable levels to *Adar1*$^{+/+}$ and *Adar1*$^{E861A/+}$ controls (Fig. 1B). Additionally, *Adar1*$^{E861A/E861A}$ embryos had elevated expression of ADAR1p150 (Fig. 1B).

Adar1$^{E861A/+}$ heterozygous mice were normal, were present at the expected Mendelian ratio, and had no discernible phenotype. No viable *Adar1*$^{E861A/E861A}$ pups were born from *Adar1*$^{E861A/+}$ intercrosses and were found to be dying at ~E13.5 (Fig. 1C). *Adar1*$^{E861A/E861A}$ yolk sacs were pale, and embryos appeared developmentally delayed compared with controls (Fig. 1D), despite being normal at E12.5 (fig. S1, D and E). At E13.5, *Adar1*$^{E861A/E861A}$ FL was smaller, with eightfold fewer viable cells (Fig. 1D and fig. S1E). We observed a failure in erythropoiesis with a severe loss of erythroblast populations (Fig. 1, E and F) and increased cell death (Fig. 1G), also apparent in other hematopoietic populations (fig. S2). Consistent with our previous analysis of the ADAR1 conditional allele (*12*), adult hematopoietic stem cells (HSCs) expressing only the catalytically inactive ADAR1 could not be maintained in vivo and were lost over time (fig. S3). The A-to-I editing activity of ADAR1 is essential for embryonic development and the maintenance of hematopoiesis in vivo.

We performed transcriptional profiling on three independent littermate *Adar1*$^{+/+}$ and *Adar1*$^{E861A/E861A}$ FLs. An absence of ADAR1 editing resulted in the up-regulation of 383 transcripts ($\log_2$FC > 2), 258 of which are IFN-stimulated genes (ISGs) (Fig. 2A and table S1). Pathway analysis revealed a profound enrichment of signatures activated after IFN treatment or viral infection (Fig. 2B and table S1). Of the 50 most differentially expressed genes, 44 were up-regulated by either type I IFN, type II IFN, or both (Fig. 2C and table S1). The derepression of ISGs was confirmed by quantitative reverse transcriptase polymerase chain reaction (qRT-PCR) (Fig. 2D). Furthermore, we demonstrated that the transcriptional response in *Adar1*$^{E861A/E861A}$ FLs closely parallels that of complete ADAR1 deficiency (*12*) (fig. S4A).

Synthetic dsRNA sequences based on endogenous RNA containing adenosine but not inosine stimulate ISGs and apoptosis in vitro by binding to MDA5 and RIG-I (*13*). We defined a gene set associated with the response to IU-dsRNA (inosine-uracil–paired dsRNA) in human cells (*13*). Gene signatures of both *Adar1*$^{E861A/E861A}$ FL and *Adar1*$^{-/-}$ HSCs were highly enriched for the IU-dsRNA response (Fig. 2E), demonstrating a species-conserved response to dsRNA that is constrained by the presence of inosine residues. Therefore, the deamination of adenosine in dsRNA by ADAR1 is necessary for suppression of the IFN response under homeostatic conditions. Furthermore, it suggested that the absence of A-to-I substitutions in endogenous dsRNA may initiate this response.

To define ADAR1-specific editing events in vivo, we analyzed A-to-I (G) mismatches within the RNA sequencing data. Across all samples, 6167 A-to-I editing sites were identified: 5540 known (*14*) and 627 previously undiscovered (Fig. 3A). Strain-specific single-nucleotide polymorphisms were excluded, and only A-to-I mismatch frequencies that differed significantly between genotypes were considered (Fig. 3B). Using these criteria, 673 A-to-I editing sites were defined (Fig. 3A). Of these, 666 sites had reduced editing in mutants, including hyperedited loci, which had no detectable editing (Fig. 3B and tables S2 and S3). This confirmed that the *Adar1*^{E861A} allele is catalytically inactive and the majority of FL A-to-I editing is ADAR1 dependent. We validated 281 of the identified A-to-I sites on independent *Adar1*$^{E861A/E861A}$ and *Adar1*$^{+/+}$ FL samples (*15*). All tested sites were confirmed as differentially edited in both FL and mouse embryonic fibroblasts (MEFs) (table S4). Sanger sequencing validated ADAR1-specific *Blcap*^{Y2C}, *Mad2l1*, *Rbbp4*, and *Klf1* editing sites from independent FL samples (Fig. 3C).

ADAR1 is required for erythropoiesis (Fig. 1, E to G). Interestingly, 40% (264 of 666) of the ADAR1-specific editing sites were within hyperedited clusters of only three genes—*Klf1*, *Oip5*, and *Optn*—which have peak or restricted expression in

[1]St. Vincent's Institute of Medical Research, Fitzroy, Victoria 3065, Australia. [2]Department of Medicine, St. Vincent's Hospital, University of Melbourne, Fitzroy, Victoria 3065, Australia. [3]Department of Genetics, Stanford University, Stanford, CA 94305, USA. [4]Department of Molecular Neurobiology, Max Planck Institute for Medical Research, 69120 Heidelberg, Germany. [5]Taconic Biosciences, 51063 Cologne, Germany.
*These authors contributed equally to this work. †Corresponding author. E-mail: cwalkley@svi.edu.au

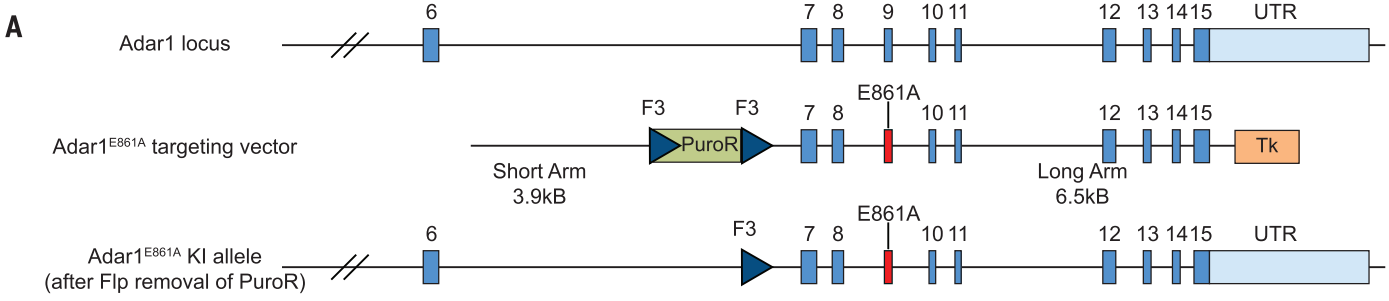
Downloaded from www.sciencemag.org on September 5, 2015

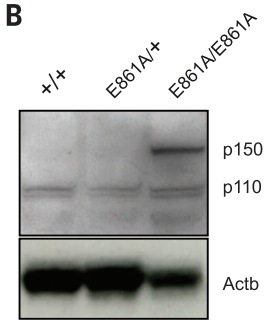
the erythroid lineage (table S3). Seventy, 61, and 133 ADAR1-specific A-to-I hyperedited loci were within long 3′ untranslated regions (3′UTRs) of *Klf1*, *Oip5*, *and Optn*, respectively. An example of hyperediting in *Klf1* is depicted in Fig. 3D. An absence of ADAR1 editing of these loci provides a possible link to the FL failure in *Adar1*$^{E861A/E861A}$ embryos.

Modeling of the predicted secondary structure of the hyperedited 3′UTRs showed that in the absence of editing there was the potential for long perfect dsRNA segments to be formed through duplexing of repetitive regions (Fig. 3E and fig. S7, A to C). The thermodynamics of inosine base pairing is not defined. Therefore, we modeled secondary structures for hyperedited substrates in two ways: (i) by predicting secondary structures of *Klf1* (Fig. 3E, left), *Optn*, and *Oip5* (fig. S7) 3′UTRs with inosine in place of adenosine, assuming no base pairing, or (ii) by replacing adenosine with guanosine (Fig. 3E, middle), assuming wobble base paring. In both cases, the predicted dsRNA structures have higher free-energy states in the presence of A-to-I or A-to-G substitutions (fig. S7, A to F). Therefore, extensive I-U mismatches would be predicted to destabilize perfect dsRNA stem loops within hyperedited 3′UTRs (Fig. 3E and fig. S7, A to F). Thus, we hypothesized that ADAR1 editing remodeled the secondary structure of endogenous RNA to abrogate the formation of long matched dsRNAs.

The transcriptional signatures in the *Adar1*$^{E861A/E861A}$ FL resembled that of RIG-I and MDA5 activation (*13*). We postulated that in the absence of ADAR1 editing, endogenous dsRNAs—such as the 3′UTRs of *Klf1*, *Oip5*, and *Optn*—could be bound by MDA5 and/or RIG-I and could activate the cellular dsRNA response. Short hairpin RNA (shRNA) knockdown of MDA5 rescued proliferation and viability (Fig. 4, A to C) and suppressed ISG induction in hematopoietic stem and progenitor cells expressing only the *Adar1*^{E861A} allele to control levels, using two independent MDA5 shRNAs (fig. S8).

Based on the in vitro rescue, we crossed *Adar1*$^{E861A/E861A}$ to MDA5$^{-/-}$ (*Ifih1*$^{-/-}$) mice. Initially we assessed embryos at E13.5, a time point when *Adar1*$^{E861A/E861A}$ embryos are no longer viable (Fig. 1C). *Adar1*$^{E861A/E861A}$*Ifih1*$^{-/-}$ double mutant yolk sac, embryo, and FL were comparable to controls and were present at the expected ratio (Fig. 4D and fig. S9A). Erythropoiesis was completely rescued, and FL ISGs were equivalent to those of control littermates (Fig. 4, E to G). Most surprisingly, viable *Adar1*$^{E861A/E861A}$*Ifih1*$^{-/-}$ mutants that survived past weaning have been identified (fig. S9B). The viable double mutants are outwardly healthy, albeit slightly smaller than littermate controls, and have not demonstrated additional phenotypes to date (Fig. 4H). The rescue of both developmental and adult viability demonstrates that MDA5 is the primary sensor

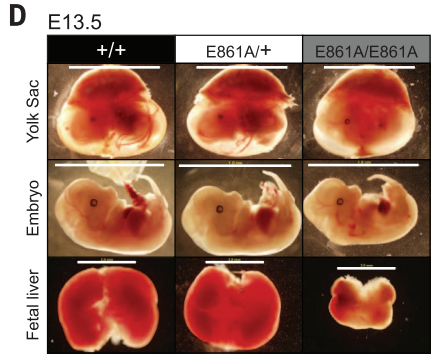


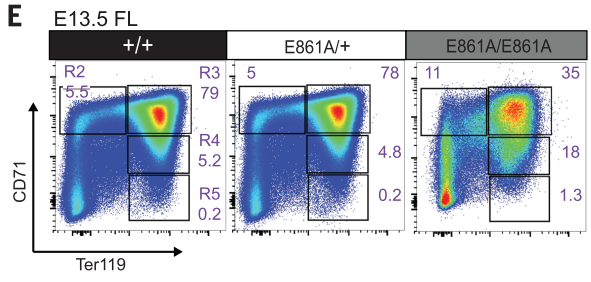


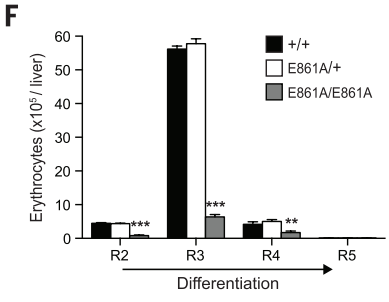
C

Adar1$^{E861A/+}$ X *Adar1*$^{E861A/+}$

Stage	Litters	+/+	E861A/+	E861A/E861A (Alive)		Expected
E10.5	1	1	7	0	-	2
E11.5	1	1	4	4	(4)	2.25
E12.5	8	12	32	21	(21)	16.25
E13.5	4	5	18	8	(3)	7.75
E14.5	2	3	11	4	(0)	4.5
P10	18	25	59	0	(0)	21







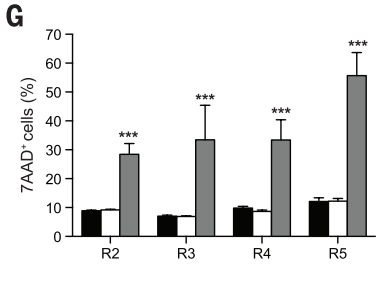


Fig. 1. *Adar1*$^{E861A/E861A}$ embryos die in utero. (**A**) Schematic of *Adar1*^{E861A} knock-in allele. (**B**) ADAR1 protein expression in whole E12.5 embryos of the indicated genotypes. (**C**) Survival data at the indicated stages. (**D**) Images of viable E13.5 yolk sacs, embryos, and FL. Scale: yolk sac and embryo, 1 cm; FL, 2 mm. Representative (**E**) fluorescence-activated cell sorting (FACS) profiles, (**F**) cell numbers, and (**G**) frequency of 7AAD$^+$ FL erythroblasts at E13.5. Results are mean ± SEM (+/+, *n* = 5 embryos; E861A/+, *n* = 18; E861A/E861A, *n* = 3). $^{**}P < 0.005$ and $^{***}P < 0.0005$ compared with *Adar1*$^{+/+}$. R2 to R5 denote erythroblast populations.

of endogenous dsRNA in the absence of ADAR1 editing.

Unlike ADAR2, the primary role of ADAR1 has not been clearly defined. Although it was assumed that RNA editing was its central function, additional RNA editing–independent roles have been proposed. The murine phenotypes and transcriptional consequences of complete ADAR1 deficiency and the specific loss of A-to-I editing are markedly similar, demonstrating that RNA editing is the primary and physiologically most important function of ADAR1. *Adar1*$^{E861A/E861A}$ embryos die ~1 to 1.5 days later than *Adar1*$^{-/-}$ embryos, suggesting limited contributions from nonediting functions of ADAR1. We believe the difference in survival is accounted for by the catalytically inactive ADAR1 retaining the ability to sequester immunogenic dsRNA (*16*). ADAR1 sequestration is not sufficient, however, to completely prevent MDA5 recognition of unedited dsRNA and subsequent signaling. Therefore, the

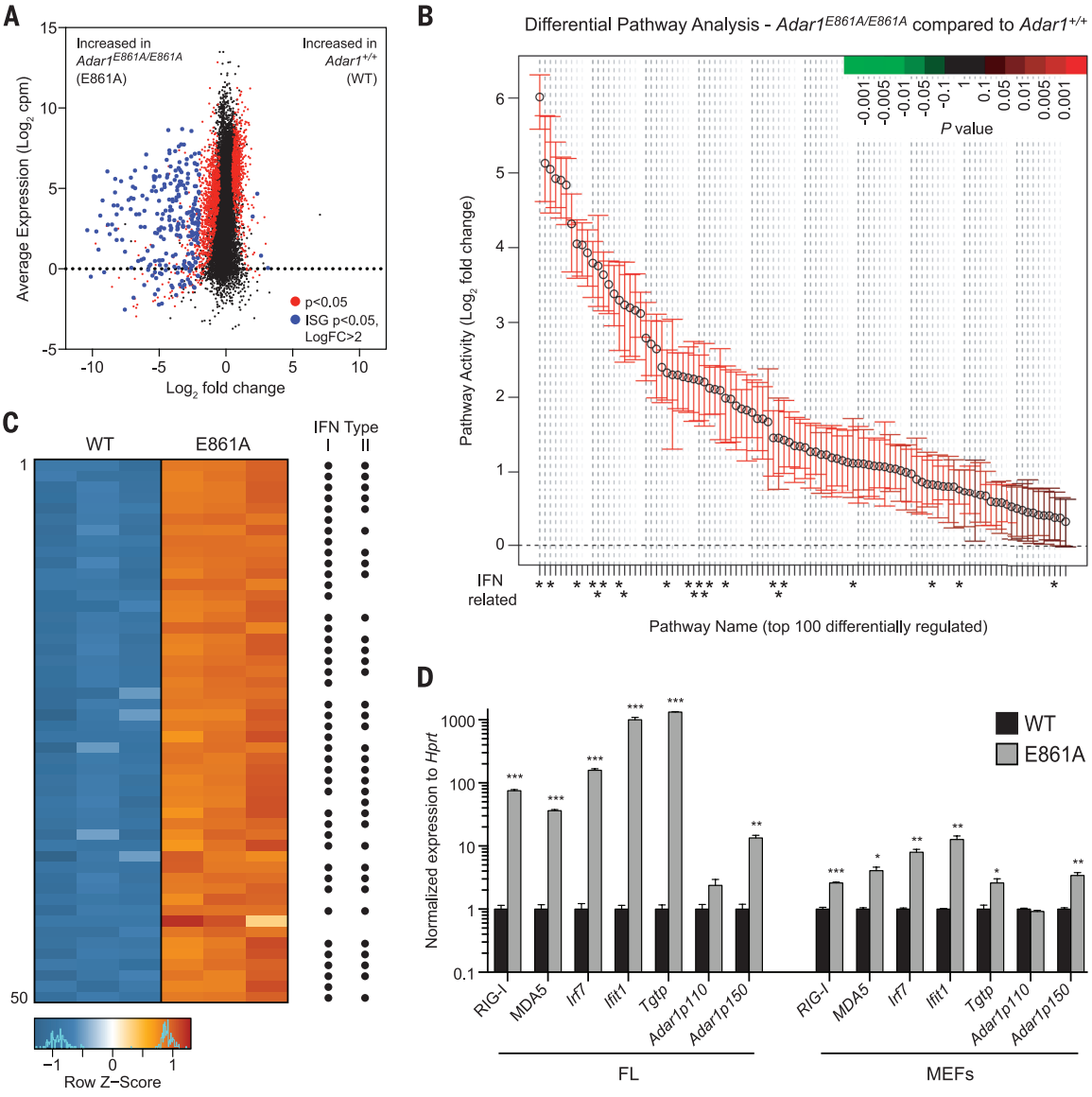


Fig. 2. Absence of editing transcriptionally phenocopies loss of ADAR1. (**A**) MA plot comparing gene expression in WT and E861A E12.5 FL. Red dots, differentially expressed genes; blue dots, differentially expressed ISGs. (**B**) QuSAGE analysis of the top 100 differential pathway signatures ranked by fold enrichment and *P* value. (**C**) Heat map of the 50 most differentially expressed genes. Black dots indicate known ISGs. (**D**) qRT-PCR of ISGs in E861A compared with controls in FL and MEFs. Results are mean ± SEM (n = 3). **P* < 0.05, ***P* < 0.005, and ****P* < 0.0005 compared with *Adar1*$^{+/+}$. (**E**) IU-dsRNA response gene set in E861A compared with WT samples (left) and *Adar1*$^{-/-}$ HSCs compared with controls (right).

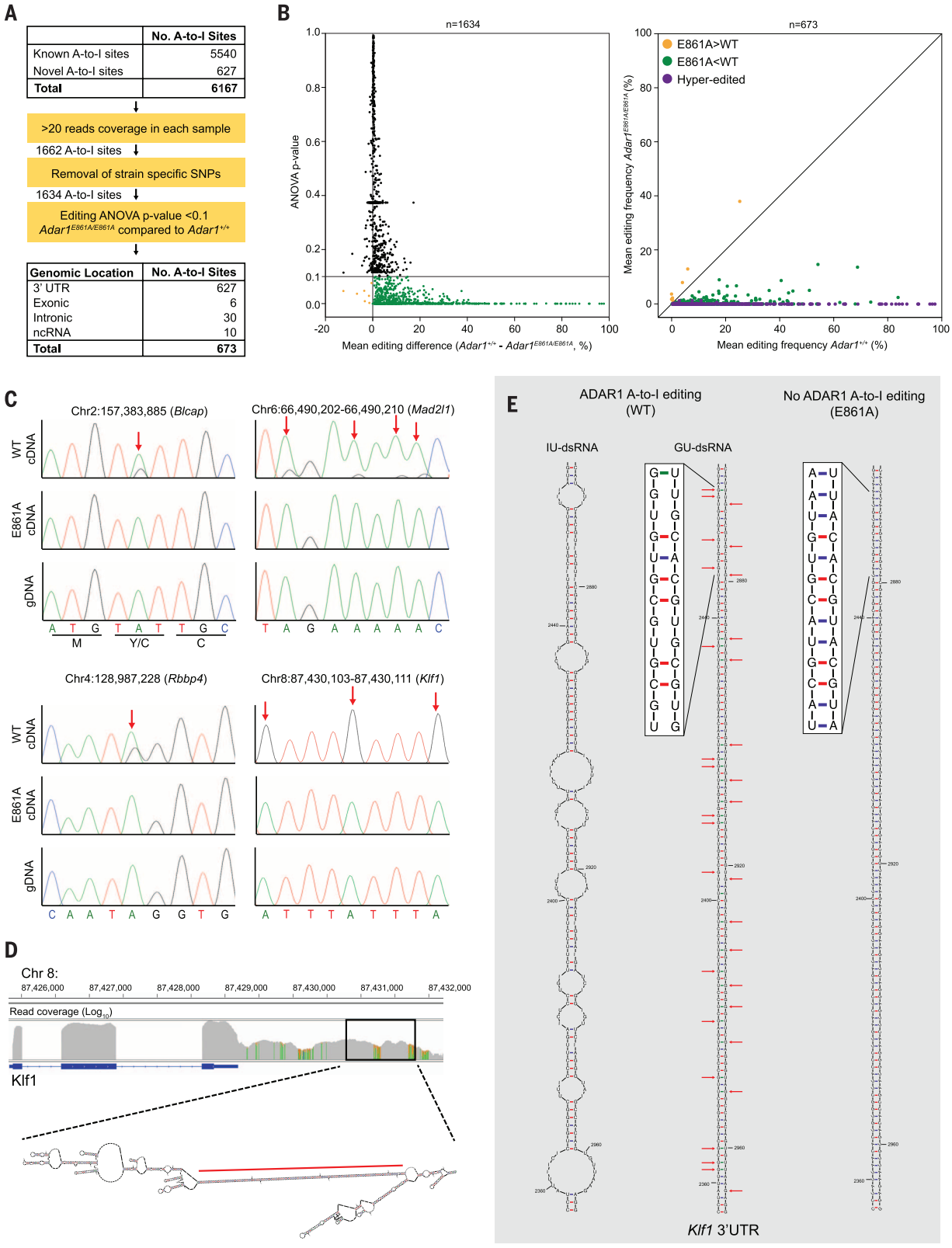


Fig. 3. Defining the ADAR1 FL editome. (**A**) Summary of A-to-I editing site analysis in FL. SNPs, single-nucleotide polymorphisms; ANOVA, analysis of variance; ncRNA, noncoding RNA. (**B**) Mean editing difference for sites with >20 reads (left, $n = 1634$). Mean editing frequency of differentially edited sites between E861A and controls (right, $n = 673$). (**C**) Genomic DNA (gDNA) (bottom) and complementary DNA (cDNA) (top and middle) Sanger sequencing validation of editing sites. Red arrows highlight edited adenosine. (**D**) Integrative Genomics Viewer image of *Klf1* in WT E12.5 FL and predicted secondary structure of 3′UTR. The red line denotes the region depicted in (E). (**E**) Predicted secondary structure of a 212–base pair dsRNA stem loop from the 3′UTR of *Klf1*, with inosine (IU-dsRNA, left) and guanosine (GU-dsRNA, middle) in place of adenosine at the edited sites. Right, predicted secondary structure with no A-to-I editing.

extended survival of the editing-deficient animals reflects a delay rather than a fundamental difference in the presentation of the same phenotype.

The data from the *Adar1*^{E861A} mutants are consistent with the type I interferonopathies of Aicardi-Goutières syndrome (AGS) patients bearing ADAR1 mutations (*17*, *18*). Editing of endogenous transcripts in ADAR1-mutant AGS patients is probably reduced, leading to retention of paired endogenous dsRNA that can be sensed by MDA5. Consistent with this, gain-of-function mutations of MDA5 have been identified in non–ADAR1-mutant AGS patients (*18*). AGS MDA5 mutations caused higher-affinity binding to self-dsRNA, resulting in the inappropriate detection of self-dsRNA (*18*). Thus, the physiological function of ADAR1 is probably conserved in mammals.

Approximately half of the mammalian genome is composed of noncoding retrotransposons such as SINEs and Alus (*19*, *20*), which typically form dsRNA duplexes. Retrotransposons are subjected to extensive A-to-I RNA editing (*3*, *4*). The location of repetitive elements may determine their immunogenicity. Retrotransposons located within introns do not persist in the cytosol and therefore cannot activate MDA5. Repetitive elements in 3′UTRs, though rare (*4*), can be retained and form duplexes, harboring the potential for recognition by MDA5. We propose that hyperediting of self-dsRNA by ADAR1 (such as the 3′UTRs of *Klf1*, *Optn*, and *Oip5*) generates multiple I-U mismatches that act to prevent MDA5 oligomerization (*21*). In the absence of ADAR1 editing, long dsRNA stem loops can form that activate MDA5 (fig. S10). However, we cannot rule out an alternate possibility that edited substrates preferentially bind MDA5 to prevent its activation by other (unidentified and nonedited) dsRNA transcripts (*13*).

Concurrent ablation of MAVS, the downstream adaptor of MDA5 and RIG-I, rescues ADAR1-null mice to birth (*22*), demonstrating a role for ADAR1 in the suppression of the RLR pathway. Our study specifically identifies the critical cytosolic sensor upstream of MAVS and demonstrates

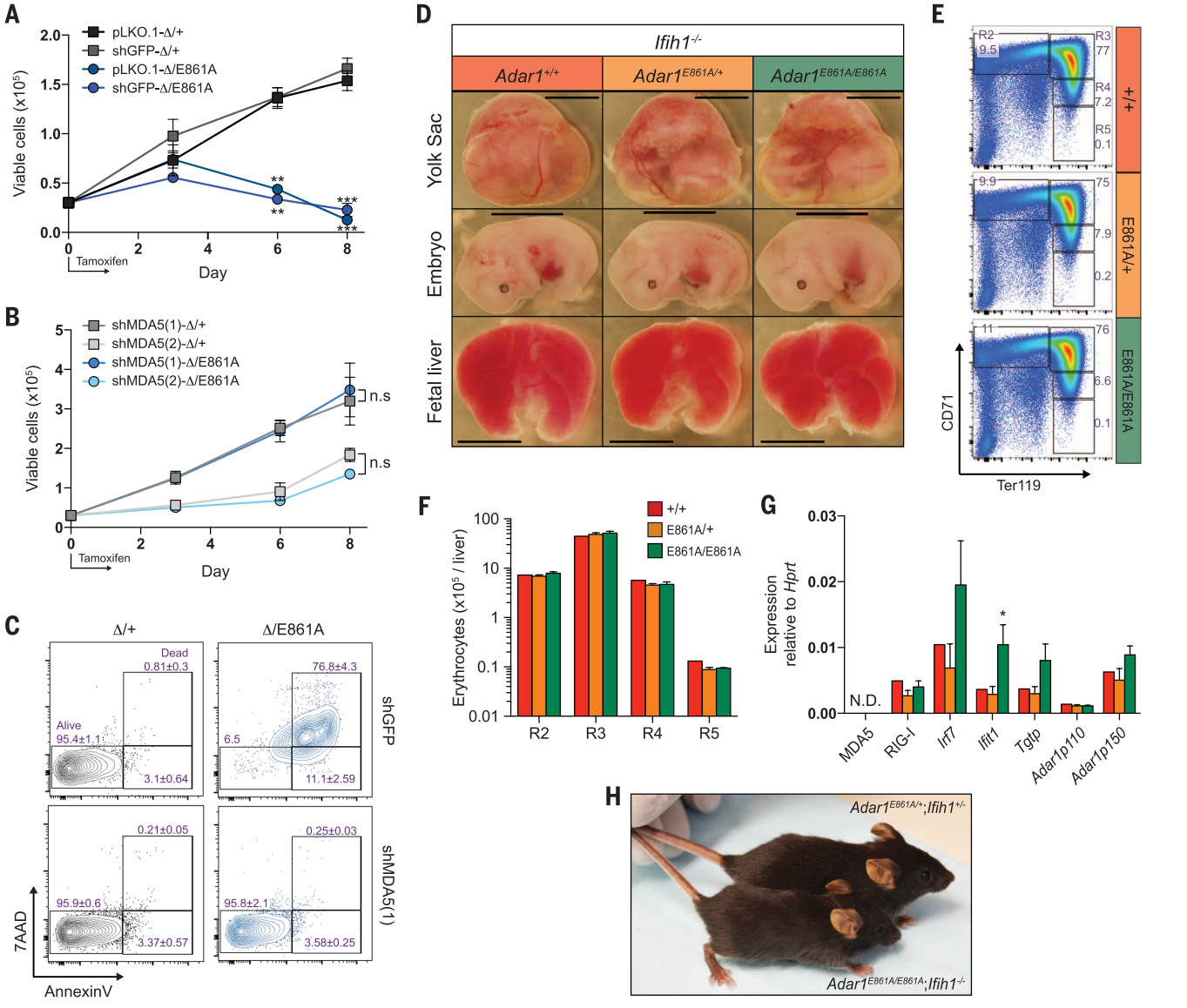


Fig. 4. Loss of MDA5 rescues *Adar1*$^{E861A/E861A}$ viability. (**A**) LKS^{+} cells isolated from *Rosa26*CreER^{T2} *Adar1*$^{fl/+}$ (Δ/+) and *Rosa26*CreER^{T2} *Adar1*$^{fl/E861A}$ (Δ/E861A) infected with pLKO.1 empty vector, shGFP, or (**B**) two independent shMDA5 [shMDA5(1) and shMDA5(2)] were cultured for 8 days. Results are mean ± SEM (n = 3). $^{**}P < 0.005$ and $^{***}P < 0.0005$ compared with Δ/+. n.s, not significant. (**C**) Analysis of apoptosis on day 8. (**D**) Images of viable E13.5 yolk sac, embryo, and FL of the indicated genotype (all *Ifih1*$^{-/-}$). Scale: yolk sac and embryo, 5 mm; FL, 1.6 mm. Representative (**E**) FACS profiles and (**F**) numbers of FL erythrocytes at E13.5. (**G**) E13.5 FL qRT-PCR of ISGs. Results are mean ± SEM (+/+, n = 2; E861A/+, n = 8; E861A/E861A, n = 4). $^{*}P < 0.05$ compared with *Adar1*$^{+/+}$*Ifih1*$^{-/-}$ controls. (**H**) Photo of an *Adar1*$^{E861A/E861A}$ *Ifih1*$^{-/-}$ mouse and an *Adar1*$^{E861A/+}$*Ifih1*$^{+/-}$ littermate at 26 days of age.

that the *Adar1*$^{E861A/E861A}$ phenotype and, by extension, *Adar1*$^{-/-}$ can be ascribed to the lack of editing of multiple substrates, resulting in the inappropriate activation of MDA5. We speculate that these unedited transcripts are sensed as nonself by MDA5 and activate innate immune signaling. ADAR1's primary physiological function is to edit endogenous dsRNA to prevent sensing of endogenous dsRNA as nonself by MDA5.

REFERENCES AND NOTES

1. P. Danecek *et al.*, *Genome Biol.* **13**, R26 (2012).
2. J. B. Li *et al.*, *Science* **324**, 1210–1213 (2009).
3. G. Ramaswami *et al.*, *Nat. Methods* **9**, 579–581 (2012).
4. Y. Neeman, E. Y. Levanon, M. F. Jantsch, E. Eisenberg, *RNA* **12**, 1802–1809 (2006).
5. J. B. Patterson, C. E. Samuel, *Mol. Cell. Biol.* **15**, 5376–5388 (1995).
6. J. C. Hartner *et al.*, *J. Biol. Chem.* **279**, 4894–4902 (2004).
7. Q. Wang *et al.*, *J. Biol. Chem.* **279**, 4952–4961 (2004).
8. S. V. Ward *et al.*, *Proc. Natl. Acad. Sci. U.S.A.* **108**, 331–336 (2011).
9. M. Higuchi *et al.*, *Cell* **75**, 1361–1370 (1993).
10. M. Higuchi *et al.*, *Nature* **406**, 78–81 (2000).
11. F. Lai, R. Drakas, K. Nishikura, *J. Biol. Chem.* **270**, 17098–17105 (1995).
12. J. C. Hartner, C. R. Walkley, J. Lu, S. H. Orkin, *Nat. Immunol.* **10**, 109–115 (2009).
13. P. Vitali, A. D. Scadden, *Nat. Struct. Mol. Biol.* **17**, 1043–1050 (2010).
14. G. Ramaswami, J. B. Li, *Nucleic Acids Res.* **42**, D109–D113 (2014).
15. R. Zhang *et al.*, *Nat. Methods* **11**, 51–54 (2014).
16. M. C. Washburn *et al.*, *Cell Reports* **6**, 599–607 (2014).
17. G. I. Rice *et al.*, *Nat. Genet.* **44**, 1243–1248 (2012).
18. G. I. Rice *et al.*, *Nat. Genet.* **46**, 503–509 (2014).
19. E. S. Lander *et al.*, *Nature* **409**, 860–921 (2001).
20. Mouse Genome Sequencing Consortium, *Nature* **420**, 520–562 (2002).
21. B. Wu *et al.*, *Cell* **152**, 276–289 (2013).
22. N. M. Mannion *et al.*, *Cell Reports* **9**, 1482–1494 (2014).

ACKNOWLEDGMENTS

We thank V. Sankaran, S. Orkin, L. Purton, and J. Heierhorst for discussion and SVH BioResources Centre for animal care. Data sets described in the paper are deposited in Gene Expression Omnibus (accession number GSE58917). This work was supported by the Leukaemia Foundation (C.R.W.), a Leukaemia Foundation Ph.D. scholarship (B.J.L), National Health and Medical Research Council (NHMRC) Project Grant 1021216, NHMRC Career Development Award 559016 (C.R.W.), a German Academic Exchange Service Postdoctoral Fellowship (R.P.), a Stanford University Dean's Fellowship (R.P.), Stanford Genome Training Program (NIH grant T32 HG000044) and Stanford Graduate Fellowship (G.R.), NIH grant R01GM102484 (J.B.L.), the Ellison Medical Foundation (J.B.L.), and the Stanford University Department of Genetics (J.B.L.). This work was also supported in part by the Victorian State Government Operational Infrastructure Support Scheme (to St. Vincent's Institute of Medical Research). C. R.W. was the Leukaemia Foundation Phillip Desbrow Senior Research Fellow. J.C.H. is an employee of Taconic Biosciences. Taconic Biosciences had no role in the preparation and content of this Report. All other authors declare no conflicts of interest. Author contributions: M.H., P.H.S., and J.C.H. generated the knock-in mouse line; B.J.L., R.P., A.M.C., G.R., J.C.H., J.B.L., and C.R.W. performed experiments and analyzed and interpreted data; M.H., P.H.S., and J.C.H. provided intellectual input and conceptual advice; and B.J.L. and C.R.W. wrote the manuscript.

SUPPLEMENTARY MATERIALS

www.sciencemag.org/content/349/6252/1115/suppl/DC1
Materials and Methods
Supplementary Text
Figs. S1 to S10
Tables S1 to S4
References (*23*–*41*)

1 June 2015; accepted 13 July 2015
Published online 23 July 2015
10.1126/science.aac7049

DNA SEGREGATION

Structures of archaeal DNA segregation machinery reveal bacterial and eukaryotic linkages

Maria A. Schumacher,[1]* Nam K. Tonthat,[1] Jeehyun Lee,[1] Fernando A. Rodriguez-Castañeda,[2] Naga Babu Chinnam,[1] Anne K. Kalliomaa-Sanford,[2] Irene W. Ng,[2] Madhuri T. Barge,[2] Porsha L. R. Shaw,[1] Daniela Barillà[2]*

Although recent studies have provided a wealth of information about archaeal biology, nothing is known about the molecular basis of DNA segregation in these organisms. Here, we unveil the machinery and assembly mechanism of the archaeal *Sulfolobus* pNOB8 partition system. This system uses three proteins: ParA; an atypical ParB adaptor; and a centromere-binding component, AspA. AspA utilizes a spreading mechanism to create a DNA superhelix onto which ParB assembles. This supercomplex links to the ParA motor, which contains a bacteria-like Walker motif. The C domain of ParB harbors structural similarity to CenpA, which dictates eukaryotic segregation. Thus, this archaeal system combines bacteria-like and eukarya-like components, which suggests the possible conservation of DNA segregation principles across the three domains of life.

DNA segregation or partition is an essential biological process ensuring faithful genomic transmission. The best-understood segregation systems at the molecular level are those used by bacterial plasmids. These simplified systems consist of a DNA centromere; ParA nucleoside triphosphatase (NTPase); and centromere-binding protein (CBP), ParB (*1*–*6*). The most common partition apparatuses use Walker-box NTPases (*7*). The segregation systems that have been identified on bacterial chromosomes also harbor Walker NTPases, although their mechanisms are less clear (*1*–*6*). In contrast to bacterial partition, eukaryotic partition is highly complex. However, the linchpin in eukaryotic segregation is the histone protein, CenpA, which is deposited in place of histone H3 at DNA centromeres and dictates assembly of the segregation machinery (*8*–*11*). Although some progress has been made in understanding DNA segregation in eukarya and bacteria, virtually nothing is known about the molecular process of segregation in archaea, the third domain of life (*12*–*14*).

To gain insight into the underpinnings of archaeal segregation, we performed a molecular dissection of the proteins encoded on the plasmid pNOB8 partition cassette harbored in *Sulfolobus* NOB8H2 (*15*). This cassette contains three open reading frames (ORFs): *orf44*, *orf45*, and *orf46*. *orf46* and *orf45* encode 315- and 470-residue proteins, respectively, which show 33 to 37% and 42 to 58% sequence similarity to bacterial ParA and ParB proteins. *orf44* generates a 93-residue protein that shows no sequence similarity to any characterized partition protein. The organization of the *orf44-parB-parA* genes (fig. S1A) is reminiscent of bacterial partition cassettes; however, the cluster is tricistronic, unlike typical bicistronic bacterial systems (*1*–*4*). Hypothesizing that the pNOB8 centromere may be located either 5′ or 3′ of the cassette as in bacteria, we analyzed pNOB8 protein binding to these regions. Unlike its bacterial counterparts, pNOB8 ParB only bound DNA nonspecifically (fig. S1B). Orf44, however, bound the upstream DNA with high affinity [apparent dissociation constant ($K_d$app) = ~50 nM] (Fig. 1A). Therefore, we named this CBP, archaeal segregation protein A (AspA). Deoxyribonuclease I (DNase I) footprinting showed that AspA interacted with a 23–base pair (bp) palindrome in the upstream region and that increasing AspA concentrations led to spreading around this site (Fig. 1B). Hence, like bacterial ParB proteins, AspA spreads nonspecifically to DNA adjacent to its centromere to form an extended "partition-complex." Although poorly characterized, higher-order partition-complexes are central to segregation, as they mediate stabilizing, dynamic interactions with ParA assemblages (*1*–*4*). Indeed, the CBP-NTPase interaction is key to the partition process. Biochemical experiments, however, showed that AspA does not bind pNOB8 ParA. Rather, ParB bound both AspA [dissociation constant (K_d = 12 μM)] and ParA (K_d = 17 μM), which indicated that it acts as an adaptor (fig. S1C). Thus, the pNOB8 partition system is composed of the CBP AspA, adaptor ParB, and ParA NTPase. This finding prompted us to perform BLAST searches for the occurrence of *aspA-parB-parA* cassettes on archaeal genomes. The results revealed that this tripartite cluster of genes is widespread across different crenarchaeal genera and is harbored on both chromosomes and plasmids (fig. S2).

[1]Department of Biochemistry, Duke University School of Medicine, 243 Nanaline H. Duke, Box 3711, Durham, NC 27710, USA. [2]Department of Biology, University of York, York YO10 5DD, UK.
*Corresponding author. E-mail: maria.schumacher@duke.edu (M.A.S.); daniela.barilla@york.ac.uk (D.B.)

The AspA structure was obtained to gain insight into its function (table S1 and fig. S3A). The structure consists of a winged helix-turn-helix module followed by a C-terminal dimerization helix. Biochemical data supported the structural analysis that AspA is dimeric (fig. S3B). The AspA fold is distinct from bacterial CBPs and shows structural similarity with the PadR family of transcription regulators, found in bacteria and archaea (*16*). Three structures were determined of AspA bound to centromere DNA sites (fig. S3C and table S1). The structures all contain multiple interacting AspA dimers bound to DNA, that, when extended, lead to the generation of the same periodically arranged left-handed protein-DNA superhelix (Fig. 1, C to E, and Fig. 2A). This superhelix bears general resemblance to the left-handed *Vibrio cholera* ParA2–adenosine triphosphate–DNA (ParA2-ATP-DNA) filament (*17*). The protein and the DNA cannot be distinguished in the low-resolution ParA2-DNA electron microscopy structure, which makes a more direct comparison difficult. However, the AspA and ParA2 protein folds and superhelices are distinct; AspA and ParA2 are PadR and Walker-box proteins, respectively; and the ParA2-ATP-DNA superhelix has a pitch of 120 Å compared with 70 Å for the AspA-DNA superhelix. The high resolution of the AspA-DNA structure allows details of binding and superhelix formation to be discerned. Specifically, the insertion of two AspA α3 recognition helices of adjacently bound AspA dimers into each expanded major groove (~13 Å compared with 11 Å for B-DNA) leads to superhelix generation. The small Ala^{53} side chain appears key in the concurrent occupation of both helices in the same major groove. Leu^{52}-Ala^{53} and Glu^{54}-Lys^{59} contacts bolster this interaction (Fig. 1C). To be capable of DNA spreading, a protein must show adaptability in DNA binding. Almost all DNA base and phosphate contacts come from two adaptable AspA elements: the N-terminal arms and glutamines from the recognition helices (fig. S3D). The AspA eight-residue N-terminal arms fold only upon DNA binding and adopt a surprising range of conformations, which allows them to insert into either the major or minor grooves, where they make base interactions, phosphate contacts, or both (Fig. 1D). Consistent with the superhelical structure, isothermal titration calorimetry (ITC) experiments revealed a stoichiometry of wild-type AspA (wtAspA) dimer to 32-oligomer duplex of 3:1. By contrast, a AspA(A53K) mutation, which replaced the small Ala^{53} side chain with a bulky residue, bound DNA with a stoichiometry of 1:1 (Fig. 2B). Further, DNase I protection revealed that AspA(A53K) was unable to spread on DNA (Fig. 2C). Thus, multiple data support the AspA-DNA superhelix structure.

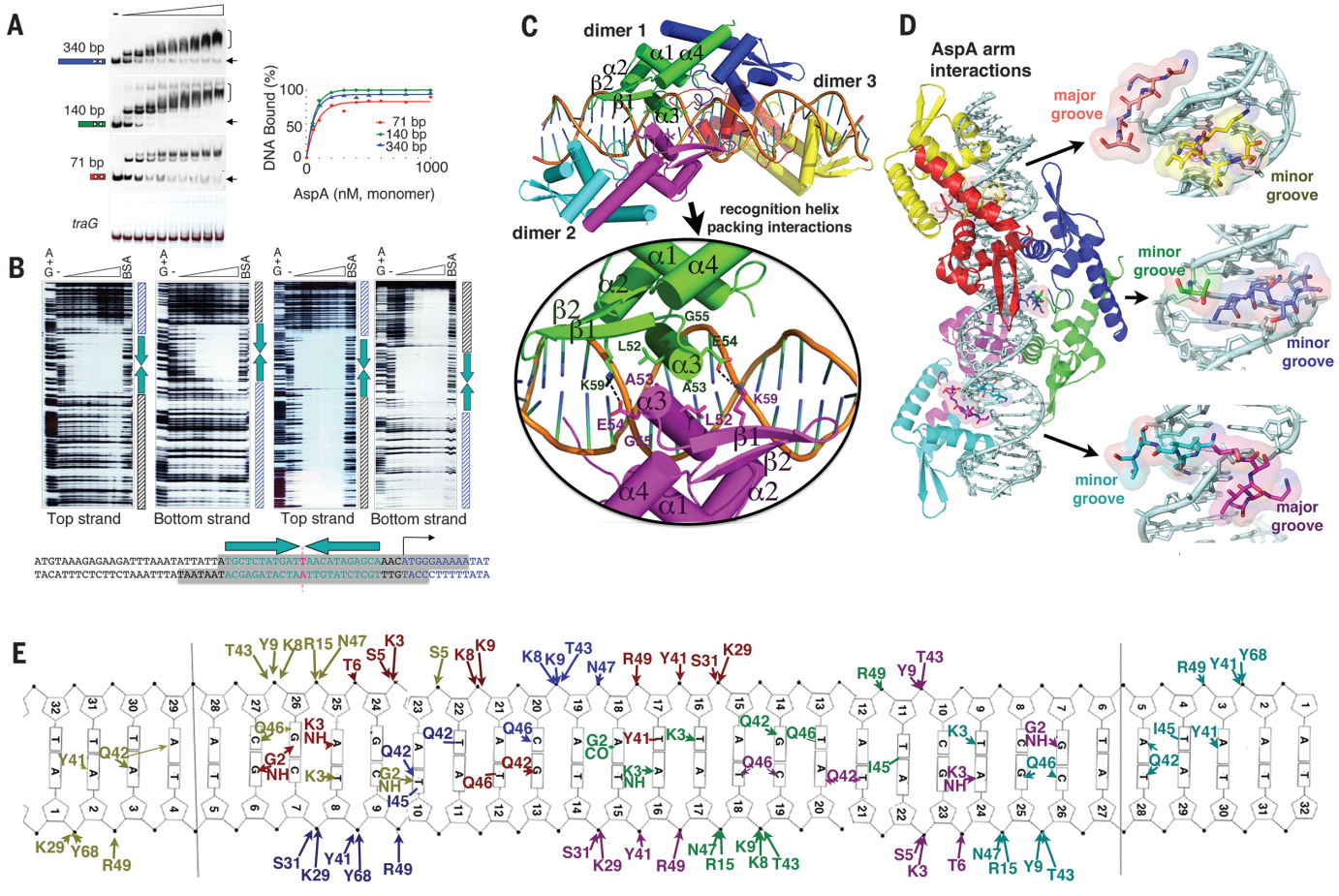


Fig. 1. Identification of pNOB8 centromere and AspA-centromere structure. (**A**) AspA (0 to 1000 nM) was incubated with three DNA fragments upstream of its gene or the pNOB8 *traG* gene and subjected to electrophoretic mobility shift assays. White triangles denote location of the palindromic centromere. Arrows, unbound DNA; brackets, high-molecular-weight AspA-DNA complexes. The percentage of bound DNA was plotted against the concentration of AspA. (**B**) DNase I footprint identifying the DNA site bound by AspA (left, 0 to 750 nM) and its ability to spread at higher concentrations (right, 0 to 3000 nM). First lane, AG ladder; last lane, bovine serum albumin control. The inverted centromere repeat is in green and the *aspA* gene in blue. Below footprints, the sequence shaded in gray indicates the extent of the AspA footprint on top and bottom strands at low-to-medium protein concentrations. (**C**) (Top) AspA–32-oligomer (AspA-32mer) structure. Three interacting AspA dimers coat the DNA, which generates a continuous superstructure. (Bottom) Close-up showing contacts between recognition helices occupying the same major groove (*31*). (**D**) AspA N-terminal arm-DNA contacts. (**E**) Schematic diagram showing AspA-centromere interactions (*31*).

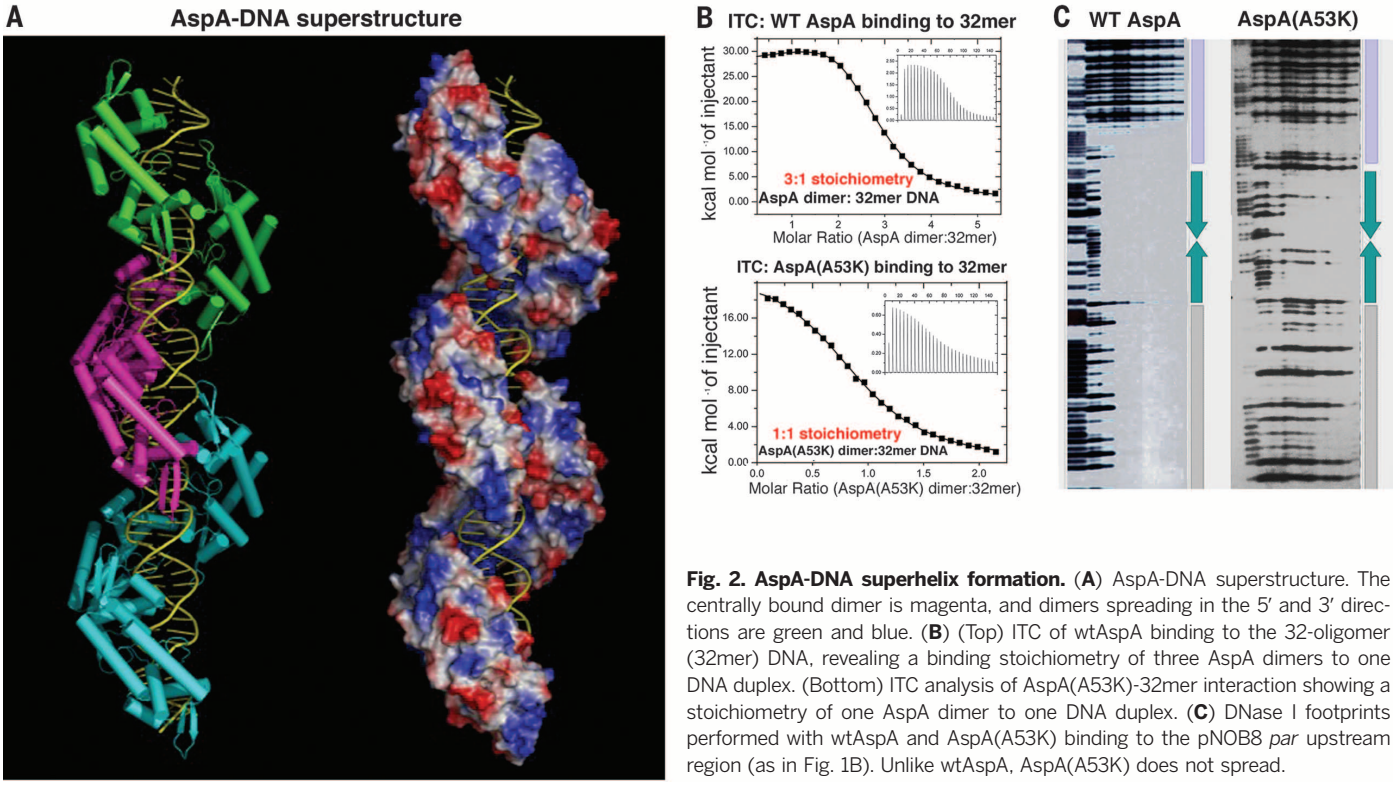


Fig. 2. AspA-DNA superhelix formation. (**A**) AspA-DNA superstructure. The centrally bound dimer is magenta, and dimers spreading in the 5′ and 3′ directions are green and blue. (**B**) (Top) ITC of wtAspA binding to the 32-oligomer (32mer) DNA, revealing a binding stoichiometry of three AspA dimers to one DNA duplex. (Bottom) ITC analysis of AspA(A53K)-32mer interaction showing a stoichiometry of one AspA dimer to one DNA duplex. (**C**) DNase I footprints performed with wtAspA and AspA(A53K) binding to the pNOB8 *par* upstream region (as in Fig. 1B). Unlike wtAspA, AspA(A53K) does not spread.

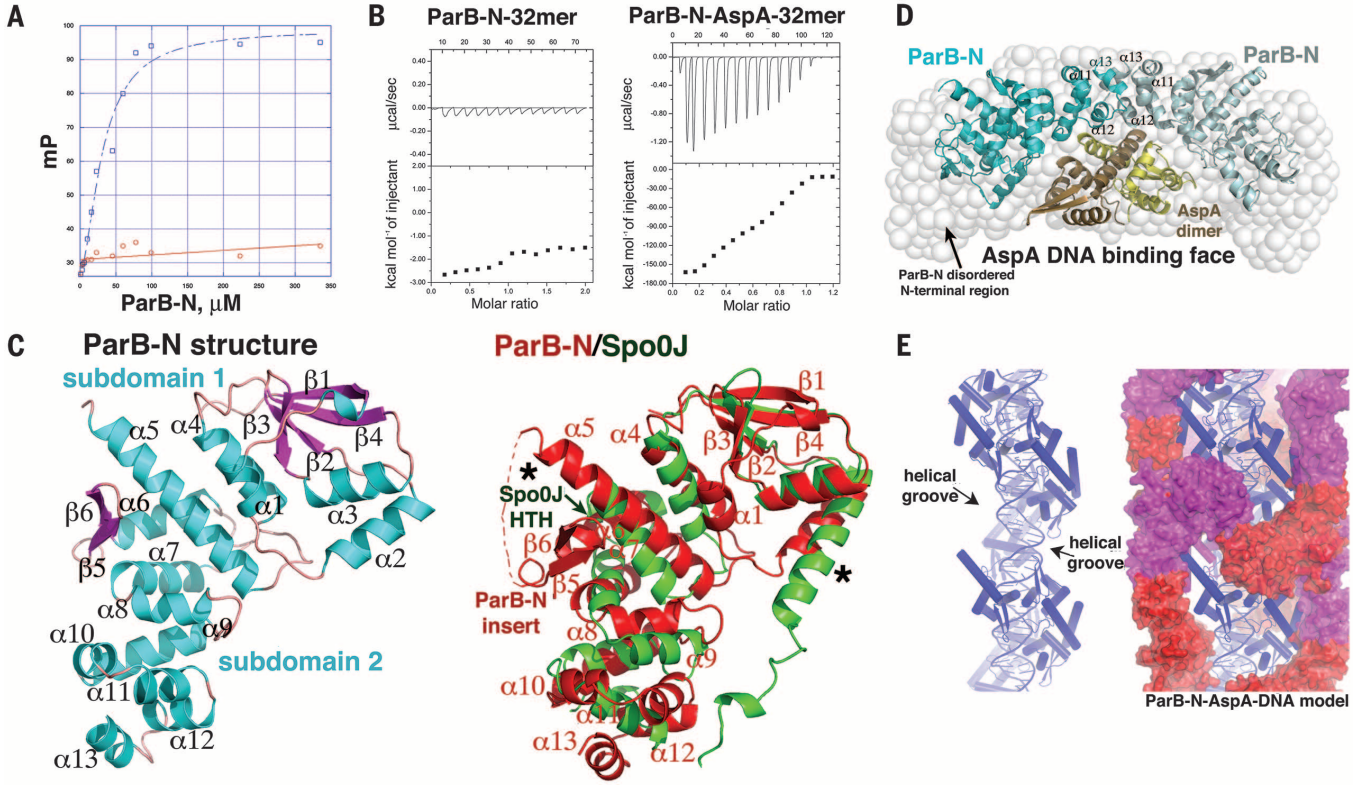


Fig. 3. Structure of ParB-N and assembly onto the AspA-DNA superhelix. (**A**) Increasing concentrations of wtParB-N (blue) or ParB-N α11-α12-α13 truncation mutant (red) were added to a preformed AspA-DNA complex to analyze binding. mP, millipolarization. (**B**) ITC analyses revealing that ParB-N does not bind DNA (left) but binds AspA-DNA (right). (**C**) (Left) pNOB8 ParB-N structure. (Right) Overlay of ParB-N onto *T. thermophilus* Spo0J. Notable structural differences are denoted by asterisks. (**D**) AspA–ParB-N model obtained by docking the AspA and ParB-N crystal structures into the SAXS envelope. (**E**) AspA–DNA–ParB-N model obtained by fitting the ParB-N–AspA model onto the AspA-DNA superhelix. The AspA-DNA superhelix is blue, and ParB-N molecules are shown as coarse cartoon surfaces, with individual molecules colored red and magenta.

The pNOB8 ParB adaptor was found to be composed of two domains, an N domain (ParB-N; residues 1–320) and a C domain (ParB-C; residues 370–470). Full-length ParB bound ParA in the presence or absence of ATP. However, neither ParB-C nor ParB-N bound ParA, which indicated that the flexible, ~50-residue interdomain linker mediates ParA binding (fig. S4, A to C). AspA did not bind ParB-C (fig. S5A) but bound ParB-N, and ITC showed the binding stoichiometry was 1:1, one AspA subunit to one ParB-N molecule (Fig. 3, A and B). The nonspecific DNA binding function of ParB was mapped to ParB-C (fig. S5B). Thus, pNOB8 ParB carries out multiple adaptor functions: binding AspA, ParA, and nonspecific DNA (fig. S4C). We next performed structural studies on ParB-N. As pNOB8 ParB-N crystals diffracted poorly, the 98:2 *Sulfolobus solfataricus* strain 98/2 chromosomal ParB (40% identity to pNOB8 ParB) N domain was used for crystallographic analyses (table S2). The ParB-N structure contains two subdomains separated by a central helix (Fig. 3C). Dali searches revealed weak structural similarity between ParB-N and one protein; the N-terminal domain of the bacterial *Thermus thermophilus* ParB homolog, Spo0J [root mean square deviation (rmsd) = 3.3 Å] (Fig. 3C, right) (*18*). However, there are large structural differences in the N-terminal subdomains and central regions of these proteins. The central region contains a loop in ParB-N and a helix-turn-helix (HTH) in Spo0J (Fig. 3C). The lack of an HTH in ParB-N is consistent with its inability to bind DNA and suggests that this domain must have evolved for an alternative function or functions, e.g., binding to AspA.

Small angle x-ray scattering (SAXS) (*19*–*22*) was used to study the AspA–ParB-N interaction and revealed a symmetric ellipsoid-like structure for the complex that could be fit by placing an AspA dimer in the center flanked by ParB-N molecules [radius of gyration (*Rg*) of model = 34.2 Å compared with 33.2 ± 0.4 Å from experimental data] (supplementary Materials and Methods). In this model, which is consistent with the ITC stoichiometry of 1:1, the AspA C-terminal helices are grasped by ParB-N helices α11-α12-α13 (Fig. 3D), which dimerize in the model; the same α11-α12-α13 dimer was observed in ParB-N structures. Note that the AspA–ParB-N model also leaves the N-terminal face of the AspA dimer free to contact DNA, consistent with our data (Fig. 3D). The AspA dimer–ParB-N SAXS model can be docked onto each AspA dimer in the AspA-DNA superhelix, which leads to the generation of a multiprotein superstructure, in which ParB-N molecules conform to AspA-DNA superhelical grooves (Fig. 3E). Multiple modeling attempts, without taking into account the SAXS data, revealed that this organization provided not only the best fit to the AspA-DNA superstructure but also the only one without a clash. These data suggest that the specific AspA-DNA superhelical structure may function as a template for ParB-N binding (Fig. 3E, left). To test the AspA–DNA–ParB-N model, we generated a stable ParB-N truncation mutant (fig. S6), lacking helices α11-α12-α13, which the model indicates as important in AspA binding. ITC and fluorescence polarization (FP) experiments (Fig. 3A) revealed no binding by the mutant.

The AspA–DNA–ParB-N superstructure exposes the ParB C terminus at the surface, which would project the long linker and attached ParB-C into the solvent, which allows these regions to contact ParA and nonspecific DNA, respectively. The ParB-C structure was solved and consists of five helices (fig. S7). ParB-C forms a tight dimer (burying 2530 Å^2), which was supported by biochemical analyses (Fig. 4A and fig. S7A). Notably, ParB-C shows structural similarity to histones, including CenpA (Fig. 4A and fig. S7B). This is important because CenpA is the histone variant that marks centromeres in eukaryotes (*8*). Although the ParB-C dimer is somewhat distinct from histone dimers, it contains an electropositive surface pattern similar to histones and as noted, it binds DNA (fig. S5B). A ParB-C–DNA model constructed by superimposition with nucleosome structures shows that the DNA is proximal to the ParB-C basic patches (Fig. 4B). A conserved feature of CBPs proteins that work in concert with Walker-box NTPases is their ability to both spread onto and bridge DNA (*23*, *24*). The presence of many dynamic CBP-ParA attachments could maintain association of CBP-centromere complexes with ParA but simultaneously allow movement. Unlike bacterial CBPs, the pNOB8 CBP, AspA, forms a linear partition complex and shows no bridging capability. The nonspecific DNA binding function of ParB-C could fulfill that role.

Partition mechanisms are dictated by their motor (NTPase) proteins, which bind CBP–centromere partition complexes. The pNOB8 ParA structure shows strong similarity to bacterial Walker-box ParA proteins (*25*–*27*) (Fig. 4C, fig. S8, and table S2). Two conformations of pNOB8 ParA were obtained: apo and adenylyl-imidodiphosphate (AMP-PNP)–bound (fig. S9, A and B). Comparison of the AMP-PNP and apo ParA dimers reveals that the so-called signature lysines make the expected intersubunit phosphate contacts in the AMP-PNP–bound state, which stabilizes dimerization and enhances ATP hydrolysis. However, these residues are too distant in the apo conformation to make the same interaction (Fig. 4D). Thus, AMP-PNP (or ATP) binding to pNOB8 ParA appears to lock in a dimer state optimal for adenosine triphosphatase (ATPase) activity. Both ATP binding and hydrolysis are required for partition by Walker-box ParAs, and current data suggest that these proteins move dynamically,

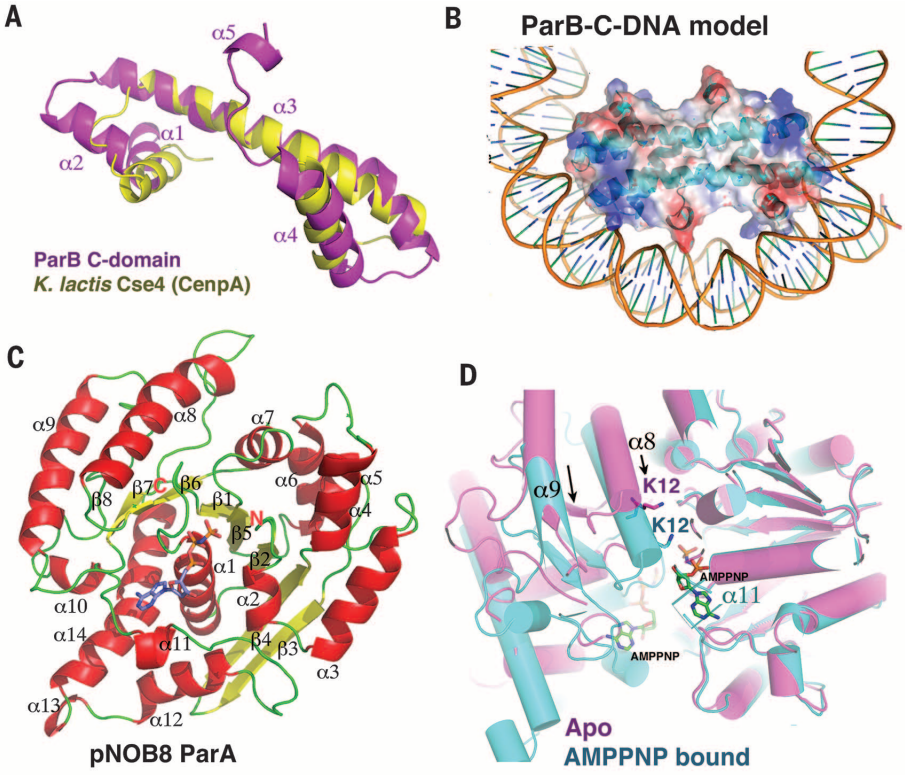


Fig. 4. pNOB8 ParB-C contains a eukaryotic histone–CenpA-like fold, and ParA harbors a bacterial Walker-box fold. (**A**) Superimposition of the ParB-C and *Kluyveromyces lactis* Cse4-CenpA structures (rmsd = 2.5 Å for Cα atoms). (**B**) ParB-C modeled onto DNA to show its electrostatic surface. (**C**) pNOB8 ParA–AMP-PNP subunit structure. (**D**) Superimposition of apo and AMP-PNP–bound ParA subunits showing relation of other subunit.

en masse, on the nucleoid DNA, which serves as a substratum (*28*, *29*). Cycles of ParA movement are driven by CBP binding, which stimulates the ATPase activity of ParA. This represents a viable segregation mechanism for archaea, which like bacteria, lack a nuclear membrane. Consistent with this, pNOB8 ParA bound DNA nonspecifically in an ATP-dependent manner, similar to bacterial ParAs (figs. S9C and S10).

In summary, this work reveals important molecular insights into DNA segregation in archaea. This includes a delineation of the partition protein structures and higher-order complexes (fig. S10). The pNOB8 ParB component was shown to harbor structural similarity to histone-CenpA, which functions as the eukaryotic CBP. On the other hand, pNOB8 ParA harbors a Walker motif similar to that of bacterial ParAs. Recent data suggest that *S. solfataricus* itself uses a chromosomal partition system with a predicted Walker-box NTPase (*30*). Thus, these findings suggest that Walker-box cassettes may be the most ubiquitous DNA segregation system in nature and also suggest the possible conservation of general segregation principles across the three domains of life.

REFERENCES AND NOTES

1. G. S. Gordon, A. Wright, *Annu. Rev. Microbiol.* **54**, 681–708 (2000).
2. F. Hayes, D. Barillà, *Nat. Rev. Microbiol.* **4**, 133–143 (2006).
3. M. Thanbichler, L. Shapiro, *J. Struct. Biol.* **156**, 292–303 (2006).
4. M. A. Schumacher, *Curr. Opin. Struct. Biol.* **22**, 72–79 (2012).
5. K. Gerdes, J. Møller-Jensen, R. B. Jensen, *Mol. Microbiol.* **37**, 455–466 (2000).
6. U. M. Pinto, K. M. Pappas, S. C. Winans, *Nat. Rev. Microbiol.* **10**, 755–765 (2012).
7. E. V. Koonin, *J. Mol. Biol.* **229**, 1165–1174 (1993).
8. H. Tachiwana *et al*., *Nature* **476**, 232–235 (2011).
9. M. M. Valdivia, K. Hamdouch, M. Ortiz, A. Astola, *Curr. Genomics* **10**, 326–335 (2009).
10. S. Henikoff, T. Furuyama, *Chromosoma* **121**, 341–352 (2012).
11. R. Bernad, P. Sánchez, A. Losada, *Exp. Cell Res.* **315**, 3233–3241 (2009).
12. S. Gribaldo, C. Brochier-Armanet, *Philos. Trans. R. Soc. Lond.* **361**, 1007–1022 (2006).
13. T. A. Williams, P. G. Foster, C. J. Cox, T. M. Embley, *Nature* **504**, 231–236 (2013).
14. J. O. McInerney, M. J. O'Connell, D. Pisani, *Nat. Rev. Microbiol.* **12**, 449–455 (2014).
15. Q. She *et al*., *Extremophiles* **2**, 417–425 (1998).
16. G. Fibriansah *et al*., *PLOS ONE* **7**, e48015 (2012).
17. M. P. Hui *et al*., *Proc. Natl. Acad. Sci. U.S.A.* **107**, 4590–4595 (2010).
18. T. A. Leonard, P. J. Butler, J. Löwe, *Mol. Microbiol.* **53**, 419–432 (2004).
19. D. I. Svergun, *Biophys. J.* **76**, 2879–2886 (1999).
20. D. I. Svergun, *J. Appl. Cryst.* **33**, 530–534 (2000).
21. D. I. Svergun, M. V. Petoukhov, M. H. Koch, *Biophys. J.* **80**, 2946–2953 (2001).
22. M. V. Petoukhov, D. I. Svergun, *Biophys. J.* **89**, 1237–1250 (2005).
23. M. A. Schumacher, B. E. Funnell, *Nature* **438**, 516–519 (2005).
24. T. G. Graham *et al*., *Genes Dev.* **28**, 1228–1238 (2014).
25. T. D. Dunham, W. Xu, B. E. Funnell, M. A. Schumacher, *EMBO J.* **28**, 1792–1802 (2009).
26. T. A. Leonard, P. J. Butler, J. Löwe, *EMBO J.* **24**, 270–282 (2005).
27. M. A. Schumacher *et al*., *J. Biol. Chem.* **287**, 26146–26154 (2012).
28. S. Ringgaard, J. van Zon, M. Howard, K. Gerdes, *Proc. Natl. Acad. Sci. U.S.A.* **106**, 19369–19374 (2009).
29. A. G. Vecchiarelli, K. C. Neuman, K. Mizuuchi, *Proc. Natl. Acad. Sci. U.S.A.* **111**, 4880–4885 (2014).
30. A. K. Kalliomaa-Sanford *et al*., *Proc. Natl. Acad. Sci. U.S.A.* **109**, 3754–3759 (2012).
31. Single-letter abbreviations for the amino acid residues are as follows: A, Ala; C, Cys; D, Asp; E, Glu; F, Phe; G, Gly; H, His; I, Ile; K, Lys; L, Leu; M, Met; N, Asn; P, Pro; Q, Gln; R, Arg; S, Ser; T, Thr; V, Val; W, Trp; and Y, Tyr.

ACKNOWLEDGMENTS

This work was supported by NIH grant GM074815 (M.A.S) and UK Biotechnology and Biological Sciences Research Council (BB/F012004/1) and Leverhulme Trust (RPG-245) grants (D.B.). SAXS and crystallographic data were collected at the Advanced Light Source (ALS). ALS is a national user facility operated by Lawrence Berkeley National Laboratory on behalf of the Office of Basic Energy Sciences, U.S. Department of Energy (DOE), through the Integrated Diffraction Analysis Technologies program, supported by the DOE Office of Biological and Environmental Research. Additional support comes from MINOS at National Center for Biotechnology Information, NIH (R01-GM105404). We thank Q. She for the kind gift of the *Sulfolobus* NOB8H2 strain and N. Matamala for initial contributions to the project. Coordinates and structure factors have been deposited with the Protein Data Bank, accession numbers 4RS7, 4RS8, 4RSB, 4RSF, 4RU7 and 4RU8.

SUPPLEMENTARY MATERIALS

www.sciencemag.org/content/349/6252/1120/suppl/DC1
Materials and Methods
Figs. S1 to S11
Tables S1 and S2
References (*32*–*41*)

11 February 2015; accepted 5 August 2015
10.1126/science.aaa9046

The Norwegian Academy of Science and Letters
announces the

CALL FOR NOMINATIONS 2016

THE KAVLI PRIZE

For outstanding scientific research in

ASTROPHYSICS • NANOSCIENCE • NEUROSCIENCE

Nomination deadline: December 1, 2015

Nominations will be reviewed by committees of
leading international scientists appointed by

The Norwegian Academy of Science and Letters
based on recommendations by

The Chinese Academy of Sciences
The French Academy of Sciences
The Max Planck Society (Germany)
The National Academy of Sciences (US)
The Royal Society (UK)

The Kavli Prize will be awarded in Oslo in September 2016
and will consist of

A gold medal • US $ 1,000,000 • A scroll

For details about the nomination process see

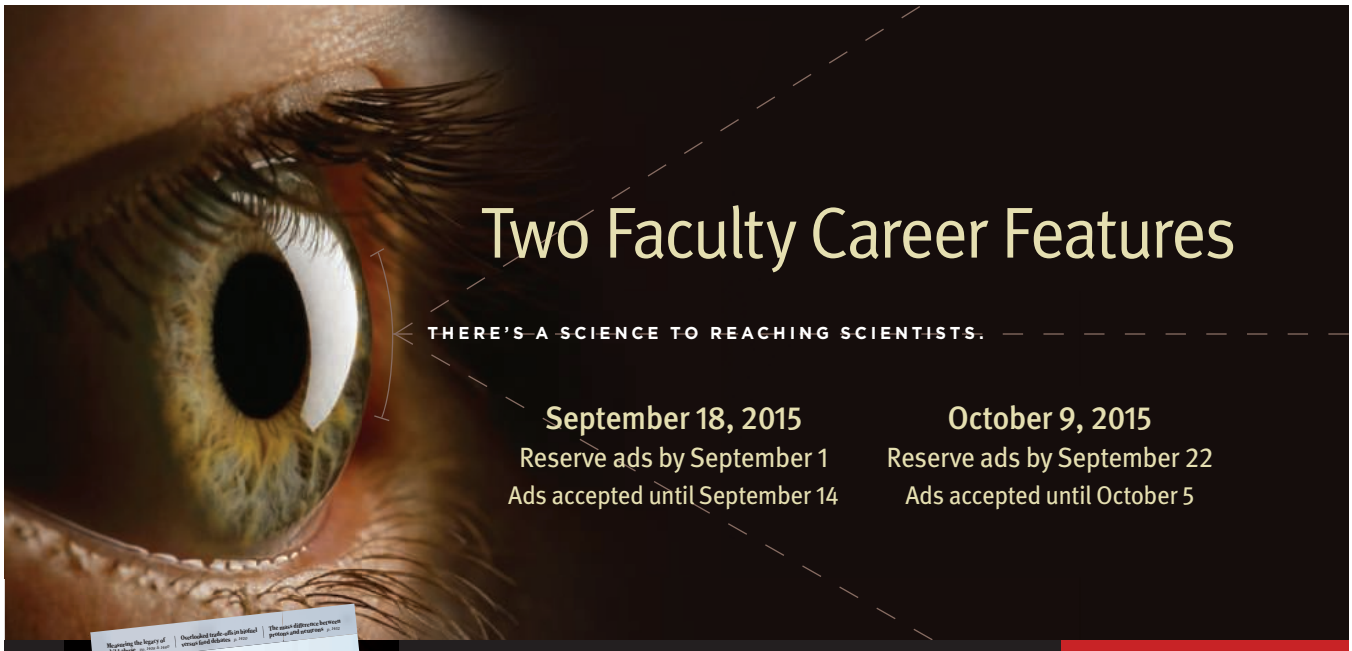
www.kavliprize.org

A partnership of

THE NORWEGIAN MINISTRY
OF EDUCATION AND RESEARCH

THE KAVLI FOUNDATION

THE NORWEGIAN ACADEMY OF SCIENCE AND LETTERS



Two Faculty Career Features

THERE'S A SCIENCE TO REACHING SCIENTISTS.

September 18, 2015
Reserve ads by September 1
Ads accepted until September 14

October 9, 2015
Reserve ads by September 22
Ads accepted until October 5

For recruitment in science, there's only one Science



Hiring faculty? Whatever your timing, we've got two special features for your **Faculty ads** this fall! The September 18 feature covers strategies and resources to build teaching skills. The October 9 feature offers strategies for moving into academia from other industries.

What makes *Science* the best choice for recruiting?

- Read and respected by 570,400 readers around the globe
- 60% of our weekly readers work in academia and 67% are Ph.D.s. *Science* connects you with more scientists in academia than any other publication
- Your ad dollars support AAAS and its programs, which strengthens the global scientific community.

Special packages available when you advertise in both features

Why choose these faculty features for your advertisement?

- Relevant ads lead off the career section with special Faculty banner
- September 18 issue will be distributed at the Biotechnica Meeting in Hanover, Germany, 6–8 October.

Expand your exposure. Post your print ad online to benefit from:

- Link on the job board homepage directly to Faculty jobs
- Dedicated landing page for faculty positions
- Additional marketing driving relevant job seekers to the job board.

SCIENCECAREERS.ORG

ScienceCareers
FROM THE JOURNAL SCIENCE AAAS

To book your ad: **advertise@sciencecareers.org**

The Americas
202-326-6582

Europe/RoW
+44(0)1223-326500

Japan
+81-3-3219-5777

China/Korea/Singapore/Taiwan
+86-186-0082-9345

NEW ENGLAND BioLabs® Inc.

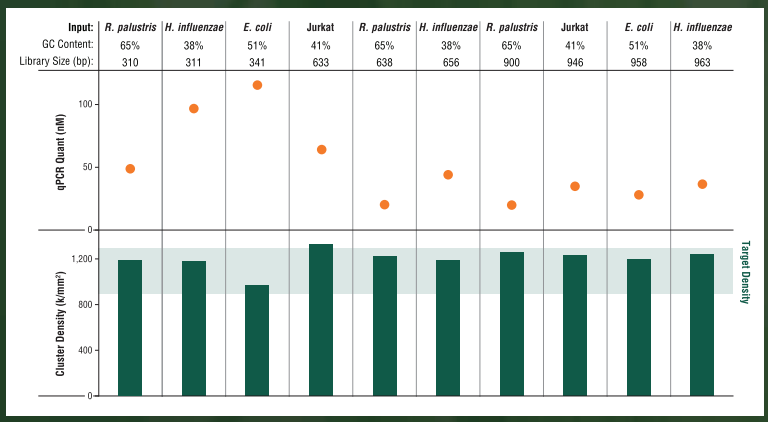
Count on it.

Introducing the NEBNext® Library Quant Kit for Illumina®

Accurate quantitation of next generation sequencing libraries is essential for maximizing sequencing data output and quality. The NEBNext Library Quant Kit for Illumina is a qPCR-based method that delivers higher consistency and reproducibility of quantitation than other currently available methods. With optimized kit components and a more convenient protocol, you can count on your quantitation values, every time.

To learn more and request a sample, visit **www.neb.com/E7630**

With the NEBNext Library Quant Kit, optimal cluster density is achieved from quantitated libraries with a broad range of library size and GC content.



Libraries of 310–963 bp from the indicated sources were quantitated using the NEBNext Library Quant Kit, then diluted to 8 pM and loaded onto a MiSeq® (v2 chemistry; MCS v2.4.1.3). Library concentrations ranged from 7–120 nM, and resulting raw cluster density for all libraries was 965–1300 k/mm2 (ave. =1199). Optimal cluster density was achieved using concentrations determined by the NEBNext Library Quant Kit for all library sizes.

NEW ENGLAND BIOLABS®, NEB® and NEBNEXT® are registered trademarks of New England Biolabs, Inc.
ILLUMINA® and MISEQ® are registered trademarks of Illumina, Inc.

appliedbiosystems

Connect—
the world is your lab

When your data are always within reach, answers are never far away. Remotely monitor your runs, access results, and collaborate with colleagues—anywhere, anytime using the Thermo Fisher Cloud—with the new Applied Biosystems™ QuantStudio™ 3 and 5 Real-Time PCR Systems.



Get connected at
thermofisher.com/quantstudio3-5

ThermoFisher SCIENTIFIC

For Research Use Only. Not for use in diagnostic procedures. © 2015 Thermo Fisher Scientific Inc. All rights reserved.
All trademarks are the property of Thermo Fisher Scientific and its subsidiaries unless otherwise specified. **CO121866 0815**

Reservoir Plate

The Echo 525 liquid handler now has expanded capabilities with the introduction of the Echo qualified reservoir, a liquid handler source plate designed to enable convenient assay assembly and efficient large reagent volume transfers. The reservoir enables scientists performing genomic, proteomic, and cell-based assays to reduce the use of costly reagents while achieving rapid fluid transfers. The Echo 525 liquid handler utilizes ultrasound acoustic droplet ejection (ADE) technology to rapidly transfer liquids between microplates in nanoliter increments. Without using pins or tips, the Echo 525 liquid handler can accurately dispense 25 nL per droplet, enabling assay miniaturization and improving data quality. The system requires no user calibration, as it adjusts the transfer parameters for each well based on the acoustic analysis of the fluid to be transferred. The product's 6-well design enables the transfer of over 15 mL from a single plate.

Labcyte
For info: 877-742-6548
www.labcyte.com

DNA/RNA/Protein Purification System

Low and medium-throughput laboratories now have an alternative to manual processes and spin-column methods for nucleic acid purification, thanks to a new automated system. Designed for research labs and small biotech firms looking to simplify DNA, RNA, and protein purification processes, the new KingFisher Duo Prime system builds upon the utility of the existing KingFisher Duo system to help improve reproducibility and deliver high-quality samples with less time and effort than traditional manual methods. With the KingFisher Duo, isolating DNA from 12 blood samples takes as little as 53 minutes and requires only 15 minutes of hands-on time compared to manual spin-column methods, which take up to 90 minutes of hands-on time. The system is designed to isolate DNA, RNA, and proteins from a variety of starting materials, including cell-free body fluids, blood, bacteria, cell cultures, tissue, and plant samples.

Thermo Fisher Scientific
For info: 800-995-2787
www.thermoscientific.com/kingfisherduoprime



qPCR Master Mix

Kapa Probe Force is a highly inhibitor-resistant quantitative polymerase chain reaction (qPCR) master mix that removes the need for DNA purification, enabling streamlined sample-to-quantitation in less than an hour. The master mix contains a high-performance engineered DNA polymerase enzyme specially designed to overcome blood, tissue, and plant PCR inhibitors. With Kapa Probe Force, crude samples can now be analyzed with comparable accuracy, reproducibility, and sensitivity as purified DNA. The product is designed for low- or high-throughput genotyping, as well as gene expression studies. Kapa Probe Force is ideally suited for direct qPCR analysis of challenging sample types without the need for purification. Users can create streamlined, cost-effective workflows designed to fit any budget, without compromise.

Kapa Biosystems
For info: 855-527-2246
www.kapabiosystems.com/probeforce

Sample Evaporator

Using a patented, vacuum-assisted vortex concentration technology, the Smart Evaporator from Asynt sets a new standard for labs tasked with drying sample tubes and vials. The spiral air flow generated by this unique concentration technology allows the Smart Evaporator to rapidly concentrate even high boiling solvents and water without heating to high temperatures. The spiral plug concentration technology works by using a vacuum to draw air/nitrogen through a spiral slit, generating a vortex that both stirs the sample and creates an increased evaporative surface area. This unique technology allows you to evaporate without the worry of solvent bumping and the need to constantly monitor the equipment. As the spiral plugs are tapered, the Smart Evaporator is compatible with almost any type of vial or sample tube. When using the Smart Evaporator, there is no need to switch sample tubes and risk losing sample or to increase the volume of solvent to evaporate because of extra washing steps.

Asynt
For info: +44-(0)-1638-781709
www.asynt.com

Thermal Mixer

The BioShake thermal mixer can now be applied to even more versatile applications of sample preparation, because a specific adapter block has been developed for the 96-well, 0.8 mL ABgene storage plate. This plate is used as a so-called MIDI plate with Illumina's sample preparation kits for next-generation sequencing. The new BioShake adapter, made of aluminum, allows precise heating and smooth mixing of the plate at 1,800 rpm. The high-frequency shaker automatically detects the adapter. Rates up to 3,000 rpm and heating up to 99°C are programmed via keypad. Additionally, a "short-mix" function and short programs can be started. In addition to the existing adapters (for tubes from 0.2 mL to 4 mL, microtiter and deep-well plates, and conical 5 mL, 15 mL, or 50 mL tubes), the new adapter expands the application variety of this compact thermal shaker.

Analytik Jena
For info: +49-(0)-36-41-77-70
www.analytik-jena.com

Electronically submit your new product description or product literature information! Go to www.sciencemag.org/products/newproducts.dtl for more information.

Newly offered instrumentation, apparatus, and laboratory materials of interest to researchers in all disciplines in academic, industrial, and governmental organizations are featured in this space. Emphasis is given to purpose, chief characteristics, and availability of products and materials. Endorsement by *Science* or AAAS of any products or materials mentioned is not implied. Additional information may be obtained from the manufacturer or supplier.

JOIN AAAS

Get instant access to *Science*. Support all of the sciences.



The American Association for the Advancement of Science (AAAS) is a non-profit community that is open to everyone, from Nobel laureates to high school students. Ours is a global membership of over 120,000 people who believe in the power of science to make the world a better place.

From the moment you join, you get immediate access to everything that AAAS's award-winning journal *Science* has to offer, including:

- 51 weeks of home delivery of *Science*;
- Instant online retrieval of every *Science* article ever published, from today, dating back to 1880;
- Anytime, anywhere access via the *Science* mobile site and apps for Android, iPad, and iPhone devices;
- Members-only newsletters; and more.

As a member, you are also making a critical contribution to AAAS's efforts to provide a public voice for all of science. With public skepticism about science increasing, and public funding for research more uncertain than ever, this work has never been more important.

AAAS is hard at work promoting science in government offices, in schools, and in the public commons all around the world—with programs like AAAS Senior Scientists and Engineers, which brings volunteer scientists into public school classrooms, or our sweeping petition drives calling for the preservation of federal R&D funding.

Visit **promo.aaas.org/joinaaas** and join today. Together we can make a difference.

Science
AAAS

CELL SIGNALING TECHNOLOGY

EPIGENETICS:
DISCOVERY THROUGH VALIDATION

692 CST antibodies for epigenetic-related targets, including histone modifications, epigenetic regulators, and general transcription factors.

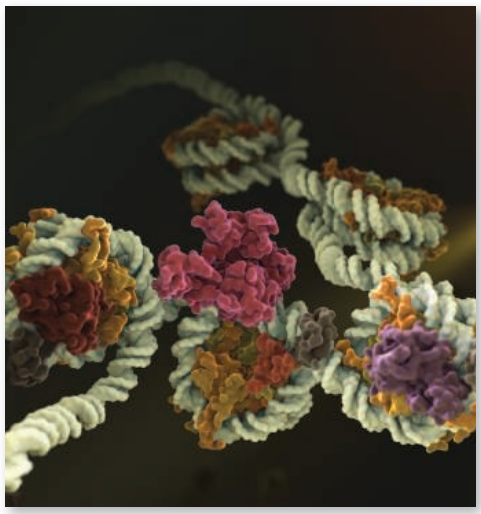
226 CST antibodies validated for ChIP according to ENCODE* Consortium guidelines.

Validated Tools for Discovery:

» SimpleChIP® Kits to facilitate Chromatin IP from cells and tissue.

» PTMScan® Kits and Services to enable MS-based discovery of methylated and acetylated proteins.

» Most ChIP-validated antibodies approved for additional applications like IHC, Flow, IF and WB.



Molecular model of chromatin.

Learn more at: www.cellsignal.com/epigeneticdiscovery

*Landt S.G. et al. (2012) *Genome Res.* 22, 1813–1831.

© 2015 Cell Signaling Technology, Inc. Cell Signaling Technology, CST, PTMScan, and SimpeChIP are trademarks of Cell Signaling Technology, Inc.

15PADEPIGNONE0079ENG_00

Cell Signaling TECHNOLOGY®

WORKING LIFE

By **Kim Hunter-Schaedle**

When science fails a scientist

In August 2012, a phone call from Scotland told me that my sister had been diagnosed with advanced breast cancer. Six weeks later she was dead. In between was a blur of travel, family tensions, and—one bright spot—making my sister laugh one more time. But my sharpest memory of those weeks is the helplessness of sitting in a hospital office learning that estrogen receptor-negative breast cancer cells in my sister's body had metastasized to her bones, lungs, and brain. We could make her comfortable, the doctor said. That was it.

When I learned about my sister's cancer, I was in the midst of a career transition—the second in my professional life. Back in my 30s, I had decided to leave the bench because I felt I could have a greater impact on the human condition as a medical research foundation administrator than I could as a decent, but not great, neuroscientist. For 6 years, I was the chief scientific officer of a foundation that researched drug treatments for benign but deforming tumors that could become malignant. I was the one sitting at the other end of the table, facing people who were relying on science to change, and possibly save, the life of their loved one. "We are going to get there," I would say. "We will find drugs that will work." I truly believed it.



"My decision has been to grab life—now."

I got the news about my sister after my husband and I had taken the radical step of moving from a city-centered life to the rural one we had fallen in love with. I was working from our new home, consulting for cancer foundations and walking my dog in the woods at lunchtime. For the first time, my career had slowed down. I was quietly torn between fully embracing this change and returning to the career fast track, but I couldn't quite figure out what it was that I missed. Was it the prestige, the salary, or leading the charge to find cancer treatments? Traveling to our annual international conference 6 years straight (always at the time of my June wedding anniversary)? Strategizing with 30 researchers and clinicians about curing brain tumors (which caused me to miss a celebration dear to my in-laws)?

After the phone call from Scotland, I emailed my sister's medical reports to many of the doctors I'd worked with while at the foundation, in the hope they could help. But their responses, though sensitive and thoughtful, could only try to prepare me for my big sister's death at age 56.

First, the helplessness grew. Then the anger: Why was hospice the only option she had? Weren't there off-label drugs or clinical trials? Shouldn't I know this? Had my sister been in denial? How could she not know she was riddled with cancer? She'd feared breast exams, so she didn't get them. We'd argued about that, and about her smoking. Eventually, my anger gave way to resignation: Her cancer had simply eluded the options science had to offer.

We knew my mother's large family had a history of breast and ovarian cancer, and one cousin had a *BRCA1* mutation. But it wasn't until after my sister's death that I investigated and mapped the family cancer tree. When my gynecologist saw it, she said wow. We'll never know if my sister had a *BRCA1* mutation, but the summer after she died I learned that I did. The decision to have prophylactic surgery was easy.

Science may have helped me protect my health, but I no longer assume that we'll have translated enough science into better drugs for cancer if I ever need them. Meanwhile, this difficult couple of years has helped me make peace with my decision to abandon the high-profile career ladder. Just a year before she died, my sister had retired and she was looking forward to freedom. So my decision has been to grab life—now. At 50, I finally have a work-life balance. I found a job in mental health administration where I can make an intellectual contribution, and which also allows me to go home and live life. I have given enough to the "cures" cause. It is a long road, and it is time for others to lead the way. ■

Kim Hunter-Schaedle lives in western Massachusetts and works at Austen Riggs Center, a psychiatric hospital in Stockbridge. For more on life and careers, visit sciencecareers.org. Send your story to SciCareerEditor@aaas.org.

ILLUSTRATION: ROBERT NEUBECKER

Downloaded from www.sciencemag.org on September 5, 2015

Published by AAAS



Science Careers Advertising

For full advertising details, go to ScienceCareers.org and click For Employers, or call one of our representatives.

Tracy Holmes
Worldwide Associate Director
Science Careers
Phone: +44 (0) 1223 326525

THE AMERICAS

E-mail: advertise@sciencecareers.org

Fax: +1 (202) 289 6742

Tina Burks
Phone: +1 (202) 326 6577

Nancy Toema
Phone: +1 (202) 326 6578

Online Job Posting Questions
Phone: +1 (202) 312 6375

EUROPE / INDIA / AUSTRALIA / NEW ZEALAND / REST OF WORLD

E-mail: ads@science-int.co.uk

Fax: +44 (0) 1223 326532

Sarah Lelarge
Phone: +44 (0) 1223 326527

Kelly Grace
Phone: +44 (0) 1223 326528

Online Job Posting Questions
Phone: +44 (0) 1223 326528

JAPAN

Katsuyoshi Fukamizu (Tokyo)
E-mail: kfukamizu@aaas.org
Phone: +81 3 3219 5777

Hiroyuki Mashiki (Kyoto)
E-mail: hmashiki@aaas.org
Phone: +81 75 823 1109

CHINA / KOREA / SINGAPORE / TAIWAN / THAILAND

Ruolei Wu
Phone: +86 186 0082 9345
E-mail: rwu@aaas.org

All ads submitted for publication must comply with applicable U.S. and non-U.S. laws. *Science* reserves the right to refuse any advertisement at its sole discretion for any reason, including without limitation for offensive language or inappropriate content, and all advertising is subject to publisher approval. *Science* encourages our readers to alert us to any ads that they feel may be discriminatory or offensive.

ScienceCareers
FROM THE JOURNAL SCIENCE AAAS

ScienceCareers.org

LEHIGH UNIVERSITY

COMPUTATIONAL BIOSCIENCE & ENGINEERING FULL OR ASSOCIATE PROFESSOR

Lehigh University invites applications for a position in **Computational Bioscience & Engineering at the rank of Full or Associate Professor with tenure**. Applicants must hold a Ph.D. in a science or engineering field, an M.D., or an MD/Ph.D. and have a demonstrated record of accomplishment and funding in computational approaches to biomedical and/or health-related research, broadly defined. Candidates from any area of computational bioscience & engineering will be considered, including but not limited to systems biology; functional genomics, proteomics, microbiomics; gene networks and connectonomics; bioinformatics; algorithms; machine learning; and modeling of dynamic behavior at the molecular, sub-cellular, cellular, organismal, and system levels. Individuals who can effectively bridge bioengineering and biological sciences, two of the university's largest programs, are preferred. The position carries an expectation of leadership in developing collaborations between the life sciences and engineering as part of the university's recently announced DATA-X initiative (http://www1.lehigh.edu/datax). An endowed chair is potentially available for a successful candidate at the Full Professor level.

Applications, including a C.V., letter of intent, descriptions of research interests and teaching philosophy, and the names of three potential references should be submitted to: **https://academicjobsonline.org/ajo/jobs/5679**. For additional information, contact **Neal G. Simon, Ph.D., Search Committee Chair, 111 Research Dr., Bethlehem, PA 18015, inbios@lehigh.edu**. Review of applications will begin on **November 9, 2015** and continue until the position is filled.

Lehigh University is especially interested in qualified candidates who can contribute, through their research, teaching, and/or service, to the diversity and excellence of the academic community. Lehigh University is a recipient of an NSF ADVANCE Institutional Transformation award for promoting the careers of women in academic sciences and engineering.

Lehigh University is an Equal Opportunity Affirmative Action Employer. The University provides comprehensive benefits including partner benefits, and a faculty dual career assistance program (http://www.lehigh.edu/~inprv/work_life_balance.html).

WestVirginiaUniversity.

The Department of Microbiology, Immunology and Cell Biology and Centers for Neuroscience West Virginia University School of Medicine invite applications for the Open Rank Faculty Position in Neuroimmunology

The Department of Microbiology, Immunology and Cell Biology (http://medicine.hsc.wvu.edu/micro/) and the Centers for Neuroscience (WVUCN; http://www.hsc.wvu.edu/wvucn/) seek a distinguished immunologist as tenure-track faculty (rank open) to further new programs in neural injury, neurodegeneration, immune senescence or neural development. The successful applicant will hold a primary faculty appointment in the Department, as well as membership in the WVUCN, in the WVU School of Medicine. This position provides an exceptional opportunity to participate in robust, interdisciplinary basic and translational research and training programs via collaborative teams of clinician and non-clinician biomedical scientists and engineering and basic science faculty. These teams are resourced to develop new technical and clinical solutions to research and clinical challenges, as part of a new campus-wide emphasis on dynamically growing neuroscience and neurotechnology research. The appointed faculty will be expected to conduct high impact and innovative research and teach immunology to medical, graduate and undergraduate students. The successful candidate will be a recognized investigator with a PhD or MD/PhD degree and a track record of independent research, demonstrated by high quality publications in peer-reviewed journals and extramural funding commensurate with years of experience. Preferably, the selected candidate will hold active extramural funding in order to integrate rapidly with ongoing research at the intersection of immunology and neuroscience. Dedicated laboratory space and competitive operating funds will be made available.

Founded in 1867, West Virginia University is 1 of only 11 research intensive land-grant institutions offering a single health sciences campus with accredited Schools of Medicine, Dentistry, Nursing, and Pharmacy and a formative School of Public Health. WVU is West Virginia's major research and development center, and its only comprehensive doctoral-granting institution. Our faculty conduct research totaling over $138 million in sponsored contracts and grants per year. The Carnegie Foundation for the Advancement of Teaching classifies WVU as a comprehensive doctoral institution with medical programs – placing it among only 50 such public and 28 private institutions nationwide.

Nominations, applications (including a cover letter, vitae, and list of 3 professional references), expressions of interest, requests for information, or confidential inquiries should be directed (preferably electronically) to: **Rosana Schafer, Ph.D., Chair, Search Committee, c/o Barbara Pritt (bpritt@hsc.wvu.edu), Department of Microbiology, Immunology and Cell Biology, West Virginia University School of Medicine, Morgantown, WV 26506-9177.** The position remains open until filled.

West Virginia University is an Affirmative Action/Equal Opportunity Employer and is the recipient of an NSF ADVANCE award for gender equity. WVU is a tobacco-free campus.

UC San Diego

Tenure Track or Tenured Professor For a New Initiative in Precision Medicine

The University of California, San Diego has made an unprecedented commitment to advance human health by applying computational biology to analyze big data in biomedical research. The University of California, San Diego invites applications from outstanding candidates for up to five separate searches for TENURE TRACK or TENURED FACULTY POSITIONS. These positions are part of a bold multi-discipline, multi-year initiative that spans the entire University. Each appointment will be made jointly between at least two departments from across the campus in order to facilitate collaborations in new inter-disciplinary fields. They include Health Science (School of Medicine and Skaggs School of Pharmacy and Pharmaceutical Sciences), the Jacobs School of Engineering, the Divisions of Physical Sciences, Biology, Social Sciences, Arts and Humanities, the School of Global Policy and Strategy, and the Scripps Institution of Oceanography (SIO). The initiative in precision medicine seeks to transform medicine through advances in omic-scale diagnosis, therapy, engineering and computer science, imaging and data integration that enable insights into disease mechanisms. Appointments generally will be at the Assistant or Associate Professorial level and in exceptional cases at the very early Professorial level. The University of California, San Diego, is committed to academic excellence and diversity within the faculty, staff, and student body.

There will be five separate areas within the overall initiative:

1. Epigenetics and Genomics;
2. Informatics and Systems Medicine;
3. Microbiome;
4. Sensors, Devices, and Imaging; and
5. Bioethics and Biomedical Policy.

Candidates may submit an application to one or more of these areas.

Successful applicants will be expected to teach both graduate and undergraduate students in the participating departments and establish a vigorous program of high-quality federally funded research that focuses on innovative approaches in one of the targeted areas. These may include, but are not limited to

- engineering, computer science and computational approaches to biological complexity and challenging biomedical problems;
- integration of multi-omics data across multiple scales from molecule to organism for deciphering disease mechanisms and improving treatment;
- soft-robotics and other engineering applications relevant to clinical and/or translational medicine;
- next generation computational and engineering approaches to personalized medical diagnosis and treatment;
- imaging and/or sensing mechanisms for clinical applications;
- application of systems medicine approaches, experimental investigations and development of new understanding of the design principles of living systems;
- quantitative pharmacology;
- biomedical innovation and regulatory policy, ethical implications of the biomedical revolution and related policy issues in these areas.

Successful applicants will complement exceptional expertise in multiple areas at UC San Diego, including cardiovascular disease, obesity and metabolic disease, cancer, aging, degenerative diseases, autoimmune diseases, infections, inflammation, and will help synergize translational design efforts.

The preferred candidate will have demonstrated strong leadership or a commitment to support diversity, equity, and inclusion in an academic setting.

The level of appointment and salary is commensurate with qualifications and based on UC pay schedules.

Review of applications will begin on October 3, 2015 and continue until the position is filled.

Applications must be submitted electronically through AP-Online Recruit website. Candidates may submit an application to one or more of these areas.

Applications at the Assistant Professor level, please refer to the links below:

1. Epigenetics and Genomics; https://apol-recruit.ucsd.edu/apply/JPF00840
2. Informatics and Systems Medicine; https://apol-recruit.ucsd.edu/apply/JPF00838
3. Microbiome; https://apol-recruit.ucsd.edu/apply/JPF00839
4. Sensors, Devices, and Imaging; https://apol-recruit.ucsd.edu/apply/JPF00841
5. Bioethics and Biomedical Policy https://apol-recruit.ucsd.edu/apply/JPF00837

Applications at the Associate or Full Professor level, please refer to the links below:

1. Epigenetics and Genomics; https://apol-recruit.ucsd.edu/apply/JPF00810
2. Informatics and Systems Medicine; https://apol-recruit.ucsd.edu/apply/JPF00829
3. Microbiome; https://apol-recruit.ucsd.edu/apply/JPF00831
4. Sensors, Devices, and Imaging; https://apol-recruit.ucsd.edu/apply/JPF00832
5. Bioethics and Biomedical Policy: https://apol-recruit.ucsd.edu/apply/JPF00830

For applicants with interest in spousal/partner employment, please see http://academicaffairs.ucsd.edu/aps/partneropp/index.html for the UC San Diego Partner Opportunities Program.

Please direct inquiries to precisionmedicinerecruit@ucsd.edu

UC San Diego is an Equal Opportunity/Affirmative Action Employer with a strong institutional commitment to excellence through diversity.

Science Careers online @sciencecareers.org

ScienceCareers online @sciencecareers.org

NIH *Eunice Kennedy Shriver* National Institute of Child Health and Human Development

Tenure-Track and Midcareer Research Positions in the *Eunice Kennedy Shriver* National Institute of Child Health and Human Development (NICHD)

The *Eunice Kennedy Shriver* National Institute of Child Health and Human Development (NICHD), National Institutes of Health (NIH), Department of Health and Human Services (DHHS), is recruiting up to four outstanding tenure-track investigators or midcareer researchers to join our dynamic and interactive faculty, who use a variety of models to study basic mechanisms of development, pediatric disease processes, and their translation into clinical treatments (see http://www.nichd.nih.gov/about/org/dir/Pages/index.aspx)

Clinical & Translational Research in Pediatric or Women's Health: One or more positions; areas of interest include, but are not limited to, endocrine, reproductive medicine, genetic, metabolic, and developmental disorders.

Cell/Developmental Biology: One or more positions using any of a wide range of animal models to study basic research questions and/or disease pathophysiology.

Basic or Translational Neuroscience: One or more positions to pursue studies using animal model systems, human disease models, or computational or theoretical approaches.

Successful applicants will perform clinical or basic research in the outstanding facilities at NICHD and NIH. These include the NIH Hatfield Clinical Research Center's facilities for human investigation with its state-of-the art biomedical imaging and metabolic assessment, (see http://clinicalcenter.nih.gov/), and NICHD's core facilities for the study of model organisms, including biological imaging, mouse, and zebrafish facilities.

All positions are located on the NIH main campus in Bethesda, Maryland They are fully supported by the intramural program of NICHD and include a start-up allowance as well as an ongoing commitment of research space, laboratory resources, and positions for staff and trainees. Successful applicants will join a faculty of 70 principal investigators whose work covers a broad range of basic and clinical research areas.

Qualifications/eligibility: Candidates must have a Ph.D., M.D., or equivalent and an established track record of accomplishment in the respective areas of recruitment as evidenced by high-quality publications in peer-reviewed journals. Appointees may be U.S. citizens, resident aliens, or nonresident aliens eligible to obtain a valid employment-authorization visa. Salary is commensurate with experience.

How to apply: Applicants must submit a CV, a two-page description of proposed research, and contact information for three professional references. These should be submitted to nichddirsearch@mail.nih.gov, specifying the applicable position in the subject line. Candidates may apply concurrently to NIH-wide hiring mechanisms, including the Earl Stadtman Investigator program (http://tenuretrack.nih.gov/apply) and the Lasker Clinical Research Scholars program (http://www.nih.gov/science/laskerscholar). **Applications will be reviewed on a continuous basis after September 15, 2015. Interviews of qualified applicants will begin November 1, and applications will be accepted until positions are filled.**

The NIH is dedicated to building an inclusive and diverse community in its training and employment programs.
DHHS, NIH, and NICHD are Equal Employment Opportunity Employers.

THE HONG KONG UNIVERSITY OF SCIENCE AND TECHNOLOGY

School of Science
Joint Faculty Positions

The School of Science of The Hong Kong University of Science and Technology seeks applicants for joint substantiation-track faculty positions at the rank of Assistant Professor or Associate Professor.

Applicants should have a doctoral degree plus several years of postdoctoral experience, as well as expertise in interdisciplinary areas, such as super-resolution imaging and biological physics, that bridge life science, physics, and chemistry. They will be expected to establish an independent, internationally recognized research program and to contribute to the undergraduate and graduate teaching missions of the School.

The School of Science is located in the vibrant international atmosphere of the University, on a quiet, picturesque sea-side campus, just 40 minutes from downtown Hong Kong. Teaching and research are carried out in an outstanding intellectual environment that is rich in technical resources. The medium of instruction in the University is English. The School of Science is committed to diversity in recruitment and strongly supports equal opportunity employment.

Salary is highly competitive and will be commensurate with qualifications and experience. Fringe benefits including medical and dental benefits, annual leave and housing will be provided where applicable. Appointment will normally be on a three-year contract. A gratuity will be payable upon successful completion of contract.

Application Procedure

Applications should include a curriculum vitae, a short statement of research interests and the names and addresses of three individuals who can serve as referees for the candidate. These materials should be sent to **Prof. Yung Hou Wong, Chair of the Adhoc Joint Search and Appointment Committee for Interdisciplinary Recruitment, Division of Life Science, The Hong Kong University of Science and Technology, Clear Water Bay, Kowloon, Hong Kong**. Electronic submissions are strongly encouraged (email: indissearch@ust.hk). Review of applications starts immediately and will continue until the positions are filled.

(Information provided by applicants will be used for recruitment and other employment-related purposes.)

Boston Children's Hospital — Harvard Medical School

Chief of Cardiology Position
Professor of Pediatrics
Department of Cardiology
Boston Children's Hospital
Harvard Medical School

Boston Children's Hospital is seeking to fill a position to serve as the Chief of Cardiology at Boston Children's Hospital, with an individual whose primary interest is Pediatric Cardiology. The candidate will be an acknowledged leader and senior statesperson in pediatrics, with superb leadership and communications skills as well as significant accomplishments in clinical service, teaching, administration and a strong desire to do innovative research.

The candidate is expected to lead one of the largest academic faculties in Pediatric Cardiology with a long track record of clinical innovation.

The successful candidate will have an M.D. or M.D./Ph.D., substantial experience and training in pediatric cardiology. Qualifications and experience should be commensurate with a full-time faculty appointment at Harvard Medical School at the Full Professor level in the Department Pediatrics. Letters of interest, a curriculum vitae and summary of research interests may be submitted to: **Pedro del Nido, M.D.; Committee Chair, c/o Dianne Hatfield, Administration, Boston Children's Hospital, 300 Longwood Ave., Wolbach 2; Boston, MA 02115**

Electronic Submission: **dianne.hatfield@childrens.harvard.edu**

We are an Equal Opportunity Employer and all qualified applicants will receive consideration for employment without regard to race, color, religion, sex, sexual orientation, gender identity, national origin, disability status, protected veteran status, or any other characteristic protected by law.

Director, National Library of Medicine, National Institutes of Health








The NIH is the center of medical and behavioral research for the Nation
----making essential medical discoveries that improve health and save lives.

Are you an exceptional candidate who can provide leadership to the preeminent institute for library science research in the world?? Are you at that point in your career where you're ready to "give back"? The Director, National Library of Medicine (NLM) position at the National Institutes of Health (NIH) offers a unique opportunity to serve as the chief visionary in this senior position with responsibilities focused on the direction and management of the world's largest biomedical library and electronic information and data resources that are used billions of times each year by millions of people and thousands of computer systems worldwide. The Director, NLM, develops goals, priorities, policies, and program activities, and keeps the Director, NIH abreast of NLM developments, accomplishments, and needs as they relate to the overall mission of the NIH. S/he is responsible for managing a high-level complex organization and demonstrates integrity and fairness, adhering in work and behavior to the highest ethical and scientific research standards. The mission of NLM is to support research that increases understanding of life processes and lays the foundation for advances in disease diagnosis, treatment, and prevention.

We are looking for applicants with a Ph.D., M.D., or comparable doctorate degree in a health science field plus senior-level scientific experience and knowledge of research programs in one or more scientific areas related to biomedical informatics, computational biology, data science and standards, biomedical communications, and health information technology, who have a commitment to excellence and the energy, enthusiasm, and innovative thinking necessary to lead a dynamic and diverse organization. Applicants should be known and respected within their profession, both nationally and internationally, as individuals of outstanding scientific competence. For further information please read the ACD's report at **http://acd.od.nih.gov/reports/Report-NLM-06112015-ACD.pdf**.

The successful candidate for this position will be appointed at a salary commensurate with his/her qualifications. Full Federal benefits will be provided including leave, health and life insurance, long-term care insurance, retirement, and savings plan (401k equivalent).

If you are ready for an exciting leadership opportunity, please see the detailed vacancy announcement at http://www.jobs.nih.gov (under Executive Jobs).
Applications will be reviewed starting October 20, 2015 and will be accepted until the position is filled.

NLM, NIH, AND DHHS ARE EQUAL OPPORTUNITY EMPLOYERS

Discovery Themes at Ohio State

Brain Injury Career Opportunities

MOLECULAR AND CELLULAR MECHANISMS OF BRAIN INJURIES

Department
Neuroscience

Position
Molecular and Cellular Mechanisms of Brain Injuries

Rank
Assistant Professor

Description
The Ohio State University Department of Neuroscience is recruiting for a tenure-track Assistant Professor. Candidates must hold a PhD (or equivalent) with research expertise in areas directly related to injury and repair of the central nervous system. This position is part of an ongoing commitment to develop distinguished research and clinical care centers at The Ohio State University focused on traumatic injuries to brain and spinal cord. In addition to a direct appointment in the Department, the successful applicant will become a member of the new Ohio State Center for Chronic Brain Injury.

Qualifications
Successful candidates are expected to contribute to the missions of the University, Department and Centers via active participation in research and teaching programs, mentoring of trainees and serving on departmental or college-level committees. Salary will be competitive and commensurate with experience.

About the University
The Ohio State University is committed to establishing a culturally and intellectually diverse environment, encouraging all members of our learning community to reach their full potential. We are responsive to dual-career families and strongly promote work-life balance to support our community members through a suite of institutionalized policies. We are an NSF Advance Institution and a member of the Ohio/Western Pennsylvania/West Virginia Higher Education Recruitment Consortium (HERC).

The Ohio State University is an equal opportunity employer. All qualified applicants will receive consideration for employment without regard to race, color, religion, sex, sexual orientation or identity, national origin, disability status or protected veteran status.

Application Instructions: Prospective candidates should send a statement of research interests, vita and a list of three references in PDF format to Michelle Semer-Bloomfield at **michelle.semer-bloomfield@osumc.edu**. Submission deadline is **1 October 2015**.

For more information about career opportunities, please visit Discovery.osu.edu.

THE OHIO STATE UNIVERSITY

ScienceCareers online @sciencecareers.org

SUNY DOWNSTATE Medical Center

University Hospital of Brooklyn

SENIOR VICE PRESIDENT OF RESEARCH

The State University of New York Health Science Center at Brooklyn (SUNY Downstate) announces a search for the next ***Senior Vice President of Research***. Downstate seeks a successful investigator and/or research administrator with a history of significant oversight responsibility for the administrative infrastructure supporting institutional research.

The State University of New York (SUNY) Downstate Medical Center is one of four academic health centers in SUNY's 64-campus system. Downstate joined the SUNY system in 1950 with a single college and has grown over the years. It now encompasses the College of Medicine, College of Nursing, College of Health Related Professions, School of Graduate Studies, School of Public Health, University Hospital of Brooklyn, and several research and biotechnology centers. Today, Downstate enrolls close to 1,800 students, has over 4,000 faculty (including full-time, part-time and voluntary), and employs some 3,000 support staff. It grants the BS, MS, MPH, RN, MD, and PhD degrees, among others, as well as advanced certificates, with approximately 80 percent of students enrolled in graduate-level programs.

The Senior Vice President for Research will also serve as the Operations Manager of the SUNY Downstate Research Foundation, an auxiliary organization of the SUNY system, which manages contract and grant funding, both pre- and post-award, for the universities in the system.

Candidates will hold an MD, PhD, MD/PhD, or equivalent and have a reputation for leadership in a medical school and/or academic medical center setting.

Forward applications to:

Warren E. Ross, M.D.
c/o **sarah.taylor@kornferry.com**
Korn Ferry International

SUNY Downstate is an Equal Opportunity / Affirmative Action Employer and Educator. Women and members of underrepresented minority groups are encouraged to apply.

KORN FERRY

UNIVERSITY *of* MISSOURI

Senior Associate Dean for Research

The University of Missouri (MU) School of Medicine in Columbia invites applications and nominations for the position of Senior Associate Dean for Research. This position reports directly to the Dean of the School of Medicine.

MU has an outstanding research infrastructure in life sciences. MU has numerous distinctions including the largest and most powerful university-owned research reactor in the country; the only NIH-funded national swine resource and research center; one of 13 regional biocontainment laboratories in the nation; one of only four Mutant Mouse Regional Resource Centers in the nation; a Rat Resource and Research Center; the only university in the nation to hold three major NIH national centers.

The Senior Associate Dean for Research will work with the Dean of the School of Medicine and campus research leaders to develop strategies that identify areas of research significance which will enable the School of Medicine to grow its research enterprise. The candidate will be expected to coordinate and lead extramural applications for research infrastructure and other large institutional awards; represent the School of Medicine to local, regional and national constituencies; and provide leadership in the area of clinical and translational research. The Senior Associate Dean will also oversee the graduate program in biomedical sciences, the research compliance programs, laboratory safety and the fiscal integrity of the research enterprise.

This individual will have an MD or PhD or equivalent degree, broad progressive administrative leadership experience in an academic health center environment; working knowledge of current national biomedical research interests with a history of sponsored funding; national recognition for achievement in research pursuits that would warrant appointment as a full professor. There should be a demonstrated record of promoting collaboration and cultivating both internal and external relations. The candidate must demonstrate the highest integrity and personal ethics and have a strong commitment to diversity.

Interested individuals should submit a letter of interest and a current CV to **Roberta Settergren**, staff for the search committee, at **settergrenr@health.missouri.edu** or **MU School of Medicine, DC018.00, Columbia, MO 65212**, telephone (573) 882-3944.

An Equal Opportunity/Access/Affirmative Action/Pro Disabled & Veteran Employer
For additional information, visit the following web sites:
http://medicine.missouri.edu/ and **http://missouri.edu/**

Georgia Tech Biology
College of Sciences

As part of a substantial expansion in the biological sciences, the **School of Biology** at **Georgia Tech** is seeking applications for tenure-track positions from candidates whose research would thrive in our community (http://www.biology.gatech.edu). Applications are particularly encouraged in the following areas:

Assistant or Associate Professor in **Ecology** including, molecular chemical ecology, microbial ecology, and behaviors and interactions that are mediated by chemical signals and cues. Candidates will be favored whose research integrates well with the department's strengths in chemical ecology, ecology and evolutionary biology, microbiology, or marine ecology.

Assistant or Associate Professor in **Neuroscience** (http://neuro.gatech.edu), including those applying genetic approaches to identify neural circuits that encode brain function and behavior.

Endowed Professor in Molecular and Cellular Biology, an outstanding mid-career or senior investigator in molecular biosciences including, cellular biology, biochemistry, structural biology, genetics, genomics and protein/cellular engineering. Candidates should have experience commercializing intellectual property from their laboratory; significant resources and partnerships are available to promote these activities.

The **Georgia Institute of Technology** is a top ranked educational/research institution and is rated as one of the best places to work. Georgia Tech is situated on an attractive campus in the heart of Atlanta, a vibrant, verdant city having great economic and cultural strengths. Research in these interdisciplinary fields at Georgia Tech benefits from strong interactions between biologists and faculty of diverse disciplines including engineering, computing, policy, and other sciences.

Candidates should submit an application online at **http://searches.biology.gatech.edu**, including a letter of application, curriculum vitae, statement of research interests and plans, and contact information for three references. Review of applications begins **October 1, 2015** and will continue until positions are filled.

Georgia Tech is a unit of the University System of Georgia and an Affirmative Action/Equal Opportunity Employer and requires compliance with the Immigration Control Reform Act of 1986.

GEORGIA INSTITUTE OF TECHNOLOGY



For recruitment in science, there's only one Science

Why choose this neuroscience section for your advertisement?

- Relevant ads lead off the career section with special Neuroscience banner
- Bonus distribution to:

  Association of Science Technology Centers (ASTC)
  October 17–20, 2015, Montreal, Canada

  Society for Neuroscience
  October 17–21, 2015, Chicago, IL.



* Ads accepted until September 28 on a first-come, first-served basis.

SCIENCECAREERS.ORG

Science Careers AAAS

To book your ad: **advertise@sciencecareers.org**

The Americas 202-326-6582	**Japan** +81-3-3219-5777
Europe/RoW +44(0)1223-326500	**China/Korea/Singapore/Taiwan** +86-186-0082-9345

University of Minnesota
Driven to Discover

Integrative Biology and Physiology
Medical School

Department of Integrative Biology and Physiology Tenure-track Faculty Positions

The Department of Integrative Biology and Physiology, University of Minnesota Medical School, seeks outstanding faculty candidates at all ranks in cardiovascular and muscle biology, and in the areas of metabolism, obesity, and diabetes.

We offer a highly collaborative and diverse research environment, generous start-up, modern laboratory space, and state-of-the-art core facilities. Successful candidates will have expertise that complements current faculty and be committed to excellence in education. Further information can be found at http://physiology.med.umn.edu.

To apply for this position, visit the University of Minnesota website at **http://www1.umn.edu/ohr/employment/** and enter job number **#301596** under jobs posted "anytime."

The University of Minnesota is an Equal Opportunity Educator and Employer.

Creating links that last a lifetime

at the International Centre for Fundamental Physics and its interfaces École normale supérieure, Paris (ENS-ICFP)

In 2015, the ENS-ICFP will hire three outstanding Junior Research Chairs at postdoctoral level for a two-year contract with a probable extension for a third year. Fellows are expected to develop new research projects within the Department of Physics at École normale supérieure.

What we offer :
- **Internationally competitive salary**
- **Attractive research funds and travel allowance**
- **Access to a cutting-edge scientific environment**
- **Complete integration into the Department of Physics through scientific exchange and teaching at the master level**

Application process and research themes can be found at http://phys.ens.fr/

Deadline to apply: October 18, 2015
Positions start in September 2016

One or two additional positions in Theoretical Physics will be made available by the Philippe Meyer Institute

The JRC positions are funded by the 10-year grant ENS-ICFP obtained through the French National Excellence initiative

PSL Research University · UPMC Sorbonne Universités · l'Observatoire de Paris · CNRS · ENS

BAYLOR UNIVERSITY

Assistant or Associate Professor of Biology—Limnology

The Department of Biology invites applications to fill this tenure/tenure-track position beginning August, 2016. Candidates should have a Ph.D. and demonstrated expertise in reservoir/lake limnology or closely related aquatic science discipline. We seek an outstanding scientist who will establish competitive and externally funded research program in reservoir or lake limnology addressing questions at the ecosystem level and which complements the broad aquatic program within the Center for Reservoir and Aquatic Science Research (CRASR) at Baylor. Applications will be reviewed beginning **October 16, 2015** and will be accepted until the position is filled. To ensure full consideration, complete applications must be submitted by **October 31, 2015**. For position details and application information please visit: **www.baylor.edu/hr/facultypositions** or from **Robert_Doyle@baylor.edu**.

Baylor University is a private Christian university and a nationally ranked research institution, consistently listed with highest honors among The Chronicle of Higher Education's "Great Colleges to Work For." Chartered in 1845 by the Republic of Texas through the efforts of Baptist pioneers, Baylor is the oldest continuously operating university in Texas. The university provides a vibrant campus community for over 15,000 students from all 50 states and more than 80 countries by blending interdisciplinary research with an international reputation for educational excellence and a faculty commitment to teaching and scholarship. Baylor is actively recruiting new faculty with a strong commitment to the classroom and an equally strong commitment to discovering new knowledge as we pursue our bold vision, *Pro Futuris*.

Baylor University is a private not-for-profit university affiliated with the Baptist General Convention of Texas. As an Affirmative Action/Equal Opportunity Employer, Baylor is committed to compliance with all applicable anti-discrimination laws, including those regarding age, race, color, sex, national origin, marital status, pregnancy status, military service, genetic information, and disability. As a religious educational institution, Baylor is lawfully permitted to consider an applicant's religion as a selection criterion. Baylor encourages women, minorities, veterans

UF UNIVERSITY of FLORIDA
The Foundation for The Gator Nation

The Department of Pharmacology and Therapeutics (http://pharmacology.med.ufl.edu) invites applications for multiple 12-mo, tenure-track faculty positions at the Assistant or Associate Professor level. We are continuing the expansion of exceptional programs in neuropharmacology, muscle therapeutics, and immunopharmacology with an emphasis on translational and regenerative medicine. Successful candidates must hold a Ph.D. and/or M.D. degree; have at least two years of postdoctoral training; have a record of significant research accomplishments; and present long-term research goals consistent with establishing and/or maintaining a highly successful research program. Candidates at the Associate Professor level should also have a history of significant research funding and serve as PI of at least one current NIH R01 grant. All Department faculty are expected to contribute to the professional and graduate education programs of the Department. We value a diverse faculty and encourage applications from women, underrepresented minorities and veterans. The Department offers outstanding laboratories, office space and shared facilities as well as a commitment to develop and enhance faculty members' full potential as researchers, educators and scholars. The University of Florida, located in Gainesville, FL, has state-of-the-art core facilities and numerous other research resources within a vibrant, collegial institution.

Candidates must apply online at **http://bit.ly/1Kmz6c0**. Applicants should upload: (1) a cover letter, (2) a CV, (3) a statement of research interests, (4) a statement of teaching philosophy and proficiency, and (5) the names and contact information for at least three references (reference letters, while not required, will be considered during the initial review of applications). Applications should be submitted by **October 15, 2015** for best consideration but will be considered until positions are filled. Please direct inquiries to **admin@pharmacology.ufl.edu**.

The University of Florida is an Equal Opportunity Employer. The selection process will be conducted in accord with the provisions of Florida's 'Government in the Sunshine' and Public Records Laws. Search committee meetings and interviews will be open to the public, and applications, resumes, and other documents related to the search will be available for public inspection.



Special Job Focus:

Genomics

25 September, 2015

Reserve space by 8 September

Ads accepted until 21 September on a first-come, first-served basis



For recruitment in science, there's only one **Science**

What makes *Science* the best choice?

- Read and respected by 570,400 readers around the globe
- 78% of readers read *Science* more often than any other journal
- Your ad sits on specially labeled pages to draw attention to the ad
- Your ad dollars support AAAS and its programs, which strengthens the global scientific community.

Why choose this genomics feature for your advertisement?

- Relevant ads lead off the career section with special Genomics banner
- Special bonus distribution to 25,000 scientists beyond our regular circulation
- Bonus distribution to:

  American Society of Human Genetics
  6–10 October, Baltimore, MD.

Expand your exposure. Post your print ad online to benefit from:

- Link on the job board homepage directly to genomics jobs
- Dedicated landing page for jobs in genomics
- Additional marketing driving relevant job seekers to the job board.

Post online and your job will be e-mailed to over 5,401 active job seekers looking for genomics jobs.

SCIENCECAREERS.ORG

ScienceCareers
FROM THE JOURNAL SCIENCE AAAS

To book your ad: **advertise@sciencecareers.org**

The Americas
202-326-6582
Europe/RoW
+44(0)1223-326500
Japan
+81-3-3219-5777
China/Korea/Singapore/Taiwan
+86-186-0082-9345

CIAT
International Center for Tropical Agriculture
Since 1967 / Science to cultivate change

GENETIC RESOURCES PROGRAM LEADER

International Center for Tropical Agriculture (CIAT) is seeking a highly motivated and experienced genebank manager and researcher as curator of the in-trust tropical forages, beans and cassava collections including supervision of CIAT's new germplasm facilities. PhD. with more than five years' experience and expertise in population genetics, breeding systems, crop evolution, seed pathology and physiology relevant to the conservation and distribution of crop genetic resources and wild relatives is highly desired. Applicants are invited to send a cover letter illustrating their suitability for the above position with a detailed curriculum vitae. All correspondence should be addressed to **Ms. Andrea Linares (e-mail: z.a.linares@cgiar.org)**, titled "Genetic Resources Program Leader". Closing date for applications: **October 13th, 2015**

ASSISTANT PROFESSOR FACULTY POSITIONS

The Department of Chemistry at the University of Michigan invites applications for an anticipated tenure-track position in any area of chemistry or biochemistry (including analytical, chemical biology, education, inorganic, materials, organic and physical) with an anticipated start date of September 1, 2016. The position is expected to be filled at the assistant professor level; but, all applicants at all levels of professor rank will be considered. This position will be a University-year appointment (9-months academic year salary with summer salary supported by research funds). Candidates are expected to develop an internationally recognized program of scholarly research and to excel in teaching at undergraduate and graduate levels.

Detailed information regarding the electronic application process and required materials is available on-line at website: **https://www.chem.lsa.umich.edu/chem/facultyrecruit/.**

Review of applications will begin on **October 1, 2015**. Information about the Chemistry Department is available at website: **www.lsa.umich.edu/chem.**

Questions about the application process may be sent to e-mail: **chemfacrecruit@umich.edu.**

The University of Michigan is an Equal Opportunity/Affirmative Action Employer and is supportive of the needs of dual career couples, women and minorities are encouraged to apply.

ASSISTANT/ASSOCIATE PROFESSOR
Ecology and Evolutionary Biology

The Department of Ecology and Evolutionary Biology, Tulane University, invites applications for one TENURE-TRACK POSITION at the level of assistant professor or associate professor. See website: **http://tulane.edu/sse/eebio/about/positions** for details about the position, department, and search. Submit letter of application, curriculum vitae, statements of research and teaching interests, selected publications, and names and addresses of three references to**: e-mail: apply.interfolio.com/30088**. Review of applications will begin **October 15, 2015**, and the search will remain open until the position is filled. *Tulane is an Equal Opportunity Employer/Minorities/Female/Veteran/Disabled employer.*

Download the
ScienceCareers
Job App

SEARCH JOBS
ON THE GO!

apps.sciencemag.org



STOWERS INSTITUTE
FOR MEDICAL RESEARCH

Faculty Position in the Life Sciences

The Stowers Institute for Medical Research invites innovative young scientists in the Life Sciences to submit applications for a faculty position. We anticipate making an appointment in 2016 at the rank of Assistant Investigator. Research programs of interest include, but are not limited to: biochemistry, quantitative biology, neuroscience, developmental and cell biology, genomics, stem cell biology, regenerative biology and epigenetics. Our interests encompass a broad gamut of experimental organisms and approaches. The successful candidate is expected to develop a groundbreaking, innovative and independent research program and will benefit from and complement the Institute's existing strengths in genetics and epigenetics, cell and chromosome biology, stem cells and regenerative biology, developmental biology and evolution, and biochemistry and neuroscience.

The position is fully funded throughout the candidate's appointment. This includes $600,000 per year for full salary support and research funding, in addition to start-up funds and ongoing needs for equipment. The initial appointment is for 6 years and is then subject to renewal every 6 to 7 years. In total, the package for a junior position is more than $3.6 million over the first term and increases significantly after promotion. In addition, investigators may take advantage of exceptional core facilities and technology centers staffed by over 100 scientists. Stowers investigators have multiple opportunities to be involved in the Institute's Graduate School program.

Candidates must have a Ph.D. or equivalent degree and postdoctoral experience demonstrating innovation and excellence in their field. Candidates will be expected to possess a long-term vision of their scientific interests, to establish a vigorous and innovative research program, and to actively contribute to the Institute's mission and collegiality.

Deadline for applications is **November 1, 2015**. Applicants should submit a cover letter, a CV, a research plan and vision statement, and arrange for the submission of three letters of reference through our application page at: **http://www.stowers.org/facultysearch**.

Questions should be directed to the Search Committee Chair, Dr. Alejandro Sánchez Alvarado (**facultysearch@stowers.org**).

The Stowers Institute for Medical Research is proud to be an Equal Opportunity Employer. All qualified applicants will be afforded equal opportunity regardless of race, creed, color, religion, gender, sexual orientation, pregnancy, national origin, age, disability, military status, or any other status protected by law.



Mid-career group leader position
Fundamental Cell Biology

The Institut Pasteur (Paris, France) announces an international call for a mid-career group leader position in the field of Fundamental Cell Biology. We encourage applications from outstanding individuals developing an ambitious research program in any area of Fundamental Cell Biology.

Successful applicants will be integrated into the cutting edge interdisciplinary environment offered within the Department of Cell Biology and Infection, which focuses on fundamental cell biology and infection biology at the interface with physics and mathematics. Further information can be found at: http://www.pasteur.fr/en/research/cell-biology-infection.

Institut Pasteur is located in central Paris and offers an unparalleled research environment through its state-of-the art research laboratories combining fundamental and translational research, integral biological services capability, cutting-edge scientific equipment, and technologically-advanced platforms (**www.pasteur.fr/en**).

Applications will be evaluated on the basis of scientific excellence. Successful candidates will be appointed with a permanent position. In addition, highly attractive packages to match the experience of the candidate will be provided, including institutional salaries (principal investigator, technician, secretary, post-doctoral fellows), a substantial contribution to running costs and equipment, access to on campus state-of-the-art technology core facilities, as well as support for relocation expenses and administrative matters.

Applicants should provide a single PDF file, containing in order:

1. A brief introductory letter
2. A Curriculum Vitae, list of 10 most important publications and a full publication list
3. A description of past and present research activities (up to 3 pages, 1.5 spacing, times or arial 11)
4. The proposed research project (up to 3 pages with 1.5 spacing, times or arial 11).

Candidates are encouraged to contact the head of the Department of Cell Biology and Infection, Chiara Zurzolo (**zurzolo@pasteur.fr**) for inquiries.

Candidates should send their formal applications by e-mail to the Director of Scientific Evaluation, Prof. Alain Israël, at the Institut Pasteur (**cellbio2015@pasteur.fr**).

Application deadline: October 31st, 2015. Short-listed candidates will be contacted in December 2015 for an interview that will take place early 2016.

ScienceCareers online @sciencecareers.org